frontiers | Research Topics

Measuring resting cerebral perfusion using magnetic resonance imaging (MRI)

Edited by
James Duffin and Alex Bhogal

Published in
Frontiers in Physiology

ISSN 1664-8714
ISBN 978-2-8325-5021-2
DOI 10.3389/978-2-8325-5021-2

About Frontiers

Frontiers is more than just an open access publisher of scholarly articles: it is a pioneering approach to the world of academia, radically improving the way scholarly research is managed. The grand vision of Frontiers is a world where all people have an equal opportunity to seek, share and generate knowledge. Frontiers provides immediate and permanent online open access to all its publications, but this alone is not enough to realize our grand goals.

Frontiers journal series

The Frontiers journal series is a multi-tier and interdisciplinary set of open-access, online journals, promising a paradigm shift from the current review, selection and dissemination processes in academic publishing. All Frontiers journals are driven by researchers for researchers; therefore, they constitute a service to the scholarly community. At the same time, the *Frontiers journal series* operates on a revolutionary invention, the tiered publishing system, initially addressing specific communities of scholars, and gradually climbing up to broader public understanding, thus serving the interests of the lay society, too.

Dedication to quality

Each Frontiers article is a landmark of the highest quality, thanks to genuinely collaborative interactions between authors and review editors, who include some of the world's best academicians. Research must be certified by peers before entering a stream of knowledge that may eventually reach the public - and shape society; therefore, Frontiers only applies the most rigorous and unbiased reviews. Frontiers revolutionizes research publishing by freely delivering the most outstanding research, evaluated with no bias from both the academic and social point of view. By applying the most advanced information technologies, Frontiers is catapulting scholarly publishing into a new generation.

What are Frontiers Research Topics?

Frontiers Research Topics are very popular trademarks of the *Frontiers journals series*: they are collections of at least ten articles, all centered on a particular subject. With their unique mix of varied contributions from Original Research to Review Articles, Frontiers Research Topics unify the most influential researchers, the latest key findings and historical advances in a hot research area.

Find out more on how to host your own Frontiers Research Topic or contribute to one as an author by contacting the Frontiers editorial office: frontiersin.org/about/contact

Measuring resting cerebral perfusion using magnetic resonance imaging (MRI)

Topic editors
James Duffin — University of Toronto, Canada
Alex Bhogal — Utrecht University, Netherlands

Citation
Duffin, J., Bhogal, A., eds. (2024). *Measuring resting cerebral perfusion using magnetic resonance imaging (MRI)*. Lausanne: Frontiers Media SA.
doi: 10.3389/978-2-8325-5021-2

Table of contents

frontiers | Frontiers in Physiology

TYPE Editorial
PUBLISHED 08 July 2024
DOI 10.3389/fphys.2024.1447417

OPEN ACCESS

EDITED AND REVIEWED BY
Irena Levitan,
University of Illinois Chicago, United States

*CORRESPONDENCE
James Duffin,
j.duffin@utoronto.ca

RECEIVED 11 June 2024
ACCEPTED 24 June 2024
PUBLISHED 08 July 2024

CITATION
Duffin J and Bhogal AA (2024), Editorial: Measuring resting cerebral perfusion using magnetic resonance imaging (MRI).
Front. Physiol. 15:1447417.
doi: 10.3389/fphys.2024.1447417

Editorial: Measuring resting cerebral perfusion using magnetic resonance imaging (MRI)

James Duffin[1,2,3]* and Alex A. Bhogal[4]

[1]Department of Anaesthesia and Pain Management, University of Toronto, Toronto, ON, Canada, [2]Department of Physiology, University of Toronto, Toronto, ON, Canada, [3]Thornhill Research Inc., Toronto, ON, Canada, [4]Center for Image Sciences, Department of Radiology, University Medical Center Utrecht, Utrecht, Netherlands

KEYWORDS

perfusion, oxygenation, MRI, DSC, arterial spin label (ASL) MRI, calibrated BOLD

Editorial on the Research Topic
Measuring resting cerebral perfusion using magnetic resonance imaging (MRI)

Cerebral perfusion

Cerebral perfusion metrics such as cerebral blood flow (CBF) provide an important assessment of cerebrovascular health and the hemodynamic consequences of cerebrovascular disease and ischemic events. For example, the detection of collateral blood circulation, which is widely recognised as a crucial protective mechanism that can significantly influence clinical outcomes following ischemic events such as stroke. Moreover, understanding cerebral blood flow distribution patterns can aid in surgical planning for interventional procedures, and assessment of their effectiveness. These considerations underscore the necessity for developing MRI-based techniques to measure perfusion metrics together with their associated post-processing methods. An advantage of MRI is the ability to deliver volumetric, temporally resolved information to which classical methods such as transcranial doppler are insensitive as Fico et al. explain. They demonstrated this aspect, showing that 4D flow MRI was more sensitive to age-related differences in cerebrovascular reactivity when comparing with analogous velocity-based measurements made using TCD. This was despite good agreement between middle cerebral artery velocity measurements as measured using each technique.

The reproducibility of MRI measurements is an important consideration when examining longitudinal changes in perfusion metrics, as Madsen et al. remind us. They examined the longitudinal reproducibility of a selection of metabolic (lactate and N-acetyl-aspartate (NAA) concentrations) and hemodynamic (cerebral blood flow, cerebral metabolic rate of oxygen consumption and global arterio-venous oxygen saturation difference) MR parameters. With the exception of lactate, MR parameters showed good within-day reproducibility, which declined between 7 days and several week measurements. Understanding physiological variability is crucial for optimizing study designs and establishing the sample sizes required to adequately power large-scale studies.

Novel methods of measuring cerebral perfusion

Dynamic susceptibility contrast (DSC) in MRI is a widely used method for perfusion imaging. Current clinical DSC-MRI involves the injection and tracking of a gadolinium (Gd) based contrast agent. However, there are safety concerns associated with Gd (Runge, 2000), as it has been shown to accumulate in the body (Kanda et al., 2014; Gulani et al., 2017) and our drinking water (Rogowska et al., 2018). Gd use is also limited in the sense that measurements are not repeatable within the same scan session since the injection can only be performed once. A novel alternative to Gd contrast is to establish an endogenous contrast bolus consisting of deoxyhemoglobin (dOHb), which is also paramagnetic. This can be done by means of a transient desaturation of arterial hemoglobin using a transient hypoxic respiratory challenge. Such an approach leads to a similar susceptibility change as Gd but is produced non-invasively. The dOHb bolus can be tracked using the same gradient-echo sequences, and as Stumpo et al. demonstrated the resulting images are in good agreement with those obtained using conventional DSC methods.

The nature of the dOHb stimulus has also provided the opportunity to apply existing analysis methods developed for hypercapnic respiratory challenges to calculate voxel-wise perfusion metrics. One such method is transfer function analysis, and Sayin et al. showed that it can also be applied to transient hypoxia-induced changes in dOHb to provide perfusion information. The use of dOHb as a novel non-invasive contrast agent is clearly promising.

Interestingly, the search for non-invasive techniques has encouraged several studies that derive perfusion-like metrics using CO_2 as a stimulus. Vu et al. implemented sinusoidal CO_2 challenges for concurrent assessment of relative cerebral blood flow and cerebral vascular reactivity (CVR) while Fitzgerald et al. exploit the sharp signal changes associated with CO_2-induced vasodilation to derive blood transit times in grey matter tissue.

However, there is an important caveat pertaining to the use of a vascular stimulus such as CO_2 for obtaining perfusion metrics. Increasing CO_2 with its associated CBF increase alters the 'baseline perfusion' state. To counteract this aspect, multi-delay arterial spin labelling methods are appealing. Pinto et al. showed that by accounting for macrovascular signal components and dispersion effects, more accurate quantification of CBF could be achieved. Similarly, Shah et al. used imputation modelling to correct measurement errors for improved CBF assessment using phase contrast MR in large cerebral vessels.

In addition to advanced modelling methods, clever acquisition strategies to maximize spatial resolution as were employed by Kashyap et al. These approaches will help advance ASL towards greater clinical adoption; particularly multi PLD variants. Indeed, Krishnamurthy et al. already showcase applications for understanding stroke etiology using ASL, while Jellema et al. highlight applications for perfusion (and complimentary) intra-operative acquisition strategies in the even the most sensitive paediatric brain tumour patients.

Measuring blood oxygenation by MRI

Finally, we must emphasize that perfusion is only one aspect of cerebral regulation, and it is closely linked brain metabolic processes which are essential for maintaining homeostasis. As suggested by Le et al., characterizing the interplay between blood oxygen delivery and tissue consumption can pave the way for novel biomarkers of microvascular disease. The work of Williams et al. also helps to better interpret functional MRI studies that often rely on the Blood Oxygenation Level Dependent (BOLD) signal contrast that originates from changes in perfusion mediated by the cerebrovascular reactivity response coupled with changes in oxygen consumption. Understanding these relationships will be key to using advanced physiological MRI towards routine clinical practice.

Conclusion

In summary, the collection of papers in this Research Topic highlight the importance of cerebral perfusion metrics in assessing cerebrovascular health. They demonstrate that there are many ways of making such measurements. Some require invasive techniques, such as the intravenous injection of the paramagnetic contrast agent Gadolinium, and others are non-invasive, such as utilizing changes in dOHb produced by controlling respired gases. They also show that improving measurement techniques and data analysis methodologies offer ways of improving the determination of resting perfusion metrics. We, the editors of this CVR Research Topic, hope that readers will benefit from the collection of articles presented. We believe that MRI perfusion metrics will become ever more useful in the assessment of cerebrovascular disease in clinical practice.

Author contributions

JD: Writing–review and editing, Writing–original draft. AB: Writing–review and editing, Writing–original draft.

Conflict of interest

Author JD was employed by Thornhill Research Inc.

The remaining author declares that the research was conducted in the absence of any commercial or financial relationships that could be construed as a potential conflict of interest.

The author(s) declared that they were an editorial board member of Frontiers, at the time of submission. This had no impact on the peer review process and the final decision.

Publisher's note

References

Gulani, V., Calamante, F., Shellock, F. G., Kanal, E., Reeder, S. B., and International Society for Magnetic Resonance in M (2017). Gadolinium deposition in the brain: summary of evidence and recommendations. *Lancet Neurol.* 16, 564–570. doi:10.1016/S1474-4422(17)30158-8

Kanda, T., Ishii, K., Kawaguchi, H., Kitajima, K., and Takenaka, D. (2014). High signal intensity in the dentate nucleus and globus pallidus on unenhanced T1-weighted MR images: relationship with increasing cumulative dose of a gadolinium-based contrast material. *Radiology* 270, 834–841. doi:10.1148/radiol.13131669

Rogowska, J., Olkowska, E., Ratajczyk, W., and Wolska, L. (2018). Gadolinium as a new emerging contaminant of aquatic environments. *Environ. Toxicol. Chem.* 37, 1523–1534. doi:10.1002/etc.4116

Runge, V. M. (2000). Safety of approved MR contrast media for intravenous injection. *J. magnetic Reson. imaging* 12, 205–213. doi:10.1002/1522-2586(200008)12:2<205::aid-jmri1>3.0.co;2-p

frontiers | Frontiers in Physiology

TYPE Original Research
PUBLISHED 09 February 2023
DOI 10.3389/fphys.2023.1102983

OPEN ACCESS

EDITED BY
Alex Bhogal,
Utrecht University, Netherlands

REVIEWED BY
Cesar Caballero-Gaudes,
Basque Center on Cognition, Brain and Language, Spain
Dengrong Jiang,
Johns Hopkins University, United States

*CORRESPONDENCE
John C. Wood,
jwood@chla.usc.edu

SPECIALTY SECTION
This article was submitted to Medical Physics and Imaging, a section of the journal Frontiers in Physiology

RECEIVED 21 November 2022
ACCEPTED 30 January 2023
PUBLISHED 09 February 2023

CITATION
Vu C, Xu B, González-Zacarías C, Shen J, Baas KPA, Choi S, Nederveen AJ and Wood JC (2023), Sinusoidal CO_2 respiratory challenge for concurrent perfusion and cerebrovascular reactivity MRI.
Front. Physiol. 14:1102983.
doi: 10.3389/fphys.2023.1102983

Sinusoidal CO_2 respiratory challenge for concurrent perfusion and cerebrovascular reactivity MRI

Chau Vu[1,2], Botian Xu[1,2], Clio González-Zacarías[2,3,4], Jian Shen[1,2], Koen P. A. Baas[5], Soyoung Choi[2,3,4], Aart J. Nederveen[5] and John C. Wood[1,2]*

[1]Department of Biomedical Engineering, University of Southern California, Los Angeles, CA, United States, [2]Division of Cardiology, Children's Hospital Los Angeles, University of Southern California, Los Angeles, CA, United States, [3]Neuroscience Graduate Program, University of Southern California, Los Angeles, CA, United States, [4]Signal and Image Processing Institute, University of Southern California, Los Angeles, CA, United States, [5]Department of Radiology and Nuclear Medicine, Amsterdam UMC, Location AMC, Amsterdam, Netherlands

Introduction: Deoxygenation-based dynamic susceptibility contrast (dDSC) has previously leveraged respiratory challenges to modulate blood oxygen content as an endogenous source of contrast alternative to gadolinium injection in perfusion-weighted MRI. This work proposed the use of sinusoidal modulation of end-tidal CO_2 pressures (*SineCO_2*), which has previously been used to measure cerebrovascular reactivity, to induce susceptibility-weighted gradient-echo signal loss to measure brain perfusion.

Methods: *SineCO_2* was performed in 10 healthy volunteers (age 37 ± 11, 60% female), and tracer kinetics model was applied in the frequency domain to calculate cerebral blood flow, cerebral blood volume, mean transit time, and temporal delay. These perfusion estimates were compared against reference techniques, including gadolinium-based DSC, arterial spin labeling, and phase contrast.

Results: Our results showed regional agreement between *SineCO_2* and the clinical comparators. *SineCO_2* was able to generate robust CVR maps in conjunction to baseline perfusion estimates.

Discussion: Overall, this work demonstrated feasibility of using sinusoidal CO_2 respiratory paradigm to simultaneously acquire both cerebral perfusion and cerebrovascular reactivity maps in one imaging sequence.

KEYWORDS

brain perfusion, respiratory challenges, cerebrovascular reactivity (CVR), carbon dioxide challenge, deoxygenation, dynamic susceptibility contrast (DSC)

1 Introduction

Perfusion magnetic resonance imaging (MRI) is a popular imaging technique for assessing hemodynamic impairments in a variety of central nervous system abnormalities such as intracranial tumors and acute strokes (Jahng et al., 2014). There are multiple different MRI techniques to measure cerebral perfusion, including phase contrast (PC), arterial spin labeling (ASL), and dynamic susceptibility contrast (DSC).

Particularly, DSC MRI is a perfusion technique that is frequently performed in clinical routines, requiring intravenous injection of a contrast agent (gadolinium chelate) and dynamic imaging to capture the passage of the contrast bolus through the vasculature (Østergaard, 2005). Based on the susceptibility-induced signal loss caused by the paramagnetic contrast, tracer

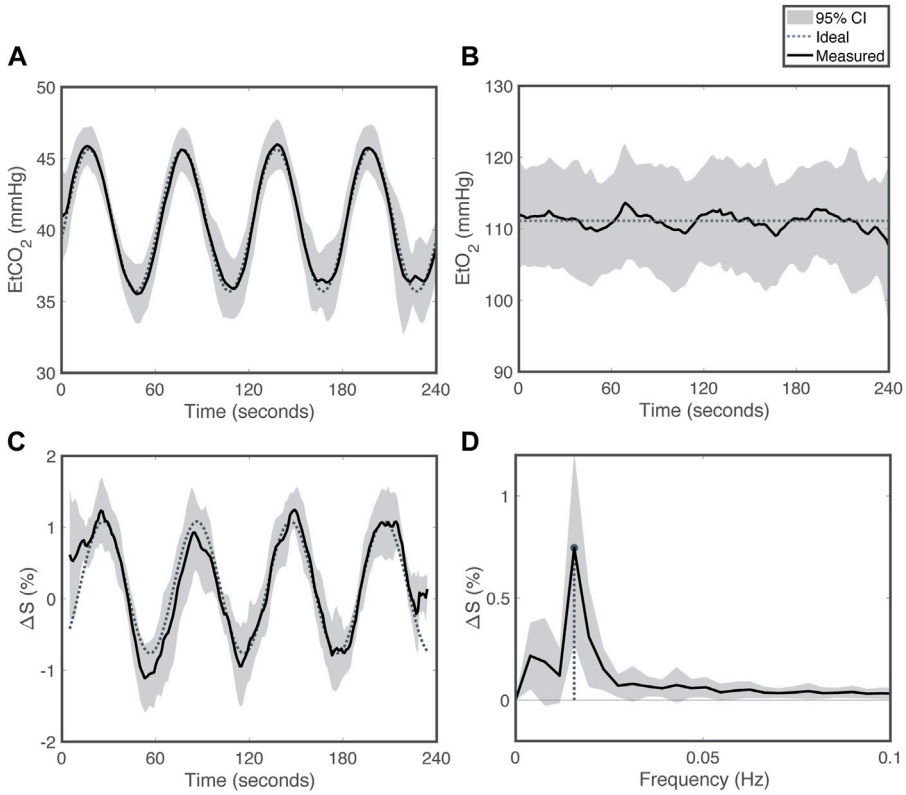

FIGURE 1
Respiratory challenge patterns for *SineCO*$_2$ **(A)** End-tidal carbon dioxide (EtCO$_2$), **(B)** end-tidal oxygen (EtO$_2$), **(C)** percent signal change in the time domain and **(D)** in the frequency domain. Grey shading reflects 95% confidence interval. Dotted line represents the targeted sequence, and solid line is the average time series measured in the cohort.

kinetics models are applied to calculate multiple perfusion parameters. Despite its popular usage and clinical utility, DSC suffers from its reliance on exogenous gadolinium contrasts, which pose increased risks of anaphylaxis, nephrogenic systemic fibrosis, (Schlaudecker and Bernheisel, 2009) and gadolinium deposition in different tissues (Strickler and Clark, 2021).

To address this drawback, recent works have proposed contrast-free deoxygenation-based DSC (dDSC) which take advantage of endogenous paramagnetic deoxyhemoglobin to induce susceptibility-weighted MRI signal losses, similar to the effects of gadolinium (MacDonald et al., 2018; Poublanc et al., 2021; Vu et al., 2021). This dDSC technique delivers boluses of deoxygenated hemoglobin through transient exposure to low-oxygen (hypoxia) or high-oxygen (hyperoxia) gas inhalation (Meier and Zierler, 1954; Østergaard et al., 1996; Østergaard, 2005) and has demonstrated feasibility in healthy volunteers as well as chronic anemia subjects who had elevated blood flow and shortened transit time (Vu et al., 2021).

One of the obstacles to perfusion quantification in both gadolinium-based and deoxygenation-based DSC is the determination of cerebral blood flow (CBF), which requires a deconvolution between the signals in the blood and in the tissue. Traditionally, this deconvolution is performed using a singular value decomposition (SVD) approach in the time domain (Østergaard et al., 1996). In this work, we propose to replace the transient contrast bolus with a sinusoidal gas challenge and compute perfusion at the fundamental sinusoidal frequency in the Fourier domain, thereby simplifying the SVD deconvolution process. We also propose to raise and lower the concentration of deoxygenated hemoglobin through modulations of end-tidal CO_2 level (Figure 1A), rather than manipulating the inspired oxygen concentration. The sinusoidal end-tidal CO_2 fluctuations (*SineCO*$_2$), and corresponding changes in oxygen delivery, trigger reciprocal changes in the gradient-echo MRI signals that can be converted into CBF estimates. In order to assess the feasibility of this new perfusion technique, we evaluated *SineCO*$_2$ on 10 healthy volunteers in comparison with perfusion measurements from standard gadolinium-based DSC, ASL, and PC MRI.

2 Materials and methods

2.1 Study protocol

The Committee on Clinical Investigation at Children's Hospital Los Angeles approved the protocol; written informed consent was obtained from all subjects (CCI#20-00050). This study was performed in accordance with the Declaration of Helsinki.

A total of 10 healthy volunteers participated in this study during the months of April and May of 2021. Exclusion criteria included pregnancy, hypertension, diabetes, stroke or other known neurologic insult, seizures, known developmental delay or learning disability, at

least one 'yes' answer to the 6-question Choyke survey (Choyke et al., 1998), and measured glomerular filtration rate (GFR) lower than 60 mL/min/1.73 mm^2 (Østergaard, 2005). Imaging, vital signs (heart rate, blood pressure, temperature, and oxygen saturation), and blood samples (for complete blood count) were collected for each subject on the same study visit date.

2.2 Respiratory challenges

Respiratory challenges were performed by prospectively targeting end-tidal O_2 (EtO_2) and end-tidal CO_2 ($EtCO_2$) partial pressures using a specialized computer-controlled gas blender (RespirAct, Thornhill Research, Toronto, Canada) (Slessarev et al., 2007). This device measures the subject's baseline EtO_2 and $EtCO_2$ during the initial preparation phase and delivers specific concentrations of oxygen and carbon-dioxide during the challenge phase to accurately target EtO_2 and $EtCO_2$ values. Fingertip pulse oximetry SpO_2 (Nonin, Plymouth, MN) was recorded continuously during gas challenges. *SineCO_2* challenge was performed, in which EtO_2 was clamped at subject-specific baseline and $EtCO_2$ was modulated in a sine wave between 35 and 45 mmHg with a period of 60 s (Blockley et al., 2011). This period was fourfold longer than the brain's characteristic rise-time in response to CO_2 (Duffin et al., 2015) and has previously been used in published CVR protocols (Blockley et al., 2011).

2.3 MRI experiment

2.3.1 Structural MRI

All MRI was acquired on a 3T Philips Achieva (Philips Medical Systems, Best, Netherlands) with a 32-channel head-coil. Pre-contrast anatomical 3D T1 was acquired with the following parameters: TR = 8 ms, TE = 3.7 ms, flip angle = 8°, and resolution = 1 mm isotropic. Total scan time was 5:18 for T1 sequence.

Pre-processing steps on structural T1-weighted images consist of brain extraction, tissue classification into grey matter (GM), white matter (WM) and segmentation using the BrainSuite Anatomical Pipeline (brainsuite.org, v.21a). Tissue segmentation into 312 regions-of-interest (ROI) was performed using the USCBrain anatomical atlas (Joshi et al., 2022), whose labels were modified to include subdelineations of deep WM tissue (manually drawn WM structures) and the cerebellum [transferred from the probabilistic atlas of the human cerebellum (Diedrichsen et al., 2009)]. All cortical ROIs were separately labeled into GM and gyral WM regions. Subsequently, these labels were transferred to each subject's structural imaging space.

2.3.2 Arterial spin labeling (ASL)

Time-encoded pseudo-continuous ASL was acquired with the following parameters: TE = 16 ms, TR = 5,040 ms, Hadamard-8 matrix with seven blocks of 2,000, 800, 500, 300, 250, 200, and 150 ms, post-label delay (PLD) = 100 ms, SENSE = 2.5, resolution = 3 mm × 3 mm × 6 mm, FOV = 240 mm × 240 mm × 114 mm, two FOCI background suppression pulses, 2D single-shot EPI readout, and 12 signal averages. M0 images were acquired by switching off labeling and background suppression and keeping the same imaging parameters, except for TR = 2,500 ms. Scan time was 8: 44 for ASL sequence and 18 s for M0 sequence.

Perfusion quantification was performed using FSL BASIL toolbox (FSL, Oxford, United Kingdom). Additional details on acquisition and processing of the time-encoded ASL sequence have been previously published (Afzali-Hashemi et al., 2021). Briefly, all perfusion weighted images were motion-corrected to the first dynamic using SPM12 (Wellcome Trust Center for Neuroimaging, London, United Kingdom). The individual acquisitions were subsequently subtracted according to a Hadamard-8 matrix to obtain perfusion weight images having PLD values of 100, 250, 450, 700, 1,000, 1,500, and 2,300 ms. The individual PLD images experienced different numbers of background suppression pulses and were divided by a correction factor of $(0.95)^N$, where N was the number of pulses. The signal variation across PLD was denoised using a spatiotemporal generalized variation model as described by (Spann et al., 2017). The denoised perfusion weighted images were processed using the BASIL toolbox which uses Bayesian inference to fit arterial transit time, arterial blood volume and CBF voxelwise using an extended kinetic model (Chappell et al., 2010). Blood T1 was derived from the subject's measured hematocrit (Lu et al., 2004). Subject-specific labeling efficiency was derived from the flow-weighted velocity measured from the phase contrast images (Aslan et al., 2010). The final maps were smoothed using a Gaussian lowpass filter with full-width half maximum value of 3.5 mm.

Subsequently, perfusion maps were registered to dDSC native space for comparison.

2.3.3 Phase contrast (PC)

Single-slice PC images were acquired above the carotid bifurcation: TR = 17 ms, TE = 10 ms, flip angle = 10°, resolution = 0.6 mm × 0.6 mm, FOV = 220 mm × 220 mm, slice thickness = 5 mm, and velocity encoding gradient of 80 cm/s. The scan was ungated and used 10 averages to compensate for pulsatility. Scan time was 1:06 for the phase contrast acquisition. Details on calculation of total CBF from four feeding arteries were published in previous works. (Cologner et al., 2020; Wymer et al., 2020). Briefly, vessel edges were derived from the complex-difference images using Canny edge detection from MATLAB (MathWorks, Natick, MA). Subsequent vessel areas were mapped to the phase-difference (velocity) images and total brain blood flow was calculated as follows:

$$\sum_{i=1}^{4}\sum_{j=1}^{N} V(j) \quad (1)$$

where V is the velocity map (after appropriate scaling for geometry and velocity encoding), the inner summation is across the N voxels in the vessel and the outer summation is across the four feeding vessels. The total CBF was then normalized to brain weight by calculating the total brain volume from the 3D T1w image (BrainSuite, brainsuite.org, v.21a) and assuming a brain density of 1.05 g/mL.

2.3.4 Gadolinium-based DSC

Traditional gadolinium DSC was acquired using a dual-echo gradient-echo blood-oxygen level dependent (BOLD) MRI sequence with the following parameters: TR = 1.5 s, TE = 8/35 ms, flip angle = 30°, FOV = 190 mm × 190 mm × 100 mm, resolution = 2.5 mm× 2.5 mm × 5 mm, 160 dynamics, SENSE = 2, and no multi-band acceleration. The FOV was aligned with the previous dDSC acquisition at the time of scanning. Scan time was 4:05.

Gadovist at 0.1 mmol/kg was injected at a rate of 4 cc per second using a 20 or 22 gauge IV. Due to the lack of a power injector at our

research facility, gadolinium contrast was injected manually by a physician. Contrast bolus was followed by 20 mL of saline flush *via* a three-way stopcock.

Gadolinium-based DSC BOLD images were preprocessed using the spatial functional processing pipeline similar to dDSC preprocessing, as detailed below. Perfusion values for CBF, cerebral blood volume (CBV), and mean transit time (MTT) were calculated based on published pipelines for gadolinium DSC (Stokes et al., 2021). Final rigid registration of perfusion images to deoxygenation DSC native space was performed for regional comparison.

2.3.5 Deoxygenation-based DSC MRI

Dynamic gradient-echo BOLD MRI was acquired for the *SineCO*$_2$ challenge with the following parameters: TR = 1.5 s, TE = 35/90 ms, flip angle = 52°, FOV = 190 mm × 190 mm × 100 mm, resolution = 2.5 mm isotropic, SENSE = 1, multi-band SENSE = 4, phase-encoding direction = AP, fat-shift direction = P, and 220 dynamics. One dynamic of reverse-gradient BOLD was acquired with the opposite fat-shift direction = A along the phase encoding direction. Scan time was 5:05 for the BOLD sequence and 9 s for the reverse-gradient BOLD.

To correct for EPI-induced distortion, BOLD images were pre-processed with field map calculated from opposite phase encoding directions. Motion correction with Analysis of Functional NeuroImages (AFNI, USA) and slice timing correction with FMRIB Software Library (FSL, Oxford, United Kingdom) were performed in that order. Registration of BOLD to T1 space was performed in BrainSuite. Finally, BOLD images were smoothed using a 4 mm × 4 mm × 4 mm Gaussian kernel.

All subsequent dDSC processing was performed in MATLAB (MathWorks, Natick, MA). Signal contribution from pial veins was suppressed by eliminating voxels with higher signal amplitude than the 98th percentile (Bhogal et al., 2022). Whole brain (WB), GM, and WM perfusion values was computed by averaging voxels within brain and tissue-specific masks in each subject's functional native space.

2.4 Data analysis for deoxygenation-based DSC

2.4.1 Gradient-echo ΔR_2^*

Perfusion measures were calculated for both the single-echo data at 35 ms and dual-echo data at TEs of 35 and 90 ms. Single echo ΔR_2^* was calculated using the following relationship:

$$\Delta R_2^*(t) = -\frac{1}{TE} ln\left(\frac{S(t)}{S_0}\right) \tag{2}$$

where $S(t)$ is the tissue signal and S_0 is the average value across $S(t)$.

Dual echo ΔR_2^* was calculated for two echoes, TE_1 = 35 ms and TE_2 = 90 ms:

$$\Delta R_2^* = \frac{1}{TE_2 - TE_1}\left[ln\left(\frac{S_{TE1}(t)}{S_{0,TE1}}\right) - ln\left(\frac{S_{TE2}(t)}{S_{0,TE2}}\right)\right] \tag{3}$$

2.4.2 Venous output function (VOF)

Venules have the largest BOLD fluctuation in response to CO_2 stimuli because the blood volume is close to 100%, instead of <10% for brain tissue. The great cerebral veins not only have the largest signal intensity changes, but they have the longest delay relative to the global BOLD signal. Individual VOFs were obtained automatically by choosing 20 voxels with the highest integrated, rectified signal intensity (Carroll et al., 2003) and delay greater than the 98th percentile (Bhogal et al., 2022). To convert ΔR_2^* to concentration-time curve $C(t)$ in both blood and tissue voxels, this manuscript assumed a linear relationship $\Delta R_2^*(t) = r_Y \times C(t)$, with coefficients $r_{Y\_tissue} = r_{Y\_blood} = 1$.

2.4.3 Time delay (TD)

Since the signal at each voxel was a sinusoid, whose phase could be estimated, TD was computed as the phase delay of tissue:

$$TD = \frac{\phi_{tissue} - \phi_{venous}}{2\pi f_c} \tag{4}$$

where f_c is the fundamental frequency of the sinusoidal stimulus and ϕ is the phase of the sine wave (Blockley et al., 2011) calculated from the Fourier transform of the BOLD signal with respect to time. The venous phase ϕ_{venous} was estimated by forming a histogram of phase delays across all voxels within the brain for each subject and selecting the 98th percentile, thus removing observer bias to obtain more consistent phase estimates (Bhogal et al., 2022).

2.4.4 Cerebral blood flow (CBF)

For traditional DSC, CBF is usually calculated by deconvolution with singular value decomposition (SVD) between the tissue signal and the blood VOF signal: (Østergaard et al., 1996):

$$C_{tissue}(t) = C_{blood}(t) \otimes (CBF \times R(t)) \tag{5}$$

For *SineCO*$_2$, CBF was calculated in the frequency domain based on the magnitude spectra of Fourier-transformed tracer kinetics model (Eq. 4):

$$\left|C_{tissue}(f)\right| = \left|C_{blood}(f)\right| \times CBF \times \left|R(f)\right| \tag{6}$$

The residue function $R(t)$ was modeled using a decaying exponential function, $R(t) = e^{-t/\tau}$ with time constant τ (Østergaard, 2005). For a first-order system at low frequencies its time constant can be approximated as the phase delay (Thompson, 2014), $\tau = TD$ calculated from Eq. 4 The magnitude spectrum of the residue function was $|R(f)| = \frac{1}{\sqrt{(1/\tau)^2 + (2\pi f)^2}}$. CBF was the only unknown in Eq. 6 and was estimated using least-squares fitting for the magnitude spectra at each voxel.

2.4.5 Cerebral blood volume (CBV)

CBV was calculated as $CBV = \frac{\kappa}{\rho}\frac{\int |C_{tissue}(t)dt|}{\int |C_{blood}(t)dt|}$, where ρ is the brain density 1.05 g/mL, κ is the hematocrit correction factor, and the limits of integration represent the start and stop of the BOLD signal response. In respiratory-based DSC, since the deoxygenation contrast is confined within red blood cells instead of plasma, κ = 1/0.69 is used to account for the difference between capillaries' and large blood vessels' hematocrits (Tudorica et al., 2002; Schulman et al., 2022).

2.4.6 Mean transit time (MTT)

MTT was computed using central volume theorem as the ratio between CBV and CBF (Stewart, 1893):

$$MTT = \frac{CBV}{CBF} \tag{7}$$

2.4.7 Cerebrovascular reactivity (CVR)

To generate the CVR maps, temporal alignment and least squares fitting were applied between the single-echo BOLD at TE of 35 ms and $EtCO_2$ signals on a voxel-by-voxel basis, with the slope term as CVR calculation (Liu et al., 2019a). Maps of voxel-wise ratio between CBF and CVR for individual subjects were generated for regional comparison between the two parameters.

2.5 Statistical analysis

Statistical analysis was performed in R statistical package (R Core Team, Vienna, Austria). Amplitude, phase, and period of sinusoidal signals were computed by fitting the BOLD signals (either single-echo at TE of 35 ms or dual-echo at TEs of 35 and 90 ms) to sine waves while minimizing least-squares errors. Temporal SNR of the sinusoidal BOLD signal was calculated as the ratio between the peak-to-peak amplitude and the standard deviation of the BOLD fluctuations after removing the fundamental sine wave.

Perfusion measurements were checked for normality with Shapiro-Wilk test. To compare global perfusions between *SineCO₂* and DSC, ASL, or PC reference, paired *t*-test was performed. Reproducibility was assessed from two iterations of two-cycle sinusoid for *SineCO₂*. Test-retest and intersubject coefficient-of-variation were reported.

Within each subject, agreement between pairs of methods was assessed using correlation and limits of agreement analyses. Pearson correlation coefficient r was calculated from the linear fit between perfusion values from 312 ROI for pairs of perfusion techniques. 95% limits of agreement were calculated as $\bar{d} \pm 1.96 \times s_d$, where $\bar{d}$ is the mean difference and s_d is the standard deviation of the differences between two methods in the ROI set. All limits of agreement were normalized by the average of the two methods and reported as percentages (Bland and Altman, 1999; Giavarina, 2015).

3 Results

3.1 Respiratory challenges

All 10 subjects successfully completed the *SineCO₂* respiratory challenge, but one subject was excluded from the group analysis because of gas leakage from the mask caused by facial hair, and one subject was excluded since the timing of the gas challenge and the BOLD imaging was incorrectly aligned at the time of the experiment.

None of the subjects reported discomfort during *SineCO₂* respiratory challenge. Baseline tidal volumes and respiration rates were 772 ± 292 mL and 17.2 ± 3.3 breaths/min and did not change significantly during CO_2 modulations ($p = 0.27$ and $p = 0.82$, respectively). Initial $EtCO_2$ and EtO_2 recordings were 41.0 ± 3.5 mmHg and 110.4 ± 7.0 mmHg in the cohort. During *SineCO₂*, continuous measurements of $EtCO_2$ demonstrated sinusoidal amplitudes of 4.6 ± 0.8 mmHg (Figure 1A), whereas EtO_2 was kept level at baseline (Figure 1B). SpO_2 remained level at 98.4% ± 0.9% during the challenge.

Under CO_2-induced vasodilation and vasoconstriction, single-echo gradient-echo MRI signal at TE of 35 ms varied in a sinusoidal pattern with peak-to-peak amplitude of 1.20% ± 0.44% ($\Delta R_2^* = 0.34 \pm 0.13\ s^{-1}$) relative to baseline (Figure 1C), higher in the GM (1.52% ± 0.57%, $\Delta R_2^* = 0.43 \pm 0.16\ s^{-1}$) compared to WM (0.58% ± 0.26%, $\Delta R_2^* = 0.17 \pm 0.07\ s^{-1}$, $p<0.01$). Temporal SNR was 1.36 ± 0.52 in the whole brain, 1.72 ± 0.66 in GM, and 0.92 ± 0.38 in WM. In the Fourier domain, global signals demonstrated a peak at 0.17 Hz, corresponding to a sine wave period of 60 s (Figure 1D).

3.2 Perfusion measurements

3.2.1 Single-echo *SineCO₂*

Perfusion parameters for the whole brain, GM, and WM are displayed in Table 1; individual CBF, CBV, TD, and MTT maps by single-echo *SineCO₂* at TE of 35 ms are shown in Figure 2. Similar spatial distribution is observed in CBF and CBV maps (Figure 2), with GM-WM ratio of 2.1 ± 0.1 for CBV and 1.9 ± 0.1 for CBF. Both TD and MTT maps showed shorter venous delay in deep WM compared to GM ($p = 0.02$ and $p<0.01$, respectively), but distribution is heterogeneous between subjects (Figure 2).

3.2.1.1 CBF

To evaluate quantitative perfusion by *SineCO₂*, mean CBF values are shown in Table 1 in comparison with gadolinium-based DSC, ASL, and PC. In the whole brain, *SineCO₂* CBF trended lower compared to ASL ($p = 0.08$) but was significantly lower than PC ($p = 0.01$) and higher than DSC ($p = 0.04$). In terms of reproducibility, there was no significant difference between two repetitions ($p = 0.47$) with a test-retest coefficient of variation of 21%. The intersubject coefficient of variation was 19%, slightly higher compared to DSC (18%), ASL (16%), and PC (13%).

Within-subject correlations and Bland-Altman analyses are shown for a representative subject in Figure 3, and individual analyses are in Supplementary Figures S1, S2, demonstrating similar correlation and width of the limits of agreement between *SineCO₂* and reference techniques compared to agreement amongst DSC and ASL references.

3.2.1.2 CBV

SineCO₂ was not different from CBV by DSC ($p = 0.36$), and regional correlation was high across ROIs and similar to agreement observed in CBF (Supplementary Figure S3). Intersubject coefficient of variation was 11%, and test-retest coefficient of variation was 20%, demonstrating no significant difference between the two repetitions ($p = 0.18$).

3.2.1.3 TD

TD values by *SineCO₂* were significantly longer compared to DSC ($p < 0.01$). Opposite trends were observed between the two techniques, with prolonged TD in WM in DSC but shortened WM delay relative to venous signal in *SineCO₂* challenge. Compared to CBF and CBV measurements, TD maps were noisier (Figure 2C), with a test-retest coefficient of variation of 25% and intersubject coefficient of variation of 35%.

3.2.1.4 MTT

Shorter MTT values were observed in *SineCO₂* compared to DSC ($p = 0.01$), and grey matter showed longer transit time than white matter ($p < 0.01$). No correlation was observed with DSC MTT (not shown). Test-retest and intersubject coefficients of variation were 17% and 23%, respectively.

3.2.2 Dual-echo *SineCO₂*

Compared to the global ΔR_2^* 0.34 ± 0.13 s^{-1} obtained at the first TE = 35 ms, dual-echo ΔR_2^* at TEs of 35 and 90 ms was 0.22 ± 0.08 s^{-1} ($p <$

TABLE 1 Regional perfusion estimates by $SineCO_2$ and three reference standards ASL, DSC, and PC in the whole brain (WB), grey matter (GM), and white matter (WM).

		CBF (mL/100 g/min)	CBV (mL/100 g)	TD (seconds)	MTT (seconds)
SineCO₂	WB	38.8 ± 7.5 (0.19)	3.1 ± 0.4 (0.11)	6.4 ± 2.2 (0.35)	4.5 ± 1.0 (0.23)
	GM	47.9 ± 9.2 (0.19)	3.9 ± 0.5 (0.12)	6.6 ± 2.2 (0.33)	4.8 ± 1.0 (0.20)
	WM	25.3 ± 5.7 (0.22)	1.7 ± 0.2 (0.11)	6.3 ± 2.2 (0.36)	4.1 ± 1.0 (0.25)
DSC	WB	29.6 ± 5.4 (0.18)	2.9 ± 0.3 (0.10)	2.4 ± 0.2 (0.10)	6.4 ± 1.0 (0.16)
	GM	35.6 ± 6.2 (0.17)	3.4 ± 0.3 (0.10)	2.1 ± 0.2 (0.11)	6.3 ± 0.9 (0.14)
	WM	20.3 ± 4.2 (0.21)	2.0 ± 0.2 (0.12)	2.6 ± 0.2 (0.08)	6.6 ± 1.3 (0.20)
ASL	WB	48.0 ± 7.8 (0.16)	NA	NA	1.13 ± 0.08 (0.7)
	GM	60.5 ± 10.8 (0.18)	NA	NA	1.07 ± 0.09 (0.08)
	WM	32.3 ± 8.0 (0.25)	NA	NA	1.22 ± 0.09 (0.07)
PC	WB	65.9 ± 8.3 (0.13)	NA	NA	NA

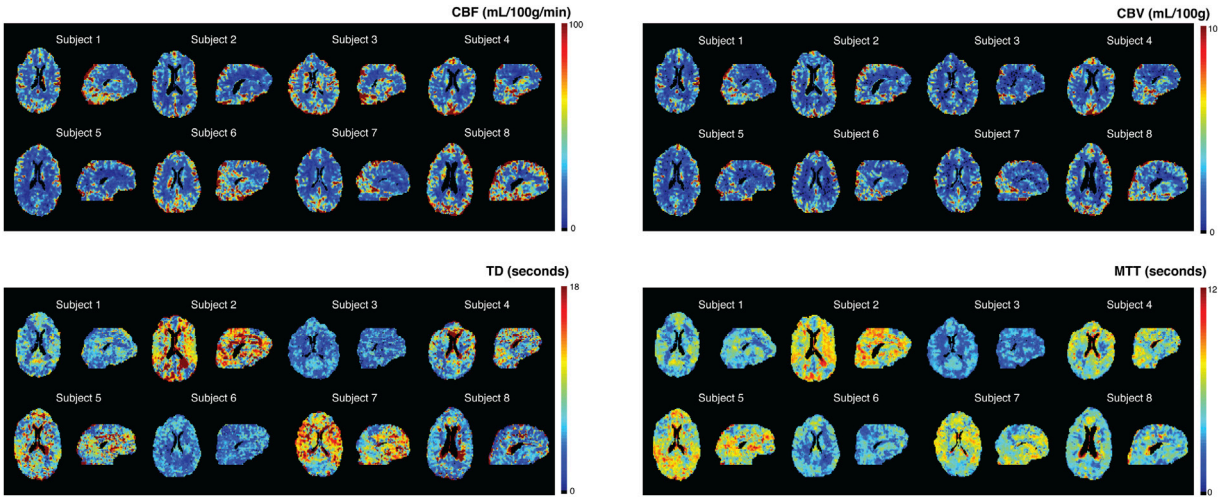

FIGURE 2
SineCO₂ CBF, CBV, TD, and MTT maps for individual subjects.

0.01). Temporal SNR was lower in the dual-echo signal (tSNR = 0.82 ± 0.32, $p = 0.03$). Individual CBF, CBV, TD, and MTT maps using the dual-echo approach (Supplementary Figure S4) show a similar spatial distribution compared to single-echo perfusion maps (Figure 2). However, dual-echo maps are noisier and yield a higher bias in CBF compared to DSC and ASL (data not shown).

3.3 Cerebrovascular reactivity

Individual CVR maps are shown in Figure 4. Mean CVR was 0.24% ± 0.06%/mmHg in the cohort, significantly higher in the GM (0.28% ± 0.07%/mmHg) compared to the WM (0.13% ± 0.03%/mmHg, $p<0.01$). Spatial patterns of CVR maps are similar to CBF and CBV maps generated from the *SineCO₂* technique. Ratio maps between CBF and CVR (Supplementary Figure S5) demonstrated areas of negative CVR in the deep white matter areas as well as disproportionally higher ratio in the white matter compared to GM.

4 Discussion

In this work, we employed a technique previously used to measure CVR with a CO_2 respiratory challenge to modulate cerebral saturation and BOLD signal in a sinusoidal pattern (Blockley et al., 2011), after which tracer kinetics equations were applied in the frequency domain to compute perfusion parameters. *SineCO₂* CBF, and CBV values were within acceptable range of literature (Grandin et al., 2005), but MTT was larger than expected (Ibaraki et al., 2007). Single-echo acquisition yielded better temporal SNR and better image quality compared to dual-echo approach. CBF estimates were compared with three reference techniques, gadolinium-based DSC, ASL, and PC, and demonstrated no bias with ASL and PC but overestimation compared to DSC. The limits of agreement were large between *SineCO₂* with ASL, and DSC but were comparable to agreement amongst the reference techniques and previously reported agreement between DSC and PET (Grandin et al., 2005). Despite the systematic biases, perfusion maps showed regional agreement

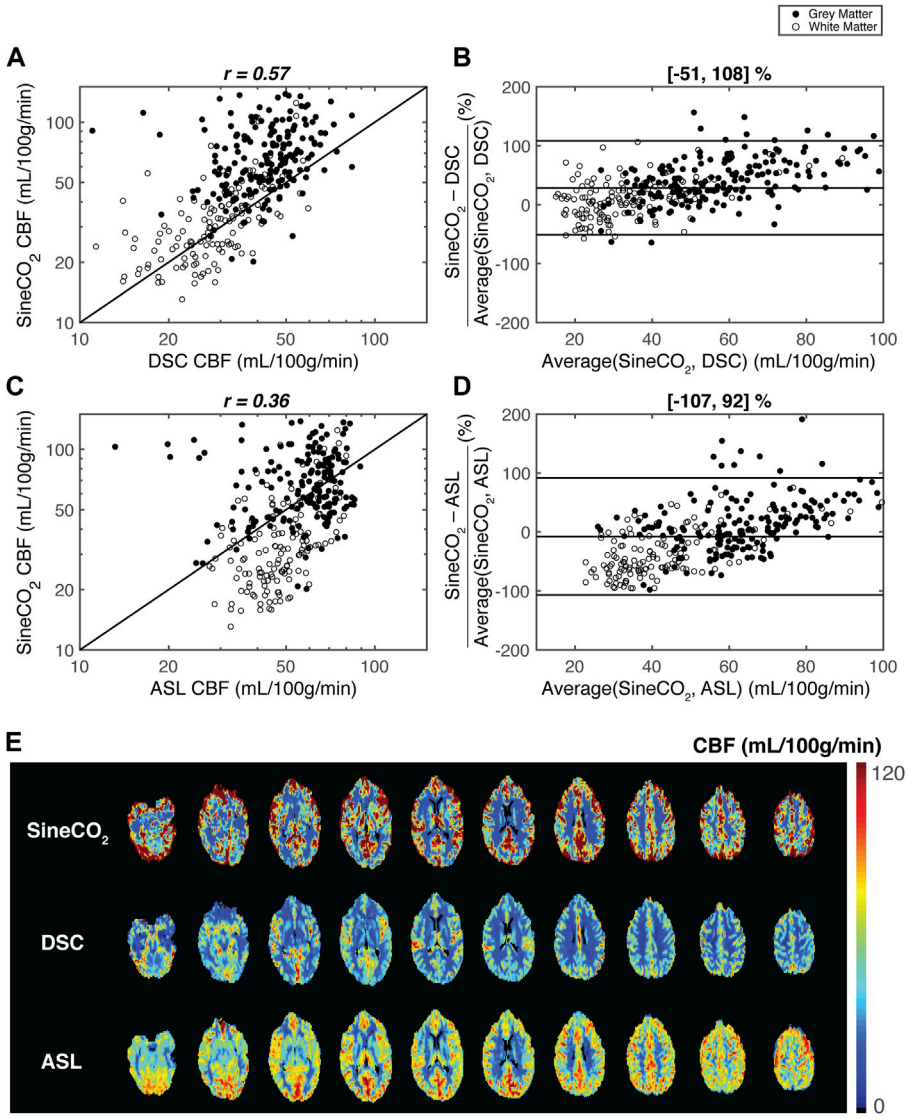

FIGURE 3
Regional agreement between respiratory challenge *SineCO$_2$* and reference standards DSC and ASL in a representation subject. Correlation and Bland-Altman limits of agreement analyses using 312 regions-of-interest between **(A–B)** *SineCO$_2$* and DSC and **(C–D)** *SineCO$_2$*, and ASL **(E)** CBF maps in representative subject by three techniques.

between the techniques, indicating that *SineCO$_2$* has the potential to differentiate diseased and normal-appearing tissue in cerebral pathologies such as ischemic strokes or brain tumors.

The use of CO_2 vasoactive stimulus represents a divergence from previous deoxygenation-based DSC studies, which utilize hypoxia or hyperoxia respiratory challenges to directly deliver boluses of deoxygenated hemoglobin (MacDonald et al., 2018; Poublanc et al., 2021; Vu et al., 2021). Capnic challenges raise and lower cerebral saturation through vasodilation and vasoconstriction within the capillary beds, so the sinusoidal modulations are not present on the arterial side but instead only in vessels undergoing oxygen exchange and large veins. Therefore, this source of contrast results in an anti-causal system where the VOF is used *in lieu* of an AIF. Conceptually, this is analogous to playing a cine-angiogram in reverse. Even though the anti-causality is not compatible with traditional tracer kinetics model (Meier and Zierler, 1954; Østergaard, 2005), computation of CBF in the frequency domain ignores the phase in favor of the magnitude, which is independent of the relative delay between tissue and VOF signals. CBV estimates in typical DSC experiments are corrected with the area-under-curve of a VOF signal, which is usually less vulnerable to partial volume effects compared to AIF (Knutsson et al., 2010); therefore, CBV measures are also independent of the use of VOF. On the other hand, TD is calculated as the delay between the phase of the tissue signal and venous phase for *SineCO$_2$* instead of arterial phase in DSC; therefore, TD maps demonstrated opposite trends between the two techniques.

The *SineCO$_2$* approach has some interesting properties. Overall, since the endogenous contrast is generated by oxygen exchange, it cannot detect actual or effective shunt flow, potentially underestimating true perfusion. The contrast change results from a cascaded transport system, in which the CO_2 stimulus passes through an initial cerebrovascular response transfer function followed by a secondary residue function that governs the propagation of

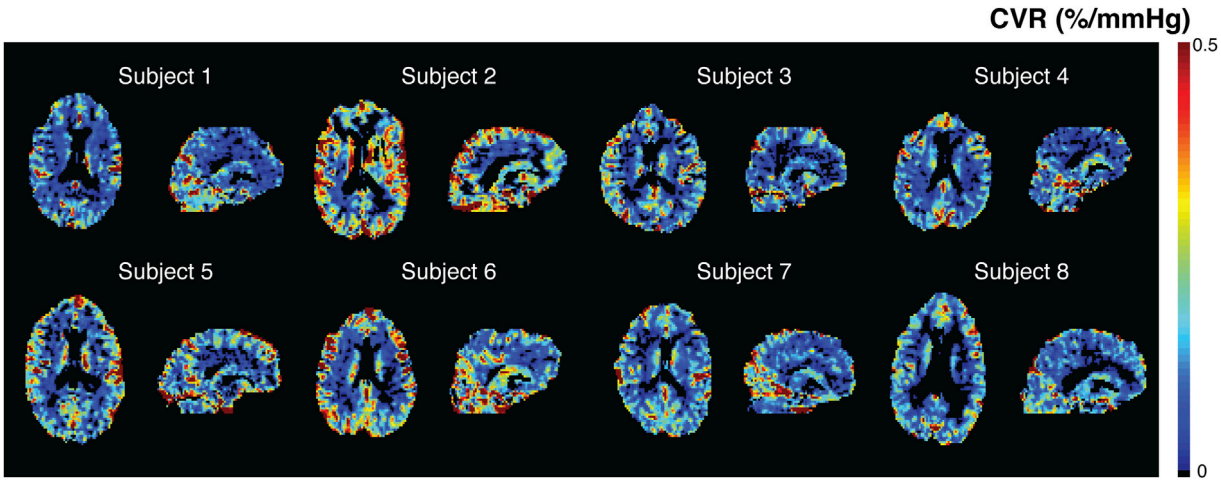

FIGURE 4
SineCO$_2$ CVR maps in individual subjects.

deoxyhemoglobin. The complexity of this higher-order system is simplified by the capability to extract a VOF signal, which relates to the signal only through the residue transfer function. The indirect mode of contrast generation also requires some cerebrovascular reactivity to generate a signal suitable for CBF estimation, hence it is not surprising that CVR, CBF, and CBV maps resemble one another. In brain regions where resting flow is preserved but CVR is abnormal, signal-to-noise of the CBF and CBV estimates will be poor.

CO_2 modulations also have complex cerebrovascular and peripheral hemodynamic effects, including changes in respiratory rates, tidal volumes, heart rates, blood pressures, and perfusion values, proportionally to the extent and duration of CO_2 inhalation. The upward swing of the CO_2 sinusoid is a hypercapnic stimulus which results in increase in CBF (Kety and Schmidt, 1948), whereas the trough of the sinusoid represents a hypocapnic stimulus with a decrease in flow. Assuming ±5 mmHg fluctuations in $EtCO_2$ remain within the autoregulatory range (Battisti-Charbonney et al., 2011), 1 mmHg change in $EtCO_2$ typically induces 1–2 mL/100 g/min change in CBF (Kety and Schmidt, 1948; Brian, 1998). Therefore, CBF in the tracer kinetic model can be written as a function of time $CBF(t) = CBF_0[1 + CVR(EtCO_2(t) - 40\,mmHg)]$, where CBF_0 is the baseline cerebral blood flow at $EtCO_2$ of 40 mmHg. With a typical grey matter CVR of 0.2%/mmHg, and a peak-to-peak amplitude of 5 mmHg, the oscillating contribution is only around 1%. Furthermore, since the oscillations are centered about the most linear portion of the CBF–$EtCO_2$ curve (Battisti-Charbonney et al., 2011), this work assumes that the value measured is the average perfusion and is comparable to baseline blood flow. However, this assumption requires validation with a dynamic acquisition of ASL or PC with high enough temporal resolution to quantify fluctuations in CBF in response to CO_2 respiratory challenge.

Additionally, the vasoactive effects of CO_2 challenge can potentially explain the divergence in regional agreement between *SineCO*$_2$ and ASL. During sustained hyperemia, cortical GM regions are prioritized compared to deep WM (Chai et al., 2019). This steal phenomenon occurs in which blood flow preferentially increases in GM at the expense of WM (Poublanc et al., 2013), causing higher sinusoid amplitudes in GM and thus overestimation of CBF in cortical regions. On the other hand, since flow changes are lower within WM, CBF measurements are not as high in WM in *SineCO*$_2$ compared to baseline measurements by ASL.

Other limitations include the study design of administering the sinusoidal stimulus about a fixed $EtCO_2$ value of 40 mmHg regardless of the subject's initial $EtCO_2$ levels; in subjects of high baseline CO_2 partial pressure, this paradigm induced hypocapnia and hyperventilation response that lengthened transit time (Ito et al., 2003) and potentially explained the heterogeneous distribution in several TD maps (Angleys et al., 2015). Clamping the average end-tidal CO_2 to 40 mmHg may also introduce a small "step" response in the BOLD signal for individuals whose resting end-tidal CO_2 is far from 40 mmHg. However, limiting our analysis to a single frequency minimized error contributions from this effect. Despite targeting a single fundamental frequency f_o in practice only a perfect sinusoid can be accomplished on positive cycles. The shape of the negative cycle depends on the subject's hyperpneic response from the previous positive cycle, thus introducing a small non-linearity and frequencies outside the target range. Lastly, since the signal is venous-weighted, SpO_2 values could not be used to convert ΔR_2^* to arterial saturation in concentration-time curves; therefore, the values presented here are only considered semi-quantitative. However, since relative perfusion is frequently used in clinical routines, semi-quantitative measurements may still offer insight into diseased tissue relative to contralateral normal-appearing tissue.

Despite the shortcomings, the most significant advantage to *SineCO*$_2$ perfusion imaging is that sinusoidal CO_2 respiratory challenge is a robust mechanism to measure CVR (Blockley et al., 2011). Previous works have demonstrated that 32% of the variation in GM CVR is explained by variation in baseline CBF (Afzali-Hashemi et al., 2021), so these two parameters are tightly coupled together and are known to vary with changes in $EtCO_2$ (Hou et al., 2020). However, measurement of CVR can still yield additional information, as illustrated by the existence of negative CVR values in deep WM unseen on CBF maps. Divergence in CBF and CVR as shown in the ratio maps typically happens in areas of low flow and long delay, in which CBF can increase in response to CO_2 but requires sufficient time to reach the hypercapnic ceiling and can potentially be classified as negative CVR (Poublanc et al., 2015). In this current technique, *SineCO*$_2$ CBF measurements are calculated purely from the

magnitude spectrum and are independent of phase delay, but CVR estimates computed from traditional general linear model approach are influenced by vascular delay (Poublanc et al., 2015; Liu et al., 2019b). Therefore, *SineCO$_2$* capability to acquire both perfusion and reactivity simultaneously in one imaging sequence is of high interest in cerebrovascular diseases and gives it an edge over other conventional perfusion MRI techniques.

Most of *SineCO$_2$* potential diagnostic power lies in perfusion imaging of strokes or gliomas, especially in more vulnerable populations in whom gadolinium injection is undesirable, such as renal-impaired or pediatric patients. However, the fundamental difference between gadolinium contrast and deoxyhemoglobin contrast may allow them to play complementary roles in perfusion imaging for these pathologies. For ischemic strokes in which the penumbra is under low oxygen delivery, CO_2-induced modulations in CBF can lead to reperfusion of the damaged regions (Brambrink and Orfanakis, 2010), which can yield a completely different perfusion distribution compared to gadolinium DSC. In brain tumors, gadolinium-based contrast extravasation through the disrupted blood-brain barrier can result in altered CBV measurements (Ho et al., 2016); on the other hand, deoxygenation-based contrast remains purely intravascular. Therefore, CBV measured using gadolinium-based DSC within gliomas might differ compared to *SineCO$_2$* CBV. These potential divergences in the two techniques require additional work to evaluate the diagnostic role of *SineCO$_2$* in different cerebrovascular pathologies.

In conclusion, this validation study established feasibility of using *SineCO$_2$* to measure perfusion and demonstrated agreement between *SineCO$_2$* against three reference perfusion techniques, DSC, ASL, and PC. Despite the systematic bias, in clinical routines, neuroradiologists typically rely on relative perfusion differences between diseased and normal-appearing tissue rather than absolute perfusion, so *SineCO$_2$* relative perfusion maps may still be useful clinically independent of VOF selection. Additionally, *SineCO$_2$* also represents an easy approach to generate CBF maps independent of confounding parameters in SVD deconvolution and minimize MRI time by simultaneous acquisition of perfusion and reactivity in one imaging sequence.

Data availability statement

De-identified imaging data and processing code will be made available to qualified researchers on a case-by-case basis after obtaining approval from the Children's Hospital Los Angeles regulatory authorities.

Ethics statement

The studies involving human participants were reviewed and approved by The Committee on Clinical Investigation at Children's Hospital Los Angeles approved the protocol (CCI#20-00050). The patients/participants provided their written informed consent to participate in this study.

Author contributions

CV and JW designed the research study and wrote the manuscript. CV, BX, CG-Z, JS, KB, and SC collected the data. CV, BX, CG-Z, JS, and SC analyzed the data. AN and JW assisted with the interpretation of the data. All authors edited and approved this manuscript.

Funding

This work was supported by National Heart, Lung, and Blood Institute (grant 1U01-HL-117718-01, 1R01-HL136484-01A1), the National Center for Research (5UL1-TR000130-05) through the Clinical Translational Science Institute at Children's Hospital Los Angeles, the National Institutes of Health (grant R01-NS074980), and the National Institute of Neurological Disorders and Stroke (grant 1F31NS106828-01A1). CV was supported by the Core Pilot Program and a Research Career Development Fellowship from the Saban Research Institute at Children's Hospital Los Angeles. Philips Healthcare provided support for protocol development and applications engineering on a support-in-kind basis.

Acknowledgments

The authors would like to thank Dr. Ashley Stokes and colleagues for the generous release of the DSC imaging sequence and processing script. We would like to thank Dr. Jon Detterich and Dr. Andrew Cheng for their help with the experiments. We would like to thank Obdulio Carreras and Silvie Suriany for subject recruitment and coordinating efforts. We would like to thank Noel Arugay, Julia Castro, Mercedes Landaverde, and Lisa Villanueva for their help with MRI scheduling and scanning. We would also like to thank Dr. Joseph Fisher, Dr. David Mikulis, Dr. Julien Poublanc, Dr. James Duffin, Dr. Olivia Sobczyk, Ece Su Sayin, and Harrison Levine for their valuable discussions and critiques.

Conflict of interest

JW: Research funding NHLBI and NIDDK of the National Institutes of Health, Research Support-in-Kind from Philips Healthcare, Consultant for BluebirdBio, Celgene, Apopharma, WorldcareClinical, and BiomeInformatics.

The remaining authors declare that the research was conducted in the absence of any commercial or financial relationships that could be construed as a potential conflict of interest.

Publisher's note

Supplementary material

The Supplementary Material for this article can be found online at: https://www.frontiersin.org/articles/10.3389/fphys.2023.1102983/full#supplementary-material

References

Afzali-Hashemi, L., Baas, K. P. A., Schrantee, A., Coolen, B. F., van Osch, M. J. P., Spann, S. M., et al. (2021). Impairment of cerebrovascular hemodynamics in patients with severe and milder forms of sickle cell disease. *Front. Physiol.* 12, 645205. doi:10.3389/FPHYS.2021.645205

Angleys, H., Østergaard, L., and Jespersen, S. N. (2015). The effects of capillary transit time heterogeneity (CTH) on brain oxygenation. *J. Cereb. Blood Flow. Metab.* 35 (5), 806–817. doi:10.1038/JCBFM.2014.254

Aslan, S., Xu, F., Wang, P. L., Uh, J., Yezhuvath, U. S., van Osch, M., et al. (2010). Estimation of labeling efficiency in pseudocontinuous arterial spin labeling. *Magn. Reson Med.* 63 (3), 765–771. doi:10.1002/mrm.22245

Battisti-Charbonney, A., Fisher, J., and Duffin, J. (2011). The cerebrovascular response to carbon dioxide in humans. *J. Physiol.* 589 (12), 3039–3048. doi:10.1113/jphysiol.2011.206052

Bhogal, A. A., Sayin, E. S., Poublanc, J., Duffin, J., Fisher, J. A., Sobcyzk, O., et al. (2022). Quantifying cerebral blood arrival times using hypoxia-mediated arterial BOLD contrast. *Neuroimage* 261, 119523. doi:10.1016/j.neuroimage.2022.119523

Bland, J. M., and Altman, D. G. (1999). Measuring agreement in method comparison studies. *Stat. Methods Med. Res.* 8 (2), 135–160. doi:10.1177/096228029900800204

Blockley, N. P., Driver, I. D., Francis, S. T., Fisher, J. A., and Gowland, P. A. (2011). An improved method for acquiring cerebrovascular reactivity maps. *Magn. Reson Med.* 65 (5), 1278–1286. doi:10.1002/mrm.22719

Brambrink, A., and Orfanakis, A. (2010). Therapeutic hypercapnia" after ischemic brain injury: Is there a potential for neuroprotection? *Anesthesiology* 112 (2), 274–276. doi:10.1097/ALN.0B013E3181CA8273

Brian, J. E. (1998). Carbon dioxide and the cerebral circulation. *Anesthesiology* 88 (5), 1365–1386. doi:10.1097/00000542-199805000-00029

Carroll, T. J., Rowley, H. A., and Haughton, V. M. (2003). Automatic calculation of the arterial input function for cerebral perfusion imaging with MR imaging. *Radiology* 227 (2), 593–600. doi:10.1148/radiol.2272020092

Chai, Y., Bush, A. M., Coloigner, J., Nederveen, A. J., Tamrazi, B., Vu, C., et al. (2019). White matter has impaired resting oxygen delivery in sickle cell patients. *Am. J. Hematol.* 94 (4), 467–474. doi:10.1002/AJH.25423

Chappell, M. A., MacIntosh, B. J., Donahue, M. J., Günther, M., Jezzard, P., and Woolrich, M. W. (2010). Separation of macrovascular signal in multi-inversion time arterial spin labelling MRI. *Magn. Reson Med.* 63 (5), 1357–1365. doi:10.1002/MRM.22320

Choyke, P., Cady, J., DePollar, S., and Austin, H. (1998). Determination of serum creatinine prior to iodinated contrast media: Is it necessary in all patients? *Tech. Urol.* 4 (2), 65–69. Available at: https://pubmed.ncbi.nlm.nih.gov/9623618/ (Accessed July 2, 2022).

Coloigner, J., Vu, C., Borzage, M., Bush, A., Choi, S., Miao, X., et al. (2020). Transient hypoxia model revealed cerebrovascular impairment in anemia using BOLD MRI and near-infrared spectroscopy. *J. Magn. Reson Imaging* 52 (5), 1400–1412. doi:10.1002/JMRI.27210

Diedrichsen, J., Balsters, J. H., Flavell, J., Cussans, E., and Ramnani, N. (2009). A probabilistic MR atlas of the human cerebellum. *Neuroimage* 46 (1), 39–46. doi:10.1016/j.neuroimage.2009.01.045

Duffin, J., Sobczyk, O., Crawley, A. P., Poublanc, J., Mikulis, D. J., and Fisher, J. A. (2015). The dynamics of cerebrovascular reactivity shown with transfer function analysis. *Neuroimage* 114, 207–216. doi:10.1016/j.neuroimage.2015.04.029

Giavarina, D. (2015). Understanding Bland altman analysis. *Biochem. medica* 25 (2), 141–151. doi:10.11613/BM.2015.015

Grandin, C., Bol, A., Smith, A., Michel, C., and Cosnard, G. (2005). Absolute CBF and CBV measurements by MRI bolus tracking before and after acetazolamide challenge: Repeatabilily and comparison with PET in humans. *Neuroimage* 26 (2), 525–535. doi:10.1016/j.neuroimage.2005.02.028

Ho, C. Y., Cardinal, J. S., Kamer, A. P., Lin, C., and Kralik, S. (2016). Contrast leakage patterns from dynamic susceptibility contrast perfusion MRI in the grading of primary pediatric brain tumors. *Am. J. Neuroradiol.* 37 (3), 544–551. doi:10.3174/ajnr.A4559

Hou, X., Liu, P., Li, Y., Jiang, D., De Vis, J. B., Lin, Z., et al. (2020). The association between BOLD-based cerebrovascular reactivity (CVR) and end-tidal CO2 in healthy subjects. *Neuroimage* 207, 116365. doi:10.1016/j.neuroimage.2019.116365

Ibaraki, M., Ito, H., Shimosegawa, E., Toyoshima, H., Ishigame, K., Takahashi, K., et al. (2007). Cerebral vascular mean transit time in healthy humans: A comparative study with PET and dynamic susceptibility contrast-enhanced MRI. *J. Cereb. Blood Flow. Metab.* 27 (2), 404–413. doi:10.1038/sj.jcbfm.9600337

Ito, H., Kanno, I., Ibaraki, M., Hatazawa, J., and Miura, S. (2003). Changes in human cerebral blood flow and cerebral blood volume during hypercapnia and hypocapnia measured by positron emission tomography. *J. Cereb. Blood Flow. Metab.* 23 (6), 665–670. doi:10.1097/01.WCB.0000067721.64998.F5

Jahng, G-H., Li, K-L., Ostergaard, L., and Calamante, F. (2014). Perfusion magnetic resonance imaging: A comprehensive update on principles and techniques. *Korean J. Radiol.* 15 (5), 554–577. doi:10.3348/kjr.2014.15.5.554

Joshi, A. A., Choi, S., Liu, Y., Chong, M., Sonkar, G., Gonzalez-Martinez, J., et al. (2022). A hybrid high-resolution anatomical MRI atlas with sub-parcellation of cortical gyri using resting fMRI. *J. Neurosci. Methods* 374, 109566. doi:10.1016/j.jneumeth.2022.109566

Kety, S. S., and Schmidt, C. F. (1948). The effects of altered arterial tensions of carbon dioxide and oxygen on cerebral blood flow and cerebral oxygen consumption of normal young men. *J. Clin. Invest.* 27 (4), 484–492. doi:10.1172/JCI101995

Knutsson, L., van Westen, D., Petersen, E. T., Bloch, K. M., Holtas, S., Stahlberg, F., et al. (2010). Absolute quantification of cerebral blood flow: Correlation between dynamic susceptibility contrast MRI and model-free arterial spin labeling. *Magn. Reson Imaging* 28 (1), 1–7. doi:10.1016/J.MRI.2009.06.006

Liu, P., De Vis, J. B., and Lu, H. (2019). Cerebrovascular reactivity (CVR) MRI with CO2 challenge: A technical review. *Neuroimage* 187, 104–115. doi:10.1016/J.NEUROIMAGE.2018.03.047

Liu, P., De Vis, J. B., and Lu, H. (2019). Cerebrovascular reactivity (CVR) MRI with CO2 challenge: A technical review. *Neuroimage* 187, 104–115. doi:10.1016/j.neuroimage.2018.03.047

Lu, H., Clingman, C., Golay, X., and Van Zijl, P. C. M. (2004). Determining the longitudinal relaxation time (T1) of blood at 3.0 Tesla. *Magn. Reson Med.* 52 (3), 679–682. doi:10.1002/MRM.20178

Ma, C., Jensen, M. M., Smets, B. F., and Thamdrup, B. (2017). Pathways and controls of N2O production in nitritation-anammox biomass. *Environ. Sci. Technol.* 51 (16), 8981–8991. doi:10.1021/acs.est.7b01225

MacDonald, M. E., Berman, A. J. L., Mazerolle, E. L., Williams, R. J., and Pike, G. B. (2018). Modeling hyperoxia-induced BOLD signal dynamics to estimate cerebral blood flow, volume and mean transit time. *Neuroimage* 178, 461–474. doi:10.1016/j.neuroimage.2018.05.066

Meier, P., and Zierler, K. L. (1954). On the theory of the indicator-dilution method for measurement of blood flow and volume. *J. Appl. Physiol.* 6 (12), 731–744. doi:10.1152/jappl.1954.6.12.731

Østergaard, L. (2005). Principles of cerebral perfusion imaging by bolus tracking. *J. Magn. Reson Imaging* 22 (6), 710–717. doi:10.1002/JMRI.20460

Østergaard, L., Weisskoff, R. M., Chesler, D. A., Gyldensted, G., and Rosen, B. R. (1996). High resolution measurement of cerebral blood flow using intravascular tracer bolus passages. Part I: Mathematical approach and statistical analysis. *Magn. Reson Med.* 36 (5), 715–725. doi:10.1002/MRM.1910360510

Poublanc, J., Crawley, A. P., Sobczyk, O., Montandon, G., Sam, K., Mandell, D. M., et al. (2015). Measuring cerebrovascular reactivity: The dynamic response to a step hypercapnic stimulus. *J. Cereb. Blood Flow. Metab.* 35 (11), 1746–1756. doi:10.1038/jcbfm.2015.114

Poublanc, J., Han, J. S., Mandell, D. M., Conklin, J., Stainsby, J. A., Fisher, J. A., et al. (2013). Vascular steal explains early paradoxical blood oxygen level-dependent cerebrovascular response in brain regions with delayed arterial transit times. *Cerebrovasc. Dis. Extra* 3 (1), 55–64. doi:10.1159/000348841

Poublanc, J., Sobczyk, O., Shafi, R., Sayin, E. S., Schulman, J., Duffin, J., et al. (2021). Perfusion MRI using endogenous deoxyhemoglobin as a contrast agent: Preliminary data. *Magn. Reson Med.* 86 (6), 3012–3021. doi:10.1002/MRM.28974

Schlaudecker, J., and Bernheisel, C. (2009). Gadolinium-associated nephrogenic systemic fibrosis. *Am. Fam. Physician* 80 (7), 711–714. Available at: https://pubmed.ncbi.nlm.nih.gov/19817341/ (Accessed January 18, 2022).

Schulman, J., Sayin, E. S., Manalac, A., Poublanc, J., Sobczyk, O., Duffin, J., et al. (2022). Perfusion quantification in the human brain using DSC MRI – simulations and validations at 3T. *bioRxiv*. doi:10.1101/2022.04.27.489686

Slessarev, M., Han, J., Mardimae, A., Prisman, E., Preiss, D., Volgyesi, G., et al. (2007). Prospective targeting and control of end-tidal CO2 and O2 concentrations. *J. Physiol.* 581, 1207–1219. doi:10.1113/jphysiol.2007.129395

Spann, S. M., Kazimierski, K. S., Aigner, C. S., Kraiger, M., Bredies, K., Stollberger, R., et al. (2017). Spatio-temporal TGV denoising for ASL perfusion imaging. *Neuroimage* 157, 81–96. doi:10.1016/j.neuroimage.2017.05.054

Stewart, G. N. (1893). Researches on the circulation time in organs and on the influences which affect it: Parts I.-III. *J. Physiol.* 15 (1-2), 1–89. doi:10.1113/jphysiol.1893.sp000462

Stokes, A. M., Bergamino, M., Alhilali, L., Hu, L. S., Karis, J. P., Baxter, L. C., et al. (2021). Evaluation of single bolus, dual-echo dynamic susceptibility contrast MRI protocols in brain tumor patients. *J. Cereb. Blood Flow. Metab.* 41 (12), 3378–3390. doi:10.1177/0271678X211039597

Strickler, S. E., and Clark, K. R. (2021). Gadolinium deposition: A study review. *Radiol. Technol.* 92 (3), 249–258. Available at: http://www.ncbi.nlm.nih.gov/pubmed/33472877.

Thompson, M. T. (2014). *Intuitive analog circuit design*. 2nd ed. Oxford: Newnes. doi:10.1016/C2012-0-03027-X

Tudorica, A., Fang Li, H., Hospod, F., Delucia-Deranja, E., Huang, W., Patlak, C. S., et al. (2002). Cerebral blood volume measurements by rapid contrast infusion andT2*-weighted echo planar MRI. *Magn. Reson Med.* 47 (6), 1145–1157. doi:10.1002/mrm.10167

Vu, C., Chai, Y., Coloigner, J., Nederveen, A. J., Borzage, M., Bush, A., et al. (2021). Quantitative perfusion mapping with induced transient hypoxia using BOLD MRI. *Magn. Reson Med.* 85 (1), 168–181. doi:10.1002/mrm.28422

Wymer, D. T., Patel, K. P., Burke, W. F., and Bhatia, V. K. (2020). Phase-contrast MRI: Physics, techniques, and clinical applications. *Radiographics* 40 (1), 122–140. doi:10.1148/RG.2020190039

frontiers | Frontiers in Physiology

TYPE Original Research
PUBLISHED 15 February 2023
DOI 10.3389/fphys.2023.1134804

OPEN ACCESS

EDITED BY
James Duffin,
University of Toronto, Canada

REVIEWED BY
Toshihiko Aso,
RIKEN Center for Biosystems Dynamics Research, Japan
Ali Golestani,
University of Calgary, Canada

*CORRESPONDENCE
Yunjie Tong,
tong61@purdue.edu

†These authors have contributed equally to this work and share first authorship

SPECIALTY SECTION
This article was submitted to Vascular Physiology, a section of the journal Frontiers in Physiology

RECEIVED 30 December 2022
ACCEPTED 01 February 2023
PUBLISHED 15 February 2023

CITATION
Fitzgerald B, Yao J, Hocke LM, Frederick BB, van Niftrik CHB and Tong Y (2023), Using carpet plots to analyze blood transit times in the brain during hypercapnic challenge magnetic resonance imaging.
Front. Physiol. 14:1134804.
doi: 10.3389/fphys.2023.1134804

Using carpet plots to analyze blood transit times in the brain during hypercapnic challenge magnetic resonance imaging

Bradley Fitzgerald[1†], Jinxia Fiona Yao[2†], Lia M. Hocke[3,4], Blaise deB. Frederick[3,4], Christiaan Hendrik Bas van Niftrik[5] and Yunjie Tong[2*]

[1]Elmore Family School of Electrical and Computer Engineering, Purdue University, West Lafayette, IN, United States, [2]Weldon School of Biomedical Engineering, Purdue University, West Lafayette, IN, United States, [3]McLean Imaging Center, McLean Hospital, Belmont, MA, United States, [4]Department of Psychiatry, Harvard Medical School, Boston, MA, , United States, [5]Department of Neurosurgery, University Hospital Zurich, Zurich, Switzerland

Blood arrival time and blood transit time are useful metrics in characterizing hemodynamic behaviors in the brain. Functional magnetic resonance imaging in combination with a hypercapnic challenge has been proposed as a non-invasive imaging tool to determine blood arrival time and replace dynamic susceptibility contrast (DSC) magnetic resonance imaging, a current gold-standard imaging tool with the downsides of invasiveness and limited repeatability. Using a hypercapnic challenge, blood arrival times can be computed by cross-correlating the administered CO_2 signal with the fMRI signal, which increases during elevated CO_2 due to vasodilation. However, whole-brain transit times derived from this method can be significantly longer than the known cerebral transit time for healthy subjects (nearing 20 s vs. the expected 5–6 s). To address this unrealistic measurement, we here propose a novel carpet plot-based method to compute improved blood transit times derived from hypercapnic blood oxygen level dependent fMRI, demonstrating that the method reduces estimated blood transit times to an average of 5.32 s. We also investigate the use of hypercapnic fMRI with cross-correlation to compute the venous blood arrival times in healthy subjects and compare the computed delay maps with DSC-MRI time to peak maps using the structural similarity index measure (SSIM). The strongest delay differences between the two methods, indicated by low structural similarity index measure, were found in areas of deep white matter and the periventricular region. SSIM measures throughout the remainder of the brain reflected a similar arrival sequence derived from the two methods despite the exaggerated spread of voxel delays computed using CO_2 fMRI.

KEYWORDS

carpet plot, hypercapnia fMRI, cerebral transit time, dynamic susceptibility contrast imaging, structural similarity index

Abbreviations: BOLD, blood oxygen level dependent; CBF, cerebral blood flow; CSF, cerebrospinal fluid; DSC, dynamic susceptibility contrast; fMRI, functional magnetic resonance imaging; GM, gray matter; MCCC, maximum cross-correlation coefficient; MRI, magnetic resonance imaging; $P_{ET}CO_2$, partial pressure end-tidal CO_2; SSIM, structural similarity index measure; TTP, time to peak; WM, white matter.

1 Introduction

Measurements related to blood arrival time throughout the brain represent important hemodynamic metrics in several contexts. Arrival time measurements are useful in characterizing cerebral hemodynamic behavior in patients; examples include the demonstration of prolonged blood arrival time in patients with multiple sclerosis (Paling et al., 2014), internal carotid artery occlusion (Bokkers et al., 2008), Moyamoya (Donahue et al., 2016), and stroke (Chalela et al., 2000; Macintosh et al., 2010). Additionally, computation of accurate blood arrival times is a key step in computing cerebral vascular reactivity (Niftrik et al., 2017; Yao et al., 2021) and is an important factor to consider when analyzing collateral perfusion (Zaharchuk et al., 2011). Further, blood transit time (the time taken for blood to pass through a region or whole of the brain) can be derived from arrival time measurements. Transit time can serve as a benchmark for evaluating the quality of region-specific (or voxel-wise) arrival time measurements, as the metric can be easily compared with known whole-brain blood transit times. Thus, the development of reliable, safe, and repeatable techniques for measuring cerebral blood arrival times and the associated cerebral blood transit times is important for the continued development of our understanding of blood dynamics in the brain.

Dynamic susceptibility contrast (DSC) imaging is frequently used to study magnetic resonance imaging (MRI) brain perfusion by imaging the first pass of an intravenously injected gadolinium-based contrast agent through the brain (Lentschig et al., 1998). DSC-MRI is a reliable reference standard for blood flow-related measurements, including transit time. However, it is a an invasive imaging technique and the side-effects of gadolinium-based agents remaining in the human body are still debatable (Essig et al., 2013), highlighting the need for a safer and more convenient alternative. Several different alternative methods for measurement of hemodynamic metrics, based on blood oxygen level dependent (BOLD) MRI, have been proposed (Aso et al., 2020; Bhogal et al., 2022; Sayin et al., 2022). Recently, an increasing number of studies have used elevated CO_2 levels as a regressor to estimate the CO_2/blood arrival time *via* BOLD MRI (Blockley et al., 2011; Thomas et al., 2013a; Duffin et al., 2015; Donahue et al., 2016). It is known that CO_2 is a vasodilator, meaning that elevated CO_2 arriving to a region of the brain can cause an increase in regional blood flow and volume, resulting in increased BOLD signals. Thus, blood flow can be observed by tracking the passage of the CO_2 throughout the brain. BOLD-CO_2 MRI offers advantages over DSC-MRI as a blood-tracking method, since CO_2-MRI is a non-invasive technique and there are no adverse side-effects of inhaling elevated CO_2 within a suitable range.

For CO_2-MRI, a voxel's estimated CO_2/blood arrival time is commonly represented by the time delay corresponding to maximum cross-correlation coefficient (MCCC) between the voxel's BOLD signal and the partial pressure of end-tidal CO_2 concentration ($P_{ET}CO_2$) measurement (Blockley et al., 2011; Poublanc et al., 2013; Niftrik et al., 2017). However, this delay time often overestimates the true CO_2 arrival time, leading to overestimation in whole-brain blood transit time assessment. This overestimation is a result of the brain's varying hemodynamic response to CO_2, as different brain regions differ in the time taken for local tissues to respond the arrival of the increased CO_2, leading to various shapes of the BOLD signal waveform deformations from the $P_{ET}CO_2$ measurement (Duffin et al., 2015; Golestani et al., 2015; Poublanc et al., 2015; Prokopiou et al., 2019). Hence the cross-correlation time delay from the deformed BOLD signal does not purely reflect the signal onset (i.e., CO_2 arrival time), but is also influenced by the CO_2 hemodynamic response of the brain region. Simulations from a previous study showed that performing cross-correlation of the measured CO_2 with various shapes of the BOLD signal waveform with a shared breakpoint (representing the same moment of CO_2 arrivals) from the baseline can obtain different delay time values when the true delay should be equivalent (Yao et al., 2021). Depending on the extent of the distortion of the BOLD waveform from the CO_2 measurement, one can obtain a delay time offset as large as 20 s (Yao et al., 2021). One study of 25 healthy subjects reported that the estimated arterial CO_2 arrival times derived from the maximum cross-correlation method can have an average span of 20.1 s across the whole brain, with a span of 15.9 s for gray matter (GM) and 25.5 s for white matter (WM) (Niftrik et al., 2017), which is inconsistent with the fact that the whole-brain blood transit time is approximately 5–6 s on average (Hoffmann et al., 2000).

Thus, it is important to evaluate the effects of these signal deformations on the accuracy of the CO_2-derived delay maps. This evaluation can be discussed through two different perspectives: first, the accuracy of the specific voxel-wise CO_2-derived delay time values can be evaluated. Second, ordering of the voxels throughout the brain based on CO_2-derived delay time values suggests a sequence of voxels corresponding to the arrival paths of the CO_2 "bolus". This sequence of voxels can also be evaluated for accuracy separately from evaluation of the delay values themselves. The use of a carpet plot to analyze CO_2-MRI data holds potential to assist with better understanding this issue of widely spread CO_2-derived delay times computed *via* the MCCC method.

A carpet plot is a 2-dimensional voxel vs. time matrix showing BOLD signal intensities, which was initially used within MRI-related studies for assessing quality of MRI signals (especially for the detection of motion artifacts) (Power, 2017). We previously made use of carpet plots for calculating the time taken for blood to pass through the brain (i.e., transit time) by ordering voxels according to delays (based on the low frequency oscillation signal delay time relative to the global averaged signal) computed using resting-state functional MRI (rs-fMRI) signals (Fitzgerald et al., 2021). The derived blood transit time from reconstructed resting-state carpet plots was shown to be comparable with that from DSC-MRI carpet plots. The same methodology can be applied to CO_2-MRI data to create CO_2-based carpet plots, in which observable signal patterns could prove useful in assessing the impact of distorted BOLD signals (caused by variations in reactivity to CO_2 throughout the brain) on the assigned venous blood/CO_2 arrival times, as well as in computing brain blood transit times using CO_2-MRI data.

In this follow-up study, we apply this novel methodology to construct sorted carpet plots from CO_2-challenge BOLD fMRI data. The purpose of this study is twofold: first, we use observed patterns in these carpet plots to group voxels based on their assigned CO_2-derived delay times and demonstrate improved estimates of the blood transit time (through the majority of the brain) which are

closer to the expected transit time values than those implied by the wide distribution of delay times computed from the cross-correlation method. Second, we aim to provide an analysis of the similarity between voxel-wise delay maps derived from CO_2-MRI and from DSC-MRI. To this end, we use the carpet plot voxel groupings to examine how the delay times computed from the two methods compare using the "structure" element of the structural similarity index measure (SSIM) (Zhou et al., 2004). In addition, we examine patterns in the BOLD signal of voxels within these groups to move towards an understanding of how varying reactivity affects the sequential ordering of assigned CO_2 delay times throughout the brain.

We acknowledge that conditions of brain perfusion differ between DSC-MRI and CO_2-MRI; here we simply aim to investigate whether similar perfusion information (i.e., blood transit time) can be derived from CO_2-MRI by utilizing our novel carpet plot methodology to tease out the confounding effects induced by the CO_2 challenge. Such analysis helps to evaluate the possibility of using CO_2-MRI as an alternative to DSC-MRI in the measurement of the blood transit time.

2 Materials and methods

2.1 Data acquisition

The Institutional Review Boards (IRB) of the institutions at which datasets were collected (McLean Hospital for DSC-MRI, Purdue University for CO_2 challenge MRI) approved all experimental protocols used in this study. All experiments followed the ethical principles of the Belmont Report, and all subjects provided written informed consent. DSC-MRI data from eight healthy subjects (1F, 7M, mean ± s.d., 33 ± 12 years) were acquired using a Siemens TIM Trio 3T scanner (Siemens Medical Solutions, Malvern, PA) with 32-channel phased array head matrix coil. A gadolinium contrast agent was given by intravenous injection for the DSC-MRI scans (TR/TE = 1510/21 m, voxel size = 1.8 × 1.8 × 3.5 mm^3, duration = 180 s). Detailed acquisition information for DSC-MRI can be found in a previous publication by Tong et al. (2017).

CO_2 challenge data was collected from a separate set of eleven subjects (5F, 6M, age ±s.d., 22.7 ± 4.4 years; three female subjects were excluded due to dropouts and/or poor quality of data) using a 3T GE Discovery MR750 MR scanner. Two out of the eight remaining participants (Subjects 1 and 2, scanned during the protocol testing phase before parameters were adjusted for the remaining subjects) underwent fMRI scanning with the following parameters: (TR/TE = 800/30 ms, voxel size = 3.75 × 3.75 × 2.5 mm^3, duration = 600 s). The remaining participants (Subjects 3–8) were scanned with the following parameters: (TR/TE = 1000/30 ms, voxel size = 3 × 3 × 3 mm^3, duration = 600 s). The elevated CO_2 challenge was controlled by a programmable computer-based gas delivery system (RespirAct, Thornhill Research Inc., Toronto, Canada) (Fisher, 2016). Each subject was fitted with a plastic face mask (covering the nose and the mouth) connected with a breathing circuit before entering the MRI scanner room. The breathing protocol consisted of 2 minutes of the "baseline" CO_2 level (i.e., the resting CO_2 level), followed by 2 minutes of elevated (10 mmHg higher than baseline) CO_2, 2 minutes of baseline CO_2, 2 minutes of elevated CO_2, and two final minutes of baseline CO_2. The system controlled and recorded the end-tidal partial pressure of CO_2 ($P_{ET}CO_2$) time series.

2.2 Data preprocessing

Data were preprocessed using the FMRIB Software Library (FSL, Oxford University, United Kingdom, v5.0 for DSC-MRI data, v6.0 for the CO_2-MRI data, https://fsl.fmrib.ox.ac.uk/fsl/fslwiki) (Jenkinson et al., 2012). Preprocessing included motion correction, slice-time correction, brain extraction, and spatial smoothing (3 mm for DSC-MRI scans, 5 mm for CO_2-MRI scan).

2.3 Constructing DSC delay maps

Gadolinium bolus delay maps were created for each DSC-MRI subject, where delay values represent the time-of-arrival of the gadolinium bolus in each brain voxel (see Figure 1). This voxel-specific delay is represented by the time to peak (TTP), which is computed as the time between initial injection until the maximum dip of the DSC signal loss. TTP was chosen over T0 (interval between injection and its first detection) because the peak can be easily and more accurately identified than the detection of the first arrival. TTP was calculated by the program Perfx using a gamma function fitting with temporal interpolation (developed by Chris Rorden, www.mccauslandcenter.sc.edu/CRNL/tools/pwi). After interpolation, the temporal resolution of DSC-MRI data for TTP was 0.0001 s.

2.4 Constructing CO_2 delay maps

CO_2 delay maps were computed using MATLAB (version R2017b or later, www.mathworks.com/). The brain-masked fMRI data was then arranged into a 2D matrix, where each row contains the measured BOLD time series for a voxel. Each voxel time series was detrended (MATLAB *detrend*) and normalized by dividing by the standard deviation of the time series. The global average time series was computed, detrended and normalized in the same way. For each voxel, the time series was oversampled by a factor of 10 (MATLAB *interpft*) to improve the temporal resolution. For the CO_2 delay map calculation, the time series was filtered using a fourth-order Butterworth bandpass filter with bandwidth 0.001–0.02 Hz to extract the very low frequency oscillations associated with CO_2-dependent fluctuations in the BOLD signal. The filtered time series was then compared with the global average time series (also oversampled by the same factor and filtered into the same frequency band) *via* cross-correlation, and the shifting-index which produced the maximum absolute correlation value between the two signals was recorded as the "delay" value for that voxel. We note that the use of the maximum absolute correlation allowed some voxel delays to be associated with a negative correlation, which is discussed in more detail in the Discussion section. Full-brain CO_2 delay maps for each subject were computed using this method. These delay maps were then

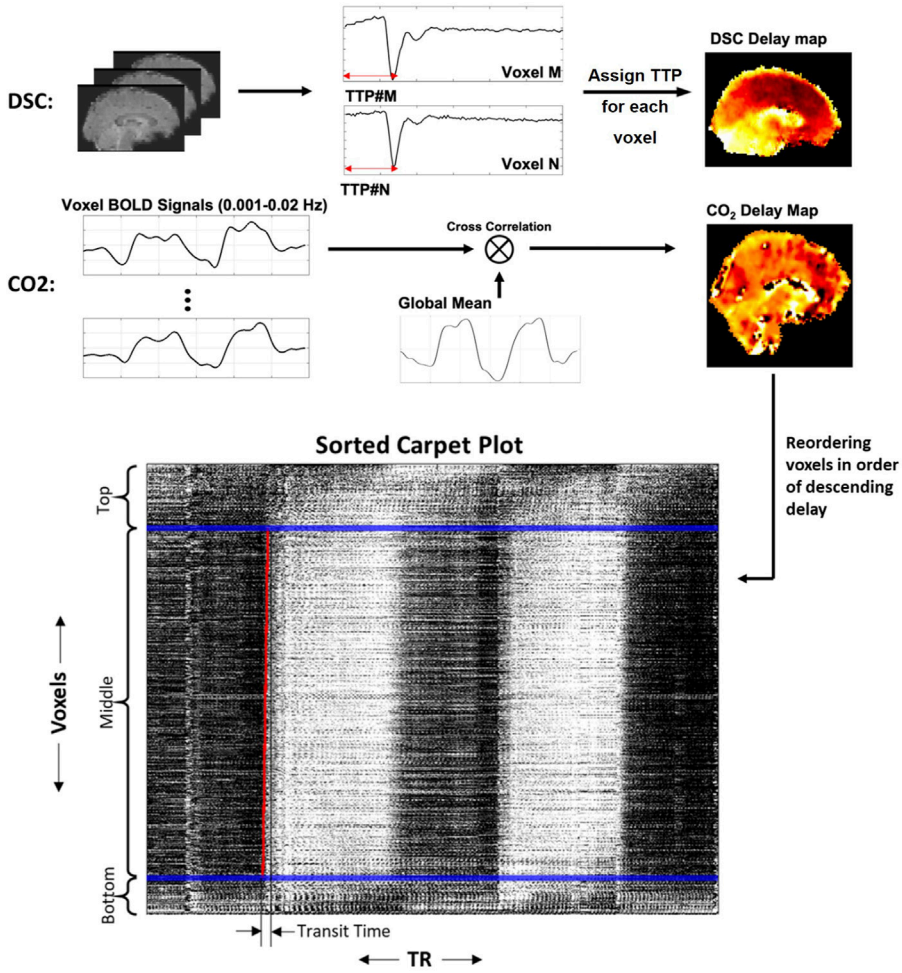

FIGURE 1
Methods for creating DSC delay maps, CO_2 delay maps and carpet plots. DSC delay maps were created by computing the voxel-wise time to peak (TTP) metric, representing the delay until peak signal decrease was obtained, which corresponds to the arrival of the gadolinium bolus in a given voxel. CO_2 delay maps were computed by performing voxel-wise cross-correlation between individual voxel time series and the global averaged time series and selecting the delay value which resulted in maximum absolute correlation. Voxels were then sorted in descending order according to the computed delay values, and the 2D carpet plot image was created by displaying the time series of all brain voxels in this sorted order (top representing largest delay, bottom representing smallest delay).

registered to a standard template space (Fonov et al., 2009), temporally aligned by subtracting the mean delay values, and averaged to produce a subject-averaged CO_2 delay map.

2.5 Constructing CO_2 carpet plots

The rows of the fMRI data matrix (where rows are voxels and columns are time points) were reordered based on descending delay values (see Figure 1; longest delay voxels at top of image, shortest delay values at bottom of image), creating a sorted carpet plot. Visual inspection of this carpet plots demonstrates that most voxel time series in the center of the image form a linear edge, while a portion of voxel time series at the top and bottom of the image (representing voxels with comparatively high or low delays, respectively) do not follow this linear edge trend. This observation is relevant because it has been shown that carpet plots constructed from DSC-MRI data yield a near-linear blood-arrival edge covering nearly all voxels (above 95%) in the brain with reasonable associated transit times (Fitzgerald et al., 2021). Using DSC-MRI as a reference standard, this suggests that isolating voxels in the CO_2 carpet plot which follow this linear trend may be useful in computing better estimates of the blood transit time. To this end, each carpet plot was divided into three vertical sections. These sections were created by defining the middle section such that it contained all voxels with delays inside a 20-s window centered at the median delay time (see window edges defined by blue lines in Figures 1, 2). The width of this window was chosen based on empirical results with visual confirmation, which suggested that such a window size served as a conservative but reliable method that could be applied consistently across all subjects to isolate those voxels which followed the linear edge trend. A brief further discussion of this window, the effect of varying its width, and testing of a subject-specific adaptive window width is presented in the Supplementary Section S1.

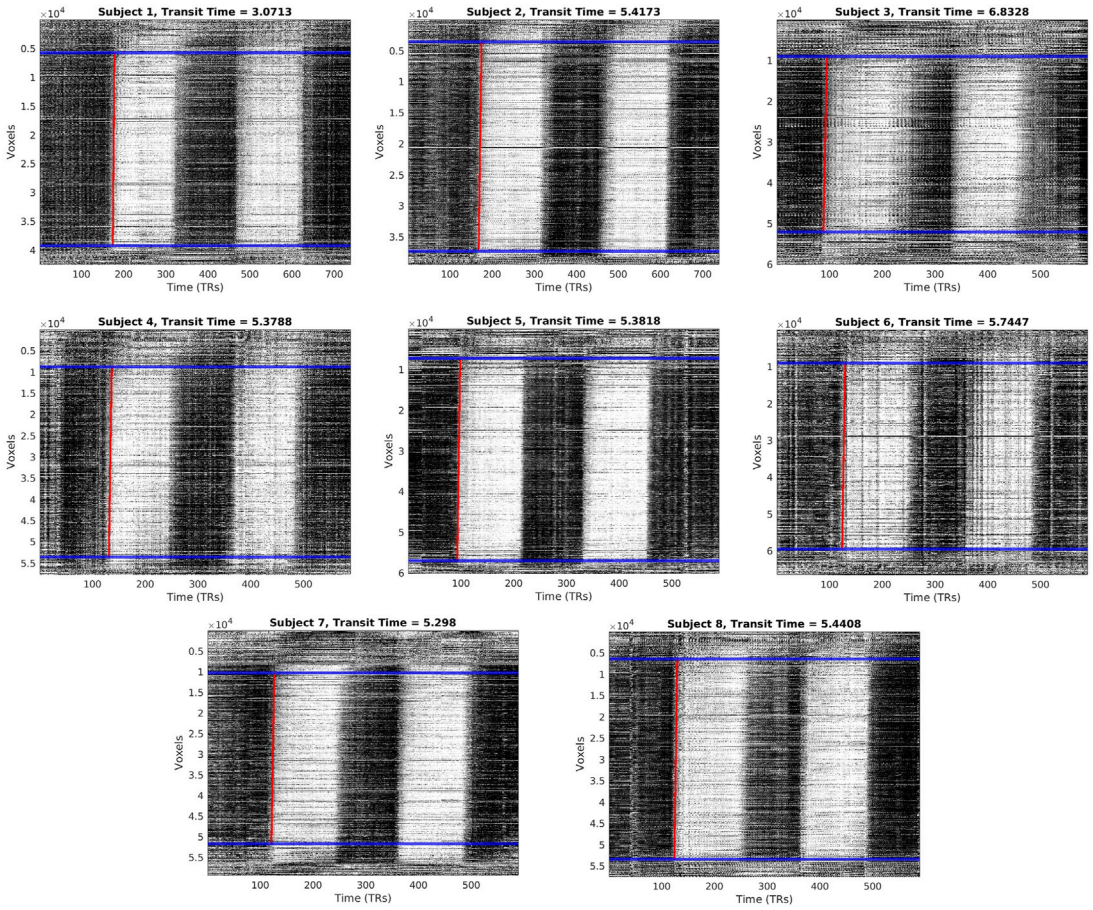

FIGURE 2
Carpet plots and transit times for each CO_2 subject. Blue lines indicate boundaries for image cropping before edge detection. Red lines indicate the computed edge associated with the arrival of the CO_2 bolus.

2.6 Carpet plot analysis

A slope detection program, introduced and discussed in our previous study (Fitzgerald et al., 2021), was used to detect and fit a linear line to the first CO_2-arrival edge present in the middle section of the CO_2 carpet plot, illustrated as a red line in Figure 1. Details regarding this slope detection program can be found in the previous publication (Fitzgerald et al., 2021); to summarize, the program estimates the linear edge present by fitting a linear trend line to a set of data points, where the data points represent the horizontal (time) point of maximum increase (i.e., maximum derivative). As such, the detected linear edge reflects the time of maximum CO_2-induced BOLD signal increase. One adjustment to the described program was made: voxel time series within the sorted carpet plot were first frequency filtered (0.001–0.02 Hz) in order to capture the signal variation resulting from CO_2 arrival while removing the variation resulting from low frequency oscillations (0.01–0.1 Hz) present in rs-fMRI data. After computation, a nearly vertical edge that is tilted slightly to the right can be observed due to the flow over time of the CO_2-arrival-based BOLD signal rise throughout the brain. The horizontal (time) duration of this estimated edge line was recorded as the transit time (i.e., time taken for CO_2 bolus to traverse all voxels present in the cropped carpet plot). Only transit times for the first carpet plot edge, corresponding to the first CO_2 bolus given, is reported here. This choice was made in order to avoid unknown complications arising from any residual effects of the first CO_2 bolus which might affect blood flow behavior during the second CO_2 bolus (see Supplementary Figure S2 for transit times of the second edge).

As discussed in the introduction, it has been shown that CO_2-derived delay times computed *via* the cross-correlation method can be skewed by varying responses of the brain to the CO_2 bolus arrival, with a primary issue being that the overall spread of delay times throughout all voxels can extend far beyond the expected time it takes for blood to flow through the whole brain (around 5–6 s) (Hoffmann et al., 2000). To further investigate this issue, we examine whether the shape of the voxel BOLD time series was associated with that voxel's assigned cross-correlation delay time (and thus the voxel's vertical location in the carpet plot). Voxel time series from the top, middle, and bottom portions of the carpet plot were averaged using two methods: first using the original, unfiltered voxel time series, and second where each individual time series was detrended, divided by the time series standard deviation, and frequency filtered (0.001–0.02 Hz). Finally, we more closely observe

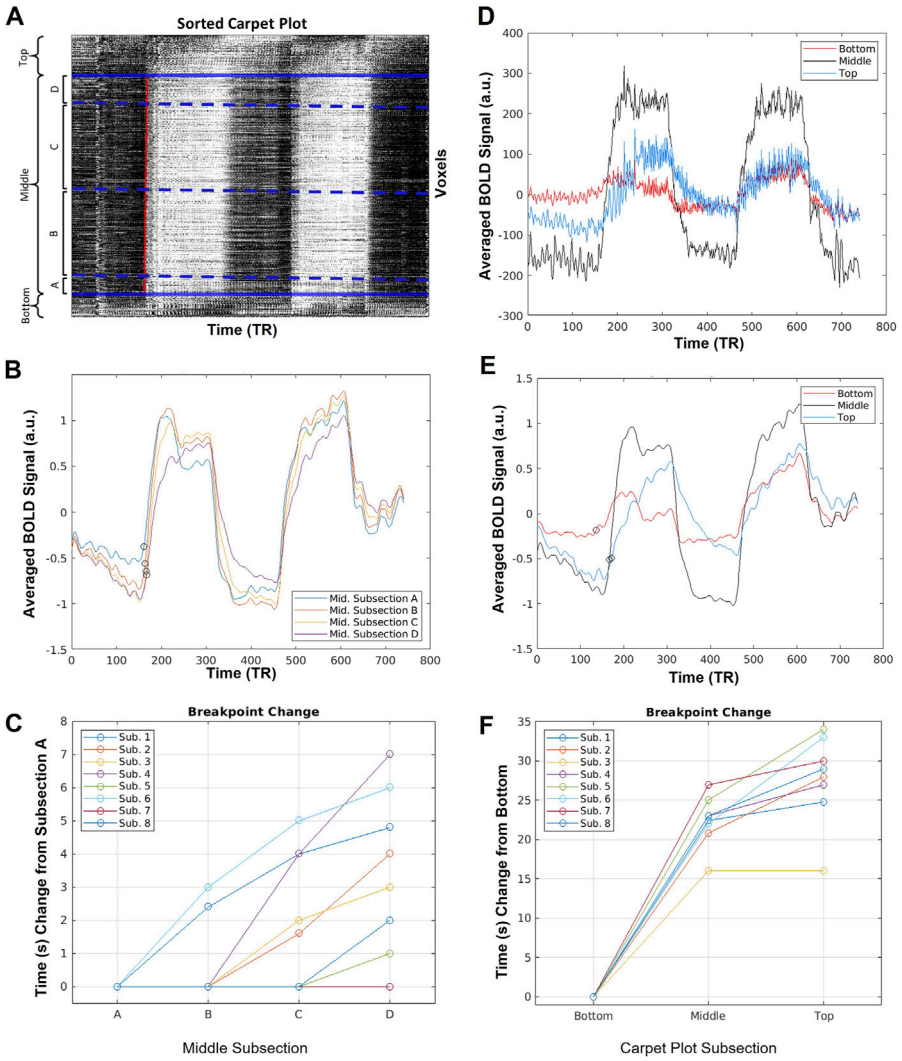

FIGURE 3
Sample averaged time series computed during carpet plot analysis. **(A)** Display of example sorted carpet plot, where the red line represents the edge computed during edge detection applied to the cropped carpet plot. Solid blue lines indicate the boundary of regions removed before edge detection, and divide the carpet plot into the "top", "middle", and "bottom" regions, as labeled. Dotted blue lines indicate boundaries for four subsections, (A–D), of the middle region; these subsections are defined by grouping voxels with assigned delay times falling within four 5-s windows (a division, into four groups, of the 20-s span of delays assigned to voxels in the middle section). **(B)** Display of the averaged time series of voxels in each middle subsection after normalization (detrending and dividing by standard deviation) of each individual voxel time series. Circles mark estimates of the time series breakpoints. **(C)** Plot of change in estimated breakpoint between middle subsection averaged time series. Plotted times indicate change relative to the estimated breakpoint of subsection A. **(D)** Display of the averaged time series of voxels from the top, middle, and bottom sections of the carpet plot without normalization of the time series. **(E)** Display of the averaged time series of voxels from the top, middle, and bottom sections of the carpet plot after normalization (detrending and dividing by standard deviation) of each time series. Circles mark estimates of the time series breakpoints. **(F)** Plot of change in estimated breakpoint between bottom, middle, and top carpet plot averaged time series. Plotted times indicate change relative to the estimated breakpoint of the bottom section.

the time series of voxels in the middle of the carpet plot by dividing it into four stacked subsections, each section representing voxels grouped into 5-s windows based on their assigned delay time (recall that the characterization of the middle section is based on voxels which are assigned delay times within a 20-s window; see Figure 3 for visualization). These four subsections will be referred to as middle subsections A through D (from lowest to highest delay grouping). Voxel time series within each middle subsection were averaged (see example displayed in Figure 3) after normalization and frequency filtering. To compare the relative signal to noise ratio between carpet plot sections, roughly reflected in the magnitude of CO_2-induced signal increase, the standard deviations of the bottom, middle, and top averaged time series (without filtering and normalization—see Figure 3D) were computed and compared using a Wilcoxon signed rank test with Bonferroni correction for multiple comparisons.

For the averaged time series of the top, middle, and bottom carpet plot regions, as well as that of each middle subsection, the

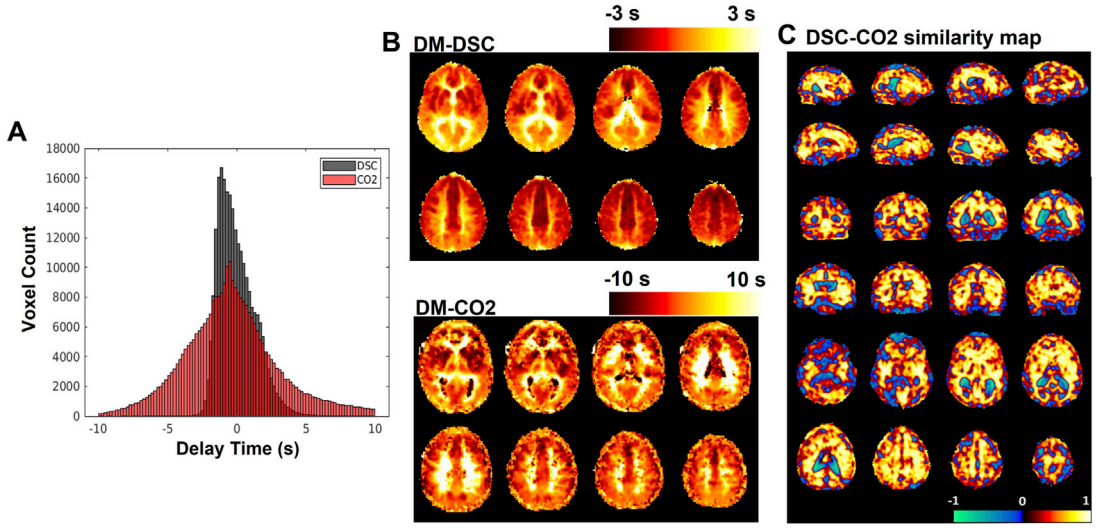

FIGURE 4
(A) Histograms of delay maps computed from DSC-MRI and CO_2-challenge fMRI. **(B)** Sample slices of subject-averaged DSC-MRI and CO_2-fMRI delay maps. **(C)** SSIM map displaying local (per-voxel) structural similarity *s* values comparing subject-averaged DSC bolus arrival delay map with the subject-averaged original CO_2 arrival delay map. The structural similarity metric *s* can be interpreted similarly to Pearson's correlation coefficient; values range from −1 to 1, where high positive values indicate higher structural similarity, lower negative values indicate inverted structural similarity, and values near zero represent little similarity.

breakpoint (i.e. time point when the time series signal begins to increase, or break from the baseline level, in correspondence with the arrival of the CO_2 bolus) was estimated following a procedure similar to that proposed by Niftrik et al. (2017). First, an estimate of the breakpoint of the whole-brain averaged time series was computed based on the start time of the measured $P_{ET}CO_2$ signal increase (see Supplementary Section S3 for details). Then, for a given averaged time series from a carpet plot section, the baseline signal level was computed as the average signal intensity during 1 minute before the estimated whole-brain breakpoint. The peak signal intensity (i.e. the signal intensity during the second minute of the first bolus of elevated CO_2) was estimated as the average signal intensity of the 1-min time span beginning 1 minute after the estimated whole-brain breakpoint. The breakpoint of the given time series was then computed as the time index when the time series first increased by 10% of the difference between the baseline and peak signal levels. The 10% breakpoint threshold was demonstrated by Niftrik et al. (2017) and is necessary to ensure that the computed time point reflects CO_2-induced BOLD signal increase (as opposed to natural signal fluctuations). Breakpoint estimates are illustrated in Figure 3.

To investigate whether the top, middle, and bottom carpet plot regions were associated with particular brain regions, masks were created which specified which voxels commonly fell within each carpet plot section. These masks were computed by creating subject-specific section masks, registering these masks to the same standardized ICBM MNI-152 space (Kötter et al., 2001; Mazziotta et al., 2001), and keeping voxels which appeared in at least half of all subjects within the standardized space. In addition, subject-specific masks of voxels which showed little CO_2-induced signal change (marked by absolute MCCC below 0.3) were created and registered to the standardized space to analyze common locations of such voxels. The carpet plot locations (top, middle, or bottom section) of such voxels were also noted.

2.7 Similarity comparison using structural similarity index (SSIM)

We employed the structural similarity index measure (SSIM) to compare the similarity between the subject-averaged DSC-TTP map and the subject-averaged CO_2-MRI delay map (Figure 4C). Unlike other common similarity metrics which only provide a single value indicating the similarity as a global assessment (such as the Pearson correlation), the SSIM provides spatial similarity information by calculating local statistics (Zhou et al., 2004). The two subject-averaged DSC and CO_2 delay maps were demeaned and masked such that only voxels that existed in both delay maps were included. For 3D images, the SSIM algorithm utilizes a cubic window with a Gaussian weighting function to compute local image metrics during the computation, meaning that the program cannot compute an SSIM value for voxels near the brain edge if background voxels do not contain some value. To resolve this issue, which would cause the loss of a large number of edge voxels during the SSIM computation, we assigned the average delay value (i.e., zero) to all voxels containing no delay value (due to either being background voxels or the DSC-TTP program not returning a valid TTP delay, especially in ventricle regions). Note that while this choice can introduce bias to the structural similarity metric, the number of empty voxels inside the brain is very small and the choice to fill empty or edge voxels with the averaged delay value should minimize any introduced bias. The SSIM comparison was then conducted using the MATLAB

10.3389/fphys.2023.1134804

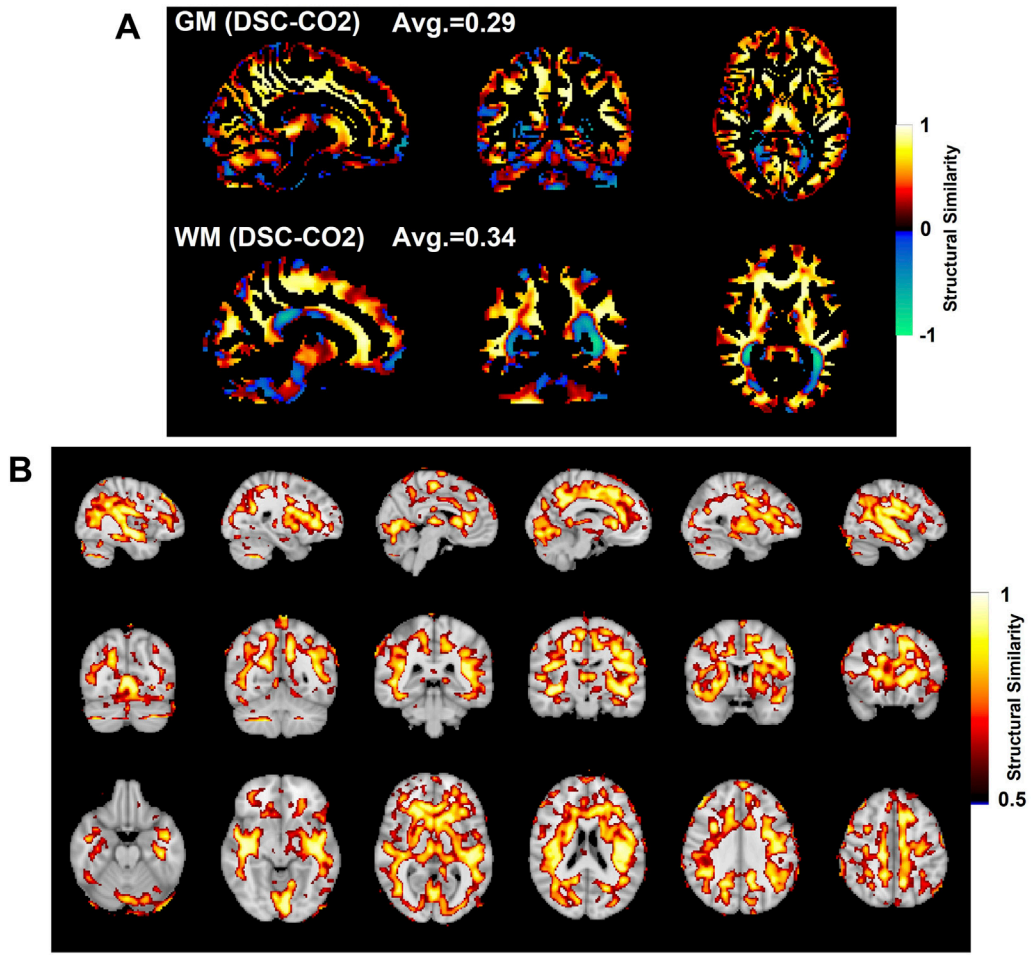

FIGURE 5
Comparison of SSIM values in gray matter (GM, top) and white matter (WM, bottom) shown in **(A)**. SSIM maps compare the subject-averaged DSC bolus arrival delay map with the subject-averaged CO_2 arrival delay map. Voxels with SSIM values greater than 0.5 are shown in **(B)**.

command *ssim*. After the SSIM computation, those voxels filled with average delay (zero) previously were masked out.

The SSIM program computes a voxel-wise similarity map, where the resulting voxel-specific index value is computed using data from a specified cubic window surrounding the voxel. The SSIM algorithm incorporates three computed measurements: luminance, contrast, and structure. For the purposes of this study, only the "structure" element of the SSIM was used (see Discussion for more details regarding this choice). The structure element s of two compared cubic windows x and y is computed as:

$$s(x,y) = \frac{\sigma_{xy} + c}{\sigma_x \sigma_y + c} \tag{1}$$

The parameters of Eq. 1 are computed as:

$$\mu_x = \sum_{i=1}^{N} w_i x_i \tag{2}$$

$$\sigma_x = \left(\sum_{i=1}^{N} w_i (x_i - \mu_x)^2 \right)^{1/2} \tag{3}$$

$$\sigma_{xy} = \sum_{i=1}^{N} w_i (x_i - \mu_x)(y_i - \mu_y) \tag{4}$$

where c is a stabilizing constant and w_i represents the weight assigned to the voxel according to the Gaussian weighting function (Zhou et al., 2004). The structure element is similar to a local estimate of Pearson's correlation coefficient between the two windows with the added adjustment of the Gaussian weighting function. For the remainder of this paper, references to "structural similarity" will refer to this structure element of the SSIM. The default window size and weighting settings were used, resulting in a window size of 11 × 11 × 11 voxels and standard deviation of the Gaussian weighting function as 1.5. This program returns a structural similarity voxel map with index values ranging from −1 to 1. Negative values indicate inverted structure between the two images surrounding a specific voxel (Zhou et al., 2004). A higher magnitude value indicates higher similarity between two images in the region within the filter window surrounding the voxel. A global average structural similarity value was computed by averaging the resulting values over all brain voxels.

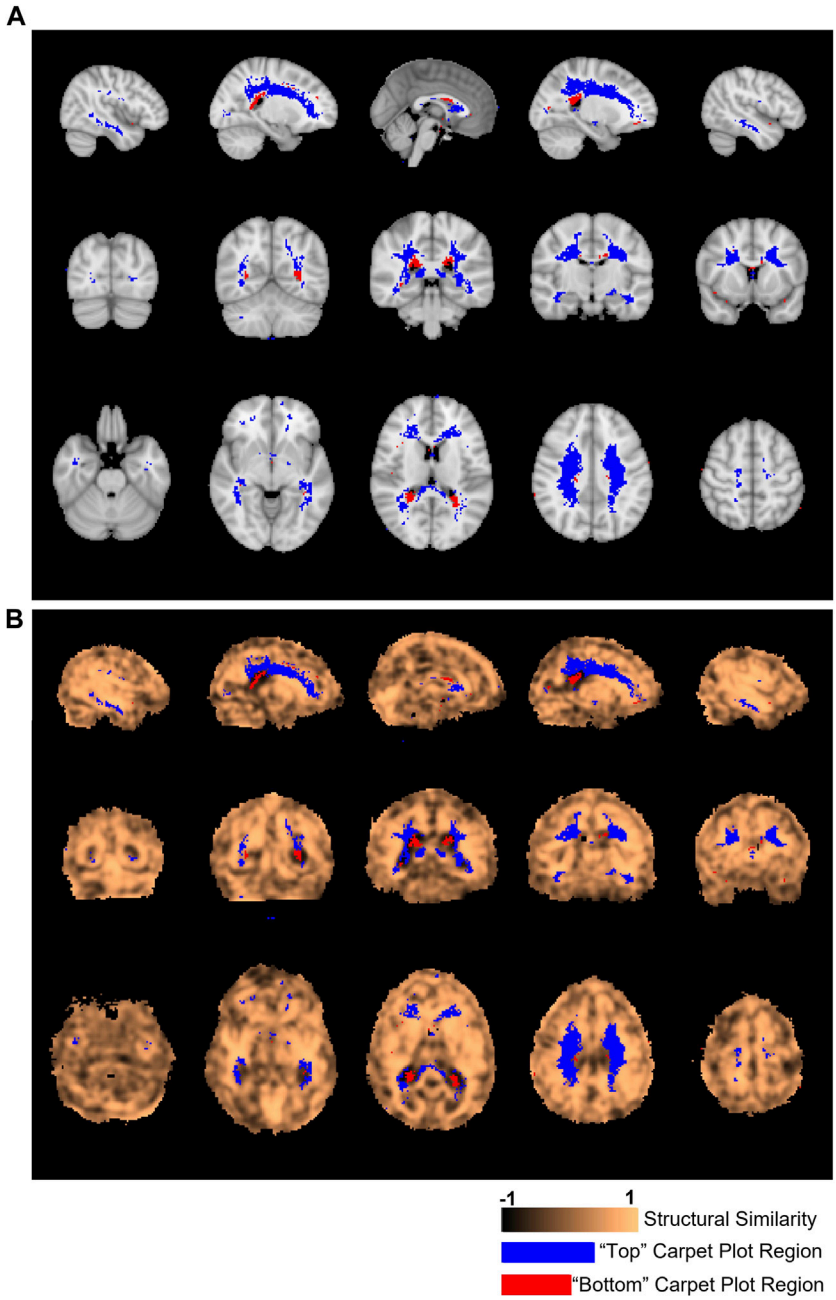

FIGURE 6
Locations of voxels located in top and bottom carpet plot regions and correspondence with structural similarity map. **(A)** Colored voxels indicate locations corresponding to voxels which were located in the top and bottom regions of CO_2 carpet plots in at least half of all subjects. Blue voxels correspond to those cropped from the top of the carpet plot (with extra long CO_2-derived delay times), while red voxels correspond to those cropped from the bottom of the carpet plot (with extra short CO_2-derived delay times). **(B)** The same cropped carpet plot voxels from **(A)** are overlaid on the structural similarity value map comparing the subject-averaged DSC-TTP delay map with the subject-averaged CO_2-arrival delay map.

Structural similarity values were averaged over GM regions and over WM regions, with these regions illustrated in Figure 5. In addition, structural similarity values were averaged over the previously detailed carpet plot section masks, which isolate the voxels which commonly belong to the top, middle, and bottom carpet plot regions. A comparison of the top and bottom carpet plot region masks with the computed structural similarity map is shown in Figure 6.

2.8 Statistical analysis

To evaluate the association between computed breakpoints and the carpet plot section from which the time series was derived, Wilcoxon signed rank tests with Bonferroni correction for multiple comparisons were performed comparing breakpoints from adjacent carpet plot sections. Wilcoxon rank sum tests (with Bonferroni correction when applicable) were applied to evaluate the differences

in SSIM values in the three sections (top, middle, and bottom) of a carpet plot and in the GM and WM regions.

3 Results

3.1 Transit times derived from CO_2 carpet plots

Carpet plots for all subjects are displayed in Figure 2. CO_2 bolus transit times were computed as the horizontal distance, measuring time, of the sloped carpet plot edge (displayed in red). The detected CO_2-arrival edges had transit times of 5.32±1.04 s (mean±s.d.). Dividing lines between the top, middle, and bottom carpet plot regions are shown in Figure 2 in blue. On average, the middle carpet plot section contained 77.8±5.4% of all voxels.

3.2 Carpet plot analysis results

Figure 3 displays sample results of the carpet plot analysis for one subject. Figure 3A illustrates the breakdown of the carpet plot into three regions—"top", "middle", and "bottom"—and illustrates the breakdown of the middle region into four smaller subgroups—middle subsections A, B, C, and D. We note that within the middle region, subsections B and C contain far more voxels than subsections A and D, since subgroups are groups of voxels with assigned delay times within a 5-s window. The distribution of delay times is primarily bell-shaped, meaning there are more voxels with assigned delay times close to the mean of the distribution. Figures 3B, D, E display the averaged time series of voxels for each grouping illustrated in (a) for the given sample subject. Figures displaying the same information in Figures 3B, D, E for all other subjects can be found in the Supplementary Figures S3–S5; the results derived from other subjects followed similar trends to those shown here.

Figures 3C, F illustrate the relationships between estimated breakpoints within the four middle subsections (C) and within the top, middle, and bottom carpet plot regions (F). These breakpoints represent an estimation of the true blood arrival time point for the voxel grouping, in contrast to the skewed arrival delay time assigned *via* cross-correlation. Analysis of these breakpoints provides an evaluation of whether voxels assigned a later venous blood arrival time *via* cross-correlation truly have a later arrival time as estimated *via* the breakpoint. This analysis was conducted on averaged subsections of voxels because computation of voxel-wise breakpoints resulted in unsatisfactory quality in the breakpoint estimates, likely due to noisiness in individual voxel time series (this is further discussed in the Discussion). The breakpoints of the middle subsections (from subsection A to D, i.e., from lower to higher delay times) are non-decreasing and demonstrate a positive association between the assigned delay time for the grouping and the breakpoint of the grouping's averaged time series. A statistically significant (Wilcoxon signed rank test, $p < 0.025$) difference is found when comparing the bottom breakpoints with the middle breakpoints, as well as the middle breakpoints with top breakpoints. A statistically significant difference (Wilcoxon signed rank test, $p < 0.016$) was found in comparing middle subsections C vs. D. For the raw averaged time series, illustrated in Figure 3D, the average standard deviation (computed as a simple metric to compare the relative signal-to-noise ratios between carpet plot sections) of the middle averaged time series signal across subjects was 154.3 (a.u.), which is significantly higher (Wilcoxon signed rank test, $p < 0.025$) than both the averaged standard deviations of 41.6 and 46.7 for the top and bottom averaged time series, respectively. Similar differences in CO_2-induced signal strength are seen in the normalized and filtered averaged time series shown in Figure 3E.

The percentage (mean ± s.d.) of voxels within the top, middle, and bottom carpet plot regions reflecting low (below 0.3) absolute MCCC were found to be 8.97% ± 4.25%, 0.85% ± 0.53%, and 13.15% ± 5.21%, respectively. Subject-specific masks of the brain locations of such voxels were created and analyzed, but the resulting masks contained very few, sporadic voxel locations which reflected little similarity between subjects; thus no further details on these results are given.

3.3 Structural similarity map with SSIM and regional comparison of SSIM

The subject-averaged delay maps computed from DSC-data and CO_2 challenge data are displayed in Figure 4B, with histograms displayed in Figure 4A. In addition, Figure 4C shows the similarity map (voxel-wise s as defined previously) acquired from comparing the averaged DSC-TTP map with the averaged BOLD-CO_2 MRI delay map *via* the SSIM structure element. For the DSC-CO_2 delay map comparison, the whole-brain average structural similarity value $\bar{s}$ is 0.28.

Figure 5A shows the SSIM value similarity maps for the DSC-CO_2 delay maps comparison broken down into GM and WM regions. The average SSIM values for each map and region are also displayed above each image. The GM and WM regions produce similar averaged SSIM values (0.29 for GM and 0.34 for WM; medians statistically different based on Wilcoxon rank sum test, $p < 0.05$). 30% of the voxels in the DSC-CO_2 similarity map were found to have relatively high (greater than 0.5) SSIM values and are displayed in Figure 5B. The percentage of relatively high SSIM values in GM and WM is 29% and 40%, respectively. Rough analysis of the presence of different tissue types in the three carpet plot sections suggested that the top carpet plot regions consisted of mostly WM, the bottom carpet plot regions contain a large number of voxels classified as neither GM or WM, and the middle carpet plot regions contain a roughly equal amount of GM and WM (see Supplementary Table S2 for further details).

Figure 6A displays the location of the top and bottom carpet plot region masks, which represent areas of the brain that were assigned to either the top or bottom carpet plot regions in at least half of subjects. These same voxel masks are overlaid in Figure 6B with the structural similarity map comparing the subject-averaged CO_2 delay map with the subject-averaged DSC delay map. The average structural similarity s within the top, middle, and bottom carpet plot regions were 0.36±0.41, 0.32±0.32, and −0.21±0.41, respectively. Significantly different distributions in s values were found between all three carpet plot regions (Wilcoxon rank sum test, $p < 0.01$ for all three comparisons).

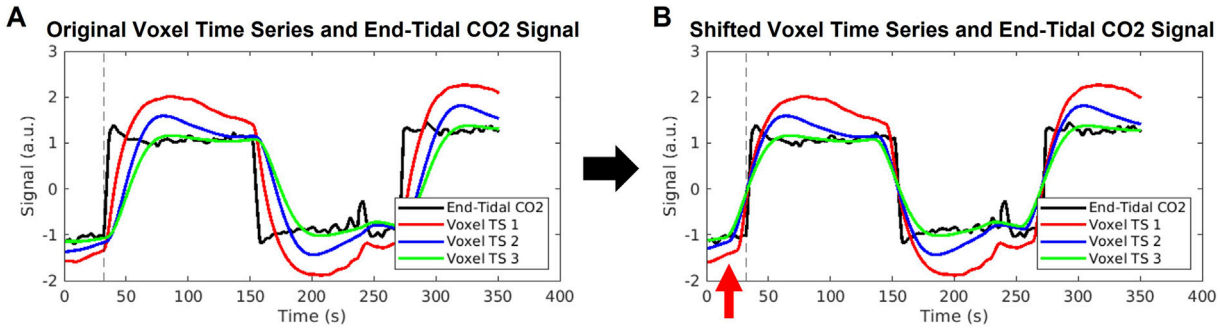

FIGURE 7
Illustration of errors stemming from cross-correlation method of delay times. **(A)** An example end-tidal CO_2 time series is shown in black, with three example voxel time series shown in red, blue, and green. These voxel time series are created by convolution of the black end-tidal CO_2 time series with three different hemodynamic response functions representative of different areas of the brain, as used in Yao et al. (2021). The common break point for all signals is illustrated by the dashed vertical line. **(B)** The voxel time series are shifted according to the maximum cross-correlation method, which aligns the signals such that maximum correlation with the end-tidal CO_2 time series is achieved. The same end-tidal CO_2 breakpoint as in **(A)** is shown by the dashed vertical line. The red arrow highlights that the voxel time series now display breakpoints occurring before the end-tidal CO_2 increase, which is not possible. The red, blue, and green voxel time series were shifted to the left by 7, 16, and 19 s, respectively, which represent unrealistically high delay values.

4 Discussion

In this study, we use carpet plots and related analyses to assess the issue of widely spread venous blood arrival delay values assigned *via* the cross-correlation method applied to CO_2-fMRI. Results (Figure 4A) indicated, as expected, that the venous blood arrival time values computed using CO_2-challenge fMRI produce a wider range of delay values than those derived from DSC-MRI. Carpet plot analysis yielded an average estimated blood transit time of 5.32 s. The analysis of averaged time series from different groups of voxels, identified in part using the carpet plot, illustrated patterns in the shape of voxel time series based on a voxel's assigned delay time, which we will further discuss in this section.

4.1 Review of known inaccuracies in the cross-correlation method

We first wish to clearly state the inaccuracy associated with computing venous blood arrival times from CO_2-challenge fMRI data using the method of maximum cross-correlation of each voxel time series with some version of the inhaled CO_2 signal. It has been previously demonstrated that the maximum cross-correlation method can yield a blood-arrival delay span of 20.1 s across the whole brain (Niftrik et al., 2017), which is inconsistent with the fact that the cerebral blood transit time is approximately 5–6 s (Hoffmann et al., 2000). To further illustrate this error stemming from cross-correlation, we cross-correlated the CO_2 measurement with three BOLD signals with different shapes while sharing the same breakpoint (see Figure 7). These three BOLD signals (in red, green, and blue) simulate voxels having the same arrival time of the elevated CO_2 (the same breakpoint), but with different response times to the elevated CO_2, and were computed by convolving the true $P_{ET}CO_2$ measurement with three different hemodynamic response functions from Yao et al. (2021). Depending on the extent of the distortion of the BOLD waveform from the CO_2 measurement, a delay time offset could be as high as 19 s. This delay time offset is not due to the real CO_2 arrival offset but the brain's CO_2 response behavior. Therefore, the delay time calculated for the CO_2-fMRI by the cross-correlation method can be skewed by this CO_2 response behavior, raising the question of whether arrival times computed *via* cross-correlation truly reflect the venous blood arrival time or are purely dominated by the CO_2 response behavior of the voxel. We address a part of this issue by demonstrating that analyzing CO_2-fMRI data using carpet plots can lead to improved estimates of the cerebral blood transit time. We also use voxel groupings suggested by inspection of the carpet plots to better understand the relationship between signal shape and assigned delay time.

4.2 Transit times

The slope detection method introduced in our previous study (Fitzgerald et al., 2021) was applied to the middle sections of carpet plots to compute blood transit time through the associated brain voxels, yielding an average estimate of 5.32 s. This observation of a linear pattern in the middle region is important because we observe this linear pattern in nearly the entire carpet plot (over 95% of voxels) for carpet plots derived from DSC-MRI; such carpet plots are illustrated in our previous paper (Fitzgerald et al., 2021); Supplementary Figure S6. The definition of the middle carpet plot section is such that it contains voxels with delays within a 20-s window, meaning that the cross-correlation method alone would suggest a 20-s blood transit time through this region of voxels. An average of 5.32 s represents an improved transit time estimate that moves much closer to the expected 5–6 s. We note that the middle carpet plot sections contained, on average, about 78% of voxels in the brain, meaning that about 22% of voxels were not directly represented by this estimated transit time. This implies that these estimated transit times could be underestimates, primarily if the voxels located in the top and bottom sections truly do experience

blood arrival after (for top voxels) or before (for bottom voxels) those in the middle section. As will be discussed, our analysis suggests that voxels within the top of the carpet plot, though they do have assigned delays that are likely skewed too long, are likely to be roughly correctly assigned sequentially, strengthening the likelihood that these transit times are underestimates of the whole-brain blood flow. However, increasing the estimated transit times by 22% (proportionally to the number of voxels not represented by the middle region) would result in an average transit time of 6.44 s, which is still much improved compared to the 20-s spread implied by the cross-correlation method alone. In addition, the middle carpet plot sections appear to be composed of roughly equal numbers of both GM and WM voxels, suggesting that the computed transit time does not reflect blood passage only through GM portions of the brain.

Other studies have presented similar methodologies for computing whole-brain blood transit times based on BOLD MRI signals, yielding similar results. Aso et al. (2020) computed voxel-wise lag (i.e., delay) maps based on cross-correlation of resting state voxel BOLD time series with an extracted seed time series intended to represent the center of the vascular tree. This was followed by computation of global transit time as the sum of estimates of the arterial transit time (computed as the average of voxels with positive lag times relative to center) and the venous transit time (computed as the average of voxels with negative lag times relative to center), with the majority of global transit time estimates falling into the range of 4–6 s (Aso et al., 2020). Additionally, Bhogal et al. (2022) implemented a carpet method for computing global transit times using controlled hypoxia as a source of BOLD contrast, yielding an average global transit time of 4.5 s. Similar investigation of using hypoxia to induce BOLD contrast has been explored in (Sayin et al., 2022). These alternative approaches demonstrate the feasibility of BOLD signal-based methods for computing global transit time which do not rely on induced hypercapnia.

4.3 Analysis of signal behavior in carpet plot regions

Figure 3 illustrates several behaviors and traits of the voxel time series within different sections of the carpet plots. First, Figures 3D, E demonstrate that the averaged time series derived from the middle of the carpet plot tends to have a more profound signal-to-noise ratio than that of the top and bottom carpet plot regions, which implies that voxels within the middle carpet plot region tend to experience a greater degree of signal change due to the arrival of the CO_2 bolus. Observing this difference in induced signal change after normalizing (detrended and divided by standard deviation) voxel time series, as in Figure 3E, demonstrates that a higher percentage of voxels within the top and bottom carpet plot regions likely display little to no CO_2-induced signal change (causing the averaged CO_2 signal strength to be weaker). One possible reason could rely on the intrinsic hemodynamic responses in some brain regions which tend to have reduced BOLD response to the same CO_2 stimulus, measured by reduced cerebrovascular reactivity (Bhogal et al., 2015; Niftrik et al., 2017). A more detailed discussion regarding the main location of top and bottom carpet plot regions and the effect on the signal behavior can be found in the next section.

In addition, it can be observed that the averaged time series from the top carpet plot section displays a notably different signal shape than that of the middle section, in that the CO_2-induced signal rise and fall is much sharper in the middle section. To help quantify this difference in signal shape, we estimated two additional metrics from the signals: the time index when the increasing CO_2 signal reached 90% of the difference between baseline and peak signal intensity (called "peak point" here), and the slope of the signal in between the estimated breakpoint and peak point. Details regarding the computation of these metrics and the associated results are listed in Supplementary Figure S7. This analysis showed that voxels in the top of the carpet plot, thus having been assigned very long delay times, do tend to have signal shapes which reflect slower rise and fall times. This is exactly the signal behavior which is demonstrated in Figure 7 to lead to excessively long delay times in the cross-correlation method. Similarly, this trend of higher delay times associated with slower responses to the CO_2 bolus can be seen in the middle carpet plot subsections illustrated in Figure 3B. Peak points and slopes for these averaged time series were also computed and demonstrated that longer delay times were associated with lower slopes and longer peak points (see Supplementary Figure S8).

These results demonstrate that, as is suggested by the discussion of Figure 7, the delay time assigned *via* cross-correlation in CO_2-fMRI is largely associated with the shape of the voxel time series, which is dependent not only upon the true arrival time of the CO_2 bolus, but also upon how quickly and how strongly a given brain region responds to the arrival of this CO_2 bolus. It has been found that various brain regions respond to the CO_2 stimuli differently (slow vs. rapid response) (Golestani et al., 2015; Poublanc et al., 2015; Fisher et al., 2017; Prokopiou et al., 2019), resulting in a variety of shapes of the BOLD waveform, which increases the difficulty of obtaining accurate delay times. The rise in signal intensity is not a result of detecting CO_2 directly, but rather is the result of increased blood flow caused by vasodilation due to the increased CO_2 presence. This raises an important question: does a delayed/weaker reactivity to the arrival of CO_2 necessarily correspond to an actual delay in the CO_2 arrival? To address this question, we computed estimates of the breakpoints of averaged time series from each carpet plot section, as displayed in Figures 3C, F. Estimating these breakpoints, as described in Niftrik et al. (2017), could serve as a better estimate of the time point of CO_2 arrival, given the known shortcomings of the cross-correlation method. Results indicated that on the averaged time signals, breakpoints do increase as the assigned delay values corresponding to the given carpet plot section increase. We note that the average change in breakpoint time between the averaged time series for middle subsections A and D was 3.75 s. Given that these four subsections were broken up according to 5-s delay windows, the cross-correlation method alone would suggest a range of delays in the realm of 15 s between the midpoints of subsections A and D. Thus the breakpoint computations show a tighter estimation of the change in venous blood arrival time, though it must be highlighted that this tighter estimation only comes through breakpoint computation on averaged BOLD time series over many voxels as opposed to individual voxel breakpoint estimates (discussed later in the Discussion). These observations provide a first point of support for the notion that the sequence of

delay values is somewhat reliable despite the heavy influence of signal shape on the computed delay time. To further assess this question, we turn to analyzing the structural similarity between the subject-averaged CO_2 and DSC delay maps.

4.4 DSC-MRI and CO_2-MRI delay maps comparison

The structural similarity metric *s* is computed somewhat like a weighted correlation coefficient between data within the two compared windows centered around a given voxel. It can provide a rough intuition for whether the structure, or sequence of assigned delay values, is similar between the two windows. In observing the structural similarity map results, we first observe the regions with relatively high structural similarity values (*s* greater than 0.5), as illustrated in Figure 5B. 30% of all brain voxels yielded *s* values greater than 0.5. Those voxels are mainly clustered in the temporal lobe, parietal lobe, occipital lobe, and WM. We note that regions of WM contained higher structural similarity values, on average, than areas of GM (Figure 5A). It is important to note, however, that since the structural similarity values *s* are computed using information within an $11 \times 11 \times 11$ voxel Gaussian-weighted window around the central voxel, meaning that each *s* value reflects the similarity within a window around the voxel, possibly from multiple tissue types.

4.4.1 Top of carpet plot

One of the primary issues of the maximum cross-correlation method applied to CO_2-MRI is the resulting wide spread of CO_2-derived delay values. To better understand this spread, we analyzed which voxel locations corresponded to those cropped from the top of CO_2 carpet plots (indicating extra long CO_2-derived delay values) and voxel locations which corresponded to those cropped from the bottom of CO_2 carpet plots (indicating extra short CO_2-derived delay times). These voxel locations are displayed in Figure 6. Observation of these voxel locations reveals that voxels with extra long CO_2-derived delay times were primarily located in areas of deep WM in the brain. This also explains the observation that these voxels have lower signal-to-noise ratio compared with those in the middle carpet plot portion. This pattern of longer delays and lower signal-to-noise ratio in areas of deep WM is consistent with the results observed in the DSC-MRI data and in previous papers (Thomas et al., 2013b; Bhogal et al., 2015; Poublanc et al., 2015; Bhogal, 2021; Poublanc et al., 2021). Further, the observed BOLD signal pattern in each voxel is impacted by both the arrival of CO_2 to the voxel and the blood vessel dilation which occurs due to CO_2 being a vasodilator. Some studies (Bhogal et al., 2015; Niftrik et al., 2017) suggest that cerebrovascular reactivity, a measure of the magnitude of the response of brain regions to the effects of CO_2 arrival, tends to be lower in regions of deep WM, which could suggest that the extra long CO_2-derived delays observed in these regions in CO_2 delay maps could also be influenced by low cerebrovascular reactivity in those areas. Additionally, results from Bhogal (2021) confirmed that reactivity in WM is notably different than that of GM and showed that the response of WM is also influenced by venous draining topology. Despite these sources of potential confounding of the assigned delay time within these voxels, analysis of the structural similarity map within the brain region mask associated with the top of the carpet plots (see Figure 6B) revealed that these voxels had equal, possible higher, structural similarity compared with those from the middle of the carpet plots. This suggests that these voxels with very long CO_2-derived delays have similar reliability in their ordering with those from the middle of the carpet plot (whose delay times are expected to be more reliable) in terms of structural similarity to the DSC delay map.

4.4.2 Bottom of carpet plot

Voxels which were removed from the bottom of the carpet plot were primarily located in regions near the boundary between WM and the lateral ventricles, particularly toward the posterior side of the brain. These voxels correspond to locations where the computed delay value was more than 10 s earlier than the average CO_2-derived delay time across the brain, which likely cannot reflect true arrival of the CO_2 given that the increased arterial CO_2 would not likely occur so early in these specific voxels. We also note that these voxels at the bottom of the carpet plot were more likely to have BOLD time series which were negatively correlated with the global average time series. Analysis of the correlation values obtained during the cross-correlation delay computations revealed that voxels with negative correlations appeared in the bottom, middle, and top carpet plot regions at rates of 35%, 2%, and 21% on average, respectively.

Such observations (namely, of negatively correlated BOLD signals near the edge of the ventricles and with signal changes earlier than most voxels across the brain) align with previous studies (Bianciardi et al., 2011; Thomas et al., 2013a; Bright et al., 2014) which suggest that negative BOLD signal correlations are predominantly due to blood volume change instead of cerebral blood flow (CBF) increase. This volume change is due to dilation of ventricular vessels accompanied by shrinkage of cerebrospinal fluid (CSF) space, resulting in signal decrease which could overpower any BOLD signal increase. This hypothesis also explains the very short CO_2-derived delays calculated for voxels with negatively correlated BOLD signals since CSF shrinkage could occur prior to the arrival of the CO_2. Alternatively, another mechanism which could cause negatively correlated BOLD signals is the cerebral "steal effect", in which multiple CBF changes (both increased and decreased CBF response in regions in and surrounding the voxel) simultaneously occur in response to the arrival of the CO_2, meaning that regions with reduced CBF are compromised due to the increased CBF in other regions (Brawley, 1968; Poublanc et al., 2013; Sobczyk et al., 2014). Finally, one might hypothesize that the Bohr effect (Riggs, 1988), under which increased concentration of CO_2 in the blood causes a decreased oxygen binding affinity in hemoglobin (thus increasing concentrations of deoxyhemoglobin), could theoretically cause a BOLD signal decrease in response to elevated blood CO_2. However, the magnitude of any such signal changes due to the Bohr effect is expected to be very small. This claim is supported by the fact that an increase of 10 mmHg from baseline in end-tidal CO_2 should only cause a very small shift in the oxyhemoglobin dissociation curve for normal blood partial pressure of O_2 (PO_2) (Levitzky, 2013), where normal arterial PO_2 typically falls within the range of 75–100 mmHg (Ortiz-Prado et al., 2019). Further investigation is still needed to definitively explain this phenomenon of certain voxels displaying decreased BOLD signal in response to the CO_2 bolus. As demonstrated in Figure 6B, the voxels with very short CO_2-derived delay values corresponded with areas of the SSIM value map which

were particularly low, indicating that these unrealistically low delay times are likely one of the main factors which differentiates the CO_2 delay maps from the DSC delay maps.

As an added evaluation of the similarity between CO_2 and DSC delay maps, CO_2 carpet plot were reconstructed by sorting voxels according to the averaged DSC delay map (after registration to the subject's native space) and transit times were recomputed. Details on these results are shared in the Supplementary Material, along with the resorted carpet plots in Supplementary Figure S9. We note that this method of sorting carpet plots resulted in varying transit time values and did appear to significantly reduce the visual clarity of the three carpet plot sections that are apparent when sorting *via* the subject-specific CO_2 delay maps. This result suggests a lack of similarity between DSC and CO_2-derived delay map sequence should be noted. The difference between these two delay map sequence could be partially explained by the different underlying mechanisms of DSC and CO_2 MRI, as DSC-MRI tracks the passage of the paramagnetic gadolinium-based contrast agent, inducing a local signal loss while not affecting the vascular tone or cerebral blood flow, whereas CO_2 stimulus induces various complicated hemodynamic reactions, resulting in changes in the BOLD signal waveform. However, it must also be acknowledged that this transit time computation method (*via* slope detection on carpet plots) is highly dependent upon precise sorting of the carpet plot voxels for each subject. Since this experiment sorted individual subject carpet plots based on an averaged delay map derived from a separate cohort of subjects, such inter-subject differences may likely account for a significant portion of the differences in carpet plot sorting. Confirmation of the similarity of carpet plots and transit times derived from CO_2 *versus* DSC delay maps would be best evaluated on a cohort where both DSC and CO_2 MRI can be conducted on the same subjects.

4.5 Alternative methods and reasoning for chosen methodology

We wish to note two alternative methods for computing venous blood arrival times from CO_2-MRI data and explain the observed shortcomings with these methods. First, the improved transit times derived from carpet plots suggest the possibility that the voxel-wise data points used to estimate the transit time edge may represent accurate CO_2 arrival times. The carpet plot edge detection method, after applying an image smoothing filter, examines each image row (voxel time series) and identifies the time point of maximum point-to-point increase (signal derivative). These time points from all voxel time series in the carpet plot are then used to estimate the observed edge *via* linear regression. In one alternative method, these maximum signal derivative time points were computed as the voxel-wise venous blood delay times. When a subject-averaged delay map using this method was compared with the DSC-MRI delay map *via* SSIM comparison, the resulting brain-wise SSIM value was 0.20, indicating lower similarity than the cross-correlation delay map SSIM value of 0.28. Visual inspection of this delay map showed that it appeared "noisier", or less smooth, than the delay map derived from cross-correlation.

Additionally, the discussion of Figure 3 would suggest that direct computation of the voxel time series "breakpoint", or the starting point of the rise of the BOLD signal associated with arrival of the CO_2 bolus, would yield a more accurate delay time than that of the cross-correlation method. This second alternative method was discussed and implemented in a study by Niftrik et al. (2017). However, implementation of this method on the data set discussed in this study failed to overcome the issue of delay-value distributions spanning a time window greater than the expected 5–6 s. One hypothesis for why these alternatives fail to out-perform the cross-correlation method is that these methods rely on direct observation of one specific portion of the voxel time series. These methods are thus very sensitive to noisiness in the voxel BOLD signal. In comparison, the cross-correlation method utilized information from the entire voxel time series, which contains two instances of rising and falling signal, which is helpful in overcoming noisiness of the signal (see Supplementary Section S8; Supplementary Figures S10–S12 for more details on alternative results).

We also wish to note the reasoning used in decisions regarding the use of the structure element of the SSIM for CO_2-MRI vs. DSC-MRI comparisons. The traditional SSIM metric is computed as the multiplication of three terms: structure, luminance, and contrast (Zhou et al., 2004). The structure term, as described in this paper, reflects the degree of scaled covariance of the data within the two compared windows. The luminance term measures the similarity between the means of the two windows, while the contrast term measures the similarity in the variance between the two windows. For the purposes of this study, multiplying each of these terms as is done in the traditional metric made it difficult to interpret precisely what caused a low SSIM value, so we elected to analyze the structure, luminance, and contrast terms individually. It was found that the structure element was useful in that it was easily interpreted (due to similarity to Pearson's correlation coefficient—see Eq. (1)), relatively insensitive to delay map normalization, and provided useful information reflecting regional similarity between the two delay maps. In contrast, the luminance and contrast elements were found to add relatively little additional information, with interpretation highly sensitive to data normalization methods (the choice of which is not trivial). Thus we chose to use the structure element as the main comparison metric for this study (see Supplementary Figure S13 for more details regarding this choice).

Another commonly used similarity metric, normalized mutual information (NMI), was also tested to evaluate the similarity between two delay maps. The NMI metric yields similarity values ranging from 0 to 1. The comparison of the spatial similarity maps derived from both metrics are shown in Supplementary Figures S14, S15. A very similar pattern of the similarity maps from both methods was observed in majority of the regions. However, the SSIM allows for highlighting inverted structure between the two maps through negative similarity values, while the NMI metric does not. This capability is the main reason the SSIM approach was chosen over the NMI approach.

4.6 Limitations and future directions

One limitation of this study is the limited number of subjects in the DSC-MRI (DSC scans on healthy subjects are rarely conducted due to the injection of the Gd contrast) and BOLD-CO_2 MRI

datasets, leading to a high variety of delay maps across subjects. Also, subjects in the CO_2-MRI dataset and the DSC-MRI dataset are from different cohorts and not gender-matched, contributing to the inconsistency between delay maps derived from these two methodologies. These factors may lead to underestimation of the similarity between the averaged DSC-TTP map and the averaged BOLD-CO_2 MRI delay map. Furthermore, in the CO_2 arrival delay adjustment methodology, a linear fitting was assumed in the edge-detection algorithm, which might not work properly in diseased patients (e.g., Moyamoya, stroke). Non-linear fitting could be considered for such subjects. Additionally, the brain operates under different conditions during DSC-MRI and BOLD-CO_2 MRI. DSC-MRI tracks the passage of the paramagnetic gadolinium-based contrast agent, which induces a local signal loss while not affecting the vascular tone or cerebral blood flow or volume. However, in BOLD-CO_2 MRI, the CO_2 stimulus induces various complicated hemodynamic reactions, which plays an important role in the BOLD signal changes. Analysis of averaged time series delays as divided by the carpet plot confirmed that the shape of voxel time series, characterized by the response of the voxel to the CO_2 bolus arrival, are largely associated with the delay times assigned *via* cross correlation in CO_2 challenge fMRI. An alternative strategy could be inducing hyperoxia (Moreton et al., 2016; Pinto et al., 2020) or hypoxia (Poublanc et al., 2021; Sayin et al., 2022) during BOLD imaging as an alternative gas stimulus to track blood flow with the benefit of less vascular reactivity changes during imaging.

A useful extension of this study would include an analysis of whether the carpet plot-based transit time computation method can be useful for quantifying blood transit times throughout localized subsections of the brain. Additionally, it may be possible to extend this methodology to use the fitted carpet plot edge line to estimate improved voxel-wise blood arrival delay times. To support such an extension, more work would need to be conducted to conclude whether the rank (i.e., ordering) of voxels in the carpet plot is truly accurate when computed based on the cross-correlation method.

5 Conclusion

In this study, we proposed a novel carpet plot-based method to reduce the estimated cerebral transit times derived from hypercapnia fMRI in healthy subjects and spatially compare the resulting delay maps with the DSC-MRI TTP maps. We demonstrated that, at least at a broad level, the sequence of voxels implied by the assigned CO_2 delay values is still similar to, though not a perfect representation of, that derived from DSC-MRI. The tilted edge in the middle CO_2 carpet plot regions mimics that observed in DSC-MRI carpet plots. Voxels in the top portion (extra long delays) were located in deep WM while those in the bottom portion were located in the periventricular region. The structural similarity (with DSC delays) of voxels associated with the top and middle carpet plot regions was shown to be positive and similar between the top and middle regions. Voxels falling within the bottom of the carpet plot were shown to have delay values that are unrealistically early and, on average, have poor (negative) structural similarity with the same voxels assigned delays *via* DSC-MRI. However, delay values of voxels in the top portion were largely affected by the hemodynamic response under CO_2 challenge. Further research should focus on inducing alternative gas challenge to eliminate the vessel response, as well as collecting both DSC-MRI and gas challenge MRI data from the same cohort of subjects.

Data availability statement

The raw data supporting the conclusions of this article will be made available by the authors, without undue reservation.

Ethics statement

The studies involving human participants were reviewed and approved by the Institutional Review Board of Purdue University and the Institutional Review Board of McLean Hospital. The patients/participants provided their written informed consent to participate in this study.

Author contributions

The study was conceptualized by YT. Data collection experiments were conducted by BBF, LH, and YT. Data processing and analysis were conducted by BF, JY, and YT. Results were reviewed and interpreted by all authors. The manuscript was drafted by BF and JY and was edited by all authors. BF and JY contributed equally to the manuscript.

Funding

This work was supported by the National Institutes of Health (NIH) R21 DA032746 (BBF), NIH R21AG068962 (YT), and NIH/National Institute on Aging R21 AG070383-01 (LMH); in part, with support from the Indiana Clinical and Translational Sciences Institute (the Pilot Funding for Research Use of Core Facilities).

Conflict of interest

The authors declare that the research was conducted in the absence of any commercial or financial relationships that could be construed as a potential conflict of interest.

Publisher's note

Supplementary material

The Supplementary Material for this article can be found online at: https://www.frontiersin.org/articles/10.3389/fphys.2023.1134804/full#supplementary-material

References

Aso, T., Sugihara, G., Murai, T., Ubukata, S., Urayama, S.-I., Ueno, T., et al. (2020). A venous mechanism of ventriculomegaly shared between traumatic brain injury and normal ageing. *Brain (London, Engl.)* 143 (6), 1843–1856. doi:10.1093/brain/awaa125

Bhogal, A. A., Philippens, M. E. P., Siero, J. C. W., Fisher, J. A., Petersen, E. T., Luijten, P. R., et al. (2015). Examining the regional and cerebral depth-dependent BOLD cerebrovascular reactivity response at 7 T. *NeuroImage* 114 (C), 239–248. doi:10.1016/j.neuroimage.2015.04.014

Bhogal, A. A., Sayin, E. S., Poublanc, J., Duffin, J., Fisher, J. A., Sobcyzk, O., et al. (2022). Quantifying cerebral blood arrival times using hypoxia-mediated arterial BOLD contrast. *NeuroImage (Orl. Fla.)* 261, 119523. doi:10.1016/j.neuroimage.2022.119523

Bhogal, A. A. (2021). Medullary vein architecture modulates the white matter BOLD cerebrovascular reactivity signal response to CO2: Observations from high-resolution T2 weighted imaging at 7T. *NeuroImage (Orl. Fla.)* 245, 118771. doi:10.1016/j.neuroimage.2021.118771

Bianciardi, M., Fukunaga, M., van Gelderen, P., de Zwart, J. A., and Duyn, J. H. (2011). Negative BOLD-fMRI signals in large cerebral veins. *J. Cereb. Blood flow Metab.* 31 (2), 401–412. doi:10.1038/jcbfm.2010.164

Blockley, N. P., Driver, I. D., Francis, S. T., Fisher, J. A., and Gowland, P. A. (2011). An improved method for acquiring cerebrovascular reactivity maps. *Magn. Reson. Med.* 65 (5), 1278–1286. doi:10.1002/mrm.22719

Bokkers, R. P. H., van Laar, P. J., van de Ven, K. C. C., Kapelle, L. J., Klijn, C. J. M., and Hendrikse, J. (2008). Arterial spin-labeling MR imaging measurements of timing parameters in patients with a carotid artery occlusion. *Am. J. Neuroradiol.* 29 (9), 1698–1703. doi:10.3174/ajnr.A1232

Brawley, B. W. (1968). The pathophysiology of intracerebral steal following carbon dioxide inhalation, an experimental study. *Scand. J. Clin. Lab. Invest.* 21, XIII-B. doi:10.3109/00365516809169045

Bright, M. G., Bianciardi, M., de Zwart, J. A., Murphy, K., and Duyn, J. H. (2014). Early anti-correlated BOLD signal changes of physiologic origin. *NeuroImage (Orl. Fla.)* 87, 287–296. doi:10.1016/j.neuroimage.2013.10.055

Chalela, J. A., Alsop, D. C., Gonzalez-Atavales, J. B., Maldjian, J. A., Kasner, S. E., and Detre, J. A. (2000). Magnetic resonance perfusion imaging in acute ischemic Stroke using continuous arterial spin labeling. *Stroke* 31 (3), 680–687. doi:10.1161/01.STR.31.3.680

Donahue, M. J., Strother, M. K., Lindsey, K. P., Hocke, L. M., Tong, Y., and Frederick, B. D. (2016). Time delay processing of hypercapnic fMRI allows quantitative parameterization of cerebrovascular reactivity and blood flow delays. *J. Cereb. Blood Flow Metab.* 36 (10), 1767–1779. doi:10.1177/0271678X15608643

Duffin, J., Sobczyk, O., Crawley, A. P., Poublanc, J., Mikulis, D. J., and Fisher, J. A. (2015). The dynamics of cerebrovascular reactivity shown with transfer function analysis. *NeuroImage* 114 (C), 207–216. doi:10.1016/j.neuroimage.2015.04.029

Essig, M., Shiroishi, M. S., Nguyen, T. B., Saake, M., Provenzale, J. M., Enterline, D., et al. (2013). Perfusion MRI: The five most frequently asked technical questions. *Am. J. Roentgenol.* 200 (1), 24–34. doi:10.2214/AJR.12.9543

Fisher, J. A., Sobczyk, O., Crawley, A., Poublanc, J., Dufort, P., Venkatraghavan, L., et al. (2017). Assessing cerebrovascular reactivity by the pattern of response to progressive hypercapnia. *Hum. Brain Mapp.* 38 (7), 3415–3427. doi:10.1002/hbm.23598

Fisher, J. A. (2016). The CO2 stimulus for cerebrovascular reactivity: Fixing inspired concentrations vs. targeting end-tidal partial pressures. *J. Cereb. Blood Flow Metab.* 36 (6), 1004–1011. doi:10.1177/0271678X16639326

Fitzgerald, B., Yao, J. F., Talavage, T. M., Hocke, L. M., Frederick, B. d., and Tong, Y. (2021). Using carpet plots to analyze transit times of low frequency oscillations in resting state fMRI. *Sci. Rep.* 11 (1), 7011. doi:10.1038/s41598-021-86402-z

Fonov, V. S., Evans, A. C., McKinstry, R. C., Almli, C. R., and Collins, D. L. (2009). Unbiased nonlinear average age-appropriate brain templates from birth to adulthood. *NeuroImage (Orl. Fla)* 47, S102. doi:10.1016/S1053-8119(09)70884-5

Golestani, A. M., Chang, C., Kwinta, J. B., Khatamian, Y. B., and Jean Chen, J. (2015). Mapping the end-tidal CO2 response function in the resting-state BOLD fMRI signal: Spatial specificity, test–retest reliability and effect of fMRI sampling rate. *NeuroImage* 104, 266–277. doi:10.1016/j.neuroimage.2014.10.031

Hoffmann, O., Weih, M., Schreiber, S., Einhäupl, K. M., and Valdueza, J. M. (2000). Measurement of cerebral circulation time by contrast-enhanced Doppler sonography. *Cerebrovasc. Dis.* 10 (2), 142–146. doi:10.1159/000016043

Jenkinson, M., Beckmann, C. F., Behrens, T. E. J., Woolrich, M. W., and Smith, S. M. (2012). FSL. *NeuroImage* 62 (2), 782–790. doi:10.1016/j.neuroimage.2011.09.015

Kötter, R., Mazziotta, J., Toga, A., Evans, A., Fox, P., Lancaster, J., et al. (2001). A probabilistic atlas and reference system for the human brain: International Consortium for Brain Mapping (ICBM). *Philos. Trans. Biol. Sci.* 356 (1412), 1293–1322. doi:10.1098/rstb.2001.0915

Lentschig, M. G., Reimer, P., Rausch-Lentschig, U. L., Allkemper, T., Oelerich, M., and Laub, G. (1998). Breath-hold gadolinium-enhanced MR angiography of the major vessels at 1.0 T: dose-response findings and angiographic correlation. *Radiology* 208 (2), 353–357. doi:10.1148/radiology.208.2.9680558

M. G. Levitzky (Editor) (2013). "Chapter 7. Transport of oxygen and carbon dioxide in the blood,". 8e [online] *Pulmonary Physiology* (McGraw-Hill). Available at: https://accessmedicine.mhmedical.com/content.aspx?bookid=575&sectionid=42512985#57346456 (Accessed: January 31, 2023).

Macintosh, B. J., Lindsay, A. C., Kylintireas, I., Kuker, W., Günther, M., Robson, M. D., et al. (2010). Multiple inflow pulsed arterial spin-labeling reveals delays in the arterial arrival time in minor stroke and transient ischemic attack. *Am. J. Neuroradiol.* 31 (10), 1892–1894. doi:10.3174/ajnr.A2008

Mazziotta, J., Toga, A., Evans, A., Fox, P., Lancaster, J., Zilles, K., et al. (2001). A four-dimensional probabilistic atlas of the human brain. *J. Am. Med. Inf. Assoc.* 8 (5), 401–430. doi:10.1136/jamia.2001.0080401

Moreton, F. C., Dani, K. A., Goutcher, C., O'Hare, K., and Muir, K. W. (2016). Respiratory challenge MRI: Practical aspects. *NeuroImage Clin.* 11 (C), 667–677. doi:10.1016/j.nicl.2016.05.003

Niftrik, C. H. B., Piccirelli, M., Bozinov, O., Pangalu, A., Fisher, J. A., Valavanis, A., et al. (2017). Iterative analysis of cerebrovascular reactivity dynamic response by temporal decomposition. *Brain Behav.* 7 (9), e00705. doi:10.1002/brb3.705

Ortiz-Prado, E., Dunn, J. F., Vasconez, J., Castillo, D., and Viscor, G. (2019). Partial pressure of oxygen in the human body: A general review. *Am. J. Blood Res.* 9 (1), 1–14.

Paling, D., Thade Petersen, E., Tozer, D. J., Altmann, D. R., Wheeler-Kingshott, C. A. M., Kapoor, R., et al. (2014). Cerebral arterial bolus arrival time is prolonged in multiple sclerosis and associated with disability. *J. Cereb. blood flow Metab.* 34 (1), 34–42. doi:10.1038/jcbfm.2013.161

Pinto, J., Bright, M. G., Bulte, D. P., and Figueiredo, P. (2020). Cerebrovascular reactivity mapping without gas challenges: A methodological guide. *Front. Physiol.* 11, 608475. doi:10.3389/fphys.2020.608475

Poublanc, J., Han, J. S., Mandell, D. M., Conklin, J., Stainsby, J. A., Fisher, J. A., et al. (2013). Vascular steal explains early paradoxical blood oxygen level-dependent cerebrovascular response in brain regions with delayed arterial transit times. *Cerebrovasc. Dis. Extra* 3 (1), 55–64. doi:10.1159/000348841

Poublanc, J., Crawley, A. P., Sobczyk, O., Montandon, G., Sam, K., Mandell, D. M., et al. (2015). Measuring cerebrovascular reactivity: the dynamic response to a step hypercapnic stimulus. *J. Cereb. Blood flow Metab. Off. J. Int. Soc. Cereb. Blood Flow Metab.* 35 (11), 1746–1756. doi:10.1038/jcbfm.2015.114

Poublanc, J., Sobczyk, O., Shafi, R., Sayin, E. S., Schulman, J., Duffin, J., et al. (2021). Perfusion MRI using endogenous deoxyhemoglobin as a contrast agent: Preliminary data. *Magn. Reson. Med.* 86 (6), 3012–3021. doi:10.1002/mrm.28974

Power, J. D. (2017). A simple but useful way to assess fMRI scan qualities. *NeuroImage* 154, 150–158. doi:10.1016/j.neuroimage.2016.08.009

Prokopiou, P. C., Pattinson, K. T. S., Wise, R. G., and Mitsis, G. D. (2019). Modeling of dynamic cerebrovascular reactivity to spontaneous and externally induced CO2 fluctuations in the human brain using BOLD-fMRI. *NeuroImage* 186, 533–548. doi:10.1016/j.neuroimage.2018.10.084

Riggs, A. F. (1988). The Bohr effect. *Annu. Rev. Physiol.* 50, 181–204. doi:10.1146/annurev.ph.50.030188.001145

Sayin, E. S., Schulman, J., Poublanc, J., Levine, H. T., Raghavan, L. V., Uludag, K., et al. (2022). Investigations of hypoxia-induced deoxyhemoglobin as a contrast agent for cerebral perfusion imaging. *Hum. Brain Mapp.* 44, 1019–1029. doi:10.1002/hbm.26131

Sobczyk, O., Battisti-Charbonney, A., Fierstra, J., Mandell, D. M., Poublanc, J., Crawley, A. P., et al. (2014). A conceptual model for CO_2-induced redistribution of cerebral blood flow with experimental confirmation using BOLD MRI. *Neuroimage* 92, 56–68. doi:10.1016/j.neuroimage.2014.01.051

Thomas, B. P., Liu, P., Aslan, S., King, K. S., van Osch, M. J. P., and Lu, H. (2013a). Physiologic underpinnings of negative BOLD cerebrovascular reactivity in brain ventricles. *NeuroImage* 83, 505–512. doi:10.1016/j.neuroimage.2013.07.005

Thomas, B. P., Liu, P., Park, D. C., van Osch, M. J. P., and Lu, H. (2013b). Cerebrovascular reactivity in the brain white matter: Magnitude, temporal characteristics, and age effects. *J. Cereb. Blood Flow Metab.* 34 (2), 242–247. doi:10.1038/jcbfm.2013.194

Tong, Y., Lindsey, K. P., Hocke, L. M., Vitaliano, G., Mintzopoulos, D., and Frederick, B. D. (2017). Perfusion information extracted from resting state functional magnetic resonance imaging. *J. Cereb. Blood Flow Metab.* 37 (2), 564–576. doi:10.1177/0271678X16631755

Yao, J. F., Yang, H.-C. S., Wang, J. H., Liang, Z., Talavage, T. M., Tamer, J. G. G., et al. (2021). A novel method of quantifying hemodynamic delays to improve hemodynamic response, and CVR estimates in CO2 challenge fMRI. *J. Cereb. Blood Flow. Metab.* 41, 1886–1898. doi:10.1177/0271678X20978582

Zaharchuk, G., Do, H. M., Marks, M. P., Rosenberg, J., Moseley, M. E., and Teinberg, G. K. S. (2011). Arterial spin-labeling MRI can identify the presence and intensity of collateral perfusion in patients with Moyamoya disease. *Stroke* 42 (9), 2485–2491. doi:10.1161/STROKEAHA.111.616466

Zhou, W., Bovik, A. C., Sheikh, H. R., and Simoncelli, E. P. (2004). Image quality assessment: from error visibility to structural similarity. *IEEE Trans. Image Process* 13 (4), 600–612. doi:10.1109/TIP.2003.819861

frontiers | Frontiers in Physiology

TYPE Original Research
PUBLISHED 20 February 2023
DOI 10.3389/fphys.2023.1096297

OPEN ACCESS

EDITED BY
Alex Bhogal,
Utrecht University, Netherlands

REVIEWED BY
Mikio Hiura,
Aomori University, Japan
Zhensen Chen,
Fudan University, China
Xiang Kong,
Nanjing General Hospital of Nanjing Military Command, China

*CORRESPONDENCE
Matthew T. Borzage,
Borzage@usc.edu

SPECIALTY SECTION
This article was submitted to Vascular Physiology, a section of the journal Frontiers in Physiology

RECEIVED 11 November 2022
ACCEPTED 24 January 2023
PUBLISHED 20 February 2023

CITATION
Shah P, Doyle E, Wood JC and Borzage MT (2023), Imputation models and error analysis for phase contrast MR cerebral blood flow measurements.
Front. Physiol. 14:1096297.
doi: 10.3389/fphys.2023.1096297

Imputation models and error analysis for phase contrast MR cerebral blood flow measurements

Payal Shah[1], Eamon Doyle[2], John C. Wood[1] and Matthew T. Borzage[3]*

[1]Division of Cardiology, Department of Pediatrics, Children's Hospital Los Angeles, Los Angeles, CA, United States, [2]Department of Radiology, Children's Hospital Los Angeles, Los Angeles, CA, United States, [3]Division of Neonatology, Department of Pediatrics, Children's Hospital Los Angeles, Keck School of Medicine, Fetal and Neonatal Institute, University of Southern California, Los Angeles, CA, United States

Cerebral blood flow (CBF) supports brain metabolism. Diseases impair CBF, and pharmacological agents modulate CBF. Many techniques measure CBF, but phase contrast (PC) MR imaging through the four arteries supplying the brain is rapid and robust. However, technician error, patient motion, or tortuous vessels degrade quality of the measurements of the internal carotid (ICA) or vertebral (VA) arteries. We hypothesized that total CBF could be imputed from measurements in subsets of these 4 feeding vessels without excessive penalties in accuracy. We analyzed PC MR imaging from 129 patients, artificially excluded 1 or more vessels to simulate degraded imaging quality, and developed models of imputation for the missing data. Our models performed well when at least one ICA was measured, and resulted in R^2 values of 0.998–0.990, normalized root mean squared error values of 0.044–0.105, and intra-class correlation coefficient of 0.982–0.935. Thus, these models were comparable or superior to the test-retest variability in CBF measured by PC MR imaging. Our imputation models allow retrospective correction for corrupted blood vessel measurements when measuring CBF and guide prospective CBF acquisitions.

KEYWORDS

magnetic resonance imaging (MRI), cerebral blood flow (CBF), phase contrast (PC), internal carotid artery (ICA), vertebral artery

Introduction

The brain requires a significant fraction of the metabolic support of the body, and it lacks the capacity to buffer disruptions in blood supply. Thus, adequate cerebral blood flow (CBF) is vital to brain health (Lassen, 1959) and CBF measurements span many areas of brain research. CBF varies markedly with brain development throughout infancy, childhood, and senescence. (Oshima et al., 2002; Liu et al., 2019; Paniukov et al., 2020). Altered CBF is associated with cardiovascular risk, (Jennings et al., 2013; King et al., 2018), small vessel disease, (Yu et al., 2020), Alzheimer's dementia, (Leijenaar et al., 2017), white matter lesions, (Hanaoka et al., 2016), anemia, (Borzage et al., 2016), stroke risk in sickle cell disease, (Vernooij et al., 2008; Prohovnik et al., 2009), and higher risk of non-cardiovascular mortality in the elderly. (Sabayan et al., 2013). CBF is a predictive biomarker for patients with severe depression, (Leaver et al., 2019), and CBF is modulated by pharmacological agents including substances of abuse, (Chen et al., 2016), alcohol, (Christie et al., 2008), and anesthetics. (Oshima et al., 2002).

The gold standard for CBF measurements are Kety-Schmidt tracer methods for whole brain measurements and Positron Emitting Tomography (PET) for spatially resolved measurements. However, both are invasive, making them poor candidates for

neurovascular screening or research applications. A non-invasive alternative CBF measurement is arterial spin labeling (ASL) magnetic resonance imaging (MRI), which uses magnetically labeled water protons in the blood as endogenous tracers to estimate brain perfusion. However, quantitation of ASL is limited by the measurement or assumption of multiple parameters, including blood-brain partition coefficient, T1 of blood, T1 of brain tissue, labeling efficiency, and arterial transit time. (Alsop et al., 2010). Estimates of each of these key parameters are provided in the literature, however experimental methods demonstrate variability for each: the blood-brain partition coefficient varies with age, underlying pathology and brain region; (Thalman et al., 2019) T1 of blood varies with red cell characteristics and hematocrit; (Lu et al., 2004) labeling efficiency is a confounding variable that depends on the blood velocity and labelling schema; (Robertson et al., 2017) and arterial transit time varies with the health, age (MacIntosh et al., 2015; Dai et al., 2017) and brain region. (Thomas et al., 2006). The reproducibility of ASL is moderate (ICC 0.74–0.78); (Yang et al., 2019) and ASL acquisitions are lengthy, with typical scan times of 5–7 min. As a result, ASL is excellent at determining relative brain perfusion in specific regions, but less suitable for measuring absolute blood flow.

Alternatively, phase contrast (PC) MRI of the internal carotid (ICA) or vertebral (VA) arteries provides rapid and robust quantification of global CBF (ml/min). The measurement yielded by PC MRI can be normalized to brain volume from brain mass estimates derived from anatomic imaging to estimate global brain perfusion in ml/100 g/min. PC MRI is reproduceable between users (ICC 0.97–0.99) and has a low coefficient of variation (4%–9%) for serial measurements. (Koerte et al., 2013; Liu et al., 2014; Sakhare et al., 2019). If phasic variation is unimportant, then accurate CBF can be collected without cardiac gating thereby greatly accelerating the acquisition. Most importantly, PC-MRI does not require modeling or parameter estimation, making it robust across pathological states.

One barrier to deploying PC MRI in clinical practice is the need to minimize contributions from partial-voluming or off-axis flow. The MR operator prevents these issues by carefully localizing the imaging plane orthonormal to the vessel being measured. The four head vessels are not parallel, thus optimal measurement of one of vessel compromises measurements from the others. To overcome this problem, the MR operator can use four PC MR images at the cost of a four-fold increase in time. However, manual optimization of each image remains dependent on operator skill. Automated methods for analyzing the anatomy of patients and planning ideal locations of four PC MR imaging slices have been proposed, but not implemented by MR scanner vendors. (Liu et al., 2014). Alternatively, placing a "best-guess" single PC MR imaging slice to measure CBF is methodologically simple and fast, but is inherently suboptimal and occasionally results in one or more vessels being too oblique for acceptable quantitation.

We postulated that flows in each vessel were sufficiently correlated with one another so that imputation could compensate for measurements corrupted by motion or obliquity, provided that one or more vessels remain measurable. To test this hypothesis, we calculated the internal correlations among the head vessels, developed a table of mathematical models to impute the flow from corrupted arterial flow measurements, and assessed the resulting error introduced by our imputations.

Materials and methods

Patient demographics

This study is a secondary analysis of existing data, which was originally approved by the Children's Hospital Los Angeles Committee on Clinical Investigations (CCI 11–00083). Informed consent was obtained from N = 129 patients recruited between 2012 and 2017. This cohort included patients with sickle cell disease (N = 55), healthy control patients (N = 42), and patients suffering from various hemoglobinopathies (N = 32). These patients were 23.5 ± 9.7 years (range 9–61 years) old (59M, 70F). Their hematocrits were 32.9% ± 7.2% and 33% (N = 42) were on chronic transfusion. (Borzage et al., 2016).

Image acquisition

The imaging methods are reported elsewhere in detail and summarized here. (Borzage et al., 2016). We obtained all images with a 3T Philips Achieva and eight-element head coil. A magnetic resonance angiogram localized the vessels in the neck, and a PC MR imaging plane was placed approximately 1 cm above the carotid bifurcation. The angiogram was collected in the axial plane with inline reformatting into sagittal and coronal planes to facilitate orthogonal placement of the PC imaging plane. Image parameters for the PC MR examination were as follows: repetition time, 12.3 ms; echo time, 7.5 ms; field of view, 260 mm; thickness, 5 mm; signal averages, 10; acquisition matrix, 204 × 201; reconstruction matrix, 448 × 448; bandwidth, 244 Hz/pixel; and velocity encoding gradient, 200 cm/s. For this retrospective data analysis, we retained only one PC MR image per patient. Figure 1 demonstrates the coronal angiogram showing the carotid and vertebral arteries together with the magnitude and phase images.

Image processing

We performed all phase-contrast image analysis using MATLAB (The MathWorks, Natick, MA). We thresholded the complex difference image to identify moving voxels (defined as greater than the mean plus two standard deviations of stationary voxels sampled from a non-vascular region). We fit the phase differences of stationary voxels using a two-dimensional second-order polynomial to remove the background phase. We identified vessel boundaries using a Canny edge-detector of the complex difference image, dilating the edge by a single voxel, and excluding any stationary voxels. We calculated the blood flow in each artery by summing the blood velocities (cm/s) within the vessel multiplied by the voxel area (cm^2). When the automatic edge detection failed (<5% of the time), the carotid or vertebral artery boundaries were identified manually by an MR researcher (JCW) with 22 years of experience analyzing PC MR images.

Modeling cerebral blood flow

We identified all 16 possible scenarios wherein combinations of two, one, or zero ICAs or VAs might be able to be analyzed from an

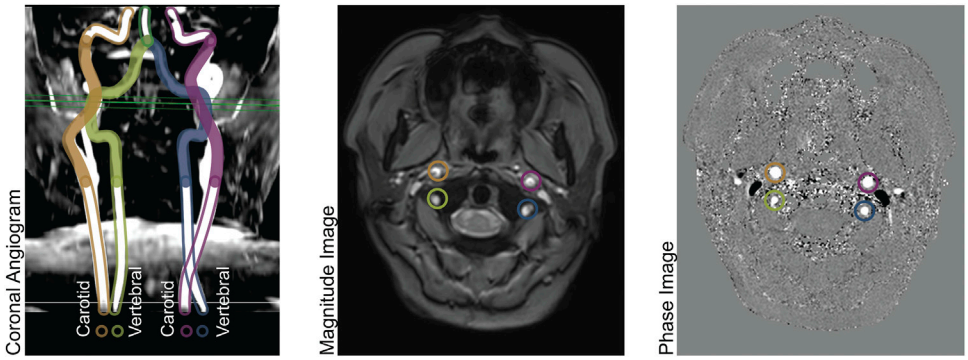

FIGURE 1
Left panel: Coronal Angiogram showing the carotid and vertebral arteries. The solid-colored portion of the vessels are above the bifurcation of the common carotid arteries, and below the level of the basilar artery. The green horizontal plane shows the location of the phase contrast slice. Center panel: a magnitude image; and right panel: a phase image, both acquired at the level indicated in the left panel.

TABLE 1 Models for computing cerebral blood flow.

Number of usable vessels		Model	Cerebral blood flow equation	RMSE	Normalized RMSE	R-Squared	ICC(2,1)
ICAs	VAs						
2	2	0	CBF = Anterior + Posterior	00.00	0.000	1.000	1.000
	1	1	CBF = 1.226 × Anterior + 0.933 × VA	41.00	0.044	0.998	0.982
	0	2	CBF = 1.426 × Anterior	69.89	0.075	0.995	0.973
1	2	3	CBF = 1.866 × ICA + 1.145 × Posterior	57.19	0.061	0.997	0.983
	1	4	CBF = 2.419 × ICA + 0.983 × VA	78.75	0.084	0.994	0.948
	0	5	CBF = 2.841 × ICA	98.20	0.105	0.990	0.935
0	2	6	CBF = 3.219 × Posterior	159.46	0.171	0.974	0.877
	1	7	CBF = 5.816 × VA	323.45	0.346	0.885	0.662
	0	8	CBF = 933.656	297.88	0.319	NA	0.000

Models for computing cerebral blood flow when vessels are missing. The models are independent of the lateral location of the vessel(s) that are imputed thereby allowing us to omit models for the combinations of different left *versus* right vessels (See Figure 3, Results). Models 1-7 are computed with an intercept of zero; model eight is the mean CBF in this study. The models followed the anticipated pattern wherein missing ICAs *versus* VAs contributed more error (e.g. model 3 *versus* 1). Abbreviations: cerebral blood flow (CBF), internal carotid artery (ICA), vertebral artery (VA), root mean square error (RMSE), intra-class correlation coefficient (ICC). An online calculator for these models is provided: https://brainflow.science/impute-cbf.

image (Table 1). We synthesized each of these 16 scenarios from each PC MR image to simulate the effects of a sub-optimal image which failed to assess the four vessels to be analyzed. We applied a standard least-squares model to model the total cerebral blood flow (CBF) as a function of the vessels able to be analyzed. In scenarios where two ICAs or two VAs were analyzed, we simplified and reduced the degrees of freedom in the models by calculating the total anterior (sum of ICAs) or posterior (sum of VAs) flow. We evaluated the quality of each model using root mean squared error, intra-class correlation coefficients (ICC), R^2 statistic. The ICC (Lassen, 1959; Liu et al., 2019) is a two-way random, single measures absolute agreement between model 0 (gold standard) and models 1-8, calculated using MATLAB. We also performed Bland-Altman analyses of all imputed models compared to total CBF. We calculated the biases as the mean difference between model 0 and each other model, and the 95% limits of agreement as twice the standard deviation of the differences of individual measurements between model 0 and each other model.

Results

We report the total cerebral blood flow (933.7 ± 297.9), anterior circulation (sum of ICAs, 652.6 ± 209.2), and posterior circulation (sum of VAs, 281.0 ± 106.2). We also report the flow in the individual arteries: left ICA (328.1 ± 110.5), right ICA (324.9 ± 105.7), left VA (145.9 ± 76.8), and right VA (134.9 ± 53.1), all values are reported in units of ml/min as mean ± standard deviation. (Figure 1, Left). We also report the ratio of flow in individual arteries *versus* total cerebral blood flow, which are: left ICA (0.352 ± 0.039), right ICA (0.348 ± 0.039), left VA (0.154 ± 0.049), and right VA (0.147 ± 0.044), all values are unitless, and reported as mean ± standard deviation. (Figure 1, Right).

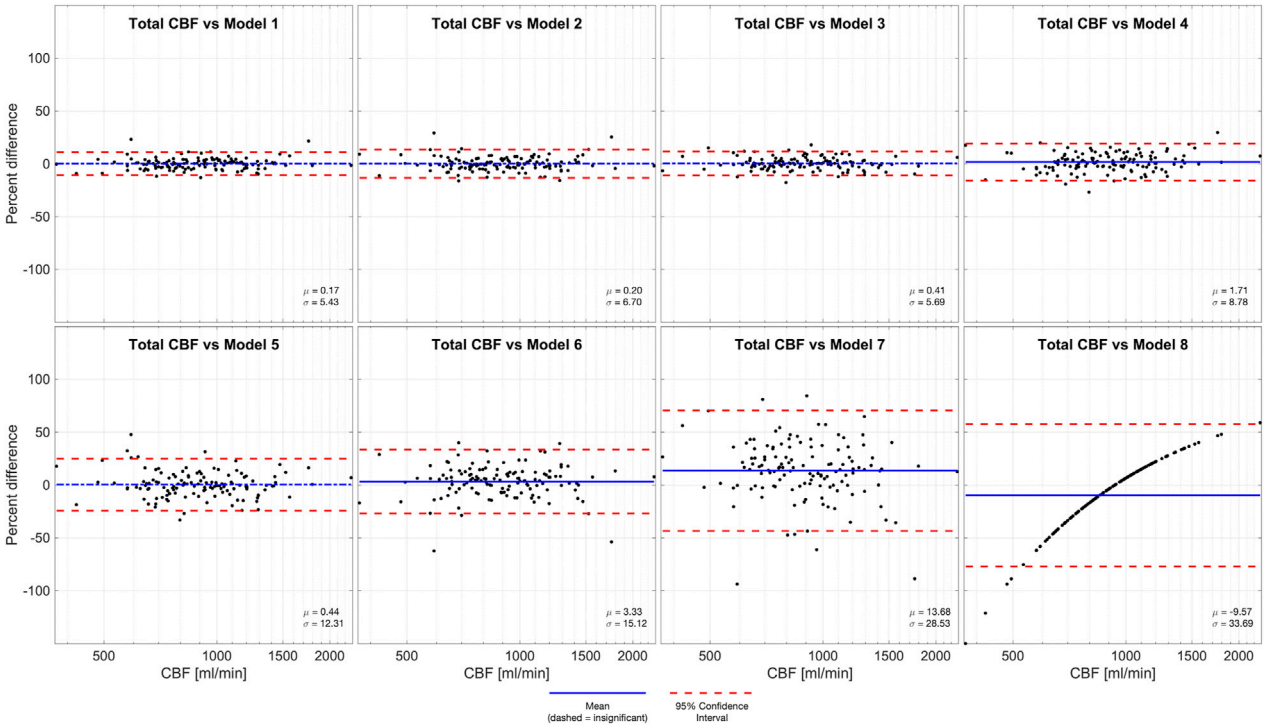

FIGURE 2
Bland-Altman analysis of total CBF quantified by PC in four vessels (model 0) *versus* various models of one or more missing vessels. Blue line demonstrates bias, dashed blue line demonstrates insignificant ($p > 0.05$) bias, and red dash lines demonstrate 95% confidence intervals. These results suggest that it is important to successfully capture at least one ICA or both VAs to impute CBF measurements.

We evaluated all four ratios (left ICA-CBF, right ICA-CBF, left VA-CBF, right VA-CBF) with an ANOVA, and tested all six pairwise comparisons with Tukey-Kramer HSD. Only two pairs of ratios were not different: the left ICA-CBF *versus* right ICA-CBF ratios ($p = 0.549$), and the left VA-CBF *versus* right VA-CBF ratios ($p = 0.549$). Thus, we simplified from 16 models to eight using symmetry of the left and right CBF ratios. All other pairs of ratios were different ($p < 0.0001$).

We created eight statistical models of CBF using standard least squares simple linear regression. We computed the performance statistics for the models, including R^2value, root mean square error (RMSE), normalized RMSE and ICC to evaluate the performance and the reliability of the models (Table 1). These models are numbered from the case with all arteries present (model 0), in ascending order of increasing expected error to the model with the most error because there are no arteries present (model 8). As anticipated from model 1 to model 8, the error in imputation (RMSE) increased and the R^2 decreased. All these models were statistically significant ($p < 0.0001$), except when there were no usable blood vessels (model 8).

We performed Bland-Altman analyses of models 1-8 compared to total CBF (model 0), demonstrated in Figure 2. Models 1-3 and 5 are all statistically unbiased ($p > 0.05$), models 4 and 6 had small biases (1.71% and 3.33%, respectively). Models 1-4 had narrow limits of agreement, with standard deviations of 5.43%–8.78%. Models 5-6 and had wider limits of agreement, with standard deviations of 12.31%–15.12%. Model 7, which was derived from a measurement in one VA, and it performed exceptionally poorly (Bias −9.57%, standard deviation 28.53%). Thus, model 7 had similar performance to model 8 (Bias −9.57% standard deviation 33.69%) wherein flow is assumed equal to the population mean.

Discussion

Our models were suitable to impute CBF for all scenarios wherein at least one ICA was usable (Model 1–5). We do not recommend attempting to impute CBF without any ICA measurements (models 6–8) because of their poor performance. We included models 6 and 7 because they were valid correlates of total cerebral blood flow, and model 8 (mean CBF) for completeness. We recommend the reader interpret our model performances in context of the accuracy and precision needed for each specific use case for measuring CBF. In any situation in which these models are used they add error *versus* the ideal situation wherein all four vessels are perfectly measured in one PC MR image. Thus, if any of the models are used, the error they introduce should be considered and the modeled results should be held with appropriate uncertainty.

The best comparisons of our model performance would be *versus* the performance of other CBF imputation models that use PC MR data. However, because our motivation for these models was the lack of any extant model we cannot ascertain how our models perform *versus* other approaches. As an imperfect alternative, we provide the reader with examples of alternative studies of CBF correlations using different measurement and

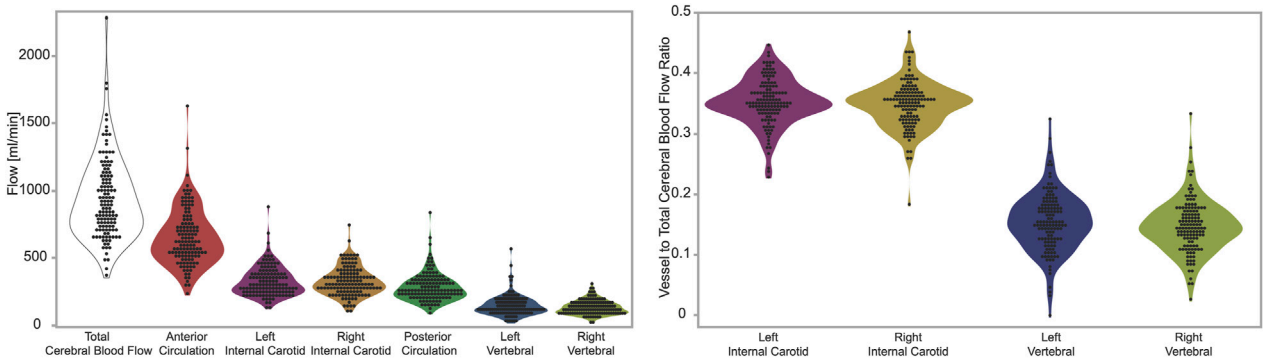

FIGURE 3
Left panel: measurements of flow in units of ml per minute. From left to right the figures shows total, anterior circulation, left internal carotid, right internal carotid, posterior circulation, left vertebral, right vertebra. Right panel: ratios of flow in individual arteries *versus* total cerebral blood flow. From left to right the figure shows left internal carotid, right internal carotid, left vertebral, right vertebra. The figures demonstrate visually (1) the range of total cerebral blood flow, (2) the contribution from individual arteries is predominantly from the anterior circulation, that flow through (3) carotid and (4) vertebral arteries are symmetric on the left and right sides.

validation approaches as context for our model performance. The correlation of arterial spin labeling *versus* ^{15}O positron emission tomography (R^2 0.47 total CBF and R^2 0.48 voxelwise blood flow); (Heijtel et al., 2014) and the intraclass correlation of test-retest measurements with PC MR with no repositioning of slice or patient (ICC 0.79). (Sakhare et al., 2019). provide context to judge our imputation performance *versus* other methods and errors commonly encountered by those who measure CBF.

Imputation error increased more when an ICA was corrupted than a VA. This was anticipated because the ICA makes a greater contribution to CBF than a VA. Thus, a single PC MR slice placement that optimizes the measurement of the two ICAs may be preferable to a single PC MR slice placement that attempts to optimize both the ICAs and VAs. The ability to accurately estimate total CBF based only on carotid measurements (one or both) is perhaps not surprising based on prior work using transcranial Doppler. While losing one carotid compromised CBF accuracy, knowledge of the posterior flow adequately compensated for this loss, reflecting the strong conservation of flow balance between the anterior and posterior circulations.

We suggest that in time-limited scanning scenarios, that the following PC MR localization be used. (A1) Acquire a low resolution, highly accelerated MR angiography scout image with sagittal and coronal maximum intensity projection (MIP) images; this can typically be performed in approximately 30 s (A2) Use the sagittal MRA image to optimize the anterior-posterior pitch of the PC MR plane for the ICAs. (A3) Use the coronal image to optimize the left-right roll of the PC MR plane for the ICAs, (A4) ensure the PC MR slice is above the external carotid artery bifurcation, and (A5) below the junction of the VAs into the basilar artery. Alternatively, if there is not adequate time to acquire the MR angiography image, it is also quite possible to use the ubiquitous initial anatomical survey image; (B1) place the PC MR imaging plane at the level of the C2 cervical vertebra, and (B2) angle it to be perpendicular to the spinal cord. Either approach will intersect all the great vessels of the neck and therefore create the images suitable for our imputation models.

Limitations

Our models are only exploiting image-based information, however we know that CBF is associated with hematocrit, sex and age. (Borzage et al., 2016; Bush et al., 2016). Thus, excluding this data limits our modeling but it also allows our approach to be suitable for scenarios in which this information is either never collected, or removed to anonymize the datasets. We assumed fixed ratios between vessel flow and total CBF. This assumption is implicit on the understanding that the flow would be proportional to the volume of tissue perfused by these vessels, and that those tissues would be present in a fixed volumetric ratio. However, the ratio of these structures may change in development or senescence which limits our model application to the developing brain and provides an opportunity for further development. (Bethlehem et al., 2021). Our model assumed the PC MR slice contains the ICAs and VAs, however with an exceptionally poor localization the image might include the common carotid arteries or basilar artery. If these are incorrectly identified as ICA or VA arteries, then it would cause overestimation of the total CBF. One opportunity for future research is developing models to impute cerebral blood flow from images of common carotid or basilar arteries. Our results demonstrate flow in the two ICAs and two VAs are statistically equivalent. However, we did not include patients with systemic or cerebrovascular disease, nor patients with profound variance in the anatomy of their arteries (e.g. patients who actually lack an ICA or VA), thus our data demonstrating lateral symmetry might not generalize to populations with vascular disease. However, patients with known vascular disease or profoundly abnormal vessels may benefit from the more time-insensitive option of ASL MR. In contrast the PC MR approach is suitable for large studies and population-based screening. Moreover, our observed inter-vessel relationships could potentially be useful in recognizing deranged blood flow distribution in conditions such as steno-occlusive disease.

We did not explore other approaches to acquisition or analysis of the PC MR image data. Our secondary analysis was unable to change the prior approach to acquisition and exploring image processing approaches is beyond the scope of this project. Moreover, our imputation results are based on vascular physiology, not imaging

technology. Thus, our results remain valid even with improved PC MR data acquisitions or image analyses. Our dimensionless approach means that even if our imaging methods are biased compared to approaches taken by others, they can use our imputation models. If our image acquisition methods have higher variance compared to approaches by others, our modeling error will be conservative and overestimate the variance compared to those their improved methods.

Conclusion

Phase contrast MR is an efficient and effective way to assess total cerebral blood flow. Our results indicate that using our imputation models based on at least one ICA flow measurement provides lower variance in results than ASL, and higher intraclass correlation than test-retest PC MR. Therefore, our methods are an important set of equations describing vascular physiology. Our equations enable a new approach for dealing with real-world data and make it easier to use PC MR to obtain measurements of CBF in large numbers of patients or volunteers.

Data availability statement

The raw data supporting the conclusion of this article will be made available by the authors, without undue reservation.

Ethics statement

The studies involving human participants were reviewed and approved by Children's Hospital Los Angeles Committee on Clinical Investigations (CCI 11-00083). Written informed consent to participate in this study was provided by the participants' legal guardian/next of kin.

Author contributions

All authors listed have made a substantial, direct, and intellectual contribution to the work and approved it for publication.

Funding

Research reported in this publication was supported by The National Heart, Lung, and Blood Institute of the National Institutes of Health under awards 5K25HL153954, 1U01-HL-117718-01 and Minority Supplement to Grant 1U01-HL-117718-01.

Conflict of interest

The authors declare that the research was conducted in the absence of any commercial or financial relationships that could be construed as a potential conflict of interest.

Publisher's note

All claims expressed in this article are solely those of the authors and do not necessarily represent those of their affiliated organizations, or those of the publisher, the editors and the reviewers. Any product that may be evaluated in this article, or claim that may be made by its manufacturer, is not guaranteed or endorsed by the publisher.

References

Alsop, D. C., Dai, W., Grossman, M., and Detre, J. A. (2010). Arterial spin labeling blood flow MRI: Its role in the early characterization of alzheimer's disease. *J. Alzheimers Dis.* 20 (3), 871–880. doi:10.3233/JAD-2010-091699

Bethlehem, R. A. I., Seidlitz, J., White, S. R., Vogel, J. W., Anderson, K. M., Adamson, C., et al. 2021.

Borzage, M. T., Bush, A. M., Choi, S., Nederveen, A. J., Václavů, L., Coates, T. D., et al. (2016). Predictors of cerebral blood flow in patients with and without anemia. *J. Appl. Physiol. (1985)* 120 (8), 976–981. doi:10.1152/japplphysiol.00994.2015

Bush, A. M., Borzage, M. T., Choi, S., Václavů, L., Tamrazi, B., Nederveen, A. J., et al. (2016). Determinants of resting cerebral blood flow in sickle cell disease. *Am. J. Hematol.* 91 (9), 912–917. doi:10.1002/ajh.24441

Chen, W., Liu, P., Volkow, N. D., Pan, Y., and Du, C. (2016). Cocaine attenuates blood flow but not neuronal responses to stimulation while preserving neurovascular coupling for resting brain activity. *Mol. Psychiatry* 21 (10), 1408–1416. doi:10.1038/mp.2015.185

Christie, I. C., Price, J., Edwards, L., Muldoon, M., Meltzer, C. C., and Jennings, J. R. (2008). Alcohol consumption and cerebral blood flow among older adults. *Alcohol* 42 (4), 269–275. doi:10.1016/j.alcohol.2008.03.132

Dai, W., Fong, T., Jones, R. N., Marcantonio, E., Schmitt, E., Inouye, S. K., et al. (2017). Effects of arterial transit delay on cerebral blood flow quantification using arterial spin labeling in an elderly cohort. *J. Magn. Reson Imaging* 45 (2), 472–481. doi:10.1002/jmri.25367

Hanaoka, T., Kimura, N., Aso, Y., Takemaru, M., Kimura, Y., Ishibashi, M., et al. (2016). Relationship between white matter lesions and regional cerebral blood flow changes during longitudinal follow up in Alzheimer's disease. *Geriatr. Gerontol. Int.* 16 (7), 836–842. doi:10.1111/ggi.12563

Heijtel, D. F., Mutsaerts, H. J., Bakker, E., Schober, P., Stevens, M. F., Petersen, E. T., et al. (2014). Accuracy and precision of pseudo-continuous arterial spin labeling perfusion during baseline and hypercapnia: A head-to-head comparison with ^{15}O H_2O positron emission tomography. *Neuroimage* 92, 182–192. doi:10.1016/j.neuroimage.2014.02.011

Jennings, J. R., Heim, A. F., Kuan, D. C., Gianaros, P. J., Muldoon, M. F., and Manuck, S. B. (2013). Use of total cerebral blood flow as an imaging biomarker of known cardiovascular risks. *Stroke* 44 (9), 2480–2485. doi:10.1161/STROKEAHA.113.001716

King, K. S., Sheng, M., Liu, P., Maroules, C. D., Rubin, C. D., Peshock, R. M., et al. (2018). Detrimental effect of systemic vascular risk factors on brain hemodynamic function assessed with MRI. *Neuroradiol. J.* 31 (3), 253–261. doi:10.1177/1971400917750375

Koerte, I., Haberl, C., Schmidt, M., Pomschar, A., Lee, S., Rapp, P., et al. (2013). Inter- and intra-rater reliability of blood and cerebrospinal fluid flow quantification by phase-contrast MRI. *J. Magn. Reson Imaging* 38 (3), 655–662. doi:10.1002/jmri.24013

Lassen, N. A. (1959). Cerebral blood flow and oxygen consumption in man. *Physiol. Rev.* 39 (2), 183–238. doi:10.1152/physrev.1959.39.2.183

Leaver, A. M., Vasavada, M., Joshi, S. H., Wade, B., Woods, R. P., Espinoza, R., et al. (2019). Mechanisms of antidepressant response to electroconvulsive therapy studied with perfusion magnetic resonance imaging. *Biol. Psychiatry* 85 (6), 466–476. doi:10.1016/j.biopsych.2018.09.021

Leijenaar, J. F., van Maurik, I. S., Kuijer, J. P. A., van der Flier, W. M., Scheltens, P., Barkhof, F., et al. (2017). Lower cerebral blood flow in subjects with Alzheimer's dementia, mild cognitive impairment, and subjective cognitive decline using two-dimensional phase-contrast magnetic resonance imaging. *Alzheimers Dement. (Amst).* 9, 76–83. doi:10.1016/j.dadm.2017.10.001

Liu, P., Lu, H., Filbey, F. M., Pinkham, A. E., McAdams, C. J., Adinoff, B., et al. (2014). Automatic and reproducible positioning of phase-contrast MRI for the quantification of global cerebral blood flow. *PLoS One* 9 (5), e95721. doi:10.1371/journal.pone.0095721

Liu, P., Qi, Y., Lin, Z., Guo, Q., Wang, X., and Lu, H. (2019). Assessment of cerebral blood flow in neonates and infants: A phase-contrast MRI study. *Neuroimage* 185, 926–933. doi:10.1016/j.neuroimage.2018.03.020

Lu, H., Clingman, C., Golay, X., and van Zijl, P. C. (2004). Determining the longitudinal relaxation time (T1) of blood at 3.0 Tesla. *Magn. Reson Med.* 52 (3), 679–682. doi:10.1002/mrm.20178

MacIntosh, B. J., Swardfager, W., Robertson, A. D., Tchistiakova, E., Saleem, M., Oh, P. I., et al. (2015). Regional cerebral arterial transit time hemodynamics correlate with vascular risk factors and cognitive function in men with coronary artery disease. *AJNR Am. J. Neuroradiol.* 36 (2), 295–301. doi:10.3174/ajnr.A4094

Oshima, T., Karasawa, F., and Satoh, T. (2002). Effects of propofol on cerebral blood flow and the metabolic rate of oxygen in humans. *Acta Anaesthesiol. Scand.* 46 (7), 831–835. doi:10.1034/j.1399-6576.2002.460713.x

Paniukov, D., Lebel, R. M., Giesbrecht, G., and Lebel, C. (2020). Cerebral blood flow increases across early childhood. *Neuroimage* 204, 116224. doi:10.1016/j.neuroimage.2019.116224

Prohovnik, I., Hurlet-Jensen, A., Adams, R., De Vivo, D., and Pavlakis, S. G. (2009). Hemodynamic etiology of elevated flow velocity and stroke in sickle-cell disease. *J. Cereb. Blood Flow. Metab.* 29 (4), 803–810. doi:10.1038/jcbfm.2009.6

Robertson, A. D., Matta, G., Basile, V. S., Black, S. E., Macgowan, C. K., Detre, J. A., et al. (2017). Temporal and spatial variances in arterial spin-labeling are inversely related to large-artery blood velocity. *AJNR Am. J. Neuroradiol.* 38 (8), 1555–1561. doi:10.3174/ajnr.A5257

Sabayan, B., van der Grond, J., Westendorp, R. G., Jukema, J. W., Ford, I., Buckley, B. M., et al. (2013). Total cerebral blood flow and mortality in old age: A 12-year follow-up study. *Neurology* 81 (22), 1922–1929. doi:10.1212/01.wnl.0000436618.48402.da

Sakhare, A. R., Barisano, G., and Pa, J. (2019). Assessing test-retest reliability of phase contrast MRI for measuring cerebrospinal fluid and cerebral blood flow dynamics. *Magn. Reson Med.* 82 (2), 658–670. doi:10.1002/mrm.27752

Thalman, S. W., Powell, D. K., Ubele, M., Norris, C. M., Head, E., and Lin, A. L. (2019). Brain-blood partition coefficient and cerebral blood flow in canines using calibrated short TR recovery (CaSTRR) correction method. *Front. Neurosci.* 13, 1189. doi:10.3389/fnins.2019.01189

Thomas, D. L., Lythgoe, M. F., van der Weerd, L., Ordidge, R. J., and Gadian, D. G. (2006). Regional variation of cerebral blood flow and arterial transit time in the normal and hypoperfused rat brain measured using continuous arterial spin labeling MRI. *J. Cereb. Blood Flow. Metab.* 26 (2), 274–282. doi:10.1038/sj.jcbfm.9600185

Vernooij, M. W., van der Lugt, A., Ikram, M. A., Wielopolski, P. A., Vrooman, H. A., Hofman, A., et al. (2008). Total cerebral blood flow and total brain perfusion in the general population: The rotterdam scan study. *J. Cereb. Blood Flow. Metab.* 28 (2), 412–419. doi:10.1038/sj.jcbfm.9600526

Yang, F. N., Xu, S., Spaeth, A., Galli, O., Zhao, K., Fang, Z., et al. (2019). Test-retest reliability of cerebral blood flow for assessing brain function at rest and during a vigilance task. *Neuroimage* 193, 157–166. doi:10.1016/j.neuroimage.2019.03.016

Yu, C., Lu, W., Qiu, J., Wang, F., Li, J., and Wang, L. (2020). Alterations of the whole cerebral blood flow in patients with different total cerebral small vessel disease burden. *Front. Aging Neurosci.* 12, 175. doi:10.3389/fnagi.2020.00175

frontiers | Frontiers in Physiology

TYPE Review
PUBLISHED 13 April 2023
DOI 10.3389/fphys.2023.1098959

OPEN ACCESS

EDITED BY
James Duffin,
University of Toronto, Canada

REVIEWED BY
Martina Sebök,
University Hospital Zürich, Switzerland
Marco Pinho,
University of Texas Southwestern Medical Center, United States

*CORRESPONDENCE
Pien E. J. Jellema,
e.j.jellema@prinsesmaximacentrum.nl

†These authors have contributed equally to this work

SPECIALTY SECTION
This article was submitted to Medical Physics and Imaging, a section of the journal Frontiers in Physiology

RECEIVED 15 November 2022
ACCEPTED 29 March 2023
PUBLISHED 13 April 2023

CITATION
Jellema PEJ, Wijnen JP, De Luca A, Mutsaerts HJMM, Obdeijn IV, van Baarsen KM, Lequin MH and Hoving EW (2023), Advanced intraoperative MRI in pediatric brain tumor surgery.
Front. Physiol. 14:1098959.
doi: 10.3389/fphys.2023.1098959

Advanced intraoperative MRI in pediatric brain tumor surgery

Pien E. J. Jellema[1,2]*, Jannie P. Wijnen[2], Alberto De Luca[2,3], Henk J. M. M. Mutsaerts[4,5], Iris V. Obdeijn[2], Kirsten M. van Baarsen[1,6], Maarten H. Lequin[1,7†] and Eelco W. Hoving[1,6†]

[1]Department of Pediatric Neuro-Oncology, Princess Máxima Centre for Pediatric Oncology, Utrecht, Netherlands, [2]Centre for Image Sciences, University Medical Centre Utrecht, Utrecht, Netherlands, [3]Department of Neurology, University Medical Center Utrecht, Utrecht, Netherlands, [4]Department of Radiology and Nuclear Medicine, Amsterdam UMC Location Vrije Universiteit Amsterdam, Amsterdam, Netherlands, [5]Amsterdam Neuroscience, Brain Imaging, Amsterdam, Netherlands, [6]Department of Neurosurgery, University Medical Centre Utrecht, Utrecht, Netherlands, [7]Department of Radiology, University Medical Centre Utrecht, Utrecht, Netherlands

Introduction: In the pediatric brain tumor surgery setting, intraoperative MRI (ioMRI) provides "real-time" imaging, allowing for evaluation of the extent of resection and detection of complications. The use of advanced MRI sequences could potentially provide additional physiological information that may aid in the preservation of healthy brain regions. This review aims to determine the added value of advanced imaging in ioMRI for pediatric brain tumor surgery compared to conventional imaging.

Methods: Our systematic literature search identified relevant articles on PubMed using keywords associated with pediatrics, ioMRI, and brain tumors. The literature search was extended using the snowball technique to gather more information on advanced MRI techniques, their technical background, their use in adult ioMRI, and their use in routine pediatric brain tumor care.

Results: The available literature was sparse and demonstrated that advanced sequences were used to reconstruct fibers to prevent damage to important structures, provide information on relative cerebral blood flow or abnormal metabolites, or to indicate the onset of hemorrhage or ischemic infarcts. The explorative literature search revealed developments within each advanced MRI field, such as multi-shell diffusion MRI, arterial spin labeling, and amide-proton transfer-weighted imaging, that have been studied in adult ioMRI but have not yet been applied in pediatrics. These techniques could have the potential to provide more accurate fiber tractography, information on intraoperative cerebral perfusion, and to match gadolinium-based T1w images without using a contrast agent.

Conclusion: The potential added value of advanced MRI in the intraoperative setting for pediatric brain tumors is to prevent damage to important structures, to provide additional physiological or metabolic information, or to indicate the onset of postoperative changes. Current developments within various advanced ioMRI sequences are promising with regard to providing in-depth tissue information.

KEYWORDS

intraoperative MRI, advanced MRI, surgical anatomy, postoperative changes, pediatric brain tumor patients

1 Introduction

Pediatric brain tumor surgery aims for a complete resection of tumor tissue while avoiding damage to healthy functional brain regions. The extent of resection (EOR) is a key indicator of the child's prognosis after surgery (Lindner et al., 2017; Tejada et al., 2018). An increased EOR could improve progression-free and overall survival (Marongiu et al., 2016; Costabile et al., 2019; Li et al., 2021) and reduce the risk of early reoperation (Shah et al., 2012; Sunderland et al., 2021).

The implementation of intraoperative magnetic resonance imaging (ioMRI) aims to sustain these goals by enabling "real-time" images of the brain, allowing for intraoperative evaluation of the extent of resection (EOR) (Marongiu et al., 2016). In 38% of pediatric ioMRI-guided surgical cases, the ioMRI was followed by additional resection leading to a substantial increase in EOR (Karsy et al., 2019; Giussani et al., 2022).

IoMRI may also contribute to alleviate a second challenge during surgery; avoiding damage to healthy functional brain regions and preserving the quality of life (Sunderland et al., 2021). Particularly, ioMRI can pinpoint intraoperative complications such as intracranial hemorrhage or tissue ischemia (Marongiu et al., 2016). IoMRI also gives a "real-time" update on the actual anatomy that may be affected by per-operative brain shift. All in all, ioMRI imaging may be used to update the neuronavigation that supports the neurosurgeon to achieve more radical tumor resections while avoiding neurological damage in surrounding brain tissue (Choudhri et al., 2015; Metwali et al., 2020; Sunderland et al., 2021).

Generally, ioMRI sites incorporate multiparametric imaging optimized for surgical aims. Conventionally used sequences in the pediatric ioMRI context are variations of 2D or 3D T1-and T2-weighted (T1w and T2w) images to visualize residual tumor tissue and to guide continuation of the neurosurgical resection (Abernethy et al., 2012; Choudhri et al., 2014; Millward et al., 2015; Giordano et al., 2017; Low et al., 2018; Tejada et al., 2018; Karsy et al., 2019).

Advanced MRI sequences, on the other hand, could potentially provide additional information on physiological aspects of the brain. For example, these sequences could assess the functional integrity of white matter tracts and blood perfusion or metabolic status of the brain tissue (Abernethy et al., 2012; Sanvito et al., 2021; Petr et al., 2022).

Potentially this might contribute to peroperative awareness and support prevention of damage to healthy functional brain regions.

In this manuscript, we systematically review the literature, aiming to answer the following question: "what is the added value of advanced imaging in ioMRI for pediatric brain tumor surgery, as compared to conventional imaging?"

2 Methods

We conducted a Pubmed search of the literature on advanced MRI in the pediatric ioMRI setting, based on the following search terms: (pediatr* OR paediatr* OR child*) AND (ioMRI OR iMRI OR iopMRI OR "intraoperative MRI" OR "intra-operative MRI") AND (tumor* OR tumour* OR glioma*). Papers were screened on title and abstract, and relevant articles were read in full text.

Articles were included based on the following criteria:

- Case series, cohorts, or trials including pediatric patients (age <19 years) undergoing ioMRI for brain (tumor) surgery.
- The reported MRI sequences were intraoperatively acquired.
- The added value of advanced MRI sequences was reported.

Literature reviews, book chapters, articles on epilepsy, *in vitro* studies, articles not written in English, or with no focus on surgery; articles on low-field MRI (<1.5 Tesla), no focus on ioMRI or no pediatric patients (age, <19 years) were excluded.

Conventional MRI sequences were defined as T1w, T2w, or fluid-attenuated inversion recovery (FLAIR) sequences (with or without gadolinium contrast) that can provide structural information about the brain (Lequin and Hendrikse, 2017). Advanced MRI sequences were defined as sequences that could also provide information on physiology and functionality, including metabolism, brain tumor cellularity, and hemodynamics (Lequin and Hendrikse, 2017; Petr et al., 2022).

The following MRI sequences were considered as advanced MRI sequences: arterial spin labelling (ASL), amide-proton transfer-weighted imaging (APTw), dynamic contrast-enhanced (DCE), dynamic susceptibility contrast (DSC), diffusion kurtosis imaging (DKI), intravoxel incoherent motion (IVIM), multicomponent-driven equilibrium single pulse observation of T1 and T2 (mcDESPOT), magnetic resonance spectroscopy (MRS), myelin water imaging (MWI), neurite orientation and dispersion density imaging (NODDI), quantitative magnetization transfer (qMT), quantitative susceptibility mapping (QSM), relaxometry, vascular, extracellular and restricted diffusion for cytometry in tumors (VERDICT) (Petr et al., 2022); diffusion-weighted imaging (DWI), diffusion tensor imaging (DTI), chemical shift imaging (CSI), susceptibility-weighted imaging (SWI), and functional MRI (Lequin and Hendrikse, 2017).

From each included study, the following data were extracted: study center, magnetic field strength (Tesla), number of brain tumor patients included, histopathological diagnosis, advanced MRI sequences used, and their added value as reported in the study.

As this search yielded limited information, we extended our search beyond the initial research question, using the snowball technique, to gain more information on the technical background of each advanced MRI technique, their use in ioMRI in adults, and their use in routine pediatric brain tumor care.

3 Results

3.1 Systematic literature review

The literature search on PubMed yielded 128 articles, of which ten met our inclusion criteria (Figure 1; Table 1) (Abernethy et al., 2012; Yousaf et al., 2012; Avula et al., 2013; Ren et al., 2013; Giordano et al., 2017; Tejada et al., 2018; Saint-Martin et al., 2019; Low et al., 2020; Avula et al., 2021; Sunderland et al., 2021). Most of these studies were cohort studies, two were case series (Abernethy et al., 2012; Ren et al., 2013), one included a review of experience (Abernethy et al., 2012), and one included a comparison of their results to existing literature (Low et al., 2020). A total of 604 ioMRI brain tumor patients were

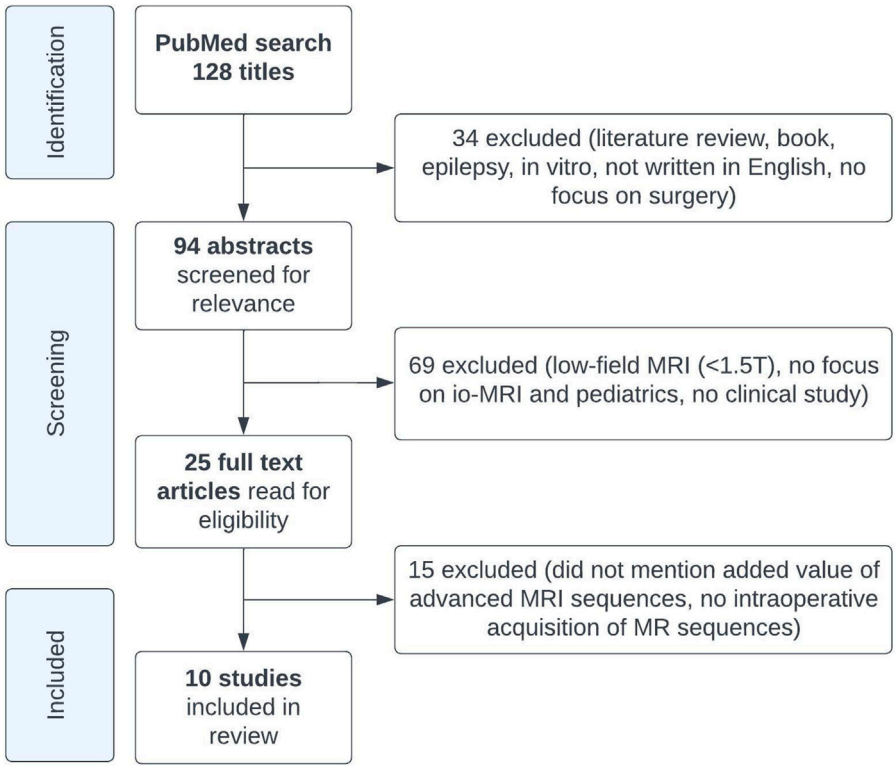

FIGURE 1
Study flowchart.

described in the included literature. All studies that resulted from our PubMed search were performed on either a 1.5 or 3 Tesla MRI scanner. These studies aimed to report the initial ioMRI experience, to evaluate early repeat resection (Avula et al., 2013), to detect ischemic infarcts on diffusion ioMRI (Saint-Martin et al., 2019), or to evaluate ioMRI scans as post-operative scans (Avula et al., 2021). The included studies described a heterogeneous group of histopathological brain tumors with advanced MRI (Table 1). Just one study focused specifically on advanced ioMRI (Saint-Martin et al., 2019) but did not perform any post-processing for further data analysis. Eight studies were evaluated as having a low risk of bias as they included consecutive patients of all histopathological brain tumors though five of these studies reported advanced imaging only in selective patients (Abernethy et al., 2012; Yousaf et al., 2012; Avula et al., 2013; Tejada et al., 2018; Low et al., 2020), introducing an increased bias risk. Two studies had a higher risk of bias as they selected based on tumor type; subendymal giant cell astrocytoma (Ren et al., 2013) or thalamic tumor patients (Sunderland et al., 2021).

The ten articles that reported the use of advanced ioMRI sequences for pediatric brain tumor surgery focused on diffusion MRI (DWI and DTI), perfusion MRI (DSC), and metabolic MRI (MRS and CSI). Diffusion MRI was used in 288 patients, covered by seven studies (Ren et al., 2013; Giordano et al., 2017; Tejada et al., 2018; Saint-Martin et al., 2019; Low et al., 2020; Avula et al., 2021; Sunderland et al., 2021). Three other studies that covered diffusion MRI did not specify the number of patients. Most authors used DWI to detect diffusion restriction that can indicate hemorrhage or ischemic infarcts and DTI for reconstructing fibers (i.e., corticospinal tract and arcuate fasciculus) to avoid damage to important structures. DTI was also used to generate B0 and apparent diffusion coefficient (ADC) maps to visualize ischemic infarcts (Saint-Martin et al., 2019). Perfusion MRI was used in 22 patients, covered by one study (Tejada et al., 2018). Three other studies also used perfusion MRI for selective patients but did not specify their numbers. Authors used DSC for early resection control and additional physiological information on relative cerebral blood flow. Metabolic MRI was used in 11 patients, covered by one study (Tejada et al., 2018). Two other studies that reported use of MRS did not specify the number of selected patients. MRS and CSI were used to evaluate the presence of abnormal high concentration of metabolites (i.e., choline) that could either represent edema or tumor invasion.

In conclusion, the sparse literature demonstrated that advanced sequences in ioMRI for pediatric brain tumor surgery was used to reconstruct fibers to prevent damage to important structures, provide information on relative cerebral blood flow or abnormal metabolites, or to indicate the onset of hemorrhage or ischemic infarcts.

3.2 Explorative literature review

The explorative literature search was confined to the same advanced MRI fields: diffusion-, perfusion-, and metabolic MRI. It focused on the technical background of the sequences, their use in the ioMRI setting for adult brain tumor surgery, and their use in routine pediatric brain tumor care.

10.3389/fphys.2023.1098959

TABLE 1 Study designs and parameters of included studies.

Study	Included pediatric ioMRI brain tumor patients [total]	Study design	Study aim	Brain tumor types described with advanced MRI (histopathology or location)	Advanced MRI sequence	Added value
Abernethy et al. (2012) Alder Hey Children's Hospital, Liverpool, United Kingdom	Not mentioned	Review of experience and case series	Report of initial ioMRI experience	Not mentioned	DTI	Reconstruction of fibers to avoid damage to important structures.
					DSC	Early resection control and information on relative cerebral blood flow.
Yousaf et al. (2012) Alder Hey Children's Hospital, Liverpool, United Kingdom	73 [73]	Cohort	Report of initial ioMRI experience	Deep-seated tumors (DTI), pathology not provided	DTI	Reconstruction of fibers to avoid damage to important structures.
					DSC	Early resection control and information on relative cerebral blood flow.
					MRS	Evaluation of presence of abnormal metabolites.
Avula et al. (2013) Alder Hey Children's Hospital, Liverpool, United Kingdom	36 [72]	Cohort	Evaluation of early repeat resection	Atypical teratoid rhabdoid tumor (MRS)	DWI	Detect diffusion restriction that can indicate hemorrhage or ischemic infarcts.
					DSC	Information on relative cerebral blood flow.
					MRS	Evaluation of presence of abnormal metabolites.
Ren et al. (2013) PLA General Hospital, Beijing, China	7 [7]	Case series	Report of initial ioMRI experience in SEGA patients	SEGA	DTI	Reconstruction of corticospinal tract and arcuate fasciculus to avoid damage to important structures.
Giordano et al. (2017) International Neuroscience Institute–Hannover, Hannover, Germany	75 [75]	Cohort	Report of ioMRI experience	Craniopharyngioma, Rathke's cleft cyst, pituitary macroadenoma, pilocytic astrocytoma, diffuse astrocytoma, glioblastoma, oligodendroglioma, angiocentric glioma, SEGA, anaplastic astrocytoma, ependymoma, cortical dysplasia, ganglioglioma, hamartoma, germinoma, PNET.	DTI	Reconstruction of fibers to avoid damage to important structures.
Tejada et al. (2018) Alder Hey Children's Hospital, Liverpool, United Kingdom	223 [223]	Cohort	Report of ioMRI experience	High-grade glioma (DTI, CSI), midline glioma, and multifocal embryonal tumor (DWI).	DWI	Detect diffusion restriction that can indicate hemorrhage or ischemic infarcts.
					DTI	Reconstruction of fibers to avoid damage to important structures.
					DSC	Information on relative cerebral blood flow.
					MRS and CSI	Evaluation of presence of abnormal metabolites that could either represent edema or tumor invasion.

(Continued on following page)

TABLE 1 (*Continued*) Study designs and parameters of included studies.

Study	Included pediatric ioMRI brain tumor patients [total]	Study design	Study aim	Brain tumor types described with advanced MRI (histopathology or location)	Advanced MRI sequence	Added value
Saint-Martin et al. (2019) The Montreal Children's Hospital, Montreal, Canada	115 [115]	Cohort	Detection of ischemic infarct on diffusion ioMRI	Medulloblastoma, pilocytic astrocytoma, glioblastoma, anaplastic ependymoma, craniopharyngioma, epidermoid cyst, anaplastic ganglioglioma, desmoplastic infantile ganglioglioma, and hypothalamic hamartoma.	DTI	Generate B0 and ADC maps to visualize ischemic infarcts.
Low et al. (2020) KK Women's and Children's Hospital, Singapore, Singapore	35 [43]	Cohort and comparison to literature	Report of ioMRI experience	Not mentioned	DTI	Reconstruction of corticospinal tract to avoid damage to important structures.
Avula et al. (2021) Alder Hey Children's Hospital, Liverpool, United Kingdom	20 [20]	Cohort	Evaluation of ioMRI scan as post-operative scan	Medulloblastoma, pilocytic astrocytoma, fibrillary astrocytoma, ganglioglioma, craniopharyngioma, high-grade glioma, pleomorphic xanthoastrocytoma, pilomyxoid astrocytoma, SEGA, and pituitary adenoma.	DWI and DTI	Detect diffusion restriction that can indicate hemorrhage or ischemic infarcts.
Sunderland et al. (2021) Alder Hey Children's Hospital, Liverpool, United Kingdom	20 [30]	Cohort	Report of ioMRI experience in thalamic tumor patients	Thalamic tumors	DTI	Reconstruction of fibers to avoid damage to important structures.

IoMRI = intraoperative MRI; DTI = diffusion tensor imaging; DSC = dynamic susceptibility contrast; MRS = magnetic spectroscopy resonance; SEGA = subependymal giant cell astrocytoma; PNET = primitive neuroectodermal tumor.

TABLE 2 Difference between single- and multi-shell diffusion MRI acquisition for brain tumor imaging.

	Single-shell diffusion MRI	Multi-shell diffusion MRI
Typical quantification methods	DTI	DKI
Typical b-values	Single, around b = 1000 s/mm^2.	Multiple, between b = 1,000 and b = 3,000 s/mm^2. For example, b = 1,000, 2000, 3,000 s/mm^2.
Fiber tractography model	Depending on the number of gradient directions: • <28, DTI. Unable to resolve crossing fibers. • ≥28, spherical deconvolution. Can (partly) resolve crossing fibers*	Advanced methods applicable if at least 28 gradient directions (45+ recommended) are collected for the largest b-value. Can resolve crossing- and kissing fibers, and account for partial volume effects (e.g., fluids).

DTI = diffusion tensor imaging; DKI = diffusion kurtosis imaging; b-value = Diffusion weighting.
*Guo et al. (2020).

3.3 Diffusion MRI

3.3.1 Technical background of diffusion MRI

Diffusion MRI (dMRI) is based on the diffusion of water molecules and provides information on the microstructural tissue organization. In dMRI, multiple diffusion-weighted images are acquired in multiple spatial directions.

Diffusion tensor imaging (DTI) leverages dMRI data acquired at a single diffusion weighting (b-value) that is therefore called single-shell acquisition (Table 2). It is the conventional dMRI quantification method in clinical practice. The acquisition of dMRI data with multiple b-values, called multi-shell, has recently become feasible within clinically acceptable acquisition times. Multi-shell dMRI allows for more advanced quantification models like diffusion kurtosis imaging (DKI).

DMRI metrics such as the apparent diffusion coefficient (ADC) and fractional anisotropy (FA) can be used to disentangle tissue components (e.g., cellular mass versus edema or other cavities) that can be useful for clinical decision-making (Lequin and Hendrikse, 2017). DKI has been shown to be more sensitive to microstructural changes than DTI (Mohammadi et al., 2015; Yeh et al., 2021). Moreover, multi-shell dMRI data allowed models that could capture the presence of multiple water components (Rydhög et al., 2017),

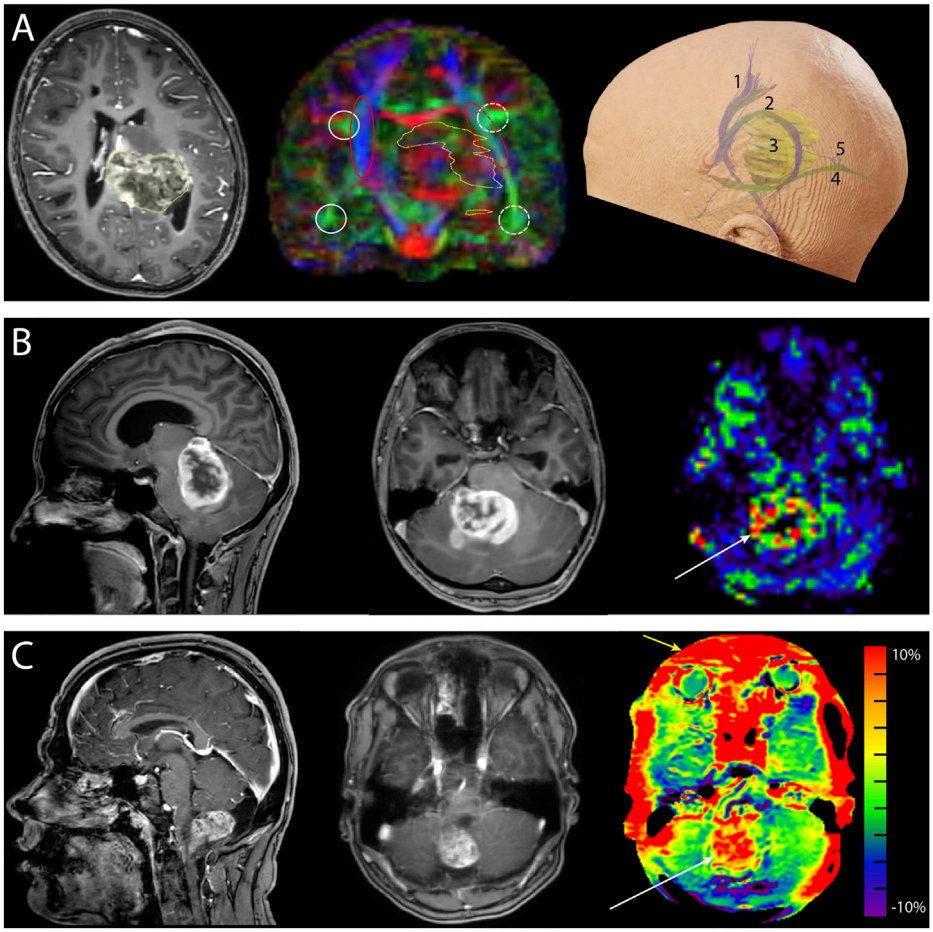

FIGURE 2
Neurosurgical cases demonstrating the added value of advanced MRI. **(A)** Preoperative images of a 10-year-old girl with a diffuse midline glioma (H3K27 mt) originating from the left posterior thalamus and mesencephalon and expanding into the atrium of the left ventricle. *Left*: the transverse T1-weighted contrast-enhanced image shows enhancement of the tumor (yellow outline). *Center:* the coronal fractional anisotropy color-coded map (single-shell diffusion MRI, 16 directions) shows left-right asymmetry demonstrating the displacement of fibers caused by the tumor (yellow outline). The white circles depict the arcuate fasciculus, and the red ovals depict the corticospinal tracts. Solid lines depict the unaffected side, and the dashed lines show the affected side. *Right:* reconstruction of the corticospinal tract 1), arcuate fasciculus 2), tumor 3), and optic radiation 4). A parietal surgical approach posterior to the arcuate fasciculus and superior to the optic radiation 5) was chosen for tumor mass reduction and histopathological diagnosis. **(B)** Preoperative images of a 17-year-old girl with neurofibromatosis type 1 and a space-occupying lesion in the fourth ventricle. *Left*: the sagittal T1-weighted contrast-enhanced images. The differential diagnosis was pilocytic astrocytoma or high-grade glioma. *Center*: transverse T1-weighted contrast-enhanced image. *Right*: the hyperperfusion (white arrow) of the unquantified arterial spin labeling image makes diagnosing a high-grade glioma more probable. Histopathological examination revealed a high-grade glioma with pilocytic features. **(C)** Preoperative images of a 17-year-old boy with a pilocytic astrocytoma. *Left:* sagittal T1-weighted contrast-enhanced image. *Center:* transverse T1-weighted contrast-enhanced image. *Right:* amide-proton transfer-weighted (APTw) image. Note the hyperintense region (white arrow) that matches the contrast enhancement on T1-weighted contrast-enhanced image. The red outer rim (yellow arrow) of the APTw image is likely caused by susceptibility-weighted air-tissue artifacts. Ethical approval from the local medical ethics committee was obtained for this study.

such as free water (e.g., edema) (Pasternak et al., 2009) or perfusion (e.g., intra-voxel incoherent motion) (De Luca et al., 2017). In addition to microstructural properties, dMRI data can be used to reconstruct the trajectory of brain white matter pathways (Figure 2A) (Jeurissen et al., 2019). When such fiber tractography models are based on multi-shell dMRI, they could typically account for crossing fibers and properties of different tissue types in the brain (e.g., white matter versus grey matter versus free fluid). Multi-shell data could be used to generate a more detailed and anatomically accurate fiber tractography than single-shell dMRI (Table 4) (Poretti et al., 2012; Mohammadi et al., 2015; Guo et al., 2020; Yeh et al., 2021). Moreover, it might be able to map the border of major white matter tracts and displaced fiber tracts more reliably (Nimsky, 2014; De Luca et al., 2020). Disadvantages of multi-shell dMRI are lower signal-to-noise ratio (SNR), which is often resolved with a lower spatial resolution or longer acquisition time, and technically demanding post-processing to increase image quality (Mohammadi et al., 2015). Both single- and multi-shell dMRI are sensitive to eddy currents and susceptibility artifacts between air and tissue (Table 3). These artifacts are increased in the intraoperative setting due to the open skull (Mohammadi et al., 2015; Lindner et al., 2022). However, this might be worse in multi-shell diffusion MRI acquisition due to the higher gradient amplitudes (Mohammadi et al., 2015).

TABLE 3 Technical considerations and details of each advanced MRI sequence.

Sequence	Estimated average scan time*	Desired resolution§	Sequence-specific artifacts and considerations
Single-shell dMRI	3 min (in case of DTI, whole-brain, about 20 directions)†	Isotropic, <2.5 mm	Susceptible to air-tissue artifacts and eddy currents; Susceptible to artifacts caused by free diffusion in tissue (e.g., edema).
Multi-shell dMRI	8 min (in case of a minimum protocol for DKI, whole-brain, about 42 directions)‡	Isotropic, <2.5 mm	Susceptible to air-tissue artifacts and eddy currents; Higher b-value acquisition results in a lower SNR that needs to be compensated by averaging or reducing the echo time; Longer acquisition time.
ASL	4 min 30 s (whole-brain)	3 × 3 × 7 mm	Susceptible to air-tissue artifacts and blood flow artifacts caused by pulsation of large blood vessels; Thick slices (7 mm) required to reach desired SNR levels in the clinical setting; Difficult to position ASL labeling box perpendicular to vessels in the neck when the patient has a twisted neck in the surgical position.
MRS (single-voxel)‖	4 min 28 s	20 × 20 × 20 mm	Susceptible to air-tissue artifacts; Long acquisition time and low spatial resolution.
APTw imaging	4 min (half-brain)	0.9 × 0.9 × 6 mm	Susceptible to air-tissue artifacts causing a B0 offset of the saturation pulse¶, thereby less specific for APTw signal; Thick slices (6 mm) required to reach desired SNR level in the clinical setting.

DMRI = diffusion MRI; DTI = diffusion tensor imaging; DKI = diffusion kurtosis imaging; SNR = signal-to-noise ratio; ASL = arterial spin labelling; MRS = magnetic resonance spectroscopy; APTw = Amide proton transfer-weighted.

*Estimated scan time when making use of accelerated imaging techniques on a 3 Tesla strength while using two single-loop receiving coils.

†Whole brain is a field of view of 240 × 240 × 160 mm.

‡The acquisition of multi-shell dMRI with single-loop receiving coils cannot be accelerated with the multi-band technique as it is only available for a conventional multi-channel head coil.

§Reconstructed voxel size.

‖Semi-LASER spectroscopy with an echo time of 35 ms.

¶Zhou et al. (2019).

3.3.2 Use of diffusion MRI in adult ioMRI setting

In the adult ioMRI setting, dMRI was used for fiber tracking of white matter fibers in eloquent brain areas (Zhang et al., 2022). Due to the brain shift after craniotomy, such fiber reconstructions had to be adjusted intraoperatively (Zhang et al., 2022). Single-shell dMRI, which is suitable for DTI, has been used more often in clinical practice than multi-shell dMRI due to its reliance on simpler data acquisition and reconstruction models (Mohammadi et al., 2015). Previous research on intraoperative single-shell dMRI reported its use in the estimation of brain shift (Metwali et al., 2020). It was also an integral part of an ioMRI protocol which was able to increase EOR from 44% to 88.5% in an adult glioblastoma population (Marongiu et al., 2016). Studies comparing EOR in groups of patients using ioMRI protocols with and without diffusion MRI are not currently available and would be helpful to determine its specific added value. Hypothetically, multi-shell dMRI might even further improve these findings (Nimsky, 2014). The feasibility of multi-shell dMRI fiber tractography was reported by Leote et al. (2018) for the pre-surgical planning of adult brain tumor surgery.

3.3.3 Use of diffusion MRI in pediatric routine brain tumor care

DMRI metrics, such as the ADC and FA, were used in routine pediatric clinical practice to grade tumor tissue and differentiate it from healthy brain tissue (Table 4) (Ouadih et al., 2022). ADC was associated with cellularity in previous studies, which was correlated with extracellular diffusion (Villanueva-Meyer et al., 2017; She et al., 2021). Reduced diffusivity (low ADC) compared to surrounding tissues could point toward high cellular tumor tissue (i.e., medulloblastoma) with little extracellular water and ischemia. Conversely, high diffusivity (high ADC) could indicate increased extracellular water, vasogenic edema, or necrotic tissue (Avula et al., 2014). FA values were also used to grade brain tumor tissue in children, where low FA has been associated with high-grade glioma (Poretti et al., 2012). Furthermore, DKI metrics were considered more promising than conventional dMRI metrics in tumor grading and prediction of the expression of Ki-67, a histopathological cell proliferation biomarker (Jiang et al., 2015; Sanvito et al., 2021).

3.4 Perfusion MRI

3.4.1 Technical background of contrast-based perfusion MRI

Brain tumor perfusion characteristics can be investigated with gadolinium contrast-based perfusion MRI sequences. Examples of such imaging methods are dynamic susceptibility contrast- (DSC) and dynamic contrast-enhanced (DCE) imaging (Lequin and Hendrikse, 2017). Gadolinium contrast is the cornerstone of MRI tumor diagnostics, but its disadvantages should be considered carefully. First, gadolinium could cause the accumulation of toxic side products, especially in renal failure patients, increasing the chance of developing nephrogenic systemic fibrosis (Sadowski et al., 2007). Second, gadolinium is a blood-pool contrast agent whose enhancement assumes an intact blood-brain barrier. However, surgical manipulation violates this assumption in the intraoperative setting. This could lead to misinterpretation of gadolinium contrast enhancement (Abernethy et al., 2012). Third, gadolinium could cause a delay in sequence repetition if readministered within 24 h. However, on the day of the surgical procedure, MR scan sessions are often repeated (e.g., intra- and post-operative MRI or multiple ioMRI sessions) (Millward et al., 2015; Keil et al., 2018). Fourth, gadolinium may pose an environmental threat (Trapasso et al., 2021). Taking these disadvantages of gadolinium contrast-based

TABLE 4 Clinical implications of advanced ioMRI in pediatrics.

Imaging technique	Promises	Pitfalls
Single-shell dMRI	Conventional quantification method in clinical practice; DTI metrics (e.g., MD and FA) are reliable to grade tumor tissue.	Data is likely not optimal for fiber tractography in presence of edema and/or fluid cavities.
Multi-shell dMRI	Sensitive to additional effects than single-shell dMRI (e.g., diffusion restrictions due to membranes). Suitable for state-of-the-art fiber tractography methods to resolve crossing- and kissing fibers and account for partial volume effects; DKI metrics can be used to grade tumor tissue and predict Ki-67 expression; Detect residual diffusion restriction effects and residual tumor tissue.	Not commonly used in clinical practice; Initially requires more expert knowledge to set-up. Lack of user-friendly tools to leverage its full potential.
ASL	Detect residual tumor tissue; Differentiate from non-tumorous gadolinium enhancement in resection cavity; Mapping of functional areas.	Artifacts in the control image can propagate in ASL difference image (e.g., false-positive hyperperfusion).
MRS (single-voxel)	Metabolic evaluation of tumor tissue; Metabolite pattern recognition could be assisted by automated processing.	Low specificity of tumor type.
APTw imaging	Replace gadolinium-based anatomical sequences to detect residual tumor; Can generate a quantified image; APTw signal could be associated with increased protein levels.	Not commonly used in clinical practice; Potentially low detection sensitivity to low-grade gliomas which are more prominent in pediatrics.

dMRI = diffusion MRI; DTI = diffusion tensor imaging; DKI = diffusion kurtosis imaging; MD = mean diffusivity; FA = fractional anisotropy; ASL = arterial spin labeling; MRS = magnetic resonance spectroscopy; APTw = amide-proton transfer-weighted.

sequences into account, we shall focus on non-invasive alternatives for this explorative literature search on perfusion MRI.

3.4.2 Technical background of non-invasive perfusion MRI

Arterial spin labelling (ASL) is a perfusion MRI sequence that can quantify absolute CBF based on endogenous blood water (Keil et al., 2018). The ASL signal is based on subtracting two consecutive images (Lindner et al., 2022). The first image labels inflowing arterial blood at the cervical level that is magnetically inverted with a radiofrequency pulse (Alsaedi et al., 2018; Keil et al., 2018). This image is acquired after an appropriate delay time, called the post-labeling delay, which depends on the speed of blood flow and thus the health of the vascular tree (Carsin-Vu et al., 2018; Keil et al., 2018). The second image is the control image that covers the same downstream cerebral region of interest but without magnetically inverting the blood in the cervical arteries (Alsaedi et al., 2018). The ASL difference image visualizes the perfusion signal from the arteries into neighboring brain tissue (Alsaedi et al., 2018). This difference image can then generate a map that represents the quantified CBF in mL/100 g brain tissue/min (Keil et al., 2018).

ASL has the advantage that it is not susceptible to blood-brain barrier leakage artifacts usually observed for gadolinium (Lindner et al., 2017; Keil et al., 2018). Another important advantage is that it can be easily repeated without any cost, except for adding the scanning duration. Lastly, the ability of ASL to quantify absolute CBF (Keil et al., 2018) is useful for assessment of cerebral vitality in surgical and eloquent areas. Disadvantages of ASL are the relatively low SNR (Table 3) and limited sensitivity in low CBF regions such as white matter (Petr et al., 2022). However, the low SNR of the ASL signal is less prominent in children (Yeom et al., 2013). The problem of limited sensitivity in the white matter could be overcome by integrating ASL and dMRI in a multiparametric model to generate a comprehensive clinical overview.

3.4.3 Use of non-invasive perfusion MRI in adult ioMRI setting

Intraoperative ASL could be used for iatrogenic changes in CBF and to depict residual tumor tissue in adults (Table 4) (Lindner et al., 2017). Lindner et al. (2017) reported the feasibility of intraoperative residual tumor detection using ASL when compared to gadolinium-contrast based T1w images (T1w-Gd) in adults with glioblastoma. They argued that ASL could make a more definite judgment of residual tumor tissue than conventional ioMRI sequences (Lindner et al., 2017). However, only a small number of patients were included in this study (n = 8). Another use of intraoperative ASL could be mapping functional areas that should not be damaged during surgery to avoid postsurgical deficits (Lindner et al., 2022). This research also focused on an adult glioblastoma population. It showed that intraoperative ASL could reliably map functional areas and residual brain tumor after post-processing special data. However, their analysis method also revealed false-positive artifacts on the resection rim that should be carefully considered.

3.4.4 Use of non-invasive perfusion MRI in pediatric routine brain tumor care

Several studies have indicated that ASL could be a reliable method to evaluate perfusion patterns of brain tumors in pediatric populations (Yeom et al., 2013; Morana et al., 2017). ASL-based CBF maps have been used routinely to grade tumor tissue in children due to its correlation with tumor vascular density (Yeom et al., 2013; Dangouloff-Ros et al., 2016; Keil et al., 2018). In such a way, hyperperfusion on ASL images could indicate the high malignity of tumor tissue, because of increased tumor tissue activity and blood flow supply (Figure 2B) (Yeom et al., 2013; Dangouloff-Ros et al., 2016; Keil et al., 2018). To illustrate this, Yeom et al. (2013) presented a case diagnosed with mixed anaplastic astrocytoma-glioblastoma that showed elevated CBF values in tumor tissue compared to non-tumoral grey matter. On the other hand, low-grade gliomas, such as dysembryoplastic neuroepithelial tumors,

showed low ASL-based CBF within the tumor region (Yeom et al., 2013; Lequin and Hendrikse, 2017).

Some limitations of ASL in pediatric routine brain tumor care should be considered. First, various ASL perfusion patterns existed for both high- and low-grade gliomas depending on vascular characteristics (e.g., vessel density and capillary exchange rate). Second, ASL hypoperfusion in children could also be caused by edema or scar tissue (Keil et al., 2018). Due to this heterogeneity of measurements in different tumor types, ASL images should be considered in combination with high-resolution anatomical images for a more definite judgement. Third, the effect of anesthesia on regional CBF should also be considered, as general anesthesia usually induces vasodilation (Carsin-Vu et al., 2018; Keil et al., 2018).

3.5 Metabolic MRI

3.5.1 Technical background in metabolic MRI

Proton magnetic resonance spectroscopy (MRS) is a non-invasive metabolic MRI technique that can detect metabolites in the tissues (Wilson et al., 2019). For example, MRS could detect the neurotransmitters glutamate, glutamine, GABA, and other metabolites such as N-acetyl aspartate, choline, creatine, and myo-inositol. Alterations in metabolite levels could give insight into the pathophysiological condition of tissue (Petr et al., 2022). A limitation of MRS is that on clinical field strengths (3 Tesla), the sensitivity is relatively low as usually, the scan time in the clinic is limited (Table 3) (Wilson et al., 2019). Therefore large voxel sizes of 8 mL are commonly used for MRS in clinical practice (Wilson et al., 2019). This could be problematic in the intraoperative setting where whole-brain images are preferred to evaluate spatial heterogeneity. In that setting, the acquisition time for whole-brain chemical shift-imaging (CSI) (or even a single slice) becomes a practical limitation. Currently, fast whole brain CSI methods are not implemented as vendor products for use in intraoperative setting.

Another metabolic MRI modality is chemical exchange saturation transfer (CEST). CEST is an MRI modality that exploits the abundance of exchangeable protons of a certain metabolite, and its chemical exchange with water protons, to image the relative concentration of a certain metabolite (Wu et al., 2016). In CEST, protons of the metabolite of interest are saturated by a prolonged saturation RF pre-pulse; during this pre-pulse, water exchanges unsaturated protons with saturated protons from the metabolites of interest, resulting in a reduction of the water signal, which can be imaged over the whole volume. This has the advantage of an easier interpretation in clinical practice compared to single-voxel MRS (Wu et al., 2016). Amide-proton transfer-weighted (APTw) imaging is a form of CEST imaging sensitive to chemical exchange of protons in water, mobile proteins, and peptides. This form of CEST has been mainly used for brain tumors (Wu et al., 2016; Suh et al., 2019).

3.5.2 Use of metabolic MRI in adult ioMRI setting

In the intraoperative setting, metabolic MRI could be used to provide biochemical information about relative metabolite concentrations of potential residual tumor tissue (Pamir et al., 2010; Yousaf et al., 2012). Pamir et al. (2010) reported that the combination of MRS with DWI effectively differentiated peritumoral changes from a residual tumor in adult low-grade glioma. APTw imaging has not yet been described in the intraoperative setting. However, APTw imaging has been reported to guide stereotactic biopsy in adults with newly diagnosed gliomas (Jiang et al., 2017). Jiang et al. (2017) showed that the APTw signal was sensitive and specific for differentiating between adult low- and high-grade gliomas.

Hypothetically, intraoperative APTw imaging might be an alternative to a T1w-Gd sequence (Figure 2C). Yu et al. (2019) reported that lesions identified on the APTw images mimicked those on the T1w-Gd images of adult meningioma patients. To add to this argument, APTw images could provide improved diagnostic specificity compared to T1w-Gd images in high-grade glioma patients (Zhou et al., 2013). APTw imaging accurately differentiated between glioblastoma and solitary brain metastases in adults (Yu et al., 2017). Also, Zhou et al. (2019) showed that APTw images added new information to the standard T1w-Gd image in an oligodendroglioma case. A disadvantage of intraoperative APTw images could be that surgery-induced blood components could produce hyperintensity artifacts on APTw images (Zhou et al., 2019; Zhang et al., 2021). Moreover, whether the thicker slices used for APTw images in the clinic still add valuable information in the surgical setting is questionable. Lastly, the open skull during surgery could increase magnetic field (B0) inhomogeneities due to the sensitivity of the APTw signal to air-tissue interfaces which decreases accuracy of the APTw signal (Zhou et al., 2019). To solve this issue, attention should be paid to remove all air bubbles in the brain and B0 shimming to avoid these susceptibility artifacts during intraoperative APTw image acquisition (Table 3). An alternative could be to focus B0 shimming and CEST acquisition on a specific region of interest instead of imaging the whole brain. Taking technical and logistical limitations into account, intraoperative APTw imaging seems to be the most useful in the case of high-grade glioma patients (Chalil and Ramaswamy, 2016; Zhang et al., 2021).

3.5.3 Use of metabolic MRI in pediatric routine brain tumor care

MRS has been used in clinical practice to support diagnosing and differentiating brain tumor subtypes in children (Faghihi et al., 2017). In such a way, spectroscopic patterns can be distinctive for tumor subtypes (Vicente et al., 2013). Aggressive features of a tumor could be indicated by an elevated choline-to-N-acetyl aspartate ratio or the presence of lactate (Choudhri et al., 2015). The recognition of these patterns could be assisted by automated processing in pediatrics (Vicente et al., 2013). Due to regional metabolic variations, MRS alone did not suffice to define all regional components of tumors (Lequin and Hendrikse, 2017). MRS should be combined with other standardized MRI methods for a more definitive diagnosis. For example, based on the metabolic profile alone, a pilocytic astrocytoma could be misdiagnosed as a more aggressive variant due to a higher choline peak than a creatine peak and an elevated lipid peak (Table 4) (Lequin and Hendrikse, 2017).

APTw imaging could also be used in pediatric brain tumor care to grade and identify the proliferative activity of tumor tissue (Zhang et al., 2021). The increased protein levels in tumor tissue could be indicated by increased APTw values that might be positively correlated with Ki-67 expression levels (Table 4) (Wu et al., 2016; Suh et al., 2019). Therefore, high-grade gliomas could be indicated by a higher APTw signal than low-grade gliomas, although these results were more heterogeneous in the pediatric population

(Suh et al., 2019; Zhang et al., 2021). Besides, APTw imaging was said to differentiate between brain tumor tissue and edema (Wen et al., 2010). Zhang et al. (2020) presented a pediatric case where the edema showed a similarly low APTw signal as the healthy surrounding tissue. However, a comparison of the APTw signal between tumor tissue and edema was missing. Due to the scarce existing literature in the pediatric population, further research is essential to reliably incorporate APTw imaging in clinical practice (Suh et al., 2019).

4 Discussion

This study is a retrospective study of the literature on the added value of advanced MRI in the intraoperative setting of pediatric brain tumors compared to conventional MR imaging. Our systematic literature search revealed that the fields of diffusion-, perfusion-, and metabolic MRI have been reported for selective cases during surgery. The available literature was sparse and demonstrated that advanced sequences were used to prevent damage to reconstruct fibers to prevent damage to important structures, provide information on relative cerebral blood flow or abnormal metabolites, or to indicate the onset of hemorrhage or ischemic infarcts.

Our explorative literature search revealed developments within each advanced MRI field that have been studied in the adult ioMRI population but have not yet been applied in pediatrics. First, multi-shell dMRI could offer "real-time" fiber tractography that was said to be more anatomically accurate than models based on single-shell data. Second, ASL could give information on intraoperative cerebral perfusion and could indicate residual tumor tissue intraoperatively without a contrast agent. Third, APTw imaging and ASL could potentially match T1w-Gd images. Despite these promising advances, the technical and practical limitations of each of these advanced MRI sequences should be carefully considered before implementing them in standard pediatric ioMRI protocols.

4.1 Future perspectives

Advanced MR images acquired during surgery could gain insight into the effect of mechanical manipulation of a child's brain. Data from these sequences could be useful for research into biomarkers predicting surgery-induced early effects of intraoperative complications (Choudhri et al., 2015; Metwali et al., 2020). For example, in research on surgery-induced cerebellar mutism syndrome (CMS), intraoperative dMRI and ASL imaging might help find biomarkers that could be used for treatment development and prevention strategies (Ahmadian et al., 2021). In such a way, CMS-related diffusion abnormalities that have been seen in the proximal efferent cerebellar pathways (Avula et al., 2014; Keil et al., 2018; Avula, 2020), could be detected earlier on by means of multi-shell fiber tractography that is more anatomically accurate. Also, the onset of supratentorial cortical hypoperfusion related to CMS could be detected earlier on intraoperative ASL perfusion maps (Ahmadian et al., 2021). Hypoperfusion in this region was previously found to result from cortico-cerebellar diaschisis (Keil et al., 2018).

Another example is the prediction of early postoperative seizures after supratentorial brain tumor surgery with intraoperative ASL and APTw imaging. These seizures have been associated with hemorrhage in the resection cavity (Chassoux and Landre, 2017; Samudra et al., 2019; Ersoy et al., 2020). As the onset of seizures in children has been associated with cortical hyperperfusion (Oishi et al., 2012; Keil et al., 2018), intraoperative perfusion imaging with ASL might be an early predictor for seizures and even lead to intraoperative monitoring and prevention (Palaniswamy et al., 2019). APTw images could have a similar effect due to the association of seizures with a reduced pH that could be picked up by a reduced APTw signal (Magnotta et al., 2012; Jin et al., 2017). However, this seizure-induced change in pH change was said to be smaller than the precision of the pH measurement derived from APTw data (Jin et al., 2017). Nevertheless, intraoperative APTw images could have the unique potential to gain more insight into the physiologic processes of postoperative seizures in young children.

Reports focusing on the added value of intraoperative use of advanced MRI, particularly metabolic MRI, in the pediatric brain tumor population are scarce to date. The existing literature was often of a descriptive nature, and randomized controlled trials are lacking. Whilst we could learn from proof of concept reports that use advanced ioMRI in the adult population (Lindner et al., 2017), a specific investigation into the pediatric population is required to understand this unique situation better. Further, the majority of the included studies of our systematic literature search originated from the same clinical center (Abernethy et al., 2012; Yousaf et al., 2012; Avula et al., 2013; 2021; Tejada et al., 2018; Sunderland et al., 2021). Their findings could therefore potentially represent overlapping patient data.

To study the effect of surgery on a child's brain, a multiparametric approach, including diffusion, perfusion, and metabolic ioMRI could be useful. Especially with the opportunity of tissue pathological validation on the spot. Recent developments regarding *in vivo* microscopy and high-speed histopathological diagnostics (Hollon et al., 2020) may facilitate immediate validation of these advanced ioMRI sequences in the near future.

Further development of accelerated imaging techniques could also be explored to reduce the acquisition time or to improve image quality. Particularly image acceleration techniques that could be used with the limited number of single-loop receiving coils that are currently available in the intraoperative setting. Alternatively, recent hardware development of thinner, more flexible, or multi-channel coils could improve image quality and reduce the transition time to and from the ioMRI suite.

The application of advanced ioMRI could be potentially valuable in providing new relevant information of the brain in the peroperative setting. The implementation might be challenging and involves close collaboration between neurosurgeons, neuroradiologists, and physicists. Collaboration among professionals from different ioMRI centres will contribute and support progress in this field.

5 Conclusion

The potential added value of advanced MRI in the intraoperative setting for pediatric brain tumors is to prevent damage to important structures, to provide additional physiological or metabolic information, or to indicate the onset of postoperative changes. Current developments within various advanced ioMRI sequences are promising with regard to providing in-depth tissue information.

Author contributions

PJ drafted the manuscript and JW helped to shape the manuscirpt. AL gave input for the diffusion MRI section, HM gave input for the perfusion MRI section, IO and JW gave input for the metabolic MRI section. KB and EH gave input for the neurosurgical perspective, ML provided input for the neuroradiological perspective. All authors reviewed the manuscript and provided critical feedback.

Funding

We gratefully acknowledge funding of the European Union: Eurostars E! 12449 IMAGINE! and the Dutch Research Council: NWO-VIDI 18361_JW.

Conflict of interest

The authors declare that the research was conducted in the absence of any commercial or financial relationships that could be construed as a potential conflict of interest.

Publisher's note

All claims expressed in this article are solely those of the authors and do not necessarily represent those of their affiliated organizations, or those of the publisher, the editors and the reviewers. Any product that may be evaluated in this article, or claim that may be made by its manufacturer, is not guaranteed or endorsed by the publisher.

References

Abernethy, L. J., Avula, S., Hughes, G. M., Wright, E. J., and Mallucci, C. L. (2012). Intra-operative 3-T MRI for paediatric brain tumours: Challenges and perspectives. *Pediatr. Radiol.* 42, 147–157. doi:10.1007/s00247-011-2280-3

Ahmadian, N., van Baarsen, K. M., Robe, P. A. J. T., and Hoving, E. W. (2021). Association between cerebral perfusion and paediatric postoperative cerebellar mutism syndrome after posterior fossa surgery—A systematic review. *Childs Nerv. Syst.* 37, 2743–2751. doi:10.1007/s00381-021-05225-5

Alsaedi, A., Thomas, D., Bisdas, S., and Golay, X. (2018). Overview and critical appraisal of arterial spin labelling technique in brain perfusion imaging. *Contrast Media Mol. Imaging* 2018, 1–15. doi:10.1155/2018/5360375

Avula, S., Pettorini, B., Abernethy, L., Pizer, B., Williams, D., and Mallucci, C. (2013). High field strength magnetic resonance imaging in paediatric brain tumour surgery - its role in prevention of early repeat resections. *Childs Nerv. Syst.* 29, 1843–1850. doi:10.1007/s00381-013-2106-8

Avula, S., Kumar, R., Pizer, B., Pettorini, B., Abernethy, L., Garlick, D., et al. (2014). Diffusion abnormalities on intraoperative magnetic resonance imaging as an early predictor for the risk of posterior fossa syndrome. *Neuro Oncol.* 17, 614–622. doi:10.1093/neuonc/nou299

Avula, S., Jaspan, T., Pizer, B., Pettorini, B., Garlick, D., Hennigan, D., et al. (2021). Comparison of intraoperative and post-operative 3-T MRI performed at 24–72 h following brain tumour resection in children. *Neuroradiology* 63, 1367–1376. doi:10.1007/s00234-021-02671-5

Avula, S. (2020). Radiology of post-operative paediatric cerebellar mutism syndrome. *Childs Nerv. Syst.* 36, 1187–1195. doi:10.1007/s00381-019-04224-x

Carsin-Vu, A., Corouge, I., Commowick, O., Bouzillé, G., Barillot, C., Ferré, J. C., et al. (2018). Measurement of pediatric regional cerebral blood flow from 6 months to 15 years of age in a clinical population. *Eur. J. Radiol.* 101, 38–44. doi:10.1016/j.ejrad.2018.02.003

Chalil, A., and Ramaswamy, V. (2016). Low grade gliomas in children. *J. Child. Neurol.* 31, 517–522. doi:10.1177/0883073815599259

Chassoux, F., and Landre, E. (2017). Prevention and management of postoperative seizures in neuro-oncology. *Neurochirurgie* 63, 197–203. doi:10.1016/j.neuchi.2016.10.013

Choudhri, X. A. F., Klimo, P., Auschwitz, T. S., Whitehead, M. T., and Boop, F. A. (2014). 3T intraoperative MRI for management of pediatric CNS neoplasms. *AJNR Am. J. Neuroradiol.* 35, 2382–2387. doi:10.3174/ajnr.A4040

Choudhri, A. F., Siddiqui, A., Klimo, P., and Boop, F. A. (2015). Intraoperative MRI in pediatric brain tumors. *Pediatr. Radiol.* 45, 397–405. doi:10.1007/s00247-015-3322-z

Costabile, J. D., Alaswad, E., D'Souza, S., Thompson, J. A., and Ormond, D. R. (2019). Current applications of diffusion tensor imaging and tractography in intracranial tumor resection. *Front. Oncol.* 9, 426–429. doi:10.3389/fonc.2019.00426

Dangouloff-Ros, V., Deroulers, C., Foissac, F., Badoual, M., Shotar, E., Grévent, D., et al. (2016). Arterial spin labeling to predict brain tumor grading in children: Correlations between histopathologic vascular density and perfusion MR imaging. *Radiology* 281, 553–566. doi:10.1148/radiol.2016152228

De Luca, A., Bertoldo, A., and Froeling, M. (2017). Effects of perfusion on DTI and DKI estimates in the skeletal muscle. *Magn. Reson Med.* 78, 233–246. doi:10.1002/mrm.26373

De Luca, A., Guo, F., Froeling, M., and Leemans, A. (2020). Spherical deconvolution with tissue-specific response functions and multi-shell diffusion MRI to estimate multiple fiber orientation distributions (mFODs). *Neuroimage* 222, 117206–117215. doi:10.1016/j.neuroimage.2020.117206

Ersoy, T. F., Ridwan, S., Grote, A., Coras, R., and Simon, M. (2020). Early postoperative seizures (EPS) in patients undergoing brain tumour surgery. *Sci. Rep.* 10, 1–10. doi:10.1038/s41598-020-70754-z

Faghihi, R., Zeinali-Rafsanjani, B., Mosleh-Shirazi, M. A., Saeedi-Moghadam, M., Lotfi, M., Jalli, R., et al. (2017). Magnetic resonance spectroscopy and its clinical applications: A review. *J. Med. Imaging Radiat. Sci.* 48, 233–253. doi:10.1016/j.jmir.2017.06.004

Giordano, M., Samii, A., Lawson McLean, A. C., Bertalanffy, H., Fahlbusch, R., Samii, M., et al. (2017). Intraoperative magnetic resonance imaging in pediatric neurosurgery: Safety and utility. *J. Neurosurg. Pediatr.* 19, 77–84. doi:10.3171/2016.8.PEDS15708

Giussani, C., Trezza, A., Ricciuti, V., Cristofori, A. D., Held, A., Isella, V., et al. (2022). Intraoperative MRI versus intraoperative ultrasound in pediatric brain tumor surgery: Is expensive better than cheap ? A review of the literature. *Childs Nerv. Syst.* 1, 1445–1454. doi:10.1007/s00381-022-05545-0

Guo, F., Leemans, A., Viergever, M. A., Dell'Acqua, F., and De Luca, A. (2020). Generalized Richardson-Lucy (GRL) for analyzing multi-shell diffusion MRI data. *Neuroimage* 218, 116948. doi:10.1016/j.neuroimage.2020.116948

Hollon, T. C., Pandian, B., Adapa, A. R., Urias, E., Save, A. V., Khalsa, S. S. S., et al. (2020). Near real-time intraoperative brain tumor diagnosis using stimulated Raman histology and deep neural networks. *Nat. Med.* 26, 52–58. doi:10.1038/s41591-019-0715-9

Jeurissen, B., Descoteaux, M., Mori, S., and Leemans, A. (2019). Diffusion MRI fiber tractography of the brain. *NMR Biomed.* 32, 1–22. doi:10.1002/nbm.3785

Jiang, R., Jiang, J., Zhao, L., Zhang, J., Zhang, S., Yao, Y., et al. (2015). Diffusion kurtosis imaging can efficiently assess the glioma grade and cellular proliferation. *Oncotarget* 6, 42380–42393. doi:10.18632/oncotarget.5675

Jiang, S., Eberhart, C. G., Zhang, Y., Heo, H. Y., Wen, Z., Blair, L., et al. (2017). Amide proton transfer-weighted magnetic resonance image-guided stereotactic biopsy in patients with newly diagnosed gliomas. *Eur. J. Cancer* 83, 9–18. doi:10.1016/j.ejca.2017.06.009

Jin, T., Wang, P., Jin, T., and Kim, S. G. (2017). Enhancing sensitivity of pH-weighted MRI with combination of amide and guanidyl CEST. *Neuroimage* 157, 341–350. doi:10.1016/j.neuroimage.2017.06.007

Karsy, M., Akbari, S. H., Limbrick, D., Leuthardt, E. C., Evans, J., Smyth, M. D., et al. (2019). Evaluation of pediatric glioma outcomes using intraoperative MRI: A multicenter cohort study. *J. Neurooncol* 143, 271–280. doi:10.1007/s11060-019-03154-7

Keil, V. C., Hartkamp, N. S., Connolly, D. J. A., Morana, G., Dremmen, M. H. G., Mutsaerts, H. J. M. M., et al. (2018). Added value of arterial spin labeling magnetic resonance imaging in pediatric neuroradiology: Pitfalls and applications. *Pediatr. Radiol.* 49, 245–253. doi:10.1007/s00247-018-4269-7

Leote, J., Nunes, R. G., Cerqueira, L., Loução, R., and Ferreira, H. A. (2018). Reconstruction of white matter fibre tracts using diffusion kurtosis tensor imaging at 1.5T: Pre-surgical planning in patients with gliomas. *Eur. J. Radiol.* 5, 20–23. doi:10.1016/j.ejro.2018.01.002

Lequin, M., and Hendrikse, J. (2017). Advanced MR imaging in pediatric brain tumors, clinical applications. *Neuroimaging Clin. N. Am.* 27, 167–190. doi:10.1016/j.nic.2016.08.007

Li, Y., Kim, M. M., Wahl, D. R., Lawrence, T. S., Parmar, H., and Cao, Y. (2021). Survival prediction analysis in glioblastoma with diffusion kurtosis imaging. *Front. Oncol.* 11, 690036–690038. doi:10.3389/fonc.2021.690036

Lindner, T., Ahmeti, H., Lübbing, I., Helle, M., Jansen, O., Synowitz, M., et al. (2017). Intraoperative resection control using arterial spin labeling — proof of concept, reproducibility of data and initial results. *Neuroimage Clin.* 15, 136–142. doi:10.1016/j.nicl.2017.04.021

Lindner, T., Ahmeti, H., Helle, M., Jansen, O., Fiehler, J., Dührsen, L., et al. (2022). Measurements of functional network connectivity using resting state arterial spin labeling during neurosurgery. *World Neurosurg.* 157, 152–158. doi:10.1016/j.wneu.2021.10.107

Low, S. Y. Y., Soh, S. Y., Chen, M. W., Ng, L. P., Low, D. C. Y., and Seow, W. T. (2018). DTI fusion with conventional MR imaging in intra-operative MRI suite for paediatric brainstem glioma biopsy. *Childs Nerv. Syst.* 34, 19–21. doi:10.1007/s00381-017-3627-3

Low, S. Y. Y., Lim, E. H. L., Loh, L. E., Mok, Y. H., Siow, Y. N., Ng, L. P., et al. (2020). Use of an offsite intraoperative MRI operating theater for pediatric brain tumor surgery: Experience from a Singapore children's hospital. *World Neurosurg.* 135, e28–e35. doi:10.1016/j.wneu.2019.10.083

Magnotta, V. A., Heo, H. Y., Dlouhy, B. J., Dahdaleh, N. S., Follmer, R. L., Thedens, D. R., et al. (2012). Detecting activity-evoked pH changes in human brain. *Proc. Natl. Acad. Sci. U. S. A.* 109, 8270–8273. doi:10.1073/pnas.1205902109

Marongiu, A., D'Andrea, G., and Raco, A. (2016). 1.5-T field intraoperative magnetic resonance imaging improves extent of resection and survival in glioblastoma removal. *World Neurosurg.* 98, 578–586. doi:10.1016/j.wneu.2016.11.013

Metwali, H., De Luca, A., Ibrahim, T., Leemans, A., and Samii, A. (2020). Data-driven identification of the regions of interest for fiber tracking in patients with brain tumors. *World Neurosurg.* 143, e275–e284. doi:10.1016/j.wneu.2020.07.107

Millward, C. P., Da Rosa, S. P., Avula, S., Ellenbogen, J. R., Spiteri, M., Lewis, E., et al. (2015). The role of early intra-operative MRI in partial resection of optic pathway/hypothalamic gliomas in children. *Childs Nerv. Syst.* 31, 2055–2062. doi:10.1007/s00381-015-2830-3

Mohammadi, S., Tabelow, K., Ruthotto, L., Feiweier, T., Polzehl, J., and Weiskopf, N. (2015). High-resolution diffusion kurtosis imaging at 3T enabled by advanced post-processing. *Front. Neurosci.* 8, 1–14. doi:10.3389/fnins.2014.00427

Morana, G., Piccardo, A., Tortora, D., Puntoni, M., Severino, M., Nozza, P., et al. (2017). Grading and outcome prediction of pediatric diffuse astrocytic tumors with diffusion and arterial spin labeling perfusion MRI in comparison with 18F–DOPA PET. *Eur. J. Nucl. Med. Mol. Imaging* 44, 2084–2093. doi:10.1007/s00259-017-3777-2

Nimsky, C. (2014). Fiber tracking - we should move beyond diffusion tensor imaging. *World Neurosurg.* 82, 35–36. doi:10.1016/j.wneu.2013.08.035

Oishi, M., Ishida, G., Morii, K., Hasegawa, K., Sato, M., and Fujii, Y. (2012). Ictal focal hyperperfusion demonstrated by arterial spin-labeling perfusion MRI in partial epilepsy status. *Neuroradiology* 54, 653–656. doi:10.1007/s00234-012-1027-7

Ouadih, Y. E., Pereira, B., Biau, J., Claise, B., Chaix, R., Verrelle, P., et al. (2022). DTI abnormalities related to glioblastoma: A prospective comparative study with metastasis and healthy subjects. *Curr. Oncol.* 29, 2823–2834. doi:10.3390/curroncol29040230

Palaniswamy, S. R., Beniwal, M., Venkataramaiah, S., and Srinivas, D. (2019). Perioperative management of pediatric giant supratentorial tumors: Challenges and management strategies. *J. Pediatr. Neurosci.* 14, 211–217. doi:10.4103/jpn.JPN_51_19

Pamir, M. N., Özduman, K., Dinçer, A., Yildiz, E., Peker, S., and Özek, M. M. (2010). First intraoperative, shared-resource, ultrahigh-field 3-Tesla magnetic resonance imaging system and its application in low-grade glioma resection: Clinical article. *J. Neurosurg.* 112, 57–69. doi:10.3171/2009.3.JNS081139

Pasternak, O., Sochen, N., Gur, Y., Intrator, N., and Assaf, Y. (2009). Free water elimination and mapping from diffusion MRI. *Magn. Reson Med.* 62, 717–730. doi:10.1002/mrm.22055

Petr, J., Hogeboom, L., Nikulin, P., Wiegers, E., Schroyen, G., Kallehauge, J., et al. (2022). A systematic review on the use of quantitative imaging to detect cancer therapy adverse effects in normal-appearing brain tissue. *MAGMA* 35, 163–186. doi:10.1007/s10334-021-00985-2

Poretti, A., Meoded, A., and Huisman, T. A. G. M. (2012). Neuroimaging of pediatric posterior fossa tumors including review of the literature. *J. Magn. Reson Imaging* 35, 32–47. doi:10.1002/jmri.22722

Ren, H., Chen, X., Sun, G., Hu, S., Zheng, G., Li, F., et al. (2013). Resection of subependymal giant cell astrocytoma guided by intraoperative magnetic resonance imaging and neuronavigation. *Childs Nerv. Syst.* 29, 1113–1121. doi:10.1007/s00381-013-2045-4

Rydhög, A. S., Szczepankiewicz, F., Wirestam, R., Ahlgren, A., Westin, C. F., Knutsson, L., et al. (2017). Separating blood and water: Perfusion and free water elimination from diffusion MRI in the human brain. *Neuroimage* 156, 423–434. doi:10.1016/j.neuroimage.2017.04.023

Sadowski, E. A., Bennett, L. K., Chan, M. R., Wentland, A. L., Garrett, A. L., Garrett, R. W., et al. (2007). Nephrogenic systemic fibrosis: Risk factors and incidence estimation. *Radiology* 243, 148–157. doi:10.1148/radiol.2431062144

Saint-Martin, C., Apuzzo, S., Salman, A., and Farmer, J. P. (2019). Hyperacute infarct on intraoperative diffusion imaging of pediatric brain tumor surgery. *Can. J. Neurol. Sci.* 46, 550–558. doi:10.1017/cjn.2019.226

Samudra, N., Zacharias, T., Plitt, A., Lega, B., and Pan, E. (2019). Seizures in glioma patients: An overview of incidence, etiology, and therapies. *J. Neurol. Sci.* 404, 80–85. doi:10.1016/j.jns.2019.07.026

Sanvito, F., Castellano, A., and Falini, A. (2021). Advancements in neuroimaging to unravel biological and molecular features of brain tumors. *Cancers (Basel)* 13, 424–425. doi:10.3390/cancers13030424

Shah, M. N., Leonard, J. R., Inder, G. E., Gao, F., Geske, M., Haydon, D. H., et al. (2012). Intraoperative magnetic resonance imaging to reduce the rate of early reoperation for lesion resection in pediatric neurosurgery: Clinical article. *J. Neurosurg. Pediatr.* 9, 259–264. doi:10.3171/2011.12.PEDS11227

She, D., Lin, S., Guo, W., Zhang, Y., Zhang, Z., and Cao, D. (2021). Grading of pediatric intracranial tumors: Are intravoxel incoherent motion and diffusional kurtosis imaging superior to conventional DWI? *AJNR Am. J. Neuroradiol.* 42, 2046–2053. doi:10.3174/ajnr.A7270

Suh, C. H., Park, J. E., Jung, S. C., Choi, C. G., Kim, S. J., and Kim, H. S. (2019). Amide proton transfer-weighted MRI in distinguishing high- and low-grade gliomas: A systematic review and meta-analysis. *Neuroradiology* 61, 525–534. doi:10.1007/s00234-018-02152-2

Sunderland, G., Foster, M. T., Pizer, B., Hennigan, D., Pettorini, B., and Mallucci, C. (2021). Evolution of surgical attitudes to paediatric thalamic tumours: The alder hey experience. *Childs Nerv. Syst.* 37, 2821–2830. doi:10.1007/s00381-021-05223-7

Tejada, S., Avula, S., Pettorini, B., Henningan, D., Abernethy, L., and Mallucci, C. (2018). The impact of intraoperative magnetic resonance in routine pediatric neurosurgical practice—A 6-year appraisal. *Childs Nerv. Syst.* 34, 617–626. doi:10.1007/s00381-018-3751-8

Trapasso, G., Chiesa, S., Freitas, R., and Pereira, E. (2021). What do we know about the ecotoxicological implications of the rare Earth element gadolinium in aquatic ecosystems? *Sci. Total Env.* 781, 146273. doi:10.1016/j.scitotenv.2021.146273

Vicente, J., Fuster-Garcia, E., Tortajada, S., García-Gómez, J. M., Davies, N., Natarajan, K., et al. (2013). Accurate classification of childhood brain tumours by *in vivo* ^{1}H MRS - a multi-centre study. *Eur. J. Cancer* 49, 658–667. doi:10.1016/j.ejca.2012.09.003

Villanueva-Meyer, J. E., Mabray, M. C., and Cha, S. (2017). Current clinical brain tumor imaging. *Neurosurgery* 81, 397–415. doi:10.1093/neuros/nyx103

Wen, Z., Hu, S., Huang, F., Wang, X., Guo, L., Quan, X., et al. (2010). MR imaging of high-grade brain tumors using endogenous protein and peptide-based contrast. *Neuroimage* 51, 616–622. doi:10.1016/j.neuroimage.2010.02.050

Wilson, M., Andronesi, O., Barker, P. B., Bartha, R., Bizzi, A., Bolan, P. J., et al. (2019). Methodological consensus on clinical proton MRS of the brain: Review and recommendations. *Magn. Reson Med.* 82, 527–550. doi:10.1002/mrm.27742

Wu, B., Warnock, G., Zaiss, M., Lin, C., Chen, M., Zhou, Z., et al. (2016). An overview of CEST MRI for non-MR physicists. *Eur. J. Nucl. Med. Mol. Imaging Phys.* 3, 19–21. doi:10.1186/s40658-016-0155-2

Yeh, F.-C., Irimia, A., Bastos, D. C. de A., and Golby, A. J. (2021). Tractography methods and findings in brain tumors and traumatic brain injury. *Neuroimage* 245, 1–22. doi:10.1016/j.neuroimage.2021.118651

Yeom, K. W., Mitchell, L. A., Lober, R. M., Barnes, P. D., Vogel, H., Fisher, P. G., et al. (2013). Arterial spin-labeled perfusion of pediatric brain tumors. *AJNR Am. J. Neuroradiol.* 35, 395–401. doi:10.3174/ajnr.A3670

Yousaf, J., Avula, S., Abernethy, L., and Mallucci, C. (2012). Importance of intraoperative magnetic resonance imaging for pediatric brain tumor surgery. *Surg. Neurol. Int.* 3, 65–72. doi:10.4103/2152-7806.95417

Yu, H., Lou, H., Zou, T., Wang, X., Jiang, S., Du, Y., et al. (2017). Applying protein-based amide proton transfer MR imaging to distinguish solitary brain metastases from glioblastoma. *Eur. Radiol.* 27, 4516–4524. doi:10.1007/s00330-017-4867-z

Yu, H., Wen, X., Wu, P., Chen, Y., Zou, T., Wang, X., et al. (2019). Can amide proton transfer–weighted imaging differentiate tumor grade and predict Ki-67 proliferation status of meningioma? *Eur. Radiol.* 29, 5298–5306. doi:10.1007/s00330-019-06115-w

Zhang, H., Tang, X., Lv, Y., Hu, D., Sun, J., Wang, Y., et al. (2020). Amide proton transfer-weighted (APTw) imaging of intracranial infection in children: Initial experience and comparison with gadolinium-enhanced T1-weighted imaging. *Biomed. Res. Int.* 2020, 1–13. doi:10.1155/2020/6418343

Zhang, H., Zhou, J., and Peng, Y. (2021). Amide proton transfer–weighted MR imaging of pediatric central nervous system diseases. *Magn. Reson Imaging Clin. N. Am.* 29, 631–641. doi:10.1016/j.mric.2021.06.012

Zhang, W., Ille, S., Schwendner, M., Wiestler, B., Meyer, B., and Krieg, S. M. (2022). Tracking motor and language eloquent white matter pathways with intraoperative fiber tracking versus preoperative tractography adjusted by intraoperative MRI-based elastic fusion. *J. Neurosurg.* 137, 1114–1123. doi:10.3171/2021.12.JNS212106

Zhou, J., Zhu, H., Lim, M., Blair, L., Quinones-Hinojosa, A., Messina, S. A., et al. (2013). Three-dimensional amide proton transfer MR imaging of gliomas: Initial experience and comparison with gadolinium enhancement. *J. Magn. Reson Imaging* 38, 1119–1128. doi:10.1002/jmri.24067

Zhou, J., Heo, H. Y., Knutsson, L., van Zijl, P. C. M., and Jiang, S. (2019). APT-weighted MRI: Techniques, current neuro applications, and challenging issues. *J. Magn. Reson Imaging* 50, 347–364. doi:10.1002/jmri.26645

frontiers | Frontiers in Physiology

TYPE Original Research
PUBLISHED 03 May 2023
DOI 10.3389/fphys.2023.1167857

OPEN ACCESS

EDITED BY
Julien Vincent Brugniaux,
Université Grenoble Alpes, France

REVIEWED BY
Stephen John Payne,
National Taiwan University, Taiwan
Mikio Hiura,
Aomori University, Japan

*CORRESPONDENCE
Ece Su Sayin,
ecesu.sayin@mail.utoronto.ca

RECEIVED 16 February 2023
ACCEPTED 07 April 2023
PUBLISHED 03 May 2023

CITATION
Sayin ES, Sobczyk O, Poublanc J, Mikulis DJ, Fisher JA and Duffin J (2023), Transfer function analysis assesses resting cerebral perfusion metrics using hypoxia-induced deoxyhemoglobin as a contrast agent.
Front. Physiol. 14:1167857.
doi: 10.3389/fphys.2023.1167857

Transfer function analysis assesses resting cerebral perfusion metrics using hypoxia-induced deoxyhemoglobin as a contrast agent

Ece Su Sayin[1,2]*, Olivia Sobczyk[2,3], Julien Poublanc[3], David J. Mikulis[3], Joseph A. Fisher[1,2,4] and James Duffin[1,2]

[1]Department of Physiology, University of Toronto, Toronto, ON, Canada, [2]Departments of Anaesthesia and Pain Management, University Health Network, Toronto, ON, Canada, [3]Joint Department of Medical Imaging and the Functional Neuroimaging Laboratory, University Health Network, Toronto, ON, Canada, [4]Toronto General Hospital Research Institute, University Health Network, University of Toronto, Toronto, ON, Canada

Introduction: Use of contrast in determining hemodynamic measures requires the deconvolution of an arterial input function (AIF) selected over a voxel in the middle cerebral artery to calculate voxel wise perfusion metrics. Transfer function analysis (TFA) offers an alternative analytic approach that does not require identifying an AIF. We hypothesised that TFA metrics Gain, Lag, and their ratio, Gain/Lag, correspond to conventional AIF resting perfusion metrics relative cerebral blood volume (rCBV), mean transit time (MTT) and relative cerebral blood flow (rCBF), respectively.

Methods: 24 healthy participants (17 M) and 1 patient with steno-occlusive disease were recruited. We used non-invasive transient hypoxia-induced deoxyhemoglobin as an MRI contrast. TFA and conventional AIF analyses were used to calculate averages of whole brain and smaller regions of interest.

Results: Maps of these average metrics had colour scales adjusted to enhance contrast and identify areas of high congruence. Regional gray matter/white matter (GM/WM) ratios for MTT and Lag, rCBF and Gain/Lag, and rCBV and Gain were compared. The GM/WM ratios were greater for TFA metrics compared to those from AIF analysis indicating an improved regional discrimination.

Discussion: Resting perfusion measures generated by The BOLD analysis resulting from a transient hypoxia induced variations in deoxyhemoglobin analyzed by TFA are congruent with those analyzed by conventional AIF analysis.

KEYWORDS

transfer function analysis, transient hypoxia, MRI, BOLD = blood oxygen level dependent, contrast agents, brain, perfusion imaging

1 Introduction

Cerebral blood flow is distributed via a complex network of vessels with flow resistances that vary depending on anatomy, vascular health, and tissue metabolism. This distribution of blood flow can be mapped using blood oxygenation level dependent (BOLD) magnetic resonance imaging (MRI) to trace a bolus of contrast agent. The BOLD signal is sensitive to

distortions in the static magnetic field caused by paramagnetic contrast agents such as gadolinium (Ogawa et al., 1990). The value of resting perfusion metrics obtained from the passage of a contrast agent during BOLD imaging, including mean transit time (MTT), relative cerebral blood volume (rCBV) and relative cerebral blood flow (rCBF), is that they can indicate regions of slowed and insufficient resting blood supply (Donahue et al., 2017). The dynamic susceptibility contrast (DSC) agent of choice used for perfusion imaging clinically is a gadolinium-based contrast agent (GBCA), injected intravenously to generate a bolus that is required to be imaged over a large artery on its first pass through the brain. Tissue BOLD signals can be analysed during passage of the GBCA bolus through the brain using the first pass arterial signal changes (arterial input function or AIF) deconvolved with tissue signal changes to obtain tissue perfusion metrics.

Transient hypoxia-induced deoxyhemoglobin (THx-dOHb) can be used as an endogenous paramagnetic contrast agent for DSC imaging. In 2021 Poublanc et al. reported the use of THx-dOHb as a non-invasive dynamic susceptibility contrast agent (Poublanc et al., 2021; Vu et al., 2021; Sayin et al., 2022a). Comparisons of resting perfusion metrics calculated from THx-dOHb were very similar to those obtained from a clinical standard, GBCA (Sayin et al., 2022a). However, a significant issue with DSC perfusion mapping is that the BOLD signal in proximity to arteries has both linear and non-linear behaviour depending on where the signal is measured. The intravascular signal exhibits a quadratic relationship with the concentrating of the paramagnetic contrast agent (Spees et al., 2001; Zhao et al., 2007) at 3 Tesla (Uludag et al., 2009), whereas the signal in tissue adjacent to the vessel is linear with contrast concentration. The nature of the AIF used for perfusion analysis is therefore dependent on location of the voxels used to measure the AIF. An AIF independent method for acquiring DSC perfusion metrics would therefore be welcomed.

1.1 Transfer function analysis

Here we introduce a frequency domain analysis technique, transfer function analysis (TFA). This technique has been used to measure dynamic pressure autoregulation of the cerebral vasculature (Blaber et al., 1997; Zhang et al., 1998; Tzeng et al., 2012), as well as the cerebrovascular response to changes in CO_2 (Duffin et al., 2015). It offers a means of characterizing the BOLD response to [dOHb] with not only an estimate of the magnitude of the response (Gain), but also the phase, or time Lag (Blockley et al., 2011) and coherence, the linear time invariance of the BOLD to SO_2 relationship. Briefly, the aligned BOLD response and SO_2 data are divided into five 50% overlapping segments (Welch algorithm (Welch, 1967)). In each segment the relation between the BOLD response signal and the contrast signal (SO_2) is analyzed in the frequency domain by resolving the two signals into their Fourier series of component sine waves (Figures 1A, B). The frequency response function, defined as the average cross-spectrum of the response signal divided by the average autospectrum of the stimulus signal, yields Gain and Phase measures, averaged for all segments. Coherence is calculated from averages of the cross- and auto-spectra as the average cross-spectrum squared divided by the product of the stimulus and response autospectra. Gain, Phase and Coherence measures are taken from the frequency spectrum at a single reference frequency (Figures 1A, B). As Figure 1C illustrates, Gain describes the amplitude ratio relating the BOLD response to the contrast signal and phase or time Lag the time relationship.

Previously, TFA was used to describe the dynamics of the BOLD response to changes in a vasoactive agent such as CO_2 (Duffin et al., 2015; Sayin et al., 2022b). In this case the phase difference between stimulus and response arises from two factors: a blood arrival time delay and a vascular response time. Differences in time delay between regions were assumed to be less than the 1.5 s sampling period (TR) so that TFA phase primarily reflects the speed of the vascular response (Duffin et al., 2015). By contrast, the phase difference between [dOHb] changes and the resulting BOLD signal is assumed to arise from both the time of passage of blood through a voxel and the arrival time delay. If the time of arrival delay is minimised, the phase difference expressed in time units is a measure related to mean transit time (MTT). We further hypothesised that if the Gain can be assumed to reflect the strength of the signal in a voxel, which is proportional to the volume of blood in a voxel, then Gain is a measure of relative cerebral volume (rCBV). In this case the ratio of Gain/Lag (CBV/MTT) is a measure of relative cerebral blood flow (rCBF), analogous to the central volume theorem (Ostergaard, 2005).

1.2 Observations

We describe the utility of transfer function analysis of the BOLD response to a series of two transient hypoxic exposures to produce corresponding changes in [dOHb] at rest. Voxel-wise maps of Gain, Lag and Gain/Lag were assembled by averaging these TFA metrics calculated and compared with maps of rCBV, MTT and rCBF respectively obtained from a deconvolution-based method using an AIF as described by Poublanc et al. (2021). Average supratentorial whole brain and posterior/anterior circulation TFA perfusion metrics were also compared to the corresponding conventional AIF analysis. In addition, we made spatial comparisons of the maps in a healthy participant and a patient with vascular insufficiency as shown in the magnetic resonance angiography (MRA) in Figure 8.

2 Materials and methods

2.1 Participant and ethics approval

This study conformed to the standards set by the latest revision of the Declaration of Helsinki and was approved by the Research Ethics Board of the University Health Network (UHN) and Health Canada. All participants provided written and informed consent to partake in this study. We recruited 24 healthy participants (7 Female) ranging from 21 to 82 (mean (SD) 38.6 ± 17.9 years, median age 30 years (Table 1) by word of mouth. The healthy participants consisted of non-smokers, not taking any medication and no known history of neurological or cardiovascular disease. In addition, a 66-year-old female participant with known cerebral vascular disease was recruited. The patient has bilateral moyamoya disease with a right MCA occlusion and distal left ICA occlusion with a previous patent left EC-IC bypass.

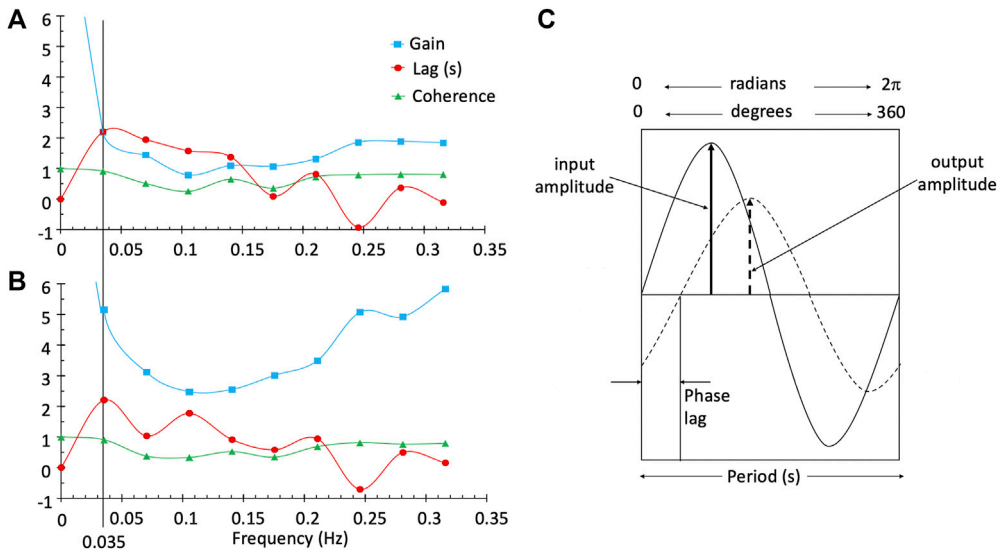

FIGURE 1
TFA provides the Gain, phase or time Lag, and Coherence measures for all frequencies in a single voxel in the white matter **(A)** and a single voxel in the grey matter **(B)**. The line at a frequency of 0.035 Hz was chosen as the single frequency representative measurement of Gain, Lag and Coherence used to characterise the BOLD response in a voxel. Diagram **(C)** illustrates a single frequency. Gain is output amplitude/input amplitude and phase is the difference in the timing of the sine waves. As illustrated, the output is positive and lags the input; consequently, phase is negative. The time lag (s) is period*phase lag (r/2π).

TABLE 1 Healthy participant characteristics.

Age range years	All	Female	Male
18 to 35	13	6	7
36 to 60	9	1	8
61 to 85	2	0	2

2.2 The contrast agent: Transient hypoxia-induced dOHb protocol

Changes in [dOHb] were achieved by controlling $P_{ET}CO_2$ and $P_{ET}O_2$ using sequential delivery of specific inspired gases with a computer-controlled gas blender (RespirAct™; Thornhill Medical Inc, Toronto, Canada) running a prospective targeting algorithm (Slessarev et al., 2007). The principles of operation of the RespirAct™ have been described elsewhere (Fisher et al., 2016). Participants breathed through a facemask sealed to the face with skin tape (Tegaderm, 3M, Saint Paul, MN, United States) to exclude all but system-supplied gas. The dOHb changes resulting from the programmed $P_{ET}O_2$ stimulus pattern of 4-min and 20 s duration is shown in Figure 2. The pattern consisted of a 60 s normoxic baseline at $P_{ET}O_2$ of 95 mmHg, a hypoxic step of $P_{ET}O_2$ to 40 mmHg for 60 s, a return to normoxia for 20 s, a second hypoxic step for 60 s, followed by a return to normoxia for 60 s. After the completion of the $P_{ET}O_2$ sequence, the participant returns to free breathing of room air. With this targeting approach, the end tidal values have been shown to be equal, within measurement error, to their respective arterial partial pressures (Ito et al., 2008; Fierstra et al., 2011).

2.3 MRI Scanning Protocol

A 3-Tesla scanner (HDx Signa platform, GE healthcare, Milwaukee, WI, USA) with an 8-channel head coil was used in these experiments. The protocol consisted of a high-resolution T1-weighted scan followed by one BOLD sequence scan. The high-resolution T1-weighted scan was acquired using a 3D spoiled gradient echo sequence with the following parameters: TI = 450 ms, TR 7.88 ms, TE = 3 ms, flip angle = 12°, voxel size = 0.859 × 0.859 × 1 mm, matrix size = 256 × 256, 146 slices, field of view = 24 × 24 cm, no interslice gap. The BOLD scan was acquired during normocapnic $P_{ET}O_2$ manipulation using a T2*-weighted gradient echoplanar imaging sequence with the following parameters: TR = 1,500 ms, TE = 30 ms, flip angle = 73°, 29 slices voxel size = 3 mm isotropic voxels and matrix size = 64 × 64.

2.4 Data Analysis

The acquired BOLD images were volume registered, slice-time corrected and co-registered to the anatomical images using AFNI software (National Institutes of Health, Bethesda, Maryland) (Cox, 1996). Arterial oxygen saturation (SaO_2) and [dOHb] were calculated from $P_{ET}O_2$ and the oxyhemoglobin dissociation curve (Balaban et al., 2013) assuming a fixed [Hb] of 130 g/L and a pH of 7.4. Two methods of analysis were employed. First, a conventional analysis using an AIF chosen over the middle cerebral artery and a deconvolution-based model was used to calculate voxel-wise maps of rCBV and MTT. The rCBF was calculated as CBV/MTT and scaled by 25. This is described in greater detail elsewhere (Poublanc et al., 2021).

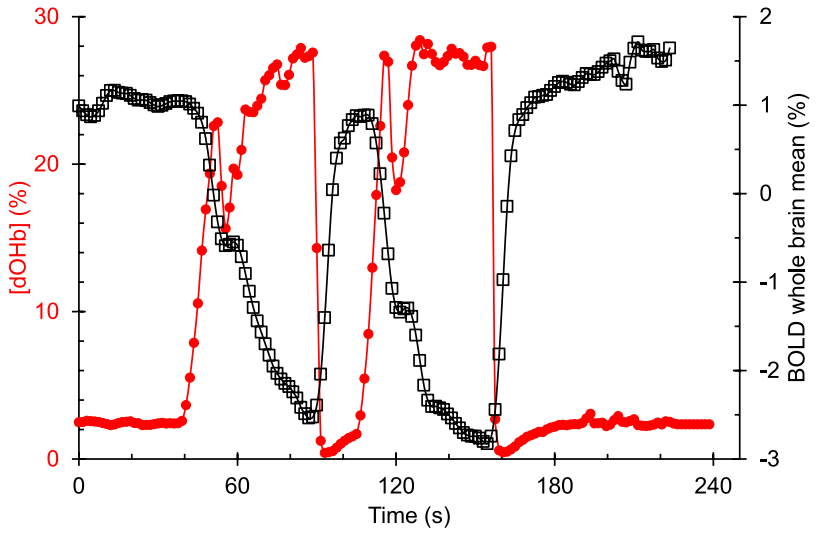

FIGURE 2
An example of the hypoxia-induced changes in [dOHb] (%) and the resulting whole brain average BOLD (%) signal response in a representative healthy control participant. [dOHb] was calculated from end tidal PO_2 using the Hill equation describing the normal oxyhemoglobin *in-vivo* O_2 dissociation curve (Balaban et al., 2013).

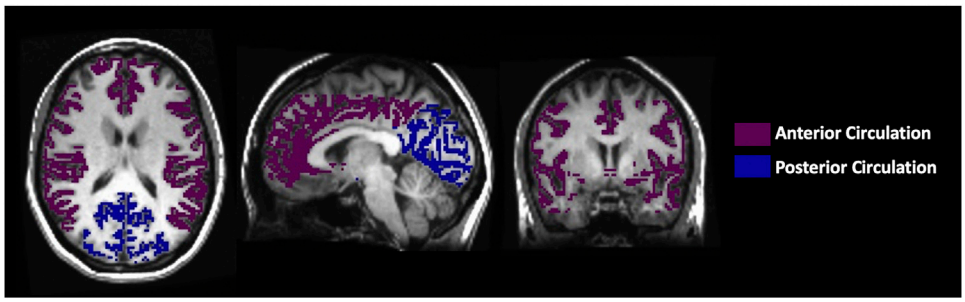

FIGURE 3
The axial, sagittal and coronal view of the manually delineated grey matter in the anterior and posterior circulation.

Second, a voxel-wise TFA of the BOLD data was analyzed using a custom program (LabVIEW, National Instruments, Texas). First, a zero-phase filter was applied to the BOLD vs. time data for all voxels to smooth the time course and reduce signal variations due to noise. The zero-phase filter applies an infinite impulse response recursive filter to the input signal such that the filtered signal has no phase distortion. Careful temporal alignment of the SO_2 and BOLD data is required for the measurement of both Lag and Gain/Lag ratio. Lag is affected by both the contrast transit time and its time of arrival. Lag was minimised by using the whole brain population histogram as a guide, adjusting the alignment of SO_2 and the whole brain mean BOLD to zero the minimum Lag. TFA calculated Gain, phase Lag, and Coherence as well as the Gain/Lag ratio for each voxel at the chosen frequency of 0.035 Hz. With this frequency the period is 28.57 s and phase Lag can be converted to time Lag (s) as period*phase lag ($r/2\pi$). SaO_2 was taken as the measure of the contrast agent and used as the AIF.

Maps of the perfusion metrics obtained from each analysis were transformed into Montreal Neurological Institute (MNI) space and overlayed onto their respective anatomical images. Analytical processing software, SPM8 (Wellcome Department of Imaging Neuroscience, Institute of Neurology, University College, London, UK), was used to segment the anatomical images (T1 weighted) into grey matter (GM) and white matter (WM). The vascular regions of interest (middle cerebral artery (MCA), posterior cerebral artery (PCA) and anterior cerebral artery (ACA)) were previously delineated manually on an anatomical MNI template. For this analysis, the supratentorial cortical grey matter MCA and ACA were combined as the anterior circulation mask and the supratentorial cortical grey matter PCA was used as the posterior circulation mask, as shown in Figure 3.

Average resting perfusion metrics using both TFA and conventional AIF analysis were calculated for specific regions for each participant in GM and WM and their ratios (GM/WM) using previously created vascular territory masks. To avoid susceptibility artifacts where the MRI signal is noisy, the slices ranging from mid

to the top of the brain (slices 40–60) were selected to calculate perfusion metrics. Comparisons between the conventional AIF analysis and TFA for perfusion metrics were not possible for relative values (expressed in arbitrary units) and were therefore limited to only TFA lag vs. MTT (expressed in seconds). To assess the spatial discrimination of the two analyses, the regional GM/WM ratios were compared. The results from the grouped 24 healthy participants were compiled together to determine normative ranges for TFA (Gain, Lag, Coherence and Gain/Lag ratio), and for conventional AIF analysis (rCBV, MTT and rCBF). This was performed for each metric and analysis by calculating a voxel-by-voxel mean and standard deviation from the co-registered maps in standard space (Sobczyk et al., 2015; Sobczyk et al., 2021).

2.5 Statistical analysis

Comparisons were made using a two-way analysis of variance (ANOVA) with factors tissue region and type of analysis using a commercial statistical package (SigmaPlot, Systat Software, San Jose, California, USA). Both a Normality Test (Shapiro-Wilk) and Equal Variance Tests were part of the ANOVA, and correction for multiple comparisons were applied by an all pairwise multiple comparison procedure (Bonferroni method). The GM/WM ratios for MTT, rCBF and rCBV were compared between the types of analysis using one-way ANOVA. Significant difference in these tests was taken as $p < 0.05$.

3 Results

3.1 Group comparisons

None of the subjects expressed distress during hypoxia and none terminated the procedure. Figure 4 presents the distribution of the data using boxplots. Figure 5 displays axial slices of the TFA and the conventional AIF analysis perfusion metrics for the grouped healthy participants. Note that colour scales minimum and maximum values were scaled to obtain the maximum colour contrast.

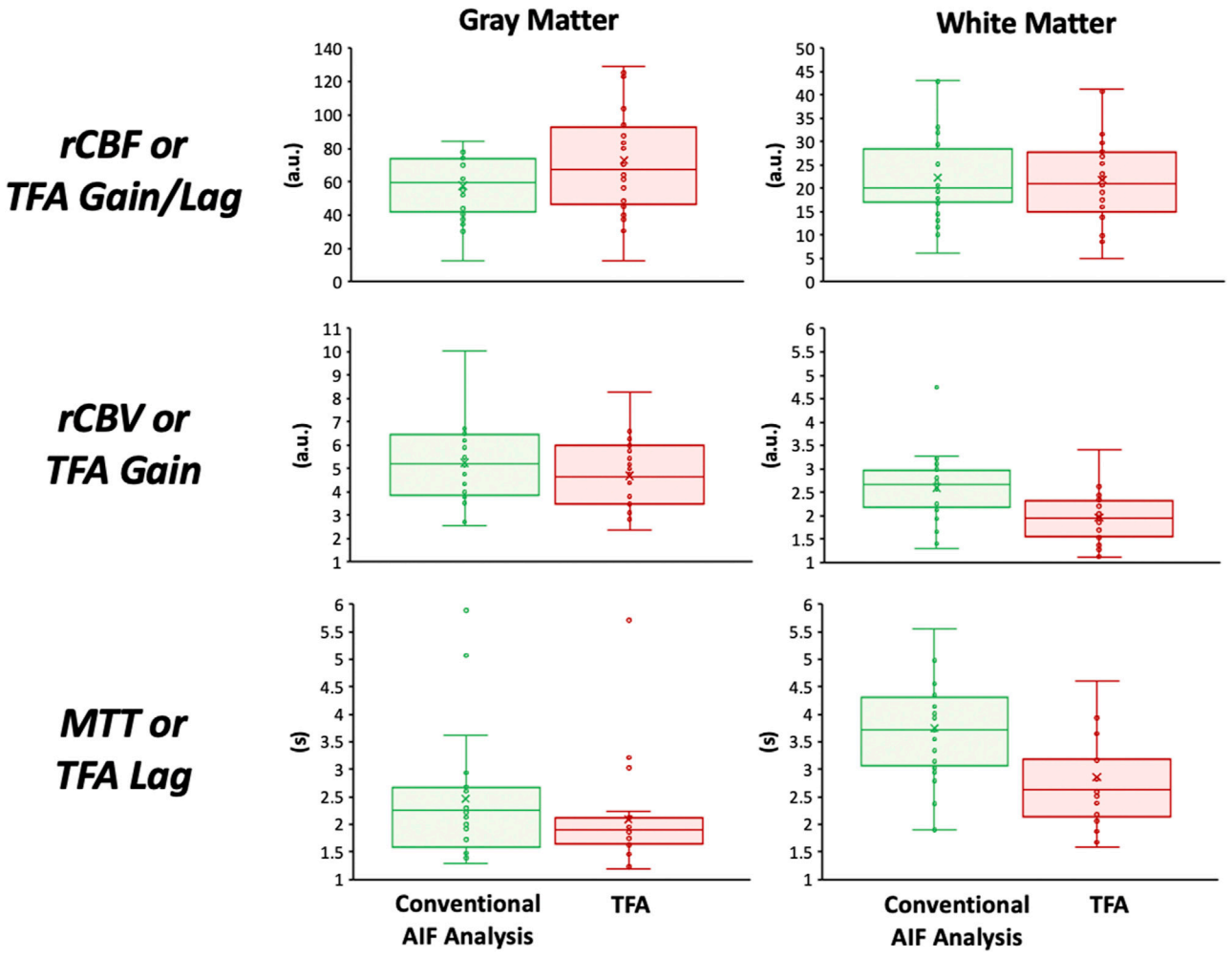

FIGURE 4
Boxplots showing the distribution of the perfusion metrics in the gray and white matter for the conventional AIF analysis (in green) and TFA (in red). The statistical summary comparing the two analysis techniques is found in Tables 2, 3.

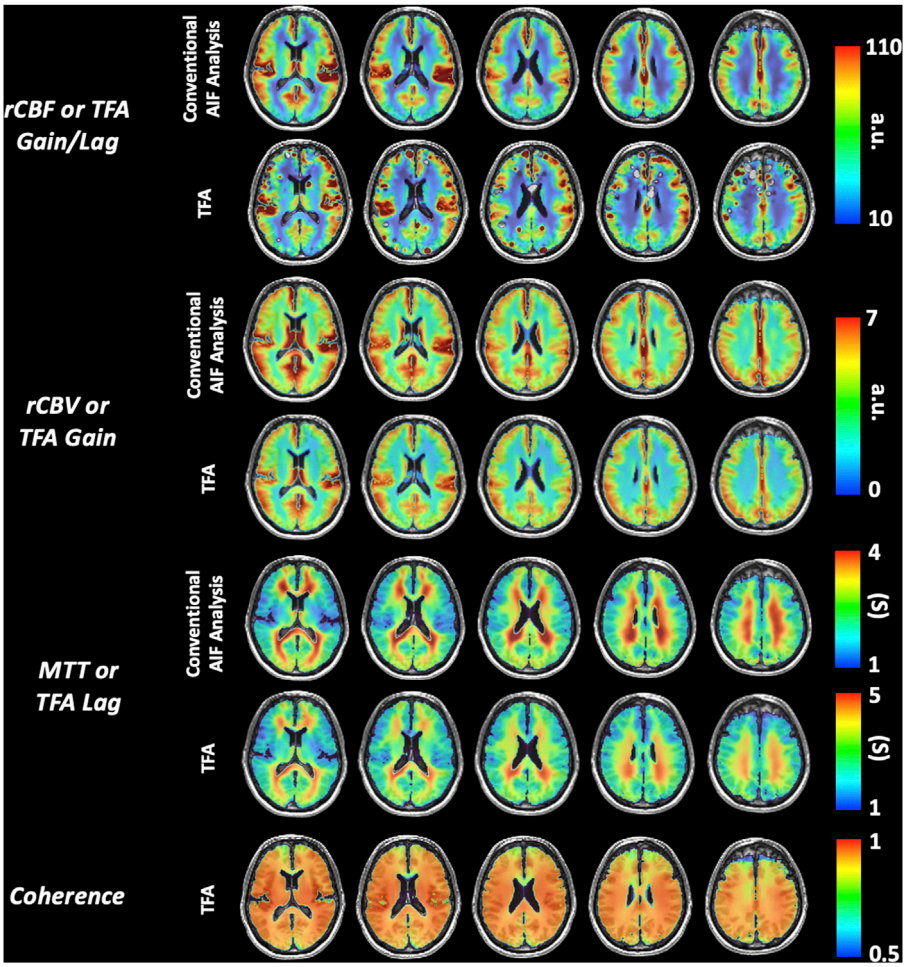

FIGURE 5
Representative axial slices of the grouped healthy participant group TFA metrics (Gain/Lag, Gain, Lag, and Coherence) and AIF metrics (rCBF, rCBV and MTT).

3.2 Statistical results

Table 2 summarises the comparison of TFA, and conventional AIF analysis metrics expressed as mean (SD) values for all the healthy participants. The Gain/rCBV and Gain/Lag/rCBF is relative and expressed in arbitrary units. Hence to be able to compare spatial discrimination between analysis methods, the GM/WM ratios were calculated. Table 3 summarises the comparison of GM/WM ratios between TFA, and conventional AIF analysis metrics expressed as mean (SD) values. The p values in Table 1 are from the two-way ANOVA with factors type of analysis and region. An All Pairwise Multiple Comparison Procedure (Bonferroni t-test) was used. The p values in Table 3 are from one-way ANOVA.

3.3 Examples of a healthy participant and patient

Figures 6, 8 display example perfusion metrics maps of a healthy individual and a selected patient. Figures 7, 9 display the histogram distribution of the perfusion metrics of a healthy individual and a selected patient.

4 Discussion

4.1 Main findings

We hypothesised that TFA metrics of Gain, Lag, and their ratio, Gain/Lag, correspond to conventional AIF resting perfusion metrics such as rCBV, MTT and rCBF, respectively. The main finding of this study is that TFA of the BOLD signal response to hypoxia induced dOHb provides perfusion metrics that are equivalent to those obtained with a conventional deconvolution-based analysis using an AIF. The grouped healthy participant maps of perfusion metrics for both types of analyses displayed high degree of similarity in relative magnitude and distribution of the perfusion metrics. The ranges of Lag and MTT values were similar with statistically significant but small differences only found in the whole brain WM. Ratios of GM/WM for each resting perfusion metric, calculated to assess their regional contrast, found Lag,

TABLE 2 A summary of the mean (SD) TFA lag vs. AIF MTT metrics for grouped healthy participants.

		Conventional AIF analysis			TFA			*p*-value lag vs. MTT
		rCBF	rCBV	MTT	Gain/Lag ("rCBF")	Gain ("rCBV")	Lag ("MTT")	
GM		57.53 (18.33)	5.26 (1.65)	2.46 (1.11)	72.78 (32.08)	4.70 (1.50)	2.09 (0.94)	0.231
WM		22.30 (9.45)	2.60 (0.71)	3.74 (1.07)	21.80 (9.07)	1.96 (0.54)	2.86 (1.17)	0.006*
Anterior Circulation	GM	59.0 (18.44)	5.23 (1.62)	2.36 (1.09)	74.80 (33.48)	4.67 (1.45)	2.03 (0.95)	0.284
Posterior Circulation	GM	52.57 (19.09)	5.35 (1.75)	2.84 (1.24)	63.82 (27.52)	4.71 (1.63)	2.30 (0.90)	0.077

p values are from a 2-way ANOVA with asterisks (*) emphasising significant differences ($p < 0.05$).

TABLE 3 Whole brain supratentorial cortical GM/WM ratios for all metrics from both analyses.

Region	MTT	Lag	*p*-value
GM/WM	0.65 (0.17)	0.74 (0.13)	0.016*
	rCBF	**Gain/Lag**	***p*-value**
	2.72 (0.65)	3.36 (0.70)	0.002*
	rCBV	**Gain**	***p*-value**
	2.02 (0.27)	2.38 (0.32)	<0.001*

p values are from one-way ANOVAs with asterisks (*) marking significant differences ($p < 0.05$).

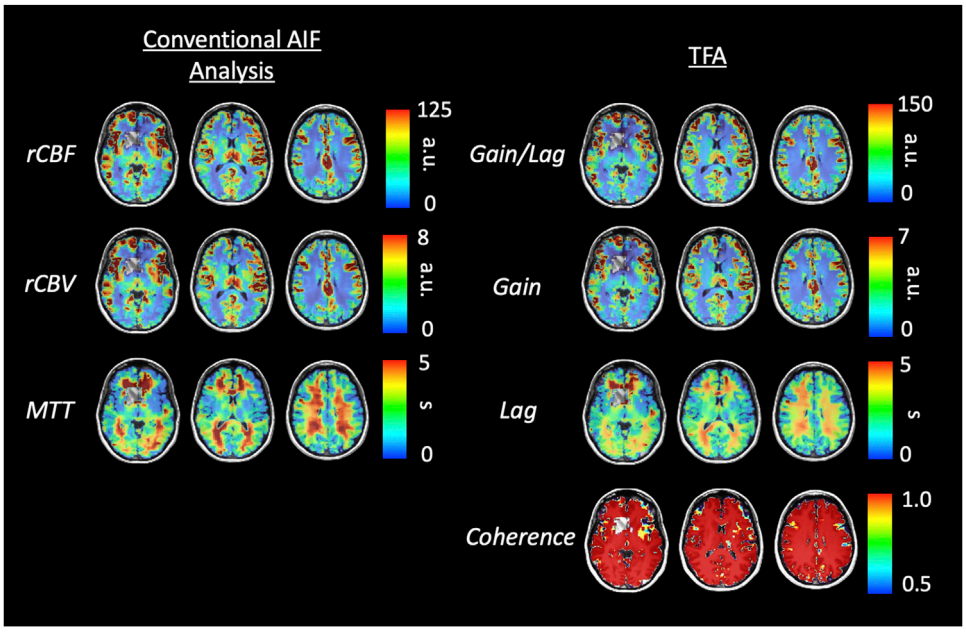

FIGURE 6
Axial slices of perfusion metrics for the conventional AIF and TFA analyses for a representative healthy control. Scales for rCBF, Gain/Lag, rCBV, and Gain are arbitrary units, and seconds for MTT and Lag.

Gain/Lag and Gain were significantly higher than MTT, rCBF and rCBV respectively, suggesting that TFA metrics provided a higher regional contrast.

We compared maps from a healthy individual to that of a patient with cerebrovascular pathology in order to determine whether TFA can identify cerebrovascular pathology seen with conventional AIF

analysis. The comparison of perfusion values generated from conventional AIF analysis and TFA in the healthy individual show high congruence. Perhaps more importantly, there is also high spatial similarity between the two perfusion methods in magnitude and spatial distribution in the patient with right MCA occlusion and distal left ICA occlusion. This finding also suggests that TFA, like the AIF conventional analysis, can identify areas of reduced cerebrovascular health at rest.

Altogether these observations indicate that analysis of the BOLD response to THx-dOHb by TFA can provide an alternative to the conventional AIF analysis.

4.2 Detailed comparisons

Perfusion metrics rCBV and rCBF from the conventional AIF analysis and their TFA counterparts Gain, and Gain/Lag ratio are in arbitrary units so that direct numerical comparisons are not possible between analyses, or with published values of these metrics. Nevertheless, the grouped healthy participant maps for these metrics are spatially very similar to each other, and to other published maps of rCBV and rCBF, with regional differences that are in general agreement with the control group average maps presented by others (Grandin et al., 2005; Ibaraki et al., 2007; Newbould et al., 2007; Watabe et al., 2014; Asaduddin et al., 2019). Furthermore, the values in GM and WM fall within the range of those from computerized tomography studies (Chen et al., 2019).

Both MTT and Lag in grouped healthy participant maps depicted regional variations of about 0–5 s with whole brain means (SD) of 3.74 (1.07) and 2.86 (1.17) s in WM and 2.46 (1.11) and 2.09 (0.94) s in GM for MTT and Lag, respectively. These values are comparable to those found for DSC MRI of 3.0 (0.6) s in GM and 4.3 (0.7) s in WM by (Helenius et al., 2003), as well as those found using positron emission tomography and DSC MRI (Ibaraki et al., 2007; Wirestam et al., 2010). A range of 0–10 s were found using carpet plots to analyze transit times from low frequency oscillations in resting state fMRI (Fitzgerald et al., 2021) and from hypoxia-induced dOHb (Bhogal et al., 2022). The MTT and Lag metrics are also within the range of MTT metrics calculated previously using hypoxia-induced changes in [dOHb] as a susceptibility contrast agent; between 0 and 12 s (Vu et al., 2021) and between 0 and 8 s (Poublanc et al., 2021; Sayin et al., 2022a).

The maps of resting perfusion metrics and their corresponding histograms presented in Figures 6–9 provide two comparisons, one between a healthy control and a patient with cerebrovascular pathology, and the other between the two analysis methods TFA and conventional AIF analysis. Comparing the maps between the two methods demonstrate the apparent spatial similarity, with regional variations that match each other despite the different analytic approaches. The main differences between analyses with respect to the regional distributions of the metrics are discernible in the histograms, whose widths display the full variability of the metrics. As noted in Table 3 comparing the GM/WM ratios, the TFA discrimination between GM and WM is higher than the conventional AIF analysis.

We also note the very apparent differences between the perfusion maps of the healthy participant and that of the patient.

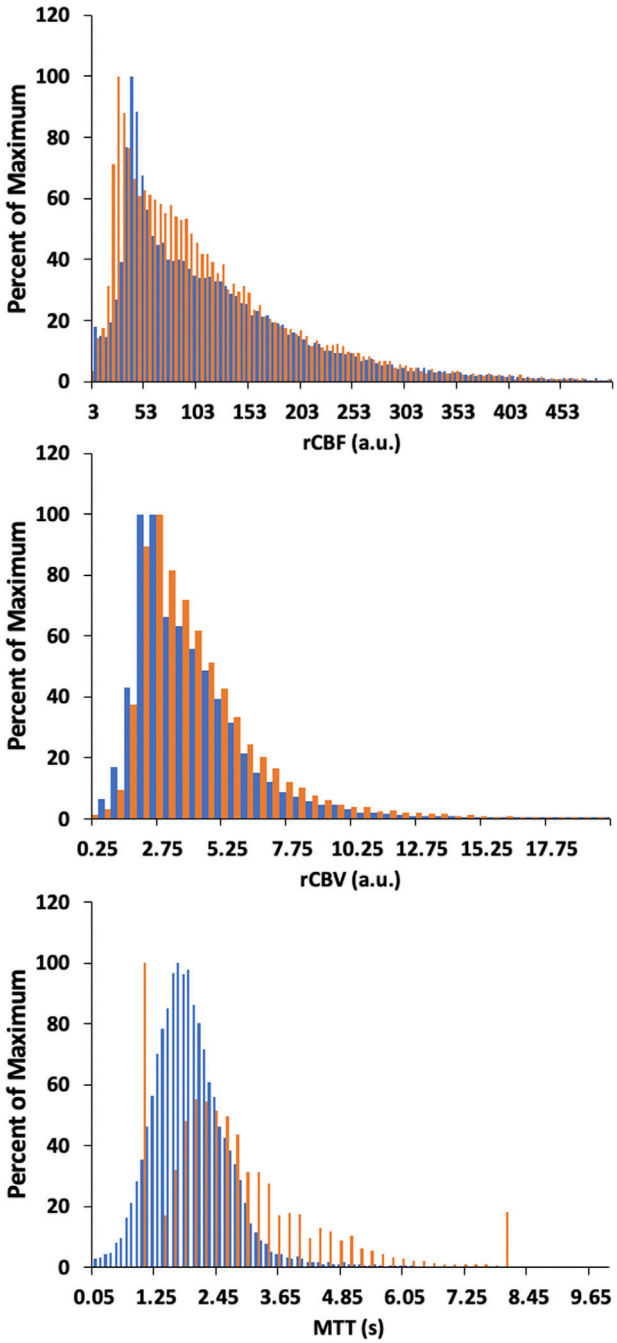

FIGURE 7
Histogram of whole brain averages for the conventional analysis (in orange) and TFA metrics (in blue) for a representative healthy control. Scales for rCBF, Gain/Lag, rCBV, and Gain are arbitrary units, and seconds for MTT and Lag.

These differences are also reflected in the histograms of the distribution of each metric. The maps of the patient example for both analyses indicate signs of the known left sided pathology with areas of increased MTT/Lag, increased rCBV/Gain and decreased rCBF/Gain/Lag ratio. We suggest that both analyses provide the clinically useful information.

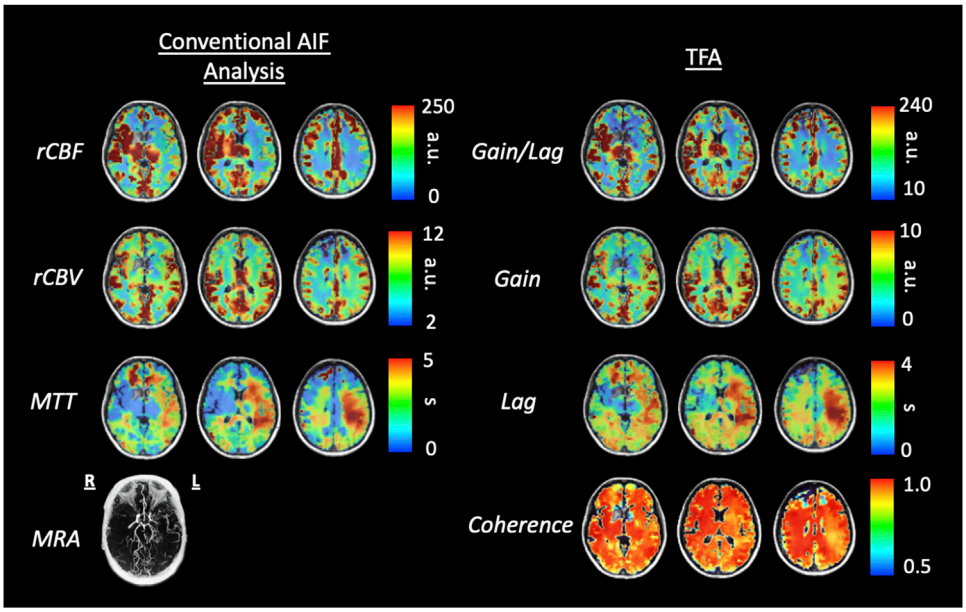

FIGURE 8
Axial slices of perfusion metrics for the conventional AIF analysis and TFA for a patient example with bilateral moyamoya disease with a right MCA occlusion and distal left ICA occlusion with a previous patent left EC-IC bypass. Note the decreased rCBF and Gain/Lag, the increased rCBV and Gain, and the prolonged MTT and Lag in all analyses reflect the vascular pathology of the patient. Scales for rCBF, Gain/Lag, rCBV and Gain are arbitrary units, seconds for MTT and Lag.

4.3 Limitations

The voxel-wise application of TFA uses the changes in SO_2 calculated from $P_{ET}O_2$ measured at the lungs as the input signal and the measured BOLD changes in a voxel as the output signal. The voxel-wise TFA therefore assumes that the SO_2 signal arrives at the voxel where BOLD is measured with the same changes as in pulmonary venous blood. Any dispersion is limited to passage through the left atrium and left ventricle, with the latter dispersion depending on the left ventricular ejection fraction.

One consideration in this study is the exposure of subjects to hypoxia. While SO_2 and [dOHb] can be quickly returned to normal by increasing inspired oxygen to 100%, the speed of reduction of SO_2 and [dOHb] by changing inspired PO_2 is limited by minute ventilation, functional residual capacity, and oxygen consumption. The rate of washout of O_2 from the functional residual capacity is limited by the lowest inspired oxygen concentration, which in the RespirAct™ is 4%, the functional residual capacity of the lungs, and minute ventilation. The two hypoxic exposures in the sequence were therefore extended to 60 s as the time to attaining PO_2 of 40 mmHg is about 15–20 s, leaving at least 30 s of hypoxia baseline. Re-establishment of normoxia is usually evoked within one breath. This provides a step change in dOHb and can also act as a safety feature. An important caution is not to induce hypoxia in patients who are already hypoxic due to congenital heart disease, sickle cell disease, severe chronic obstructive and restrictive pulmonary disease, presence of lung atelectasis, pneumonia, asthma, and pulmonary shunting associated with COVID-19.

As Table 1 notes, the healthy participant group was small and varied in age and sex, so that the results cannot be differentiated by age or sex. Indeed, our purpose in recruiting was to sample a wide variety of individuals to gain a general sense of the range of perfusion metrics and their regional variation.

It is assumed that the brief hypoxic exposures do not cause any change in cerebral blood flow. This assumption is based partly on the observation that the vasculature does not begin to respond to hypoxia at resting $P_{ET}CO_2$ until $P_{ET}O_2$ is below 50 mmHg (Mardimae et al., 2012), and partly on the consideration that the vascular response time constant is too long (80 s) for the brief hypoxia to affect the flow (Poulin et al., 1996). We note that the conversion of $P_{ET}O_2$ to SO_2 assumed a fixed [Hb] of 130 g/L and a pH = 7.4 and suggest that if actual measures are available, adjustments to the calculation of perfusion metrics be applied for each individual.

5 Conclusion

In this study THx-dOHb was used to produce a rapid variation in [dOHb], which induced sufficient BOLD signal changes to enable the calculation of resting perfusion metrics using TFA. We hypothesised that perfusion metrics derived from TFA analysis would be congruent with those derived from standard DSC processing using deconvolution of the AIF with the tissue response function such that TFA Gain would be analogous to rCBV, TFA Lag to MTT and the ratio Gain/Lag to rCBF. The truth of this hypothesis was first verified by showing high

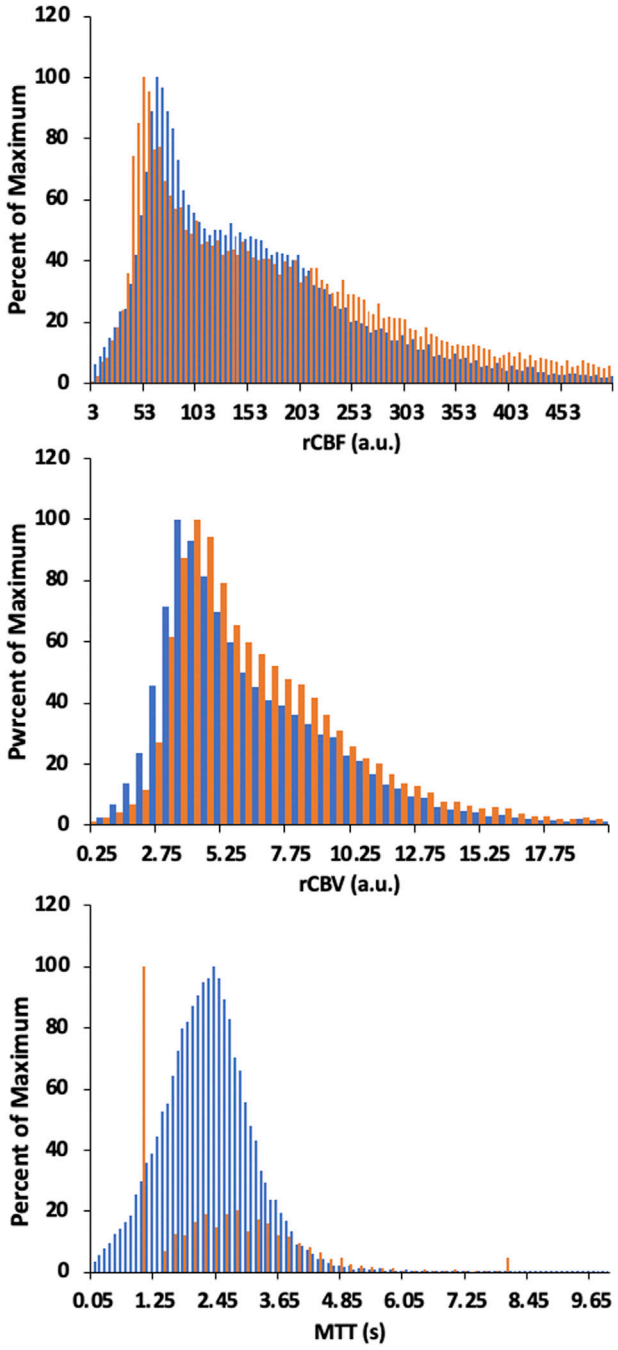

FIGURE 9
Histogram of whole brain averages for the conventional analysis (in orange) and TFA metrics (in blue) for a patient example with bilateral moyamoya disease with a right MCA occlusion and distal left ICA occlusion with a previous patent left EC-IC bypass. Scales for rCBF, Gain/Lag, rCBV, and Gain are arbitrary units, and seconds for MTT and Lag. Colour scales are adjusted to assist comparisons.

congruence between perfusion maps generated by both analytical methods in a healthy group of participants. A second confirmation was obtained by showing that TFA was able to discriminate between healthy and diseased tissue in a patient with a right MCA occlusion and distal left ICA occlusion with a previous patent left EC-IC bypass in a manner that was also highly consistent with the conventional analysis. We conclude that TFA of the BOLD changes resulting from THx-dOHb can be used to provide an alternative analysis method of determining resting perfusion metrics in individuals, which eliminates the requirement of an AIF selection and complex deconvolution calculations based on an assumed kinetic model. Furthermore, TFA has the potential to be applied to perfusion analysis for DSC imaging using GBCAs.

Data availability statement

The original contributions presented in the study are included in the article/Supplementary Material, further inquiries can be directed to the corresponding author.

Ethics statement

The studies involving human participants were reviewed and approved by Research Ethics Board at University Health Network. The patients/participants provided their written informed consent to participate in this study.

Author contributions

JD conceived the study and implemented the analyses. DM selected and reviewed all subjects for suitability. ES, OS, and JP executed the experiments to acquire the data. JD and ES analysed the data. JD, ES, and JF wrote the initial draft of the manuscript. All authors participated in the preparation and revision of the final version of the manuscript.

Acknowledgments

The authors thank the MR technologist at Toronto Western Hospital.

Conflict of interest

JF and DM contributed to the development of the automated end-tidal targeting device, RespirAct™ (Thornhill Research Inc., TRI) used in this study and have equity in the company. OS and JD receive salary support from TRI. TRI provided no other support for the study.

The remaining authors declare that the research was conducted in the absence of any commercial or financial relationships that could be construed as a potential conflict of interest.

Publisher's note

References

Asaduddin, M., Do, W.-J., Kim, E. Y., and Park, S.-H. (2019). Mapping cerebral perfusion from time-resolved contrast-enhanced MR angiographic data. *Magn. Reson. Imaging* 61, 143–148. doi:10.1016/j.mri.2019.05.040

Balaban, D. Y., Duffin, J., Preiss, D., Mardimae, A., Vesely, A., Slessarev, M., et al. (2013). The *in-vivo* oxyhaemoglobin dissociation curve at sea level and high altitude. *Respir. Physiol. Neurobiol.* 186, 45–52. doi:10.1016/j.resp.2012.12.011

Bhogal, A. A., Sayin, E. S., Poublanc, J., Duffin, J., Fisher, J. A., Sobcyzk, O., et al. (2022). Quantifying cerebral blood arrival times using hypoxia-mediated arterial BOLD contrast. *NeuroImage* 261, 119523. doi:10.1016/j.neuroimage.2022.119523

Blaber, A. P., Bondar, R. L., Stein, F., Dunphy, P. T., Moradshahi, P., Kassam, M. S., et al. (1997). Transfer function analysis of cerebral autoregulation dynamics in autonomic failure patients. *Stroke* 28, 1686–1692. doi:10.1161/01.str.28.9.1686

Blockley, N. P., Driver, I. D., Francis, S. T., Fisher, J. A., and Gowland, P. A. (2011). An improved method for acquiring cerebrovascular reactivity maps. *Magn. Reson Med.* 65, 1278–1286. doi:10.1002/mrm.22719

Chen, C., Bivard, A., Lin, L., Levi, C. R., Spratt, N. J., and Parsons, M. W. (2019). Thresholds for infarction vary between gray matter and white matter in acute ischemic stroke: A ct perfusion study. *J. Cereb. Blood Flow. Metab.* 39, 536–546. doi:10.1177/0271678X17744453

Cox, R. W. (1996). Afni: Software for analysis and visualization of functional magnetic resonance neuroimages. *Comput. Biomed. Res.* 29, 162–173. doi:10.1006/cbmr.1996.0014

Donahue, M. J., Achten, E., Cogswell, P. M., De Leeuw, F. E., Derdeyn, C. P., Dijkhuizen, R. M., et al. (2017). Consensus statement on current and emerging methods for the diagnosis and evaluation of cerebrovascular disease. *J. Cereb. Blood Flow. Metab.* 38, 1391–1417. doi:10.1177/0271678X17721830

Duffin, J., Sobczyk, O., Crawley, A. P., Poublanc, J., Mikulis, D. J., and Fisher, J. A. (2015). The dynamics of cerebrovascular reactivity shown with transfer function analysis. *NeuroImage* 114, 207–216. doi:10.1016/j.neuroimage.2015.04.029

Fierstra, J., Machina, M., Battisti-Charbonney, A., Duffin, J., Fisher, J. A., and Minkovich, L. (2011). End-inspiratory rebreathing reduces the end-tidal to arterial PCO(2) gradient in mechanically ventilated pigs. *Intensive Care Med.* 37, 1543–1550. doi:10.1007/s00134-011-2260-y

Fisher, J. A., Iscoe, S., and Duffin, J. (2016). Sequential gas delivery provides precise control of alveolar gas exchange. *Respir. Physiol. Neurobiol.* 225, 60–69. doi:10.1016/j.resp.2016.01.004

Fitzgerald, B., Yao, J. F., Talavage, T. M., Hocke, L. M., Frederick, B. D., and Tong, Y. (2021). Using carpet plots to analyze transit times of low frequency oscillations in resting state fMRI. *Sci. Rep.* 11, 7011. doi:10.1038/s41598-021-86402-z

Grandin, C. B., Bol, A., Smith, A. M., Michel, C., and Cosnard, G. (2005). Absolute CBF and CBV measurements by MRI bolus tracking before and after acetazolamide challenge: Repeatabilily and comparison with PET in humans. *Neuroimage* 26, 525–535. doi:10.1016/j.neuroimage.2005.02.028

Helenius, J., Perkio, J., Soinne, L., Ostergaard, L., Carano, R. A., Salonen, O., et al. (2003). Cerebral hemodynamics in a healthy population measured by dynamic susceptibility contrast MR imaging. *Acta Radiol.* 44, 538–546. doi:10.1034/j.1600-0455.2003.00104.x

Ibaraki, M., Ito, H., Shimosegawa, E., Toyoshima, H., Ishigame, K., Takahashi, K., et al. (2007). Cerebral vascular mean transit time in healthy humans: A comparative study with PET and dynamic susceptibility contrast-enhanced MRI. *J. Cereb. Blood Flow. Metab.* 27, 404–413. doi:10.1038/sj.jcbfm.9600337

Ito, S., Mardimae, A., Han, J., Duffin, J., Wells, G., Fedorko, L., et al. (2008). Non-invasive prospective targeting of arterial PCO2 in subjects at rest. *J. Physiol.* 586, 3675–3682. doi:10.1113/jphysiol.2008.154716

Mardimae, A., Balaban, D. Y., Machina, M. A., Han, J. S., Katznelson, R., Minkovich, L. L., et al. (2012). The interaction of carbon dioxide and hypoxia in the control of cerebral blood flow. *Pflugers Arch. - Eur. J. Physiol.* 464, 345–351. doi:10.1007/s00424-012-1148-1

Newbould, R. D., Skare, S. T., Jochimsen, T. H., Alley, M. T., Moseley, M. E., Albers, G. W., et al. (2007). Perfusion mapping with multiecho multishot parallel imaging EPI. *Magnetic Reson. Med.* 58, 70–81. doi:10.1002/mrm.21255

Ogawa, S., Lee, T. M., Kay, A. R., and Tank, D. W. (1990). Brain magnetic resonance imaging with contrast dependent on blood oxygenation. *Proc. Natl. Acad. Sci. U. S. A.* 87, 9868–9872. doi:10.1073/pnas.87.24.9868

Ostergaard, L. (2005). Principles of cerebral perfusion imaging by bolus tracking. *J. Magn. Reson Imaging* 22, 710–717. doi:10.1002/jmri.20460

Poublanc, J., Sobczyk, O., Shafi, R., Sayin, E. S., Schulman, J., Duffin, J., et al. (2021). Perfusion MRI using endogenous deoxyhemoglobin as a contrast agent: Preliminary data. *Magnetic Reson. Med.* 86 (6), 3012–3021. doi:10.1002/mrm.28974

Poulin, M. J., Liang, P. J., and Robbins, P. A. (1996). Dynamics of the cerebral blood flow response to step changes in end-tidal PCO2 and PO2 in humans. *J. Appl. Physiology* 81, 1084–1095. doi:10.1152/jappl.1996.81.3.1084

Sayin, E. S., Schulman, J., Poublanc, J., Levine, H. T., Raghavan, L. V., Uludag, K., et al. (2022a). Investigations of hypoxia-induced deoxyhemoglobin as a contrast agent for cerebral perfusion imaging. *Hum. Brain Mapp.* 44, 1019–1029. doi:10.1002/hbm.26131

Sayin, E. S., Sobczyk, O., Poublanc, J., Mikulis, D. J., Fisher, J. A., Kuo, K. H. M., et al. (2022b). Assessment of cerebrovascular function in patients with sickle cell disease using transfer function analysis. *Physiol. Rep.* 10, e15472. doi:10.14814/phy2.15472

Slessarev, M., Han, J., Mardimae, A., Prisman, E., Preiss, D., Volgyesi, G., et al. (2007). Prospective targeting and control of end-tidal CO2 and O2 concentrations. *J. Physiol.* 581, 1207–1219. doi:10.1113/jphysiol.2007.129395

Sobczyk, O., Battisti-Charbonney, A., Poublanc, J., Crawley, A. P., Sam, K., Fierstra, J., et al. (2015). Assessing cerebrovascular reactivity abnormality by comparison to a reference atlas. *J. Cereb. Blood Flow. Metab.* 35, 213–220. doi:10.1038/jcbfm.2014.184

Sobczyk, O., Sayin, E. S., Sam, K., Poublanc, J., Duffin, J., Fisher, J. A., et al. (2021). The reproducibility of cerebrovascular reactivity across MRI scanners. *Front. physiology* 12, 668662. doi:10.3389/fphys.2021.668662

Spees, W. M., Yablonskiy, D. A., Oswood, M. C., and Ackerman, J. J. (2001). Water proton MR properties of human blood at 1.5 Tesla: Magnetic susceptibility, T(1), T(2), T*(2), and non-lorentzian signal behavior. *Magn. Reson Med.* 45, 533–542. doi:10.1002/mrm.1072

Tzeng, Y. C., Ainslie, P. N., Cooke, W. H., Peebles, K. C., Willie, C. K., Macrae, B. A., et al. (2012). Assessment of cerebral autoregulation: The quandary of quantification. *Am. J. Physiol. Heart Circ. Physiol.* 303, H658–H671. doi:10.1152/ajpheart.00328.2012

Uludag, K., Muller-Bierl, B., and Ugurbil, K. (2009). An integrative model for neuronal activity-induced signal changes for gradient and spin echo functional imaging. *Neuroimage* 48, 150–165. doi:10.1016/j.neuroimage.2009.05.051

Vu, C., Chai, Y., Coloigner, J., Nederveen, A. J., Borzage, M., Bush, A., et al. (2021). Quantitative perfusion mapping with induced transient hypoxia using BOLD MRI. *Magnetic Reson. Med.* 85, 168–181. doi:10.1002/mrm.28422

Watabe, T., Shimosegawa, E., Kato, H., Isohashi, K., Ishibashi, M., and Hatazawa, J. (2014). CBF/CBV maps in normal volunteers studied with (15)O PET: A possible index of cerebral perfusion pressure. *Neurosci. Bull.* 30, 857–862. doi:10.1007/s12264-013-1458-0

Welch, P. (1967). The use of fast fourier transform for the estimation of power spectra: A method based on time averaging over short, modified periodograms. *IEEE Trans. Audio Electroacoustics* 15, 70–73. doi:10.1109/tau.1967.1161901

Wirestam, R., Thilmann, O., Knutsson, L., Bjorkman-Burtscher, I. M., Larsson, E. M., and Stahlberg, F. (2010). Comparison of quantitative dynamic susceptibility-contrast MRI perfusion estimates obtained using different contrast-agent administration schemes at 3T. *Eur. J. Radiol.* 75, e86–e91. doi:10.1016/j.ejrad.2009.07.038

Zhang, R., Zuckerman, J. H., Giller, C. A., and Levine, B. D. (1998). Transfer function analysis of dynamic cerebral autoregulation in humans. *Am. J. Physiol.* 274, H233–H241. doi:10.1152/ajpheart.1998.274.1.h233

Zhao, J. M., Clingman, C. S., Narvainen, M. J., Kauppinen, R. A., and Van Zijl, P. C. (2007). Oxygenation and hematocrit dependence of transverse relaxation rates of blood at 3T. *Magn. Reson Med.* 58, 592–597. doi:10.1002/mrm.21342

frontiers | Frontiers in Physiology

TYPE Original Research
PUBLISHED 09 May 2023
DOI 10.3389/fphys.2023.1167148

OPEN ACCESS

EDITED BY
James Duffin,
University of Toronto, Canada

REVIEWED BY
Alex Bhogal,
Utrecht University, Netherlands
Ruiliang Bai,
Zhejiang University, China

*CORRESPONDENCE
Rebecca J. Williams,
rebecca.williams@cdu.edu.au

RECEIVED 16 February 2023
ACCEPTED 24 April 2023
PUBLISHED 09 May 2023

CITATION
Williams RJ, Specht JL, Mazerolle EL, Lebel RM, MacDonald ME and Pike GB (2023), Correspondence between BOLD fMRI task response and cerebrovascular reactivity across the cerebral cortex. *Front. Physiol.* 14:1167148. doi: 10.3389/fphys.2023.1167148

Correspondence between BOLD fMRI task response and cerebrovascular reactivity across the cerebral cortex

Rebecca J. Williams[1]*, Jacinta L. Specht[2,3,4], Erin L. Mazerolle[5], R. Marc Lebel[3,6], M. Ethan MacDonald[3,4,7,8] and G. Bruce Pike[2,3,4]

[1]Faculty of Health, School of Human Services, Charles Darwin University, Darwin, NT, Australia, [2]Department of Clinical Neuroscience, Cumming School of Medicine, University of Calgary, Calgary, AB, Canada, [3]Department of Radiology, Cumming School of Medicine, University of Calgary, Calgary, AB, Canada, [4]Hotchkiss Brain Institute, Cumming School of Medicine, University of Calgary, Calgary, AB, Canada, [5]Departments of Psychology and Computer Science, St. Francis Xavier University, Antigonish, NS, Canada, [6]GE HealthCare, Calgary, AB, Canada, [7]Department of Biomedical Engineering, Schulich School of Engineering, University of Calgary, Calgary, AB, Canada, [8]Department of Electrical and Software Engineering, Schulich School of Engineering, University of Calgary, Calgary, AB, Canada

BOLD sensitivity to baseline perfusion and blood volume is a well-acknowledged fMRI confound. Vascular correction techniques based on cerebrovascular reactivity (CVR) might reduce variance due to baseline cerebral blood volume, however this is predicated on an invariant linear relationship between CVR and BOLD signal magnitude. Cognitive paradigms have relatively low signal, high variance and involve spatially heterogenous cortical regions; it is therefore unclear whether the BOLD response magnitude to complex paradigms can be predicted by CVR. The feasibility of predicting BOLD signal magnitude from CVR was explored in the present work across two experiments using different CVR approaches. The first utilized a large database containing breath-hold BOLD responses and 3 different cognitive tasks. The second experiment, in an independent sample, calculated CVR using the delivery of a fixed concentration of carbon dioxide and a different cognitive task. An atlas-based regression approach was implemented for both experiments to evaluate the shared variance between task-invoked BOLD responses and CVR across the cerebral cortex. Both experiments found significant relationships between CVR and task-based BOLD magnitude, with activation in the right cuneus (R^2 = 0.64) and paracentral gyrus (R^2 = 0.71), and the left pars opercularis (R^2 = 0.67), superior frontal gyrus (R^2 = 0.62) and inferior parietal cortex (R^2 = 0.63) strongly predicted by CVR. The parietal regions bilaterally were highly consistent, with linear regressions significant in these regions for all four tasks. Group analyses showed that CVR correction increased BOLD sensitivity. Overall, this work suggests that BOLD signal response magnitudes to cognitive tasks are predicted by CVR across different regions of the cerebral cortex, providing support for the use of correction based on baseline vascular physiology.

KEYWORDS

BOLD, cerebrovascular reactivity, hypercapnia, functional magnet resonance imaging (fMRI), cerebral blood blow, vascular physiology, attention, cognition

1 Introduction

Functional MRI (fMRI) based on blood oxygen level-dependent (BOLD) contrast is widely used in neuroscience research and represents a composite signal arising from changes in total intravoxel deoxyhemoglobin (Kim and Ogawa, 2012). Transient reductions in deoxyhemoglobin due to changes in cerebral blood flow, blood volume and cerebral metabolic of oxygen give rise to BOLD signal changes capitalized by both task-based and resting-state fMRI to probe neural networks (Hoge et al., 1999; Pike, 2012). These dynamic changes are highly dependent on basal physiology, with resting perfusion, blood volume and venous oxygenation having strong modulatory effects on the BOLD signal (Stefanovic et al., 2006; Liu et al., 2013a; Chu et al., 2018). The negative consequences of this includes increased inter-subject variation and the problematic interpretation of BOLD fMRI signal changes in situations where independent basal perfusion changes occur, such as in aging (Chen et al., 2011; Chen, 2019; MacDonald et al., 2020; Juttukonda et al., 2021) and cerebrovascular disease (Blicher et al., 2012; MacDonald et al., 2016; Williams et al., 2017; Mazerolle et al., 2018). Scaling techniques have been proposed to address BOLD signal magnitude differences due to basal physiology (Biswal et al., 2007; Kannurpatti and Biswal, 2008; Tsvetanov et al., 2015; Kazan et al., 2016; Tsvetanov et al., 2021b). Hypercapnic normalization is a scaling technique where measurements of cerebrovascular reactivity (CVR) are implemented to reduce fMRI activation map dependence on baseline cerebral blood volume (Bandettini and Wong, 1997; Cohen et al., 2004; Liau and Liu, 2009). CVR refers to the ability of blood vessels to dynamically regulate cerebral blood flow and is often measured with MRI in the assessment of vascular health (Pillai and Mikulis, 2015; Chen, 2018). While CVR is traditionally defined as the change in flow due to vasoactive stimulus (Fisher and Mikulis, 2021), BOLD contrast is often used as a surrogate measure of cerebral blood flow with the assumption of the vasoactive stimulus being isometabolic (Chen and Pike, 2010).

There are different vasoactive stimuli that can be applied to measure CVR, the two most common being acetazolamide and carbon dioxide (CO_2). Breath-hold induced hypercapnia and the delivery of air mixtures with increased concentrations of CO_2 are the most commonly used approaches in MRI research studies. Participants holding their breath for short (10–30 s) epochs is a relatively easy and reliable technique for inducing mild hypercapnia (Bright and Murphy, 2013; Pinto et al., 2020). Breath-hold based measures of CVR have also shown good correspondence with those obtained with respiratory manipulation via the delivery of gas mixtures containing elevated concentrations of CO_2 (Tancredi and Hoge, 2013). This latter approach involves both the delivery of gases and the precise recording of end-tidal gases and has been shown to have good test-retest reliability in non-patient groups (Liu et al., 2021).

Blood flow modulations underpinning BOLD responses to neural activity are caused by neurovascular coupling, where changes in regional flow reflect modulations in neural activity and metabolic demand (Hosford and Gourine, 2019). This is independent from the mechanisms related to acidosis that regulate cerebral blood flow increases under hypercapnic conditions (Battisti-Charbonney et al., 2011; Duffin et al., 2021). Despite these different pathways leading to hyperemia, contributions from mutual physiology such as baseline cerebral blood volume suggests that CVR may be a BOLD signal modulator. This is critical for the implementation of hypercapnic normalization, which is predicated on a linear relationship between CVR and neural activity-induced BOLD signal changes. There is some evidence supporting this relationship. For instance, when investigating how different baseline measures of vascular physiology modulate task-induced BOLD signals, Liu et al. showed a correspondence between BOLD signal magnitude to a visual scene-categorization task and CVR in four different regions-of-interest (ROIs) including the early visual areas, medial temporal lobe, and bilateral inferior frontal gyrus (Liu et al., 2013a). Another study characterised the relationship between breath-hold BOLD and task-BOLD signal changes in younger and older adults (Kannurpatti et al., 2014). The tasks included a motor and a cognitive task associated with executive control function. When evaluating the relationship between task and breath-hold BOLD responses in significantly activated voxels, the authors found a linear relationship for the younger group only (Kannurpatti et al., 2014). Addressing discrepancies in CVR and task-based BOLD responses between younger and older adults was the aim of research by Liu et al. (2013b). In this study, hypercapnic normalization was implemented where CVR maps were calculated on a per-subject basis to normalize BOLD activation maps to a memory task in older and younger adults. Age-related decreases in BOLD signal were found primarily in the posterior visual cortex and temporal lobe; however, these decreases were no longer observed following normalization. This study suggested that vascular-driven age-related differences in BOLD activation to a memory task can be addressed using hypercapnic normalization.

These findings highlight that one of the potential benefits of adding CVR to a task-based fMRI experiment is to correct age-related differences in BOLD responses due to baseline vasculature. This benefit would extend to all populations in group fMRI studies by reducing inter-subject variability attributable to baseline vasculature. Hypercapnic normalization has been shown to reduce variability using breath-hold CVR in young adults (Thomason et al., 2007), and it can be concluded from the literature, summarized above, that activation magnitude can be predicted by CVR for a small number of tasks in some regions of cortex. This suggests that CVR can be incorporated into a linear model to account for variance and reduce error. An important consideration however is that these conclusions are based on a small number of studies that are limited in both sample sizes and the tasks evaluated. An under-explored question is whether vascular correction is applicable for all fMRI paradigms and brain regions. Cortical regions subserving higher-order cognitive processes show more inter-subject variability than primary sensory cortices in both structure (Sydnor et al., 2021) and function (Mueller et al., 2013). Spatial disparity has also been observed in blood flow and metabolic coupling (Chiarelli et al., 2007), underscoring the importance of characterizing the relationship between vascular physiology and neural-activity mediated BOLD signal on a regional level. Relative to sensory tasks targeting the unimodality regions such as the primary visual or motor cortices, cognitive fMRI tasks have lower sensitivity due to the use of multiple experimental conditions and cognitive subtraction (Logothetis, 2008). It has been suggested that cognitive paradigms are dominated by neural response

variability, and vascular correction might therefore be ineffective (Kannurpatti et al., 2010). Further work investigating the utility of vascular correction for cognitive paradigms is warranted. Furthermore, all studies to date have implemented only one type of CVR technique; whether the hypercapnic approach affects the relationship between CVR and task-related BOLD signal remains undetermined.

The aim of the present research was to thoroughly investigate the relationship between CVR and BOLD responses to cognitive tasks implicating different neural networks. Two experimental studies were implemented to meet this aim, each utilizing different approaches to measure CVR using hypercapnia: breath-hold and gas inhalation. It was hypothesized that neural-activity mediated BOLD responses would be linearly related to CVR across the cerebral cortex for both hypercapnic approaches. The first experiment involved the analysis of an open-source dataset containing breath-hold and task-based BOLD fMRI data from the UCLA Consortium for Neuropsychiatric Phenomics (CNP) LA5c Study (Poldrack et al., 2016). In this first experiment, the linear relationship between CVR, inferred using breath-hold BOLD responses, and task-based BOLD responses across different cognitive networks was measured. Group analyses were performed to determine if vascular scaling using breath-hold BOLD responses reduces variability in large datasets. The second experiment attempted to determine if the results from the first experiment generalize to gas-inhalation CVR. This was achieved by characterizing the relationship between CVR and BOLD activation to an attention task in an independent sample with CO_2-administered hypercapnia.

2 Methods and materials

2.1 Experiment 1: Breath-hold CVR

2.1.1 Participants

For study 1, all data were obtained from the OpenfMRI database (Bilder et al., 2020). Data were downloaded from https://openneuro.org/datasets/ds000030/versions/1.0.0. Full details regarding participant recruitment, inclusion and exclusion criteria are provided in the study protocol paper (Poldrack et al., 2016). All participants gave written informed consent, and the study was approved by the Institutional Review Board at UCLA. The complete dataset contains images from healthy control subjects, and those diagnosed with schizophrenia, bipolar disorder, and attention deficit/hyperactivity disorder. Only the data from control subjects were utilised in this work. All control participants with task-based fMRI including the 3 paradigms utilized in the present study (detailed in task descriptions below) and T_1-weighted structural data were included in the present analysis, resulting in a total of 114 participants (mean age = 31.46 ± 8.78 years, range = 21–50 years, 54 F).

2.1.2 Imaging acquisition

All MRI data for Study 1 were acquired on one of two 3 T Siemens Trio scanners. Subjects completed two separate scanning sessions in a counterbalanced order. The structural and fMRI data used in the present analysis were acquired in different sessions. An MPRAGE was acquired in the sagittal orientation (TR/TE/TI = 1900/2.26/1,100 ms, FOV = 250 mm, matrix = 256 × 256, flip angle = 7°, slice thickness = 1 mm, 176 slices). The fMRI data (cognitive tasks and breath-hold) were acquired using T_2*-weighted echo planar imaging with TR/TE = 2000/30 ms, flip angle = 90°, FOV = 192 mm, matrix = 64 × 64, slice thickness = 4 mm, 34 slices.

2.1.3 Task descriptions

Study participants completed a battery of cognitive paradigms during the fMRI scans, including three event-related cognitive tasks and one breath-holding task. While more than three cognitive tasks were available, not every participant completed the full battery. The following three cognitive tasks were specifically chosen for this analysis because they were completed by the most participants, resulting in the final sample size of 114. A detailed description of the tasks is given in (Poldrack et al., 2016).

The first of the three cognitive tasks, the Spatial Capacity Task (SCAP), targeted spatial working memory (Glahn et al., 2003), where stimuli included pseudo-randomly displayed yellow circles (1, 3, 5 or 7) around a central fixation cross, presented for 2 s per trial. After a short delay (1.5, 3 or 4.5 s), a single green circle appeared. The participant was required to indicate whether the green circle was in the same position as one of the yellow target circles. A total of 48 trials were presented. The manipulated variables were number of target circles, with 4 levels (1, 3, 5, 7) and delay in seconds (1.5, 3 or 4.5).

The second task was the stop-signal task, a measure of response inhibition (Logan et al., 1984). The participants were instructed to press a button as quickly as possible in response to a presented 'go' stimulus (arrows pointing to the left or to the right). In 25% of trials, the arrow stimulus was presented with an auditory tone (presented through headphones for 250 ms), which indicated a 'stop' signal. Participants were instructed to withhold all button presses for trials with the 'stop' signal. There was a total of 128 trials, of which 32 were stop trials. Trials were 1,000 ms in duration and interspersed with a jittered baseline period consisting of a fixation cross.

The third cognitive task was a task-switching paradigm (Miyake et al., 2004). For each trial, one of four stimuli including a red triangle, red circle, green triangle, or green circle was presented. Participants made a button-press response as quickly as possible in response to the stimulus to indicate the color (red or green) or shape (triangle or circle). A cue presented directly prior to the onset of the stimulus instructed the participant to respond to either the color or the shape of the stimulus. This cue was either the full word ('Color' or 'Shape'), or the first letter ('C' or 'S'). A total of 96 trials were presented, with 33% of all trials involving a switch of instructions compared to prior trials.

To measure CVR, a breath-hold task was performed. Participants held their breath for periods of 13.5 s, interspersed with 16.5 s of regular breathing. A visual cue was presented to prepare and pace the breath-holding challenge. There were 5 epochs of breath-holding across a total of 2.5 min. A respiratory belt was worn by participants during the breath-hold task, although these data was not analyzed in this analysis.

2.1.4 fMRI preprocessing

A schematic summarizing the pre-processing pipeline for experiment 1 is shown in Figure 1. All fMRI data underwent slice timing correction and motion correction using SPM12

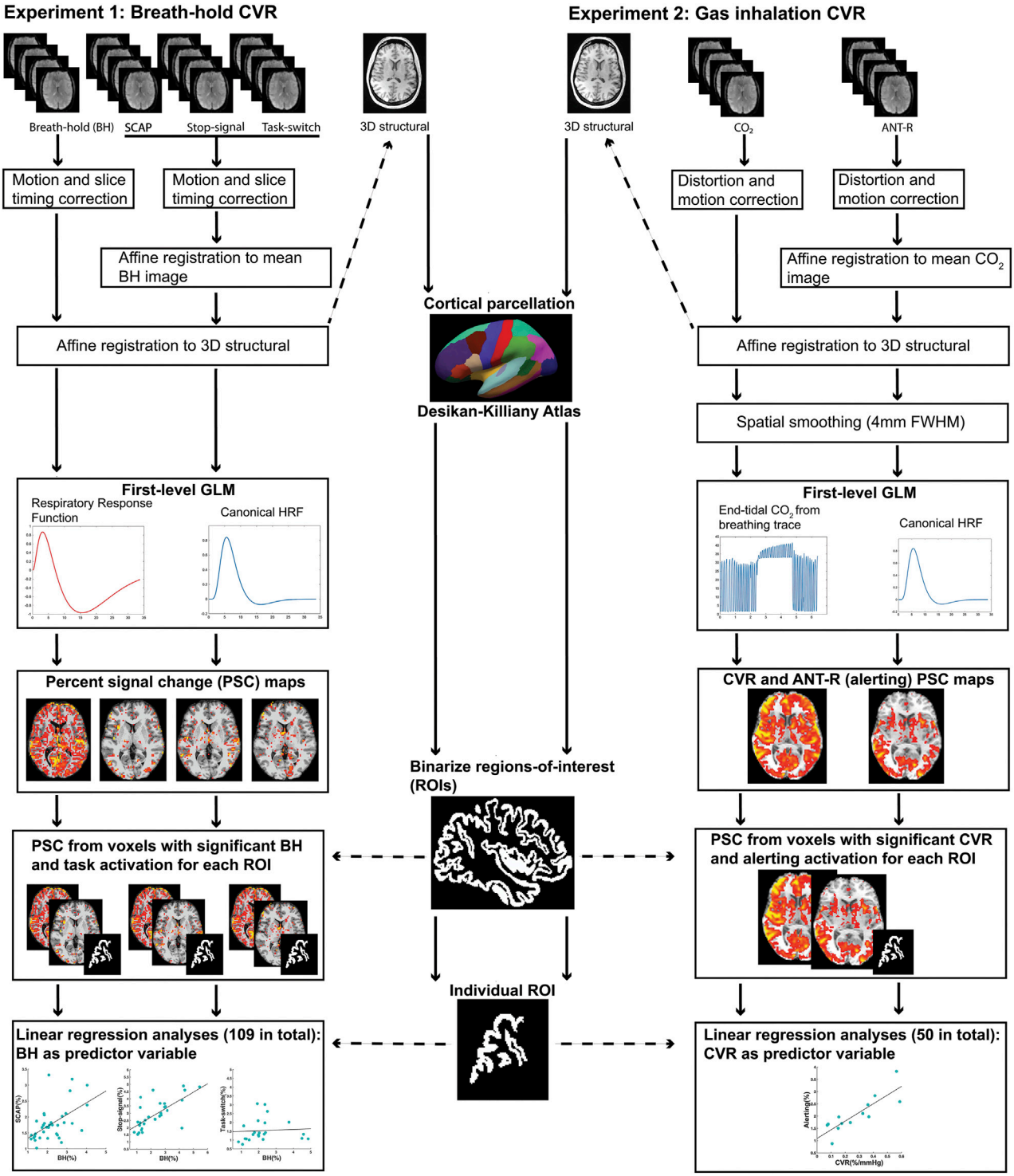

FIGURE 1
Schematic diagram summarizing the pre-processing and first-level analysis pipeline for experiment 1 (left) and experiment 2 (right).

(https://www.fil.ion.ucl.ac.uk/spm/). To ensure precise registration between breath-hold and cognitive tasks, for each subject all fMRIs were aligned using affine registration with Advanced Normalization Tools (Avants et al., 2011; Avants et al., 2014). Affine registration between each subject's fMRIs and structural T_1 MPRAGE, and normalisation of the T_1 image to the MNI template, was performed using Unified Segmentation in SPM12 (Ashburner and Friston, 2005). Deformation fields from the T_1 image segmentation were used to normalize the fMRIs to the MNI template. No spatial smoothing was performed.

2.1.5 fMRI first-level analyses

The fMRI data corresponding to the three tasks were individually entered into first-level general linear models. Modelling of the SCAP task included separate regressors for all 4 levels of load (1, 3, 5, 7) at each delay time (1.5, 3, 5 s) resulting in 12 task-related regressors. The contrast of interest was load 5 (averaged over all delays) relative to baseline, as this load has been implemented previously to interrogate working memory within capacity limits (Todd and Marois, 2004; Montojo et al., 2014). The model for the stop-signal task included 4 task-related regressors: successful go, failed go, successful stop, and failed stop. The contrast of interest was successful stop. The model for the task-switching task included individual regressors for the 4 types of cue ('SHAPE', 'S', 'COLOR', 'C') and whether each cue was a switch or a no-switch trial, resulting in a total of 8 task-related regressors. The contrast of interest was the effect of the switch trials averaged over all cues. For all 3 cognitive paradigms, the task-related regressors were modelled using delta functions corresponding to the onset times of the trials, convolved with the canonical hemodynamic response function. Only correct responses were included in the task-related regressors, with incorrect responses modelled as separate regressors of no interest. Each model also included six motion parameters to account for variability due to head motion.

The BOLD responses to the breath-hold epochs were modelled using a ramp function convolved with a respiratory response function (Birn et al., 2008). A ramp function was used instead of a typical boxcar approach to model the accumulation of CO_2 over the course of the breath-hold epoch. The respiratory response function was established by Birn et al. (2008) to accurately model hypercapnia-induced BOLD responses to breath-hold. Similar to prior work modelling the hemodynamic response function (Handwerker et al., 2004; Williams et al., 2014; Williams et al., 2016), the respiratory version is modelled by the difference between two gamma functions but characterised by a longer, larger post-stimulus under-shoot. Both response functions can both be observed in Figure 1. For a small subset of participants (15/114, or 13%), the respiratory response function was not a good fit and resulted in too few significant voxels available for the ROI analysis. Rather than exclude these participants from further analysis, the hemodynamic response function convolved with the ramp function was implemented instead as this was a better fit for their breath-hold data. To account for possible delays in BOLD responses to breath-hold induced hypercapnia, different general linear models were created for each participant with staggered onset times. The onset times increased in increments of 1 TR (2 s), up to a maximum of 12 s. The model with the most significant voxels for each individual subject was utilized for further analyses. The contrast of interest used in further analyses was the effect of the breath-hold epochs greater than baseline.

2.1.6 ROI analysis

Structural ROIs were obtained on a per-subject basis using each participant's T_1-weighted image and cortical reconstruction with the recon-all function in FreeSurfer image analysis suite (Dale et al., 1999; Fischl et al., 1999; Fischl et al., 2004). This included automatic labelling of all cortical regions based on the Desikan-Killiany Atlas (Desikan et al., 2006). This atlas parcellates each of the cerebral hemispheres into 34 distinct regions based on gyral anatomy, resulting in 68 anatomical ROIs per subject.

To perform the ROI analysis, BOLD voxel-wise percent signal change (PSC) values for each of the cognitive and breath-hold tasks were extracted from each anatomical ROI on a per-subject basis. The following procedure was performed on individual activation maps from the first-level analysis. First, PSC maps were calculated for each task using the contrast images corresponding to the contrast of interest (outlined in the 'fMRI first-level analyses' section above) and the baseline images. The PSC maps were thresholded so that only significant ($p < 0.001$ uncorrected for multiple comparisons) voxels were included in the ROI analyses.

Once the thresholded PSC maps were calculated for all 4 fMRI tasks (3 cognitive tasks and breath-hold), each of the anatomical ROIs were binarized and transformed into fMRI space. The voxel values of the thresholded PSC maps were then extracted for each anatomical ROI. For each of the 3 cognitive tasks, only voxels with both significant task activation and a significant BOLD response to the breath-hold task were included. The voxels values were then averaged for each ROI, resulting in 6 averaged ROI PSC values for each participant: one for each of the 3 cognitive tasks, and its corresponding breath-hold. Any individuals with breath-hold ROI values that were considered outliers for the ROI were removed from the analysis in order to minimize effects from large vessels. Outliers were determined as values greater than 3 mean absolute deviations. If fewer than 10 participants demonstrated significant activation within an ROI, that ROI was removed from the analysis. Prior research showing that a sample size of 8 is sufficient for regression models with little variance, while a minimum of 25 is required for models with high variance (Jenkins and Quintana-Ascencio, 2020). For the present research it was anticipated that variance would differ between ROIs, and choosing too high a threshold in terms of number of subjects with significant activation might eliminate important results.

For each cognitive task, linear regression analyses were run for each ROI PSC, with the breath-hold PSC as the predictor variable. This resulted in a possible 204 regressions (68 ROIs x 3 cognitive tasks), although not all participants showed significant activation in all ROIs and therefore a subset was excluded. The final number of regression analyses performed across all 3 tasks was 109. Outliers were removed prior to regression analyses, with outliers defined as data points greater than 3 standard deviations from the group mean. All linear regression analyses were run in MATLAB. Due to inflated probability of making a Type I error due to the number of linear regressions performed, False Discovery Rate (FDR) correction ($p < 0.05$) was implemented.

2.1.7 Group-level analyses

The aim of the group-level analyses was to determine whether correcting for CVR by including breath-hold covariates into the general linear model reduced variance and increased sensitivity. The inclusion of covariates has shown to be a robust method to correct for CVR (Liau and Liu, 2009), and can be achieved either at the voxel-wise or the ROI level. Both voxel and ROI methods were explored here. For the voxel-wise approach, the breath-hold contrast image for each subject was entered into the model as a covariate. This was achieved using the extended version (Yang et al., 2011) of the Biological Parametric Mapping toolbox (Casanova et al., 2007), an SPM toolbox which allows for image covariates by implementing a separate general linear model for each voxel. CVR uncorrected

analyses for the voxel-wise method were standard group-level one-sample *t*-test performed in SPM12 for each task separately. All *t*-maps output were thresholded at $p < 0.05$ cluster-corrected for multiple comparisons using AFNI functions 3dFWHMx and 3dClustSim. For the ROI method, regions were chosen from the significant ROIs from the linear regression analyses (outlined in section 2.1.6). The averaged breath-hold value for each ROI was entered for each individual subject into the model as a covariate, and the statistical search limited to the ROI using binary masks. The CVR uncorrected analyses for the ROI method were identical except no covariate was included into the model. This was achieved using standard second-level analyses in SPM12.

2.2 Experiment 2: Gas inhalation CVR

2.2.1 Participants

For the second study, 17 participants completed a single scan session consisting of a cognitive fMRI scan, a hypercapnic fMRI scan with delivered CO_2 gas mixtures (see task and CO_2 paradigm descriptions below), and a structural scan. All participants reported no history of neurologic or respiratory disease. Data from 2 participants were removed due to excessive head motion and incomplete CO_2 scan. The final analysis presented here consisted of 15 participants (mean age = 38.5 ± 13.5 years, age range = 22–58 years, 8 F, all right-handed). This study was approved by the University of Calgary Conjoint Health Research Ethics Board and all participants provided written informed consent.

2.2.2 Imaging acquisition

All images for study 2 were acquired on a 3 T GE MRI scanner (Discovery MR750) with a 32-channel head coil from Nova Medical. The fMRI acquisition consisted of T_2*-weighted echo planar images with multiband (MB) acceleration (MB factor = 3), TR/TE = 1800/30 ms, flip angle = 70°, FOV = 256 mm, slice thickness = 2 mm, 63 slices, ARC factor = 2. There were 5 runs of fMRI (4 task, 1 CO_2) acquired in total. A B_0 field map was acquired for each fMRI run using a multi-echo fast spoiled gradient recalled echo sequence with TR = 500 ms, TE_{1-4} = 2.3/4.5/6.6/8.7 ms, flip angle = 30°, matched to the fMRI sequence. A sagittal 3D T_1-weighted BRAVO structural image was acquired with TR/TE/TI = 6.7/2.9/650 ms, flip angle = 10°, matrix = 256 × 256, 1 mm^3 isotropic voxels, 192 slices, ASSET factor = 2.

2.2.3 Task description

The attention network task-revised (ANT-R) was the cognitive paradigm implemented in study 2 (Fan et al., 2005; Fan et al., 2009; Fan et al., 2012; Xuan et al., 2016). Attention is the cognitive domain that guides detection and prioritization of relevant features, and is comprised of 3 distinct networks: alerting, orienting and executive control (Petersen and Posner, 2012; Mackie et al., 2013). The ANT-R is the most recent version (at the time of testing) of a widely implemented behavioural paradigm that independently assesses the three attention networks and with fMRI, delineates the regions associated with each network (Fan et al., 2009; Xuan et al., 2016; Markett et al., 2022). The alerting network, responsible for anticipation and arousal, is associated with numerous widespread cortical regions including the anterior cingulate cortex, inferior occipital, precentral gyrus and parietal lobule, mid temporal and fusiform gyri, and superior frontal regions (Xuan et al., 2016). The orienting network is responsible for shifting focus to the prioritized stimuli, and has anatomical associations with the parietal lobule, frontal eye fields, the superior colliculi and thalamus. The executive control network identifies relevant information amongst competing, irrelevant stimuli, and is associated with the frontal regions including the anterior cingulate and lateral prefrontal cortex (Fan et al., 2009). The ANT-R was implemented because of these well-known anatomical correlates widely dispersed across the cerebral cortex.

The ANT-R is described in detail in (Fan et al., 2009) and (Xuan et al., 2016). The task is a cued flanker paradigm, where a central fixation cross and two rectangles to the left and right of the cross remain on the screen throughout the entirety of the task. For each trial, a row of 5 arrows is briefly presented (500 ms) in one of the two rectangles. The participants' task is to indicate as rapidly as possible whether the centre (third) target arrow is pointing to the left or to the right. This is achieved with a button press of their dominant hand using either the index or middle finger. The centre arrow was either congruent with the other 4 arrows (pointing the same direction) or incongruent. Prior to the onset of the target arrows, a transient visual cue appeared in most trials (60 out of 72 trials, or 83.3%). The cue was a short (100 ms duration) brightening of the rectangle. There were 4 types of cue conditions: no cue, double cue (where both rectangles brightened), valid spatial cue (rectangle that was going to contain the target arrows brightened) and invalid spatial cue (rectangle that did not contain the target arrows brightened). The time delay between the cue and arrow targets was randomly assigned per trial as either 0, 400 or 800 ms. The baseline period between trials (the inter-stimulus interval) was pseudo-randomised and between 2,000 and 12,000 ms. There was a total of 72 trials per run, and with a total of 260 volumes collected per run, with each run lasting 7 min and 48 s. A total of 4 ANT-R runs were acquired per participant.

2.2.4 CO_2 challenge

An MR-compatible breathing circuit was used to achieve mild hypercapnia during the fMRI scan. The apparatus consisted of a non-rebreathing facemask with unidirectional valves for separate gas delivery and sampling of end-tidal gases (Tancredi et al., 2014; MacDonald et al., 2018). Outside the scanner, an automatic gas delivery system consisting of a Digital Flo-Box and Mass Flow Controllers (Sierra Instruments, Monterey, CA) and BIOPAC sampling equipment (BIOPAC Systems Inc., Goleta, CA) controlled gas delivery and sampling. BIOPAC modules CO2100C and O2100C continually sampled CO_2 and O_2 throughout the duration of the scan (sampling rate = 100 mL/min). The hypercapnia paradigm consisted of 2 min of delivered gas mixture with increased CO_2 (gas mixture of 5% CO_2 and 95% medical air) interspersed with 2 min of medical air, resulting in a total scan time of 6 min.

2.2.5 fMRI preprocessing

The schematic summarizing the data analysis pipeline for experiment 2 is shown in Figure 1. All fMRIs underwent distortion correction using the B_0 field maps and FieldMap Toolbox in SPM (Jezzard and Balaban, 1995; Jenkinson, 2003). Motion correction was performed in SPM12 (https://www.fil.ion.

10.3389/fphys.2023.1167148

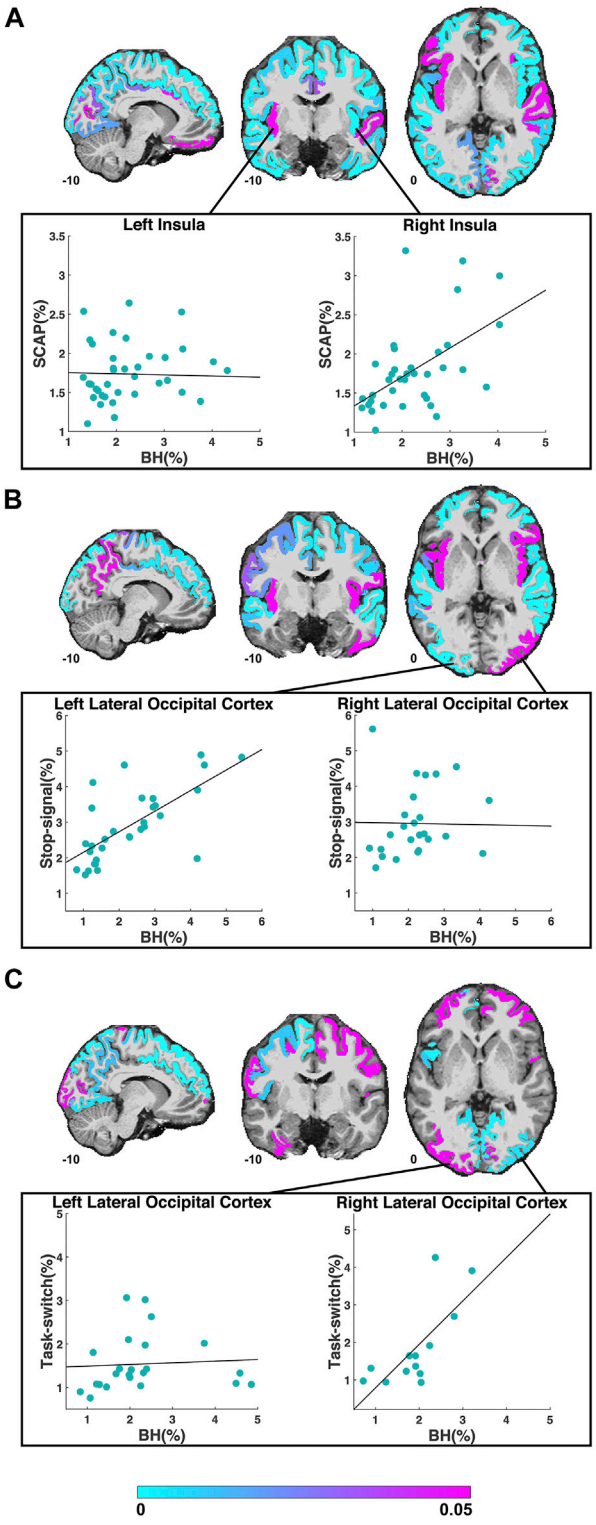

FIGURE 2
ROIs included in the regression analyses for the SCAP **(A)**, stop-signal **(B)** and task-switch **(C)** tasks are shown in cyan-magenta. ROIs where the task did not result in significant activation in at least 10 participants are not coloured. Images in coronal, sagittal and axial planes are shown in neurological orientation with MNI coordinates. The color bar indicates *p*-values from the regressions; regions in magenta did not show a significant linear relationship between breath-hold (BH) BOLD PSC and task PSC. The scatter plots in **(A)** demonstrate the PSC (breath-hold and SCAP) from the left and

(*Continued*)

FIGURE 2 (Continued)
right insula to the SCAP task. The regression for the left insula (shown in magenta in the coronal plane) was non-significant, while the right insula (shown in cyan in the coronal plane) was significant. The scatter plots in **(B)** show an example of a significant (left lateral occipital cortex) and non-significant (right lateral occipital cortex) ROI for the stop-signal task. The scatter plots in **(C)** also show the left and right lateral occipital cortex, but to the task-switch paradigm. For this task, the regression for the left lateral occipital cortex was non-significant, while the right was significant. For all scatter plots, each data point represents one subject's averaged PSC from that ROI.

TABLE 1 Regions-of-interest (ROI) with most significant (top 10) and non-significant (all) linear relationships between SCAP PSC and breath-hold PSC. *P* and R^2 values from the linear regression analyses shown.

ROI	*p*-value	R^2	*n*
Top 10 significant ROIs			
R precuneus	1.1×10^{-8}	0.39	68
L superior temporal gyrus	5.3×10^{-8}	0.57	38
R supramarginal gyrus	3.1×10^{-7}	0.29	78
R inferior temporal gyrus	2.1×10^{-6}	0.39	48
R inferior parietal cortex	3.2×10^{-6}	0.23	85
R pars triangularis	7.9×10^{-6}	0.48	33
L caudal middle frontal gyrus	1.3×10^{-5}	0.30	54
L paracentral lobule	2.1×10^{-5}	0.59	23
L supramarginal gyrus	4.7×10^{-5}	0.17	90
L postcental gyrus	7.0×10^{-5}	0.17	87
Non-significant ROIs			
L insula	0.84	0.001	39
L bank of the superior temporal sulcus	0.65	0.01	18
L pericalcarine cortex	0.32	0.05	23
R pericalcarine cortex	0.21	0.17	11
L caudal anterior cingulate	0.19	0.09	21
R bank of the superior temporal sulcus	0.11	0.20	14
L pars triangularis	0.09	0.13	23
L lateral orbitofrontal cortex	0.06	0.19	19
R lateral orbitofrontal cortex	0.05	0.12	32
R superior temporal gyrus	0.05	0.21	19

R^2 = coefficient of determination, *n* = number of participants.
R = right hemisphere, L = left hemisphere.

ucl.ac.uk/spm/). All within-subject fMRI runs (4 x ANT-R and 1 x CO_2) were aligned using affine registration with Advanced Normalization Tools (ANTs) (Avants et al., 2011; Avants et al., 2014). Affine registration between each subject's fMRIs and structural T_1, and normalisation of the T_1 image to the MNI template, was performed using Unified Segmentation in SPM12

(Ashburner and Friston, 2005). Deformation fields from the T_1 image segmentation were applied to the fMRIs, which were normalised to the MNI template. Minimal spatial smoothing (4 mm full-width at half-maximum) was performed to improve signal to noise ratio. Smoothing was performed here but not in experiment 1 because of the differences in spatial resolution.

2.2.6 fMRI first-level analyses

The general linear model for the ANT-R task included 16 task-related regressors, corresponding to cue condition (no cue, double cue, valid, invalid), the direction of the centre target arrow relative to the surrounding arrows (congruent, incongruent) and the target location (left rectangle, right rectangle). Only correct trials were modelled in these tasks regressors; incorrect trials were modelled separately as regressors of no interest. Six motion parameters were also included as regressors. Weighted linear contrasts calculated from the estimated beta images corresponded to the three attention networks. However, due to having the most robust and spatially extensive cortical activation, the alerting network was the contrast of interest for the present study. The alerting network was defined as the contrast of double cue relative to baseline, similar to prior work (Xuan et al., 2016).

First-level analysis of the hypercapnia paradigm modelled the BOLD signal change to increased CO_2 using end tidal partial-pressure of CO_2 from the CO_2 module breathing traces. On a per-subject basis, the end tidal CO_2 was extracted from the breathing trace and interpolated to match the temporal resolution of the fMRI time-series. The mean BOLD time-course was extracted from each subjects' grey matter mask and cross-correlated with the end tidal CO_2 trace. For the cross-correlations, the end tidal CO_2 time-course was systematically shifted by 1 TR (1.8 s) until the maximum correlation between the mean grey matter BOLD time-course and end tidal CO_2 was found. The end tidal CO_2 with maximal BOLD correlation was entered into the general linear model as the regressor of interest. The six motion parameters were entered into the model as regressors of no interest.

2.2.7 ROI analyses

The procedure for ROI definition was consistent with experiment 1. PSC maps were calculated from the alerting contrast and CO_2 challenge using only these significant voxels. CVR maps were obtained by dividing the CO_2 PSC maps by the maximum change in end tidal CO_2 (mm Hg) during the CO_2 challenge. ROI-averaged CVR values were input to the linear regression analyses, with ROI values greater than 3 mean absolute deviations removed from the analysis.The same procedure as study 1 was implemented for the linear regressions, where only ROIs with significant activation in at least 10 participants were considered.

2.2.8 Group-level analyses

The aim and methods of the group-level analyses outlined in experiment 1 (section 2.1.7) were identical to experiment 2. The group analyses for experiment 2 were run with both voxel-wise CVR correction using the Biological Parametric Mapping toolbox, and at the ROI level using SPM only. All analyses used alerting contrast images.

3 Results

3.1 Experiment 1: Breath-hold CVR

3.1.1 fMRI first-level analyses

The SCAP task produced robust bilateral activation across the insula and frontal and parietal lobes. The successful inhibition contrast from the stop-signal task significantly activated the superior temporal gyrus bilaterally, left insula, medial cingulate cortex, and right middle frontal gyrus. The task-switch paradigm resulted in significant activation in the left posterior-medial frontal gyrus, left inferior parietal lobule, bilateral calcarine gyrus, and left postcentral gyrus, insula, and lingual gyrus.

3.1.2 ROI analyses

The anatomical ROIs ranged in mean volume from 1,016 (±284) mm^3 for the left frontal pole to 30,102 (±2,639) mm^3 for the left superior frontal gyrus. All 68 of the anatomical ROIs and their volumes are available in Supplementary Table S1.

The first cognitive task, the SCAP paradigm, had 51 ROIs with significant BOLD responses (to both SCAP and breath-hold) in 10 or more participants. The majority of these ROIs showed a significant linear relationship between SCAP activation and BOLD PSC to breath-hold, with 41 (80.1%) ROIs in total showing significant regression results (after FDR-correction for number of ROIs). ROIs and their corresponding original (prior to FDR-correction) *p*-values are displayed in Figure 2A; Table 1 outlines the top 10 ROIs with the strongest linear relationship between SCAP activation and breath-hold, as defined by *p*-values. The 10 ROIs that did not result in a significant regression are also outlined in Table 1. As shown in Table 1, these non-significant ROIs typically had a smaller sample size (i.e., fewer participants with significant activation in that ROI), as indicated by the '*n*' column. There were exceptions however; one being the left insula. This ROI did not demonstrate a linear relationship between SCAP activation and breath-hold response but had similar activation and a larger *n* than the right insula, which did show a significant linear relationship ($p = 0.0008$, $R^2 = 0.29$, $n = 36$). The mean percent signal changes were similar between the two insula ROIs (right insula $M = 1.79$ and 2.24%, left insula $M = 1.73$ and 2.27% for SCAP and breath-hold respectively). Scatter plots for the left and right insula are shown in Figure 2A. All ROIs evaluated for the SCAP are given in the Supplementary Table S2.

The second cognitive task, the stop-signal paradigm had 34 ROIs with adequate BOLD responses (>10 participants) for linear regression analyses. Out of these 34 ROIs, 25 (73.5%) showed a significant linear relationship between stop-signal BOLD activation and breath-hold response. These ROIs and their original *p*-values from the regression analyses are shown in Figure 2B. The scatter plots in this figure show an example significant and non-significant ROI. Table 2 outlines the top 10 ROIs with the strongest linear relationship, and the 9 ROIs that were non-significant. All evaluated ROIs are shown in the Supplementary Table S3.

TABLE 2 Regions-of-interest (ROI) with most significant (top 10) and non-significant (all) linear relationships between stop-signal PSC and breath-hold PSC. *P* and R^2 values from the linear regression analyses shown.

ROI	*p*-value	R^2	*n*
Top 10 significant ROIs			
R inferior parietal cortex	8.6×10^{-9}	0.58	41
R superior temporal gyrus	1.8×10^{-7}	0.38	60
R supramarginal gyrus	8.0×10^{-7}	0.36	58
L supramarginal gyrus	1.6×10^{-6}	0.42	45
L inferior parietal cortex	2.1×10^{-6}	0.63	25
L superior parietal cortex	8.9×10^{-6}	0.54	28
L lateral occipital cortex	1.6×10^{-5}	0.48	31
R superior frontal gyrus	2.2×10^{-5}	0.47	31
R middle temporal gyrus	3.4×10^{-5}	0.36	41
R rostral middle frontal gyrus	6.0×10^{-5}	0.38	37
Non-significant ROIs			
R lateral occipital cortex	0.91	0.0005	26
R inferior temporal gyrus	0.78	0.0006	14
R postcentral gyrus	0.58	0.02	15
L pars opercularis	0.48	0.07	10
R insula	0.15	0.12	18
L bank of the superior temporal sulcus	0.13	0.15	17
L insula	0.08	0.23	14
R pars triangularis	0.07	0.33	11
R lateral orbitofrontal cortex	0.04	0.36	12

R^2 = coefficient of determination, *n* = number of participants.
R = right hemisphere, L = left hemisphere.

TABLE 3 Regions-of-interest (ROI) with most significant (top 10) and non-significant (all) linear relationships between task-switch PSC and breath-hold PSC. *P* and R^2 values from the linear regression analyses shown.

ROI	*p*-value	R^2	*n*
Top 10 significant ROIs			
L superior frontal gyrus	1.8×10^{-4}	0.62	17
L superior parietal cortex	0.0006	0.31	34
L pars opercularis	0.001	0.67	12
R lingual gyrus	0.002	0.31	28
R precuneus	0.002	0.45	18
L inferior parietal cortex	0.004	0.31	24
R lateral occipital cortex	0.005	0.53	13
L lingual gyrus	0.005	0.22	34
L precentral gyrus	0.01	0.23	28
L precuneus	0.01	0.34	18
Non-significant ROIs			
R pericalcarine	0.94	0.0006	11
R rostral middle frontal gyrus	0.85	0.003	16
L lateral occipital cortex	0.77	0.004	23
R superior frontal gyrus	0.44	0.08	10
L caudal middle frontal gyrus	0.39	0.06	15
L postcentral gyrus	0.30	0.06	19
R inferior parietal cortex	0.21	0.11	17
L fusiform	0.14	0.13	18
R precentral gyrus	0.09	0.22	14
L rostral middle frontal gyrus	0.08	0.13	24
R superior parietal cortex	0.06	0.17	22
L pericalcarine	0.05	0.21	19
R supramarginal gyrus	0.04	0.37	12

R^2 = coefficient of determination, *n* = number of participants.
R = right hemisphere, L = left hemisphere.

The third cognitive task, the task-switch paradigm showed a total of 24 ROIs with adequate BOLD responses (in 10 or more participants) for linear regression analyses. Out of these, 11 ROIs (45.8%) were significant. These ROIs and their original *p*-values from the regression analyses are shown in Figure 2C; Table 3 demonstrates the top 10 ROIs with the strongest linear relationship, and all 13 ROIs that were non-significant. Similar to the previous two paradigms, the ROIs that did not show significant relationships between task-switch activation and breath-hold BOLD responses tended to demonstrate smaller *n* sizes. The exception was the left lateral occipital cortex, which was non-significant but had a larger *n* than the right lateral occipital cortex. The right, conversely, was highly significant. The mean PSC was similar between the two lateral occipital cortices (right M = 1.84 and 1.91%, and left M = 1.54 and 2.27% for task-switch and breath-hold respectively). The scatter plots comparing the left and right lateral occipital cortex are shown in Figure 2C. The linear regression results for all evaluated ROIs are given in the Supplementary Table S4.

The regions that showed a significant linear relationship between task and breath-hold BOLD responses for all 3 cognitive tasks were the left inferior parietal cortex, precentral gyrus, superior frontal gyrus, and supramarginal gyrus; and the right precuneus. These ROIs are displayed in the Supplementary Figure S1. The ROIs with adequate responses (significant activation to at least one task and breath-hold in >10 participants) but failed to show significant regressions in any of the 3 tasks were the left bank of the superior temporal sulcus, left caudal anterior cingulate cortex, left insula, and left pars triangularis; the pericalcarine cortex bilaterally, and the lateral orbitofrontal cortex bilaterally.

3.1.3 Group-level analyses

Activation maps in Figure 3 show the group activation to the SCAP, stop-signal and task-switch paradigms both with and without CVR correction using the voxel-wise image covariate approach.

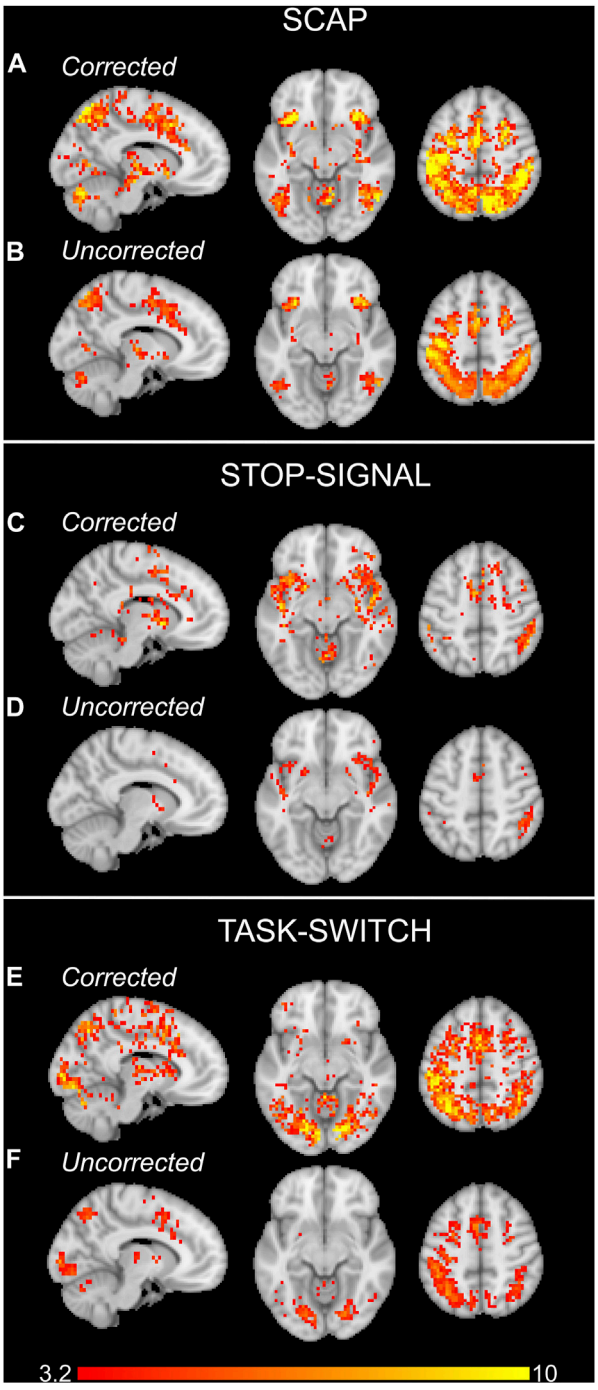

FIGURE 3
Group activation maps for the SCAP **(A, B)**, stop-signal **(C, D)** and task-switch **(E, F)** paradigms for experiment 1. The upper rows of each task **(A, C, E)** show the activation maps which were corrected for CVR by including the breath-hold contrast images as covariates. The lower row for each task **(B, D, F)** are the standard, uncorrected for CVR, group activation maps. All images cluster-corrected for multiple comparisons ($p < 0.05$). The colour bar indicates t-values.

Figures 3A, C, E show maps that have been corrected for CVR by including breath-hold as an image covariate in the Biological Parametric Mapping toolbox, and Figures 3B, D, F demonstrate the standard analyses without correction (i.e., no image covariate). For all 3 tasks, the corrected group-level analyses showed a greater number of significant voxels than their uncorrected counterparts. The corrected activation maps also had higher peak voxel *t*-values for SCAP, stop-signal and task-switch (t = 18.65, 13.69 and 15.00 respectively) compared to the uncorrected maps (t = 12.63, 7.84, 8.50). The ROI approach was also applied to correct for CVR, however there were no differences between CVR corrected and uncorrected activation maps for this method.

3.2 Gas inhalation CVR

3.2.1 CO_2 challenge

At baseline when participants were exposed to medical air only, the mean end tidal CO_2 was 35.38 (±4.1) mmHg (elevation of testing location was 1,100 m). During the 2-min hypercapnia period when participants were exposed to 5% CO_2, the mean maximum end tidal CO_2 was 45.19 (±3.59) mmHg. The mean change in end tidal CO_2 between baseline and hypercapnia was 9.81 (±3.06) mmHg.

3.2.2 fMRI analyses

The alerting contrast produced robust activation across the cerebral cortex with peak activation in the left inferior parietal lobule, right inferior frontal gyrus, left fusiform gyrus, left posterior medial-frontal gyrus, right inferior occipital gyrus, right superior parietal lobule, and right middle frontal gyrus. The CO_2 challenge produced increased BOLD responses across the cerebral cortex, particularly from the large sinuses. An example CVR map is shown in Figure 4A, and the group activation map to the alerting contrast is shown in Figure 4B.

3.2.3 ROI analyses

The mean volumes of the anatomical ROIs ranged from 820 (±255) mm^3 for the right transverse temporal cortex to 25,196 (±4,472) mm^3 for the left superior frontal gyrus. All 68 of the anatomical ROIs and their mean volumes are displayed in Supplementary Table S1.

A total of 50 ROIs had significant activation in 10 or more participants and were entered into linear regression analyses. Out of these 50 ROIs, 5 showed an uncorrected ($p < 0.05$, before FDR-correction for multiple comparisons) significant linear relationship between alerting activation and CVR: right paracentral gyrus (p = 0.0003, R^2 = 0.71, n = 13), right cuneus (p = 0.001, R^2 = 0.64, n = 13), right pericalcarine (p = 0.004, R^2 = 0.51, n = 14), left paracentral lobule (p = 0.02, R^2 = 0.42, n = 12), and right inferior parietal cortex (p = 0.04, R^2 = 0.28, n = 15). The first two (right paracentral gyrus and cuneus) were the only ROIs to survive FDR correction for multiple comparisons. These five ROIs are shown in Figure 5, along with their respective scatter plots. The linear regression results from all evaluated ROIs can be found in the Supplementary Table S5.

R^2 values from all ROIs, from both studies (breath-hold and gas-induced hypercapnia) are displayed in a polar plot in Figure 6. This plot indicates that when activated by a task, most ROIs showed at least a moderate linear relationship between task-induced signal magnitude and CVR. Low correspondence between ROI activation and CVR (indicated by small R^2 on Figure 6) typically reflects lack of activation by the task.

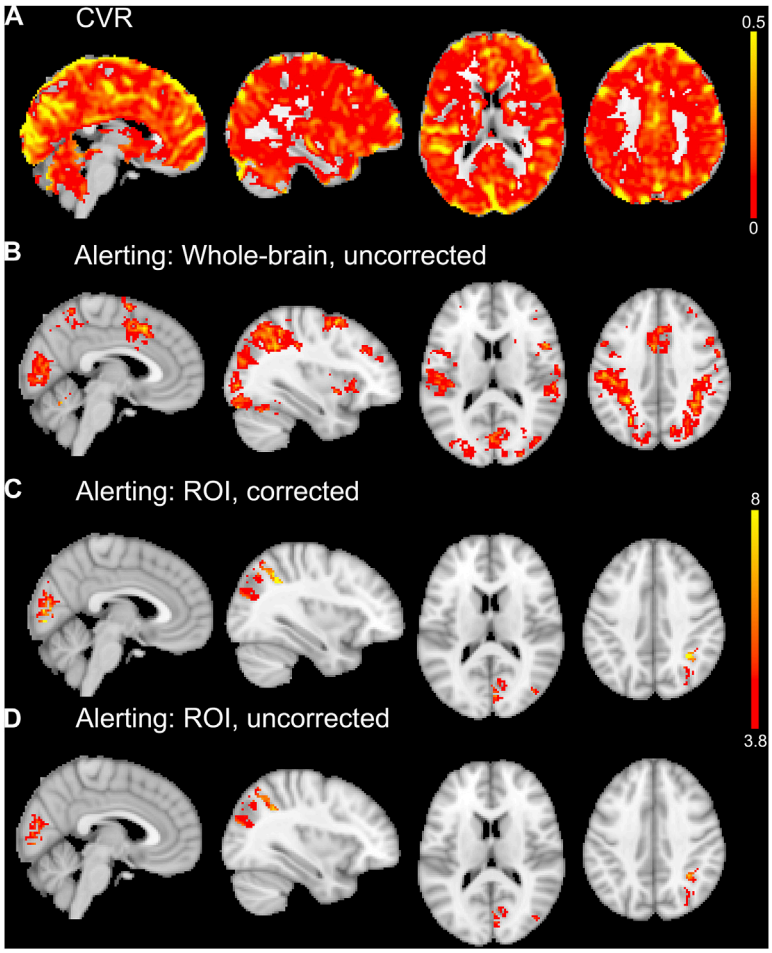

FIGURE 4
An example CVR map of a single subject is shown in **(A)**. Whole-brain average group maps for the alerting contrast of the ANT-R shown in **(B)**. The ROI analyses of the alerting contrast shown in **(C)** and **(D)** included explicit masks comprised of the five significant ROIs from the linear regression analyses for experiment 2. For the vascular corrected ROI analysis in **(C)**, the mean CVR values for each ROI were entered into the model as covariates. The vascular uncorrected ROI analysis shown in **(D)** included the explicit masks only with no covariates. The group maps in **(B, C, D)** were thresholded at $p < 0.001$ uncorrected for multiple comparisons. The upper colour bar indicates %BOLD/mmHg for the CVR map in **(A)**. The lower colour bar indicates t-values for **(B, C, D)**.

3.2.4 Group-level analyses

The first approach to CVR correction using voxel-wise general linear models and the Biological Parametric Mapping toolbox was not optimal for experiment 2, as it resulted in less activation than the uncorrected (i.e., standard one-sample *t*-test) group analysis. The second ROI approach to CVR correction implemented only the five significant ROIs from the linear regression analyses (right paracentral gyrus, right cuneus, right pericalcarine, left paracentral lobule, right inferior parietal cortex). This ROI approach resulted in small increases in the number of significant voxels (at $p < 0.001$ uncorrected for multiple comparisons) for the vascular corrected compared to the uncorrected analyses. The largest differences were observed in the right inferior parietal cortex (+27 voxels for vascular corrected vs. uncorrected) and right cuneus (+24 voxels for vascular corrected vs. uncorrected). There were increases in the peak *t*-values for most of the vascular corrected ROIs compared to the uncorrected ROIs (right cuneus: $t = 8.94$ and 6.36; right pericalcarine: $t = 8.78$ and 7.03; left paracentral lobule: $t = 6.26$ and 6.49; right inferior parietal cortex: $t = 9.33$ and 7.25 for vascular corrected and uncorrected respectively). The right paracentral gyrus is unreported as there were no suprathreshold voxels for both vascular corrected and uncorrected analyses. Activation maps from the vascular corrected and uncorrected ROI analyses are shown in Figures 4C, D respectively.

4 Discussion

This research aimed to evaluate whether basal vascular physiology, assessed using CVR, can predict task-induced BOLD responses across multiple cognitive tasks activating different cortical regions. The hypothesis that linear relationships between CVR and task-based BOLD responses would be observed across all brain regions evaluated was largely supported. Evidence for this can be found in the polar plot in Figure 6, showing that the majority of regions investigated showed at least a moderate ($R^2 > 0.20$)

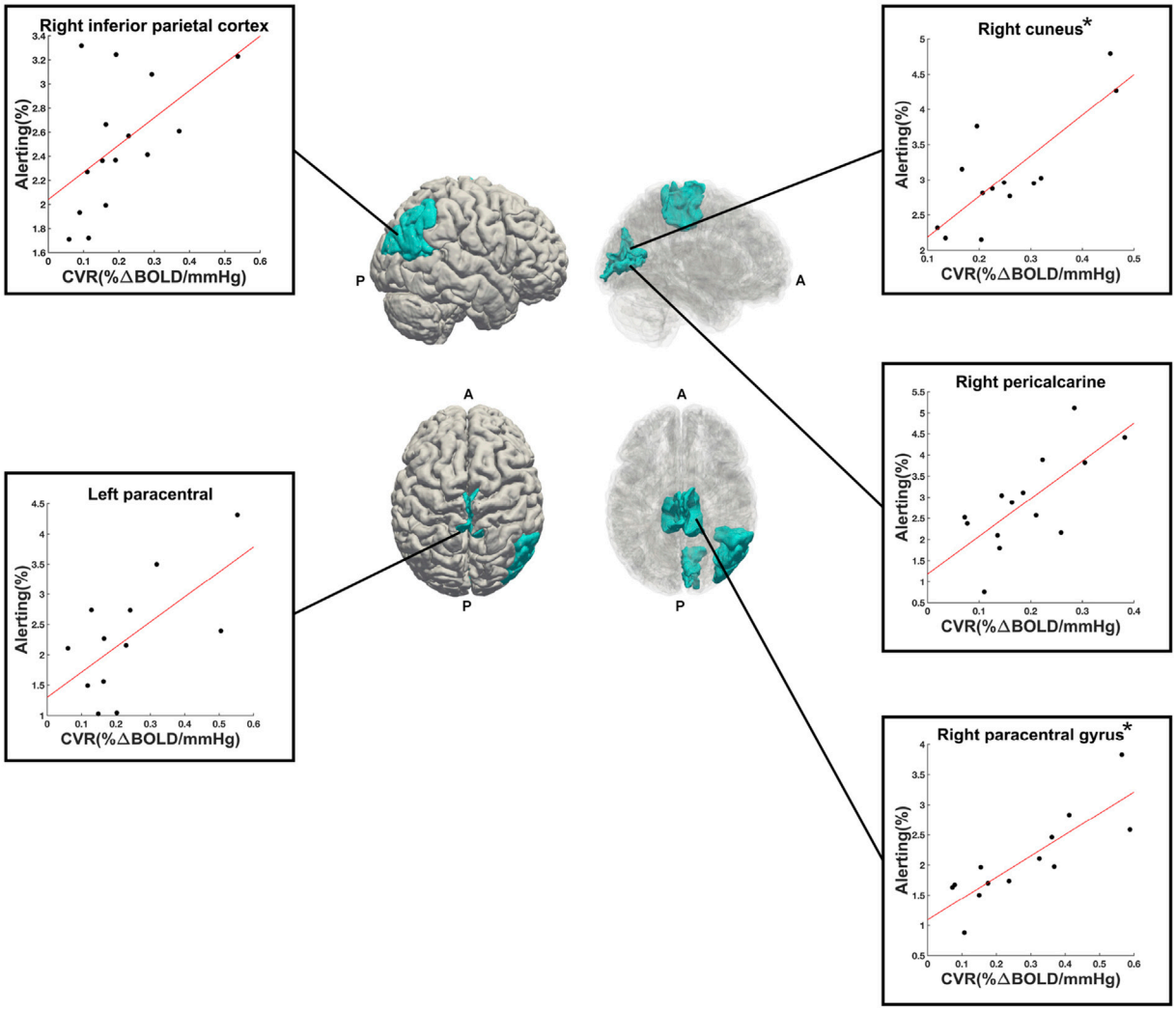

FIGURE 5
Right (upper) and superior (lower) views of the significant ROIs (in cyan) from the alerting contrast of the ANT-R task. Reduced opacity images on the right highlight medial aspects. Scatter plots show the linear relationship between alerting PSC (*y*-axis) and CVR (*x*-axis) for each ROI. The (*) next to right cuneus and right paracentral gyrus indicate that these two ROIs were significant following FDR-correction for multiple comparisons. A = anterior, P = posterior.

relationship between BOLD activation magnitude and CVR to at least one task. These findings highlight that the relationship between neural activity-mediated BOLD signal and vascular physiology is mostly preserved across the cerebral cortex, to different cognitive tasks and with different CVR approaches.

For experiment 1, task activation was predicted by breath-hold BOLD responses for the majority of evaluated ROIs, although some exceptions were found. Most of these exceptions could be explained by smaller sample size, as fewer participants demonstrated significant task and/or breath-hold BOLD responses compared to ROIs that were significant. This relationship between variance explained by breath-hold responses and sample size can be appreciated from the information presented in Tables 1–3 where both R^2 and '*n*' are reported for significant and non-significant ROIs. There were two exceptions found, however. For the SCAP task, a paradigm of spatial memory, the insula showed strong BOLD responses bilaterally, however, only activation from the right insula showed a linear relationship with CVR. Likewise, for the task-switch paradigm, the lateral occipital cortex showed strong bilateral BOLD responses but only the right hemisphere showed a significant linear relationship with CVR. These two non-significant ROIs (left insula and lateral occipital cortex) cannot be fully explained by small sample size, as they had more participants with significant activation than their contralateral counterpart. Differences in mean PSC between these ROIs is another potential explanation but does not appear relevant here as these were also highly consistent between hemispheres. Moreover, the left insula failed to show a significant linear relationship with CVR across all paradigms; this includes the SCAP, the stop-signal task with a sample size of 14 participants, and the ANT-R with 12 participants. Similarly,

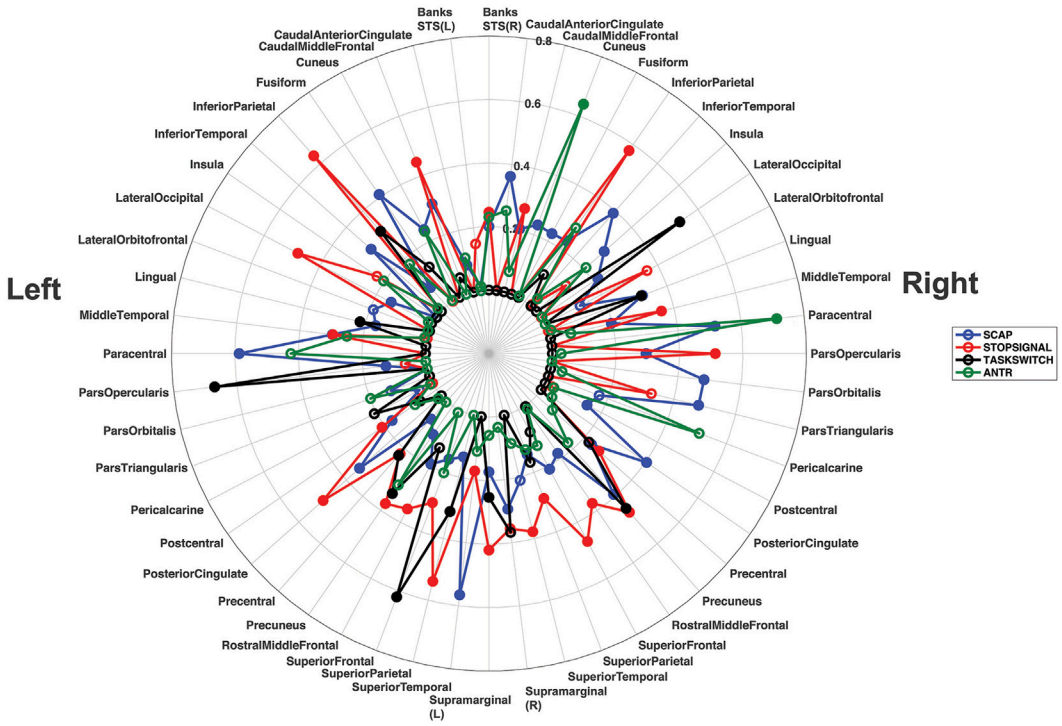

FIGURE 6
Polar plot displaying the R^2 values for all ROIs from all linear regression analyses, across both experiments. Each ROI shows its corresponding R^2 value for the left and right hemisphere separately. The R^2 values for the SCAP are shown in blue, stop-signal in red, task-switch in black and ANT-R in green. The open-coloured markers ('o') indicate that the ROI was not significant after FDR correction for multiple corrections, while the closed markers were significant. The concentric circles indicate the R^2 value, with values increasing with radius to a maximum of R^2 = 0.80.

the right insula was activated by the stop-signal (n = 18) and ANT-R (n = 13) tasks but was non-significant in the ROI analyses. Bilaterally the insula was not activated by the task-switch paradigm and was not included in the linear regression analyses for this task. One possible explanation is that left insula activation to the SCAP task and its relationship with breath-hold BOLD responses varied across participants of different ages. Further analyses were therefore run, separating the youngest age group (participants aged in their 20's at time from testing) from the oldest age group (people aged 40–50 years at time of testing). The scatter plot shown in the Supplementary Figure S2, shows a difference between these two groups which may explain the non-significant finding. Supplementary Figure S2 shows a negative (albeit non-significant) relationship between task-based activation and breath-hold BOLD responses for the older group, while the younger group showed a significant positive relationship. The present study lacks the sample size to fully investigate this age effect observed in the left insula, however it is hoped that these preliminary data provide impetus for future research.

Unlike the insula, the lateral occipital cortex showed a more task-dependent relationship with CVR. For this region, the left hemisphere regression (with breath-hold as the predictor variable) was significant in the stop-signal task (n = 31) but the right was not (n = 26). This was the opposite for the task-switch paradigm, where the left was non-significant (n = 23) and the right significant (n = 13). For the SCAP, both the right (n = 44) and the left (n = 53) lateral occipital cortices were significant. Both left and right lateral occipital cortices were non-significant in the ANT-R (n = 15 for both). Unlike the insula, this appears to be a region that has strong correspondence with vascular physiology. However, task-related variability in how each task recruited this region, and the strength with which each participant individually recruited this region, was observed.

The regions that showed significant linear regressions across all three cognitive paradigms in experiment 1 were mainly left-lateralized and showed parietal lobe dominance. Out of the 5 ROIs that were consistently significant across the three tasks, only one was outside the parietal region: the left superior frontal gyrus. This left-lateralized consistency may reflect strong BOLD responses within this region due to the common task requirement, a motor response (button press) with their dominant hand. However, the bilateral parietal lobes were dominant in experiment 2. For the five ROIs significant at $p < 0.05$ (uncorrected for multiple comparisons) in this gas-inhalation study, three were in the parietal lobe (two right hemisphere). There was a button-press response required by the dominant hand for the ANT-R task, and all participants in this study were right-handed. Motor responses might explain some of the left parietal dominance (for example, the left paracentral ROI in the ANT-R task), however further consideration is required as the inferior parietal cortex (IPC) is spatially discrete from the motor cortex. The IPC was the only region to be significantly related to CVR across all four tasks, in the two separate experiments, with the left IPC in study 1 and the right

IPC in experiment 2. Regions such as the parietal cortex where activation was strongly and consistently predicted by CVR might be particularly prone to confounding task-related BOLD signal changes due to CVR, such as those observed in aging.

Brain aging leads to cerebrovascular changes, with vascular stiffening and endothelial dysfunction compromising a vessel's ability to respond to CO_2 (Abdelkarim et al., 2019). CVR decline with advancing age has been reported (Bhogal et al., 2016; McKetton et al., 2018; Peng et al., 2018). Changes in neural activity-mediated BOLD signal also change with age (West et al., 2019), and disentangling the neural and non-neural contributions is vital for the appropriate interpretation of BOLD fMRI (Tsvetanov et al., 2021b). Addressing age-related vascular physiology differences is an area where vascular correction such as hypercapnic normalization should be considered essential. In these applications however, it is important to consider partial voluming and the increased contribution of cerebrospinal fluid. This might be a particularly important consideration in studies of aging where cortical atrophy occurs, increasing the likelihood of voxel cerebrospinal fluid contributions. In these instances, factors to prevent partial voluming such as increased spatial resolution should be considered. However, there are other applications outside of aging that would benefit from correction of baseline physiology. For example, acute sleep deprivation in healthy subjects has shown to increase regional cerebral blood flow (Elvsåshagen et al., 2019). Evidence for CVR changes due to acute sleep deprivation is lacking, however chronic sleep deprivation in subjects with obstructive sleep apnea has shown to be associated with increases in CVR (Ryan et al., 2018). Differences in habitual sleep patterns are a likely source of BOLD inter-subject variability, and the variability due to vascular changes might be addressed with vascular correction. Similarly, caffeine is a known vasoconstrictor that affects fMRI activation (Mulderink et al., 2002; Laurienti et al., 2003; Griffeth et al., 2011; Specht et al., 2019), however research addressing whether vascular correction can address vascular changes is lacking and highly warranted (Williams et al., 2021a). It is possible that medication can also affect BOLD signal, although this is medication-dependent and only certain medications have, to date, been evaluated in various patient groups (Goozee et al., 2016; Delfin et al., 2020; Williams et al., 2021b). Nonetheless, vascular correction in studies comparing medication-taking versus medically naive groups would improve interpretation of BOLD signal changes by separating variability due to vascular and non-vascular factors. Vascular correction might also improve the accuracy of BOLD fMRI magnitudes to scale with neural activity, such as experimental designs with increasing cognitive load or sensory load (for example, visual studies with partial to full visual field stimulation). This is because the vascular corrected activation map might have reduced dependence on larger blood vessels, thereby improving the accuracy of the map to reflect neural activity. Further research on this is required.

An important area of research that might benefit from vascular correction includes comparisons of patient and healthy control groups where cerebrovascular changes due to disease processes in the patient group produce confounding results. This has been highlighted in patients with Moyamoya disease where significant arterial stenosis changes the distribution of cerebral blood flow during activation and hypercapnia (Mazerolle et al., 2018; Hauser et al., 2019). One consideration is whether patients with CVR impairment will demonstrate a linear response to CO_2. There is evidence supporting a sigmoidal rather than linear relationship between CVR response and end-tidal partial pressure of CO_2. In a study of healthy participants, Bhogal et al. (2014) showed that the linearity between BOLD percent signal change and end-tidal CO_2 did not hold at high CO_2 stimulation (Bhogal et al., 2014). Patients with impaired vascular reactivity due to vessel pre-dilation may demonstrate a shift in the sigmoidal response such that BOLD responses are diminished at weaker levels of CO_2 stimulation. With hypercapnic normalization, it's assumed that a pre-dilated vessel would show a corresponding diminished BOLD activation to a task. It has been shown that task-based BOLD activation is reduced when baseline vasodilatory potential is reduced due to increased baseline end-tidal CO_2 (van Niftrik et al., 2018), suggesting that hypercapnic normalization would be ideally implemented in participants with impaired vascular reactivity.

When discussing fMRI vascular correction using hypercapnia-based approaches such as CVR, it is critical to address the assumption of iso-metabolism. When CVR studies are performed, it is assumed that metabolism remains consistent across hypercapnic and normocapnic epochs, however recent research findings have challenged this. Deckers et al. (2022) reported a mean decrease of 13.4% in cerebral metabolic rate of oxygen during inhalation of 5% CO_2 in air (Deckers et al., 2022). This is a concern for calibrated fMRI studies that aim to calculate cerebral metabolic rate of oxygen (Blockley et al., 2015), and it should also be a consideration for CVR studies using BOLD. The BOLD amplitude will be overestimated in the context of reduced deoxyhemoglobin concentrations, thereby overestimating the calculated CVR. Alternative approaches for acquiring CVR maps for vascular correction might include the use of arterial spin labelling rather than BOLD, and altering the gas mixtures to induce a slight hypoxic component (Peng et al., 2017). There is emerging research suggesting that CVR can be calculated from gas-free methods such as resting-state BOLD, which is also a possibility for future research using vascular correction (Wise et al., 2004; Kannurpatti and Biswal, 2008; Kannurpatti et al., 2012; Tsvetanov et al., 2015; Golestani et al., 2016a; Golestani et al., 2016b; Kazan et al., 2016; Wang et al., 2016; Jahanian et al., 2017; Liu et al., 2017; Pinto et al., 2020; Tsvetanov et al., 2021a; Stickland et al., 2021; Addeh et al., 2023). Other alternatives to the breath-hold and fixed concentration CO_2 hypercapnic stimuli that were utilised in the current study are targeted gas systems, where an end-tidal CO_2 value above baseline is targeted. This approach may provide further benefit to hypercapnic normalization as it reduces the variability associated with arterial CO_2 concentrations, which may then reduce inter-subject variation in CVR maps (Slessarev et al., 2007).

The group analyses in experiment 1 showed that vascular correction at the group level, performed by including the individual breath-hold contrast images as voxel-wise covariates, increased sensitivity to BOLD signal change as indicated by both the number of significant voxels and the peak *t*-values. The ROI approach to vascular correction had no effect on the activation maps from experiment 1, but in experiment 2 this approach resulted in minor improvements for the CVR corrected maps through increases in *t*-values. Linear regression analyses from experiment 2 revealed only five ROIs that predicted BOLD activation from CVR, which might explain why the whole-brain voxel-wise covariate approach that

benefitted experiment 1 did not benefit group analyses in experiment 2. This raises the question of whether vascular correction applied in a voxel-wise manner only benefits larger sample sizes, as experiment 1 had a much larger sample size than experiment 2. Sample size is one contributing factor, but others should also be considered when determining whether vascular correction is worthwhile. Groups with substantial inter-subject variability due to vascular physiology would benefit more from vascular correction than highly homogenous groups, even when sample sizes are small. In first-level modelling, precision in the estimate of the effect of interest is another pertinent factor, and this will depend on within-subject variability. This, in turn, is highly dependent on the task implemented and the number of runs, conditions, and if a cognitive task-the number of correct responses and subject variability due to attention and habituation (Chen et al., 2012). The hardware (e.g., scanner field strength and head coil) and software (e.g., use of simultaneous multi-slice, parallel imaging) might also vary the effect estimate when comparing across datasets and sites.

The small sample size for experiment 2 ($n = 15$) is a limitation of the present study, and the relatively smaller number of significant ROIs (5 out of 50 at $P < 0.05$, and 2 out of 50 after FDR-correction) compared to experiment 1 may have reflected this. Another limitation to the present study is that the voxel selection process for the linear regression analyses meant that only robustly activated brain regions were included. This could inflate R^2 values due to decreased inter-subject variability, a result of choosing only voxels above a set threshold. The alternative would be to include all voxels regardless of whether they were activated by a task; however, this alternative was considered less optimal as investigating whether task magnitudes could be predicted by CVR require a hemodynamic response.

In summary, the present study showed that CVR is mostly predictive of cognitive task-based fMRI activation across the cerebral cortex. The parietal regions were consistently related to CVR across all tasks and CVR approaches, suggesting that BOLD activations in these areas scale with baseline vascular physiology and might be prone to BOLD signal variability due to vascular changes. Most regions that were strongly activated by a task also showed a significant relationship with CVR; although, the left insula was one activated region that did not show this relationship. For the left insula, non-vascular factors such as neural variability might better explain inter-subject variability. The group analyses showed that including vascular covariates increased statistical significance of activation maps. Overall, these results provide support for the close relationship between CVR and BOLD response magnitude to complex fMRI paradigms. This suggests that vascular correction techniques such as hypercapnic normalization should be considered for all fMRI paradigms to disentangle vascular and non-vascular variability in BOLD signal magnitude.

Data availability statement

The raw data supporting the conclusion of this article will be made available by the authors, without undue reservation.

Ethics statement

The studies involving human participants were reviewed and approved by University of Calgary Conjoint Health Research Ethics Board. The patients/participants provided their written informed consent to participate in this study.

Author contributions

RW: research idea conception, study design, data collection and analysis, results interpretation and wrote the manuscript. JS: study design, data collection and analysis, results interpretation. EM: study design, results interpretation. RL: data collection and analysis. MM: data analysis, results interpretation. GP: research idea conception, study design, data collection and analysis, results interpretation. All authors reviewed and edited the manuscript.

Funding

EM is funded by the Natural Science and Engineering Research Council (NSERC) and the StFX University Council for Research. MM holds an NSERC Discovery Grant (RGPIN-2022-03552). GP would like to acknowledge financial support from the Canadian Institutes for Health Research (CIHR FDN-143290), the Natural Science and Engineering Research Council (NSERC RGPIN-2017-03880), and the Campus Alberta Innovation Program (CAIP).

Conflict of interest

RL was employed by GE Healthcare.

The remaining authors declare that the research was conducted in the absence of any commercial or financial relationships that could be construed as a potential conflict of interest.

Publisher's note

Supplementary material

The Supplementary Material for this article can be found online at: https://www.frontiersin.org/articles/10.3389/fphys.2023.1167148/full#supplementary-material

References

Abdelkarim, D., Zhao, Y., Turner, M. P., Sivakolundu, D. K., Lu, H., and Rypma, B. (2019). A neural-vascular complex of age-related changes in the human brain: Anatomy, physiology, and implications for neurocognitive aging. *Neurosci. Biobehav Rev.* 107, 927–944. doi:10.1016/j.neubiorev.2019.09.005

Addeh, A., Vega, F., Medi, P. R., Williams, R. J., Pike, G. B., and Macdonald, M. E. (2023). Direct machine learning reconstruction of respiratory variation waveforms from resting state fMRI data in a pediatric population. *Neuroimage* 269, 119904. doi:10.1016/j.neuroimage.2023.119904

Ashburner, J., and Friston, K. J. (2005). Unified segmentation. *NeuroImage* 26, 839–851. doi:10.1016/j.neuroimage.2005.02.018

Avants, B. B., Tustison, N. J., Song, G., Cook, P. A., Klein, A., and Gee, J. C. (2011). A reproducible evaluation of ANTs similarity metric performance in brain image registration. *Neuroimage* 54, 2033–2044. doi:10.1016/j.neuroimage.2010.09.025

Avants, B. B., Tustison, N. J., Stauffer, M., Song, G., Wu, B., and Gee, J. C. (2014). The Insight ToolKit image registration framework. *Front. Neuroinform* 8, 44. doi:10.3389/fninf.2014.00044

Bandettini, P. A., and Wong, E. C. (1997). A hypercapnia-based normalization method for improved spatial localization of human brain activation with fMRI. *NMR Biomed.* 10, 197–203. doi:10.1002/(sici)1099-1492(199706/08)10:4/5<197::aid-nbm466>3.0.co;2-s

Battisti-Charbonney, A., Fisher, J., and Duffin, J. (2011). The cerebrovascular response to carbon dioxide in humans. *J. Physiol.* 589, 3039–3048. doi:10.1113/jphysiol.2011.206052

Bhogal, A. A., De Vis, J. B., Siero, J. C. W., Petersen, E. T., Luijten, P. R., Hendrikse, J., et al. (2016). The BOLD cerebrovascular reactivity response to progressive hypercapnia in young and elderly. *Neuroimage* 139, 94–102. doi:10.1016/j.neuroimage.2016.06.010

Bhogal, A. A., Siero, J. C., Fisher, J. A., Froeling, M., Luijten, P., Philippens, M., et al. (2014). Investigating the non-linearity of the BOLD cerebrovascular reactivity response to targeted hypo/hypercapnia at 7T. *Neuroimage* 98, 296–305. doi:10.1016/j.neuroimage.2014.05.006

Bilder, R., Poldrack, R., Cannon, T., London, E., Freimer, N., Congdon, E., et al. (2020). UCLA Consortium for neuropsychatric Phenomics LA5c study. *OpenNeuro*. doi:10.18112/openneuro.ds000030.v1.0.0

Birn, R. M., Smith, M. A., Jones, T. B., and Bandettini, P. A. (2008). The respiration response function: The temporal dynamics of fMRI signal fluctuations related to changes in respiration. *Neuroimage* 40, 644–654. doi:10.1016/j.neuroimage.2007.11.059

Biswal, B. B., Kannurpatti, S. S., and Rypma, B. (2007). Hemodynamic scaling of fMRI-BOLD signal: Validation of low-frequency spectral amplitude as a scalability factor. *Magn. Reson Imaging* 25, 1358–1369. doi:10.1016/j.mri.2007.03.022

Blicher, J. U., Stagg, C. J., O'Shea, J., Østergaard, L., Macintosh, B. J., Johansen-Berg, H., et al. (2012). Visualization of altered neurovascular coupling in chronic stroke patients using multimodal functional MRI. *J. Cereb. Blood Flow. Metab.* 32, 2044–2054. doi:10.1038/jcbfm.2012.105

Blockley, N. P., Griffeth, V. E., Stone, A. J., Hare, H. V., and Bulte, D. P. (2015). Sources of systematic error in calibrated BOLD based mapping of baseline oxygen extraction fraction. *Neuroimage* 122, 105–113. doi:10.1016/j.neuroimage.2015.07.059

Bright, M. G., and Murphy, K. (2013). Reliable quantification of BOLD fMRI cerebrovascular reactivity despite poor breath-hold performance. *Neuroimage* 83, 559–568. doi:10.1016/j.neuroimage.2013.07.007

Casanova, R., Srikanth, R., Baer, A., Laurienti, P. J., Burdette, J. H., Hayasaka, S., et al. (2007). Biological parametric mapping: A statistical toolbox for multimodality brain image analysis. *Neuroimage* 34, 137–143. doi:10.1016/j.neuroimage.2006.09.011

Chen, G., Saad, Z. S., Nath, A. R., Beauchamp, M. S., and Cox, R. W. (2012). FMRI group analysis combining effect estimates and their variances. *Neuroimage* 60, 747–765. doi:10.1016/j.neuroimage.2011.12.060

Chen, J. J. (2018). Cerebrovascular-reactivity mapping using MRI: Considerations for alzheimer's disease. *Front. Aging Neurosci.* 10, 170. doi:10.3389/fnagi.2018.00170

Chen, J. J. (2019). Functional MRI of brain physiology in aging and neurodegenerative diseases. *Neuroimage* 187, 209–225. doi:10.1016/j.neuroimage.2018.05.050

Chen, J. J., and Pike, G. B. (2010). Global cerebral oxidative metabolism during hypercapnia and hypocapnia in humans: Implications for BOLD fMRI. *J. Cereb. blood flow metabolism* 30, 1094–1099. doi:10.1038/jcbfm.2010.42

Chen, J. J., Rosas, H. D., and Salat, D. H. (2011). Age-associated reductions in cerebral blood flow are independent from regional atrophy. *NeuroImage* 55, 468–478. doi:10.1016/j.neuroimage.2010.12.032

Chiarelli, P. A., Bulte, D. P., Gallichan, D., Piechnik, S. K., Wise, R., and Jezzard, P. (2007). Flow-metabolism coupling in human visual, motor, and supplementary motor areas assessed by magnetic resonance imaging. *Magn. Reson Med.* 57, 538–547. doi:10.1002/mrm.21171

Chu, P. P. W., Golestani, A. M., Kwinta, J. B., Khatamian, Y. B., and Chen, J. J. (2018). Characterizing the modulation of resting-state fMRI metrics by baseline physiology. *Neuroimage* 173, 72–87. doi:10.1016/j.neuroimage.2018.02.004

Cohen, E. R., Rostrup, E., Sidaros, K., Lund, T. E., Paulson, O. B., Ugurbil, K., et al. (2004). Hypercapnic normalization of BOLD fMRI: Comparison across field strengths and pulse sequences. *Neuroimage* 23, 613–624. doi:10.1016/j.neuroimage.2004.06.021

Dale, A. M., Fischl, B., and Sereno, M. I. (1999). Cortical surface-based analysis. I. Segmentation and surface reconstruction. *Neuroimage* 9, 179–194. doi:10.1006/nimg.1998.0395

Deckers, P. T., Bhogal, A. A., Dijsselhof, M. B., Faraco, C. C., Liu, P., Lu, H., et al. (2022). Hemodynamic and metabolic changes during hypercapnia with normoxia and hyperoxia using pCASL and TRUST MRI in healthy adults. *J. Cereb. Blood Flow. Metab.* 42, 861–875. doi:10.1177/0271678X211064572

Delfin, C., Reckless, G. E., Bolstad, I., Groote, I., Andreassen, O. A., and Jensen, J. (2020). Exploring the effects of an acute dose of antipsychotic medication on motivation-mediated BOLD activity using fMRI and a perceptual decision-making task. *Neuroscience* 440, 146–159. doi:10.1016/j.neuroscience.2020.05.035

Desikan, R. S., Ségonne, F., Fischl, B., Quinn, B. T., Dickerson, B. C., Blacker, D., et al. (2006). An automated labeling system for subdividing the human cerebral cortex on MRI scans into gyral based regions of interest. *Neuroimage* 31, 968–980. doi:10.1016/j.neuroimage.2006.01.021

Duffin, J., Mikulis, D. J., and Fisher, J. A. (2021). Control of cerebral blood flow by blood gases. *Front. Physiol.* 12, 640075. doi:10.3389/fphys.2021.640075

Elvsåshagen, T., Mutsaerts, H. J., Zak, N., Norbom, L. B., Quraishi, S. H., Pedersen, P., et al. (2019). Cerebral blood flow changes after a day of wake, sleep, and sleep deprivation. *Neuroimage* 186, 497–509. doi:10.1016/j.neuroimage.2018.11.032

Fan, J., Bernardi, S., Van Dam, N. T., Anagnostou, E., Gu, X., Martin, L., et al. (2012). Functional deficits of the attentional networks in autism. *Brain Behav.* 2, 647–660. doi:10.1002/brb3.90

Fan, J., Gu, X., Guise, K. G., Liu, X., Fossella, J., Wang, H., et al. (2009). Testing the behavioral interaction and integration of attentional networks. *Brain cognition* 70, 209–220. doi:10.1016/j.bandc.2009.02.002

Fan, J., Mccandliss, B. D., Fossella, J., Flombaum, J. I., and Posner, M. I. (2005). The activation of attentional networks. *NeuroImage* 26, 471–479. doi:10.1016/j.neuroimage.2005.02.004

Fischl, B., Sereno, M. I., and Dale, A. M. (1999). Cortical surface-based analysis. II: Inflation, flattening, and a surface-based coordinate system. *Neuroimage* 9, 195–207. doi:10.1006/nimg.1998.0396

Fischl, B., Van Der Kouwe, A., Destrieux, C., Halgren, E., Ségonne, F., Salat, D. H., et al. (2004). Automatically parcellating the human cerebral cortex. *Cereb. Cortex* 14, 11–22. doi:10.1093/cercor/bhg087

Fisher, J. A., and Mikulis, D. J. (2021). Cerebrovascular reactivity: Purpose, optimizing methods, and limitations to interpretation - a personal 20-year odyssey of (Re)searching. *Front. Physiol.* 12, 629651. doi:10.3389/fphys.2021.629651

Glahn, D. C., Therman, S., Manninen, M., Huttunen, M., Kaprio, J., Lönnqvist, J., et al. (2003). Spatial working memory as an endophenotype for schizophrenia. *Biol. Psychiatry* 53, 624–626. doi:10.1016/s0006-3223(02)01641-4

Golestani, A. M., Kwinta, J. B., Strother, S. C., Khatamian, Y. B., and Chen, J. J. (2016a). The association between cerebrovascular reactivity and resting-state fMRI functional connectivity in healthy adults: The influence of basal carbon dioxide. *Neuroimage* 132, 301–313. doi:10.1016/j.neuroimage.2016.02.051

Golestani, A. M., Wei, L. L., and Chen, J. J. (2016b). Quantitative mapping of cerebrovascular reactivity using resting-state BOLD fMRI: Validation in healthy adults. *Neuroimage* 138, 147–163. doi:10.1016/j.neuroimage.2016.05.025

Goozee, R., Reinders, A. A. T. S., Handley, R., Marques, T., Taylor, H., O'Daly, O., et al. (2016). Effects of aripiprazole and haloperidol on neural activation during the n-back in healthy individuals: A functional MRI study. *Schizophr. Res.* 173, 174–181. doi:10.1016/j.schres.2015.02.023

Griffeth, V. E., Perthen, J. E., and Buxton, R. B. (2011). Prospects for quantitative fMRI: Investigating the effects of caffeine on baseline oxygen metabolism and the response to a visual stimulus in humans. *Neuroimage* 57, 809–816. doi:10.1016/j.neuroimage.2011.04.064

Handwerker, D. A., Ollinger, J. M., and D'Esposito, M. (2004). Variation of BOLD hemodynamic responses across subjects and brain regions and their effects on statistical analyses. *NeuroImage* 21, 1639–1651. doi:10.1016/j.neuroimage.2003.11.029

Hauser, T. K., Seeger, A., Bender, B., Klose, U., Thurow, J., Ernemann, U., et al. (2019). Hypercapnic BOLD MRI compared to $H_2{}^{15}O$ PET/CT for the hemodynamic evaluation of patients with Moyamoya disease. *Neuroimage Clin.* 22, 101713. doi:10.1016/j.nicl.2019.101713

Hoge, R. D., Atkinson, J., Gill, B., Crelier, G. R., Marrett, S., and Pike, G. B. (1999). Investigation of BOLD signal dependence on cerebral blood flow and oxygen consumption: The deoxyhemoglobin dilution model. *Magnetic Reson. Med.* 42, 849–863. doi:10.1002/(sici)1522-2594(199911)42:5<849::aid-mrm4>3.0.co;2-z

Hosford, P. S., and Gourine, A. V. (2019). What is the key mediator of the neurovascular coupling response? *Neurosci. Biobehav Rev.* 96, 174–181. doi:10.1016/j.neubiorev.2018.11.011

Jahanian, H., Christen, T., Moseley, M. E., Pajewski, N. M., Wright, C. B., Tamura, M. K., et al. (2017). Measuring vascular reactivity with resting-state blood oxygenation level-dependent (BOLD) signal fluctuations: A potential alternative to the breath-holding challenge? *J. Cereb. Blood Flow. Metab.* 37, 2526–2538. doi:10.1177/0271678X16670921

Jenkins, D. G., and Quintana-Ascencio, P. F. (2020). A solution to minimum sample size for regressions. *PLoS One* 15, e0229345. doi:10.1371/journal.pone.0229345

Jenkinson, M. (2003). Fast, automated, N-dimensional phase-unwrapping algorithm. *Magn. Reson Med.* 49, 193–197. doi:10.1002/mrm.10354

Jezzard, P., and Balaban, R. S. (1995). Correction for geometric distortion in echo planar images from B0 field variations. *Magn. Reson Med.* 34, 65–73. doi:10.1002/mrm.1910340111

Juttukonda, M. R., Li, B., Almaktoum, R., Stephens, K. A., Yochim, K. M., Yacoub, E., et al. (2021). Characterizing cerebral hemodynamics across the adult lifespan with arterial spin labeling MRI data from the Human Connectome Project-Aging. *Neuroimage* 230, 117807. doi:10.1016/j.neuroimage.2021.117807

Kannurpatti, S. S., and Biswal, B. B. (2008). Detection and scaling of task-induced fMRI-BOLD response using resting state fluctuations. *Neuroimage* 40, 1567–1574. doi:10.1016/j.neuroimage.2007.09.040

Kannurpatti, S. S., Motes, M. A., Biswal, B. B., and Rypma, B. (2014). Assessment of unconstrained cerebrovascular reactivity marker for large age-range FMRI studies. *PLoS One* 9, e88751. doi:10.1371/journal.pone.0088751

Kannurpatti, S. S., Motes, M. A., Rypma, B., and Biswal, B. B. (2010). Neural and vascular variability and the fMRI-BOLD response in normal aging. *Magn. Reson Imaging* 28, 466–476. doi:10.1016/j.mri.2009.12.007

Kannurpatti, S. S., Rypma, B., and Biswal, B. B. (2012). Prediction of task-related BOLD fMRI with amplitude signatures of resting-state fMRI. *Front. Syst. Neurosci.* 6, 7. doi:10.3389/fnsys.2012.00007

Kazan, S. M., Mohammadi, S., Callaghan, M. F., Flandin, G., Huber, L., Leech, R., et al. (2016). Vascular autorescaling of fMRI (VasA fMRI) improves sensitivity of population studies: A pilot study. *Neuroimage* 124, 794–805. doi:10.1016/j.neuroimage.2015.09.033

Kim, S. G., and Ogawa, S. (2012). Biophysical and physiological origins of blood oxygenation level-dependent fMRI signals. *J. Cereb. blood flow metabolism* 32, 1188–1206. doi:10.1038/jcbfm.2012.23

Laurienti, P. J., Field, A. S., Burdette, J. H., Maldjian, J. A., Yen, Y. F., and Moody, D. M. (2003). Relationship between caffeine-induced changes in resting cerebral perfusion and blood oxygenation level-dependent signal. *AJNR Am. J. Neuroradiol.* 24, 1607–1611.

Liau, J., and Liu, T. T. (2009). Inter-subject variability in hypercapnic normalization of the BOLD fMRI response. *Neuroimage* 45, 420–430. doi:10.1016/j.neuroimage.2008.11.032

Liu, P., Hebrank, A. C., Rodrigue, K. M., Kennedy, K. M., Park, D. C., and Lu, H. (2013a). A comparison of physiologic modulators of fMRI signals. *Hum. Brain Mapp.* 34, 2078–2088. doi:10.1002/hbm.22053

Liu, P., Hebrank, A. C., Rodrigue, K. M., Kennedy, K. M., Section, J., Park, D. C., et al. (2013b). Age-related differences in memory-encoding fMRI responses after accounting for decline in vascular reactivity. *NeuroImage* 78, 415–425. doi:10.1016/j.neuroimage.2013.04.053

Liu, P., Jiang, D., Albert, M., Bauer, C. E., Caprihan, A., Gold, B. T., et al. (2021). Multi-vendor and multisite evaluation of cerebrovascular reactivity mapping using hypercapnia challenge. *Neuroimage* 245, 118754. doi:10.1016/j.neuroimage.2021.118754

Liu, P., Li, Y., Pinho, M., Park, D. C., Welch, B. G., and Lu, H. (2017). Cerebrovascular reactivity mapping without gas challenges. *Neuroimage* 146, 320–326. doi:10.1016/j.neuroimage.2016.11.054

Logan, G. D., Cowan, W. B., and Davis, K. A. (1984). On the ability to inhibit simple and choice reaction time responses: A model and a method. *J. Exp. Psychol. Hum. Percept. Perform.* 10, 276–291. doi:10.1037//0096-1523.10.2.276

Logothetis, N. K. (2008). What we can do and what we cannot do with fMRI. *Nature* 453, 869–878. doi:10.1038/nature06976

Macdonald, M. E., Berman, A. J. L., Mazerolle, E. L., Williams, R. J., and Pike, G. B. (2018). Modeling hyperoxia-induced BOLD signal dynamics to estimate cerebral blood flow, volume and mean transit time. *Neuroimage* 178, 461–474. doi:10.1016/j.neuroimage.2018.05.066

Macdonald, M. E., Dolati, P., Mitha, A. P., Wong, J. H., and Frayne, R. (2016). Flow and pressure measurements in aneurysms and arteriovenous malformations with phase contrast MR imaging. *Magn. Reson Imaging* 34, 1322–1328. doi:10.1016/j.mri.2016.07.007

Macdonald, M. E., Williams, R. J., Rajashekar, D., Stafford, R. B., Hanganu, A., Sun, H., et al. (2020). Age related differences in cerebral blood flow and cortical thickness with an application to age prediction. *Neurobiol. Aging* 95, 131–142. doi:10.1016/j.neurobiolaging.2020.06.019

Mackie, M. A., Van Dam, N. T., and Fan, J. (2013). Cognitive control and attentional functions. *Brain Cogn.* 82, 301–312. doi:10.1016/j.bandc.2013.05.004

Markett, S., Nothdurfter, D., Focsa, A., Reuter, M., and Jawinski, P. (2022). Attention networks and the intrinsic network structure of the human brain. *Hum. Brain Mapp.* 43, 1431–1448. doi:10.1002/hbm.25734

Mazerolle, E. L., Ma, Y., Sinclair, D., and Pike, G. B. (2018). Impact of abnormal cerebrovascular reactivity on BOLD fMRI: A preliminary investigation of moyamoya disease. *Clin. Physiol. Funct. Imaging* 38, 87–92. doi:10.1111/cpf.12387

Mcketton, L., Sobczyk, O., Duffin, J., Poublanc, J., Sam, K., Crawley, A., et al. (2018). The aging brain and cerebrovascular reactivity. *Neuroimage* 181, 132–141. doi:10.1016/j.neuroimage.2018.07.007

Miyake, A., Emerson, M. J., Padilla, F., and Ahn, J. C. (2004). Inner speech as a retrieval aid for task goals: The effects of cue type and articulatory suppression in the random task cuing paradigm. *Acta Psychol. (Amst)* 115, 123–142. doi:10.1016/j.actpsy.2003.12.004

Montojo, C. A., Ibrahim, A., Karlsgodt, K. H., Chow, C., Hilton, A. E., Jonas, R. K., et al. (2014). Disrupted working memory circuitry and psychotic symptoms in 22q11.2 deletion syndrome. *Neuroimage Clin.* 4, 392–402. doi:10.1016/j.nicl.2014.01.010

Mueller, S., Wang, D., Fox, M. D., Yeo, B. T., Sepulcre, J., Sabuncu, M. R., et al. (2013). Individual variability in functional connectivity architecture of the human brain. *Neuron* 77, 586–595. doi:10.1016/j.neuron.2012.12.028

Mulderink, T. A., Gitelman, D. R., Mesulam, M. M., and Parrish, T. B. (2002). On the use of caffeine as a contrast booster for BOLD fMRI studies. *Neuroimage* 15, 37–44. doi:10.1006/nimg.2001.0973

Peng, S. L., Chen, X., Li, Y., Rodrigue, K. M., Park, D. C., and Lu, H. (2018). Age-related changes in cerebrovascular reactivity and their relationship to cognition: A four-year longitudinal study. *Neuroimage* 174, 257–262. doi:10.1016/j.neuroimage.2018.03.033

Peng, S. L., Ravi, H., Sheng, M., Thomas, B. P., and Lu, H. (2017). Searching for a truly "iso-metabolic" gas challenge in physiological MRI. *J. Cereb. Blood Flow. Metab.* 37, 715–725. doi:10.1177/0271678X16638103

Petersen, S. E., and Posner, M. I. (2012). The attention system of the human brain: 20 years after. *Annu. Rev. Neurosci.* 35, 73–89. doi:10.1146/annurev-neuro-062111-150525

Pike, G. B. (2012). Quantitative functional MRI: Concepts, issues and future challenges. *NeuroImage* 62, 1234–1240. doi:10.1016/j.neuroimage.2011.10.046

Pillai, J. J., and Mikulis, D. J. (2015). Cerebrovascular reactivity mapping: An evolving standard for clinical functional imaging. *AJNR Am. J. Neuroradiol.* 36, 7–13. doi:10.3174/ajnr.A3941

Pinto, J., Bright, M. G., Bulte, D. P., and Figueiredo, P. (2020). Cerebrovascular reactivity mapping without gas challenges: A methodological guide. *Front. Physiol.* 11, 608475. doi:10.3389/fphys.2020.608475

Poldrack, R. A., Congdon, E., Triplett, W., Gorgolewski, K. J., Karlsgodt, K. H., Mumford, J. A., et al. (2016). A phenome-wide examination of neural and cognitive function. *Sci. Data* 3, 160110. doi:10.1038/sdata.2016.110

Ryan, C. M., Battisti-Charbonney, A., Sobczyk, O., Mikulis, D. J., Duffin, J., Fisher, J. A., et al. (2018). Evaluation of cerebrovascular reactivity in subjects with and without obstructive sleep apnea. *J. Stroke Cerebrovasc. Dis.* 27, 162–168. doi:10.1016/j.jstrokecerebrovasdis.2017.08.015

Slessarev, M., Han, J., Mardimae, A., Prisman, E., Preiss, D., Volgyesi, G., et al. (2007). Prospective targeting and control of end-tidal CO2 and O2 concentrations. *J. Physiol.* 581, 1207–1219. doi:10.1113/jphysiol.2007.129395

Specht, J. L., Williams, R. J., Mazerolle, E. L., and Pike, G. B. (2019). "Hypercapnic normalization to correct for caffeine-induced changes in task-based BOLD fMRI responses," in 27th International Society for Magnetic Resonance in Medicine Annual Meeting, Montreal, Canada, 11-16 May 2019.

Stefanovic, B., Warnking, J. M., Rylander, K. M., and Pike, G. B. (2006). The effect of global cerebral vasodilation on focal activation hemodynamics. *NeuroImage* 30, 726–734. doi:10.1016/j.neuroimage.2005.10.038

Stickland, R. C., Zvolanek, K. M., Moia, S., Ayyagari, A., Caballero-Gaudes, C., and Bright, M. G. (2021). A practical modification to a resting state fMRI protocol for improved characterization of cerebrovascular function. *Neuroimage* 239, 118306. doi:10.1016/j.neuroimage.2021.118306

Sydnor, V. J., Larsen, B., Bassett, D. S., Alexander-Bloch, A., Fair, D. A., Liston, C., et al. (2021). Neurodevelopment of the association cortices: Patterns, mechanisms, and implications for psychopathology. *Neuron* 109, 2820–2846. doi:10.1016/j.neuron.2021.06.016

Tancredi, F. B., and Hoge, R. D. (2013). Comparison of cerebral vascular reactivity measures obtained using breath-holding and CO2 inhalation. *J. Cereb. Blood Flow. Metab.* 33, 1066–1074. doi:10.1038/jcbfm.2013.48

Tancredi, F. B., Lajoie, I., and Hoge, R. D. (2014). A simple breathing circuit allowing precise control of inspiratory gases for experimental respiratory manipulations. *BMC Res. Notes* 7, 235. doi:10.1186/1756-0500-7-235

Thomason, M. E., Foland, L. C., and Glover, G. H. (2007). Calibration of BOLD fMRI using breath holding reduces group variance during a cognitive task. *Hum. Brain Mapp.* 28, 59–68. doi:10.1002/hbm.20241

Todd, J. J., and Marois, R. (2004). Capacity limit of visual short-term memory in human posterior parietal cortex. *Nature* 428, 751–754. doi:10.1038/nature02466

Tsvetanov, K. A., Henson, R. N. A., Jones, P. S., Mutsaerts, H., Fuhrmann, D., Tyler, L. K., et al. (2021a). The effects of age on resting-state BOLD signal variability is explained by cardiovascular and cerebrovascular factors. *Psychophysiology* 58, e13714. doi:10.1111/psyp.13714

Tsvetanov, K. A., Henson, R. N. A., and Rowe, J. B. (2021b). Separating vascular and neuronal effects of age on fMRI BOLD signals. *Philos. Trans. R. Soc. Lond B Biol. Sci.* 376, 20190631. doi:10.1098/rstb.2019.0631

Tsvetanov, K. A., Henson, R. N., Tyler, L. K., Davis, S. W., Shafto, M. A., Taylor, J. R., et al. (2015). The effect of ageing on fMRI: Correction for the confounding effects of vascular reactivity evaluated by joint fMRI and MEG in 335 adults. *Hum. Brain Mapp.* 36, 2248–2269. doi:10.1002/hbm.22768

Van Niftrik, C. H. B., Piccirelli, M., Bozinov, O., Maldaner, N., Strittmatter, C., Pangalu, A., et al. (2018). Impact of baseline CO_2 on Blood-Oxygenation-Level-Dependent MRI measurements of cerebrovascular reactivity and task-evoked signal activation. *Magn. Reson Imaging* 49, 123–130. doi:10.1016/j.mri.2018.02.002

Wang, P., Hou, P., Kesler, S., Colen, R., Kumar, A., Prabhu, S., et al. (2016). SU-G-IeP1-11: Resting-State fluctuation of BOLD signal amplitude for mapping cerebrovascular reactivity in presurgical functional MRI. *Med. Phys.* 43, 3646–3647. doi:10.1118/1.4956971

West, K. L., Zuppichini, M. D., Turner, M. P., Sivakolundu, D. K., Zhao, Y., Abdelkarim, D., et al. (2019). BOLD hemodynamic response function changes significantly with healthy aging. *Neuroimage* 188, 198–207. doi:10.1016/j.neuroimage.2018.12.012

Williams, R. J., Brown, E. C., Clark, D. L., Pike, G. B., and Ramasubbu, R. (2021b). Early post-treatment blood oxygenation level-dependent responses to emotion processing associated with clinical response to pharmacological treatment in major depressive disorder. *Brain Behav.* 11, e2287. doi:10.1002/brb3.2287

Williams, R. J., Goodyear, B. G., Peca, S., Mccreary, C. R., Frayne, R., Smith, E. E., et al. (2017). Identification of neurovascular changes associated with cerebral amyloid angiopathy from subject-specific hemodynamic response functions. *J. Cereb. Blood Flow. Metab.* 37, 3433–3445. doi:10.1177/0271678X17691056

Williams, R. J., Mcmahon, K. L., Hocking, J., and Reutens, D. C. (2014). Comparison of block and event-related experimental designs in diffusion-weighted functional MRI. *J. magnetic Reson. imaging JMRI* 40, 367–375. doi:10.1002/jmri.24353

Williams, R. J., Reutens, D. C., and Hocking, J. (2016). Influence of BOLD contributions to diffusion fMRI activation of the visual cortex. *Front. Neurosci.* 10, 279. doi:10.3389/fnins.2016.00279

Williams, R., Macdonald, M., Mazerolle, E., and Pike, G. (2021a). The relationship between cognition and cerebrovascular reactivity: Implications for task-based fMRI. *Front. Phys.* 9. doi:10.3389/fphy.2021.645249

Wise, R. G., Ide, K., Poulin, M. J., and Tracey, I. (2004). Resting fluctuations in arterial carbon dioxide induce significant low frequency variations in BOLD signal. *Neuroimage* 21, 1652–1664. doi:10.1016/j.neuroimage.2003.11.025

Xuan, B., Mackie, M. A., Spagna, A., Wu, T., Tian, Y., Hof, P. R., et al. (2016). The activation of interactive attentional networks. *NeuroImage* 129, 308–319. doi:10.1016/j.neuroimage.2016.01.017

Yang, X., Beason-Held, L., Resnick, S. M., and Landman, B. A. (2011). Biological parametric mapping with robust and non-parametric statistics. *Neuroimage* 57, 423–430. doi:10.1016/j.neuroimage.2011.04.046

frontiers | Frontiers in Physiology

TYPE Original Research
PUBLISHED 23 May 2023
DOI 10.3389/fphys.2023.1198615

OPEN ACCESS

EDITED BY
James Duffin,
University of Toronto, Canada

REVIEWED BY
Ali Golestani,
University of Calgary, Canada
Ethan MacDonald,
University of Calgary, Canada

*CORRESPONDENCE
Jill N. Barnes,
jnbarnes@wisc.edu

RECEIVED 01 April 2023
ACCEPTED 09 May 2023
PUBLISHED 23 May 2023

CITATION
Fico BG, Miller KB, Rivera-Rivera LA, Corkery AT, Pearson AG, Loggie NA, Howery AJ, Rowley HA, Johnson KM, Johnson SC, Wieben O and Barnes JN (2023), Cerebral hemodynamics comparison using transcranial doppler ultrasound and 4D flow MRI. *Front. Physiol.* 14:1198615. doi: 10.3389/fphys.2023.1198615

Cerebral hemodynamics comparison using transcranial doppler ultrasound and 4D flow MRI

Brandon G. Fico[1], Kathleen B. Miller[1], Leonardo A. Rivera-Rivera[2,3], Adam T. Corkery[1], Andrew G. Pearson[1], Nicole A. Loggie[1], Anna J. Howery[1], Howard A. Rowley[2,4], Kevin M. Johnson[2,3], Sterling C. Johnson[2,5], Oliver Wieben[3] and Jill N. Barnes[1]*

[1]Department of Kinesiology, Bruno Balke Biodynamics Laboratory, University of Wisconsin-Madison, Madison, WI, United States, [2]Wisconsin Alzheimer's Disease Research Center, School of Medicine and Public Health, University of Wisconsin-Madison, Madison, WI, United States, [3]Department of Medical Physics, School of Medicine and Public Health, University of Wisconsin-Madison, Madison, WI, United States, [4]Department of Radiology, School of Medicine and Public Health, University of Wisconsin-Madison, Madison, WI, United States, [5]Geriatric Research Education and Clinical Center, William S. Middleton Memorial Veteran's Hospital, Madison, WI, United States

Introduction: Age-related changes in cerebral hemodynamics are controversial and discrepancies may be due to experimental techniques. As such, the purpose of this study was to compare cerebral hemodynamics measurements of the middle cerebral artery (MCA) between transcranial Doppler ultrasound (TCD) and four-dimensional flow MRI (4D flow MRI).

Methods: Twenty young (25 ± 3 years) and 19 older (62 ± 6 years) participants underwent two randomized study visits to evaluate hemodynamics at baseline (normocapnia) and in response to stepped hypercapnia (4% CO_2, and 6% CO_2) using TCD and 4D flow MRI. Cerebral hemodynamic measures included MCA velocity, MCA flow, cerebral pulsatility index (PI) and cerebrovascular reactivity to hypercapnia. MCA flow was only assessed using 4D flow MRI.

Results: MCA velocity between the TCD and 4D flow MRI methods was positively correlated across the normocapnia and hypercapnia conditions (r = 0.262; p = 0.004). Additionally, cerebral PI was significantly correlated between TCD and 4D flow MRI across the conditions (r = 0.236; p = 0.010). However, there was no significant association between MCA velocity using TCD and MCA flow using 4D flow MRI across the conditions (r = 0.079; p = 0.397). When age-associated differences in cerebrovascular reactivity using conductance were compared using both methodologies, cerebrovascular reactivity was greater in young adults compared to older adults when using 4D flow MRI (2.11 ± 1.68 mL/min/mmHg/mmHg vs. 0.78 ± 1.68 mL/min/mmHg/mmHg; p = 0.019), but not with TCD (0.88 ± 1.01 cm/s/mmHg/mmHg vs. 0.68 ± 0.94 cm/s/mmHg/mmHg; p = 0.513).

Conclusion: Our results demonstrated good agreement between the methods at measuring MCA velocity during normocapnia and in response to hypercapnia, but MCA velocity and MCA flow were not related. In addition, measurements using 4D flow MRI revealed effects of aging on cerebral hemodynamics that were not apparent using TCD.

KEYWORDS

aging, cerebral pulsatility, cerebrovascular reactivity, middle cerebral artery, transcranial doppler ultrasound, 4D flow magnetic resonance imaging

Introduction

Cerebral hemodynamics are important biomarkers of brain health (Kleiser and Widder, 1992) and have been shown to be impaired with advancing age. These hemodynamic impairments include a reduction in cerebral blood flow (CBF), even in individuals free of cardiovascular disease (Wu et al., 2016; Alwatban et al., 2021). Another measure of cerebral hemodynamics, cerebral pulsatility, is elevated with advancing age (Alwatban et al., 2021; Fico et al., 2022). When the cerebral vasculature is challenged using elevations in CO_2 (i.e., hypercapnia), cerebrovascular reactivity is lower in healthy older adults compared to young adults (Barnes et al., 2012; Leoni et al., 2017; Yew et al., 2022). Importantly, these cerebral hemodynamic alterations with age (including lower CBF and elevated cerebral pulsatility) and impaired cerebrovascular reactivity to hypercapnia are associated with Alzheimer's disease and vascular-related dementias (Richiardi et al., 2015; Rivera-Rivera et al., 2016; Leeuwis et al., 2017; Wolters et al., 2017).

A commonly used method to assess cerebral hemodynamics is transcranial Doppler ultrasound (TCD), which transmits ultrasound waves from the Doppler probe and detects reflected waves from red blood cells passing through the vessel of interest. TCD ultrasound provides rapid, noninvasive measures of cerebral artery blood velocity with excellent temporal resolution and can be utilized by researchers in a variety of settings (Purkayastha and Sorond, 2013). TCD has been used to demonstrate age-related reductions in middle cerebral artery blood velocity and elevations in pulsatility index with advancing age (Alwatban et al., 2021).

Studies using TCD have demonstrated age-related differences in cerebrovascular reactivity based on cerebral artery blood velocity (Bakker et al., 2004; Barnes et al., 2012; Flück et al., 2014). These findings are contrary to studies that show no difference with age (Murrell et al., 2013; Miller et al., 2018), higher values in older adults (Galvin et al., 2010), or sex specific differences (Kastrup et al., 1998). Moreover, when participants are evaluated with multiple methods, such as TCD and magnetic resonance imaging (MRI), these age-related comparisons are inconsistent (Burley et al., 2021a). The discrepancy between reports in age differences in cerebral hemodynamics and cerebrovascular reactivity may be dependent on the sensitivity of the techniques used. A well-known limitation of TCD is the ability to measure blood velocity only, and not blood flow volume rate, because imaging of the arterial diameter or cross-sectional area is not possible. Additionally, the TCD measurement of blood velocity is sensitive to the angle of insonation with error increasing at greater angles (Purkayastha and Sorond, 2013). Thus, if TCD is used to obtain blood velocity, as a surrogate for blood flow, this may result in inconsistent results (Hoiland and Ainslie, 2016b; Brothers and Zhang, 2016).

There are several MRI or neuroimaging methods used to quantify cerebral hemodynamics and cerebrovascular reactivity (Williams et al., 2021). Specifically, blood oxygen level dependent (BOLD) MRI measures the relative levels of oxyhemoglobin and deoxyhemoglobin, which is an indirect measure of CBF and represents activity at the capillary level (Ogawa et al., 1990). Other MRI techniques such as arterial spin labelling (ASL) measures microvascular perfusion (Alsop et al., 2015) and phase contrast angiography (PCA) measures blood flow through the large cerebral vessels such as the middle cerebral artery (MCA). More recently, four-dimensional flow MRI (4D flow MRI or 3D time-resolved PCA) has been used to measure blood velocity in all three spatial dimensions throughout the duration of the cardiac cycle allowing for a direct calculation of blood flow (Markl et al., 2012; Schrauben et al., 2015). However, 4D flow MRI is sensitive to partial volume effects especially when a region of interest is oversized (Tang et al., 1993). Interestingly, MRI based analyses of age-related differences in cerebral hemodynamics and cerebrovascular reactivity also have inconsistent findings (Burley et al., 2021a; Burley et al., 2021b). For example, Burley et al. (2021a) showed that older adults had higher cerebrovascular reactivity to hypercapnia using TCD, but lower cerebrovascular reactivity using BOLD, compared with young adults, further emphasizing the importance of the measurement used to quantify CBF. The discrepancy in findings is likely due to fundamental differences in the MRI methodology and what is quantified. As such, the agreement between the various measurement techniques for cerebral hemodynamics and cerebrovascular reactivity is necessary to be able to compare studies. The commonly used TCD technique may provide various age-related results based on the hypercapnia protocol used (Al-Khazraji et al., 2021) due to its inherent limitation of only capturing blood velocity. Therefore, a more direct method (4D flow MRI) of assessing cerebral blood flow in response hypercapnia may provide further insight into age-related differences.

To our knowledge, no study has directly compared 4D flow MRI with TCD technique to investigate cerebral hemodynamics and cerebrovascular reactivity to hypercapnia in young and older healthy adults. Therefore, the purpose of this study was to compare cerebral hemodynamics of the MCA between TCD and 4D flow MRI in young and older adults at rest and in response to hypercapnia. We hypothesized that the MCA velocity measured using TCD and 4D flow MRI would be correlated and demonstrate good agreement between the two methods. In contrast, we hypothesized that there would be disagreement between the methods when we compared MCA blood velocity using TCD with MCA blood flow volume rate using 4D flow MRI. We also hypothesized that age-associated differences in cerebral hemodynamics and cerebrovascular reactivity would be detected using 4D flow MRI, but not TCD.

Materials and methods

Participants

Twenty young (between 18 and 35 years) and nineteen older (between 50 and 68 years) physically active healthy adults participated in the study. Participants were excluded from the

study if they had a body mass index (BMI) > 30 kg/m^2, and if they 1) were current smokers; 2) were diagnosed with hypertension based on the latest guidelines (Whelton et al., 2018) or taking blood pressure medications; 3) presented with a history or evidence of hepatic or renal disease, hematological disease, peripheral vascular disease, stroke, neurovascular disease, cardiovascular disease, diabetes; or 4) had contraindications for a MRI scan (as determined by a health history questionnaire and MRI screening form). All scans were reviewed by a neuroradiologist (HAR) for incidental findings. Of note, data from the participants in this study were also included in our previous publication (Miller et al., 2019). All study procedures were approved by the Institutional Review Board of the University of Wisconsin–Madison and were performed according to the Declaration of Helsinki, including obtaining written informed consent from each participant. This study was registered under ClinicalTrials.gov #NCT02840851.

Experimental procedures

All procedures were completed at the Bruno Balke Biodynamics Laboratory and the Wisconsin Institutes for Medical Research at the University of Wisconsin–Madison. The study consisted of a screen day visit and two experimental study days. The two experimental study days, with an average of 8 days apart, were randomized and utilized identical protocols for cerebral hemodynamics testing. For each participant, the randomized study days were scheduled for the same time of day to limit the effects of diurnal variation. Premenopausal women were studied in the early follicular phase of their menstrual cycle (or the low-hormone phase of oral contraceptive use) to minimize the influence of ovarian hormone status. Due to the potential influence of diet and exercise on cerebrovascular function, participants were asked to record 3 days of normal dietary intake and exercise prior to their first study day and asked to repeat these prior to their second study day. Prior to the study days, participants were asked to fast for 4 h, to abstain from non-steroidal anti-inflammatory drugs (NSAIDs) for 5 days, avoid nicotine for 2 h, and to abstain from caffeine, exercise, and alcohol for 24 h prior to the visits. Additionally, participants did not take any over the counter medications, vitamins or supplements on the days of the study visits. All tests were conducted in controlled ambient temperature between 20°C and 22°C.

Screen day visit

Upon arrival to the Bruno Balke Biodynamics Laboratory, height and weight were measured using a standard scale (Seca no. 769, Vogel & Halke, Hamburg, Germany). BMI was calculated as kg/m^2. Physical activity was determined using a weekly exercise log and physical activity questionnaire (Amireault and Godin, 2015). After 10 min of supine rest, mean arterial pressure (MAP) was taken in triplicate with a non-invasive brachial blood pressure cuff (Datex Ohmeda, GE Healthcare, Fairfield, CT, United States). Participants then had a familiarization session that included TCD set-up with probe location being noted.

Experimental study day: TCD

We utilized a 2 MHz TCD probe (Spencer Technologies, Redmond, WA, United States) to measure left MCAv (Bishop et al., 1986; Poulin and Robbins, 1996). The 2 MHz probe was placed over the temporal bone above the zygomatic arch between the frontal process and front of the ear with the participants lying supine. The probe was secured using a headband to ensure optimal insonation position and angle throughout the study hypercapnia protocol (Barnes et al., 2012).

Experimental study day: MRI

Cranial MRI scans were performed at the Wisconsin Institutes for Medical Research using a 3T clinical MRI system (MR750, GE Healthcare, Waukesha, WI, United States) and a 32-channel head coil (Nova Medical Head Coil, Nova Medical, Wilmington, MA, United States) with a gradient strength of 50 mT/m, and a gradient slew rate of 200 mT/m/ms. Left and right middle cerebral artery hemodynamics were assessed using 4D flow Phase Contrast MRI using a 3D radially undersampled sequence that included volumetric, time-resolved PC MRI data with three-directional velocity encoding (PC-VIPR) (Gu et al., 2005; Johnson et al., 2008). Comparisons between TCD and 4D flow MRI utilized the left MCA since TCD measured left MCAv, unless otherwise noted. The imaging parameters were as follows: velocity encoding (Venc) = 80 cm/s, field of view = 220 mm, acquired isotropic spatial resolution = 0.7 mm × 0.7 mm × 0.7 mm, repetition time (TR) = 7.4 ms, echo time (TE) = 2.7 ms, flip angle = 10°, bandwidth = 83.3 kHz, 14,000 projection angles and scan time ~7 min. Time-resolved velocity and magnitude data were reconstructed offline by retrospectively gating into 20 cardiac phases using temporal interpolation (Jing et al., 2006; Miller et al., 2019).

Cerebrovascular reactivity to hypercapnia

Hypercapnia trials were performed as previously described in detail using a steady-state, open-circuit technique (Berkenbosch et al., 1989; Miller et al., 2019). Briefly, for both experimental study day visits (study day TCD and study day MRI) participants were in the supine position and fitted with a mask covering their nose and mouth containing a one-way valve to prevent re-breathing (Hans Rudolph Inc., Shawnee, KS, United States). After baseline (using medical grade normocapnic gas), stepwise elevations of 4% and 6% inspired CO_2, 21% oxygen, and balanced nitrogen were administered. Between stepwise elevations in CO_2, 2 min were allowed to reach steady state $ETCO_2$ prior to collecting cerebral hemodynamics. $ETCO_2$ was elevated and maintained constant for approximately 9 min at each level of inspired CO_2.

Data analysis

Data from the TCD were collected at 250 Hz and analyzed off-line using signal processing software (WinDaq, DATAQ Instruments, Akron, OH, United States). Cerebral hemodynamics included MCAv and pulsatility index. When using TCD, pulsatility index was calculated as (maximum velocity–minimum velocity)/mean velocity. Beat-by-beat hemodynamic measurements were averaged over 1 min of steady state during normocapnic gas, 4% inspired CO_2, and 6% inspired CO_2. To account for changes in perfusion pressure that may affect MCAv, cerebrovascular reactivity was calculated as the linear relationship between cerebrovascular conductance index (CVCi) calculated as MCAv/MAP and changes in $ETCO_2$ during hypercapnia (cm/s/mmHg/mmHg).

The 4D flow MRI scans were also evaluated offline. The scans underwent background phase offset correction, eddy current correction (Schrauben et al., 2015) and automatic phase unwrapping to minimize potential for velocity aliasing (Loecher et al., 2016). Vessel segmentation of the left and right MCA was performed in MATLAB using an in-house tool as previously described for semi-automated cerebrovascular hemodynamic analysis (Schrauben et al., 2015). The MCA was measured at the M1 segment. Measurements included MCAv, blood flow volume rate, and vessel cross sectional area. Hemodynamic measurements were averaged during steady state at normocapnic gas, 4% inspired CO_2, and 6% inspired CO_2. When using 4D flow MRI, pulsatility index was calculated as (maximum flow–minimum flow)/mean flow. To account for changes in perfusion pressure that may affect flow, cerebrovascular reactivity was calculated as the linear relationship between cerebrovascular conductance (CVC) calculated as [(blood flow/MAP) x 100] and changes in $ETCO_2$ during hypercapnia (mL/min/mmHg/mmHg).

Statistical analyses

Data analyses were performed using the Statistical Package for the Social Sciences version 28 (SPSS, IBM Corp., Armonk, NY, United States). Statistical differences in participant characteristics were evaluated by the Student's *t*-tests for unpaired data. Cerebrovascular measurements between young and older adults across conditions were evaluated using two-way (group x condition) analysis of variance. The Greenhouse-Geisser correction of degrees of freedom was used when sphericity assumptions were violated. Significant effects were further analyzed with Bonferroni *post hoc* comparisons. Cerebrovascular reactivity statistical differences between TCD vs. 4D flow MRI were evaluated by the Student's *t*-tests for paired data and age-related comparisons were evaluated by the Student's *t*-tests for unpaired data. Associations of interest were analyzed by Pearson correlational analyses and intraclass correlation coefficients were used to determine reproducibility. The intraclass correlation coefficients differs from the Pearson correlations by taking into account differences in the means of the measures being considered (the data are centered and scaled using a pooled mean and standard deviation). The differences between TCD and 4D flow MRI may be minimal at baseline, but the differences may expand at higher levels of CO_2, due to vessel responses. Using intraclass correlation coefficients we evaluated whether the changes in response to a vasodilatory stimulus agreed between the two methods, at each condition. The statistical procedure proposed by Bland and Altman was used to compare the 2 different methods of TCD vs. 4D flow MRI (Bland and Altman, 1986). Statistical significance was set α priori at $p < 0.05$.

Results

Participant characteristics

Participant characteristics are presented in Table 1. There were no group differences between the young and older adults for height, weight, BMI, resting heart rate, metabolic equivalent minutes per week, systolic blood pressure, and MAP. However, the older adults had elevated diastolic blood pressure compared with the young adults.

MCAv comparisons using TCD vs. 4D flow MRI

We first compared MCAv obtained using TCD with MCAv obtained using 4D flow MRI in the left MCA. There was a significant difference in MCAv between the two imaging methods, with higher MCAv being observed with TCD compared with 4D flow MRI across all conditions (all $p < 0.001$; Table 2). Additionally, the percent change in MCAv from normocapnia to 6% CO_2 was significantly different between TCD and 4D flow MRI ($p < 0.001$; Table 2). Despite these differences, there was a significant intra class correlation coefficient ($r = 0.329$, $p = 0.016$) between the two methods for MCAv, highlighting repeatability. Moreover, although biased, this agreement between MCAv measurements was consistent with the results of the Bland–Altman plot (Figure 1B), and MCAv between the methods was significantly correlated ($r = 0.262$; $p = 0.004$) (Figure 1A).

MCAv and MCA flow comparisons using TCD vs. 4D flow MRI

We compared MCAv obtained using TCD with MCA flow obtained using 4D flow MRI. The percent change in MCAv from normocapnia to 6% CO_2 using TCD vs. the percent change in MCA flow using 4D flow MRI was similar ($p = 0.327$; Table 2). There was no correlation between the left MCAv using TCD and left MCA flow using 4D flow MRI ($r = 0.079$; $p = 0.397$; Figure 1C); however, the Bland-Altman plot suggested moderate agreement (Figure 1D).

Pulsatility index comparisons using TCD vs. 4D flow MRI

When directly comparing pulsatility index using TCD (calculated from velocity) vs. pulsatility index using 4D flow MRI (calculated from flow), there were significant differences between the methods at normocapnia ($p < 0.001$), and during hypercapnia at 4% CO_2 ($p < 0.001$) and 6% CO_2 ($p < 0.001$; Table 2). However, the percent change

TABLE 1 Characteristics of participants.

Variable	Young adults N = 20	Older adults N = 19	*p*-value
Males/Females (n)	10/10	10/9	
Age (years)	25 ± 3	62 ± 6	< **0.001**
Height (cm)	173 ± 8	172 ± 9	0.678
Weight (kg)	71 ± 10	70 ± 15	0.841
Body Mass Index (kg/m^2)	23 ± 2	23 ± 3	0.900
Heart rate at rest (beats per minute)	53 ± 8	55 ± 7	0.488
MET minutes per week	3,259 ± 1839	3,973 ± 2,383	0.300
Systolic blood pressure (mmHg)	120 ± 11	122 ± 11	0.707
Diastolic blood pressure (mmHg)	69 ± 6	74 ± 8	**0.026**
Mean arterial pressure (mmHg)	86 ± 7	90 ± 9	0.120

Data are presented as mean ± standard deviation. MET, metabolic equivalent.
Statistical significance was set α priori at p < 0.05 with significant p-values indicated in bold.

TABLE 2 Cerebral hemodynamics during normocapnia and hypercapnia.

Variable	TCD N = 39	4D flow MRI N = 39	*p*-value
MCAv (cm/s)			
Normocapnia	53 ± 12	31 ± 7	< **0.001**
4% CO_2	60 ± 14	32 ± 6	< **0.001**
6% CO_2	64 ± 15	33 ± 7	< **0.001**
MCAv (%Δ)			
Normocapnia to 6% CO_2	16 ± 10	6 ± 10	< **0.001**
MCAv (%Δ) vs. MCA Flow (%Δ)			
Normocapnia to 6% CO_2	16 ± 10	13 ± 10	0.327
Pulsatility Index (a.u.)			
Normocapnia	0.78 ± 0.13	1.07 ± 0.21	< **0.001**
4% CO_2	0.73 ± 0.09	1.03 ± 0.17	< **0.001**
6% CO_2	0.71 ± 0.09	1.00 ± 0.17	< **0.001**
Pulsatility Index (%Δ)			
Normocapnia to 6% CO_2	−9 ± 9	−5 ± 12	0.141

Data are presented as mean ± standard deviation. MCA, middle cerebral artery; MCAv, middle cerebral artery velocity.
Statistical significance was set α priori at p < 0.05 with significant p-values indicated in bold.

in pulsatility index from normocapnia to 6% CO_2 was similar between TCD and 4D flow MRI ($p = 0.141$; Table 2). Additionally, there was a significant intra class correlation coefficient ($r = 0.345$, $p = 0.012$) between the two methods for pulsatility index measurements, highlighting repeatability. Moreover, there was a significant positive correlation between the pulsatility index measurements using TCD vs. 4D flow MRI ($r = 0.236$; $p = 0.010$; Figure 1E), but with weak agreement based on the results of the Bland–Altman plot (Figure 1F).

Cerebrovascular reactivity comparisons using TCD vs. 4D flow MRI

Cerebrovascular reactivity values between the two methods were not correlated ($r = 0.104$; $p = 0.528$). Using TCD, there were no age-related differences in cerebrovascular reactivity between young and older adults (0.88 ± 1.01 cm/s/mmHg^2 vs. 0.68 ± 0.94 cm/s/mmHg^2, respectively; $p = 0.513$; Figure 2A). In contrast, using 4D flow MRI, cerebrovascular reactivity was higher in young adults compared with

10.3389/fphys.2023.1198615

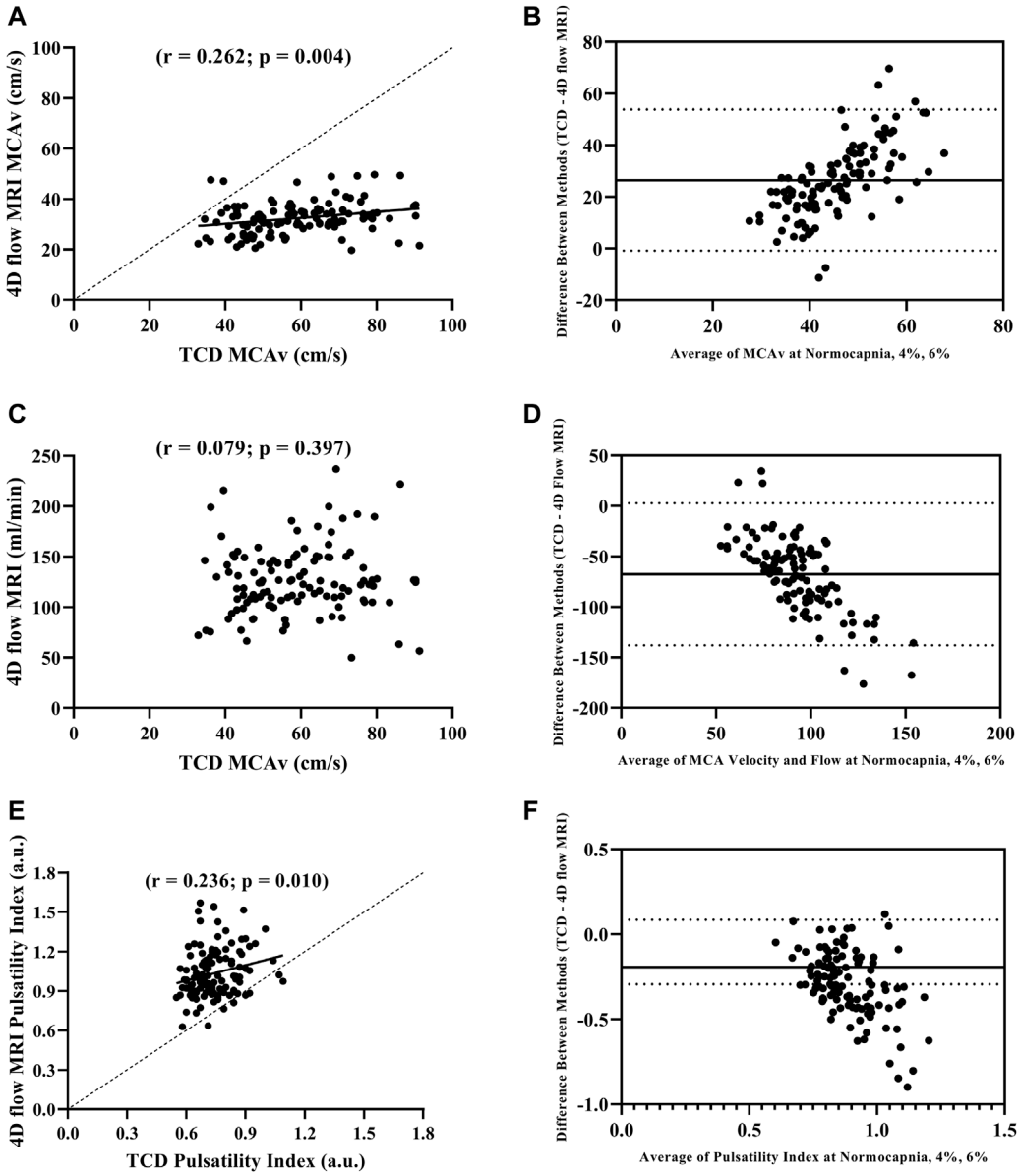

FIGURE 1
Pearson correlation between MCAv with TCD and 4D flow MRI **(A)**, Bland-Altman plot evaluating agreement between MCAv with TCD and 4D flow MRI **(B)**, Pearson correlation between MCAv with TCD and blood flow volume rate with 4D flow MRI **(C)**, Bland-Altman plot evaluating agreement between MCAv with TCD and blood flow volume rate with 4D flow MRI **(D)**, Pearson correlation between pulsatility index with TCD and 4D flow MRI **(E)**, and Bland-Altman plot evaluating agreement pulsatility index with TCD and 4D flow MRI **(F)** during normocapnia, 4% CO_2, and 6% CO_2 including all participants (N = 39).

older adults (2.11 ± 1.68 mL/min/mmHg/mmHg vs. 0.78 ± 1.68 mL/min/mmHg/mmHg, respectively; p = 0.019; Figure 2B).

Age group comparisons in hemodynamics using TCD vs. 4D flow MRI

Comparisons between young and older adults revealed age group differences in MCA blood flow volume rate (using 4D flow MRI) at each condition (p < 0.001; Figure 3B). Specifically, young adults had higher blood flow volume rate at normocapnia (p = 0.016), 4% CO_2 (p = 0.008), and 6% CO_2 (p = 0.004) as demonstrated in Table 3. There was no difference between young and older adults in MCAv (using TCD) at normocapnia (p = 0.069), 4% CO_2 (p = 0.116) and 6% CO_2 (p = 0.080) as demonstrated in Table 3, although there is a significant overall age group effect (p = 0.003; Figure 3A). These results highlight that cerebral blood flow measured using 4D flow MRI is more sensitive to age group differences than blood velocity measured using TCD at each condition. Importantly, this is independent of MCA diameter, as there were no differences between

10.3389/fphys.2023.1198615

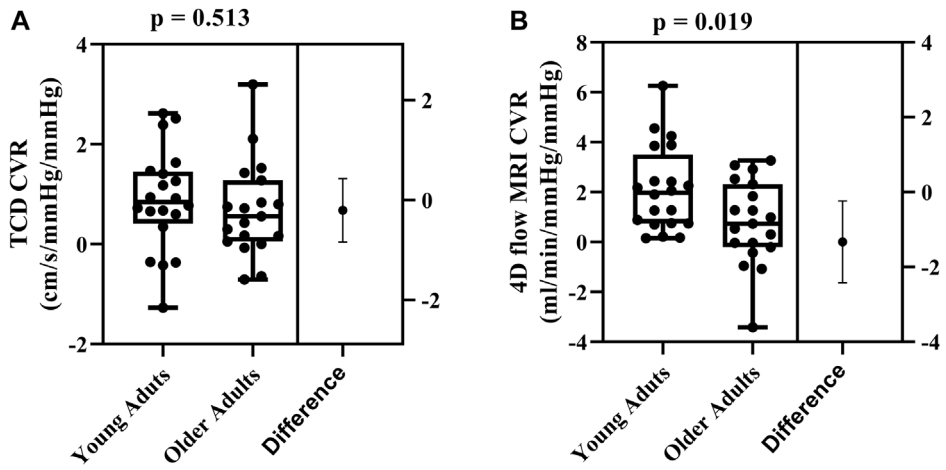

FIGURE 2
Differences in cerebrovascular reactivity (CVR) between young (N = 20) and older adults (N = 19) evaluated using TCD **(A)** and 4D flow MRI CVR **(B)**. Comparisons were made using Student's *t*-tests for unpaired data. Data are presented using box and whiskers plots with the boxes indicating where 50% of the data are found, horizontal lines are the medians, and whiskers identify the minimum and maximum values. The mean difference is presented on the far right of each panel with the error bars showing the standard deviation.

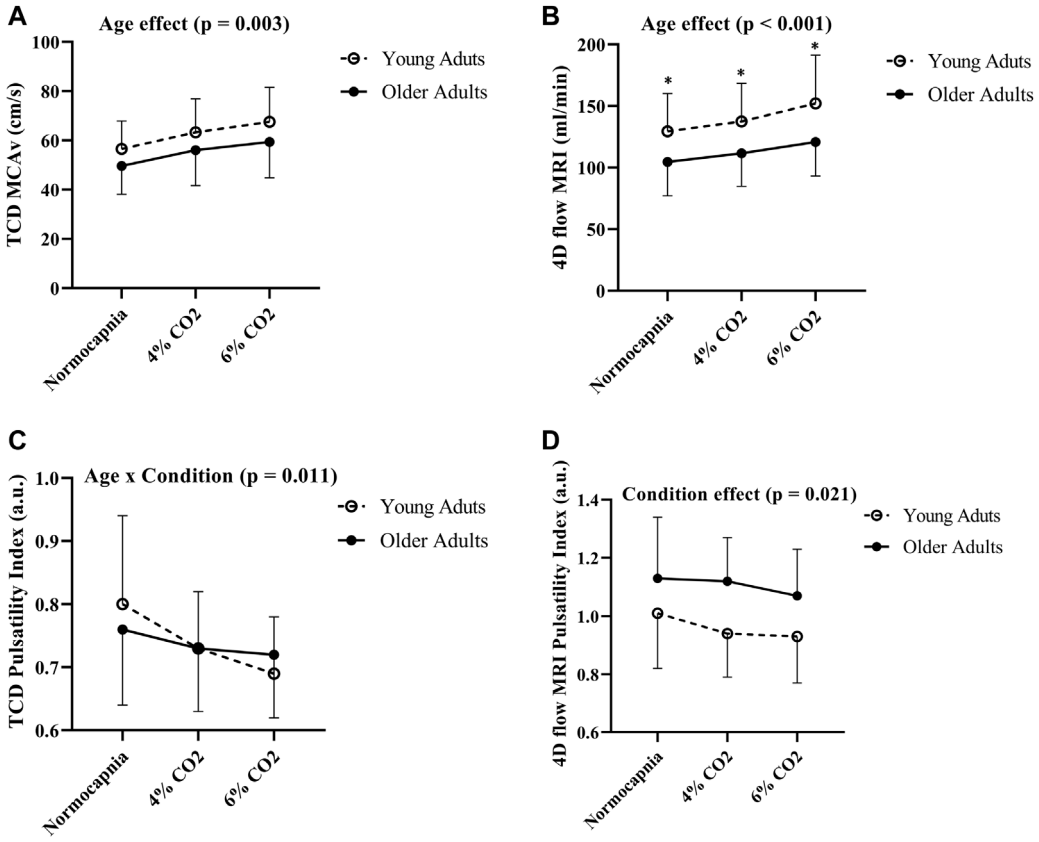

FIGURE 3
Differences in MCAv **(A)**, blood flow volume rate **(B)**, pulsatility index using TCD **(C)** and pulsatility index using 4D flow MRI **(D)** between young (N = 20) and older adults (N = 19) across all conditions. Age group differences were evaluated using two-way (age group x condition) analysis of variance. Error bars show the standard deviation across the group, * denotes a significant difference ($p < 0.05$) using pairwise comparisons between age groups at each condition.

10.3389/fphys.2023.1198615

TABLE 3 Age comparisons of cerebral hemodynamics during normocapnia and hypercapnia.

Variable	Young adults N = 20	Older adults N = 19	*p*-value
MCAv with TCD (cm/s)			
Normocapnia	57 ± 11	50 ± 12	0.069
4% CO_2	63 ± 14	56 ± 14	0.116
6% CO_2	68 ± 14	59 ± 15	0.080
Flow with 4D flow MRI (mL/min)			
Normocapnia	129 ± 31	105 ± 28	**0.016**
4% CO_2	137 ± 31	112 ± 27	**0.008**
6% CO_2	152 ± 39	121 ± 28	**0.004**
MCA diameter with 4D flow MRI (mm)			
Normocapnia	2.96 ± 0.14	2.97 ± 0.26	0.886
4% CO_2	2.95 ± 0.15	2.98 ± 0.27	0.720
6% CO_2	3.00 ± 0.17	2.99 ± 0.29	0.891
CVCi with TCD (cm/s/mmHg)			
Normocapnia	68 ± 15	59 ± 17	0.085
CVC using 4D flow MRI (mL/min/mmHg)			
Normocapnia	139 ± 35	105 ± 28	**0.001**
Pulsatility Index with TCD (a.u.)			
Normocapnia	0.80 ± 0.14	0.76 ± 0.12	0.249
4% CO_2	0.73 ± 0.09	0.73 ± 0.10	0.983
6% CO_2	0.69 ± 0.09	0.72 ± 0.10	0.449
Pulsatility Index with 4D flow MRI (a.u.)			
Normocapnia	1.01 ± 0.19	1.13 ± 0.21	0.061
4% CO_2	0.94 ± 0.15	1.12 ± 0.15	**0.001**
6% CO_2	0.93 ± 0.16	1.07 ± 0.16	**0.008**

Data are presented as mean ± standard deviation. CVC, cerebral vascular conductance; CVCi, cerebral vascular conductance index; MCA, middle cerebral artery; MCAv, middle cerebral artery velocity. Statistical significance was set α priori at $p < 0.05$ with significant p-values indicated in bold.

the young and older adults MCA diameters at normocapnia, 4% CO_2 and 6% CO_2 as demonstrated in Table 3. Additionally, during normocapnia the difference in CVCi (using TCD) between young and older adults did not reach the threshold of significance (Table 3), while CVC (using 4D flow MRI) is higher in young adults compared to older adults (Table 3).

Pulsatility index age group comparisons using TCD vs. 4D flow MRI

There were no differences in cerebral pulsatility index (using TCD) between the young and older adults during normocapnia (Table 3). Similarly, cerebral pulsatility index measured using 4D flow MRI was not different between young and older adults during normocapnia (Table 3). There was an interaction effect showing that young adults had a steeper decline in cerebral pulsatility index (measured using TCD) during hypercapnia, compared with the older adults ($p = 0.011$; Figure 3C). Using 4D flow MRI, there was only a condition effect with a similar decrease with hypercapnia between the young and older adults ($p = 0.021$; Figure 3D).

Discussion

This is the first study to compare cerebral hemodynamics between TCD and 4D flow MRI in healthy adults during normocapnic and hypercapnic conditions. Our results indicate

good agreement between the methods for MCAv measured by TCD and MCAv measured by 4D flow MRI. Yet, there was no significant correlation between MCAv measured by TCD and MCA flow measured by 4D flow MRI or cerebrovascular reactivity measured between the two methods. When examining the effect of age, 4D flow MRI was more sensitive to age-related differences in cerebral hemodynamics in response to hypercapnia compared with TCD. Thus, 4D flow MRI may be a useful tool to investigate the impact of age on cerebral hemodynamics.

Our findings that MCAv are in agreement between methods is consistent with recent work demonstrating TCD and 4D flow MRI correlated well for MCAv at normocapnia (Ha et al., 2021). We have further expanded this by comparing MCAv between TCD and 4D flow MRI methods during normocapnia and in response to hypercapnia where cerebral blood flow increases. We demonstrated that MCAv increases with hypercapnia using both TCD and 4D flow MRI; however, the increase in MCAv was greater using TCD when compared to 4D flow MRI. Interestingly, we observed a trend for MCA dilation in response to hypercapnia, which may contribute to the linear bias seen with increasing MCAv between TCD and 4D flow MRI. In other words, we are demonstrating increasing variance between the two methods in response to hypercapnia. It should be noted that there is variability in the literature between the TCD and 4D flow MRI values for MCAv. For example, previous work has demonstrated approximately 30% lower mean velocities with 4D flow MRI compared to TCD (Chang et al., 2011). These differences are likely due to limited insonation angle correction and lack of verification of the same region of interest of vessel segment selected with TCD (Tsuchiya et al., 1991; Hoksbergen et al., 1999). In this context, 4D flow MRI uses velocity encoding multi-directionally inside a 3D volume across time, within a specific vessel segment of interest, allowing for a more averaged MCAv measurement compared to TCD (Markl et al., 2012; Meckel et al., 2013). We speculate that MCAv using TCD is higher than the values reported using 4D flow MRI because the sample volume (region of interest) with TCD is narrower and captures the velocity in the middle of the vessel where the velocity is the highest due to laminar flow. While 4D flow MRI captures and averages the MCAv throughout the entire vessel (average velocity across the voxels included in the region of interest), this lowers the average MCAv compared with TCD. In addition, TCD is highly operator dependent and could limit reproducibility (Baumgartner et al., 1994), while 4D flow MRI has been demonstrated to have good test-retest reliability, multicenter reproducibility, and interobserver agreement (Wen et al., 2019).

The benefit of using 4D flow MRI is that assessments of blood flow volume rate (rather than only blood velocity) can be made because of the cross-sectional area data (Markl et al., 2012). In addition, 4D flow MRI allows for simultaneous segmentation of multiple cerebral vessels (Markl et al., 2012; Rivera-Rivera et al., 2016; Miller et al., 2019). In the present study, we were interested in comparing cerebrovascular hemodynamics using blood flow volume rate with 4D flow MRI vs. blood velocity with TCD. Importantly, we observed similar increases in blood flow volume rate and blood velocity in response to hypercapnia. We also observed moderate agreement between blood flow volume rate using 4D flow MRI and blood velocity using TCD. Taken together, our results indicate MCAv can be used as an indicator for blood flow responses to hypercapnia in healthy young and older adults.

In the present study, we were interested in comparing changes in cerebral pulsatility in response to hypercapnia with both imaging modalities. We observed similar decreases in cerebral pulsatility with TCD and 4D flow MRI. We also evaluated age-related differences between the methods. For example, cerebral pulsatility index decreased similarly in response to hypercapnia in the young and older participants with 4D flow MRI, yet we reported a steeper decrease in young adults compared with older adults when using TCD. Our results are in agreement with previous research demonstrating cerebral pulsatility decreases in response to mild hypercapnia using 4.5% CO_2 (DuBose et al., 2022). Importantly, we demonstrated TCD provided agreement and similar age-related results for MCAv when compared with the more advanced measurement technique of 4D flow MRI.

Previous work has demonstrated variability in age-related findings of cerebrovascular reactivity, particularly when comparing young and older adults (Peng et al., 2018; Miller et al., 2019). When investigating age-related differences using two methods TCD vs. MRI (BOLD; PCA), Burley et al. (2021a) reported higher cerebrovascular reactivity using TCD in older adults compared to younger adults, but the opposite results when using BOLD MRI, with younger adults having greater cerebrovascular reactivity than the older adults. Our results showed age-related differences in cerebrovascular reactivity between young and older adults, when using 4D flow MRI, but not with TCD. One possible reason for these differences is based on methods because TCD relies on the assumption that the MCA diameter does not change during hypercapnia. Based on this assumption, MCAv would be a reasonable surrogate for MCA flow; however, this assumption is still debated (Hoiland and Ainslie, 2016a; Brothers and Zhang, 2016). Although the present study did not show a correlation between MCAv and MCA flow in response to hypercapnia, it is possible that age may influence MCA cross-sectional area (Miller et al., 2019), and explain why the results regarding age differences were linked to the specific methodology. The discrepancies in the previous research may be explained by potential MCA cross sectional area changes (Verbree et al., 2014), with evidence that percent change increases in MCA cross-sectional area with hypercapnia are attenuated in older adults compared to young adults (Coverdale et al., 2017; Miller et al., 2019). Because of the user-dependent nature of TCD, it is possible that the lack of age-related differences in cerebrovascular reactivity in this study was related to sample size. In order to detect significant age differences in cerebrovascular reactivity using TCD, a greater sample size may be necessary.

Cerebral hemodynamics and cerebrovascular reactivity are emerging biomarkers for a range of conditions, including Alzheimer's disease (Roher et al., 2012; Rivera-Rivera et al., 2017; Sur et al., 2020). Because there is currently no "gold standard" for cerebral hemodynamic measurements, the purpose of this project was to compare two common methods to assess cerebral hemodynamics. 4D flow MRI is a newer method of assessing vessel-specific flow parameters compared with TCD and offers many benefits including the ability to measure cerebral hemodynamics in multiple vessels simultaneously. There are other benefits to TCD compared with MRI, including 1) portability; 2) that it is comparatively cost-

effective; and 3) TCD can be less invasive/intrusive than MRI procedures (Ghorbani et al., 2010). In the present study TCD was able to distinguish a greater decrease in cerebral pulsatility in the young adults compared to older adults. In addition, TCD has excellent temporal resolution for rapid physiological responses, which are not yet available with MRI. Additionally, TCD has clinical applications such as diagnosing cerebral vasospasm, guiding transfusion therapy, and providing preoperative evaluation for patients with cerebrovascular disease (Kincaid, 2008). Our findings may help future studies in determining the methodology that provides the best approach for the intended research question.

This study is not without limitations. For example, it was not possible to capture TCD and 4D flow MRI hemodynamics on the same day. Therefore, some variability between the measurements would be expected due to individual variation in hemodynamics (Rickards and Tzeng, 2014; Ismaili et al., 2018). A strength of the study is we attempted to minimize day-to-day variability by replicating the same procedures for each visit within a relatively short time frame with strict diet and exercise routines being duplicated. Specifically, we had participants record 3 days of normal dietary intake and exercise prior to their first study day and asked them to repeat these prior to their second study day. As mentioned, an inherent limitation when comparing TCD vs. 4D flow MRI is TCD relies on the assumption that blood velocity is a surrogate for blood flow and may not be ideal in experimental set-ups that elicit MCA dilation. Another limitation is that the instrumentation between visits was not identical due to constraints with MRI compatibility. Additionally, we did not examine relationships between TCD or 4D flow MRI with BOLD-based cerebrovascular reactivity measurements, which are commonly used. The goal of this project was to investigate MCA vessel-specific velocity and flow responses, but future studies could compare 4D flow MRI with BOLD-based cerebrovascular reactivity assessments. A final limitation is that the older adults included in this study were healthy and met or exceeded published physical activity guidelines, which may limit the translation of this study to the general population who are sedentary, may have vascular risk factors or established disease.

In conclusion, our study demonstrated good agreement between the two imaging methods for MCAv. There was no correlation between MCAv measured by TCD and MCA flow measured by 4D flow MRI or cerebrovascular reactivity measured between the two methods. When performing age-related comparisons, 4D flow MRI was more sensitive to age-related differences between young and older adults. Due to these capabilities when using 4D flow MRI, we were able to demonstrate lower blood flow volume rate and CVC in older adults when compared to younger adults, which was not possible with TCD. Additionally, 4D flow MRI provides clinical utility such as characterizing changes in cerebrovascular hemodynamics with Alzheimer's disease (Rivera-Rivera et al., 2016; Berman et al., 2017; Rivera-Rivera et al., 2017). Future studies could compare cerebral hemodynamics and cerebrovascular reactivity between 4D flow MRI and other MRI techniques (e.g., BOLD, ASL) to help determine the appropriate methodology for the proposed research questions.

Data availability statement

The raw data supporting the conclusion of this article will be made available by the authors, without undue reservation.

Ethics statement

The studies involving human participants were reviewed and approved by Institutional Review Board of the University of Wisconsin–Madison. The patients/participants provided their written informed consent to participate in this study.

Author contributions

KM and JB designed the experiments. KM, AC, AH, NL, AP, and JB collected the data. BF, KM, AH, LR-R, HR, and JB analyzed the data. BF, KM, LR-R, OW, KJ, SJ, and JB interpreted the data. BF and JB wrote the manuscript and prepared figures. All authors listed have made a substantial, direct, and intellectual contribution to the work and approved it for publication.

Funding

This study was supported by the National Institutes of Health (R00HL118154 and NS117746 to JB). This investigation was also supported by the National Institutes of Health, Ruth L. Kirschstein National Research Service Award T32's under the National Institute on Aging to the University of Wisconsin–Madison Biology of Aging & Age-Related Diseases (AG000213 to BF) and under the National Heart Lung and Blood Institute to the University of Wisconsin–Madison Cardiovascular Research Center (HL007936 to KM) as well as the Wisconsin Alumni Research Foundation (JB). This study was also supported by Alzheimer's Association Research Fellowship (AARF-22-924325 to BF).

Conflict of interest

The authors declare that the research was conducted in the absence of any commercial or financial relationships that could be construed as a potential conflict of interest.

Publisher's note

References

Al-Khazraji, B. K., Buch, S., Kadem, M., Matushewski, B. J., Norozi, K., Menon, R. S., et al. (2021). Protocol-dependence of middle cerebral artery dilation to modest hypercapnia. *Appl. Physiol. Nutr. Metab.* 46 (9), 1038–1046. doi:10.1139/apnm-2021-0220

Alsop, D. C., Detre, J. A., Golay, X., Günther, M., Hendrikse, J., Hernandez-Garcia, L., et al. (2015). Recommended implementation of arterial spin-labeled perfusion MRI for clinical applications: A consensus of the ismrm perfusion study group and the European consortium for ASL in dementia. *Magn. Reson Med.* 73 (1), 102–116. doi:10.1002/mrm.25197

Alwatban, M. R., Aaron, S. E., Kaufman, C. S., Barnes, J. N., Brassard, P., Ward, J. L., et al. (2021). Effects of age and sex on middle cerebral artery blood velocity and flow pulsatility index across the adult lifespan. *J. Appl. Physiology* 130 (6), 1675–1683. doi:10.1152/japplphysiol.00926.2020

Amireault, S., and Godin, G. (2015). The godin-shephard leisure-time physical activity questionnaire: Validity evidence supporting its use for classifying healthy adults into active and insufficiently active categories. *Percept. Mot. Ski.* 120 (2), 604–622. doi:10.2466/03.27.pms.120v19x7

Bakker, S. L., de Leeuw, F. E., den Heijer, T., Koudstaal, P. J., Hofman, A., and Breteler, M. M. (2004). Cerebral haemodynamics in the elderly: The rotterdam study. *Neuroepidemiology* 23 (4), 178–184. doi:10.1159/000078503

Barnes, J. N., Schmidt, J. E., Nicholson, W. T., and Joyner, M. J. (2012). Cyclooxygenase inhibition abolishes age-related differences in cerebral vasodilator responses to hypercapnia. *J. Appl. Physiol.* 112(11), 1884–1890. doi:10.1152/japplphysiol.01270.2011

Baumgartner, R. W., Mathis, J., Sturzenegger, M., and Mattle, H. P. (1994). A validation study on the intraobserver reproducibility of transcranial color-coded duplex sonography velocity measurements. *Ultrasound Med. Biol.* 20 (3), 233–237. doi:10.1016/0301-5629(94)90063-9

Berkenbosch, A., Bovill, J. G., Dahan, A., DeGoede, J., and Olievier, I. C. (1989). The ventilatory CO2 sensitivities from Read's rebreathing method and the steady-state method are not equal in man. *J. Physiol.* 411, 367–377. doi:10.1113/jphysiol.1989.sp017578

Berman, S. E., Clark, L. R., Rivera-Rivera, L. A., Norton, D., Racine, A. M., Rowley, H. A., et al. (2017). Intracranial arterial 4D flow in individuals with mild cognitive impairment is associated with cognitive performance and amyloid positivity. *J. Alzheimer's Dis.* 60 (1), 243–252. doi:10.3233/jad-170402

Bishop, C. C., Powell, S., Rutt, D., and Browse, N. L. (1986). Transcranial Doppler measurement of middle cerebral artery blood flow velocity: A validation study. *Stroke* 17 (5), 913–915. doi:10.1161/01.str.17.5.913

Bland, J. M., and Altman, D. G. (1986). Statistical methods for assessing agreement between two methods of clinical measurement. *Lancet* 1 (8476), 307–310. doi:10.1016/s0140-6736(86)90837-8

Brothers, R. M., and Zhang, R. (2016). CrossTalk opposing view: The middle cerebral artery diameter does not change during alterations in arterial blood gases and blood pressure. *J. Physiology* 594 (15), 4077–4079. doi:10.1113/jp271884

Burley, C. V., Francis, S. T., Thomas, K. N., Whittaker, A. C., Lucas, S. J., and Mullinger, K. J. (2021a). Contrasting measures of cerebrovascular reactivity between MRI and Doppler: A cross-sectional study of younger and older healthy individuals. *Front. physiology* 12, 656746. doi:10.3389/fphys.2021.656746

Burley, C. V., Francis, S. T., Whittaker, A. C., Mullinger, K. J., and Lucas, S. J. E. (2021b). Measuring resting cerebral haemodynamics using MRI arterial spin labelling and transcranial Doppler ultrasound: Comparison in younger and older adults. *Brain Behav.* 11 (7), e02126. doi:10.1002/brb3.2126

Chang, W., Landgraf, B., Johnson, K. M., Kecskemeti, S., Wu, Y., Velikina, J., et al. (2011). Velocity measurements in the middle cerebral arteries of healthy volunteers using 3D radial phase-contrast HYPRFlow: Comparison with transcranial Doppler sonography and 2D phase-contrast MR imaging. *Am. J. Neuroradiol.* 32 (1), 54–59. doi:10.3174/ajnr.a2240

Coverdale, N. S., Badrov, M. B., and Shoemaker, J. K. (2017). Impact of age on cerebrovascular dilation versus reactivity to hypercapnia. *J. Cereb. Blood Flow Metabolism* 37 (1), 344–355. doi:10.1177/0271678x15626156

DuBose, N., Ainslie, P., Sherman, S., Baynard, T., Hoiland, R., Smith, K., et al. (2022). Exercise and hypercapnia differentially modify ratios of extracranial and intracranial pulsatility. *FASEB J.* 36. doi:10.1096/fasebj.2022.36.S1.R5027

Fico, B. G., Miller, K. B., Rivera-Rivera, L. A., Corkery, A. T., Pearson, A. G., Eisenmann, N. A., et al. (2022). The impact of aging on the association between aortic stiffness and cerebral pulsatility index. *Front. Cardiovasc. Med.* 9, 821151. doi:10.3389/fcvm.2022.821151

Flück, D., Beaudin, A. E., Steinback, C. D., Kumarpillai, G., Shobha, N., McCreary, C. R., et al. (2014). Effects of aging on the association between cerebrovascular responses to visual stimulation, hypercapnia and arterial stiffness. *Front. physiology* 5, 49. doi:10.3389/fphys.2014.00049

Galvin, S. D., Celi, L. A., Thomas, K. N., Clendon, T. R., Galvin, I. F., Bunton, R. W., et al. (2010). Effects of age and coronary artery disease on cerebrovascular reactivity to carbon dioxide in humans. *Anaesth. Intensive Care* 38 (4), 710–717. doi:10.1177/0310057x1003800415

Ghorbani, A., Ashtari, F., and Fatehi, F. (2010). The assessment value of transcranial Doppler sonography versus magnetic resonance angiography in vertebrobasilar stroke. *J. Res. Med. Sci.* 15 (3), 133–139.

Gu, T., Korosec, F. R., Block, W. F., Fain, S. B., Turk, Q., Lum, D., et al. (2005). PC vipr: A high-speed 3D phase-contrast method for flow quantification and high-resolution angiography. *AJNR Am. J. Neuroradiol.* 26 (4), 743–749.

Ha, S. Y., Kang, Y., Lee, H. J., Hwang, M., Baik, J., and Park, S. (2021). Intracranial flow velocity quantification using non-contrast four-dimensional flow MRI: A prospective comparative study with transcranial Doppler ultrasound. *Diagn. (Basel)* 12 (1), 23. doi:10.3390/diagnostics12010023

Hoiland, R. L., and Ainslie, P. N. (2016a). CrossTalk proposal: The middle cerebral artery diameter does change during alterations in arterial blood gases and blood pressure. *J. Physiology* 594 (15), 4073–4075. doi:10.1113/jp271981

Hoiland, R. L., and Ainslie, P. N. (2016b). Rebuttal from ryan L. Hoiland and philip N. Ainslie. *J. Physiology* 594 (15), 4081. doi:10.1113/jp272241

Hoksbergen, A. W., Legemate, D. A., Ubbink, D. T., and Jacobs, M. J. (1999). Success rate of transcranial color-coded duplex ultrasonography in visualizing the basal cerebral arteries in vascular patients over 60 years of age. *Stroke* 30 (7), 1450–1455. doi:10.1161/01.str.30.7.1450

Ismaili, A. R. A., Vestergaard, M. B., Hansen, A. E., Larsson, H. B. W., Johannesen, H. H., Law, I., et al. (2018). Components of day-to-day variability of cerebral perfusion measurements – analysis of phase contrast mapping magnetic resonance imaging measurements in healthy volunteers. *PLOS ONE* 13 (6), e0197807. doi:10.1371/journal.pone.0197807

Jing, L., Redmond, M. J., Brodsky, E. K., Alexander, A. L., Aiming, L., Thornton, F. J., et al. (2006). Generation and visualization of four-dimensional MR angiography data using an undersampled 3-D projection trajectory. *IEEE Trans. Med. Imaging* 25 (2), 148–157. doi:10.1109/tmi.2005.861706

Johnson, K. M., Lum, D. P., Turski, P. A., Block, W. F., Mistretta, C. A., and Wieben, O. (2008). Improved 3D phase contrast MRI with off-resonance corrected dual echo VIPR. *Magnetic Reson. Med.* 60 (6), 1329–1336. doi:10.1002/mrm.21763

Kastrup, A., Dichgans, J., Niemeier, M., and Schabet, M. (1998). Changes of cerebrovascular CO2 reactivity during normal aging. *Stroke* 29 (7), 1311–1314. doi:10.1161/01.str.29.7.1311

Kincaid, M. S. (2008). Transcranial Doppler ultrasonography: A diagnostic tool of increasing utility. *Curr. Opin. Anaesthesiol.* 21 (5), 552–559. doi:10.1097/ACO.0b013e32830edc0b

Kleiser, B., and Widder, B. (1992). Course of carotid artery occlusions with impaired cerebrovascular reactivity. *Stroke* 23 (2), 171–174. doi:10.1161/01.str.23.2.171

Leeuwis, A. E., Benedictus, M. R., Kuijer, J. P. A., Binnewijzend, M. A. A., Hooghiemstra, A. M., Verfaillie, S. C. J., et al. (2017). Lower cerebral blood flow is associated with impairment in multiple cognitive domains in Alzheimer's disease. *Alzheimer's Dementia* 13 (5), 531–540. doi:10.1016/j.jalz.2016.08.013

Leoni, R., Oliveira, I., Pontes-Neto, O., Santos, A., and Leite, J. (2017). Cerebral blood flow and vasoreactivity in aging: An arterial spin labeling study. *Braz. J. Med. Biol. Res.* 50, e5670. doi:10.1590/1414-431X20175670

Loecher, M., Schrauben, E., Johnson, K. M., and Wieben, O. (2016). Phase unwrapping in 4D MR flow with a 4D single-step laplacian algorithm. *J. Magnetic Reson. Imaging* 43 (4), 833–842. doi:10.1002/jmri.25045

Markl, M., Frydrychowicz, A., Kozerke, S., Hope, M., and Wieben, O. (2012). 4D flow MRI. *J. Magnetic Reson. Imaging* 36 (5), 1015–1036. doi:10.1002/jmri.23632

Meckel, S., Leitner, L., Bonati, L. H., Santini, F., Schubert, T., Stalder, A. F., et al. (2013). Intracranial artery velocity measurement using 4D PC MRI at 3 T: comparison with transcranial ultrasound techniques and 2D PC MRI. *Neuroradiology* 55 (4), 389–398. doi:10.1007/s00234-012-1103-z

Miller, K. B., Howery, A. J., Harvey, R. E., Eldridge, M. W., and Barnes, J. N. (2018). Cerebrovascular reactivity and central arterial stiffness in habitually exercising healthy adults. *Front. Physiology* 9, 1096. doi:10.3389/fphys.2018.01096

Miller, K. B., Howery, A. J., Rivera-Rivera, L. A., Johnson, S. C., Rowley, H. A., Wieben, O., et al. (2019). Age-related reductions in cerebrovascular reactivity using 4D flow MRI. *Front. Aging Neurosci.* 11, 281. doi:10.3389/fnagi.2019.00281

Murrell, C. J., Cotter, J. D., Thomas, K. N., Lucas, S. J. E., Williams, M. J. A., and Ainslie, P. N. (2013). Cerebral blood flow and cerebrovascular reactivity at rest and during sub-maximal exercise: Effect of age and 12-week exercise training. *AGE* 35 (3), 905–920. doi:10.1007/s11357-012-9414-x

Ogawa, S., Lee, T. M., Kay, A. R., and Tank, D. W. (1990). Brain magnetic resonance imaging with contrast dependent on blood oxygenation. *Proc. Natl. Acad. Sci. U. S. A.* 87 (24), 9868–9872. doi:10.1073/pnas.87.24.9868

Peng, S.-L., Chen, X., Li, Y., Rodrigue, K. M., Park, D. C., and Lu, H. (2018). Age-related changes in cerebrovascular reactivity and their relationship to cognition: A four-

year longitudinal study. *NeuroImage* 174, 257–262. doi:10.1016/j.neuroimage.2018.03.033

Poulin, M. J., and Robbins, P. A. (1996). Indexes of flow and cross-sectional area of the middle cerebral artery using Doppler ultrasound during hypoxia and hypercapnia in humans. *Stroke* 27 (12), 2244–2250. doi:10.1161/01.str.27.12.2244

Purkayastha, S., and Sorond, F. (2013). Transcranial Doppler ultrasound: Technique and application. *Seminars Neurology* 32 (04), 411–420. doi:10.1055/s-0032-1331812

Richiardi, J., Monsch, A. U., Haas, T., Barkhof, F., Van de Ville, D., Radü, E. W., et al. (2015). Altered cerebrovascular reactivity velocity in mild cognitive impairment and Alzheimer's disease. *Neurobiol. aging* 36 (1), 33–41. doi:10.1016/j.neurobiolaging.2014.07.020

Rickards, C. A., and Tzeng, Y. C. (2014). Arterial pressure and cerebral blood flow variability: Friend or foe? A review. *Front. Physiol.* 5, 120. doi:10.3389/fphys.2014.00120

Rivera-Rivera, L. A., Schubert, T., Turski, P., Johnson, K. M., Berman, S. E., Rowley, H. A., et al. (2017). Changes in intracranial venous blood flow and pulsatility in Alzheimer's disease: A 4D flow MRI study. *J. Cereb. Blood Flow Metabolism* 37 (6), 2149–2158. doi:10.1177/0271678x16661340

Rivera-Rivera, L. A., Turski, P., Johnson, K. M., Hoffman, C., Berman, S. E., Kilgas, P., et al. (2016). 4D flow MRI for intracranial hemodynamics assessment in Alzheimer's disease. *J. Cereb. Blood Flow Metabolism* 36 (10), 1718–1730. doi:10.1177/0271678x15617171

Roher, A. E., Debbins, J. P., Malek-Ahmadi, M., Chen, K., Pipe, J. G., Maze, S., et al. (2012). Cerebral blood flow in Alzheimer's disease. *Vasc. Health Risk Manag.* 599. doi:10.2147/vhrm.s34874

Schrauben, E., Wåhlin, A., Ambarki, K., Spaak, E., Malm, J., Wieben, O., et al. (2015). Fast 4D flow MRI intracranial segmentation and quantification in tortuous arteries. *J. Magnetic Reson. Imaging* 42 (5), 1458–1464. doi:10.1002/jmri.24900

Sur, S., Lin, Z., Li, Y., Yasar, S., Rosenberg, P., Moghekar, A., et al. (2020). Association of cerebrovascular reactivity and Alzheimer pathologic markers with cognitive performance. *Neurology* 95 (8), e962–e972. doi:10.1212/WNL.0000000000010133

Tang, C., Blatter, D. D., and Parker, D. L. (1993). Accuracy of phase-contrast flow measurements in the presence of partial-volume effects. *J. Magnetic Reson. Imaging* 3 (2), 377–385. doi:10.1002/jmri.1880030213

Tsuchiya, T., Yasaka, M., Yamaguchi, T., Kimura, K., and Omae, T. (1991). Imaging of the basal cerebral arteries and measurement of blood velocity in adults by using transcranial real-time color flow Doppler sonography. *AJNR Am. J. Neuroradiol.* 12 (3), 497–502.

Verbree, J., Bronzwaer, A.-S. G., Ghariq, E., Versluis, M. J., Daemen, M. J., van Buchem, M. A., et al. (2014). Assessment of middle cerebral artery diameter during hypocapnia and hypercapnia in humans using ultra-high-field MRI. *J. Appl. physiology* 117 (10), 1084–1089. doi:10.1152/japplphysiol.00651.2014

Wen, B., Tian, S., Cheng, J., Li, Y., Zhang, H., Xue, K., et al. (2019). Test–retest multisite reproducibility of neurovascular 4D flow MRI. *J. Magnetic Reson. Imaging* 49 (6), 1543–1552. doi:10.1002/jmri.26564

Whelton, P. K., Carey, R. M., Aronow, W. S., Casey, D. E., Collins, K. J., Dennison Himmelfarb, C., et al. (2018). 2017 ACC/AHA/AAPA/ABC/ACPM/AGS/APhA/ASH/ASPC/NMA/PCNA guideline for the prevention, detection, evaluation, and management of high blood pressure in adults: A report of the American college of cardiology/American heart association task force on clinical practice guidelines. *Hypertension* 71 (6), e13–e115. doi:10.1161/hyp.0000000000000065

Williams, R. J., MacDonald, M. E., Mazerolle, E. L., and Pike, G. B. (2021). The relationship between cognition and cerebrovascular reactivity: Implications for task-based fMRI. *Front. Phys.* 9, 645249. doi:10.3389/fphy.2021.645249

Wolters, F. J., Zonneveld, H. I., Hofman, A., van der Lugt, A., Koudstaal, P. J., Vernooij, M. W., et al. (2017). Cerebral perfusion and the risk of dementia: A population-based study. *Circulation* 136 (8), 719–728. doi:10.1161/circulationaha.117.027448

Wu, C., Honarmand, A. R., Schnell, S., Kuhn, R., Schoeneman, S. E., Ansari, S. A., et al. (2016). Age-related changes of normal cerebral and cardiac blood flow in children and adults aged 7 Months to 61 years. *J. Am. Heart Assoc.* 5 (1), e002657. doi:10.1161/jaha.115.002657

Yew, B., Jang, J. Y., Dutt, S., Li, Y., Sible, I. J., Gaubert, A., et al. (2022). Cerebrovascular reactivity deficits in cognitively unimpaired older adults: Vasodilatory versus vasoconstrictive responses. *Neurobiol. Aging* 113, 55–62. doi:10.1016/j.neurobiolaging.2022.02.006

frontiers | Frontiers in Physiology

TYPE Original Research
PUBLISHED 26 May 2023
DOI 10.3389/fphys.2023.1142359

OPEN ACCESS

EDITED BY
Alex Bhogal,
Utrecht University, Netherlands

REVIEWED BY
Jan Petr,
Helmholtz Association of German Research Centres (HZ), Germany
James Duffin,
University of Toronto, Canada

*CORRESPONDENCE
Joana Pinto,
joana.pinto@eng.ox.ac.uk

RECEIVED 11 January 2023
ACCEPTED 14 April 2023
PUBLISHED 26 May 2023

CITATION
Pinto J, Blockley NP, Harkin JW and Bulte DP (2023), Modelling spatiotemporal dynamics of cerebral blood flow using multiple-timepoint arterial spin labelling MRI.
Front. Physiol. 14:1142359.
doi: 10.3389/fphys.2023.1142359

Modelling spatiotemporal dynamics of cerebral blood flow using multiple-timepoint arterial spin labelling MRI

Joana Pinto[1]*, Nicholas P. Blockley[2], James W. Harkin[3] and Daniel P. Bulte[1]

[1]Institute of Biomedical Engineering, Department of Engineering Science, University of Oxford, Oxford, United Kingdom, [2]David Greenfield Human Physiology Unit, School of Life Sciences, University of Nottingham, Nottingham, United Kingdom, [3]Poole Hospital NHS Foundation Trust, Poole, United Kingdom

Introduction: Cerebral blood flow (CBF) is an important physiological parameter that can be quantified non-invasively using arterial spin labelling (ASL) imaging. Although most ASL studies are based on single-timepoint strategies, multi-timepoint approaches (multiple-PLD) in combination with appropriate model fitting strategies may be beneficial not only to improve CBF quantification but also to retrieve other physiological information of interest.

Methods: In this work, we tested several kinetic models for the fitting of multiple-PLD pCASL data in a group of 10 healthy subjects. In particular, we extended the standard kinetic model by incorporating dispersion effects and the macrovascular contribution and assessed their individual and combined effect on CBF quantification. These assessments were performed using two pseudo-continuous ASL (pCASL) datasets acquired in the same subjects but during two conditions mimicking different CBF dynamics: normocapnia and hypercapnia (achieved through a CO_2 stimulus).

Results: All kinetic models quantified and highlighted the different CBF spatiotemporal dynamics between the two conditions. Hypercapnia led to an increase in CBF whilst decreasing arterial transit time (ATT) and arterial blood volume (aBV). When comparing the different kinetic models, the incorporation of dispersion effects yielded a significant decrease in CBF (~10–22%) and ATT (~17–26%), whilst aBV (~44–74%) increased, and this was observed in both conditions. The extended model that includes dispersion effects and the macrovascular component has been shown to provide the best fit to both datasets.

Conclusion: Our results support the use of extended models that include the macrovascular component and dispersion effects when modelling multiple-PLD pCASL data.

KEYWORDS

arterial spin labelling, cerebral blood flow, functional MRI, kinetic modelling, cerebral haemodynamic

1 Introduction

Imaging studies quantifying cerebral blood flow (CBF) have been increasingly applied in an effort to characterize brain health and baseline CBF has been known to be an important physiological parameter that is commonly altered at earlier stages of several pathological conditions, including Alzheimer's disease, stroke and small vessel disease (Alsop et al., 2015; Haller et al., 2016; De Vis et al., 2018; Lindner et al., 2023). CBF can be quantified non-invasively using the arterial spin labelling (ASL) MRI contrast, with most studies using single timepoint approaches (Alsop et al., 2015). However, in specific pathologies, as well as under certain physiological states where CBF dynamics are altered, single timepoint acquisition schemes and their assumptions might be invalid, ultimately compromising CBF quantification. One of those conditions is when acquiring data during a hypercapnia challenge, which is the case when evaluating cerebrovascular reactivity (CVR). CVR is the intrinsic mechanism of cerebral blood vessels of adjusting their calibre in response to a vasoactive stimulus. CVR has been shown to also be impaired in several pathologies, possibly providing additional or complementary information to baseline CBF (Catchlove et al., 2018; Chen, 2018). The most common way to evaluate CVR is by increasing arterial blood partial pressure of carbon dioxide ($PaCO_2$) (Moreton et al., 2016; Pinto et al., 2021) and imaging the concomitant CBF changes using an appropriate modality such as ASL. In this case, CVR can be quantified as the change in CBF in response to a change in $PaCO_2$ (Mandell et al., 2008; Sobczyk et al., 2015).

However, an increase in $PaCO_2$ concentration is also expected to alter blood flow dynamics, with an increase in blood flow velocity and shortening of transit times (Donahue et al., 2016). This can potentially make approaches and assumptions commonly used for baseline CBF quantification inaccurate under these conditions (e.g., fixed transit time, unchanged bolus shape). This issue can be partially overcome by using an ASL multiple time-point acquisition strategy (multiple-PLD) and fitting this signal using an appropriate physiological model. This approach allows estimation of CBF as well as other related features, such as the time it takes for the labelled blood to flow from the labelling region to the vascular or tissue compartment of the imaging regions (arterial transit time, ATT) (Donahue et al., 2016; Zhao et al., 2021), or the volume of blood signal arising from larger arteries that is destined for more distal tissues (arterial blood volume, aBV) (Chappell et al., 2010). Additionally, most ASL studies assume that the shape of the labelled blood bolus remains unaltered during the transit time of the label through the vasculature. However, due to effects collectively known as dispersion and including different laminar flow profiles, vessel architecture, or diffusion of the labelled water, the bolus shape is in fact altered throughout the vascular tree (Wu et al., 2007; Gallichan and Jezzard, 2008; Kazan et al., 2009; Chappell et al., 2013). By correcting for this effect, as some dispersed spins might not have arrived at their final destination, CBF estimation can be improved while potentially also refining the separation between the aBV and tissue components (if these are modelled separately). The impact of modelling dispersion and aBV effects in ASL has been recently investigated during normocapnia (van der Plas et al., 2022), however, given the change in blood velocity and CBF temporal features that occurs during hypercapnia or in pathologies that alter CBF dynamics, the impact of these modelling strategies might be different. In this work, we test several modelling strategies that include dispersion and/or macrovascular contribution and assess their effect on the quantification of CBF spatiotemporal dynamics during two different physiological states, normocapnia and hypercapnia.

2 Materials and methods

2.1 Data acquisition

A group of 10 healthy subjects (5 M, 20.4 ± 0.8 years old) was studied on a 3 T Siemens Prisma Scanner with a 32 channel receive only head coil (Blockley et al., 2016). All participants provided written, informed consent in order to take part in the study and ethical approval was obtained from the Central University Research Ethics Committee (CUREC) at Oxford University.

Functional MR scanning included a multiple-PLD pseudocontinuous ASL (pCASL) sequence (Okell et al., 2013) with a 2D multi-slice GE-EPI readout, background suppression, and the following parameters: spatial resolution = 3.5 × 3.5 × 5 mm^3, TR/TE = 4,100/14 ms, bolus duration = 1400 ms, 6 PLDs (250, 500, 750, 1,000, 1,250, and 1,500 ms), 8 averages for each PLD, number of slices = 24, time per slice = 46 ms and total acquisition time of 6 min and 40 s. Background suppression was achieved with a pre-saturation module (WET) and optimally timed global hyperbolic secant inversion pulses. An M_0 calibration image with no labelling or background suppression was also collected. A field map was acquired using a 2D Fast Low Angle Shot (FLASH) method with the following parameters: TR 378 ms, TE1/TE2 4.92 ms/7.38 ms, FOV of 220 mm × 220 mm, matrix 64 × 64, slices 24, slice thickness 4.5 mm, slice gap 0.45 mm, flip angle 45°. A T_1-weighted structural image was also acquired for each subject using a 3D Magnetisation Prepared Rapid Acquisition Gradient Echo (MPRAGE) pulse sequence with the following parameters: TR 1.9 s, TE 3.74 ms, FOV 174 mm × 192 mm × 192 mm, matrix 116 × 128 × 128, flip angle 8°, inversion time (TI) 904 ms.

The gas challenge was delivered by a computer controlled gas blender (RespirAct™ Gen 3, Thornhill Research Inc., Toronto, Canada) that implements a prospective algorithm for the targeting and maintenance of end-tidal CO_2 partial pressure ($PETCO_2$) and end-tidal O_2 partial pressure ($PETO_2$) concentrations (Slessarev et al., 2007). The gas protocol (Figure 1A) was personalised to each subject's $PETCO_2$ and $PETO_2$ baseline values. Modulations in $PETCO_2$ were targeted relative to baseline, whilst maintaining $PETO_2$ constant (Figure 1B). Other details on the gas challenge setup can be found in (Blockley et al., 2017). The pCASL gas protocol consisted of a baseline period of normocapnia followed by a period of hypercapnia ($PETCO_2$ step change of +10 mmHg). Both periods lasted 6 min and 40 s (Figure 1A).

2.2 Data analysis

Offline data processing was performed using FSL 6.0.3 [FMRIB Software Library (Jenkinson et al., 2012)], Matlab R2019b (Mathworks, Natick, MA, United States), and the IBM SPSS statistics tool (v.27).

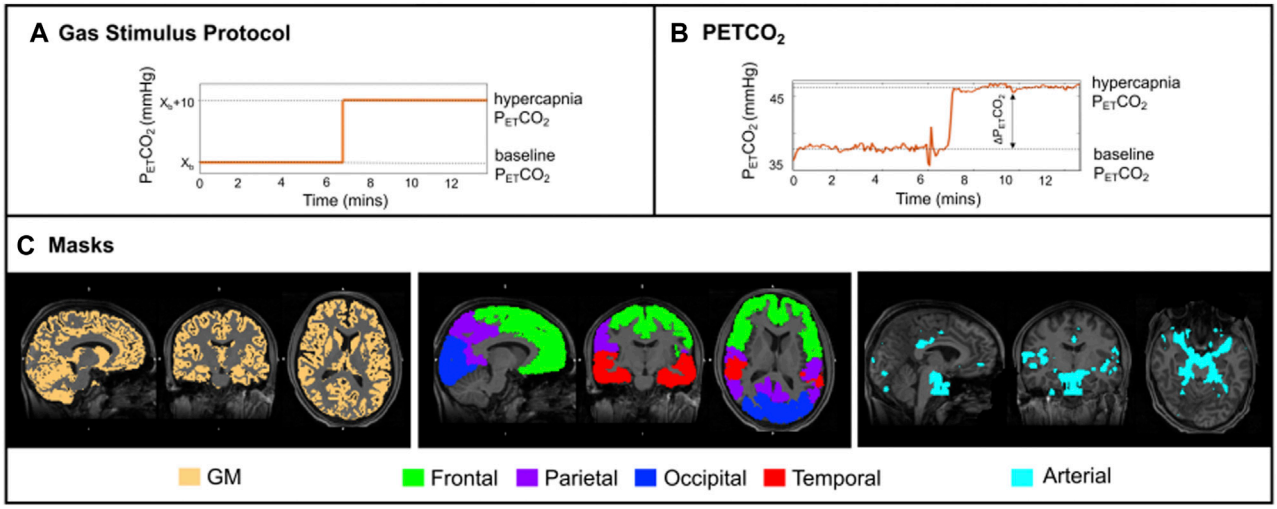

FIGURE 1
(A) Schematic of the stimulus paradigm; **(B)** $PETCO_2$ trace of one illustrative subject. ASL data acquisition was performed only during the plateau periods; **(C)** Orthogonal representations, for one illustrative subject, overlaid on the structural image: (left) thresholded GM mask in yellow; (middle) four regions of interest (ROIs—frontal, parietal, occipital, and temporal lobes); (right) arterial mask in light blue.

Structural images were tissue segmented using FAST (Zhang et al., 2001), to produce grey matter (GM), white matter and cerebrospinal fluid partial volume estimate (PVE) maps. The GM PVE maps were further thresholded at 0.3, creating restrictive GM masks whilst maintaining a significant number of voxels within regions of interest (Figure 1C). Co-registration from functional to structural space was performed using a linear registration tool, FLIRT (BBR) (Jenkinson et al., 2002), and from structural to standard (MNI) space was done using FLIRT and a non-linear registration (FNIRT) tool (Andersson et al., 2007). These registrations were also used to transform four regions of the MNI structural atlas (frontal, parietal, temporal and occipital lobes, Figure 1C) (Mazziotta et al., 2001) and the segmented structural images to functional space. Individual arterial masks were also considered, and these were obtained by thresholding the arterial masks that resulted from model fitting (more details below).

The multiple-PLD pCASL datasets underwent standard pre-processing using FSL. Steps included extraction of first volume (M_0), removing non-brain structures using BET (Smith, 2002), motion correction using MCFLIRT (Jenkinson et al., 2002), and distortion correction using a field-map strategy (FUGUE). Pairwise subtraction of label and control images was then performed in order to generate perfusion-weighted images (ΔM).

Model fitting of the multiple-PLD pCASL data for parameter quantification was performed by applying a Bayesian approach with the default parameter prior information (BASIL, http://fsl.fmrib.ox.ac.uk/fsl/fslwiki/BASIL). Bayesian modelling strategies have been shown to provide robust and reliable results for ASL data quantification, by using prior knowledge based on physically realistic ranges of the parameters (Chappell et al., 2009). In particular, in this work we have modelled our ASL data using a standard kinetic model (Buxton et al., 1998), and incorporating other physiological contributions, creating extended models (Chappell et al., 2009). In particular, we have explored the impact of modelling the intravascular blood water that is destined to perfuse more distant tissues (also known as macrovascular or arterial component, aBV) using the model proposed by (Chappell et al., 2010) (aBV with an automatic relevancy determination prior and ATT prior with mean set at 1 and precision set at 1). Additionally, we also tested for the impact of modelling dispersion effects, using a gamma distribution shaped kernel as proposed by (Chappell et al., 2013), with parameters: time to peak (p) and sharpness (s) [parameters reparametrized and subject to a Gaussian prior with means described by log (s) = 2 and log (s*p) = −0.3 and precision set at 1]. All models are implemented in BASIL. A combination of different modelling strategies was used to assess the impact of these on parameter estimation when using different conditions (normocapnia and hypercapnia) (Table 1). Four different models were tested: 1) with arterial component but without dispersion effects ($M_{art}M_{nodisp}$), 2) with the arterial component and dispersion effects ($M_{art}M_{disp}$), 3) without arterial component and dispersion effects ($M_{noart}M_{nodisp}$), and 4) without arterial component but with dispersion effects ($M_{noart}M_{disp}$).

The resulting CBF and aBV maps were calibrated using a voxelwise approach within BASIL, assuming a labelling efficiency of 0.85 (Pinto et al., 2020). CVR was computed as CBF

TABLE 1 The four different extended models including dispersion and/or macrovascular contributions.

Model Options			
		Dispersion	
		Yes	No
Macrovascular Component	Yes	$M_{art}M_{disp}$	$M_{art}M_{nodisp}$
	No	$M_{noart}M_{disp}$	$M_{noart}M_{nodisp}$

change due to hypercapnia normalized by the corresponding change in $PETCO_2$.

Average parameter values were computed for the following regions intersected with the total GM mask: frontal, parietal, temporal, and occipital (Figure 1C, middle). A total GM mask was also considered (Figure 1C, left), as well as an arterial mask obtained by thresholding the corresponding arterial blood volume maps results from the model that includes dispersion and the arterial component, $M_{art}M_{disp}$ (visually optimised threshold of aBV > 0.7, Figures 1, 4). The Bayesian approach used in this study also allows for model comparisons to be performed through the estimation of the free energy (FE) (Chappell et al., 2009). FE approximates the Bayesian evidence for a model, and thus combines the accuracy of a model's fit to the data with a penalty for the number of free parameters in the model. The closer FE is to zero the better the model is at explaining the data.

To evaluate differences between average parameters across regions, models, and conditions, a repeated-measures 3-way Analysis of Variance (rm-3-way-ANOVA, $p < 0.05$, Greenhouse-Geisser correction for sphericity), with factors: condition, region, and model, was applied. Post-hoc analysis was done using simple effects tests and pairwise comparisons with Bonferroni correction for multiple comparisons.

3 Results

Table 2 summarizes the main demographic descriptors of each subject as well as the corresponding $\Delta PETCO_2$ values acquired during the multiple-PLD pCASL acquisitions. The inhalation of a gas mixture with higher content of CO_2 (hypercapnia) significantly altered individual $PETCO_2$ values with an average increase of approximately 8 mmHg ($p < 0.001$).

Figure 2A shows illustrative images of the ASL difference normalized by the corresponding M_0 image, $\Delta M/M_0$, across time (τ + PLDs) for the two conditions (normocapnia and hypercapnia). The corresponding kinetic curves for a representative voxel highlighted in Figure 2A can be seen in Figure 2B.

Figure 3 shows two illustrative ΔM maps. Several voxels were selected and their corresponding four model fittings for each one of the conditions can be seen. This figure further highlights the different dynamics between conditions and the impact of the different modelling strategies.

Figure 4 displays the CBF, ATT, and aBV maps averaged across subjects, obtained using the four different modelling strategies, and during the two conditions, as well as the corresponding differences in CBF (CVR), ATT (ΔATT) and aBV (ΔaBV) across conditions maps. Representations of illustrative individual CBF, ATT, and aBV maps can be found in the Supplementary Material.

Several differences can be observed across the parameter maps. For instance, when comparing the conditions regardless of the model used, hypercapnia yielded maps showing higher CBF, shorter ATT in most regions, and less-defined areas of thresholded aBV (aBV with lower values).

The tested models also led to differences across the haemodynamic parameter maps. Specifically, for CBF maps, brighter areas localised around the major arteries can be seen in models that do not account for the macrovascular component or dispersion effects. Models that account for dispersion effects also tend to yield lower CBF values across the brain, and the model that includes both the macrovascular component and dispersion effects produced more homogeneous CBF maps in both conditions, and in the CVR maps (CBF difference maps). The CVR maps also show high and unrealistic values in some regions including brain edges and WM regions, but this might be due to low SNR resulting in poor fitting (Figure 3), that is amplified when computing CVR due to the normalization step. These erroneous high CVR regions appear to be less frequent when including the arterial and dispersion components into the model.

Regarding ATT, the occipital and superior areas tend to display higher values in all models/conditions tested in comparison with other brain regions. When using models that include dispersion effects, the corresponding ATT maps show higher contrast between

TABLE 2 Demographic data and $PETCO_2$ values for each subject. Bottom row corresponds to the mean and standard deviation (mean ± SD) across subjects. M stands for male and F for female.

Subject	Age	Sex	$PETCO_2$ normocapnia	$PETCO_2$ hypercapnia	$\Delta PETCO_2$
1	21	M	38.0 ± 0.5	46.2 ± 0.4	8.2
2	21	M	37.8 ± 0.8	44.2 ± 0.4	6.4
3	21	M	42.1 ± 0.8	50.5 ± 0.4	8.4
4	19	M	42.6 ± 0.8	49.8 ± 0.3	7.2
5	20	F	39.3 ± 1.2	47.7 ± 0.5	8.4
6	21	F	33.0 ± 2.8	41.6 ± 0.9	8.6
7	21	F	38.7 ± 0.6	47.3 ± 0.3	8.7
8	21	M	39.9 ± 0.8	47.7 ± 0.3	7.8
9	19	F	38.4 ± 0.9	45.5 ± 1.2	7.1
10	20	F	38.2 ± 0.7	45.5 ± 2.0	7.3
mean ± SD	20.4 ± 0.8	5 F/5 M	38.8 ± 2.6	46.6 ± 2.6	7.8 ± 0.8

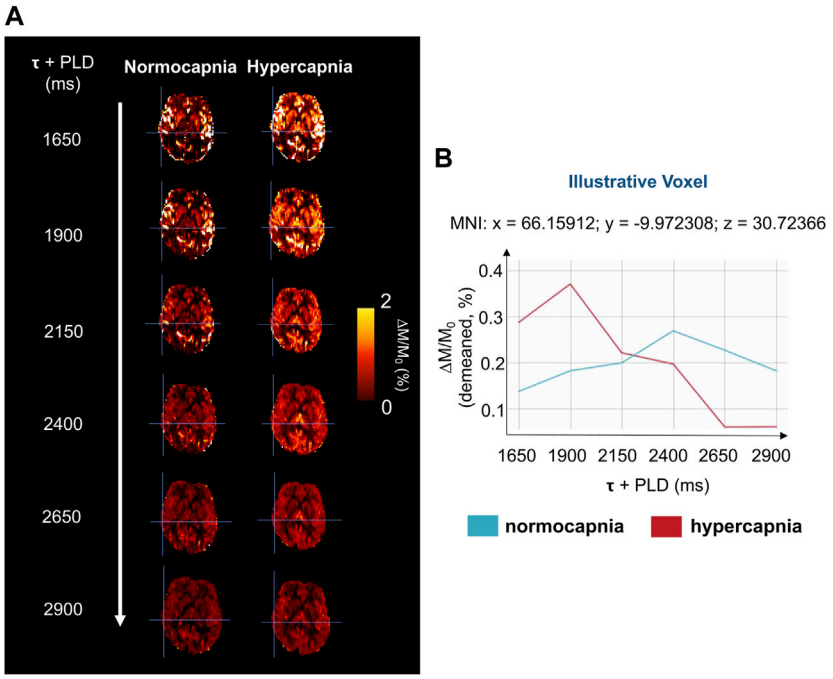

FIGURE 2
(A) Illustrative magnetization difference images (control-label, ΔM) normalized by corresponding calibration image (M_0), of a representative subject and brain slice, throughout the different τ + PLDs. **(B)** Kinetic curves of a representative voxel (highlighted in Figure 2A), for the two gas challenges. The curves have been demeaned for clarity and better visualization.

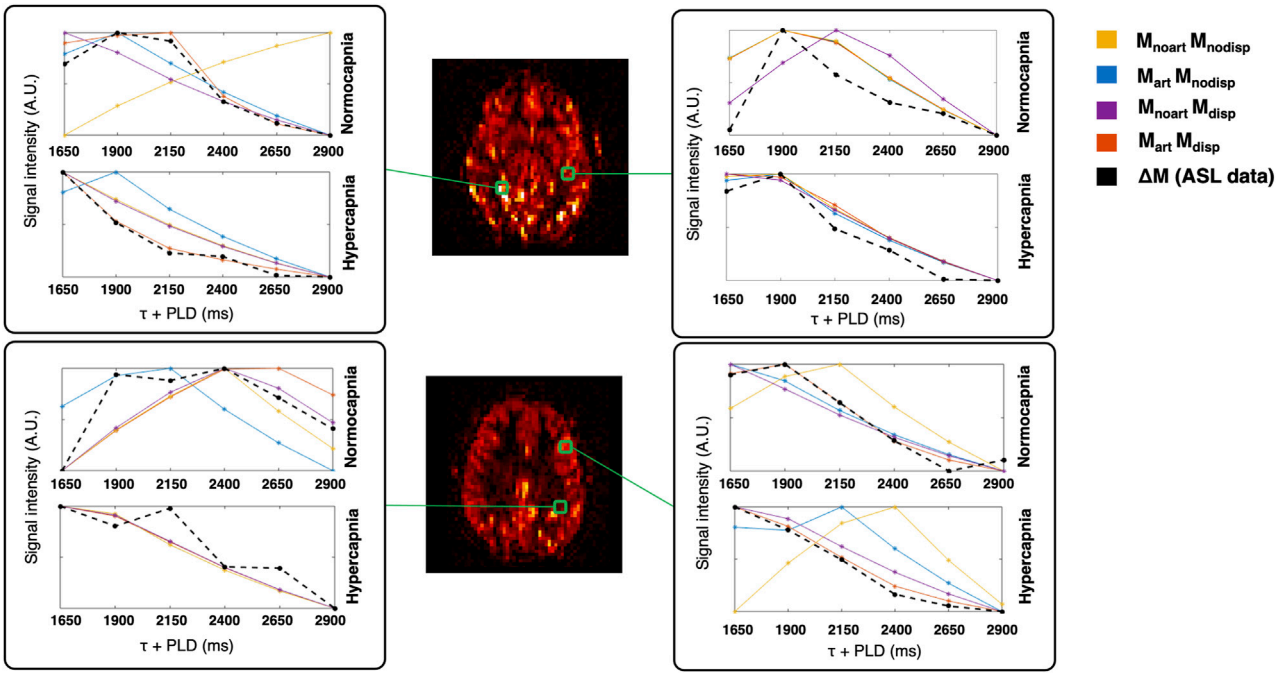

FIGURE 3
Illustrative ΔM maps (two different axial slices, normocapnia, signal intensity in arbitrary units). Four different voxels were selected (green) and the corresponding voxelwise model fittings are displayed in different colours for each condition.

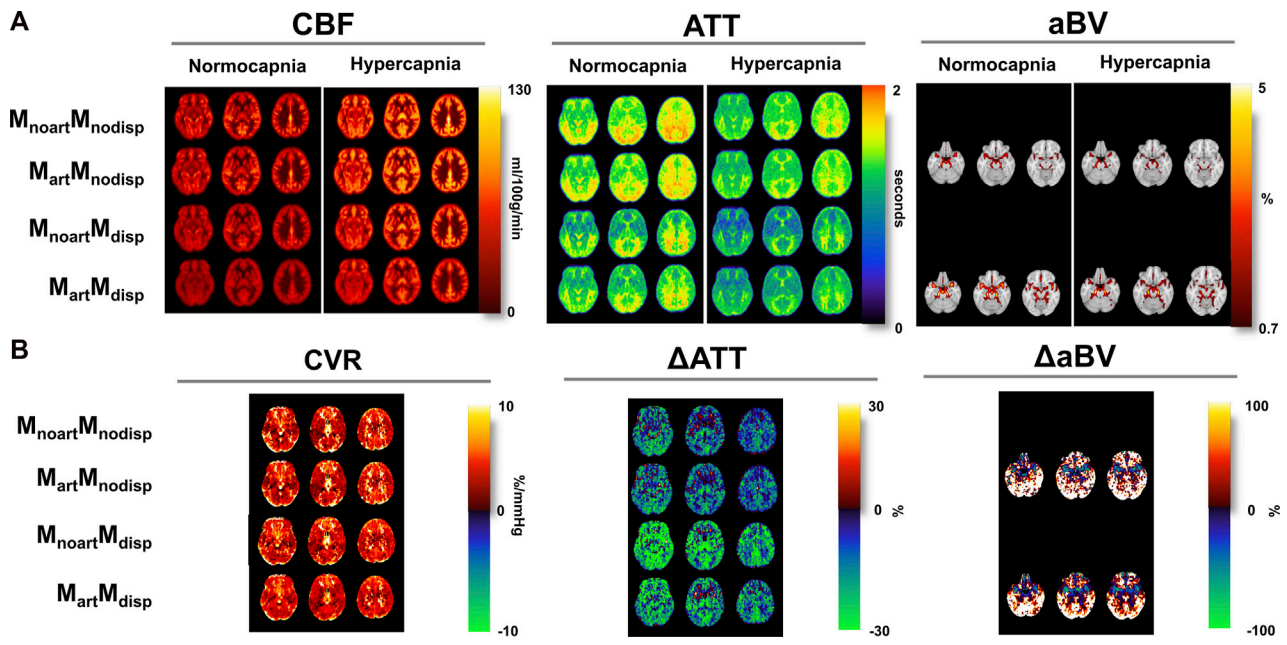

FIGURE 4
(A) Orthogonal representations of group average of the CBF, ATT, and aBV maps for the two conditions (normocapnia and hypercapnia) obtained using different modelling strategies (MNI space). **(B)** CVR, and difference ATT (ΔATT) and aBV (ΔaBV) maps (difference between hypercapnia and normocapnia). aBV and ΔaBV maps were only obtained when using strategies where the macrovascular component was modelled (M_{art}).

specific regions such as GM/WM as well as cortical/sub-cortical areas (e.g., lower ATT in the putamen and globus pallidus). The differences between conditions, displayed by the ΔATT, are higher when using the dispersion models. ΔATT is also higher during hypercapnia (positive values), in some specific frontal areas.

Including dispersion in the modelling also leads to higher aBV areas, in particular, in lateral regions further downstream. The differences between conditions are higher if including dispersion effects into the model.

Figure 5 shows the results of the regional analysis for CBF, ATT, aBV, and FE for each model and condition and the corresponding regional change in CBF (CVR), ΔATT and ΔaBV values between conditions for each model. Statistically significant main effects in CBF were observed for all factors tested (condition, model, and regions), as well as for the interactions between these (all $p \leq 0.01$). Post-hoc comparisons of CBF across models yielded significant differences ($p < 0.05$), except for the inclusion of an arterial component in models that do not account for dispersion ($M_{noart}M_{nodisp}$ and $M_{art}M_{nodisp}$; blue bar plots) in specific regions/conditions (GM changes across the different models in relation to $M_{noart}M_{nodisp}$: ~0.6–22%). Significant main effects in ATT measures were also observed for all factors tested and pairwise interactions ($p < 0.05$). Pairwise comparisons of ATT across models and conditions yielded significant differences ($p < 0.05$) except for $M_{noart}M_{nodisp}$ and $M_{art}M_{nodisp}$ (blue bar plots) and for $M_{noart}M_{disp}$ and $M_{art}M_{disp}$ (red/orange bar plots) in specific regions/conditions (GM changes across the different models in relation to $M_{noart}M_{nodisp}$: ~0.6–19%). For average aBV, significant main effects were obtained for condition and model and their interaction ($p < 0.01$). Pairwise comparisons between the two models were all significant in both conditions (in relation to $M_{art}M_{nodisp}$ ~ 74 and 44% for normocapnia and hypercapnia, respectively). Statistically significant main effects were observed in FE for all factors/interactions ($p < 0.05$), except for factor condition ($p = 0.077$). Regardless of the condition and region tested, significant differences were obtained when comparing models except for $M_{noart}M_{nodisp}$ and $M_{noart}M_{disp}$. The model including dispersion and macrovascular components consistently yields FE values closer to zero across models, i.e., better model fit.

Focusing on differences between conditions, there was a significant main effect for the factor model ($p < 0.01$), but not for factors region/interaction. While CBF changes (CVR) were significantly higher with the model that includes dispersion and the arterial component in specific areas including GM, for ATT the highest changes were obtained when modelling only dispersion, thus there seems to be an interaction between these two modelling options that depends on the parameter estimated.

4 Discussion

In this work, we analysed pCASL data during two conditions (normocapnia and hypercapnia) and using different kinetic models. Our results highlight the different CBF spatiotemporal dynamics across conditions: hypercapnia led to a significant increase in CBF and ATT, whilst aBV decreased significantly. Moreover, parameter quantification was also significantly affected by model selection. Incorporation of dispersion effects yielded a significant decrease in CBF and ATT and aBV increased in both conditions. Overall, the

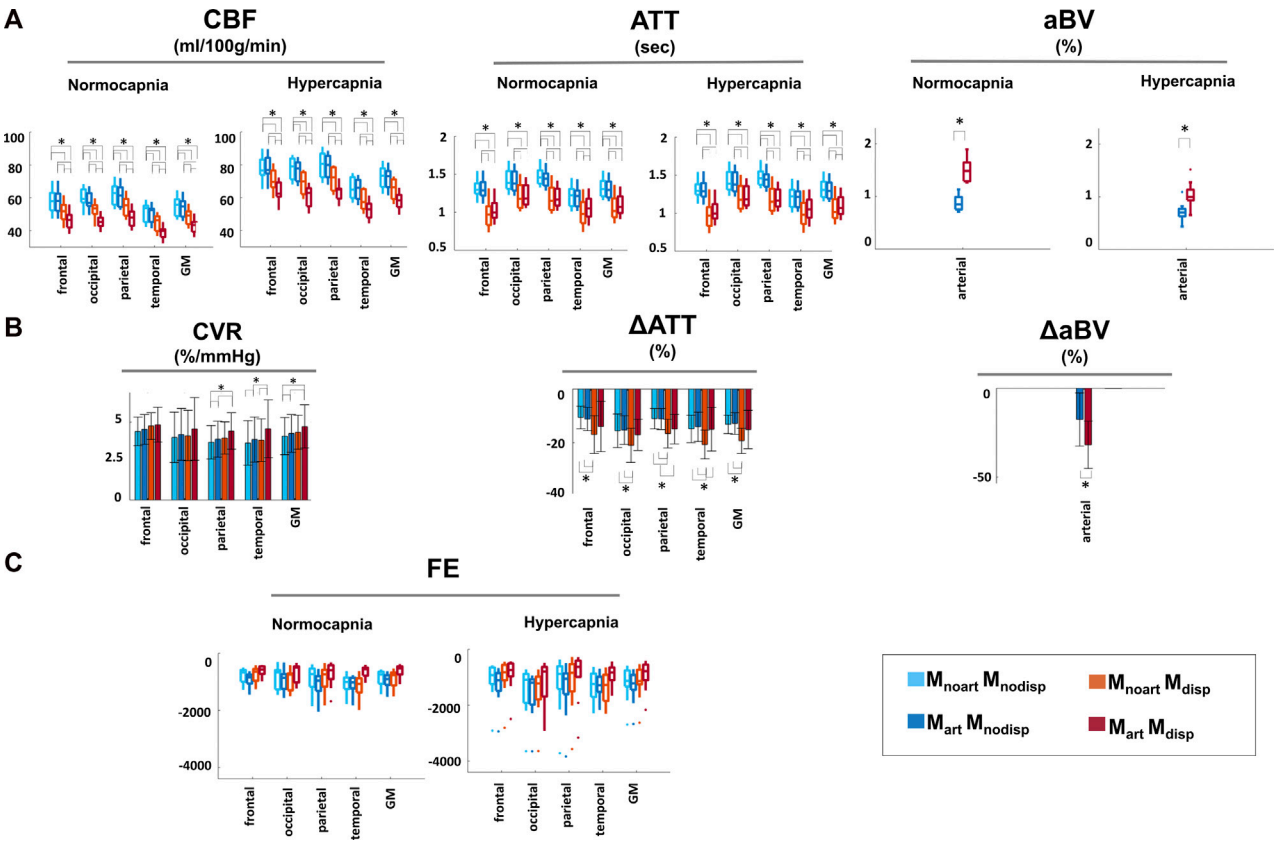

FIGURE 5
Regional analysis of: **(A)** CBF, ATT, and aBV with the different modelling strategies and conditions. **(B)** Percentage change of CBF, ATT and aBV normocapnia vs. hypercapnia. CVR corresponds to CBF change normalized against the change in the individual $PETCO_2$ level (%/mmHg). **(C)** Regional FE for each of the different modelling strategies and conditions Statistically significant results ($p < 0.05$) are highlighted with *.

extended model that includes dispersion effects and the macrovascular component provides the best fit to both datasets (in terms of FE).

4.1 Data acquisition and gas challenge

Hypercapnia was attained through a respiratory challenge that increased the CO_2 content of arterial blood by applying a prospective end-tidal targeting and maintenance method using a computer-controlled gas blender. This approach has been shown to be a robust and reliable way to prospectively induce changes in the arterial blood CO_2 content, whilst targeting and maintaining stable O_2 levels (Fierstra et al., 2013). Although the target value of an increase of 10 mmHg to each subject's baseline $PETCO_2$ was not attained, all subjects completed the gas challenge and experienced a similar $PETCO_2$ change within a standard deviation of 0.8 mmHg (Table 2). The two conditions yielded statistically significantly different $PETCO_2$ average values ($p < 0.01$) (Table 2).

4.2 Impact of different conditions on CBF dynamics quantification

Although literature on the effect of hypercapnia using multiple-PLD ASL is still limited, our results are in agreement with other reports that confirm a change in CBF dynamics with an increase in amplitude and a faster response due to hypercapnia (Donahue et al., 2016). These different dynamics can be perceived even before model fitting, as illustrated by the $\Delta M/M_0$ maps and curves of the two conditions (Figure 2), and during model fitting (Figure 3).

Our quantitative changes of CBF (~33%) and ATT (~15%) are slightly higher than the ones previously reported, although these differences might be partially explained by the different stimuli and processing analyses used. Donahue et al. reported reductions in ATT in the order of 4.6%–7.7% and a CBF increase of 8.2%–27.8% when using a pCASL sequence with a fixed-inspired challenge (inspired fraction of 5%) (Donahue et al., 2016), while Ho and others observed a GM CBF increase of around 21% and an ATT decrease in the GM of approximately 5% when using an ASL-QUASAR strategy in combination with an increase in $PETCO_2$ content by a third of the subject's baseline (~14 mm Hg) (Ho et al., 2011).

The spatiotemporal patterns in the dynamics during hypercapnia are also in line with previous reports (MacIntosh et al., 2010; Donahue et al., 2014). While the impact of hypercapnia on CBF appears to be statistically significant across the brain, for ATT, hypercapnia appears to mainly affect posterior and lateral regions, without statistically significant changes in frontal regions. Other ASL studies have also indicated prolonged ATT in border zone regions between the major cerebral artery territories

(Petersen et al., 2010), highlighting the dependence of these areas on the individual vascular architecture and geometry (Wong et al., 1997).

The arterial component during hypercapnia also seems to be lower and less defined than during normocapnia. This can be explained by the increased flow velocity in arteries resulting in the tagged blood arriving earlier in combination with the non-optimal ASL sampling scheme in terms of PLDs during hypercapnia. Ho et al. also investigated the impact of hypercapnia on the arterial component, observing dissociations in the dynamics between large vessels and GM. In particular, there were significant changes in the aBV of the larger arteries (~11%) and this difference was approximately half of the CBF increase (Ho et al., 2011).

4.3 Impact of model strategies on CBF dynamics quantification during different conditions

To our knowledge, this is the first study to assess the individual and combined impact of modelling dispersion and macrovascular components in multiple-PLD ASL haemodynamic parameter quantification during hypercapnia. Our results highlight the influence of modelling strategies on parameter quantification, even when not taking different conditions into account, which is in line with previous reports. In particular, the inclusion of dispersion into the model yielded lower CBF, ATT, and higher aBV, while more arterial signal was fitted, particularly in arteries further downstream. This can be seen visually in the parameter maps of Figure 4, where including dispersion led to less variable CBF maps in both conditions, while correcting for macrovascular areas. In fact, there seems to be an interaction between these two modelling aspects, with no significant difference in parameter quantification when introducing a macrovascular component in most regions/conditions if dispersion is not included. If dispersion is already included, adding the macrovascular component leads to significant differences in parameter quantification, with an overall decrease in CBF and an increase in ATT, likely due to better tissue and arterial signal separation. This is confirmed by the signal changes when comparing the two conditions, as CBF changes between conditions (CVR) are higher when including the arterial component, while for ATT are higher without including this component.

The impact of including dispersion also appears to be region dependent. For instance, the contrast between WM in relation to cortical GM seems to be higher when introducing dispersion into the model which is in line with the expectation that the impact of dispersion modelling will be more pronounced deeper into the vascular tree, hence, introducing this component might improve modelling and ATT quantification across WM (Figure 4). Subcortical GM areas also tend to display a different profile ratio in relation to cortical GM when including dispersion, where ATT values in subcortical areas are lower than in cortical areas.

Similarly, the impact of modelling strategies in parameter changes due to hypercapnia are also model and region dependent. For example, while the CBF changes when using $M_{noart}M_{disp}$ or $M_{art}M_{disp}$ in the frontal area are not significantly different, for other areas such as temporal or occipital regions, these two models yield significant differences. These regional differences and model/parameter dependencies might be due to the distinctive dynamics of blood coming from different main feeding arteries and their interaction with model fitting. Including both the dispersion and the macrovascular component seems to incorporate/alleviate some of these vascular differences.

The arterial component is also better distinguished when adding dispersion into the model, particularly in regions further downstream, which is in line with the assumption of a higher impact of dispersion modelling in deeper areas within the vascular tree. This effect seems to be higher during normocapnia, as the increase in blood velocity due to hypercapnia possibly makes the multi-PLD sampling scheme not optimised for this condition, as the earliest PLD might be too long to accurately detect the macrovascular contribution.

Moreover, our FE values also support the application of the model that includes dispersion and the macrovascular component, since this combination yielded the FE values closest to zero across models and conditions (i.e., better fit to the data). Although, the CVR maps obtained seem to be similar across the models tested, the model that includes both dispersion and the macrovascular component appears to create maps with lower variability, also yielding significantly higher regional values of CVR when compared with the other models.

Most of these parameter quantification differences due to modelling strategies are in line with previous reports on normocapnia (Zhang et al., 2021; van der Plas et al., 2022). A recent study comparing different ASL sequence optimization strategies in normocapnia, showed that sequences optimized for both ATT and CBF estimation are sensitive to macrovascular signal and that including dispersion effects and the macrovascular component leads to significant decreases in CBF and ATT estimation errors (Zhang et al., 2021).

As seen in other ASL studies, our CVR maps also do not display the clear GM/WM contrast commonly seen in BOLD CVR maps. Some studies argue that the tissue difference in BOLD CVR maps might be the result of the complex interaction between several physiological parameters, and the lack of differences in ASL might be reasonable as both baseline CBF and CBF induced changes by hypercapnia might be lower in WM (Taneja et al., 2019).

4.4 Limitations and future work

Although differences between parameters across conditions and models were observed and quantified, a major limitation of this work is the lack of a gold standard measure to compare our results with. In the future, a comparison with other methodologies such as PET imaging should be performed (Zhao et al., 2021). Additionally, although hypercapnic stimuli are commonly used for CVR mapping, some pathological conditions might mimic the spatiotemporal changes in CBF dynamics seen with hypercapnia (for example, if the basal vascular tone is altered or arterial blood velocities are reduced (Bright et al., 2011)). Another major limitation of this work is the small sample size (n = 10). Additionally, some of the analysis options used in this work were dependent on the ASL acquisition parameters/strategies. Given the faster flow in large arteries and the earlier arrival times of labelled blood during hypercapnia, it might be important to investigate the impact of optimising the ASL sampling scheme when acquiring data during this condition (Woods et al., 2019). Regarding the macrovascular signal, alternative strategies can be used to remove this component during

acquisition, such as including the use of flow crusher gradients. However, this approach has been discouraged (Alsop et al., 2015) and by removing this component, important clinical information might be overlooked. Another aspect that warrants further investigation is the large variability in anatomical features across and within individuals (different vascular architecture and territories) and its impact on ASL modelling, particularly in dispersion effects. Including a combination of functional and structural information might be beneficial to better model the ASL signal by taking these vascular differences into account (Li et al., 2018). Conflicting results have been reported when comparing the impact of blood flow velocity on ASL imaging (Aslan et al., 2010; Heijtel et al., 2014; Dolui et al., 2016). Although these differences can impact CVR results, these will not affect our conclusions regarding the impact of the different model strategies within each conditions, as the effect of the different labelling efficiencies will be the same across the models tested.

Importantly, our observations regarding the impact of the different models on parameter quantification can also have implications when evaluating CBF in pathologies. In several conditions, including steno-occlusive diseases, brain tumors or arteriovenous malformations (Amemiya et al., 2022; Hirschler et al., 2023), the dynamics of blood vessels and flow are known to be altered and these will likely depend on the degree of disease severity and underlying etiology. In those cases, using multi-PLD ASL strategies in combination with modelling strategies that take into account these differences, including models with dispersion and macrovascular component, might be beneficial for a more accurate estimation of CBF parameters. Further work on ASL modelling strategies should focus on translating/validating these findings in clinical applications.

5 Conclusion

This work highlights the significance of acquiring ASL data using a multiple-PLD approach to allow a larger flexibility in ASL parameter estimation, and the critical aspect of making anatomically and physiologically valid assumptions when modelling ASL data. Here we recommend the use of extended models that include the macrovascular component and dispersion effects when modelling multiple-PLD pCASL data. This is of particular importance when imaging abnormal states such as increased or decreased global CBF as induced by respiratory challenges or vasoactive substances, or in subjects with pathologies that may impact their cerebral perfusion.

Data availability statement

The datasets presented in this study can be found in online repositories. The names of the repository/repositories and accession number (s) can be found below: Oxford Research Archive Repository, https://doi.org/10.5287/bodleian:Xk48adQAO.

Ethics statement

The studies involving human participants were reviewed and approved by the Central University Research Ethics Committee (CUREC) at the University of Oxford. The patients/participants provided their written informed consent to participate in this study.

Author contributions

NB, JH, and DB performed data acquisition. JP performed data analysis and produced the first draft of the manuscript. All authors contributed to the manuscript revision and editing and approved the submitted version.

Funding

This work was supported by Engineering and Physical Sciences Research Council (EPSRC) grants EP/S021507/1 and EP/K025716/1.

Conflict of interest

The authors declare that the research was conducted in the absence of any commercial or financial relationships that could be construed as a potential conflict of interest.

Publisher's note

Supplementary material

The Supplementary Material for this article can be found online at: https://www.frontiersin.org/articles/10.3389/fphys.2023.1142359/full#supplementary-material

References

Alsop, D. C., Detre, J. A., Golay, X., Günther, M., Hendrikse, J., Hernandez-Garcia, L., et al. (2015). Recommended implementation of arterial spin-labeled perfusion MRI for clinical applications: A consensus of the ismrm perfusion study group and the European consortium for ASL in dementia. *Magn. Reson. Med.* 73, 102–116. doi:10.1002/mrm.25197

Amemiya, S., Takao, H., Watanabe, Y., Takei, N., Ueyama, T., Kato, S., et al. (2022). Reliability and sensitivity to longitudinal CBF changes in steno-occlusive diseases: ASL versus 123I-IMP-SPECT. *J. Magn. Reson. Imaging* 55, 1723–1732. doi:10.1002/JMRI.27996

Andersson, J., Jenkinson, M., and Smith, S. (2007). *Non-linear registration aka Spatial normalisation*. United Kingdom: FMRIB Technical Report TR07 JA2.

Aslan, S., Xu, F., Wang, P. L., Uh, J., Yezhuvath, U. S., Van Osch, M., et al. (2010). Estimation of labeling efficiency in pseudocontinuous arterial spin labeling. *Magn. Reson. Med.* 63, 765–771. doi:10.1002/mrm.22245

Blockley, N., Harkin, J., Stone, A., and Bulte, D. (2016). *Data acquired to investigate new approaches to cerebrovascular reactivity mapping using MRI*. Oxford: ORA - Oxford

Univ. Res. Arch. Available at: https://ora.ox.ac.uk/objects/uuid:1801af1b-4872-40da-92df-a9ecbe839e4f (Accessed 5 5, 22).

Blockley, N. P., Harkin, J. W., and Bulte, D. P. (2017). Rapid cerebrovascular reactivity mapping: Enabling vascular reactivity information to be routinely acquired. *Neuroimage* 159, 214–223. doi:10.1016/J.NEUROIMAGE.2017.07.048

Bright, M. G., Donahue, M. J., Duyn, J. H., Jezzard, P., and Bulte, D. P. (2011). The effect of basal vasodilation on hypercapnic and hypocapnic reactivity measured using magnetic resonance imaging. *J. Cereb. Blood Flow. Metab.* 31, 426–438. doi:10.1038/jcbfm.2010.187

Buxton, R. B., Frank, L. R., Wong, E. C., Siewert, B., Warach, S., and Edelman, R. R. (1998). A general kinetic model for quantitative perfusion imaging with arterial spin labeling. *Magn. Reson. Med.* 40, 383–396. doi:10.1002/mrm.1910400308

Catchlove, S. J., Pipingas, A., Hughes, M. E., and Macpherson, H. (2018). Magnetic resonance imaging for assessment of cerebrovascular reactivity and its relationship to cognition: A systematic review. *BMC Neurosci.* 19, 21–15. doi:10.1186/s12868-018-0421-4

Chappell, M. A., Groves, A. R., Whitcher, B., and Woolrich, M. W. (2009). Variational bayesian inference for a nonlinear forward model. *IEEE Trans. Signal Process.* 57, 223–236. doi:10.1109/TSP.2008.2005752

Chappell, M. A., MacIntosh, B. J., Donahue, M. J., Günther, M., Jezzard, P., and Woolrich, M. W. (2010). Separation of macrovascular signal in multi-inversion time arterial spin labelling MRI. *Magn. Reson. Med.* 63, 1357–1365. doi:10.1002/mrm.22320

Chappell, M. A., Woolrich, M. W., Kazan, S., Jezzard, P., Payne, S. J., and MacIntosh, B. J. (2013). Modeling dispersion in arterial spin labeling: Validation using dynamic angiographic measurements. *Magn. Reson. Med.* 69, 563–570. doi:10.1002/mrm.24260

Chen, J. J. (2018). Cerebrovascular-reactivity mapping using MRI: Considerations for Alzheimer's disease. *Front. Aging Neurosci.* 11, 170–179. doi:10.3389/fnagi.2018.00170

De Vis, J. B., Bhogal, A. A., Hendrikse, J., Petersen, E. T., and Siero, J. C. W. (2018). Effect sizes of BOLD CVR, resting-state signal fluctuations and time delay measures for the assessment of hemodynamic impairment in carotid occlusion patients. *Neuroimage* 179, 530–539. doi:10.1016/j.neuroimage.2018.06.017

Dolui, S., Wang, Z., Wang, D. J. J., Mattay, R., Finkel, M., Elliott, M., et al. (2016). Comparison of non-invasive MRI measurements of cerebral blood flow in a large multisite cohort. *J. Cereb. Blood Flow. Metab.* 36, 1244–1256. doi:10.1177/0271678X16646124

Donahue, M. J., Faraco, C. C., Strother, M. K., Chappell, M. A., Rane, S., Dethrage, L. M., et al. (2014). Bolus arrival time and cerebral blood flow responses to hypercarbia. *J. Cereb. Blood Flow. Metab.* 34, 1243–1252. doi:10.1038/jcbfm.2014.81

Donahue, M. J., Strother, M. K., Lindsey, K. P., Hocke, L. M., Tong, Y., and Frederick, B. deB. (2016). Time delay processing of hypercapnic fMRI allows quantitative parameterization of cerebrovascular reactivity and blood flow delays. *J. Cereb. Blood Flow. Metab.* 36, 1767–1779. doi:10.1177/0271678X15608643

Fierstra, J., Sobczyk, O., Battisti-Charbonney, A., Mandell, D. M., Poublanc, J., Crawley, A. P., et al. (2013). Measuring cerebrovascular reactivity: What stimulus to use? *J. Physiol.* 591, 5809–5821. doi:10.1113/jphysiol.2013.259150

Gallichan, D., and Jezzard, P. (2008). Modeling the effects of dispersion and pulsatility of blood flow in pulsed arterial spin labeling. *Magn. Reson. Med.* 60, 53–63. doi:10.1002/mrm.21654

Haller, S., Zaharchuk, G., Thomas, D. L., Lovblad, K. O., Barkhof, F., and Golay, X. (2016). Arterial spin labeling perfusion of the brain: Emerging clinical applications. *Radiology* 281, 337–356. doi:10.1148/RADIOL.2016150789

Heijtel, D. F. R., Mutsaerts, H. J. M. M., Bakker, E., Schober, P., Stevens, M. F., Petersen, E. T., et al. (2014). Accuracy and precision of pseudo-continuous arterial spin labeling perfusion during baseline and hypercapnia: A head-to-head comparison with ^{15}O H_2O positron emission tomography. *Neuroimage* 92, 182–192. doi:10.1016/j.neuroimage.2014.02.011

Hirschler, L., Sollmann, N., Schmitz-Abecassis, B., Pinto, J., Arzanforoosh, F., Barkhof, F., et al. (2023). Advanced MR techniques for preoperative glioma characterization: Part 1. *J. Magn. Reson. Imaging* 2023, 28662. doi:10.1002/JMRI.28662

Ho, Y. C. L., Petersen, E. T., Zimine, I., and Golay, X. (2011). Similarities and differences in arterial responses to hypercapnia and visual stimulation. *J. Cereb. Blood Flow. Metab.* 31, 560–571. doi:10.1038/JCBFM.2010.126

Jenkinson, M., Bannister, P., Brady, M., and Smith, S. (2002). Improved optimization for the robust and accurate linear registration and motion correction of brain images. *Neuroimage* 17, 825–841. doi:10.1016/s1053-8119(02)91132-8

Jenkinson, M., Beckmann, C. F., Behrens, T. E. J., Woolrich, M. W., and Smith, S. M. (2012). *FSL. Neuroimage* 62, 782–790. doi:10.1016/j.neuroimage.2011.09.015

Kazan, S. M., Chappell, M. A., and Payne, S. J. (2009). Modeling the effects of flow dispersion in arterial spin labeling. *IEEE Trans. Biomed. Eng.* 56, 1635–1643. doi:10.1109/TBME.2009.2016977

Li, Y., Mao, D., Li, Z., Schär, M., Pillai, J. J., Pipe, J. G., et al. (2018). Cardiac-triggered pseudo-continuous arterial-spin-labeling: A cost-effective scheme to further enhance the reliability of arterial-spin-labeling MRI. *Magn. Reson. Med.* 80, 969–975. doi:10.1002/MRM.27090

Lindner, T., Bolar, D. S., Achten, E., Barkhof, F., Bastos-Leite, A. J., Detre, J. A., et al. (2023). Current state and guidance on arterial spin labeling perfusion MRI in clinical neuroimaging. *Magn. Reson. Med.* 89, 2024–2047. doi:10.1002/MRM.29572

MacIntosh, B. J., Lindsay, A. C., Kylintireas, I., Kuker, W., Gunther, M., Robson, M. D., et al. (2010). Multiple inflow pulsed arterial spin-labeling reveals delays in the arterial arrival time in minor stroke and transient ischemic attack. *Am. J. Neuroradiol.* 31, 1892–1894. doi:10.3174/ajnr.A2008

Mandell, D. M., Han, J. S., Poublanc, J., Crawley, A. P., Kassner, A., Fisher, J. A., et al. (2008). Selective reduction of blood flow to white matter during hypercapnia corresponds with leukoaraiosis. *Stroke* 39, 1993–1998. doi:10.1161/STROKEAHA.107.501692

Mazziotta, J., Toga, A., Evans, A., Fox, P., Lancaster, J., Zilles, K., et al. (2001). A probabilistic atlas and reference system for the human brain: International Consortium for Brain Mapping (ICBM). *Philos. Trans. R. Soc. B Biol. Sci.* 356, 1293–1322. doi:10.1098/rstb.2001.0915

Moreton, F. C., Dani, K. A., Goutcher, C., O'Hare, K., and Muir, K. W. (2016). Respiratory challenge MRI: Practical aspects. *NeuroImage Clin.* 11, 667–677. doi:10.1016/j.nicl.2016.05.003

Okell, T. W., Chappell, M. A., Kelly, M. E., and Jezzard, P. (2013). Cerebral blood flow quantification using vessel-encoded arterial spin labeling. *J. Cereb. Blood Flow. Metab.* 33, 1716–1724. doi:10.1038/jcbfm.2013.129

Petersen, E. T., Mouridsen, K., and Golay, X. (2010). The QUASAR reproducibility study, Part II: Results from a multi-center Arterial Spin Labeling test-retest study. *Neuroimage* 49, 104–113. doi:10.1016/j.neuroimage.2009.07.068

Pinto, J., Bright, M. G., Bulte, D. P., and Figueiredo, P. (2021). Cerebrovascular reactivity mapping without gas challenges: A methodological guide. *Front. Physiol.* 11, 608475. doi:10.3389/fphys.2020.608475

Pinto, J., Chappell, M. A., Okell, T. W., Mezue, M., Segerdahl, A. R., Tracey, I., et al. (2020). Calibration of arterial spin labeling data—Potential pitfalls in post-processing. *Magn. Reson. Med.* 83, 1222–1234. doi:10.1002/mrm.28000

Slessarev, M., Han, J., Mardimae, A., Prisman, E., Preiss, D., Volgyesi, G., et al. (2007). Prospective targeting and control of end-tidal CO2 and O2 concentrations. *J. Physiol.* 581, 1207–1219. doi:10.1113/jphysiol.2007.129395

Smith, S. (2002). Fast robust automated brain extraction. *Hum. Brain Mapp.* 17, 143–155. doi:10.1002/hbm.10062

Sobczyk, O., Battisti-Charbonney, A., Poublanc, J., Crawley, A. P., Sam, K., Fierstra, J., et al. (2015). Assessing cerebrovascular reactivity abnormality by comparison to a reference atlas. *J. Cereb. Blood Flow. Metab.* 35, 213–220. doi:10.1038/JCBFM.2014.184

Taneja, K., Lu, H., Welch, B. G., Thomas, B. P., Pinho, M., Lin, D., et al. (2019). Evaluation of cerebrovascular reserve in patients with cerebrovascular diseases using resting-state MRI: A feasibility study. *Magn. Reson. Imaging* 59, 46–52. doi:10.1016/j.mri.2019.03.003

van der Plas, M. C. E., Craig, M., Schmid, S., Chappell, M. A., and van Osch, M. J. P. (2022). Validation of the estimation of the macrovascular contribution in multi-timepoint arterial spin labeling MRI using a 2-component kinetic model. *Magn. Reson. Med.* 87, 85–101. doi:10.1002/MRM.28960

Wong, E. C., Buxton, R. B., and Frank, L. R. (1997). Implementation of quantitative perfusion imaging techniques for functional brain mapping using pulsed arterial spin labeling. *NMR Biomed.* 10, 237–249. doi:10.1002/(sici)1099-1492(199706/08)10:4/5<237:aid-nbm475>3.0.co;2-x

Woods, J. G., Chappell, M. A., and Okell, T. W. (2019). A general framework for optimizing arterial spin labeling MRI experiments. *Magn. Reson. Med.* 81, 2474–2488. doi:10.1002/MRM.27580

Wu, W. C., Mazaheri, Y., and Wong, E. C. (2007). The effects of flow dispersion and cardiac pulsation in arterial spin labeling. *IEEE Trans. Med. Imaging* 26, 84–92. doi:10.1109/TMI.2006.886807

Zhang, L. X., Woods, J. G., Okell, T. W., and Chappell, M. A. (2021). Examination of optimized protocols for pCASL: Sensitivity to macrovascular contamination, flow dispersion, and prolonged arterial transit time. *Magn. Reson. Med.* 86, 2208–2219. doi:10.1002/MRM.28839

Zhang, Y., Brady, M., and Smith, S. (2001). Segmentation of brain MR images through a hidden Markov random field model and the expectation-maximization algorithm. *IEEE Trans. Med. Imaging* 20, 45–57. doi:10.1109/42.906424

Zhao, M. Y., Fan, A. P., Chen, D. Y. T., Sokolska, M. J., Guo, J., Ishii, Y., et al. (2021). Cerebrovascular reactivity measurements using simultaneous 15 O-water PET and ASL MRI: Impacts of arterial transit time, labeling efficiency, and hematocrit. *Neuroimage* 233, 117955. doi:10.1016/J.NEUROIMAGE.2021.117955

frontiers | Frontiers in Physiology

TYPE Original Research
PUBLISHED 20 July 2023
DOI 10.3389/fphys.2023.1240992

OPEN ACCESS

EDITED BY
Alex Bhogal,
Utrecht University, Netherlands

REVIEWED BY
Alan C. Seifert,
Icahn School of Medicine at Mount Sinai, United States
Danny J. J. Wang,
University of Southern California, United States

*CORRESPONDENCE
Lisa C. Krishnamurthy,
lkrishnamurthy@gsu.edu

RECEIVED 15 June 2023
ACCEPTED 11 July 2023
PUBLISHED 20 July 2023

CITATION
Krishnamurthy LC, Glassman C, Han JH, Song SE, Denmon C, Weatherill M, Rodriguez AD, Crosson BA and Krishnamurthy V (2023), ASL MRI informs blood flow to chronic stroke lesions in patients with aphasia.
Front. Physiol. 14:1240992.
doi: 10.3389/fphys.2023.1240992

ASL MRI informs blood flow to chronic stroke lesions in patients with aphasia

Lisa C. Krishnamurthy[1,2,3,4]*, Clara Glassman[1], Joo H. Han[1], Serena E. Song[1], Chanse Denmon[1], Maryanne Weatherill[1], Amy D. Rodriguez[1,5], Bruce A. Crosson[1,5] and Venkatagiri Krishnamurthy[5,6,7]

[1]Center for Visual and Neurocognitive Rehabilitation, Atlanta VA Health Care System, Decatur, GA, United States, [2]Joint GSU, Georgia Tech, and Emory Center for Translational Research in Neuroimaging and Data Science (TReNDS), Atlanta, GA, United States, [3]Department of Physics and Astronomy, Georgia State University, Atlanta, GA, United States, [4]Department of Radiology and Imaging Sciences, Emory University, Atlanta, GA, United States, [5]Department of Neurology, Emory University, Atlanta, GA, United States, [6]Division of Geriatrics and Gerontology, Department of Medicine, Emory University, Atlanta, GA, United States, [7]Department of Veterans Affairs (VA) Health Care System, Decatur, GA, United States

Introduction: Response to post-stroke aphasia language rehabilitation is difficult to anticipate, mainly because few predictors can help identify optimal, individualized treatment options. Imaging techniques, such as Voxel-based Lesion Symptom Mapping have been useful in linking specific brain areas to language behavior; however, further development is required to optimize the use of structural and physiological information in guiding individualized treatment for persons with aphasia (PWA). In this study, we will determine if cerebral blood flow (CBF) mapped in patients with chronic strokes can be further used to understand stroke-related factors and behavior.

Methods: We collected perfusion MRI data using pseudo-Continuous Arterial Spin Labeling (pCASL) using a single post-labeling delay of 2,200 ms in 14 chronic PWA, along with high-resolution structural MRI to compute maps of tissue damage using Tissue Integrity Gradation via T2w T1w Ratio (TIGR). To quantify the CBF in chronic stroke lesions, we tested at what point spatial smoothing should be applied in the ASL analysis pipeline. We then related CBF to tissue damage, time since stroke, age, sex, and their respective cross-terms to further understand the variability in lesion CBF. Finally, we assessed the feasibility of computing multivariate brain-behavior maps using CBF and compared them to brain-behavior maps extracted with TIGR MRI.

Results: We found that the CBF in chronic stroke lesions is significantly reduced compared to its homologue grey and white matter regions. However, a reliable CBF signal (although smaller than expected) was detected to reveal a negative relationship between CBF and increasing tissue damage. Further, the relationship between the lesion CBF and age, sex, time since stroke, and tissue damage and cross-terms suggested an aging-by-disease interaction. This relationship was strongest when smoothing was applied in the template space. Finally, we show that whole-brain CBF relates to domain-general visuospatial functioning in PWA. The CBF-based brain-behavior maps provide unique and complementary information to structural (lesion-based) brain-behavior maps.

Discussion: Therefore, CBF can be detected in chronic stroke lesions using a standard pCASL MRI acquisition and is informative at the whole-brain level in

identifying stroke rehabilitation targets in PWAs due to its relationship with demographic factors, stroke-related factors, and behavior.

KEYWORDS

chronic stroke lesion, cerebral blood flow, TIGR MRI, brain-behavior maps, stroke rehabilitation targets

Introduction

The most common cause of acquired language impairment (also known as aphasia) is stroke. Aphasia presents in up to 40% of people who experience acute strokes and persists in approximately 61% of individuals after 1 year (Pedersen et al., 2004). Unfortunately, response to post-stroke aphasia rehabilitation is variable, and identifying the best treatment options for a specific patient has been difficult. Researchers are increasingly using structural and functional imaging to inform and augment treatment development, which heralds improved language outcomes (Meinzer et al., 2011; Crosson et al., 2017; Crosson et al., 2019). However, using imaging data to inform clinical decisions is still in its infancy. A review of imaging studies in aphasia reveals that a diverse range of lesion locations and subsequent brain physiology changes hamper efforts to select appropriate interventions to optimize treatment outcomes (Charidimou et al., 2014). However, there is evidence that mapping each patient's unique brain anatomy (structural imaging) and physiology (cerebral blood flow imaging) to their language deficits (Fridriksson, 2010) could result in more individualized intervention.

Several imaging methodologies can provide associations between lesion location and language behavior, including Voxel-based Lesion Symptom Mapping (VLSM), which has been popular in stroke research since Bates et al. (2003) introduced the method in 2003. The technique acquires detailed images of the patient's brain using high-resolution T1-weighted (T1w) anatomical Magnetic Resonance Imaging (MRI) scans. An experienced neuroimager then can manually demarcate the lesion. The area of the lesion is transformed into a subject-specific binary mask and entered into a t-test analysis to define which lesion location corresponds to specific language deficits. VLSM is an elegant algorithm that defines structure-behavior associations and implicitly takes advantage of the heterogeneity of language behavior and lesion location. Using functional and structural imaging to study persons with aphasia (PWA) facilitates linking a specific brain area to specific language behaviors and deficits. VLSM (Bates et al., 2003), is a simple yet elegant method used to define structure-behavior associations. However, the technique has several limitations in that it depends on binary "all-or-nothing" lesion masks to define areas of structural compromise and does not offer a comprehensive picture of brain health.

In 2005, Tyler et al. (2005) advanced VLSM by discarding the binary lesion masking step by correlating the continuous T1w image signal intensity with continuous language measures. According to Tyler et al. (2005), judging whether cortical tissue is intact or damaged with an "all-or-none distinction fails to capture a much larger range of potentially informative gradations in the degree of structural damage." This is a reasonable assessment, as the damage from stroke is not limited to the Cerebral Spinal Fluid (CSF) filled cavitation, and includes regions of gliosis and Wallerian degeneration, all with varying impact on behavior. It was demonstrated that T1w image signal intensity has high correlations with word processing abilities using a lexical decision task. Though the small number of subjects ($n = 19$) could have led to issues with statistical power (Kimberg et al., 2007), this study established the feasibility and utility of correlating the MRI signal intensity with language behavior. Despite this important step forward, the methodology of using the T1w signal has some limitations in the MRI signal normalization process, as it is dependent on highly variable anatomical attributes across stroke survivors. To address the methodological issues from Tyler et al. (2005), we developed Tissue Integrity Gradation via T2w T1w Ratio (TIGR) MRI (Krishnamurthy et al., 2021) by using a ratio of T2w and T1w signals and by normalizing the signals using bounds determined by the grey matter and cerebrospinal fluid signal intensities of intact regions. Therefore, regardless of atrophy, headsize, or coil loading characteristics, the normalization procedure in TIGR is comparable across all participants within a cohort and does not require a control sample of intact brains to perform the analysis.

Although the predominant line of thinking by clinicians and scientists alike is that everything within the stroke lesion is necrotic, we have evidence that this may not be the case. Using Tissue Integrity Gradation via T2w T1w Ratio (TIGR) MRI, we can objectively identify the necrotic cavitation and surrounding pericavitational regions within the lesion (Krishnamurthy et al., 2021). The pericavitational regions are defined as "damaged tissue within the lesion surrounding the core cavitation that may still contain living cell bodies" and have been observed in animal and *in vitro* models (Clarkson et al., 2010; Anderson et al., 2014; Burda and Sofroniew, 2014; Adams and Gallo, 2018; Joy and Carmichael, 2021). The pericavitational regions can be engaged using task fMRI, are functionally connected at rest to the remaining brain network and demonstrate evidence of residual blood flow to the lesion (Krishnamurthy et al., 2021). One downside to using only structural imaging to assess brain-behavior relationships is that language is processed in a network of brain regions that must work in concert, and language deficits can arise from disconnected or disrupted regions far away from the lesion. These disconnected regions can be identified by their changes in physiology (Metter et al., 1989). Therefore, to advance the field of stroke and aphasia rehabilitation, it is imperative to expand the current imaging models to not only relate anatomy to behavior but integrate both anatomy and physiology into behavior. To further understand the tissue health of chronic stroke lesions, we expand upon our previous findings and improve upon the detection of cerebral blood flow in chronic stroke lesions in PWA.

Cerebral blood flow (CBF) can be quantified non-invasively using a neuroimaging technology called pseudo-Continuous Arterial

TABLE 1 Participant demographic, aphasia, and lesion characteristics.

Sub	Age at scan	Sex	Months since stroke	WAB-AQ	Aphasia type	Lesion volume (mL)	Cavitation volume (mL)	% Cavitation
S01	51	M	24	59	Anomic	97,078	35,999	37.1
S02	59	M	38	65.9	Anomic	84,630	20,796	24.6
S03	50	M	85	75.3	Anomic	133,145	52,620	39.5
S04	71	F	24	67.1	Transcortical Motor	126,144	13,215	10.5
S05	61	M	121	74.5	Anomic	137,945	53,874	39.1
S06	24	F	23	55.3	Broca's	133,655	38,924	29.1
S07	35	M	9	27.4	Broca's	126,164	6,537	5.2
S08	47	M	44	75.6	Anomic	105,421	42,877	40.7
S09	43	F	49	80.6	Anomic	64,703	21,073	32.6
S10	81	F	60	74.1	Conduction	114,099	31,687	27.8
S11	73	M	55	79.6	Anomic	124,145	64,475	51.9
S12	45	M	14	78.6	Anomic	148,123	14,366	9.7
S13	50	M	70	59.4	Conduction	95,516	28,115	29.4
S14	60	M	9	52.4	Wernicke's	132,319	44,429	33.6

Spin Labeling (pCASL) which is a sub-class of arterial spin labeling (ASL) MRI methods available. Generally, the ASL experiment collects one set of images that contain signals from both tissue and blood compartments (the "control" image) and one set of images that contain signals from tissue and magnetically labeled blood to reduce the contribution of the blood signal (the "label" image). The difference between control and label images removes the tissue signal to reveal an image of pure blood signal (the "perfusion" image). To convert the perfusion image to physiological units (the "CBF" image), the perfusion image is further divided by a separately acquired proton density (M0) calibration image and modeled with sequence-specific factors such as post-labeling delay and physiological factors such as arterial blood T1. The consensus paper provides a comprehensive description of the technology (Alsop et al., 2015). Often these computations are achieved in native space–or the space in which the image was acquired–but most comparative studies require all participant CBF images to be normalized to template space. One current issue in the ASL MRI field is the standardization of processing steps to obtain absolute CBF maps (Pinto et al., 2020). For example, it is unclear whether some post-processing steps such as spatial smoothing should be applied in native or template space, if at all. Spatial smoothing is a process of spatially weighting the signal intensity from neighboring voxels to decrease the impact of instrumentation noise. There is a clear need for consistent post-processing options with a complete description of all post-processing steps, including spatial smoothing, to achieve absolute CBF quantification (Pinto et al., 2020). Steps such as spatial smoothing have an even greater impact when quantifying CBF in chronic stroke lesions due to the rapid transitions in microstructural damage (Burda and Sofroniew, 2014) and the impact on brain metabolism and corresponding CBF.

The objective of this project is to advance the ability of ASL MRI to reliably detect the CBF within the lesion and facilitate characterizing how lesion CBF relates to clinical factors relevant to aphasia. To accomplish this objective, we will optimize at what stage spatial smoothing should be applied in the ASL analysis pipeline. We hypothesize that the blood flow in chronic stroke lesions will reduce with increasing tissue damage. We also hypothesize that both stroke- and demographic-related factors will relate to lesion CBF. Finally, in an exploratory analysis, we will generate brain-behavior relationships between CBF and verbal learning or visuospatial learning and compare them to structural lesion-based brain-behavior maps.

Materials and methods

General procedures

Imaging and behavioral data from 14 English-speaking PWA (Table 1; age range 24–81 years old) who were >6 months post-left-hemisphere ischemic stroke (range of time since stroke 9–121 months) were analyzed for this study. Participants with a history of mental health disorders or other neurological disorders were excluded. Participants with hemorrhagic strokes were excluded due to the limitations of quantifying tissue damage in the presence of hemosiderin. Western Aphasia Battery Aphasia Quotient (WAB AQ) (range 27.4–80.6). The participants were asked to undergo an MRI session and a language assessment session which included the administration of the Western Aphasia Battery-Revised (WAB-R) (Kertesz, 2007), the Hopkins Verbal Learning Test-Revised (HVLT-R) (Benedict et al., 1998), and the Brief Visual Memory Test-Revised (BVMT-R) (Benedict et al., 1996). This study used raw scores from the HVLT-R and BVMT-R total recall, delayed recall, and recognition hits to compute brain-behavior relationships with CBF. This study was carried out in accordance with the recommendations of the joint

review committee at Emory University and Atlanta Veterans Affairs Medical Center. All participants gave written informed consent in accordance with the Declaration of Helsinki.

MRI acquisition

MRI scans were acquired on a 3T Siemens Prisma (Erlangen, Germany) using the body coil for radio frequency (RF) transmission and a 32-channel phased-array head coil for RF receiving. Two types of anatomical MRI scans were acquired on each subject: 1) a T1-weighted high-resolution anatomical image (T1-MPRAGE, TR = 2,530 ms, TE = 2.96 ms, TI = 1,100 ms, FA = 7°, isotropic resolution = 1 × 1 × 1 mm (Crosson et al., 2017), acquisition bandwidth = 130 Hz), and 2) a T2-weighted high-resolution anatomical image (T2-SPACE, TR = 3200 ms, TE = 285 ms, FA = 120°, isotropic resolution = 1 × 1 × 1 mm (Crosson et al., 2017), acquisition bandwidth = 700 Hz).

Pseudo–Continuous Arterial Spin Labeling (pCASL) MRI was collected to measure regional whole-brain cerebral blood flow (CBF) maps (2D ascending gradient echo EPI acquisition, 35 slices, slice thickness = 4 mm, 10% gap, matrix = 74 × 74, FoV = 220 × 220 mm^2, in-plane resolution = 3 × 3 mm^2, GRAPPA = 2, no Partial Fourier, acquisition bandwidth = 2,505 Hz, TR = 5,060 ms, TE = 13 ms, slice acquisition time = 37.5 ms, PLD = 2,200 ms, labeling duration = 1,500 ms, label offset = 90 mm). The pCASL method acquires interleaved control and label images, the subtraction of which yields a pure-blood signal that is directly proportional to CBF and can be mapped on a voxel-wise basis to obtain whole-brain regional blood flow information. An additional M0 scan was acquired with the same brain coverage as the pCASL scan, except for a longer repetition time (TR = 10 s) to allow for fully relaxed magnetization to remove proton density effects during CBF quantification.

Estimation of tissue damage using TIGR maps

The workflow of calculating the Tissue Integrity Gradation via T2-weighted T1-weighted Ratio (TIGR) maps has been described previously (Krishnamurthy et al., 2021). Briefly, the user input includes a T1w and T2w image, as well as a binary lesion mask in native space. The T1w and T2w images are denoised (Coupe et al., 2008; Wiest-Daessle et al., 2008) and coregistered together via FreeSurfer's boundary-based registration (Greve and Fischl, 2009). The values in each voxel of the T2w images are divided by the value of the corresponding voxel in the aligned T1w image (T2w/T1w). Each type of image (T1w and T2w) encodes unique signal information of the underlying tissue morphology. Taking the T2w/T1w ratio combines both types of information into one image to highlight the gradient of tissue damage within the lesion. To scale the T2w/T1w signals to a subject-specific value that can be compared across the entire cohort, the signal intensity is bounded by GM (lower bound:0.1; from the contra-lesional anterior grey matter ribbon eroded by one voxel) and CSF (upper bound:1.0; from the contra-lesional anterior lateral ventricle eroded by one voxel) and classified into nine "bins" between 0.1 ("least damaged") and 1.0 ("most damaged") to maintain comparability with binary lesion maps characterized by 0's and 1's that are often used in the field. Only the voxels within the user-defined lesion mask are classified into the tissue gradient "bins," creating the final TIGR map used in group analysis. We further define all lesioned areas with a TIGR score of 1.0 as necrotic cavitation and all other regions (0.1–0.9) as surrounding pericavitational regions. To compare TIGR maps and CBF maps across PWA and generate brain-behavior relationships, the T2w/T1w ratio maps are spatially normalized to MNI template space using a "chimera" spatial normalization [described in the Supplementary Section of Krishnamurthy et al. (2021)]. The overlap of all participant's lesions in the MNI template space is accomplished using afni's 3dOverlap. The average of all participant's TIGR scores in the MNI template space is accomplished using afni's 3dmerge.

Three analysis pipelines to compute CBF

The analysis of pCASL data is accomplished with in-house scripts using a combination of afni (version 22.2.10) and FSL (version 6.0.1) commands. The "no blur" pipeline uses the following analysis steps: 1) bulk-head motion correction is computed with afni's 3dAllineate using 6 degrees of freedom. 2) The motion parameters are used to censor pairs of label and control images that contain motion of >0.7 mm and >5 degrees of rotation. A minimum of 32 pairs (out of a maximum of 40 pairs) were used for every participant's dataset. 3) The label and control images were subtracted in native space to obtain the difference signal (=control-label) using afni's 3dcalc and then averaged before conversion to physiological units. 4) To obtain CBF in physiological units, the difference signal (=control-label) and M0 image are combined with a single-compartment model to obtain units of mL/100 g/min (Buxton et al., 1998; Alsop et al., 2015). 5) The CBF map was then transformed into MNI space by registering to T1w space using FreeSurfer's bbregister and subsequently applying the chimera warp into MNI space (FSL's applywarp). All CBF results reported here are in 1 × 1 × 1 mm^3 MNI space, which also conforms to the voxel size in the TIGR MRI map of tissue damage.

The "blur 4 in MNI" analysis pipeline uses the output of the "no blur" pipeline and applies spatial smoothing (or blurring) within the brain using a 4 mm full-width-half-maximum (FWHM) Gaussian kernel (afni's 3dmerge) to increase the signal-to-noise ratio (SNR). The "blur 4 in native" analysis pipeline introduces a 4 mm FWHM Gaussian kernel smoothing before the subtraction of control and label images in native space to increase the SNR before subtraction. The same transformations into T1w and MNI space computed for the "no blur" images were then applied to the "blur 4 in native" images to maintain comparability across all datasets. The general difference between the three analysis pipelines is depicted in Figure 1 with group average output images.

Comparison between ASL analysis pipelines

To assess the impact of each of the ASL analysis pipelines on the non-lesioned CBF values in MNI space, we extracted a 15 mm radius sphere in the anterior cingulate cortex [ACC, MNI coordinates x = 0, y = 44 (anterior), z = 18 (superior)]. We ensured that the ACC 15 mm region of interest (ROI) did not overlap with any individual

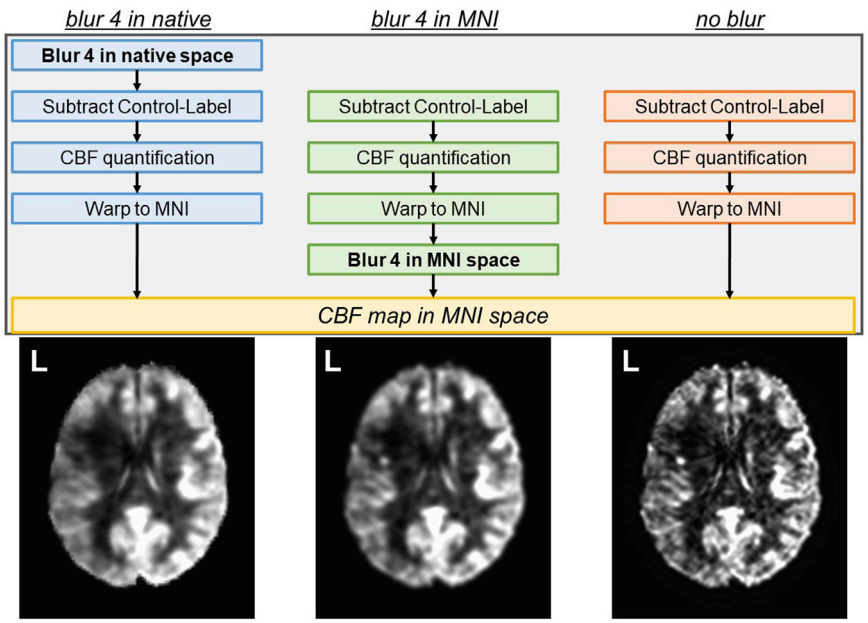

FIGURE 1
Three analysis pipelines to compute CBF were tested. The spatial smoothing in the "blur 4 in native" pipeline occurs in the native space, prior to the subtraction of control and label images. The spatial smoothing in the "blur 4 in MNI" pipeline occurs in the MNI space, and the "no blur" pipeline does not have spatial smoothing applied to the images. The resulting CBF map is always in MNI space. Average CBF maps from 14 participants (all left hemisphere lesions) for each analysis pipeline are shown as a reference.

participant's lesion. We then applied the grey matter (GM) and white matter (WM) segmentations computed on each participant's T1w image using FSL's fast algorithm (Zhang et al., 2001) to extract ACC GM and WM CBF values. The average CBF under each participant's individual GM and WM CBF maps were extracted with afni's 3dmaskave. A separate 15 mm spherical ROI outside of the brain and head was used to extract the standard deviation of the noise in the air. The following metrics were computed to assess the quality of the quantified CBF from each pipeline:

Signal-to-Noise Ratio (SNR)

$$SNR = \frac{\mu_{tissue}}{\sigma_{air}} \quad (1)$$

Coefficient of Variation (CoV)

$$CoV = \frac{\sigma_{tissue}}{\mu_{tissue}} \quad (2)$$

Grey matter to White matter Contrast-to-Noise Ratio (CNR)

$$CNR = \frac{\mu_{GM} - \mu_{WM}}{\sigma_{air}} \quad (3)$$

Where σ represents the standard deviation of the CBF within the ROI and μ represents the average CBF within the ROI.

Relationship between TIGR-quantified tissue damage and CBF

We previously related perilesional regions (TIGR score = 0 within 10 mm of the lesion), low damage lesion regions (TIGR score 0.1–0.3), medium damage lesion regions (TIGR score 0.4–0.7), and high damage lesion regions (TIGR score 0.8–1.0) to decrease in cerebral blood flow in six participants (Krishnamurthy et al., 2021). We now expand upon this finding by leveraging the interpolated 1 × 1 × 1 mm^3 CBF image to directly relate with the 1 × 1 × 1 mm^3 TIGR map in 14 participants, allowing us to use the computed TIGR score rather than averaging over a range of TIGR scores. An ROI for each TIGR score was generated (0.1, 0.2, 0.3, . . . , 1.0) which is unique to each subject based on their lesion location, TIGR map profile, and ROI size. For each participant, an average CBF value was computed for each ROI.

To assess the relationship between CBF and tissue damage within the lesion, a linear regression was performed in JMP Pro16 (Cary, NC) for each participant. The fit of the linear model is reported with R^2 and F-statistic, with the corresponding p-value. To account for multiple tests being performed, significance was assessed using the Bonferroni corrected p-value of 0.01 divided by $N = 14$ participants.

Further, given that both demographic and stroke-specific factors may govern the amount of blood flow to the lesion, we completed an ANOVA in JMP Pro16 to test if factors (tissue damage) along with (time since stroke), (sex), (age), and cross terms (tissue damage*time since stroke), (tissue damage*sex), (tissue damage*age), (time since stroke*sex), (time since stroke*age), and (sex*age) explain CBF within the lesion. The results of the model are reported with F-statistic and subsequent t-tests are performed to determine which terms had a significant effect. We also tested a separate model that included WAB-AQ, as the aphasia quotient can be used in the clinical setting.

10.3389/fphys.2023.1240992

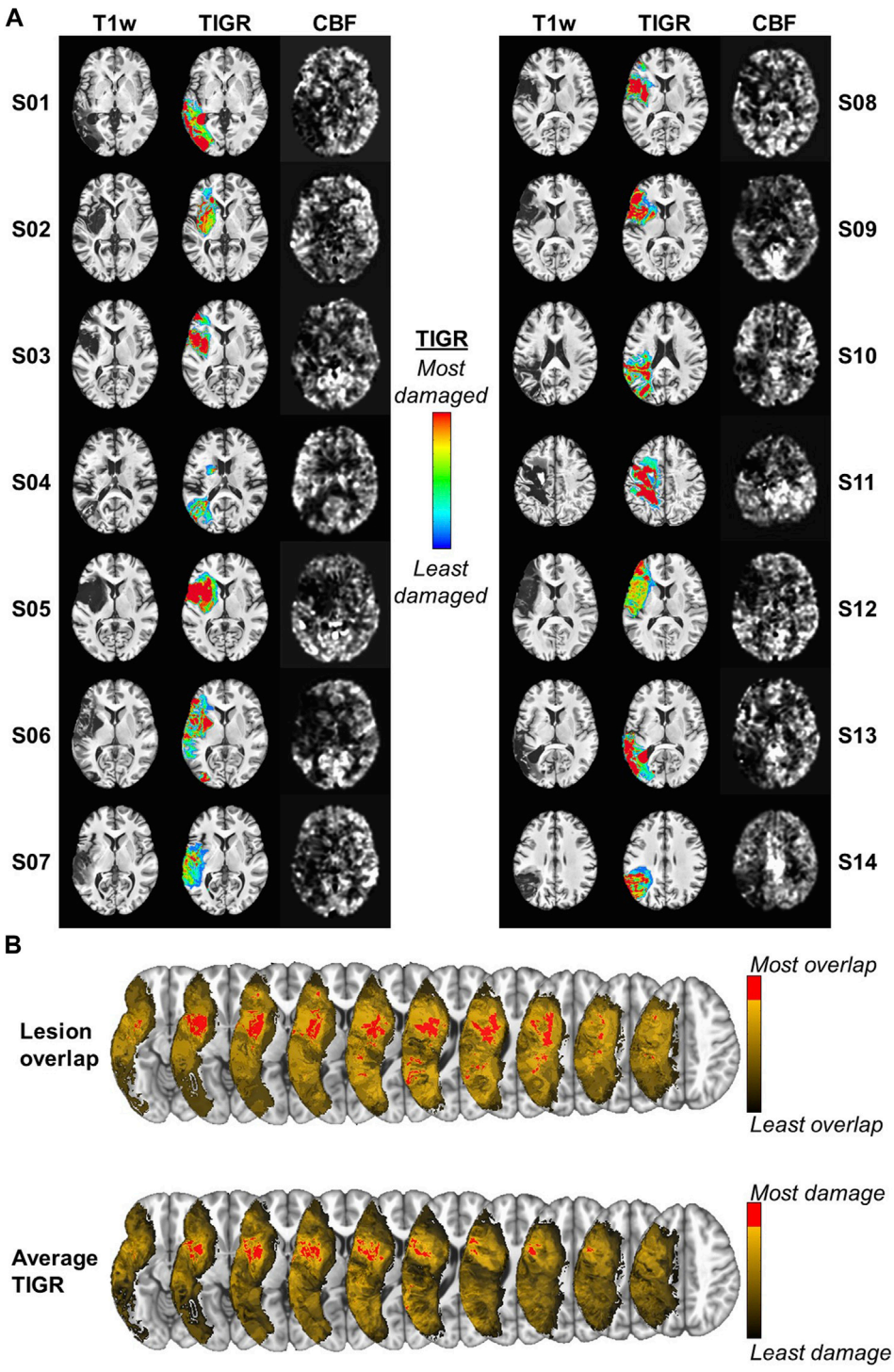

FIGURE 2
(A) The T1w, TIGR MRI, and CBF map from each individual participant, showing the heterogeneity of lesion location, tissue damage, and CBF maps. **(B)** The maximum lesion overlap and the maximum average TIGR scores are in adjacent, but only partially overlapping, areas. Note: Left is left in the images.

Multivariate brain-behavior relationships

We recently established that whole-brain task-fMRI data can be used to quantify brain-behavior maps in PWA (Song et al., 2023). Based on these promising results, we built upon this multi-variate framework by using whole-brain CBF maps. We assessed the feasibility of quantifying brain-behavior relationships between whole-brain CBF maps and either HVLT-R or BVMT-R behavioral measures using LESYMAP's sparse canonical correlation analysis (sccan) (Pustina et al., 2018) thresholded at

$p < 0.05$. Because LESYMAP's sccan models all voxels simultaneously, no multiple comparison corrections are necessary. To determine if whole-brain CBF maps can capture brain-behavior results above and beyond structural imaging modalities, we show results for TIGR maps and CBF maps, all in MNI template space to facilitate group statistics and comparison across methodologies. To account for the effects of lesion on the CBF values, we covaried two lesion-derived metrics from each voxel only if the relationship was significant: 1) lesion volume and 2) cavitation volume. There were no other covariates such as age entered into the modeling of the brain-behavior relationship. Due to the whole-brain nature of CBF data, a whole-brain mask was generated by overlapping binarized anatomical brain masks from each participant (afni 3dOverlap) and thresholded at a minimum of $N = 10$ participants represented in each voxel (afni 3dcalc). The k-fold cross-validation for sccan was set to 7 and the output results were clustered at 1,000 contiguous voxels.

Results

General results

PWA characteristics are shown in Table 1. All 14 participants were ensured to have good-quality T1w, T2w, and pCASL images via careful image pre-processing and quality control. The lesion location was heterogeneous across the MCA territory and the CBF visually decreased in their respective lesioned areas (Figure 2A). The false-color TIGR map ranges from blue (0.1, least damaged) to red (1.0, most damaged) and estimates the degree of tissue damage in the lesioned area (Figure 2A). Of the 14 participants, the maximum number of lesions that overlapped in any given region was 9 but did not overlap with the maximally damaged regions as quantified by TIGR (Figure 2B). The red portion of the colorbar in Figure 2B represents the highest 80% of the maximum overlap or average tissue damage. The lesion overlap is greater in white matter regions, whereas the greatest average tissue damage is in gray matter regions (Figure 2B).

Comparison of ASL analysis pipelines in intact brain regions and the whole lesion

The average ACC GM CBF was 46.7 ± 7.7 mL/100 g/min for blur-4-in-native, 47.7 ± 8.0 mL/100/min for blur-4-in-MNI, and 51.2 ± 8.5 mL/100 g/min for no-blur ASL analysis pipelines. The average ACC WM CBF was 36.2 ± 7.4 mL/100 g/min for blur-4-in-native, 33.9 ± 7.7 mL/100 g/min for blur-4-in-MNI, and 30.5 ± 8.5 mL/100 g/min for no-blur ASL analysis pipelines. An ANOVA testing the effect of ASL analysis pipeline and tissue type on average CBF values was significant [$F(3,80) = 23.66$, $p < 0.0001$], but indicated that only the tissue type had a significant effect on average CBF values ($F = 70.87$, $p < 0.0001$), while the ASL analysis pipeline did not have a significant effect on average CBF values ($F = 0.06$, $p = 0.95$). There is, however, a small effect of the ASL analysis pipeline on GM-WM CNR [$F(2,39) = 4.64$, $p = 0.02$], indicating that the no-blur ASL analysis pipeline provided a greater CNR (2.8 ± 1.3) than the blur-4-in-MNI (CNR = 2.1 ± 1.2) and the blur-4-in-native (CNR = 1.5 ± 0.9). This translates to the increased pairwise t-statistic in GM and WM (Figure 3A), where blur-4-in-native has pairwise GM-WM difference with $t(13) = 7.8$ ($p < 0.0001$), blur-4—in-MNI has a pairwise GM-WM difference with $t(13) = 9.3$ ($p < 0.0001$), and no-blur has the greatest pairwise GM-WM difference with $t(13) = 10.4$ ($p < 0.0001$). A significant decline with age in ACC GM CBF was detected ($t = -2.2$, $p = 0.04$), but not in ACC WM CBF ($t = 0.5$, $p = 0.60$).

The lesion CBF is significantly lower than the homologue WM CBF ($t = 11.2–12.8$, $p < 0.0001$), which is remarkably lower than the homologue GM CBF ($t = 5.6–6.1$, $p < 0.0001$), regardless of ASL analysis pipeline (Figure 3B). The CoV of the CBF in the lesion area is greater than in GM or WM, suggesting that more transitions in CBF are captured within the entire lesion ROI compared to other tissue types. Because not all lesioned tissue is equal, and some regions may have more or less blood flow due to the degree of tissue damage, it supports our expectation that a relationship between tissue damage and CBF may be detectable.

Assessing the relationship between lesion CBF and tissue damage

To assess the impact of tissue damage on blood flow, we plotted the average lesion CBF against the TIGR score for each participant. Most participants tend to have a higher CBF in less damaged tissue and a lower CBF in more damaged tissue (Figure 4). To assess if the relationship between CBF and TIGR is significant, linear regression was applied to each participant's dataset for each analysis pipeline. As seen in Table 2, 6 out of 14 participants had a Bonferroni-corrected significant relationship between CBF and TIGR. Further, an additional 5 participants had non-Bonferroni corrected significant relationships between CBF and TIGR. Only one participant (S13) did not indicate any relationship between CBF and TIGR score. Further, 12 out of 14 participants showed the expected negative relationship between CBF and TIGR as indicated by the column "sign of the slope" in Table 2. One participant showed a significant positive relationship between CBF and TIGR. It is also evident in Figure 4 that there is a lot of variability in the lesion CBF that is not explained by tissue damage. For example, there is variability in the CBF of the least damaged regions (TIGR = 0.1), which ranges from 11–36 mL/100 g/min. Therefore, in the next section, we introduce a model with more explanatory factors to further describe the CBF within the lesion.

Modeling the effect of tissue damage, time since stroke, age, and sex on blood flow to the lesion

The CBF within the lesion was modeled with a group-level ANOVA to further account for the variability by introducing stroke-related factors tissue damage (from TIGR) and time since stroke, and demographic-related factors age and sex, as well as their cross terms. The CBF output from each of the three ASL-analysis pipelines was modeled in separate ANOVAs and the factor outputs are summarized in Table 3. The significant factors include tissue damage, time since stroke, sex, age, and

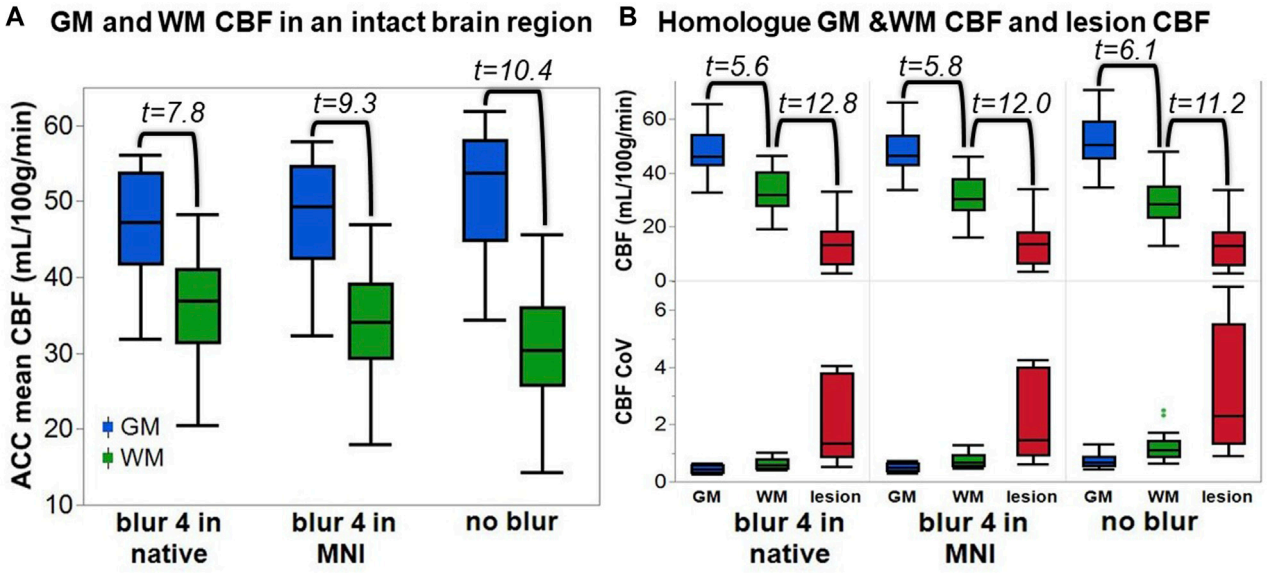

FIGURE 3
The quantified CBF from each ASL analysis pipeline. **(A)** The anterior cingulate cortex (ACC) GM and WM CBF. The number represents the t-statistic of a paired t-test between tissue types. **(B)** Top row: The CBF of the lesion and its homologue GM and WM. The number represents the t-statistic of a paired t-test between regions. Bottom row: The CoV of the CBF across the same tissue regions for each analysis pipeline.

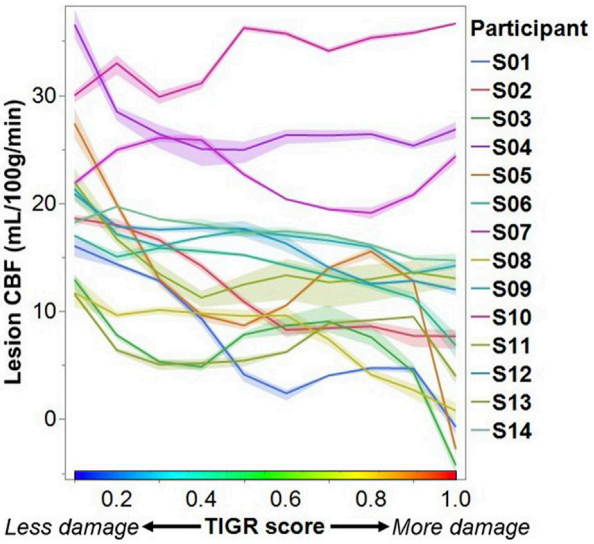

FIGURE 4
Each participant's lesion CBF at each TIGR score. Each line represents the average CBF computed from all three ASL analysis pipelines. The error envelope is constructed using the maximum and minimum CBF computed from all three pipelines.

cross-terms age-by-sex and time since stroke-by-age. These factors were significant, regardless of the analysis pipeline, but the best fit of the lesion CBF was provided by the blur-4-in-MNI ASL-analysis pipeline ($F = 55.62$, $p < 0.0001$). Although the no-blur pipeline provided the greatest GM-WM contrast in intact brain regions (Figure 3), the resulting ANOVA for the no-blur CBF provided the lowest fit as indicated by the F-statistic (Table 3). Because WAB-AQ is also a clinical (stroke-related) factor, we tested the addition of WAB-AQ to the model but found that no terms with WAB-AQ remained significantly related to lesion CBF. Therefore, we only consider the model without WAB-AQ factors.

As indicated by Figure 5, more regional tissue damage within the stroke lesion is related to a lower CBF within that region (defined by the TIGR maps). Further, if more time has elapsed since the stroke, the lesion CBF is also lower. The model also suggests that the lesion CBF is higher in older participants compared to younger, which is opposite to the intact ACC GM CBF. The model also identified that Females tend to have a greater lesion CBF compared to Males. Finally, there was an interaction between the two demographic factors age-by-sex, but more interestingly, the model also indicated a significant interaction between stroke and demographic-related factors age-by-time since stroke. Because the blur-4-in-MNI CBF output resulted in the best fit of stroke and demographic-related factors, this CBF value is further graduated to determine if brain-behavior relationships could be identified with CBF maps.

Multivariate brain-behavior relationships

If a voxel's CBF value across the group was significantly related to either lesion or cavitation volume, the relationship was covaried out to reduce any confounds in the identified brain-behavior relationships. No significant relationships between lesion volume or cavitation volume were identified with TIGR maps and therefore not regressed out.

Significant multivariate brain-behavior relationships (thresholded at $p < 0.05$) were found for BVMT total recall and BVMT recognition for

TABLE 2 The statistics describing the linear relationship between CBF and TIGR for each subject (Sub) and each analysis method: blur-4-in-native, blur-4-in-MNI, and no-blur. The * in the *p*-value column indicates significance at a Bonferroni corrected $p = 0.01$. The sign of the slope column indicates if the relationship is negative (−) or positive (+). The bolded numbers correspond to the values with a * (significance at a Bonferroni corrected $p = 0.01$).

Sub	Blur 4 in native			Blur 4 in MNI			No blur			Sign of the slope
	R^2	F (1,8)	*p*-value	R^2	F (1,8)	*p*-value	R^2	F (1,8)	*p*-value	
S01	0.84	43.34	**0.0002***	0.82	37.70	**0.0003***	0.78	28.67	**0.0007***	-
S02	0.86	48.30	**0.0001***	0.88	56.39	**<0.0001***	0.90	73.98	**<0.0001***	-
S03	0.45	6.52	0.03	0.46	8.82	0.03	0.29	3.34	0.10	-
S04	0.35	4.27	0.07	0.36	4.57	0.07	0.25	2.65	0.14	-
S05	0.50	7.99	0.02	0.48	7.27	0.03	0.46	6.73	0.03	-
S06	0.82	36.22	**0.0003***	0.81	33.69	**0.0004***	0.75	24.05	0.001	-
S07	0.23	2.40	0.16	0.18	1.75	0.22	0.17	1.67	0.23	-
S08	0.85	45.44	**0.0001***	0.81	34.52	**0.0004***	0.82	37.45	**0.0003***	-
S09	0.62	13.29	0.007	0.64	14.36	0.005	0.63	13.56	0.006	-
S10	0.71	19.63	0.002	0.66	15.70	0.004	0.57	10.44	0.01	+
S11	0.44	6.27	0.04	0.34	4.05	0.08	0.24	2.59	0.15	-
S12	0.94	127.32	**<0.0001***	0.92	90.70	**<0.0001***	0.86	50.82	**<0.0001***	-
S13	0.02	0.16	0.70	0.01	0.07	0.80	0.01	0.07	0.80	
S14	0.87	55.28	**<0.0001***	0.90	75.63	**<0.0001***	0.77	26.65	0.0009	-

TABLE 3 The ANOVA model output for each ASL analysis pipeline. The numbers indicate a t-statistic, except the bottom row, which is an F-statistic. The red box indicates that blur-4-in-MNI produces the CBF values that are best described by the model. Note: For each model factor, **** indicates $p < 0.0001$, *** indicates $p < 0.001$, ** indicates $p < 0.01$, * indicates $p < 0.05$, and N/S is not significant. The bolded numbers indicate the greatest t or F statistic in that row (if significant).

Model factor	Blur 4 in native	Blur 4 in MNI	No blur
sex	**11.83****	11.19****	9.96****
age at scan	9.40****	**10.47****	9.25****
age at scan × time since stroke	8.37****	**8.91****	8.12****
age at scan × sex	**6.80****	6.34****	5.74****
tissue damage (TIGR)	−4.72****	**−5.16****	−5.04****
time since stroke	**−4.11****	−3.95***	−3.25**
tissue damage × sex	2.32*	2.03*	1.93$^{N/S}$
tissue damage × age at scan	1.55$^{N/S}$	1.59$^{N/S}$	1.44$^{N/S}$
tissue damage × time since stroke	−0.96$^{N/S}$	−0.96$^{N/S}$	−0.84$^{N/S}$
time since stroke × sex	−0.34$^{N/S}$	−0.07$^{N/S}$	0.25$^{N/S}$
F(10,129) =	*54.90****	***55.62****	*45.36****

both cavitation and lesion-corrected CBF data (Figure 6). TIGR maps resulted in significant brain-behavior relationships with BVMT total recall. The cavitation-corrected CBF maps show fewer brain-behavior areas than the lesion-corrected CBF brain-behavior maps, although the two input data tend to agree on the areas where both are significant. The results in Figure 6 show that CBF-derived brain-behavior maps for BVMT–total recall are distinct from the brain-behavior maps for BVMT–recognition, suggesting that whole-brain CBF maps can generate behavior-specific information. Further, the TIGR relationship with BVMT total recall shows one overlapping and one unique area compared to the CBF relationships with BVMT total recall, suggesting the structural and functional modalities are complementary. The BVMT total recall maps include the anterior thalamus and retrosplenial cortex, both of which are associated with spatial-memory-related behavior (Vann et al., 2009). Conversely, the BVMT–recognition shows areas of the default mode network and the right executive function network, which are involved in decision-making (Sridharan et al., 2008). Finally, the HVLT behavior did not

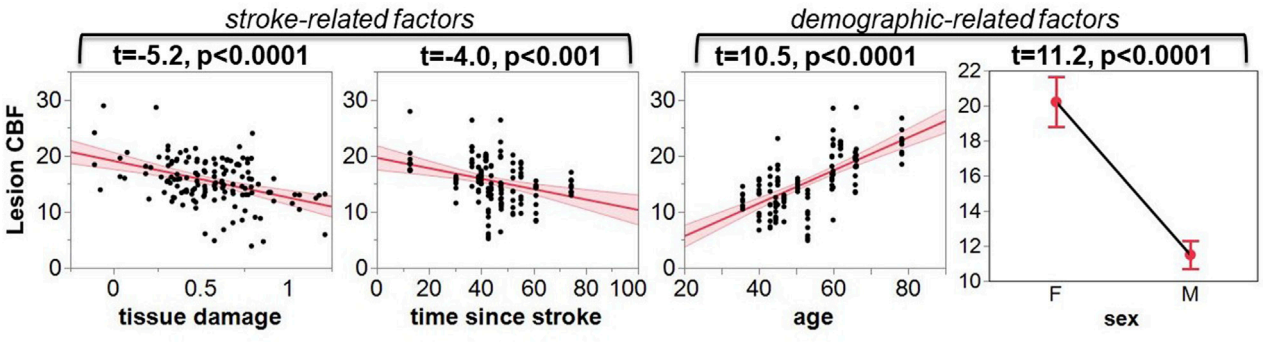

FIGURE 5
The leverage plots for the ANOVA model output. The lesion CBF is significantly associated with stroke-related factors of tissue damage and time since stroke, and demographic-related factors of age and sex.

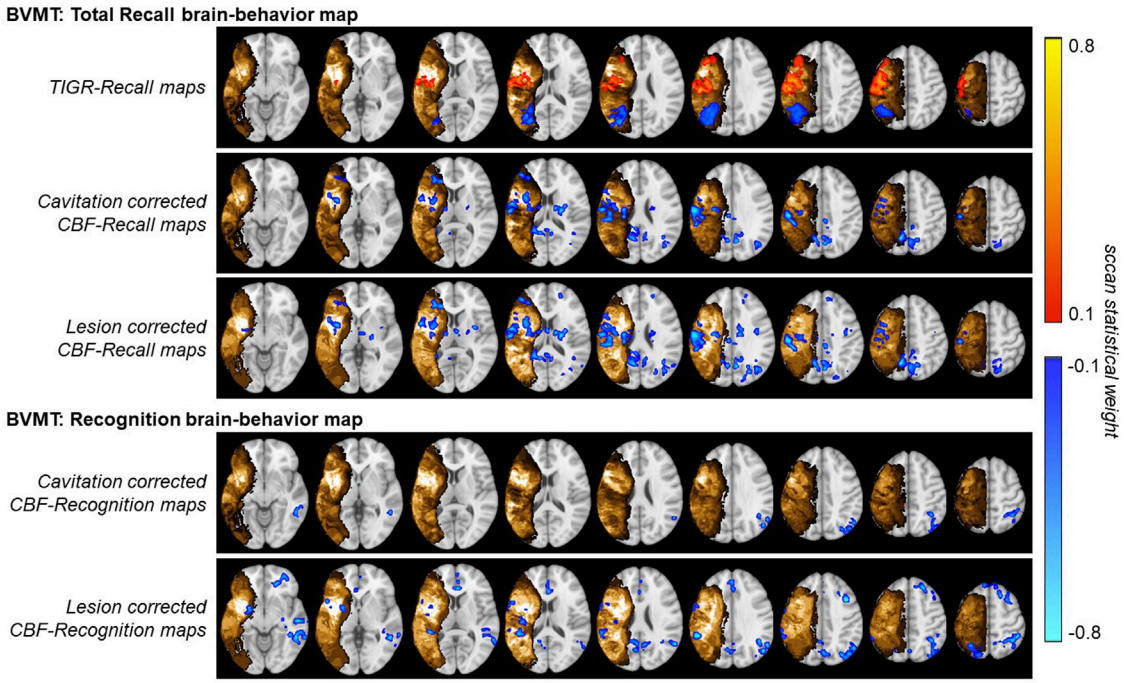

FIGURE 6
Multivariate brain-behavior maps using TIGR MRI and either cavitation-corrected or lesion-corrected cerebral blood flow (CBF) for BVMT total recall and BVMT recognition. The gold indicates either mean TIGR (cavitation corrected) or lesion overlap (lesion corrected). The red and blue indicate regions of significant multivariate brain-behavior relationships.

result in significant brain-behavior maps using LESYMAP's sccan multivariate analysis for either TIGR or CBF imaging inputs.

Discussion

The results of this study demonstrate that CBF is detectable in chronic stroke lesions, suggesting that the pericavitational regions may be viable and can be engaged and targeted during aphasia and stroke rehabilitation. We recommend that at least in chronic stroke datasets, spatial smoothing should be applied in the MNI template space during the CBF analysis to increase the grey matter and white matter contrast while maintaining sensitivity to changes in tissue damage. We showed for the first time that the CBF in chronic stroke lesions decreases with increasing tissue damage as quantified by TIGR MRI. Further, we showed that demographic and stroke-related factors also influence the lesion blood flow, suggesting that individualization of stroke intervention strategies is a priority to achieve optimal treatment outcomes. Finally, using an advanced multivariate approach, for the first time, we demonstrated that whole brain CBF in PWA is related to visual-spatial learning and memory and can serve as complementary information to lesion-based brain-behavior maps.

Comparison of ASL analysis pipelines

Measuring cerebral blood flow within chronic stroke lesions is challenging because of the small ASL signal and additional reductions caused by tissue damage. However, we have shown that standard pCASL MRI can effectively measure CBF within these lesions. We improved the detection sensitivity of changes in CBF in rapidly transitioning tissue damage by optimizing the step in which spatial smoothing is applied within the ASL analysis pipeline. Our approach increases the sensitivity to differences in tissue types, including grey matter and white matter, as well as quantifying tissue damage using the TIGR score. It is well accepted that GM has a higher CBF than WM and previous studies have determined that pCASL MRI can reliably detect WM perfusion (van Osch et al., 2009). Therefore, we first assessed the effects of spatial smoothing on the non-lesioned ACC and determined that the GM-WM differences are detectable regardless if smoothing is applied in native space, MNI template space, or not at all. However, there was an increase in tissue contrast, when smoothing was applied in MNI template space compared to native space, but the highest GM-WM CNR was found if no smoothing was applied. Given these results, we thought that no smoothing would provide the best snapshot of lesion CBF, however, when modeling the CBF with demographic and stroke-related factors (Table 3), it became apparent that spatial smoothing in MNI template space was the most appropriate.

As is well known from the functional and physiological MRI literature, spatial smoothing provides stability to the regional MR signal, generally benefitting the ASL perfusion signal (Wang et al., 2005; Fazlollahi et al., 2015) and minimizing the anatomic variability in group-level analyses (Scouten et al., 2006; Mikl et al., 2008). However, there are also some negative outcomes of spatial smoothing such as reductions in tissue CNR (Molloy et al., 2014), loss in precision of cluster extent (Hagler et al., 2006), and increased Type-1 errors in the estimation of group-level significant maps (Vul et al., 2009). While we observed the expected decrease in the tissue CNR, such a limitation should be evaluated within the context of study goals. For clinical neuroradiological evaluation of CBF maps at the individual level, perhaps tissue CNR becomes more important. Instead, for group-level investigational research studies, we show that the improved relationship between stroke and demographic-related factors outweighs the reduced CNR. Although the tissue damage transitions in the TIGR images can be as rapid as 1–2 mm, possibly limited by the resolution of the T1w and T2w images, blurring the CBF maps still improved the overall relationship with tissue damage and other factors. It will be of interest to repeat this study at the higher field strength of 7T, where submillimeter resolution ASL data can be collected (Zuo et al., 2013) and the SNR is 3-fold compared to 3T (Shao et al., 2021). Perhaps due to these inherent signal improvements, smaller transitions in the stroke lesion CBF signal can be detected at 7T. However, technical limitations for implementing ASL at 7T such as specific absorption rate (SAR) limits and the ability to achieve reasonably strong labeling at a reasonably large labeling-plane offset may preclude a widespread adaptation of TIGR and ASL data collection in stroke participants and will likely serve as a validation of the present findings. Instead, translating the current approach to wide-bore research and clinical systems with lower gradient amplitudes may help the translation of the approach into the clinic, particularly for post-stroke individualization of rehabilitation approaches. Finally, the impact of spatial smoothing and smoothing kernel size in MNI space and its effect on the extent of detected cluster size and Type-1 errors is important but was not the focus of the current study. Future work should consider advancing the stroke ASL analysis pipelines to investigate these questions using larger datasets.

Another challenge to CBF quantification is the estimation of tissue proton density (M0) to calibrate the perfusion signal. We used a separately acquired M0 image to calibrate the perfusion data on a voxel-by-voxel basis, rather than using the whole brain difference signal or intact region as the calibration reference signal, as has previously been used to reduce inter-subject variability (Aslan and Lu, 2010). We hypothesize that the M0 voxel-by-voxel normalization may be the most appropriate for stroke brains because a whole-brain average will be influenced by lesion size and location, possibly introducing more inter-subject variability, and the intact control region may be affected by changes in blood flow distal to the lesion (i.e., diaschisis), further introducing more inter-subject variability. Future work should compare and contrast the different CBF normalization techniques.

The relationship between lesion CBF and tissue damage

We assessed the relationship between lesion CBF and tissue damage using linear regression. A significantly decreasing CBF with increasing tissue damage was detected in 6 out of 14 participants at a Bonferroni corrected $p = 0.01$ and in an additional five participants at a non-Bonferroni corrected value (Table 2) suggesting that this relationship will be detectable in most chronic ischemic stroke lesions. In one participant, who is characterized as a 50-year-old Male, 70 months post-stroke, with Conduction aphasia, no relationship between CBF and tissue damage was found; however, this was also the participant with the lowest CBF value at a TIGR score of 0.1 (least tissue damage). Therefore, the detectability of further tissue-damage-related CBF decreases may be minimal for this participant. Further, the CBF for this participant does decrease between TIGR scores 0.1 and 0.6, but then rises again to peak at TIGR score 0.9 and then falls to a minimum in the cavitation (TIGR score 1.0). Indeed, the rise of CBF at a mid-level TIGR score is observed in approximately half of the participants (Figure 4), indicating that there may be a tissue-type transition. We speculate that perhaps the lower TIGR scores of 0.1–0.5 (less damage) are mapped to white matter, while TIGR scores of 0.6–0.9 (more damage) are mapped to grey matter. This would explain the "jump" in CBF mid-way through the tissue damage scores because GM always has higher CBF than WM but is now confounded by the amount of damage impacting the tissue. This does not mean that GM is necessarily always more damaged than white matter, but may perhaps stem from the inherent differences in tissue properties (cell type and morphology, tissue T1 and T2, etc.) that are a latent confound to TIGR tissue damage classification. The cavitation (TIGR score 1.0) is mapped indiscriminately to either tissue type. It is worth noting that the ratio of T1w to T2w anatomical images is

known, rightly or wrongly, in other contexts as the "myelin map" (Glasser and Van Essen, 2011; Boaventura et al., 2022) due to its strong association with myelin content in the non-lesioned brain. The ratio of T1 to T2 in myelin maps or T2 to T1 in TIGR maps is a representation of microstructure differences across brain regions–which, in a healthy brain can grossly be attributed to regional differences in myelination. In stroke lesions, or most neurological diseases, it is not so simple because the microstructural changes are so vast and varied that the change in the ratio cannot be attributed to a single cell type. Empirical data to further investigate these observations does not yet exist, and will likely rely on models to determine the previous individual sulcal and gyral patterns of the lesioned tissue. These models may also take into account atrophy and pressure-related changes in sulcal patterns. All other participants showed a significant reduction in CBF with increasing tissue damage, as hypothesized, except for one, which may be due to the pCASL MRI sequence, which is discussed later in the Limitations section.

Lesion CBF relates to stroke and demographic factors

The model output showed that CBF within the lesion was significantly described by demographic factors "age" and "sex" and stroke-related factors "time since stroke" and "tissue damage." CBF is a complex measure of vascular and metabolic supply to the tissue (Drake and Iadecola, 2007), and incorporating all of these factors in the model allows for an improved understanding of clinically-relevant factors that are important for diagnosis and treatment planning (Table 3; Figure 5).

It is well accepted that CBF reduces with age in healthy participants (Mokhber et al., 2021), which we also detected in the intact ACC GM ROI establishing the validity of our analysis pipeline. However, the model result showing that lesion CBF is more preserved in older individuals compared to younger individuals is somewhat counterintuitive (Figure 5). It may be that the global aging-related decline in brain connections results in a reduced impact on blood flow to the lesion, or may have an impact on post-stroke vascular dynamics. While it is encouraging that our results reflect these exciting findings, empirical evidence of such a relationship does not yet exist and more sophisticated multi-modal work is needed to characterize the lesion physiology and microstructure in humans.

The model also showed that Females have more preserved blood flow to the lesion than Males, but this finding conforms to the bulk of the literature on healthy aging, where cortical CBF in Females is greater than in Males, at least at an age less than 65 (Aanerud et al., 2017). The significant age-by-sex interaction term further indicates that the lesion CBF may be sensitive to Male-Female CBF differences that change with age. However, the small sample size of Females ($N = 4$, age 24–81) compared to Males ($N = 10$, age 35–73) strongly indicates that this finding needs to be replicated with a much larger cohort with a wide range in age and balanced representation of Males to Females.

The stroke-related factor "time-since-stroke" showed that lesion CBF declines as more time passes since the stroke. This may indicate that metabolic and vascular declines are perhaps still occurring in the chronic stages of stroke in the lesioned area, plausibly due to the loss of neural cells due to lack of blood supply. This is an interesting finding, as subcortical structures downstream from the lesion do not change their volume in the chronic stages (Krishnamurthy et al., 2020), indicating that these are subtle metabolic and vascular processes that may occur locally and closer to the lesion. Furthermore, the significant age-by-time since stroke interaction further indicates that the rate of decline in CBF after stroke may depend on the age at which the stroke occurred. This is one of the first pieces of evidence that aging-by-disease interactions can be quantified to help in individualized patient treatment planning.

The data indicated that lesion CBF decreases significantly with increasing tissue damage (Table 2; Figure 4). This result was reinforced in the model that accounted for both stroke and demographic-related factors (Table 3; Figure 5). Therefore, if TIGR MRI indicates that a region of the chronic stroke lesion is pericavitational, it is likely that the damaged-but-intact tissue is viable and can be reengaged with targeted rehabilitation.

Brain-behavior relationships

When examining the relationship between the brain and behavior, researchers have relied on lesion information for over 200 years (Baldo et al., 2022). Although powerful and highly informative, this approach limits the search for relationships to only the areas where lesions occur. In PWA, that usually means only the left hemisphere middle cerebral artery (MCA) territory is inspected for brain-behavior relationships. Instead, using whole-brain cerebral blood flow maps with CBF that is detectable in the lesioned areas allows the entire brain now to become available when assessing functional and physiological brain-behavior relationships. First, we will examine the lesion-level brain-behavior relationships and then extend the results into the CBF-based brain-behavior relationships.

We previously showed that brain-behavior maps extracted with TIGR show similar brain-behavior maps compared to binary lesions (Krishnamurthy et al., 2021), but may have more statistical power due to the continuous nature of TIGR compared to the binary "all-or-none" nature of lesions maps. Therefore, given the small sample size of $N = 14$ participants, we chose to evaluate lesion-based brain-behavior maps using TIGR as the input. The BVMT total recall related significantly to two regions of the group-level TIGR maps: 1) a left frontal region encompassing primary sensory-motor, dorsal pre-motor, and dorsal lateral prefrontal cortices, as well as the posterior insula, and 2) a left parietal region encompassing supramarginal gyrus and angular gyrus. The frontal region is positively related to tissue damage, which indicates that damage to these regions predicts better visuospatial function. This result is counterintuitive because damage to any brain region will likely result in some level of worse behavioral outcome. However, it may be that damage to the frontal regions indicates a lower probability of damage to the parietal regions, which instead shows a negative relationship between tissue damage and BVMT total recall. In PWA, the left inferior parietal lobule (IPL) is often associated with language processes, but in the case of the visuospatial learning captured by the BVMT total recall, it may be that this finding suggests that

visuospatial learning is processed in both the right and left parietal cortices because functions such as new learning are not clearly localized (Goodglass et al., 1979). The clues to this can be gathered from the CBF-derived brain-behavior maps.

The CBF-derived brain behavior maps show multiple distinct areas, both within the lesion and distal to the lesion. The CBF-derived brain-behavior region overlaps with the TIGR-based frontal region, while the TIGR-based parietal brain-behavior region does not overlap with the CBF-derived region. Therefore, the left parietal involvement identified with only the TIGR information may represent complementary information. It is not clear why the CBF-related regions do not overlap with all TIGR-related regions, especially since the TIGR ad CBF scores are linearly related. However, other regions outside of the lesion are highlighted when using CBF: specifically the right IPL. Therefore, the L-IPL from TIGR and R-IPL from CBF together point to both hemispheres' involvement in BVMT total recall, showing that visuospatial learning is related to the baseline blood flow to the right parietal areas (as traditionally implicated in visuospatial tasks) as well as the left parietal areas. The BVMT recognition task, which recalls which shapes were encountered, has more right lateralization in the CBF brain-behavior maps. This interpretation would have been difficult when assessing lesion-derived brain-behavior maps in the absence of the CBF-derived maps because the additional network information is missing when confined to only the lesion overlap areas. We recommend that the brain-behavior mapping field go beyond lesion-based maps and start incorporating whole-brain functional and physiological maps as inputs. Both types of maps may agree on some regions but seem to also provide unique and complementary information that together helps improve our understanding of the brain and determine targets of intervention.

We did not identify significant brain-behavior relationships with verbal learning as measured with the HVLT-R, although the reasons for this are not clear as the behavior was well distributed between low and high values, and the lesion locations were also distributed across the MCA territory. Perhaps the CBF maps did not show a relationship to HVLT-R because verbal learning is more confined to the left hemisphere compared to visuospatial learning. However, TIGR MRI also did not relate to HVLT-R which was disappointing as verbal learning in PWA is a predictor of rehabilitation success (Dignam et al., 2017), and identifying the hubs of the brain network involved in verbal learning may have been informative for treatment planning.

In this report, we also assessed the effects of covarying the lesion volume versus the cavitation volume from the CBF maps before computing the brain-behavior maps. Both cavitation volume and lesion volume had areas of significant correlation with CBF, and both cavitation-corrected and lesion-corrected CBF resulted in significant brain-behavior maps with similar regions (Figure 6). Based on the number of significant regions captured by each modality, we recommend that the field continue to correct by lesion volume, not by cavitation volume. The cavitation-corrected CBF, at least at this small sample size, seems to lose some statistical sensitivity relating to behavior (both subcortical and frontal regions are missing when correcting by cavitation size). Although the cavitation represents the part of the lesion that is fully damaged, it may be that the distal blood flow is more impacted by the size of the lesion, regardless of how much potentially viable tissue is still present in the lesion.

Finally, all brain-behavior results using CBF show a negative relationship, indicating that greater blood flow to those brain regions predicts a worse behavioral outcome. Such a result, though counterintuitive, is not beyond the realm of possibility. A theoretical, yet empirically elusive, construct in the stroke literature is the concept of diaschisis (Carrera and Tononi, 2014)—defined as "neurophysiological changes that occur distant to a focal brain lesion." It may be that loss of input and output to a region distal to the lesion may cause an increase in blood flow due to a reduction in inhibitory tone (Blicher et al., 2015), which together (i.e., GABA and CBF) influence cognitive decline (Krishnamurthy V. et al., 2022; Krishnamurthy L. C. et al., 2022). Therefore, an increased CBF distal to the lesion may indicate a failure of the network and lead to worse behavioral outcomes.

Limitations

This study is the first of its kind to assess the CBF in chronic stroke lesions and relate to the underlying tissue damage of the lesion. While the study has many novel discoveries, there are a few limitations that also need to be highlighted. First, the study sample size of $N = 14$ chronic stroke participants is small and therefore should be viewed strictly as a proof-of-principle. Particularly the model output and the brain-behavior relationships require further testing with larger cohorts, as these statistical tests usually require dozens of participants to identify significant relationships (Sperber et al., 2019). However, advanced multivariate approaches (such as Lesymap's sccan) are tailored to produce meaningful results from small sample datasets. It may be that the input of a whole-brain CBF map to the multivariate brain-behavior analysis allowed the model to converge because the entire network is represented in the data input, rather than a subset often defined by a lesion overlap mask.

Another limitation of this study is the MRI sequence parameters used to collect perfusion-weighted images. Our pCASL MRI sequence used a 2D EPI acquisition without background suppression and a single post-labeling delay. The current recommendations of the field (Alsop et al., 2015) are to use a 3D acquisition to remove the difference in blood arrival between slices and to apply background suppression to improve the computation of the difference signal by reducing the overlying tissue signal. We chose not to use background suppression because we are interested in quantifying the CBF of the lesion, but the T1 of lesioned tissue is not known and requires an additional MRI scan to quantify. Therefore, background suppression in ASL sequences must still be optimized for the chronic stroke brain, but will likely improve the relationship between lesion CBF and tissue damage quantified using TIGR. The lesion CBF of S10 likely suffered from an inadequate subtraction and caused the relationship between CBF and tissue damage to be positive, when all other participants had the expected negative relationship. Further, the intact WM CBF was consistently quantified at ~30 mL/100 g/min

in this cohort, which is higher than the literature WM CBF of ~20 mL/100 g/min (Mokhber et al., 2021), possibly due to an incomplete tissue subtraction. The other limitation of the pCASL MRI sequence used in this study is the single post-labeling delay of 2,200 ms, which is relatively long, but will not provide additional information about blood arriving at a later time due to collateral flow (Lou et al., 2019). It may be ideal to collect two or more PLDs (perhaps up to 2,800 ms) to improve upon the CBF quantification after stroke or use the more advanced MR ASL fingerprinting (Su et al., 2017) to quantify multiple physiological parameters such as CBF and bolus arrival time using a single acquisition. Collecting MRS ASL fingerprinting data could also rule out arterial transit time artifacts that may occur in and around the lesion, which may be responsible for the "jump" in CBF midway through the tissue damage scores. The increased information from MR ASL fingerprinting within chronic stroke lesions could help improve the modeling of demographic and stroke-related factors, as well as brain-behavior relationships.

The removal of physiological noise from the perfusion-weighted signal was also not undertaken. We did not collect either cardiac or respiratory information during the pCASL MRI acquisition, as such data was not readily available using our setup. It has been shown that removing both cardiac and respiratory fluctuations during the ASL analysis can help improve the stability of the signals and remove spurious regional variations (Hassanpour et al., 2018). It may be that the slight negative CBF of highly damaged (i.e., cavitated) regions in some participants may be a result of physiological pulsatility causing a greater label signal compared to the control signal. Another means of removing physiological noise in ASL images is to use ICA-denoising approaches (Carone et al., 2019), but optimization and development of ICA denoising on stroke ASL data was beyond the scope of this report.

Conclusion

In summary, we presented for the first time that CBF can be detected in chronic stroke lesions, demonstrating that this signal relates to tissue damage, with adequate fidelity to model with stroke and demographic-related factors and to relate to behavior.

Data availability statement

The raw data supporting the conclusion of this article will be made available by the authors, without undue reservation.

Ethics statement

The studies involving human participants were reviewed and approved by Emory University and Atlanta Veterans Affairs Medical Center. The patients/participants provided their written informed consent to participate in this study.

Author contributions

Conceptualization of the study and methodological development: LK, VK, CG, and BC; MR data collection: LK, AR, CD, and MW; Participant screening: LK, AR, and MW; Data analysis: LK, VK, CD, SS, and JH; Manuscript writing and editing: LK, VK, CG, JH, SS, CD, MW, AR, and BC. All authors contributed to the article and approved the submitted version.

Funding

This study was supported by the Center grant award (I50RX002358) sponsored by Veterans Health Administration. LK received funding from the Veterans Affairs Rehabilitation Research and Development Service (United States) grant IK1RX002629, I21RX003581, and I01RX003093. VK received funding from the Veterans Affairs Rehabilitation Research and Development Service (United States) grant IK2RX002934. AR received funding from the Veterans Affairs Rehabilitation Research and Development Service (United States) grant I01RX003093 and I21RX003474. MW received funding from I50RX002358, I21RX003474, and I01RX003093.

Conflict of interest

The authors declare that the research was conducted in the absence of any commercial or financial relationships that could be construed as a potential conflict of interest.

Publisher's note

All claims expressed in this article are solely those of the authors and do not necessarily represent those of their affiliated organizations, or those of the publisher, the editors and the reviewers. Any product that may be evaluated in this article, or claim that may be made by its manufacturer, is not guaranteed or endorsed by the publisher.

References

Aanerud, J., Borghammer, P., Rodell, A., Jonsdottir, K. Y., and Gjedde, A. (2017). Sex differences of human cortical blood flow and energy metabolism. *J. Cereb. Blood Flow Metabolism* 37, 2433–2440. doi:10.1177/0271678X16668536

Adams, K. L., and Gallo, V. (2018). The diversity and disparity of the glial scar. *Nat. Neurosci.* 21, 9–15. doi:10.1038/s41593-017-0033-9

Alsop, D. C., Detre, J. A., Golay, X., Günther, M., Hendrikse, J., Hernandez-Garcia, L., et al. (2015). Recommended implementation of arterial spin-labeled perfusion MRI for clinical applications: A consensus of the ISMRM perfusion study group and the European consortium for ASL in dementia. *Magnetic Reson. Med.* 73, 102–116. doi:10.1002/mrm.25197

Anderson, M. A., Ao, Y., and Sofroniew, M. V. (2014). Heterogeneity of reactive astrocytes. *Neurosci. Lett.* 565, 23–29. doi:10.1016/j.neulet.2013.12.030

Aslan, S., and Lu, H. (2010). On the sensitivity of ASL MRI in detecting regional differences in cerebral blood flow. *Magn. Reson Imaging* 28, 928–935. doi:10.1016/j.mri.2010.03.037

Baldo, J. V., Ivanova, M. V., Herron, T. J., Wilson, S. M., and Dronkers, N. F. (2022). in *Lesion-to-Symptom mapping: Principles and tools* (Berlin, Heidelberg: Springer US).

Bates, E., Wilson, S. M., Saygin, A. P., Dick, F., Sereno, M. I., Knight, R. T., et al. (2003). Voxel-based lesion-symptom mapping. *Nat. Neurosci.* 6, 448–450. doi:10.1038/nn1050

Benedict, R. H. B., Schretlen, D., Groninger, L., and Brandt, J. (1998). Hopkins verbal learning test–revised: Normative data and analysis of inter-form and test-retest reliability. *Clin. Neuropsychologist* 12, 43–55. doi:10.1076/clin.12.1.43.1726

Benedict, R. H. B., Schretlen, D., Groninger, L., Dobraski, M., and Shpritz, B. (1996). Revision of the Brief visuospatial memory test: Studies of normal performance, reliability, and validity. *Psychol. Assess.* 8, 145–153. doi:10.1037/1040-3590.8.2.145

Blicher, J. U., Near, J., Næss-Schmidt, E., Stagg, C. J., Johansen-Berg, H., Nielsen, J. F., et al. (2015). GABA levels are decreased after stroke and GABA changes during rehabilitation correlate with motor improvement. *Neurorehabil Neural Repair* 29, 278–286. doi:10.1177/1545968314543652

Boaventura, M., Sastre-Garriga, J., Garcia-Vidal, A., Vidal-Jordana, A., Quartana, D., Carvajal, R., et al. (2022). T1/T2-weighted ratio in multiple sclerosis: A longitudinal study with clinical associations. *Neuroimage Clin.* 34, 102967. doi:10.1016/j.nicl.2022.102967

Burda, J. E., and Sofroniew, M. V. (2014). Reactive gliosis and the multicellular response to CNS damage and disease. *Neuron* 81, 229–248. doi:10.1016/j.neuron.2013.12.034

Buxton, R. B., Frank, L. R., Wong, E. C., Siewert, B., Warach, S., and Edelman, R. R. (1998). A general kinetic model for quantitative perfusion imaging with arterial spin labeling. *Magnetic Reson. Med.* 40, 383–396. doi:10.1002/mrm.1910400308

Carone, D., Harston, G. W. J., Garrard, J., De Angeli, F., Griffanti, L., Okell, T. W., et al. (2019). ICA-based denoising for ASL perfusion imaging. *NeuroImage* 200, 363–372. doi:10.1016/j.neuroimage.2019.07.002

Carrera, E., and Tononi, G. (2014). Diaschisis: Past, present, future. *Brain* 137, 2408–2422. doi:10.1093/brain/awu101

Charidimou, A., Kasselimis, D., Varkanitsa, M., Selai, C., Potagas, C., and Evdokimidis, I. (2014). Why is it difficult to predict language impairment and outcome in patients with aphasia after stroke? *J. Clin. Neurol.* 10, 75–83. doi:10.3988/jcn.2014.10.2.75

Clarkson, A. N., Huang, B. S., Macisaac, S. E., Mody, I., and Carmichael, S. T. (2010). Reducing excessive GABA-mediated tonic inhibition promotes functional recovery after stroke. *Nature* 468, 305–309. doi:10.1038/nature09511

Coupe, P., Yger, P., Prima, S., Hellier, P., Kervrann, C., and Barillot, C. (2008). An optimized blockwise nonlocal means denoising filter for 3-D magnetic resonance images. *IEEE Trans. Med. Imaging* 27, 425–441. doi:10.1109/TMI.2007.906087

Crosson, B., Hampstead, B. M., Krishnamurthy, L. C., Krishnamurthy, V., McGregor, K. M., Nocera, J. R., et al. (2017). Advances in neurocognitive rehabilitation research from 1992 to 2017: The ascension of neural plasticity. *Neuropsychology* 31, 900–920. doi:10.1037/neu0000396

Crosson, B., Rodriguez, A. D., Copland, D., Fridriksson, J., Krishnamurthy, L. C., Meinzer, M., et al. (2019). Neuroplasticity and aphasia treatments: New approaches for an old problem. *J. Neurol. Neurosurg. Psychiatry* 90, 1147–1155. doi:10.1136/jnnp-2018-319649

Dignam, J., Copland, D., O'Brien, K., Burfein, P., Khan, A., and Rodriguez, A. D. (2017). Influence of cognitive ability on therapy outcomes for anomia in adults with chronic poststroke aphasia. *J. Speech, Lang. Hear. Res.* 60, 406–421. doi:10.1044/2016_JSLHR-L-15-0384

Drake, C. T., and Iadecola, C. (2007). The role of neuronal signaling in controlling cerebral blood flow. *Brain Lang.* 102, 141–152. doi:10.1016/j.bandl.2006.08.002

Fazlollahi, A., Bourgeat, P., Liang, X., Meriaudeau, F., Connelly, A., Salvado, O., et al. (2015). Reproducibility of multiphase pseudo-continuous arterial spin labeling and the effect of post-processing analysis methods. *NeuroImage* 117, 191–201. doi:10.1016/j.neuroimage.2015.05.048

Fridriksson, J. (2010). Preservation and modulation of specific left hemisphere regions is vital for treated recovery from anomia in stroke. *J. Neurosci.* 30, 11558–11564. doi:10.1523/jneurosci.2227-10.2010

Glasser, M. F., and Van Essen, D. C. (2011). Mapping human cortical areas *in vivo* based on myelin content as revealed by T1-and T2-weighted MRI. *J. Neurosci.* 31, 11597–11616. doi:10.1523/jneurosci.2180-11.2011

Goodglass, H., and Kaplan, E. (1979). in *Neuropsychology* Editor M. S. Gazzaniga (Berlin, Heidelberg: Springer US).

Greve, D. N., and Fischl, B. (2009). Accurate and robust brain image alignment using boundary-based registration. *Neuroimage* 48, 63–72. doi:10.1016/j.neuroimage.2009.06.060

Hagler, D. J., Saygin, A. P., and Sereno, M. I. (2006). Smoothing and cluster thresholding for cortical surface-based group analysis of fMRI data. *NeuroImage* 33, 1093–1103. doi:10.1016/j.neuroimage.2006.07.036

Hassanpour, M. S., Luo, Q., Simmons, W. K., Feinstein, J. S., Paulus, M. P., Luh, W. M., et al. (2018). Cardiorespiratory noise correction improves the ASL signal. *Hum. Brain Mapp.* 39, 2353–2367. doi:10.1002/hbm.24000

Joy, M. T., and Carmichael, S. T. (2021). Encouraging an excitable brain state: Mechanisms of brain repair in stroke. *Nat. Rev. Neurosci.* 22, 38–53. doi:10.1038/s41583-020-00396-7

Kertesz, A. (2007). *Western aphasia battery-revised (WAB-R)*. United Kingdom: PsychCorp.

Kimberg, D. Y., Coslett, H. B., and Schwartz, M. F. (2007). Power in Voxel-based lesion-symptom mapping. *J. Cogn. Neurosci.* 19, 1067–1080. doi:10.1162/jocn.2007.19.7.1067

Krishnamurthy, L. C., Champion, G. N., McGregor, K. M., Krishnamurthy, V., Turabi, A., Roberts, S. R., et al. (2020). The effect of time since stroke, gender, age, and lesion size on thalamus volume in chronic stroke: A pilot study. *Sci. Rep.* 10, 20488. doi:10.1038/s41598-020-76382-x

Krishnamurthy, L. C., Krishnamurthy, V., Rodriguez, A. D., McGregor, K. M., Glassman, C. N., Champion, G. S., et al. (2021). Not all lesioned tissue is equal: Identifying pericavitational areas in chronic stroke with tissue integrity gradation via T2w T1w ratio. *Front. Neurosci.* 15, 665707. doi:10.3389/fnins.2021.665707

Krishnamurthy, L. C., Paredes Spir, I., Rocha, N. O., Soher, B. J., Auerbach, E. J., Crosson, B. A., et al. (2022b). The association between language-based task-functional magnetic resonance imaging hemodynamics and baseline GABA+ and glutamate-glutamine measured in pre-supplementary motor area: A pilot study in an aging model. *Front. Psychiatry* 13, 904845. doi:10.3389/fpsyt.2022.904845

Krishnamurthy, V., Paredes Spir, I., Mammino, K. M., Nocera, J. R., McGregor, K. M., Crosson, B. A., et al. (2022a). The relationship between resting cerebral blood flow, neurometabolites, cardio-respiratory fitness and aging-related cognitive decline. *Front. Psychiatry* 13, 923076. doi:10.3389/fpsyt.2022.923076

Lou, X., Ma, X., Liebeskind, D. S., Ma, N., Tian, C., Lyu, J., et al. (2019). Collateral perfusion using arterial spin labeling in symptomatic versus asymptomatic middle cerebral artery stenosis. *J. Cereb. Blood Flow. Metab.* 39, 108–117. doi:10.1177/0271678x17725212

Meinzer, M., Harnish, S., Conway, T., and Crosson, B. (2011). Recent developments in functional and structural imaging of aphasia recovery after stroke. *Aphasiology* 25, 271–290. doi:10.1080/02687038.2010.530672

Metter, E. J., Kempler, D., Jackson, C., Hanson, W. R., Mazziotta, J. C., and Phelps, M. E. (1989). Cerebral glucose metabolism in Wernicke's, Broca's, and conduction aphasia. *Arch. Neurol.* 46, 27–34. doi:10.1001/archneur.1989.00520370029014

Mikl, M., Marecek, R., Hlustík, P., Pavlicová, M., Drastich, A., Chlebus, P., et al. (2008). Effects of spatial smoothing on fMRI group inferences. *Magn. Reson. Imaging* 26, 490–503. doi:10.1016/j.mri.2007.08.006

Mokhber, N., Shariatzadeh, A., Avan, A., Saber, H., Babaei, G. S., Chaimowitz, G., et al. (2021). Cerebral blood flow changes during aging process and in cognitive disorders: A review. *Neuroradiol. J.* 34, 300–307. doi:10.1177/19714009211002778

Molloy, E. K., Meyerand, M. E., and Birn, R. M. (2014). The influence of spatial resolution and smoothing on the detectability of resting-state and task fMRI. *Neuroimage* 86, 221–230. doi:10.1016/j.neuroimage.2013.09.001

Pedersen, P. M., Vinter, K., and Olsen, T. S. (2004). Aphasia after stroke: Type, severity and prognosis. The copenhagen aphasia study. *Cerebrovasc. Dis.* 17, 35–43. doi:10.1159/000073896

Pinto, J., Chappell, M. A., Okell, T. W., Mezue, M., Segerdahl, A. R., Tracey, I., et al. (2020). Calibration of arterial spin labeling data—Potential pitfalls in post-processing. *Magnetic Reson. Med.* 83, 1222–1234. doi:10.1002/mrm.28000

Pustina, D., Avants, B., Faseyitan, O. K., Medaglia, J. D., and Coslett, H. B. (2018). Improved accuracy of lesion to symptom mapping with multivariate sparse canonical correlations. *Neuropsychologia* 115, 154–166. doi:10.1016/j.neuropsychologia.2017.08.027

Scouten, A., Papademetris, X., and Constable, R. T. (2006). Spatial resolution, signal-to-noise ratio, and smoothing in multi-subject functional MRI studies. *NeuroImage* 30, 787–793. doi:10.1016/j.neuroimage.2005.10.022

Shao, X., Yan, L., Ma, S. J., Wang, K., and Wang, D. J. J. (2021). High-resolution neurovascular imaging at 7T: Arterial spin labeling perfusion, 4-dimensional MR angiography, and black blood MR imaging. *Magn. Reson Imaging Clin. N. Am.* 29, 53–65. doi:10.1016/j.mric.2020.09.003

Song, S. E., Krishnamurthy, L. C., Rodriguez, A. D., Han, J. H., Crosson, B. A., and Krishnamurthy, V. (2023). Methodologies for task-fMRI based prognostic biomarkers in response to aphasia treatment. *Behav. Brain Res.* 2023, 114575. (in press). doi:10.1016/j.bbr.2023.114575

Sperber, C., Wiesen, D., and Karnath, H.-O. (2019). An empirical evaluation of multivariate lesion behaviour mapping using support vector regression. *Hum. Brain Mapp.* 40, 1381–1390. doi:10.1002/hbm.24476

Sridharan, D., Levitin, D. J., and Menon, V. (2008). A critical role for the right fronto-insular cortex in switching between central-executive and default-mode networks. *Proc. Natl. Acad. Sci.* 105, 12569–12574. doi:10.1073/pnas.0800005105

Su, P., Mao, D., Liu, P., Li, Y., Pinho, M. C., Welch, B. G., et al. (2017). Multiparametric estimation of brain hemodynamics with MR fingerprinting ASL. *Magn. Reson Med.* 78, 1812–1823. doi:10.1002/mrm.26587

Tyler, L. K., Marslen-Wilson, W., and Stamatakis, E. A. (2005). Dissociating neuro-cognitive component processes: Voxel-based correlational methodology. *Neuropsychologia* 43, 771–778. doi:10.1016/j.neuropsychologia.2004.07.020

van Osch, M. J. P., Teeuwisse, W. M., van Walderveen, M. A. A., Hendrikse, J., Kies, D. A., and van Buchem, M. A. (2009). Can arterial spin labeling detect white matter perfusion signal? *Magnetic Reson. Med.* 62, 165–173. doi:10.1002/mrm.22002

Vann, S. D., Aggleton, J. P., and Maguire, E. A. (2009). What does the retrosplenial cortex do? *Nat. Rev. Neurosci.* 10, 792–802. doi:10.1038/nrn2733

Vul, E., Harris, C., Winkielman, P., and Pashler, H. (2009). Puzzlingly high correlations in fMRI studies of emotion, personality, and social cognition. *Perspect. Psychol. Sci.* 4, 274–290. doi:10.1111/j.1745-6924.2009.01125.x

Wang, J., Wang, Z., Aguirre, G. K., and Detre, J. A. (2005). To smooth or not to smooth? ROC analysis of perfusion fMRI data. *Magn. Reson. Imaging* 23, 75–81. doi:10.1016/j.mri.2004.11.009

Wiest-Daessle, N., Prima, S., Coupe, P., Morrissey, S. P., and Barillot, C. (2008). Rician noise removal by non-local means filtering for low signal-to-noise ratio MRI: Applications to DT-MRI. *Lect. Notes Comput. S. C.* 5242, 171–179. doi:10.1007/978-3-540-85990-1_21

Zhang, Y., Brady, M., and Smith, S. (2001). Segmentation of brain MR images through a hidden Markov random field model and the expectation-maximization algorithm. *IEEE Trans. Med. imaging* 20, 45–57. doi:10.1109/42.906424

Zuo, Z., Wang, R., Zhuo, Y., Xue, R., St Lawrence, K. S., and Wang, D. J. J. (2013). Turbo-FLASH based arterial spin labeled perfusion MRI at 7 T. *PLOS ONE* 8, e66612. doi:10.1371/journal.pone.0066612

frontiers | Frontiers in Physiology

TYPE Original Research
PUBLISHED 05 September 2023
DOI 10.3389/fphys.2023.1213352

OPEN ACCESS

EDITED BY
Alex Bhogal,
Utrecht University, Netherlands

REVIEWED BY
Binu P. Thomas,
University of Texas Southwestern Medical Center, United States
Henk J. M. M. Mutsaerts,
VU Medical Center, Netherlands

*CORRESPONDENCE
Mark Bitsch Vestergaard,
mark.bitsch.vestergaard@regionh.dk

†These authors have contributed equally to this work and share first authorship

RECEIVED 27 April 2023
ACCEPTED 21 August 2023
PUBLISHED 05 September 2023

CITATION
Madsen SS, Lindberg U, Asghar S, Olsen KS, Møller K, Larsson HBW and Vestergaard MB (2023), Reproducibility of cerebral blood flow, oxygen metabolism, and lactate and N-acetyl-aspartate concentrations measured using magnetic resonance imaging and spectroscopy.
Front. Physiol. 14:1213352.
doi: 10.3389/fphys.2023.1213352

Reproducibility of cerebral blood flow, oxygen metabolism, and lactate and N-acetyl-aspartate concentrations measured using magnetic resonance imaging and spectroscopy

Signe Sloth Madsen[1†], Ulrich Lindberg[2†], Sohail Asghar[3], Karsten Skovgaard Olsen[1], Kirsten Møller[4,5], Henrik Bo Wiberg Larsson[2,5] and Mark Bitsch Vestergaard[2*]

[1]Department of Anaesthesiology, Pain and Respiratory Support, Neuroscience Centre, Copenhagen University Hospital–Rigshospitalet, Glostrup, Denmark, [2]Functional Imaging Unit, Department of Clinical Physiology and Nuclear Medicine, Copenhagen University Hospital—Rigshospitalet, Copenhagen, Denmark, [3]Anesthesiology and Intensive Care, Department of Clinical Sciences, Faculty of Medicine, Lund University, Lund, Sweden, [4]Department of Neuroanaesthesiology, Neuroscience Centre, Copenhagen University Hospital–Rigshospitalet, Copenhagen, Denmark, [5]Department of Clinical Medicine, Faculty of Health and Medical Sciences, University of Copenhagen, Copenhagen, Denmark

In humans, resting cerebral perfusion, oxygen consumption and energy metabolism demonstrate large intersubject variation regardless of methodology. Whether a similar large variation is also present longitudinally in individual subjects is much less studied, but knowing the time variance in reproducibility is important when designing and interpreting longitudinal follow-up studies examining brain physiology. Therefore, we examined the reproducibility of cerebral blood flow (CBF), global cerebral metabolic rate of oxygen ($CMRO_2$), global arteriovenous oxygen saturation difference (A-$V.O_2$), and cerebral lactate and N-acetyl-aspartate (NAA) concentrations measured using magnetic resonance imaging (MRI) and spectroscopy (MRS) techniques through repeated measurements at 6 h, 24 h, 7 days and several weeks after initial baseline measurements in young healthy adults (N = 26, 13 females, age range 18–35 years). Using this setup, we calculated the correlation, limit of agreement (LoA) and within-subject coefficient of variation (CoV_{WS}) between baseline values and the subsequent repeated measurements to examine the longitudinal variation in individual cerebral physiology. CBF and $CMRO_2$ correlated significantly between baseline and all subsequent measurements. The strength of the correlations (R^2) and reproducibility metrics (LoA and CoV_{WS}) demonstrated the best reproducibility for the within-day measurements and generally declined with longer time between

Abbreviations: A-$V.O_2$, Arteriovenous oxygen saturation difference; ASL, Arterial spin labelling; CBF, Cerebral blood flow; $CMRO_2$, Cerebral metabolic rate of oxygen; CoV_{ws}, Within-subject coefficient of variation; CSF, Cerebrospinal fluid; FOV, Field of view; LoA, Limit of agreement; MRS, Magnetic resonance spectroscopy; NAA, N-acetyl aspartate; pCASL, Pseudo-continuous arterial spin labelling; PCM, Phase contrast mapping; PET, positron emission tomography; SBO, susceptibility-based oximetry; SaO_2, oxygen saturation of the arterial blood; SvO_2, oxygen saturation of the venous blood; TD, Saturation delay; TE, Echo time; TI, Inversion time; TR, Repetition time.

measurements. Cerebral lactate and NAA concentrations also correlated significantly for all measurements, except between baseline and the 7-day measurement for lactate. Similar to CBF and $CMRO_2$, lactate and NAA demonstrated the best reproducibility for within-day repeated measurements. The gradual decline in reproducibility over time should be considered when designing and interpreting studies on brain physiology, for example, in the evaluation of treatment efficacy.

KEYWORDS

cerebral blood flow, cerebral metabolic rate of oxygen, cerebral lactate, phase contrast mapping, arterial spin labelling, reproducibility, N-acetyl-aspartate

1 Introduction

Measurements of cerebral blood flow (CBF), oxygen consumption and energy metabolism are of considerable interest when studying brain physiology and pathophysiology. Numerous research studies have examined the effects of disease or certain interventions on cerebral physiology (Powers et al., 1985; Liddle et al., 1992; Oshima et al., 2003; Peng et al., 2014; Snyder et al., 2015; Wolters et al., 2017; Younis et al., 2021; Vestergaard et al., 2022). However, cerebral physiology, both CBF and energy metabolism, demonstrates very large intersubject variability, which makes it difficult to observe small effects of intervention or disease. Multiple factors modulate CBF both acutely and over longer time periods (Kety and Schmidt, 1948; Lassen, 1959; Iida et al., 2004; Coles et al., 2006; Henriksen et al., 2013); for example, changes in arterial carbon dioxide or oxygen tension as well as oxygen saturation affect CBF (Paulson et al., 1990; Vestergaard et al., 2016; Vestergaard and Larsson, 2019). The cerebral metabolic rate of oxygen ($CMRO_2$) has similarly a large intersubject variability but demonstrates smaller acute fluctuations than CBF (Iida et al., 2004; Coles et al., 2006; Peng et al., 2014; Vestergaard et al., 2020) A key role of the regulation of CBF is to maintain $CMRO_2$ at constant levels.

Studies have examined intersubject variation in cerebral physiology, but normal longitudinal intrasubject variation is much less examined and has mainly focused only on CBF. However, longitudinal studies on cerebral physiology, for example, in terms of disease progression or intervention, require knowledge of normal longitudinal intrasubject variation for correct scaling of the project and interpretation of the results. Studies have examined the reproducibility of CBF using various techniques, but typically only two measurements were acquired, often with only a short time between scans (hours or a few days).

In the present study, we aimed to measure intrasubject variation in cerebral physiology by performing multiple repeated measurements in the same subjects with 6 h, 1 day, 7 days and several weeks between examinations. We used MRI techniques to acquire brain physiological parameters. Due to the noninvasiveness of MRI, it is possible to obtain multiple repeated measurements with only minor considerations related to patient safety. For example, exposure to radiation is not a concern, as would be the case if using positron emission tomography (PET) imaging. MRI techniques were therefore chosen as the most suitable examination method. Global average CBF and $CMRO_2$ were acquired using phase contrast mapping (PCM) and susceptibility-based oximetry (SBO) MRI. CBF maps were obtained using the arterial spin labelling (ASL) MRI technique.

In addition to CBF and $CMRO_2$, we also measured the concentrations of cerebral lactate and N-acetyl-aspartate (NAA) by magnetic resonance spectroscopy (MRS). In the healthy brain, most of the glucose for energy production is fully oxidized, resulting in an oxygen-to-glucose ratio close to 6. However, in the young healthy brain, approximately 10% of glucose goes through oxygen-free glycolysis with lactate as the end-product (Goyal et al., 2014; Hyder et al., 2016). By measuring the cerebral lactate concentration, we can examine the consistency of this glycolytic activity over time. NAA is predominantly synthesized in neurons and is primarily a marker of neuronal density. The NAA concentration is lower in patients with dementia and is reduced after stroke where it correlates with neuron loss. However, NAA is also affected by neuronal metabolic activity. For example, during disease activity in multiple sclerosis and after traumatic brain injury, the NAA concentration is reduced. Yet, this reduction is reversed during recovery. This suggests that NAA concentration is also affected by metabolic integrity, in addition to neuronal density. (Bitsch et al., 1999; Moffett et al., 2007). In healthy subjects, as examined in the current study, the NAA concentration is expected to be stable, however knowing the normal variation is important to correctly use NAA as a marker of neuronal function.

Overall, we examined intrasubject longitudinal variation in CBF, $CMRO_2$, arteriovenous oxygen saturation difference ($A\text{-}V.O_2$), cerebral lactate concentration, and cerebral NAA concentration in healthy humans through repeated MRI scan sessions. By measuring all these parameters, we obtained a comprehensive examination of longitudinal intrasubject variation in several markers of cerebral physiology.

2 Materials and methods

2.1 Subjects

Two groups of young healthy subjects participated in the study. All participants were healthy, right-handed, non-smokers, with a body mass index of 18–30 kg/m^2 and normal physical and neurological examinations. Female participants were non-pregnant. The participants were instructed to have no intake or use of caffeine, alcohol, medication or other substances known to influence the parameters measured in the study prior to study participation. Detailed description regarding the inclusion criteria

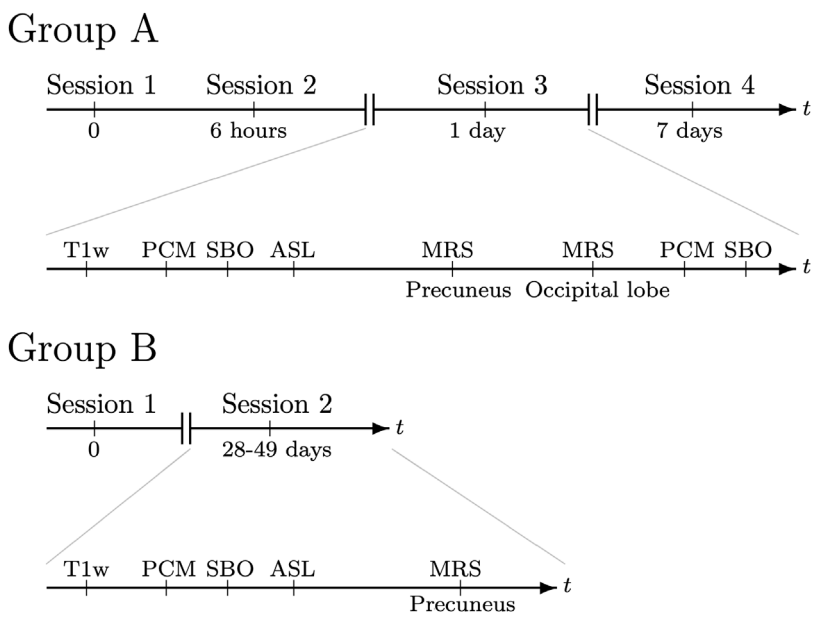

FIGURE 1
Outline of the MRI sessions and acquisition of cerebral physiology parameters allowing for examination of reproducibility. Group A underwent MRI scans four times, with 6 h, 1 day and 7 days between reacquisitions after an initial baseline measurement. Group B underwent MRI scans two times, with the second scan 28–49 days after the initial baseline scan. In each session, structural brain images were acquired using a T1-weighted high-resolution anatomical MRI sequence (T1w). Cerebral blood flow (CBF) was measured using phase contrast mapping (PCM) and arterial spin labelling (ASL) MRI techniques. Susceptibility-based oximetry (SBO) was used to measure the venous oxygen saturation of the blood leaving the brain, from which the cerebral metabolic rate of oxygen ($CMRO_2$) was calculated. Cerebral NAA and lactate concentrations were measured using magnetic resonance spectroscopy (MRS).

of the participants are provided in Madsen et al. (2020). In the first group (Group A), ten young healthy subjects (5 females) with a mean age of 25.4 years (range 18–35 years) were included and examined in four MRI sessions with repeated measurements acquired at 6 h, 1 day, and 7 days after an initial baseline measurement. All participants adhered to the same schedule, aligning the weekdays and timing of all scans and measurements. All participants were fasting 2 h for clear liquids and 6 h for all other intake before baseline scans. Between baseline and the second scan on the same day, the participants were served a light meal and drinks adhering to protocol (e.g., no caffeine, alcohol or medication). Next, we examined a second group (Group B), which included sixteen young healthy subjects (8 females) with a mean age of 23.9 years (range 18–32 years) who were examined twice with 28–49 days (mean 31.9 days) between examinations. Thus, we investigated short-term repeatability (up to 7 days) in Group A and repeatability after several weeks in Group B. Group B was included as a follow-up analysis due to the highly stable correlations observed in Group A, and we wanted to examine whether correlations were maintained after several weeks. All participants in Group B also adhered to a strict schedule, aligning the weekdays and timing of all scans and measurements, and following the same fasting regime for all scans used in this study. The participants from Group B were part of a study on the effect of general anaesthesia on brain structure and physiology; none of these subjects underwent anaesthesia during the present study (Madsen et al., 2020). Data from Group A was acquired in 2019, and data from Group B was acquired subsequently, in 2019–2021.

In all sessions, we measured global CBF and $CMRO_2$ twice (run 1 and run 2) at the beginning and end of the session to determine within-session reproducibility of these measurements. The remaining parameters were measured once in each session. The study setup is depicted in Figure 1.

Participants were recruited through advertisement on a Danish recruitment website (www.forsøgsperson.dk). Exclusion criteria were known neurological diseases and contraindications for MRI, such as metal implants and recent operations or pregnancy. The study was approved by the scientific ethical committee of the Capital Region of Denmark (H-18020364 and H-18028925) and was carried out according to the Declaration of Helsinki.

2.2 Magnetic resonance imaging

All scans were acquired on a 3 T Philips (Philips Medical Systems, Best, Netherlands) Achieva dStream (software release 5.4.1) equipped with a 32-channel phased-array receive head coil. The scanner was subjected to ongoing maintenance from the manufacture (Philips Healthcare); and we performed quality control and monitored the scanner and coil performance every week. There were no major software updates or hardware changes during data collection for this study.

The heart rate, arterial oxygen saturation and end tidal CO_2 partial pressure ($PetCO_2$) were measured continuously throughout the MRI scans using a Veris Monitor system

TABLE 1 Summary of the acquired parameters from each MRI session. The means ± standard deviations are noted. Abbreviations: A-V.O_2, arteriovenous oxygen saturation difference; CBF, cerebral blood flow; $CMRO_2$, cerebral metabolic rate of oxygen; NAA, N-acetyl-aspartate.

	Group A				Group B	
	Baseline	6 hours	1 day	7 days	Baseline	28–49 days
Phase Contrast Mapping						
CBF (Whole brain mean) [ml/100 g/min]	57.5 ± 8.3	58.4 ± 8.6	55.3 ± 6.3	56.9 ± 7.0	62.5 ± 7.8	62.8 ± 7.2
Arterial Spin Labelling						
CBF (Grey matter mean) [ml/100 g/min]	59.2 ± 13.4	57.7 ± 13.1	56.3 ± 9.1	63.3 ± 11.8	67.7 ± 10.7	68.1 ± 8.9
Susceptibility-Based Oximetry						
A-V.O_2 [%]	28.7 ± 5.2	29.3 ± 5.5	27.1 ± 6.1	29.6 ± 5.8	29.4 ± 6.3	29.3 ± 3.8
$CMRO_2$ [μmol/100 g/min]	143.2 ± 32.6	145.9 ± 30.6	128.7 ± 32.0	148.4 ± 38.6	156.4 ± 36.2	156.4 ± 24.7
MR Spectroscopy						
Lactate—precuneus [mmol/l]	0.51 ± 0.12	0.49 ± 0.11	0.50 ± 0.14	0.49 ± 0.10	0.50 ± 8.5	0.52 ± 12.3
Lactate—occipital lobe [mmol/l]	0.51 ± 0.12	0.49 ± 0.11	0.48 ± 0.11	0.52 ± 0.10		
NAA—precuneus [mmol/l]	10.1 ± 2.0	9.7 ± 1.5	9.7 ± 1.5	10.1 ± 1.5	9.4 ± 2.1	9.3 ± 2.1
NAA—occipital lobe [mmol/l]	8.2 ± 2.4	8.2 ± 2.6	7.7 ± 2.1	8.2 ± 2.5		
Cardiovascular parameters						
Haemoglobin concentration [mmol/l]	9.1 ± 1.2	9.0 ± 1.1	9.0 ± 1.2	9.1 ± 1.2	8.7 ± 0.9	8.6 ± 0.9
Arterial saturation [%]	97.5 ± 1.6	97.0 ± +0.7	97.7 ± 1.0	97.2 ± 1.4	97.9 ± 1.2	97.9 ± 0.7
Mean arterial blood pressure [mmHg]	88.3 ± 3.6	90.3 ± 3.7	88.6 ± 7.5	86.7 ± 5.7	92.1 ± 8.4	86.2 ± 6.6
End-tidal CO_2 partial pressure [kPa]	4.7 ± 1.2	5.1 ± 0.5	4.9 ± 0.5	4.9 ± 0.5	4.8 ± 0.7	4.7 ± 0.8
Heart rate [bpm]	59.8 ± 5.4	62.8 ± 5.8	61.4 ± 5.9	63.8 ± 5.6	64.0 ± 9.7	59.8 ± 10.0

(MEDRAD, Pittsburgh, Pennsylvania, USA). The blood pressure was measured with regular intervals during the examinations. The average values of these measurements throughout the scans are presented in Table 1. A venous blood sample was drawn before each scan session and analysed for haemoglobin (Hgb) concentration using a blood gas analyser XN 9000 (Sysmex, Kobe, Japan).

2.2.1 Structural images

Structural brain images were acquired using a sagittal three-dimensional T1-weighted high-resolution Magnetization Prepared Rapid Gradient Echo (MPRAGE) scan (echo time (TE) = 2.8 ms, repetition time (TR) = 6.9 ms, inversion time (TI) = 900 ms; flip angle = 9°, 137 slices, field-of-view (FOV) = 262 × 280 × 150 mm^3; voxel size = 1.1 × 1.1 × 1.1 mm^3). Bias field correction and segmentation of the brain into grey matter, white matter and cerebrospinal fluid (CSF) was carried out using FAST (FSL 5.0.11, FMRIB, Oxford, UK) (Jenkinson et al., 2012) to estimate brain volume. The anatomical images were additionally used for structural normalisation for the ASL analysis.

2.2.2 Arterial spin labelling (ASL)

Cerebral blood flow maps were acquired using arterial spin labelling (ASL). A dual-echo two-dimensional echo planar imaging pseudo-continuous arterial spin labelling (pCASL) sequence scan with 2 background suppression pulses was used (16 transverse slices (6 mm thick); TE_1/TE_2 = 12.56/31.66 ms; TR = 4550 ms (for one image); flip angle = 90°; FOV = 240 × 240 mm^2; matrix size = 88 × 88 (acquired), 128 × 128 (reconstructed); labelling duration = 1800 ms; postlabelling delay = 1800 ms with an additional slice acquisition time of 32 ms; background suppression (BS) pulses = BS_1/BS_2: 1813/3135 ms; 60 dynamics, 30 label/control pairs). A calibration scan was acquired with the same imaging parameters using a 16-phase look-locker readout after saturation (saturation delay (TD) = 50 ms; TR = 520 ms; slice timing difference = 32 ms; flip angle = 30°; 2 dynamics). R1 (relaxation rate R1 = 1/T1) was fitted from the saturation recovery signal using Eq. 1 by in-house developed MATLAB (version 9.10.0 (R2021a), The MathWorks Inc, Natick, Massachusetts, United States) programs utilizing a nonlinear least squares Levenberg–Marquardt method.

$$S(t) = S_0 \sin(\alpha)\left[\left(1 - e^{-TD\cdot R_1}\right)\left(\cos(\alpha)e^{-TR\cdot R_1}\right)^{n-1} + \left(1 - e^{-TR\cdot R_1}\right)\frac{1 - \left(\cos(\alpha)e^{-TR\cdot R_1}\right)^{n-1}}{1 - \cos(\alpha)e^{-TR\cdot R_1}}\right] \quad (1)$$

TD is the time since saturation, corrected for individual slice timing; TR is the time interval between two consecutive alpha pulses; and n is the index of the alpha pulses, which for this sequence took the values n = [1:16]. The R_1 value was used to

calculate M_0 from the initial six pCASL control measurements using Eq. 2.

$$M_0 = \frac{\frac{1}{6}\sum_{j=1}^{6} M_{ctr,j}}{[(1-e^{-R_1(TD-BS_2)}) + (-(1-e^{-R_1(BS_2-BS_1)}) + (1-e^{-R_1 BS_1})e^{-R_1(BS_2-BS_1)})e^{-R_1(TD-BS_2)}]} \quad (2)$$

BS_1/BS_2 are the timing of the background suppression pulses and M_{ctr} is the control part of the ASL data pairs. TD is the read-out time after saturation, corrected for slice timing differences.

$$TD = 3.6s + \text{slicedt} \cdot i, \text{ where } i = 0, 1, \cdots 15$$

The perfusion weighted maps were converted to quantitative CBF maps using the voxel-wise M_0 signal from Eq. 2 in the BASIL tool (FSL) (Chappell et al., 2009) with additional correction of tissue T_1-and R_2*-decay. T_1 of blood was corrected for each subject's session-specific haemoglobin concentration using the arterial equation from Lu et al. (Lu et al., 2004). Grey matter mean CBF values were extracted from the grey matter segmentations of the structural images resliced into ASL space using the oxford_asl (part of FSL) tool with the default threshold parameter of 0.8.

2.2.3 Phase contrast mapping

Global mean CBF was acquired using the PCM technique by measuring the blood flow supplying the brain through the carotid and basilary arteries (Bakker et al., 1995; Vestergaard et al., 2017). Velocity maps were acquired by a velocity-encoding turbo field echo sequence (1 slice, FOV = 240 × 240 mm^2; voxel size = 0.75 × 0.75 × 8 mm^3; TE/TR = 7.33/27.63 ms; flip angle = 10°; velocity encoding = 100 cm/s, without cardiac gating; 10 dynamics). The sequence was recorded twice to obtain optimal perpendicular slice positions on both internal carotid arteries (first scan) and the basilar artery (second scan). Each feeding artery was manually delineated using in-house developed MATLAB scripts. The blood flow to the brain was then calculated as the mean blood velocity times the cross-sectional area of the delineated cerebral arteries. The resulting flow was normalised to brain weight to obtain values in ml/100 g/min. Brain weight was estimated from the segmentation of the structural MRI image, including grey matter and white matter but excluding CSF and assuming a brain density of 1.05 g/ml (Torack et al., 1976).

2.2.4 Susceptibility-based oximetry (SBO)

Cerebral arteriovenous oxygen saturation differences (A-$V.O_2$) and $CMRO_2$ were acquired using susceptibility-based oximetry (SBO) MRI (Jain et al., 2010). Using the SBO technique, the oxygen saturation of the venous blood (SvO_2) leaving the brain in the sagittal sinus can be measured. The technique utilizes the magnetic properties of deoxyhaemoglobin in venous blood changes the intravascular magnetic susceptibility, which can be measured by MRI phase images. Susceptibility-weighted phase maps were acquired using a dual-echo gradient-echo sequence (1 slice, FOV = 220 × 190 mm^2; voxel size = 0.69 × 0.69 × 8 mm^3; TR = 23.1 ms; TE_1/TE_2 = 8.16/17.83 ms; flip angle = 30°; SENSE factor = 2; 10 dynamics, velocity encoding = 100 cm/s). The imaging plane was placed orthogonal to the sagittal sinus. By manual delineation of the sagittal sinus and the surrounding tissue, SvO_2 was calculated. An in-depth description of the postprocessing has been previously published (Vestergaard and Larsson, 2019). A-$V.O_2$ was calculated by subtracting SvO_2 from arterial saturation (SaO_2) measured using pulse oximetry. $CMRO_2$ was then calculated using the Fick principle (Eq. 3). Haemoglobin (Hgb) concentrations were measured from venous blood sampling.

$$CMRO_2 = Hgb \cdot CBF \cdot A - V.O_2 \quad (3)$$

From this sequence, we simultaneously also acquired phase information from which we could calculate the blood flow in the sagittal sinus by a similar approach as that used for calculating the flow in the feeding cerebral arteries by manual delineation of the sagittal sinus.

2.2.5 Magnetic resonance spectroscopy (MRS)

Cerebral NAA and lactate concentrations were measured using a single-voxel water-suppressed point-resolved 1H-spectroscopy (PRESS) sequence (TE/TR = 288/2000 ms; voxel size = 30 × 35 × 30 mm^3; 176 averages, 1,024 complex data points). Precuneus is a part of the default mode network and relatively metabolic stable, whereas the occipital cortex is a region which possibly could demonstrate more metabolic variation. These two regions could therefore possibly demonstrate different reproducibilities. For Group A, two measurements were acquired, one in the precuneus and a second in the occipital lobe. For Group B, only measurements in the precuneus were acquired due to the similar concentrations in the precuneus and occipital lobe observed in Group A.

Postprocessing and quantification of the spectra were performed using LCModel (LCModel, Version 6.3-1F, Toronto, Canada). The water peak acquired in the spectrum was used as reference to the measured metabolites. The water concentration in the spectroscopy voxel was estimated from the content of grey matter, white matter, and CSF within the voxel using the tissue segmentations from the structural images (Quadrelli et al., 2016). NAA and lactate concentrations were corrected for T_2 decay using literature values ($T_{2,H2O}$ = 95 ms; $T_{2,NAA}$ = 247 ms; $T_{2,Lac}$ = 240 ms) (Wansapura et al., 1999; Träber et al., 2004).

2.3 Statistics

All values are reported as means ± standard deviations. *p*-values less than 0.05 were considered significant. Reproducibility between the baseline measurement and subsequent repeated measurements was assessed by linear regression models and Bland–Altman analysis. R^2 values from the regression models and limit of agreement (LoA) metrics and within-subject coefficient of variation (CoV_{ws}) from Bland–Altman analysis were used to assess the reproducibility of the measurements. LoA was calculated as 1.96 times the mean standard deviation of the pairwise differences between baseline and each subsequent measurement.

2.4 Data availability

The parameters derived from the MRI-images and supporting data are available upon reasonable request. The MRI images are not publicly available due to privacy restrictions.

TABLE 2 Summary of R^2, limit of agreement (LoA) and within-subject coefficient of variation (CoV_{ws}) for the correlations between baseline and the subsequent measurements. Limit of agreement is defined as 1.96 standard deviations from Bland–Altman analysis. Abbreviations: A-V.O_2, arteriovenous oxygen saturation difference; CBF, cerebral blood flow; $CMRO_2$, cerebral metabolic rate of oxygen; NAA, N-acetyl-aspartate.

	Group A												Group B		
	1 hour (within-scan session)			6 hours			1 day			7 days			28–49 days		
	N = 40			*N* = 10			*N* = 10			*N* = 10			*N* = 16		
	R^2	LoA	CoV_{ws} [%]	R^2	LoA	CoV_{ws} [%]	R^2	LoA	CoV_{ws} [%]	R^2	LoA	CoV_{ws} [%]	R^2	LoA	CoV_{ws} [%]
Phase Contrast Mapping															
CBF (Whole brain mean) [ml/100 g/min]	0.84	8.1	7.4	0.86	6.3	5.6	0.71	8.9	8.1	0.57	10.6	9.5	0.31	13.8	11.2
Arterial Spin Labelling															
CBF (Grey matter mean) [ml/100 g/min]				0.85	10.7	9.3	0.71	14.6	12.8	0.69	16.7	13.9	0.31	18.3	13.1
Susceptibility-Based Oximetry															
A-V.O_2 [%]	0.87	4.0	7.0	0.57	7.7	13.7	0.47	9.12	16.7	0.26	10.7	18.6	0.29	12.4	19.1
$CMRO_2$ [µmol/100 g/min]	0.89	23.8	8.8	0.55	45.6	16.2	0.43	52.74	20.0	0.56	49.9	17.5	0.29	60.9	19.8
MR Spectroscopy															
Lactate—precuneus [mmol/l]				0.79	0.11	11.0	0.45	0.21	20.9	0.10	0.25	25.9	0.50	0.17	17.0
Lactate—occipital lobe [mmol/l]				0.51	0.17	17.4	0.41	0.19	19.4	0.32	0.21	20.4			
NAA—precuneus [mmol/l]				0.87	1.78	11.0	0.39	3.87	19.2	0.45	3.89	24.3	0.75	2.08	11.2
NAA—occipital lobe [mmol/l]				0.81	1.83	9.5	0.87	1.57	8.1	0.77	1.94	9.8			

2.5 Code availability

Software used for calculating CBF by the PCM technique is available at https://github.com/MarkVestergaard/PCMCalculator/. Software used to calculate SvO_2 from the SBO technique is available at https://github.com/MarkVestergaard/SBOCalculator/.

3 Results

For one subject in Group A, ASL analysis at the baseline measurement failed and this subject was removed from the further analysis of ASL reproducibility. Furthermore, the ASL analysis failed in one subject at the 6-h measurement and two subjects at the 7-day measurement in Group A. The failure to analyse these ASL measurements was due to technical issues with the calibration scan. For the other parameters, all data were satisfactorily acquired.

The average values of the acquired metrics in each MRI session are provided in Table 1. A summary of R^2 values from the linear regression, LoA from Bland–Altman analysis and CoV_{ws} for all parameters and correlations are summarized in Table 2. There were no significant differences in baseline values between group A and B.

The correlations and Bland–Altman analysis for global CBF, $CMRO_2$ and A-V.O_2 are demonstrated in Figure 2. The correlations for CBF, $CMRO_2$ and A-V.O_2 were significant for all comparisons. Correlations and reproducibilities were best for within-day measurements for all parameters (LoA = 6.3 ml/100 g/min; CoV_{ws} = 5.6% for CBF and LoA = 45.6 µmol/100 g/min, CoV_{ws} = 16.2% for $CMRO_2$) and gradually declined for longer time periods between measurements. The within-session reproducibility of CBF and $CMRO_2$ (Figure 2) demonstrated good reproducibility with low LoA (8.1 ml/100 g/min and 23.8 µmol/100 g/min) and highly significant correlations (R^2 = 0.84 and 0.89). However, CBF also demonstrated a significant bias towards lower values for the second measurement in the session compared to the first measurement (first measurement = 57.5 ± 8.3 ml/100 g/min; second measurement = 54.4 ± 7.2 ml/100 g/min, p = 0.0003).

Global CBF values across all sessions were significantly correlated with both haemoglobin concentration ($p < 10^{-4}$) and A-V.O_2 (p = 0.006) (Supplementary Figure S1). Reproducibility of

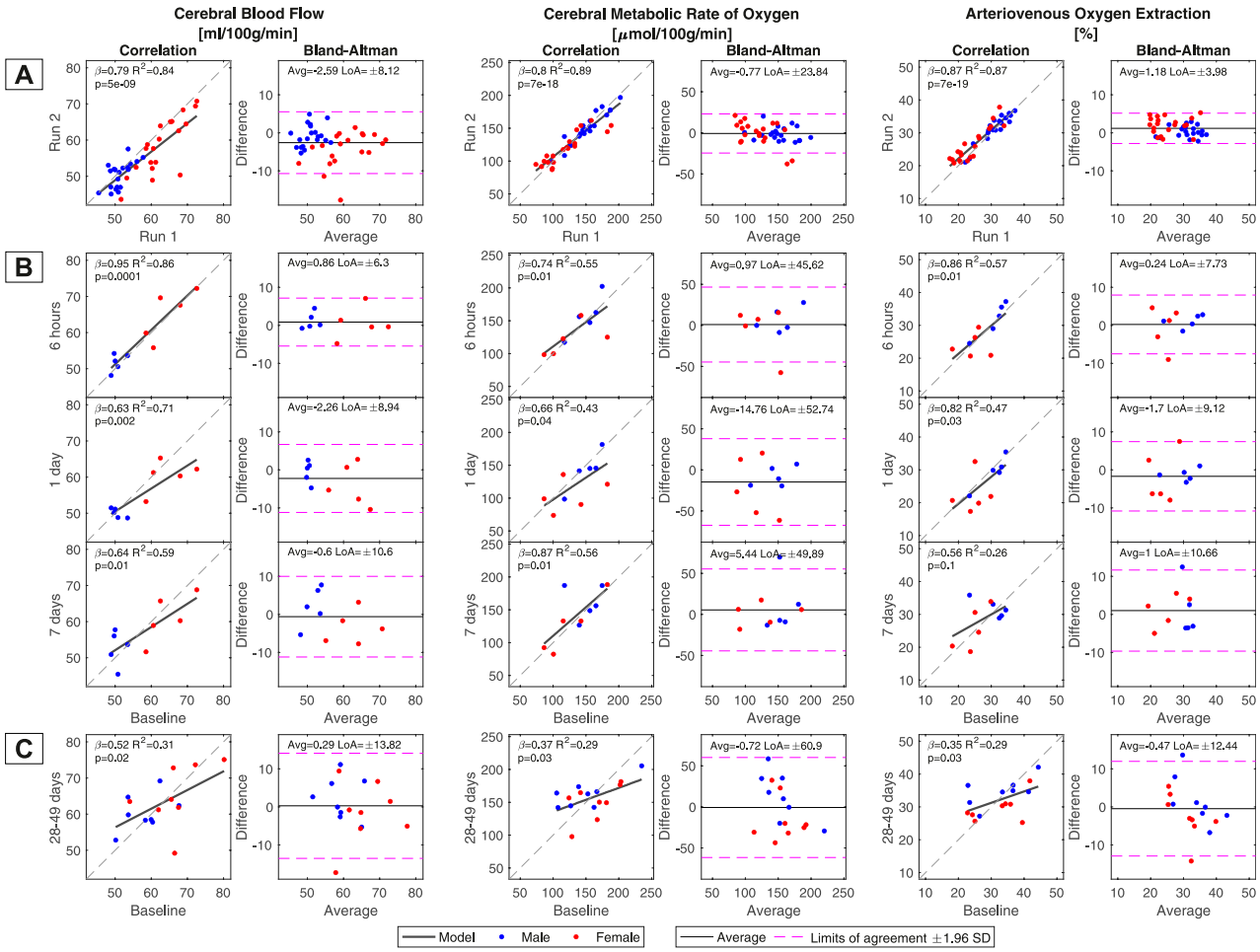

FIGURE 2
Correlation and reproducibility between baseline measurements and the subsequent acquisitions of global cerebral blood flow (CBF), cerebral metabolic rate of oxygen ($CMRO_2$) and arteriovenous oxygen saturation difference (A-$V.O_2$). **(A)** The within-session correlation was calculated from the duplicate measurements of CBF, A-$V.O_2$ and $CMRO_2$ that were acquired in each MRI session. The correlations between baseline and values from each subsequent MRI from Group A are shown in **(B)**. The correlations between baseline and values remeasured 28–49 days after the initial examination in Group B are shown in **(C)**. A general pattern of weaker correlation with increasing time between sessions is noted. Limits of agreement (LoAs) in the Bland–Altman analysis were calculated as 1.96 standard deviations of the pairwise subtracted values. Sex was not part of the regression model but is highlighted for visual interpretation. The regression slopes (β), R^2 coefficients, *p*-values and LoAs are noted in each panel.

the venous blood flow leaving the brain in the sagittal sinus is presented in Supplementary Figure S2A–C. The blood flow in the sagittal sinus demonstrated similar reproducibility to CBF, including a bias towards lower values at the second compared to the first measurement during the baseline session. There was also a significant correlation between CBF and blood flow in the sagittal sinus (Supplementary Figure S2D).

The mean regional CBF maps from the ASL acquisition and the correlation between the grey matter mean CBF from each session are shown in Figure 3. No significant difference was observed between each session. The voxel-wise LoA maps also did not demonstrate any regional differences in reproducibility for measurements up to 7 days apart. For measurements taken 28–49 days apart, the LoA was generally higher in the cortex than in the rest of the brain. Grey matter mean CBF values from the ASL measurement demonstrated the best reproducibility for within-day measurements and worse reproducibility for the remaining sessions, similar to global CBF values obtained by the PCM method.

Measurements of brain size and changes in haemoglobin concentration will affect the calculation of CBF and $CMRO_2$, and we therefore examined the reproducibility of these measurements as well (Supplementary Figure S3). Both estimation of brain size and haemoglobin concentration demonstrated very high reproducibility and therefore only minorly affected the longitudinal variant in CBF and $CMRO_2$ observed in this study. CBF was higher in women across all measurements as also demonstrated in multiple previous studies (Rodriguez et al., 1988; Esposito et al., 1996). There were no sex differences for the remaining parameters.

The correlations and Bland–Altman analysis of lactate and NAA concentrations are shown in Figure 4. All comparisons demonstrated significant correlations between baseline and subsequent measurements, except for lactate measurements after 7 days, which were only near significant for the measurement in the

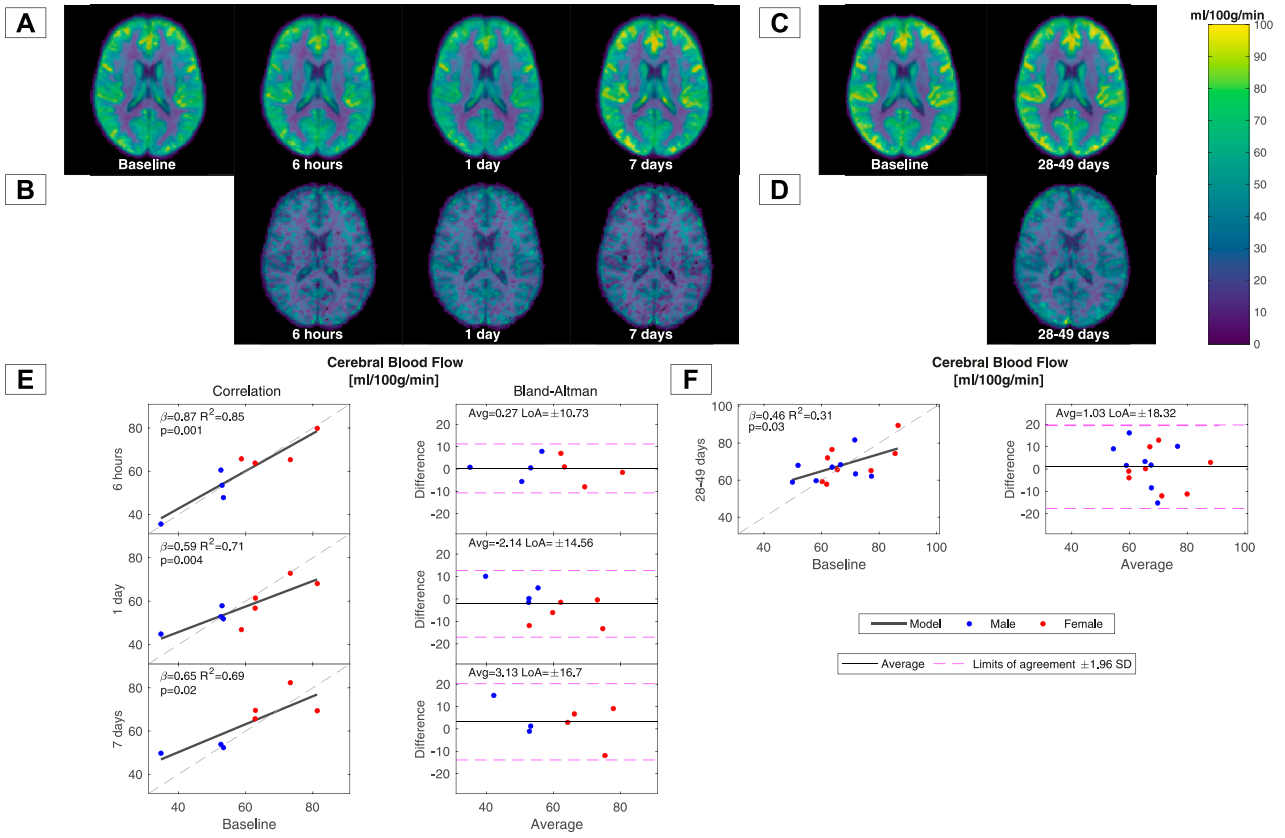

FIGURE 3
CBF maps acquired using arterial spin labelling and correlations of grey matter mean values between baseline and subsequent measurements. Average CBF maps of all subjects in Group A for each session in MNI-152 standard space are shown in **(A)**. Maps demonstrating voxel-wise limits of agreement (LoAs) between the baseline and subsequent measurements in Group A are shown in **(B)**. Average CBF maps from all subjects in Group B at the two MRI sessions are shown in **(C)**. Maps demonstrating voxel-wise LoAs between the baseline measurement and subsequent measurements 28–49 days after the initial examination of Group B are shown in **(D)**. Correlations and Bland–Altman analysis between the grey matter mean CBF values from the ASL measurement at baseline and subsequent sessions are shown in **(E)** for Group A and in **(F)** for Group B. The regression slopes (β), R^2 coefficients, *p*-values, and limits of agreement (LoAs) are noted in each panel.

occipital lobe ($p = 0.09$) and nonsignificant for the measurement in the precuneus ($p = 0.40$). The reproducibility was best for the within-day measurements for both lactate and NAA and similarly worse for the longer time periods between measurements. The quality parameters for the MRS data were signal-to-noise (SNR) = 38.8 ± 4.4, full width at half maximum (FWHM) = 0.05 ± 0.01, Cramer-Rao lower bounds (CRLB) for lactate = 25.9 ± 10.8%, CRLB for NAA = 2.9 ± 1.1% for the measurements in the occipital lobe and SNR = 42.5 ± 2.7, FWMH = 0.04 ± 0.01, CRLB for lactate = 20.2 ± 3.9% and CRLB for NAA = 2.1 ± 0.4% for the measurements in precuneus.

4 Discussion

We observed that repeated measurements of CBF, A-V.O_2, $CMRO_2$, lactate and NAA correlated and demonstrated good reproducibility, including up to several weeks between measurements. For CBF and $CMRO_2$, the reproducibility was best for within-day measurements and gradually declined for longer times between measurements. The reproducibility of lactate and NAA in the occipital lobe was similarly best for within-day measurements and gradually declined for the repeated measurements after 1 and 7 days. For lactate and NAA in the precuneus, the reproducibility was again best for within-day measurements and was equally worse for the remaining repeated measurements.

The variation in repeated measurements is caused by both measurement errors from the equipment and physiological changes. Modifications to the MRI scanner could influence the performance and affect the measurement error. Alterations to the MRI scanner, such as updating the scanner software or replacing the MRI coils, might also modify the reproducibility. However, there were no such modifications on the MRI scanner in the current study, and we do not anticipate the scanner to have significantly deteriorated during the project duration. Overall, we believe that the measurement error of the MRI scanner was similar in all MRI sessions, and we do not expect that any systematic changes occurred. Consequently, we think that the gradual decline in reproducibility we noticed with longer spans between measurements is due to physiological variation. The decreased reproducibility is therefore expected to be similar when using modalities other than MRI scans.

10.3389/fphys.2023.1213352

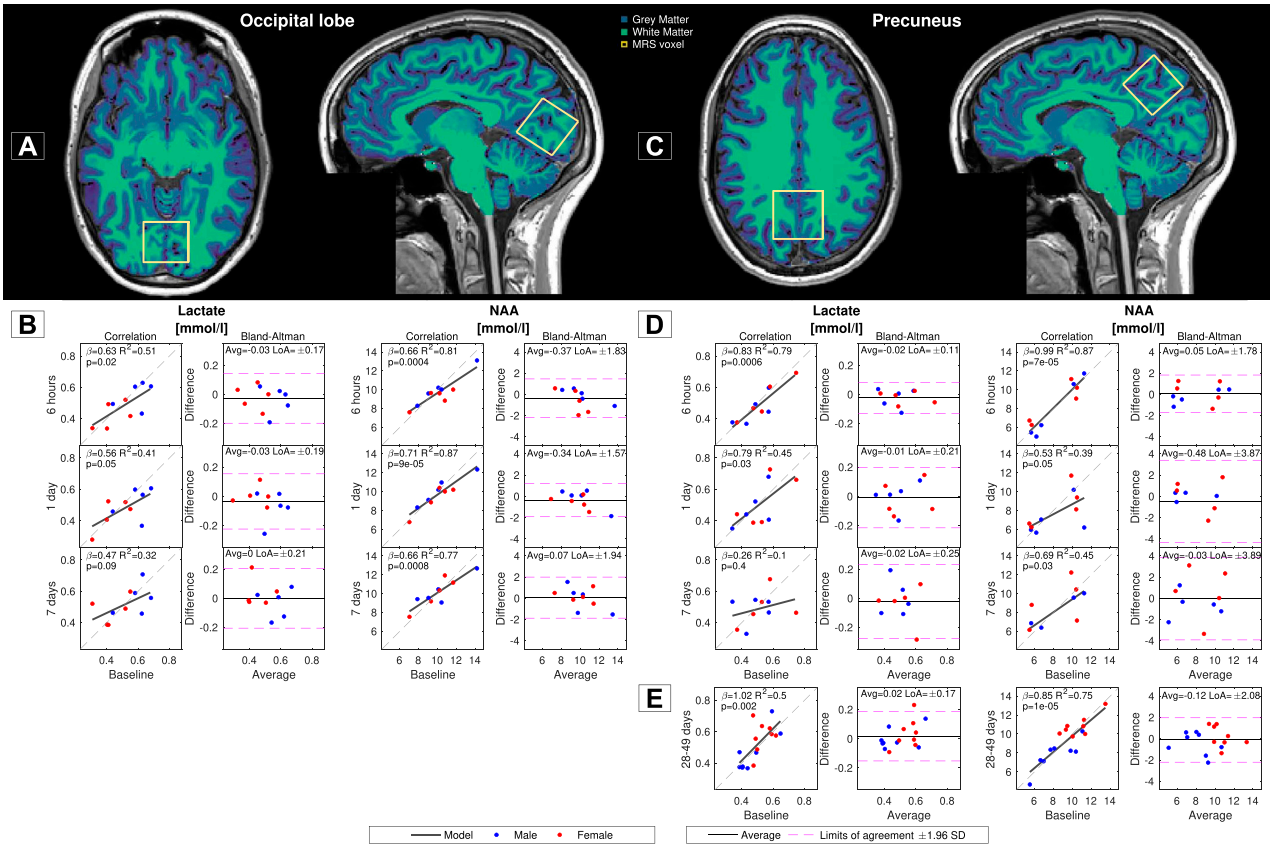

FIGURE 4
Correlation and reproducibility between baseline measurements and the subsequent acquisitions of cerebral lactate and N-acetyl-aspartate (NAA) concentrations. Lactate and NAA concentrations were measured in the occipital lobe **(A)** and precuneus **(C)**. Correlations and Bland–Altman analysis of the lactate and NAA concentrations in the occipital lobe between baseline and the subsequent acquisitions from Group A are shown in **(B)** and those from Group B in **(E)**. Correlations and Bland–Altman analysis of the lactate and NAA concentrations in the precuneus between baseline and the subsequent acquisitions from Group A are shown in **(D)** and those from Group B in **(E)**. The regression slopes (β), R^2 coefficients, *p*-values from the regressions and limits of agreement (LoAs) from Bland–Altman analysis are noted in each panel.

4.1 CBF

The techniques we used to measure CBF are noninvasive and widely available on MRI scanners, making them ideal for studies requiring multiple repeated measurements. Both PCM and ASL are therefore extensively used in research on brain physiology. We found CBF values similar to previously reported values using the same methods.

Cerebral perfusion is dynamically regulated to ensure sufficient delivery of nutrients, most notably oxygen, to the brain. Numerous factors affect CBF, for example, changes in blood gas tension, such as oxygen and CO_2; haemoglobin concentration; and hormonal variations (Kety and Schmidt, 1948; Henriksen et al., 2013; Vestergaard and Larsson, 2019). Intake of certain compounds, such as caffeine or nicotine, will also affect CBF (Zubieta et al., 2005; Krause et al., 2006). Therefore, it is to be expected that CBF will also vary within subjects and knowing the reproducibility over different time periods is important when studying CBF. Generally, we observed better reproducibility for shorter periods between examinations, with the lowest LoA and best correlation for the within-session measurements. However, we also observed a small but significant bias towards lower CBF at the second measurement in the within-session examination, also resulting in a relatively high CoV_{ws}. There were approximately 60 min between these two measurements. Interestingly, this lower CBF did not reflect changes in $CMRO_2$, suggesting that the effect on CBF from lying in the scanner is not due to changes in cerebral energy metabolism but rather an effect directly on CBF. An effect on CBF from lying for a prolonged time in an MRI scanner should therefore be considered when designing experiments on brain physiology with interventions in the scanner. Prior studies on the reproducibility of CBF have often included just two repeated examinations; therefore, the time variant effects could not be investigated. However, studies on within-day or within-session repeated measurements have generally shown good reproducibility, and studies using longer periods between examinations have similarly shown poorer reproducibility (Fan et al., 2016). A previous study on the reproducibility of CBF measurement by PCM demonstrated slightly worse reproducibility for within-session and within-day examinations compared to our study and similar reproducibility for between-day examinations (Spilt et al., 2002). Another study using 7 weeks between measurements and the ASL technique for the measurement

of CBF found reproducibility for whole-brain values similar to our data (Hermes et al., 2007). A study using PET imaging with oxygen-15-labelled water [^{15}O-H_2O] as the radiotracer and a study using ASL MRI found slightly worse within-session reproducibility compared to our study (Coles et al., 2006; Gevers et al., 2009). A study comparing CBF values obtained from ASL MRI against values acquired by ^{15}O-H_2O PET found similar reproducibilities for measurements with 25–45 days apart compared to our reproducibility for measurements with 28–49 days apart but poorer within-session reproducibility (Heijtel et al., 2014). A study using the dynamic contrast-enhanced (DCE) MRI technique found similar reproducibility for the measurement of grey and white matter separately 1 week apart compared to our whole-brain measurement (Cramer et al., 2023). Overall, the results from our study suggest that the differences in reproducibility observed in different studies are likely, at least partly, a result of the various lengths of time between examinations used in the studies.

Most studies on CBF reproducibility examine homogenous groups of healthy young adults, as was the case for this study. For example, the subjects examined had similar ages, were non-smokers and did not have any diseases or take medicine that could affect vascular function. Investigations of less homogenous groups could likely demonstrate poorer reproducibility.

4.2 $CMRO_2$

For $CMRO_2$, we observed values similar to those acquired using invasive PET imaging (Bremmer et al., 2011; Kudomi et al., 2013) or blood sampling from jugular vein catheters (Ainslie et al., 2014). The SBO technique used to measure venous oxygen saturation in the sagittal sinus for calculation of $CMRO_2$ has been validated against blood samples acquired by catheter from the jugular vein during MRI scanning (Miao et al., 2019). Reproducibility of $CMRO_2$ has been far less studied than CBF, likely due to the technical difficulties in acquisition compared to CBF. A study using T2-Relaxation-Under-Spin-Tagging (TRUST) MRI for the measurement of venous oxygen saturation and PCM for CBF found reproducibility for within-session repeated measurements comparable to our study but better between-day (1–14 days) reproducibility (Liu et al., 2013). A study using calibrated BOLD imaging and a complicated calibration scheme involving inhalation of hypercapnic and hyperoxic air to quantify $CMRO_2$ observed a slightly worse between day reproducibility of grey matter $CMRO_2$ compared to our whole brain $CMRO_2$ (Lajoie et al., 2016). The method relies on many parameters which are either fitted or derived from literature values and inaccuracies in these parameters could be the cause for the slightly poorer reproducibility.

Studies using PET imaging and inhalation of oxygen-15 as a radiotracer for $CMRO_2$ measurements have demonstrated very high reproducibility for within-session repeated measurements (Coles et al., 2006). Another PET study examining $CMRO_2$ using inhalation of oxygen-15 with an interval of 3 to 54 days between measurements found significantly better reproducibility than our results with 7 days or several weeks between measurements (Bremmer et al., 2011). Overall, this suggests that the PET technique for $CMRO_2$ measurements has better reproducibility than using combined PCM and SBO, as in this study. However, using PET and oxygen-15 is also significantly more cumbersome, time-consuming, and invasive than MRI techniques. Generally, studies on the reproducibility of $CMRO_2$ are few, and more studies using different techniques and with different timespans between examinations should be performed in the future.

4.3 Lactate and NAA

We observed relatively stable and reproducible concentrations for both lactate and NAA in both the occipital lobe and precuneus. Generally, we observed similar trends in correlations and reproducibility for lactate and $CMRO_2$, both related to energy metabolism, suggesting that the variation in lactate and $CMRO_2$ could be due to fluctuations in overall energy metabolism.

Studies on the reproducibility of MRS, similar to those on CBF and $CMRO_2$, have often compared only two repeated examinations, and time variant effects were not considered. Furthermore, the various placements of the MRS voxels, the exact technique used, and the patient groups studied make it difficult to compare results.

It has been shown that NAA can be affected by brain diseases which impairs the brain metabolism, such as dementia or multiple sclerosis, however it would be expected that in healthy subjects the NAA concentration is relatively stable over time (Moffett et al., 2007). One study has demonstrated a very high intersession reproducibility of NAA with a voxel primarily located in white matter (Brooks et al., 1999). Another study using spectroscopic imaging with repeated measurements between a few days and several months apart found reasonable reproducibility of the NAA/creatine ratio in grey matter (Tedeschi et al., 1996). Studies using a 7 T MRI scanner found a reproducibility for NAA of 5.3% in the anterior cingulate cortex with 2-3 months between visits, which is better than the reproducibility we observed in the precuneus (Wijtenburg et al., 2019). The higher field strength of the MRI scanner in that study compared to ours could be a reason for the better reproducibility. Studies on lactate reproducibility are very limited; however, one study examined the reproducibility of lactate in the posterior cingulate using 7 T MRI with 1 week between measurements and found similar values to our measurement of lactate in the precuneus with 1 week between measurements (Terpstra et al., 2016).

4.4 Strengths and limitations

The main strength of the study is that we measured multiple parameters in the same subjects and acquired data from multiple repeated measurements at distinct time points after the initial baseline measurement. This enables us to examine time variant changes in reproducibility.

A limitation is that we only examined young healthy subjects. In cohorts of older individuals or subjects with certain diseases, the reproducibility might be lower than in young subjects. This should be considered when applying the results in projects conducting research on other subject groups. It should also be noted that all parameters in this study are measured on the same scanner with optimised MRI sequence parameters set for our purposes. Thus, this does not guarantee

a direct translation to different scanners or sequence parameters, e.g., single echo pCASL instead of dual echo pCASL.

Another limitation is that we do not have a sufficient number of participants to examine which and to what extend the systemic factors explain the variation of the cerebral physiology. Systemic factors, such as SaO_2 or arterial CO_2 partial pressure, are known to impact CBF and changes in these parameters could account for some of the alterations in cerebral physiology over time. We observed, on average, stable values of SaO_2, $PetCO_2$, heart rate and blood pressure between the MRI sessions and a relatively narrow span of values across participants, suggesting limited effect from changes of these parameters. Nevertheless, individual natural fluctuations of systemic factors could likely still explain some of the variation in the cerebral physiology. Larger studies are needed to quantify the contributions arising from fluctuations in the various systemic factors on the cerebral physiology.

4.5 Conclusion

Overall, the results from the present study demonstrate satisfactorily good reproducibility of cerebral physiology measurements using non-invasive MRI techniques. We observed the best reproducibility for short timespans between the examinations and, generally, a gradual worsening of the reproducibility for longer times between measurements. Reproducibility in the context of evaluating an intervention or disease evolution should therefore be estimated based on the time scale of the study.

Data availability statement

The datasets presented in this article are not readily available because of privacy restrictions. The parameters derived from the MRI-images and supporting data are available upon reasonable request. Requests to access the datasets should be directed to mark.bitsch.vestergaard@regionh.dk.

Ethics statement

The studies involving humans were approved by the Scientific Ethical Committee of the Capital Region of Denmark. The studies were conducted in accordance with the local legislation and institutional requirements. The participants provided their written informed consent to participate in this study.

Author contributions

SM: conceptualisation, investigation, writing—original draft. UL: methodology, data curation, formal analysis, software, visualization, writing—original draft. SA: conceptualization, project administration, funding acquisition, resources, writing—review and editing. KO: project administration, writing—review and editing. KM: conceptualisation, project administration, resources, writing—review and editing. HL: conceptualisation, methodology, formal analysis, writing—review and editing. MV: conceptualisation, methodology, data curation, formal analysis, software, writing—original draft. All authors contributed to the article and approved the submitted version.

Funding

The study was supported by fundings from Læge Sofus Carl Emil Friis og Hustru Olga Doris Friis Legat and AP Møller Fonden. MV was funded by grant from the Lundbeck Foundation (R347-2020-217).

Acknowledgments

The authors thank Maria Højberg Knudsen for invaluable help executing MRI sessions, and research assistants Mathilde Aya Røen, Kübra Hidiroglu, Ingeborg By Raaum, Nanna Eriksen, Maryam Noory and Bardha Murtezaj for a steady team effort during data collection. Special thanks to all participants for making our research possible.

Conflict of interest

The authors declare that the research was conducted in the absence of any commercial or financial relationships that could be construed as a potential conflict of interest.

Publisher's note

All claims expressed in this article are solely those of the authors and do not necessarily represent those of their affiliated organizations, or those of the publisher, the editors and the reviewers. Any product that may be evaluated in this article, or claim that may be made by its manufacturer, is not guaranteed or endorsed by the publisher.

Supplementary material

The Supplementary Material for this article can be found online at: https://www.frontiersin.org/articles/10.3389/fphys.2023.1213352/full#supplementary-material

References

Ainslie, P. N., Shaw, A. D., Smith, K. J., Willie, C. K., Ikeda, K., Graham, J., et al. (2014). Stability of cerebral metabolism and substrate availability in humans during hypoxia and hyperoxia. *Clin. Sci.* 126, 661. doi:10.1042/CS20130343

Bakker, C. J. G., Kouwenhoven, M., Hartkamp, M. J., Hoogeveen, R. M., and Mali, W. P. T. M. (1995). Accuracy and precision of time-averaged flow as measured by nontriggered 2D phase-contrast MR angiography, a phantom evaluation. *Magn. Reson. Imaging* 13, 959–965. doi:10.1016/0730-725X(95)02005-E

Bitsch, A., Bruhn, H., Vougioukas, V., Stringaris, A., Lassmann, H., Frahm, J., et al. (1999). Inflammatory CNS demyelination: histopathologic correlation with *in vivo* quantitative proton MR spectroscopy. *AJNR Am. J. Neuroradiol.* 20, 1619–1627.

Bremmer, J. P., Van Berckel, B. N. M., Persoon, S., Kappelle, L. J., Lammertsma, A. A., Kloet, R., et al. (2011). Day-to-Day test–retest variability of CBF, CMRO2, and OEF measurements using dynamic 15O PET studies. *Mol. Imaging Biol.* 13, 759–768. doi:10.1007/s11307-010-0382-1

Brooks, W. M., Friedman, S. D., and Stidley, C. A. (1999). Reproducibility of1H-MRS *in vivo*. *Magn. Reson. Med.* 41, 193–197. doi:10.1002/(SICI)1522-2594

Chappell, M. A., Groves, A. R., Whitcher, B., and Woolrich, M. W. (2009). Variational bayesian inference for a nonlinear forward model. *IEEE Trans. Signal Process.* 57, 223–236. doi:10.1109/TSP.2008.2005752

Coles, J. P., Fryer, T. D., Bradley, P. G., Nortje, J., Smielewski, P., Rice, K., et al. (2006). Intersubject variability and reproducibility of ^{15} O PET studies. *J. Cereb. Blood Flow. Metab.* 26, 48–57. doi:10.1038/sj.jcbfm.9600179

Cramer, S. P., Larsson, H. B. W., Knudsen, M. H., Simonsen, H. J., Vestergaard, M. B., and Lindberg, U. (2023). Reproducibility and optimal arterial input function selection in dynamic contrast-enhanced perfusion MRI in the healthy brain. *J. Magn. Reson. Imaging* 57, 1229–1240. doi:10.1002/jmri.28380

Esposito, G., Van Horn, J. D., Weinberger, D. R., and Berman, K. F. (1996). Gender differences in cerebral blood flow as a function of cognitive state with PET. *J. Nucl. Med. Off. Publ. Soc. Nucl. Med.* 37, 559–564.

Fan, A. P., Jahanian, H., Holdsworth, S. J., and Zaharchuk, G. (2016). Comparison of cerebral blood flow measurement with [^{15} O]-water positron emission tomography and arterial spin labeling magnetic resonance imaging: A systematic review. *J. Cereb. Blood Flow. Metab.* 36, 842–861. doi:10.1177/0271678X16636393

Gevers, S., Majoie, C. B. L. M., Van Den Tweel, X. W., Lavini, C., and Nederveen, A. J. (2009). Acquisition time and reproducibility of continuous arterial spin-labeling perfusion imaging at 3T. *Am. J. Neuroradiol.* 30, 968–971. doi:10.3174/ajnr.A1454

Goyal, M. S., Hawrylycz, M., Miller, J. A., Snyder, A. Z., and Raichle, M. E. (2014). Aerobic glycolysis in the human brain is associated with development and neotenous gene expression. *Cell. Metab.* 19, 49–57. doi:10.1016/j.cmet.2013.11.020

Heijtel, D. F. R., Mutsaerts, H. J. M. M., Bakker, E., Schober, P., Stevens, M. F., Petersen, E. T., et al. (2014). Accuracy and precision of pseudo-continuous arterial spin labeling perfusion during baseline and hypercapnia: A head-to-head comparison with ^{15}O H_2O positron emission tomography. *NeuroImage* 92, 182–192. doi:10.1016/j.neuroimage.2014.02.011

Henriksen, O. M., Kruuse, C., Olesen, J., Jensen, L. T., Larsson, H. B., Birk, S., et al. (2013). Sources of variability of resting cerebral blood flow in healthy subjects: A study using ^{133} Xe spect measurements. *J. Cereb. Blood Flow. Metab.* 33, 787–792. doi:10.1038/jcbfm.2013.17

Hermes, M., Hagemann, D., Britz, P., Lieser, S., Rock, J., Naumann, E., et al. (2007). Reproducibility of continuous arterial spin labeling perfusion MRI after 7 weeks. *Magn. Reson. Mat. Phys. Biol. Med.* 20, 103–115. doi:10.1007/s10334-007-0073-3

Hyder, F., Herman, P., Bailey, C. J., Møller, A., Globinsky, R., Fulbright, R. K., et al. (2016). Uniform distributions of glucose oxidation and oxygen extraction in gray matter of normal human brain: no evidence of regional differences of aerobic glycolysis. *J. Cereb. Blood Flow. Metab.* 36, 903–916. doi:10.1177/0271678X15625349

Iida, A., Okazawa, H., Hayashida, K., Tsuyuguchi, N., Ishii, K., Kuwabara, Y., et al. (2004). Database of normal human cerebral blood flow, cerebral blood volume, cerebral oxygen extraction fraction and cerebral metabolic rate of oxygen measured by positron emission tomography with 15 O-labelled carbon dioxide or water, carbon monoxide and oxygen: A multicentre study in Japan. *Eur. J. Nucl. Med. Mol. Imaging* 31, 635–643. doi:10.1007/s00259-003-1430-8

Jain, V., Langham, M. C., and Wehrli, F. W. (2010). MRI estimation of global brain oxygen consumption rate. *J. Cereb. Blood Flow. Metab.* 30, 1598–1607. doi:10.1038/jcbfm.2010.49

Jenkinson, M., Beckmann, C. F., Behrens, T. E. J., Woolrich, M. W., and Smith, S. M. (2012). *FSL*. NeuroImage 62, 782–790. doi:10.1016/j.neuroimage.2011.09.015

Kety, S. S., and Schmidt, C. F. (1948). The effects of altered arterial tensions of carbon dioxide and oxygen on cerebral blood flow and cerebral oxygen consumption of normal young men. *J. Clin. Investig.* 27, 484–492. doi:10.1172/JCI101995

Krause, D. N., Duckles, S. P., and Pelligrino, D. A. (2006). Influence of sex steroid hormones on cerebrovascular function. *J. Appl. Physiol.* 101, 1252–1261. doi:10.1152/japplphysiol.01095.2005

Kudomi, N., Hirano, Y., Koshino, K., Hayashi, T., Watabe, H., Fukushima, K., et al. (2013). Rapid quantitative *CBF* and *CMRO* $_2$ measurements from a single *PET* scan with sequential administration of dual ^{15} O-labeled tracers. *J. Cereb. Blood Flow. Metab.* 33, 440–448. doi:10.1038/jcbfm.2012.188

Lajoie, I., Tancredi, F. B., and Hoge, R. D. (2016). Regional reproducibility of BOLD calibration parameter M, OEF and resting-state CMRO2 measurements with QUO2 MRI. *PLoS ONE* 11, 01630711–e163131. doi:10.1371/journal.pone.0163071

Lassen, N. A. (1959). Cerebral blood flow and oxygen consumption in man. *Physiol. Rev.* 39, 183–238. doi:10.1152/physrev.1959.39.2.183

Liddle, P. F., Friston, K. J., Frith, C. D., Hirsch, S. R., Jones, T., and Frackowiak, R. S. J. (1992). Patterns of cerebral blood flow in schizophrenia. *Br. J. Psychiatry* 160, 179–186. doi:10.1192/bjp.160.2.179

Liu, P., Xu, F., and Lu, H. (2013). Test-retest reproducibility of a rapid method to measure brain oxygen metabolism. *Magn. Reson. Med.* 69, 675–681. doi:10.1002/mrm.24295

Lu, H., Clingman, C., Golay, X., and Van Zijl, P. C. M. (2004). Determining the longitudinal relaxation time (T1) of blood at 3.0 Tesla. *Magn. Reson. Med.* 52, 679–682. doi:10.1002/mrm.20178

Madsen, S. S., Møller, K., Olsen, K. S., Vestergaard, M. B., Lindberg, U., Larsson, H. B. W., et al. (2020). Neuroplasticity induced by general anaesthesia: study protocol for a randomised cross-over clinical trial exploring the effects of sevoflurane and propofol on the brain – a 3-T magnetic resonance imaging study of healthy volunteers. *Trials* 21, 805. doi:10.1186/s13063-020-04468-y

Miao, X., Nayak, K. S., and Wood, J. C. (2019). *In vivo* validation of T2- and susceptibility-based $S_v O_2$ measurements with jugular vein catheterization under hypoxia and hypercapnia. *Magn. Reson. Med.* 82, 2188–2198. doi:10.1002/mrm.27871

Moffett, J., Ross, B., Arun, P., Madhavarao, C., and Namboodiri, A. (2007). N-Acetylaspartate in the CNS: from neurodiagnostics to neurobiology. *Prog. Neurobiol.* 81, 89–131. doi:10.1016/j.pneurobio.2006.12.003

Oshima, T., Karasawa, F., Okazaki, Y., Wada, H., and Satoh, T. (2003). Effects of sevoflurane on cerebral blood flow and cerebral metabolic rate of oxygen in human beings: A comparison with isoflurane. *Eur. J. Anaesthesiol.* 20, 543–547. doi:10.1017/S0265021503000863

Paulson, O. B., Strandgaard, S., and Edvinsson, L. (1990). Cerebral autoregulation. *Cerebrovasc. Brain Metab. Rev.* 2, 161–192.

Peng, S.-L., Dumas, J. A., Park, D. C., Liu, P., Filbey, F. M., McAdams, C. J., et al. (2014). Age-related increase of resting metabolic rate in the human brain. *NeuroImage* 98, 176–183. doi:10.1016/j.neuroimage.2014.04.078

Powers, W. J., Grubb, R. L., Darriet, D., and Raichle, M. E. (1985). Cerebral blood flow and cerebral metabolic rate of oxygen requirements for cerebral function and viability in humans. *J. Cereb. Blood Flow. Metab.* 5, 600–608. doi:10.1038/jcbfm.1985.89

Quadrelli, S., Mountford, C., and Ramadan, S. (2016). Hitchhiker'S guide to voxel segmentation for partial volume correction of *in vivo* magnetic resonance spectroscopy. *Magn. Reson. Insights* 9, 1–8. MRI. doi:10.4137/MRI.S32903

Rodriguez, G., Warkentin, S., Risberg, J., and Rosadini, G. (1988). Sex differences in regional cerebral blood flow. *J. Cereb. Blood Flow. Metab.* 8, 783–789. doi:10.1038/jcbfm.1988.133

Snyder, H. M., Corriveau, R. A., Craft, S., Faber, J. E., Greenberg, S. M., Knopman, D., et al. (2015). Vascular contributions to cognitive impairment and dementia including Alzheimer's disease. *Alzheimers Dement.* 11, 710–717. doi:10.1016/j.jalz.2014.10.008

Spilt, A., Box, F. M. A., Van Der Geest, R. J., Reiber, J. H. C., Kunz, P., Kamper, A. M., et al. (2002). Reproducibility of total cerebral blood flow measurements using phase contrast magnetic resonance imaging. *J. Magn. Reson. Imaging* 16, 1–5. doi:10.1002/jmri.10133

Tedeschi, G., Bertolino, A., Campbell, G., Barnett, A. S., Duyn, J. H., Jacob, P. K., et al. (1996). Reproducibility of proton MR spectroscopic imaging findings. *AJNR Am. J. Neuroradiol.* 17, 1871–1879.

Terpstra, M., Cheong, I., Lyu, T., Deelchand, D. K., Emir, U. E., Bednařík, P., et al. (2016). Test-retest reproducibility of neurochemical profiles with short-echo, single-voxel MR spectroscopy at 3T and 7T: test-Retest Reproducibility of Neurochemical Profiles at 3T and 7T. *Magn. Reson. Med.* 76, 1083–1091. doi:10.1002/mrm.26022

Torack, R. M., Alcala, H., Gado, M., and Burton, R. (1976). Correlative assay of computerized cranial tomography (CCT), water content and specific gravity in normal and pathological postmortem brain. *J. Neuropathol. Exp. Neurol.* 35, 385–392. doi:10.1097/00005072-197607000-00001

Träber, F., Block, W., Lamerichs, R., Gieseke, J., and Schild, H. H. (2004). ^{1} H metabolite relaxation times at 3.0 tesla: measurements of T1 and T2 values in normal brain and determination of regional differences in transverse relaxation: ^{1} h metabolite relaxation times at 3.0 T. *J. Magn. Reson. Imaging* 19, 537–545. doi:10.1002/jmri.20053

Vestergaard, M. B., Ghanizada, H., Lindberg, U., Arngrim, N., Paulson, O. B., Gjedde, A., et al. (2022). Human cerebral perfusion, oxygen consumption, and lactate production in response to hypoxic exposure. *Cereb. Cortex* 32, 1295–1306. doi:10.1093/cercor/bhab294

Vestergaard, M. B., Jensen, M. L., Arngrim, N., Lindberg, U., and Larsson, H. B. (2020). Higher physiological vulnerability to hypoxic exposure with advancing age in the human brain. *J. Cereb. Blood Flow. Metab.* 40, 341–353. doi:10.1177/0271678X18818291

Vestergaard, M. B., and Larsson, H. B. (2019). Cerebral metabolism and vascular reactivity during breath-hold and hypoxic challenge in freedivers and healthy controls. *J. Cereb. Blood Flow. Metab.* 39, 834–848. doi:10.1177/0271678X17737909

Vestergaard, M. B., Lindberg, U., Aachmann-Andersen, N. J., Lisbjerg, K., Christensen, S. J., Law, I., et al. (2016). Acute hypoxia increases the cerebral metabolic rate – A magnetic resonance imaging study. *J. Cereb. Blood Flow. Metab.* 36, 1046–1058. doi:10.1177/0271678X15606460

Vestergaard, M. B., Lindberg, U., Aachmann-Andersen, N. J., Lisbjerg, K., Christensen, S. J., Rasmussen, P., et al. (2017). Comparison of global cerebral blood flow measured by phase-contrast mapping MRI with ^{15}O-H$_2$O positron emission tomography: CBF measured by PCM MRI and ^{15}O-H$_2$O PET. *J. Magn. Reson. Imaging* 45, 692–699. doi:10.1002/jmri.25442

Wansapura, J. P., Holland, S. K., Dunn, R. S., and Ball, W. S. (1999). NMR relaxation times in the human brain at 3.0 tesla. *J. Magn. Reson. Imaging* 9, 531–538. doi:10.1002/(SICI)1522-2586

Wijtenburg, S. A., Rowland, L. M., Oeltzschner, G., Barker, P. B., Workman, C. I., and Smith, G. S. (2019). Reproducibility of brain MRS in older healthy adults at 7T. *NMR Biomed.* 32, e4040. doi:10.1002/nbm.4040

Wolters, F. J., Zonneveld, H. I., Hofman, A., Van Der Lugt, A., Koudstaal, P. J., Vernooij, M. W., et al. (2017). Cerebral perfusion and the risk of dementia: A population-based study. *Circulation* 136, 719–728. doi:10.1161/CIRCULATIONAHA.117.027448

Younis, S., Christensen, C. E., Vestergaard, M. B., Lindberg, U., Tolnai, D., Paulson, O. B., et al. (2021). Glutamate levels and perfusion in pons during migraine attacks: A 3T MRI study using proton spectroscopy and arterial spin labeling. *J. Cereb. Blood Flow. Metab.* 41, 604–616. doi:10.1177/0271678X20906902

Zubieta, J.-K., Heitzeg, M. M., Xu, Y., Koeppe, R. A., Ni, L., Guthrie, S., et al. (2005). Regional cerebral blood flow responses to smoking in tobacco smokers after overnight abstinence. *Am. J. Psychiatry* 162, 567–577. doi:10.1176/appi.ajp.162.3.567

frontiers | Frontiers in Physiology

TYPE Original Research
PUBLISHED 06 October 2023
DOI 10.3389/fphys.2023.1231793

OPEN ACCESS

EDITED BY
Alex Bhogal,
Utrecht University, Netherlands

REVIEWED BY
Dengrong Jiang,
Johns Hopkins University, United States
Avery Berman,
Carleton University, Canada

*CORRESPONDENCE
Linh N. N. Le,
lnnle@ucdavis.edu

RECEIVED 31 May 2023
ACCEPTED 25 September 2023
PUBLISHED 06 October 2023

CITATION
Le LNN, Wheeler GJ, Holy EN, Donnay CA, Blockley NP, Yee AH, Ng KL and Fan AP (2023), Cortical oxygen extraction fraction using quantitative BOLD MRI and cerebral blood flow during vasodilation.
Front. Physiol. 14:1231793.
doi: 10.3389/fphys.2023.1231793

Cortical oxygen extraction fraction using quantitative BOLD MRI and cerebral blood flow during vasodilation

Linh N. N. Le[1]*, Gregory J. Wheeler[1], Emily N. Holy[2], Corinne A. Donnay[2], Nicholas P. Blockley[3], Alan H. Yee[2], Kwan L. Ng[2] and Audrey P. Fan[1,2]

[1]Department of Biomedical Engineering, University of California, Davis, Davis, CA, United States, [2]Department of Neurology, University of California, Davis, Davis, CA, United States, [3]School of Medicine and Health Sciences, University of Nottingham, Nottingham, United Kingdom

Introduction: We aimed to demonstrate non-invasive measurements of regional oxygen extraction fraction (OEF) from quantitative BOLD MRI modeling at baseline and after pharmacological vasodilation. We hypothesized that OEF decreases in response to vasodilation with acetazolamide (ACZ) in healthy conditions, reflecting compensation in regions with increased cerebral blood flow (CBF), while cerebral metabolic rate of oxygen ($CMRO_2$) remained unchanged. We also aimed to assess the relationship between OEF and perfusion in the default mode network (DMN) regions that have shown associations with vascular risk factors and cerebrovascular reactivity in different neurological conditions.

Material and methods: Eight healthy subjects (47 ± 13 years, 6 female) were scanned on a 3 T scanner with a 32-channel head coil before and after administration of 15 mg/kg ACZ as a pharmacological vasodilator. The MR imaging acquisition protocols included: 1) A Gradient Echo Slice Excitation Profile Imaging Asymmetric Spin Echo scan to quantify OEF, deoxygenated blood volume, and reversible transverse relaxation rate (R_2') and 2) a multi-post labeling delay arterial spin labeling scan to measure CBF. To assess changes in each parameter due to vasodilation, two-way *t*-tests were performed for all pairs (baseline versus vasodilation) in the DMN brain regions with Bonferroni correction for multiple comparisons. The relationships between CBF versus OEF and CBF versus R_2' were analyzed and compared across DMN regions using linear, mixed-effect models.

Results: During vasodilation, CBF significantly increased in the medial frontal cortex ($P = 0.004$), posterior cingulate gyrus (pCG) ($P = 0.004$), precuneus cortex (PCun) ($P = 0.004$), and occipital pole ($P = 0.001$). Concurrently, a significant decrease in OEF was observed only in the pCG (8.8%, $P = 0.003$) and PCun (8.7%, $P = 0.001$). $CMRO_2$ showed a trend of increased values after vasodilation, but these differences were not significant after correction for multiple comparisons. Although R_2' showed a slightly decreasing trend, no statistically significant changes were found in any regions in response to ACZ. The CBF response to ACZ exhibited a stronger negative correlation with OEF ($\beta = -0.104 \pm 0.027$; $t = -3.852, P < 0.001$), than with R_2' ($\beta = -0.016 \pm 0.006$; $t = -2.692, P = 0.008$).

Conclusion: Quantitative BOLD modeling can reliably measure OEF across multiple physiological conditions and captures vascular changes with higher

sensitivity than R_2' values. The inverse correlation between OEF and CBF across regions in DMN, suggests that these two measurements, in response to ACZ vasodilation, are reliable indicators of tissue health in this healthy cohort.

KEYWORDS

Oxygen extraction fraction (OEF), cerebral blood flow (CBF), vasodilation, arterial spin labeling (ASL) MRI, quantitative BOLD (qBOLD), magnetic resonance imaging (MRI)

1 Introduction

The brain has a high metabolic demand for oxygen compared to other organs since the human brain comprises just 2% of the total body mass but consumes 20% of available oxygen for normal function (Rolfe and Brown, 1997), so regulation of cerebral blood flow (CBF) and oxygen delivery is critically important. Oxygen extraction fraction (OEF) is a key hemodynamic parameter to measure the brain's energy metabolism and is altered in aging and disease processes, including cerebrovascular disorders (Watchmaker et al., 2018; Fan et al., 2022; Liu et al., 2023), neurodegeneration (Jiang et al., 2020; Robb et al., 2022), and neuroinflammation (Cleland et al., 2021). In some pathological mechanisms, OEF is reduced concurrently with hypoperfusion due to decreased neural activity and lower oxygen metabolic demand (Ishii et al., 1996; Brown and Thore, 2011); while in other distinct mechanisms, OEF is elevated in areas of hypoperfusion, indicating physiological compensation in tissue that is at ischemic risk (Gupta et al., 2014; Fan et al., 2020; Lin et al., 2022). Therefore, it is important to measure OEF in tandem with CBF to understand overall oxygen consumption and brain tissue health.

In addition to resting state, imaging brain hemodynamics in varying physiological conditions, such as those created by controlled vasoactive stimuli, adds valuable information about cerebrovascular reactivity (CVR) and brain vascular health. These cerebrovascular "stress tests" monitor the CVR, or the brain's hemodynamic response to hypercapnic gas paradigms or to pharmacological vasodilation, e.g., with acetazolamide (ACZ) (Handwerker et al., 2007). CVR measurements reveal unique pathophysiological changes in intracranial stenosis (Lattanzi et al., 2018) and in aging that correlate with cognitive status (Silvestrini et al., 2006; Kim et al., 2021). During these vasoactive challenges, brain hemodynamics are typically monitored with the blood-oxygenation-level-dependent (BOLD) MRI signal due to its fast acquisition and ease of use; however, BOLD signal changes reflect multiple neuronal and vascular contributions and cannot be interpreted in the context of a specific hemodynamic parameter. Other investigations have used arterial spin labeling (ASL) MRI to directly assess the perfusion reactivity deficits in steno-occlusive disease and validate the BOLD response in the same patients (Mandell et al., 2008; Smeeing et al., 2016), highlighting ASL as a robust biomarker to quantify CBF in different physiological states and disease. Acetazolamide has been commonly used to assess the vasodilatory capacity of circulation because ACZ is more easily administered through intravenous or oral means than carbon dioxide, which requires a gas delivery system. In patients with major cerebral arterial occlusive diseases, ACZ also identified reduced reactivity in the hemisphere with the occlusive lesion even in patients who appeared to have preserved CO_2 reactivity (Kazumata et al., 1996). However, few studies have directly assessed OEF changes during vasoactive stimuli, largely because of a lack of non-invasive imaging approaches. [^{15}O]-PET scans have measured CBF changes in response to ACZ vasodilation in patients with cerebrovascular stenoses and showed a non-linear association between this perfusion reactivity and baseline OEF PET for various ischemic disease stages (Imaizumi et al., 2004; Nemoto et al., 2004; Yamauchi et al., 2004; Hokari et al., 2008). Unfortunately, these OEF PET measures are not easily available in different physiological states due to the complexity of the experiments and the need to administer multiple short-lived radiotracers for each condition. MRI-based OEF measures have recently been tested with ACZ administration and showed expected global OEF reductions after vasodilation using multiple T_2 relaxation-based measures (Baas et al., 2022). Venous blood oxygenation (Y_v), which can be derived from venous blood T_2 relaxation values in the sagittal sinus, combined with global cerebral metabolic rate of oxygen, has shown poorer oxygen utilization in patients with sickle cell disease compared to controls after vasodilation (Václavů et al., 2020), albeit with some bias between various T_2-based MRI methods. Decreased OEF after ACZ vasodilation has also been demonstrated using 3-dimensional quantitative susceptibility mapping MRI (Buch et al., 2017). However, these values were averaged from larger, resolvable internal cerebral veins, thus limiting regional information on OEF response across the brain.

As an alternative to global OEF measurements using T_2 relaxation-based approach, quantitative blood-oxygenation-level-dependent (qBOLD) is a non-invasive MRI approach that models the temporal signal due to reversible transverse relaxation rate (R_2') to non-invasively extract OEF and deoxygenated blood volume (DBV) (Yablonskiy and Haacke, 1994). This method allows for voxelwise estimation of tissue OEF from asymmetric spin echo (ASE) scans, which can be useful in identifying areas of the brain that may be at risk for ischemia in stroke (Stone et al., 2019) or sickle cell disease (Guilliams et al., 2018; Wang et al., 2021). These clinical studies used qBOLD to identify regional, individualized pathophysiology in different ischemic tissue types (core, infarct growth, and contralateral tissue) in acute stroke. On the other hand, in patients with sickle cell anemia, abnormal OEF elevations were observed specifically in the deep white matter, consistent with microstructural damage, that were reduced post-blood transfusion. Additionally, OEF activation has been reported to decrease in brain areas relating to motor task execution (Yin et al., 2018), especially under hypoxic conditions (Yin et al., 2021). In aging, studies have identified CVR reductions in brain regions that overlap with the default mode network (DMN), which is related to underlying vascular risk factors and suggests CVR in the DMN-CVR

to be an important marker for brain health (Haight et al., 2015). Additional investigation of the reliability of qBOLD MRI in sensitive brain areas, including the DMN, across physiological states is thus critical to advance regional OEF as an informative biomarker in cerebrovascular disease and aging.

This study aimed to demonstrate a quantitative BOLD modeling MRI method for measuring OEF values in healthy participants during a physiological perturbation with ACZ. Previous studies have shown that OEF decreases in response to an increase in CBF from various vasodilating challenges, while $CMRO_2$ remains unaffected using different techniques (Kety and Schmidt, 1948; Vorstrup et al., 1984; Václavů et al., 2020; Vestergaard et al., 2023). We aimed to demonstrate this method by showing that OEF measured with qBOLD MRI is directly related to regional alterations in CBF. A secondary aim was to compare regional OEF with R_2' values in detecting an alteration with vasodilation and their correlation with perfusion. Furthermore, we focused on assessing the OEF relationship to perfusion in the DMN due to its functional associations with vascular risk factors (Tchistiakova et al., 2015) and cerebrovascular reactivity in cognitive impairment (Richiardi et al., 2015) to identify which DMN regions show the most significant OEF effect with vasodilation.

2 Materials and methods

2.1 Study population

Eight healthy subjects (47 ± 13 years, 6 female) were recruited and gave written informed consent to participate in the study. Participants must be at least 18 years old to participate in this study. Exclusion criteria included pregnancy, anemia, history of renal disease, hypertension, diabetes, stroke, or other known neurological diseases. Subjects with peripheral vasculopathy or Raynaud's disease that precludes IV administration and a history of allergy to sulfa drugs were excluded. In addition, participants that could not receive MRI due to the inability to lie motionless in the scanner, pacemakers, aneurysm clips, neurostimulators, artificial heart valves, metal objects in eyes, ear implants, and claustrophobia were excluded. This study was performed with approval from the Institutional Review Board at the University of California, Davis.

2.2 Vasodilatory stimulus

After baseline MRI scanning, all participants were given a slow administration dosage of 15 mg/kg ACZ as a pharmacological vasodilator over 2 min. After at least 15 min of uptake time to capture the full effect of pharmacological vasodilation, the participant received repeated scans in the post-ACZ state.

2.3 MRI acquisition

Each participant underwent scanning on a 3-T MRI scanner (Siemens MAGNETOM Tim Trio, Erlangen, Germany) with a 32-channel phase array head coil. T_1-weighted anatomic images were acquired using a multi-echo magnetization-prepared rapid gradient echo (MEMPRAGE) sequence before vasodilation. These sagittal scans were acquired with repetition time (TR) = 2530 ms; echo times (TE) = 1.64, 3.5, 5.36, and 7.22 ms; inversion time (TI) = 1,200 ms; spatial resolution = 1.0 mm^3 × 1.0 mm^3 × 1.0 mm^3; in-plane matrix = 256 × 256; 176 slices with thickness = 1.0 mm; flip angle = 7.0°; and acquisition time of 6 min and 2 s.

For OEF measurements, the Gradient Echo Slice Excitation Profile Imaging (GESEPI) ASE images were acquired with an echo planar imaging (EPI) readout with specialized z-shim gradients mitigating through-slice inhomogeneities (Blockley and Stone, 2016). Scan parameters included TR = 3,000 ms; TE = 56 ms; slice thickness = 1.25 mm; resolution = 2.3 mm^3 × 2.3 mm^3 × 1.25 mm^3; flip angle = 90°; bandwidth = 2,004 Hz/Pixel; matrix size = 96 × 96 with 80 slices; field of view (FOV) = 224 mm with 7 values of the spin echo displacement time (τ) from 16 to 40 ms in the step of 4 ms. A total of 20 slabs were acquired, and each slab was constructed by averaging four 1.25-mm slices to correct for macroscopic field gradients with 100% partition oversampling (total 8 k-space partitions). The total acquisition time of the main ASE sequence was 2 min and 54 s to cover the whole brain with 80 slices. A separate spin-echo ASE scan ($\tau = 0$) was collected with the same scan parameters as described, with an acquisition time of 24 s.

To generate quantitative CBF maps, we performed multi post-labeling-delay (PLD) 3D pseudo-continuous ASL (pcASL) MRI. The parameters were five different PLDs (0.9 s, 1.2 s, 1.4 s, 1.8 s, and 2.1 s) and effective labeling durations = 2 s; TR/TE = 4,700 ms/14 ms; slice thickness = 4 mm; spatial resolution = 3.4 mm^3 × 3.4 mm^3 × 4.0 mm^3; FOV = 220 mm (Li et al., 2015). Multi-band EPI readout was used with slice-acceleration factor of 6, FOV shift factor of 3, and EPI factor of 64. Including calibration scans with similar imaging parameters but no labeling to estimate longitudinal magnetization (M_0), the total acquisition time was approximately 6 min. The ASE and pcASL scans were acquired twice—once at baseline and once after vasodilation.

2.4 Image analysis

2.4.1 Image preprocessing

Prior to qBOLD modeling, ASE data were preprocessed first with motion correction of all echoes to the spin echo volume using *MCFLIRT* (Jenkinson et al., 2002). Next, the spin echo image was brain extracted using *BET* (Smith, 2002) to create a binary mask of the brain tissue, which was applied to all ASE R_2'-weighted images. ASE data were finally smoothed with a Gaussian kernel ($\sigma = 4$ mm) in FSL (Jenkinson et al., 2012) to reduce the effect of noisy voxels. The empirical tradeoff between spatial resolution and noise reduction is shown in Supplementary Figure S4.

For pcASL data, images from all five PLDs were merged and underwent the same preprocessing steps as the ASE data. First, motion correction was applied with reference to the first pcASL image, followed by smoothing with a Gaussian kernel of 1.5 mm. Then, the M_0 image was brain extracted using *BET* to create the binary mask of the brain tissue, which was used for registration.

2.4.2 OEF quantification

2.4.2.1 Two-compartment model theory for quantitative BOLD

Quantitative measurements of the BOLD signal were used to non-invasively map hemodynamic parameters relating to brain metabolism and function. The quantitative BOLD (qBOLD) model (Yablonskiy and Haacke, 1994) measures oxygen extraction fraction from the measured reversible transverse relaxation rate, R_2' (where $R_2' = R_2^* - R_2$). A complete qBOLD model with R_2'-weighted measurements can be achieved using asymmetric spin echoes (An and Lin, 2003), such as the GESEPI-ASE pulse sequence described above. qBOLD modeling was performed with two compartments (tissue and blood), as this approach provides reliable estimates of OEF with a full range of echoes for fitting, including those before the spin echo (Cherukara et al., 2019).

The objective of qBOLD modeling is to separate OEF and DBV effects from the ASE signal and generate a brain map of OEF. The (1) tissue signal, (Yablonskiy and Haacke, 1994), S^t is:

$$S^t(\tau) = \begin{cases} S_0\, exp(-R_2^t \times TE) \times exp\left(-\frac{3}{10} DBV\,(\delta\omega \times \tau)\right)^2 & |\tau| < T_c \\ S_0\, exp(-R_2^t \times TE) \times exp(DBV - DBV \times (\delta\omega \times \tau)) & |\tau| > T_c \end{cases} \quad (1)$$

where $\delta\omega$ is the characteristic frequency (with $R_2' = DBV \times \delta\omega$), t_c is the characteristic time, and R_2^t is the irreversible transverse relaxation rate of bulk tissue. The R_2'-weighted signal has different behavior in two different regimes of the parameter τ (Eq. 1). The boundary between these regimes is considered to be at $T_c = 1.76 t_c$ (Cherukara et al., 2019). The characteristic time t_c was defined as $t_c = \frac{1}{\delta\omega}$ (Lee et al., 2018). The time variable τ corresponds to the spin echo displacement values of the ASE acquisition. The (2) blood signal, S^b, (Sukstanskii and Yablonskiy, 2001; Yablonskiy et al., 2013) is:

$$S^b(\tau) = exp\left(-R_2^b \times TE + i\frac{\delta\omega \times \tau}{2}\right) \frac{C(\eta) - iS(\eta)}{(\eta)} \quad (2)$$

where $C(\eta)$ and $S(\eta)$ are Fresnel function, and $\eta = (\frac{3\delta\omega|\tau|}{\pi})^2$. R_2^b is the transverse relaxation rate of blood and is described as a function of the fractional hematocrit (Hct) and OEF of the intravascular compartment (Simon et al., 2016):

$$R_2^b = (16.4Hct + 4.5) + (165.2Hct + 55.7) \times OEF^2 \quad (3)$$

The total signal calculated from a voxel in this two-compartment tissue model is the sum of the signal from each compartment:

$$S^{Total}(\tau) = S_0\left(DBV \times S^b(\tau) + (1 - DBV) \times S^t(\tau)\right) \quad (4)$$

After fitting the two-compartment tissue qBOLD model, R_2' and DBV were estimated. Then, OEF was determined by the relationship between R_2' and DBV with known constants:

$$OEF = \frac{3 \times R_2'}{4\pi \times \gamma B_0 \times \Delta\chi_0 \times Hct \times DBV} \quad (5)$$

where Hct is the patient's fractional hematocrit, $\Delta\chi_0$ is the magnetic susceptibility difference between oxygenated and deoxygenated red blood cells, B_0 is the magnetic field, γ is proton gyromagnetic ratio.

R_2'-weighting was acquired by shifting the spin echo refocusing pulse for 7 values of the spin echo displacement time, τ, in the step of 4 ms from 16 ms to 40 ms. The spin echo ($\tau = 0$ ms) was collected in separate scan. Hct was assumed at 0.40 (Nicoll et al., 2012). Other physiological parameters were also set as constant values as follows: $\Delta\chi_0 = 0.264 \times 10^{-6}$ (Spees et al., 2001); $R_2^t = 11.5 s^{-1}$ (He and Yablonskiy, 2007). $R_2^t = 11.5 s^{-1}$. Additionally, acquisition parameter values used for the model were B_0 = 3T, $TE = 56ms$, and $TR = 3s$.

2.4.2.2 Bayesian inference for mapping OEF with qBOLD

Fitting the acquired ASE signals to the two-compartment tissue model allows us to separate OEF (our parameter of interest) and DBV per voxel. To fit our ASE signal data, we used a Bayesian framework that estimates R_2' and DBV, which have shown to be more separable parameters with a suitable posterior distribution for the estimation (Cherukara et al., 2019). Given the total signal S^{Total} in Eq. 4, the Bayesian approach will find the optimal pair of (**DBV** and $\mathbf{R_2}$') using a variational Bayesian (VB) inference scheme implemented in FAST ASL and BOLD Bayesian Estimation Routine (FABBER) toolkit (Woolrich et al., 2006; Chappell et al., 2009; Groves et al., 2009) in FSL (version 6.0.5, Oxford, United Kingdom), as illustrated in Figure 1A. VB inference was performed with fixed prior mean values, μ_0, and standard deviations, σ_0 The mean values for R_2' and DBV for healthy subjects were 2.6 s^{-1} and 3.6%, respectively (Stone and Blockley, 2017). The optimal prior standard deviation was chosen as $\sigma_0(R_2') = 10^{\frac{3}{2}} s^{-1}$ and $\sigma_0(DBV) = 10^{\frac{1}{2}}$% based on numerical simulations (Le et al., 2023). After implementing Bayesian estimation to map DBV and R_2' in each participant, OEF was calculated voxelwise based on the proportion between DBV and R_2' with known constants from Eq. 5. All qBOLD model analyses were done in native space.

2.4.3 The relationship between OEF and $CMRO_2$

The relationship between $CMRO_2$ (μmol/100 g/min) and OEF (%) (Kety and Schmidt, 1948) can be expressed as

$$CMRO_2 = CBF \times OEF \times [Hb]_a \quad (6)$$

Where CBF is the cerebral blood flow (mL/100 g/min), and $[Hb]_a$ is the oxygenated hemoglobin concentration in the arteriole (8.272 μmol/mL) This is calculated from $[Hb]_a = [Hb]_t \times Y_a$, where $[Hb]_t$ (8.441 μmol/mL) is the hemoglobin concentration in the tissue blood with assumption of hematocrit of Hct = 0.40 (Zhang et al., 2018). Y_a is the arterial oxygenation, which is assumed to be 0.98.

2.4.4 Perfusion measurements

The complete procedure to measure cerebral blood flow is shown in Figure 1B. We used the Bayesian Inference for Arterial Spin Labeling MRI (BASIL) toolkit (Chappell et al., 2009) implemented in FSL (version 6.0.5, Oxford, United Kingdom) for analyzing ASL data and quantifying perfusion maps. This approach allows fitting a two-compartment model to separate macrovascular and tissue information in ASL signal to quantify CBF maps (Groves et al., 2009; Chappell et al., 2010).

The two-compartment model assumed that the walls of arterial vessels do not allow any substance to pass through them, and that

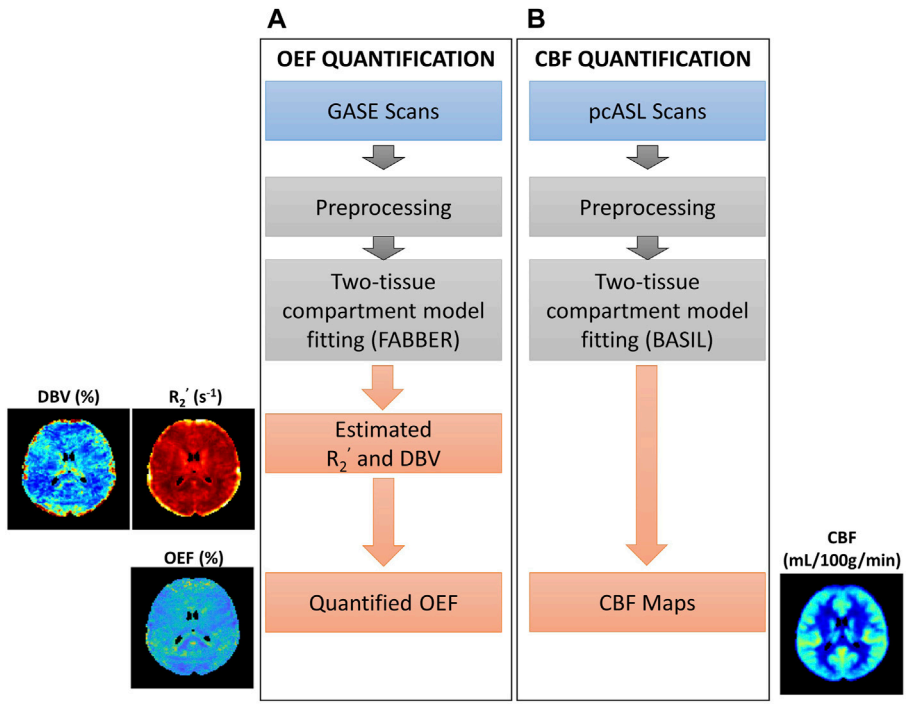

FIGURE 1
Overview of procedures for parameter quantification. **(A)** Oxygen extraction fraction (OEF) quantification using GASE scans was achieved through fitting with two-tissue compartment qBOLD model in FABBER (Woolrich et al., 2006; Chappell et al., 2009; Groves et al., 2009). **(B)** Cerebral blood flow (CBF) quantification using pseudo-continuous ASL (pcASL) scans fitted with two-tissue compartment model in BASIL (Chappell et al., 2009; Chappell et al., 2010). This pipeline was repeated before and after acetazolamide injection.

blood in the arteries moves through the voxel immediately. The total signal from any voxel is the sum of both tissue and intravascular components. CBF maps underwent a voxelwise calibration method using the measured M_0 maps (Pinto et al., 2020). Fix label duration was applied, and initial parameter values were assumed as following: initial arterial transit time (ATT) = 1.3 s; T_1 values for tissue (T_{1t}) = 1.3 s (based on 3 T field strength); T_1 values for blood (T_{1b}) = 1.65 s; brain/blood partition coefficient (λ) = 0.9 mL/g; and labeling efficiency (α) = 0.85 (Alsop et al., 2015). Analyses to compute CBF maps were done in native ASL space.

2.4.5 Image registration

To assess the regional relationship between hemodynamic parameters, especially OEF and perfusion across subjects, all quantitative maps were registered to Montreal Neurological Institute (MNI) space (Collins et al., 1999; Fonov et al., 2009; Fonov et al., 2011). For hemodynamics parameter maps, including OEF, DBV, and R_2', the spin echo image from the ASE scans was linearly co-registered, with FMRIB's Linear Image Registration Tool (FLIRT) (Jenkinson and Smith, 2001; Jenkinson et al., 2002; Greve and Fischl, 2009), to subject-specific T_1-structural space and then non-linearly co-registered, with FMRIB's Non-linear Image Registration Tool (FNIRT) (Andersson et al., 2010), to MNI space. All parameter maps were then warped to MNI space with combined transformation parameters from those two registrations. To register CBF maps to MNI space, we first performed linear registration (FLIRT) of proton density (M_0) images to T_1 images; then, all CBF maps were transformed into MNI space using non-linear co-registration as described above.

2.5 Data analysis

2.5.1 Mean ROI calculation

Before assessing parameters of interest (CBF, OEF, and R_2') across brain regions and calculating the average for each ROI, we excluded voxels with unphysiological extreme values. Voxels with OEF values greater than 100%, and with estimated R_2' greater than 20 s^{-1} were excluded from analysis. The thresholds were set consistently to prior relevant studies (Stone and Blockley, 2017; Cherukara et al., 2019). For group average parameter maps across all participants, we calculated the mean only for MNI voxels having at least 50% of the population (i.e., at least 4 subjects) within physiological values. Intermediate processing steps, including subject masks in MNI space, are shown in Supplementary Material, Supplementary Figure S1 (for OEF), Supplementary Figure S2 (for DBV), and Supplementary Figure S3 (for R_2').

In MNI space, the Harvard-Oxford cortical atlas (Frazier et al., 2005; Desikan et al., 2006; Makris et al., 2006; Goldstein et al., 2007) was used to delineate nine brain regions of interest (ROIs) within the DMN. Regions within the DMN included the posterior cingulate gyrus (pCG), precuneus (PCun), anterior cingulate gyrus (aCG), angular gyrus (AG), supramarginal gyrus (SG) (including in inferior parietal lobe), and medial frontal gyrus (MFG) (Broyd et al., 2009). As a reference for comparison for this study, we chose other cortical

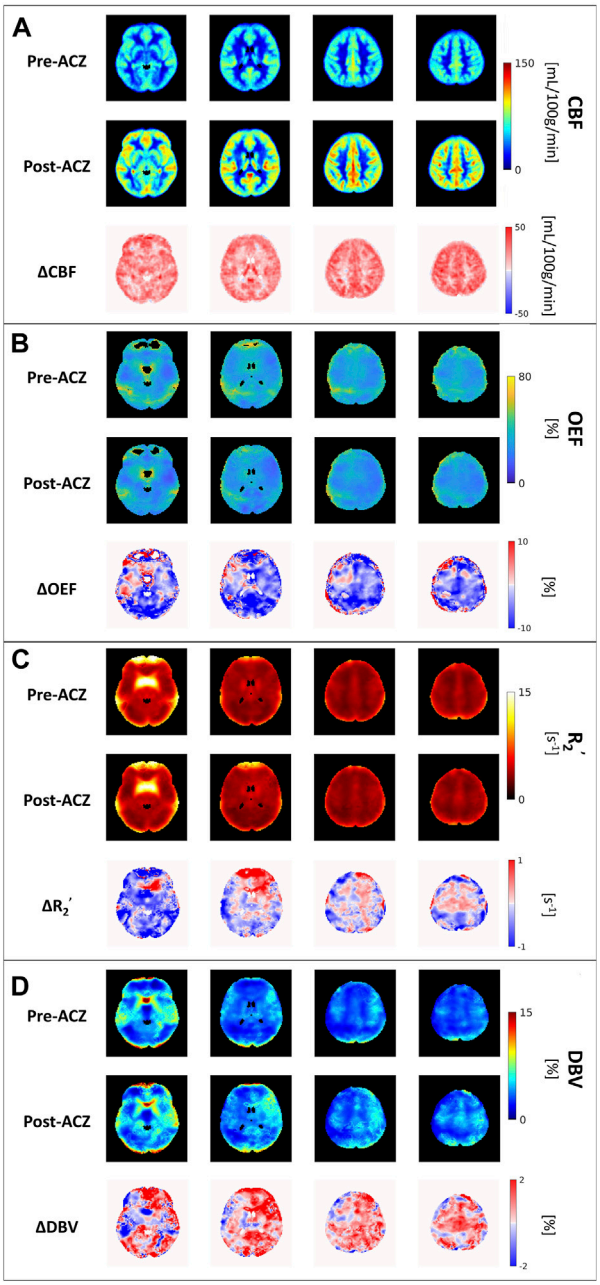

FIGURE 2
The group average of **(A)** cerebral blood flow (CBF) maps (in mL/100 g/min), **(B)** oxygen extraction fraction (OEF) maps (in %), **(C)** transverse relaxation rate (R_2') (in s^{-1}) and **(D)** deoxygenated blood volume (DBV) across all eight healthy subjects before (Pre-ACZ) and after (Post-ACZ) vasodilation with the corresponding absolute difference maps between two conditions for each parameter (ΔCBF, ΔOEF, $\Delta R_2'$, and ΔDBV). All maps were registered to Montreal Neurological Institute (MNI) space.

brain regions, including the occipital pole (OP), inferior temporal gyrus (ITG), and middle temporal gyrus (MTG), to represent non-DMN regions.

2.5.2 Statistical analysis

All statistical analyses were performed using MATLAB R2021a (MathWorks, Natick, MA, 2016). Differences between before and after vasodilation were assessed using a pairwise two-way *t*-test with Bonferroni correction for nine ROIs. A *p*-value of less than 0.006 (where $\alpha = \frac{0.05}{number\ of\ comparisons}$) was considered statistically significant for this analysis.

To evaluate the relationship of OEF and CBF across regions during vasodilation, a linear mixed-effects model was conducted using OEF as the dependent variable and CBF as the independent variable, with subject and region as random effects. We also investigated the correlation of R_2' and CBF across regions during vasodilation, using a separate linear mixed-effects model with R_2' as the dependent variable and CBF as the independent variable. For both models, subjects and regions were used as random effects to adjust for inherent physiological variations across individuals and regions. Each mixed model was fit separately using the MATLAB software package *"fitlme"* (Pinheiro and Bates, 1996). A *p*-value of less than 0.05 was considered statistically significant.

3 Results

All eight healthy participants received MRI scans consisting of the GESEPI-ASE sequence for quantitative BOLD modeling to estimate hemodynamic parameters, including R_2', DBV, and OEF (our parameter of interest). After excluding unphysiological voxels, group average maps of each parameter before and after vasodilation are shown in Figure 2. Excluded voxels were primarily located in frontal brain areas prone to air-tissue bulk magnetic susceptibility effects. The percentage of voxels removed due to thresholding in the two conditions is shown in Supplementary Table S1 (Pre-ACZ: DBV = 0.21%, R_2' = 2.05%, OEF = 13.1%; Post-ACZ: DBV = 0.16%, R_2' = 1.84%, OEF = 10.93%. We focused on parameters that are sensitive to brain oxygenation (OEF and R_2') and perfusion; the corresponding DBV maps are shown in Figure 2.

Compared to the baseline condition, increased CBF and decreased OEF were observed across multiple areas in the brain at the group average level (Figures 2A, B). We also observed a decreasing trend in R_2' (Figure 2C) and an increasing trend in DBV (Figure 2D) during vasodilation. Mean parameter values, including CBF, OEF, R_2', DBV and $CMRO_2$ for all subjects across selected regions for each condition are presented in Table 1. Additionally, the distribution of changes in OEF, R_2', DBV and CBF in response to ACZ for each selected region were plotted in Figure 3.

Paired two-way *t*-test with Bonferroni correction showed statistically significant differences in CBF and OEF estimates in selected regions during vasodilation (i.e., Pre-ACZ versus Post-ACZ), as presented in Table 1. With the injection of ACZ, CBF increased across all chosen regions before correction for multiple comparisons. After correction, elevated CBF remained significant in MFG ($P = 0.004$), pCG ($P = 0.004$), PCun ($P = 0.004$), and OP ($P = 0.001$) regions. In parallel, a significant reduction in OEF from qBOLD was observed only in pCG ($P = 0.003$) and PCun ($P = 0.001$) after correction, with a trend of decreased OEF also in the angular gyrus. In addition, a slight trend of DBV increase during vasodilation was observed only in pCG ($P = 0.045$) before correction. For R_2', there was a small reduction trend during vasodilation; however, we found no region showing statistically significant change with ACZ (Table 1). Additionally, while there was a trend of increased $CMRO_2$ after vasodilation in several brain

TABLE 1 Average cerebral blood flow (CBF) (in mL/100 g/min), oxygen extraction fraction (OEF) (in %), transverse relaxation rate (R_2') (in s^{-1}), deoxygenated blood volume (DBV) (in %) and cerebral metabolic rate of oxygen ($CMRO_2$) (in μmol/100 g/min) before (Pre) and after (Post) vasodilation across all healthy subjects (mean ± std) in different regions of interest (ROIs): angular gyrus (AG), medial frontal gyrus (MFG), anterior cingulate gyrus (aCG), posterior cingulate gyrus (pCG), precuneus (PCun), occipital pole (OP), supramarginal gyrus (SG), middle temporal gyrus (MTG), and inferior temporal gyrus (ITG). All tests were performed using a two-sided paired *t*-test with Bonferroni correction. (*$p < 0.05$, significant raw *p*-value; **$p < 0.006$, significant *p*-value after correction).

		AG	MFG	aCG	pCG	PCun	SG	OP	MTG	ITG
CBF (mL/100 g/min)	Pre-ACZ	60.7 ± 15.6	43.2 ± 10.6	68.6 ± 14.5	76.3 ± 14.8	61.6 ± 11.1	54.9 ± 14.1	40.0 ± 9.7	54.5 ± 13.7	40.2 ± 10.7
	Post-ACZ	81.8 ± 22.4	74.8 ± 23.2	93.3 ± 21.3	104.4 ± 17.8	87.6 ± 18.1	76.4 ± 22.2	58.4 ± 8.8	76.1 ± 20.7	57.6 ± 13.5
	P-val	0.046*	0.004**	0.017*	0.004**	0.004**	0.037*	0.001**	0.027*	0.018*
OEF (%)	Pre-ACZ	44.4 ± 4.1	32.4 ± 10.9	35.9 ± 4.7	34.5 ± 4.8	39.6 ± 4.2	43.2 ± 5.2	30.7 ± 8.3	25.9 ± 3.0	29.3 ± 3.1
	Post-ACZ	38.2 ± 3.8	30.3 ± 11.6	30.7 ± 6.5	25.7 ± 4.7	30.9 ± 4.1	39.1 ± 2.5	27.2 ± 7.2	25.1 ± 3.0	27.1 ± 2.3
	P-val	0.008*	0.717	0.085	0.003**	0.001**	0.070	0.381	0.609	0.134
R_2' (s^{-1})	Pre-ACZ	4.8 ± 1.0	9.1 ± 2.6	3.8 ± 0.4	3.7 ± 0.3	4.0 ± 0.7	5.1 ± 0.5	7.1 ± 1.6	7.8 ± 1.0	11.1 ± 1.2
	Post-ACZ	4.3 ± 0.8	9.0 ± 2.1	3.9 ± 0.7	3.7 ± 0.5	3.6 ± 0.7	4.7 ± 0.6	6.5 ± 0.7	7.1 ± 0.8	10.4 ± 1.9
	P-val	0.270	0.900	0.856	0.816	0.233	0.199	0.348	0.154	0.404
DBV (%)	Pre-ACZ	3.1 ± 0.7	11.0 ± 6.1	3.2 ± 0.4	3.4 ± 0.8	3.2 ± 0.7	3.1 ± 0.9	7.8 ± 2.2	11.5 ± 2.8	17.6 ± 3.1
	Post-ACZ	3.5 ± 0.7	12.2 ± 6.0	4.3 ± 1.4	4.5 ± 1.3	3.7 ± 0.7	3.4 ± 0.9	8.2 ± 2.1	10.7 ± 2.5	16.1 ± 3.6
	P-val	0.270	0.694	0.067	0.045*	0.114	0.496	0.721	0.550	0.425
$CMRO_2$ (μmol/100 g/min)	Pre-ACZ	223.0 ± 58.2	117.1 ± 47.7	206.3 ± 57.1	216.9 ± 51.8	201.7 ± 43.8	194.9 ± 51.3	103.2 ± 38.9	115.6 ± 28.8	100.3 ± 28.1
	Post-ACZ	260.8 ± 80.1	173.5 ± 40.6	238.4 ± 82.3	221.5 ± 51.1	223.1 ± 54.0	246.7 ± 70.6	130.4 ± 35.8	154.9 ± 33.5	130.3 ± 35.8
	P-val	0.298	0.023*	0.379	0.859	0.399	0.116	0.168	0.025*	0.083

areas, especially the MFG and MTG, $CMRO_2$ showed no significant change in all regions after correction for multiple comparisons (Table 1).

The CBF response to ACZ showed a significant negative linear relationship to OEF value at baseline and after vasodilation using a mixed-linear effects model with subject clustering ($\beta = -0.104 \pm 0.027$; $t = -3.852, P < 0.001$) (Figure 4A; Table 2). We further investigated the relationship between CBF and R_2' using the same mixed-effects model. The CBF response to ACZ was also correlated with R_2' ($\beta = -0.016 \pm 0.006$; $t = -2.692, P = 0.008$) (Figure 4B; Table 2).

4 Discussion

The purpose of this study was to demonstrate qBOLD modeling of ASE scans in healthy volunteers to detect regional OEF decreases in key ROIs of the DMN during concomitant perfusion increase with ACZ vasodilation. The main findings were as follows: 1) Across baseline and vasodilation states, OEF was inversely related to quantitative perfusion as expected, indicating a compensation to maintain oxygen metabolism and reliability of the local OEF measures. 2) Similar changes with ACZ observed using R_2' relaxation estimates from the same ASE acquisitions, which highlights the utility of qBOLD compartment modeling to non-invasively measure specific OEF imaging markers. 3) OEF reduction was observed in critical DMN regions, including the precuneus and posterior cingulate gyrus.

4.1 Baseline OEF and change with acetazolamide in healthy participants

The observed mean baseline OEF across selected brain regions of 35.1% is consistent with the physiological range of previous PET and MRI studies (Yamaguchi et al., 1986; Leenders et al., 1990; Cho et al., 2021; Jiang et al., 2023). We observed an OEF reduction of 6.2%–8.7% (absolute oxygenation) in significant DMN regions, which was smaller in magnitude than the 15.6% absolute OEF decrease in the sagittal sinus from past ACZ studies on healthy controls (Václavů et al., 2020). This discrepancy could be due to methodological differences, as previous studies focused on global OEF values and used a distinct contrast mechanism and calibration with T_2-prepared inversion recovery sequences (Václavů et al., 2020; Baas et al., 2022). The qBOLD method adopted here may also have lower sensitivity to OEF changes due to noise contributions in the model fitting *in vivo*. Of note, the T_2-based study also reported a larger magnitude of perfusion increase (69.3% increase) using pcASL with ACZ than our study (average 43.4% increase across

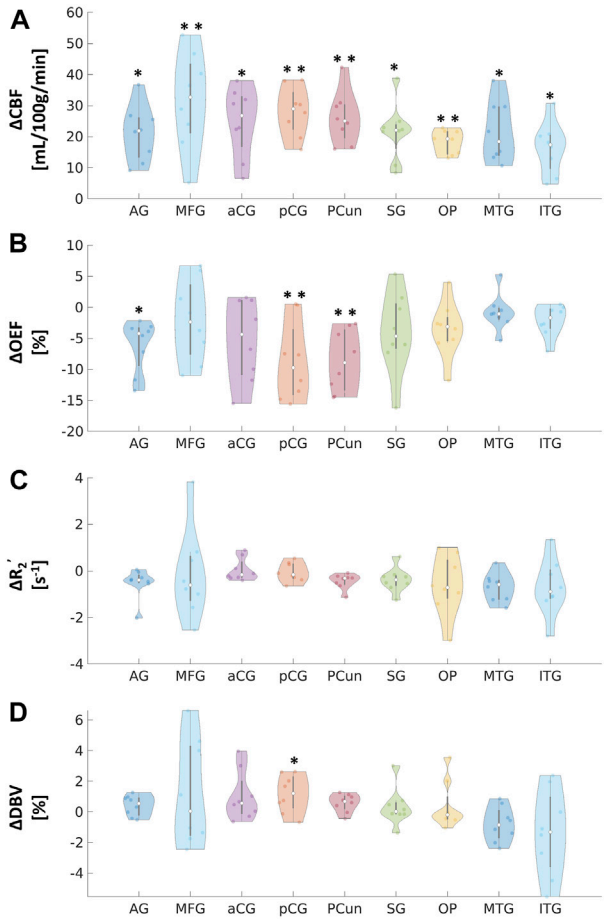

FIGURE 3
Absolute changes in **(A)** cerebral blood flow (CBF) in mL/100 g/min, **(B)** oxygen extraction fraction (OEF) in %, **(C)** transverse relaxation rate (R_2') in s^{-1}, and **(D)** deoxygenated blood volume (DBV) in % in response to acetazolamide (ACZ) in different regions of interest (ROIs): angular gyrus (AG), medial frontal gyrus (MFG), anterior cingulate gyrus (aCG), posterior cingulate gyrus (pCG), precuneus (Pcun), occipital pole (OP), supramarginal gyrus (SG), middle temporal gyrus (MTG), and inferior temporal gyrus (ITG). All tests were performed using pairwise two-way *t*-tests between pre- and post-vasodilation with Bonferroni correction. (*$p < 0.05$, significant raw *p*-value; **$p < 0.006$, significant *p*-value after correction).

regions). Therefore, direct comparison of the OEF imaging approaches in the same participants and improvement to sensitivity of our qBOLD approach is warranted in future work.

4.2 Correlation between hemodynamic parameters and perfusion

Although R_2' has been used as a surrogate marker for brain OEF in previous studies (Ni et al., 2015), including identification of putative oxygenation changes in cerebrovascular disease (Ni et al., 2017; Kaczmarz et al., 2021), this work suggests that qBOLD compartmental modeling outperforms R_2' measures in detecting physiological OEF changes in healthy volunteers. While significant OEF reductions were measured in the pCG and PCun with qBOLD, none of the ROIs showed a significant R_2' change with ACZ. Additionally, the expected inverse relationship between OEF and CBF across baseline and vasodilatory states was stronger using qBOLD than between R_2' and CBF. One rationale could be that R_2' is proportional to both OEF and DBV, such that OEF reductions concurrently with potential DBV elevations during vasodilation lead to overall smaller changes in R_2' values. Because qBOLD compartment modeling uses multiple asymmetric echoes to disentangle contributions from OEF and DBV, the resulting regional OEF measures are likely to be more sensitive than R_2', as observed in our results. In addition to the Bayesian fitting for R_2', a supplementary analysis of the monoexponential fits based on streamline qBOLD (Stone and Blockley, 2017) was also performed. Our more complex modeling approach may produce R_2' measures that are noisier compared to monoexponential fits for the relaxation parameter (Supplementary Figure S5), which may contribute to lack of sensitivity of R_2' to changes during vasodilation. Besides, in whole group level analysis with monoexponential fits, there was a slight decrease for R_2' in pCG ($P = 0.028$) and OP ($P = 0.039$) before correction (Supplementary Table S2). However, in this analysis, we chose to compare OEF and R_2' values that were both derived from Bayesian fitting for consistency. R_2' measures are also susceptible to contributions from orientation effects of the blood vessels (Kaczmarz et al., 2021) and artifacts from non-heme susceptibility sources (iron, myelin). These contributions will also manifest differently on OEF values from qBOLD modeling, which requires further evaluation with related multi-parametric qBOLD approaches that acquire separate R_2 and R_2^* maps measures to assess oxygenation (Gersing et al., 2015). Such multi-parametric qBOLD have been used to identify reduced baseline oxygen metabolism in the affected middle cerebral artery territory with moderate ischemia and may provide an alternative to ASE acquisitions (Bouvier et al., 2015).

A good validation for our qBOLD method to measure OEF is to test the hypothesis that $CMRO_2$ is unchanged during vasodilation, i.e., that OEF decreases are commensurate with the increase in CBF during acetazolamide. From this study, we found no significant $CMRO_2$ change after Bonferroni correction in all selected regions, which is consistent with our hypothesis and reflects reliability of the qBOLD method. However, we observed a slight increasing trend in $CMRO_2$, which may reflect residual underestimation bias in OEF values (i.e., underestimating the OEF decrease) and limited sensitivity of the qBOLD model to OEF. While CBF significantly increased in all selected regions, OEF only showed a significant decrease in pCG and PCun (Table 1). Therefore, there was an overall trend of increased $CMRO_2$ in several regions, even though we observed the expected compensation of OEF and CBF during vasodilation. Future work will enhance the accuracy and sensitivity of qBOLD modeling with refined physiological prior information and improved fitting routines that are more robust to noise contributions.

4.3 Effects of vasodilation in cerebral regions

This study imaged the regional effects of vasodilation on OEF across the entire cerebral cortex, focusing on DMN (Figures 2, 3). We found that most DMN regions showed increased CBF during vasodilation, and decreased OEF was observed in pCG and PCun. In

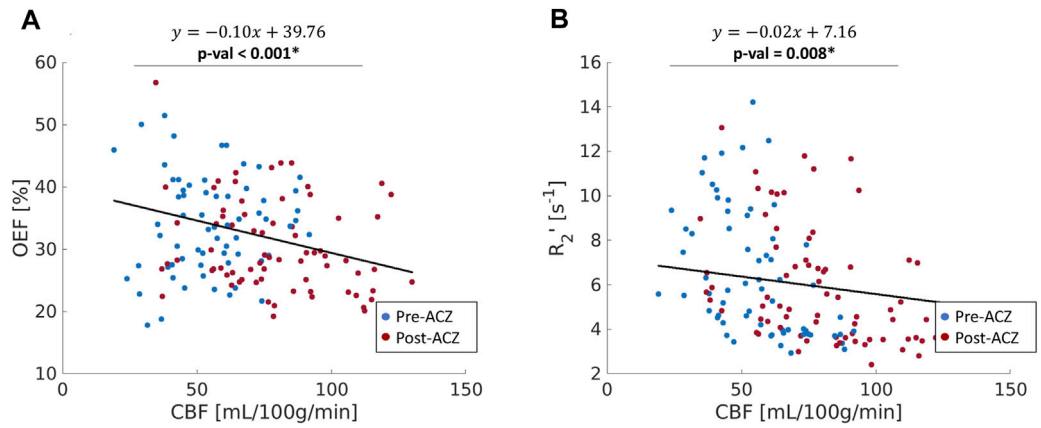

FIGURE 4
(A) The correlation between oxygen extraction fraction OEF (%) and cerebral blood flow (CBF); **(B)** the relationship between R_2' (s^{-1}) and CBF across all healthy subjects in nine ROIs (red: before vasodilation (Pre-ACZ); blue: after vasodilation (Post-ACZ). The solid black line represents the fitted line from mixed-effect models. Linear mixed-effect models with adjustment for subject clustering and region were performed separately for OEF and R_2'. $p < 0.05$* Mixed-effects model: OEF~CBF + (1|Region) + (1|Subject).

TABLE 2 Linear mixed-effects models between OEF, R_2', and CBF in the whole group ($N = 8$) across 9 ROIs. In both models, subjects and regions were used as random effects. *$p < 0.05$ β: standardized beta coefficient; SE: standardized error; OEF: oxygen extraction fraction; R_2': transverse relaxation rate; CBF: cerebral blood flow.

Dependent variables	Independent variables	$\beta \pm SE$	*t*-statistics	*p*-value
OEF	CBF	−0.104 ± 0.027	−3.852	<0.001*
R_2'	CBF	−0.016 ± 0.006	−2.692	0.008*

contrast, the non-DMN regions did not show a significant response in any hemodynamic parameters. One potential implication of this finding is that DMN regions show a strong sensitivity to vasodilation in those regions, which is consistent with well-established mechanisms of vasodilation with ACZ (Kleinschmidt et al., 1995; Wang et al., 2015). In addition, BOLD fMRI studies during hypercapnia have identified co-fluctuations in brain hemodynamics that spatially resemble the DMN but are responsive to vasoactive (not neuronal) stimuli (Bright et al., 2020). Such "vascular networks" may have unique OEF properties at baseline and in vasodilated conditions, and methods such as the qBOLD approach can characterize such physiological mechanisms of brain functional network emergence. These capabilities will enable important future studies to assess the link between oxygen metabolism in other brain networks and their disorders. Outside of the DMN, the medial temporal lobe (MTL) has been known as a key early region that is affected by many brain diseases (Clifford R. Jack et al., 1997; Tam et al., 2005; Burton et al., 2009). OEF can serve as a functional biomarker due to its sensitivity in the early stages of brain diseases and aging, as neural activity is tightly linked to the brain's oxygen consumption (Watts et al., 2018). At baseline, average OEF values in the medial temporal lobe were measured to be 25.9% ± 3.0% (Table 1), consistent with prior MRI studies' measurement of OEF in vessels supplying the MTL of 23.9% using T_2-relaxation-under-phase-contrast approach (Jiang et al., 2023). Even though there was a decreasing trend, we observed no significant change in MTL OEF during vasodilation ($P = 0.609$). This observation contrasts with Jiang et al., who observed increased MTL OEF after vasoactive challenge with caffeine ingestion. Caffeine is a common vasoconstrictor, which is known to reduce CBF and increase OEF to maintain the same amount of total oxygen consumption (Xu et al., 2015). Both ACZ and caffeine are vasoactive stimuli with minimal neuroactive effects, although they are in opposite directions. For the MTL, Jiang et al. observed a 9.1% OEF increase due to caffeine, while our study observed an average of 12.7% OEF decrease across regions due to ACZ vasodilation. More studies are needed to characterize the accuracy of qBOLD to detect changes in MTL OEF with physiological changes or aging and may require additional corrections for signal loss or distortion due to susceptibility effects in some MTL subregions (Olman et al., 2009).

4.4 Limitations

To perform qBOLD modeling, we have used an ASE sequence to directly estimate R_2' with consistent R_2-weighting across echoes (An and Lin, 2003). One main limitation of the qBOLD model is that the separation of DBV and OEF effects in the qBOLD model depends mainly on the subtle change in decay patterns. Therefore, it requires high signal-to-noise-ratio (SNR) to accurately estimate OEF from the ASE signals (An and Lin, 2000). Due to challenging low SNR from our sequence, OEF values estimated from qBOLD model still had unreasonable physiological values in particular voxels that we had to remove. To address this noise limitation, a benefit to fitting this multi-compartment with the Bayesian framework is the ability

to include prior knowledge to improve parameter estimates. In this study, prior mean values and standard deviations were taken from previous studies (Stone and Blockley, 2017; Cherukara et al., 2019; Le et al., 2023). Moreover, it has been suggested that prior means do not significantly affect the parameter estimation (Cherukara et al., 2019). However, the prior standard deviations were optimized based on a broader range of R_2'-weighted images (24 R_2'-images in Cherukara et al., 2019, and 14 in Le et al., 2023) than acquired in this MRI protocol. For this data, we also investigated the effect of prior standard deviations to the parameter estimation by comparing between the chosen prior standard deviations ($\sigma(DBV) = 10^{\frac{3}{2}}\%$; $\sigma(R_2') = 10^{\frac{1}{2}} s^{-1}$) with a broader one ($\sigma(DBV) = 10^{\frac{5}{2}}\%$; $\sigma(R_2') = 10^{\frac{5}{2}} s^{-1}$). We found that the broader standard deviation, which places less weight on prior information, resulted in more unphysiological values compared to our chosen value as shown in Supplementary Table S1. Further optimization for prior information will be assessed to maintain a robust estimation of OEF.

Hct was assumed as 0.40 based on the literature value for general circulation (Nicoll et al., 2012), which is consistent with average hematocrit in healthy subjects from other studies (Brown et al., 1962; Jeong et al., 2021). On the other hand, prior relevant studies have used a lower *Hct* of 0.34 (He and Yablonskiy, 2007) because of lower *Hct* in small vessels. Because *Hct* influences quantification specifically of the intravascular compartment, for our two-compartment model, changing *Hct* has a non-linear effect on the parameter estimates. For instance, using a *Hct* of 0.34 (i.e., a 15% lower value of *Hct*) and without spatial regularization, Cherakura et al. observed the same mean DBV values but a 3% higher mean OEF values compared to analysis with *Hct* of 0.40. However, it is unclear how much the *Hct* varies throughout the brain, which may propagate to additional regional differences of OEF estimates from the qBOLD signal. Finally, this study adopted a Bayesian framework that aims for the maximal free energy of the approximate posterior to better estimate the data (Chappell et al., 2009). This approach was chosen to ensure that applying additional smoothing (Gaussian smoothing with kernel of 4 mm) did not affect the fitting. Because the qBOLD-OEF measurement requires more complex models, it is more sensitive to the presence of noise compared to CBF quantification from ASL. Therefore, we applied a larger kernel of smoothing (i.e., 4 mm) for OEF, which is consistent to previous studies (Cho et al., 2021; Uchida et al., 2022). This kernel was empirically chosen after comparing multiple kernel sizes on our data to reduce unstructured noise and heterogeneity in the OEF maps but has the drawback of decreasing the spatial resolution of regional OEF measures. The relatively small sample size of our study is also a limitation and should be expanded in future studies to include larger cohorts with various ages and cerebrovascular conditions.

5 Conclusion

We demonstrated that regional OEF measurements from qBOLD are reliable across multiple physiological conditions and evaluated OEF through correlation with ASL perfusion in response to ACZ vasodilation as reliable indicators of tissue health in healthy cohort. This study enhances our understanding of the relationship between OEF and CBF with regional alterations in brain vasculature and has implications for the future use of oxygenation MRI to study vascular alterations in cognitive impairment and cerebrovascular diseases.

Data availability statement

The datasets presented in this study can be found in online repositories. The names of the repository/repositories and accession number(s) can be found below: https://github.com/fanlab-ucdavis/hemodynamics-data.

Ethics statement

The studies involving humans were approved by the Institutional Review Board at University of California, Davis. The studies were conducted in accordance with the local legislation and institutional requirements. The participants provided their written informed consent to participate in this study.

Author contributions

Designed research, LL, NB, and AF. Collected the data, EH, CD, and AF. Analyzed the data, LL, GW, EH, and AF. Interpreted the data, LL, GW, EH, NB, AY, KN, and AF. Prepared figures, LL. Writing—Original Draft, LL, and AF. Writing—Review and Edit, LL, GW, EH, NB, AY, KN, and AF. All authors contributed to the article and approved the submitted version.

Funding

This study received funding from the National Institute of Health (grant number R00-NS102884).

Conflict of interest

The authors declare that the research was conducted in the absence of any commercial or financial relationships that could be construed as a potential conflict of interest.

Publisher's note

All claims expressed in this article are solely those of the authors and do not necessarily represent those of their affiliated organizations, or those of the publisher, the editors and the reviewers. Any product that may be evaluated in this article, or claim that may be made by its manufacturer, is not guaranteed or endorsed by the publisher.

Supplementary material

The Supplementary Material for this article can be found online at: https://www.frontiersin.org/articles/10.3389/fphys.2023.1231793/full#supplementary-material

References

Alsop, D. C., Detre, J. A., Golay, X., Günther, M., Hendrikse, J., Hernandez-Garcia, L., et al. (2015). Recommended implementation of arterial spin-labeled perfusion MRI for clinical applications: A consensus of the ismrm perfusion study group and the European consortium for ASL in dementia. *Magn. Reson. Med.* 73, 102–116. doi:10.1002/mrm.25197

An, H., and Lin, W. (2003). Impact of intravascular signal on quantitative measures of cerebral oxygen extraction and blood volume under normo- and hypercapnic conditions using an asymmetric spin echo approach. *Magn. Reson. Med.* 50, 708–716. doi:10.1002/mrm.10576

An, H., and Lin, W. (2000). Quantitative measurements of cerebral blood oxygen saturation using magnetic resonance imaging. *J. Cereb. Blood Flow. Metab.* 20, 1225–1236. doi:10.1097/00004647-200008000-00008

Andersson, J. L. R., Jenkinson, M., and Smith, S. (2010). *Non-linear registration, aka spatial normalisation FMRIB technical report TR07JA2.*

Baas, K. P. A., Coolen, B. F., Petersen, E. T., Biemond, B. J., Strijkers, G. J., and Nederveen, A. J. (2022). Comparative analysis of blood T2 values measured by T2 -trir and TRUST. *J. Magn. Reson Imaging* 56, 516–526. doi:10.1002/jmri.28066

Blockley, N. P., and Stone, A. J. (2016). Improving the specificity of R2' to the deoxyhaemoglobin content of brain tissue: prospective correction of macroscopic magnetic field gradients. *NeuroImage* 135, 253–260. doi:10.1016/j.neuroimage.2016.04.013

Bouvier, J., Detante, O., Tahon, F., Attye, A., Perret, T., Chechin, D., et al. (2015). Reduced $CMRO_2$ and cerebrovascular reserve in patients with severe intracranial arterial stenosis: A combined multiparametric qBOLD oxygenation and BOLD fMRI study. *Hum. Brain Mapp.* 36, 695–706. doi:10.1002/hbm.22657

Bright, M. G., Whittaker, J. R., Driver, I. D., and Murphy, K. (2020). Vascular physiology drives functional brain networks. *NeuroImage* 217, 116907. doi:10.1016/j.neuroimage.2020.116907

Brown, E., Hopper, J., Hodges, J. L., Bradley, B., Wennesland, R., and Yamauchi, H. (1962). Red cell, plasma, and blood volume in the healthy women measured by radiochromium cell-labeling and hematocrit. *J. Clin. Invest.* 41, 2182–2190. doi:10.1172/JCI104677

Brown, W. R., and Thore, C. R. (2011). Review: cerebral microvascular pathology in ageing and neurodegeneration. *Neuropathol. Appl. Neurobiol.* 37, 56–74. doi:10.1111/j.1365-2990.2010.01139.x

Broyd, S. J., Demanuele, C., Debener, S., Helps, S. K., James, C. J., and Sonuga-Barke, E. J. S. (2009). Default-mode brain dysfunction in mental disorders: A systematic review. *Neurosci. Biobehav. Rev.* 33, 279–296. doi:10.1016/j.neubiorev.2008.09.002

Buch, S., Ye, Y., and Haacke, E. M. (2017). Quantifying the changes in oxygen extraction fraction and cerebral activity caused by caffeine and acetazolamide. *J. Cereb. Blood Flow. Metab.* 37, 825–836. doi:10.1177/0271678X16641129

Burton, E. J., Barber, R., Mukaetova-Ladinska, E. B., Robson, J., Perry, R. H., Jaros, E., et al. (2009). Medial temporal lobe atrophy on MRI differentiates alzheimer's disease from dementia with lewy bodies and vascular cognitive impairment: A prospective study with pathological verification of diagnosis. *Brain* 132, 195–203. doi:10.1093/brain/awn298

Chappell, M. A., Groves, A. R., Whitcher, B., and Woolrich, M. W. (2009). Variational bayesian inference for a nonlinear forward model. *IEEE Trans. Signal Process.* 57, 223–236. doi:10.1109/TSP.2008.2005752

Chappell, M. A., MacIntosh, B. J., Donahue, M. J., Günther, M., Jezzard, P., and Woolrich, M. W. (2010). Separation of macrovascular signal in multi-inversion time arterial spin labelling MRI. *Magn. Reson. Med.* 63, 1357–1365. doi:10.1002/mrm.22320

Cherukara, M. T., Stone, A. J., Chappell, M. A., and Blockley, N. P. (2019). Model-based Bayesian inference of brain oxygenation using quantitative BOLD. *NeuroImage* 202, 116106. doi:10.1016/j.neuroimage.2019.116106

Cho, J., Lee, J., An, H., Goyal, M. S., Su, Y., and Wang, Y. (2021). Cerebral oxygen extraction fraction (OEF): comparison of challenge-free gradient echo qsm+qbold (qq) with 15o pet in healthy adults. *J. Cereb. Blood Flow. Metab.* 41, 1658–1668. doi:10.1177/0271678X20973951

Cleland, N. R. W., Al-Juboori, S. I., Dobrinskikh, E., and Bruce, K. D. (2021). Altered substrate metabolism in neurodegenerative disease: new insights from metabolic imaging. *J. Neuroinflammation* 18, 248. doi:10.1186/s12974-021-02305-w

Clifford, R., Jack, J., Petersen, R. C., Yue Cheng Xu, Waring, S. C., O'Brien, P. C., et al. (1997). Medial temporal atrophy on MRI in normal aging and very mild Alzheimer's disease. *Neurology* 49, 786–794. doi:10.1212/WNL.49.3.786

Coalson, T. S., Van Essen, D. C., and Glasser, M. F. (2018). The impact of traditional neuroimaging methods on the spatial localization of cortical areas. *Proc. Natl. Acad. Sci.* 115, E6356–E6365. doi:10.1073/pnas.1801582115

Collins, D. L., Zijdenbos, A. P., Baaré, W. F. C., and Evans, A. C. (1999). "ANIMAL+INSECT: improved cortical structure segmentation," in *Information processing in medical imaging lecture notes in computer science*. A. Kuba, M. Šáamal, and A. Todd-Pokropek (Berlin, Heidelberg: Springer), 210–223. doi:10.1007/3-540-48714-X_16

Desikan, R. S., Ségonne, F., Fischl, B., Quinn, B. T., Dickerson, B. C., Blacker, D., et al. (2006). An automated labeling system for subdividing the human cerebral cortex on MRI scans into gyral based regions of interest. *NeuroImage* 31, 968–980. doi:10.1016/j.neuroimage.2006.01.021

Fan, A. P., Khalil, A. A., Fiebach, J. B., Zaharchuk, G., Villringer, A., Villringer, K., et al. (2020). Elevated brain oxygen extraction fraction measured by MRI susceptibility relates to perfusion status in acute ischemic stroke. *J. Cereb. Blood Flow. Metab.* 40, 539–551. doi:10.1177/0271678X19827944

Fan, J.-L., Nogueira, R. C., Brassard, P., Rickards, C. A., Page, M., Nasr, N., et al. (2022). Integrative physiological assessment of cerebral hemodynamics and metabolism in acute ischemic stroke. *J. Cereb. Blood Flow. Metab. Off. J. Int. Soc. Cereb. Blood Flow. Metab.* 42, 454–470. doi:10.1177/0271678X211033732

Fonov, V., Evans, A. C., Botteron, K., Almli, C. R., McKinstry, R. C., Collins, D. L., et al. (2011). Unbiased average age-appropriate atlases for pediatric studies. *NeuroImage* 54, 313–327. doi:10.1016/j.neuroimage.2010.07.033

Fonov, V., Evans, A., McKinstry, R., Almli, C., and Collins, D. (2009). Unbiased nonlinear average age-appropriate brain templates from birth to adulthood. *NeuroImage* 47, S102. doi:10.1016/S1053-8119(09)70884-5

Frazier, J. A., Chiu, S., Breeze, J. L., Makris, N., Lange, N., Kennedy, D. N., et al. (2005). Structural brain magnetic resonance imaging of limbic and thalamic volumes in pediatric bipolar disorder. *Am. J. Psychiatry* 162, 1256–1265. doi:10.1176/appi.ajp.162.7.1256

Groves, A. R., Chappell, M. A., and Woolrich, M. W. (2009). Combined spatial and non-spatial prior for inference on MRI time-series. *NeuroImage* 45, 795–809. doi:10.1016/j.neuroimage.2008.12.027

Gersing, A. S., Ankenbrank, M., Schwaiger, B. J., Toth, V., Janssen, I., Kooijman, H., et al. (2015). Mapping of cerebral metabolic rate of oxygen using dynamic susceptibility contrast and blood oxygen level dependent MR imaging in acute ischemic stroke. *Neuroradiology* 57, 1253–1261. doi:10.1007/s00234-015-1592-7

Goldstein, J. M., Seidman, L. J., Makris, N., Ahern, T., O'Brien, L. M., Caviness, V. S., et al. (2007). Hypothalamic abnormalities in schizophrenia: sex effects and genetic vulnerability. *Biol. Psychiatry* 61, 935–945. doi:10.1016/j.biopsych.2006.06.027

Greve, D. N., and Fischl, B. (2009). Accurate and robust brain image alignment using boundary-based registration. *NeuroImage* 48, 63–72. doi:10.1016/j.neuroimage.2009.06.060

Guilliams, K. P., Fields, M. E., Ragan, D. K., Eldeniz, C., Binkley, M. M., Chen, Y., et al. (2018). Red cell exchange transfusions lower cerebral blood flow and oxygen extraction fraction in pediatric sickle cell anemia. *Blood* 131, 1012–1021. doi:10.1182/blood-2017-06-789842

Gupta, A., Baradaran, H., Schweitzer, A. D., Kamel, H., Pandya, A., Delgado, D., et al. (2014). Oxygen extraction fraction and stroke risk in patients with carotid stenosis or occlusion: A systematic review and meta-analysis. *Am. J. Neuroradiol.* 35, 250–255. doi:10.3174/ajnr.A3668

Haight, T. J., Bryan, R. N., Erus, G., Davatzikos, C., Jacobs, D. R., D'Esposito, M., et al. (2015). Vascular risk factors, cerebrovascular reactivity, and the default-mode brain network. *NeuroImage* 115, 7–16. doi:10.1016/j.neuroimage.2015.04.039

Handwerker, D. A., Gazzaley, A., Inglis, B. A., and D'Esposito, M. (2007). Reducing vascular variability of fMRI data across aging populations using a breathholding task. *Hum. Brain Mapp.* 28, 846–859. doi:10.1002/hbm.20307

He, X., and Yablonskiy, D. A. (2007). Quantitative BOLD: mapping of human cerebral deoxygenated blood volume and oxygen extraction fraction: default state. *Magn. Reson. Med.* 57, 115–126. doi:10.1002/mrm.21108

Hokari, M., Kuroda, S., Shiga, T., Nakayama, N., Tamaki, N., and Iwasaki, Y. (2008). Combination of a mean transit time measurement with an acetazolamide test increases predictive power to identify elevated oxygen extraction fraction in occlusive carotid artery diseases. *J. Nucl. Med.* 49, 1922–1927. doi:10.2967/jnumed.108.054379

Imaizumi, M., Kitagawa, K., Oku, N., Hashikawa, K., Takasawa, M., Yosmkawa, T., et al. (2004). Clinical significance of cerebrovascular reserve in acetazolamide challenge—Comparison with acetazolamide challenge H2O-PET and gas-PET. *Ann. Nucl. Med.* 18, 369–374. doi:10.1007/BF02984479

Ishii, K., Kitagaki, H., Kono, M., and Mori, E. (1996). Decreased medial temporal oxygen metabolism in alzheimer's disease shown by PET. *J. Nucl. Med.* 37, 1159–1165.

Jenkinson, M., Bannister, P., Brady, M., and Smith, S. (2002). Improved optimization for the robust and accurate linear registration and motion correction of brain images. *NeuroImage* 17, 825–841. doi:10.1016/s1053-8119(02)91132-8

Jenkinson, M., Beckmann, C. F., Behrens, T. E. J., Woolrich, M. W., and Smith, S. M. (2012). Fsl. *NeuroImage* 62, 782–790. doi:10.1016/j.neuroimage.2011.09.015

Jenkinson, M., and Smith, S. (2001). A global optimisation method for robust affine registration of brain images. *Med. Image Anal.* 5, 143–156. doi:10.1016/S1361-8415(01)00036-6

Jeong, H. R., Shim, Y. S., Lee, H. S., and Hwang, J. S. (2021). Hemoglobin and hematocrit levels are positively associated with blood pressure in children and adolescents 10 to 18 years old. *Sci. Rep.* 11, 19052. doi:10.1038/s41598-021-98472-0

Jiang, D., Lin, Z., Liu, P., Sur, S., Xu, C., Hazel, K., et al. (2020). Brain oxygen extraction is differentially altered by alzheimer's and vascular diseases. *J. Magnetic Reson. Imaging* 52, 1829–1837. doi:10.1002/jmri.27264

Jiang, D., Liu, P., Lin, Z., Hazel, K., Pottanat, G., Lucke, E., et al. (2023). MRI assessment of cerebral oxygen extraction fraction in the medial temporal lobe. *NeuroImage* 266, 119829. doi:10.1016/j.neuroimage.2022.119829

Kaczmarz, S., Göttler, J., Petr, J., Hansen, M. B., Mouridsen, K., Zimmer, C., et al. (2021). Hemodynamic impairments within individual watershed areas in asymptomatic carotid artery stenosis by multimodal MRI. *J. Cereb. Blood Flow. Metab. Off. J. Int. Soc. Cereb. Blood Flow. Metab.* 41, 380–396. doi:10.1177/0271678X20912364

Kazumata, K., Tanaka, N., Ishikawa, T., Kuroda, S., Houkin, K., and Mitsumori, K. (1996). Dissociation of vasoreactivity to acetazolamide and hypercapnia. Comparative study in patients with chronic occlusive major cerebral artery disease. *Stroke* 27, 2052–2058. doi:10.1161/01.STR.27.11.2052

Kety, S. S., and Schmidt, C. F. (1948). The nitrous oxide method for the quantitative determination of cerebral blood flow in man: theory, procedure and normal values. *J. Clin. Invest.* 27, 476–483. doi:10.1172/JCI101994

Kim, D., Hughes, T. M., Lipford, M. E., Craft, S., Baker, L. D., Lockhart, S. N., et al. (2021). Relationship between cerebrovascular reactivity and cognition among people with risk of cognitive decline. *Front. Physiol.* 12, 645342. doi:10.3389/fphys.2021.645342

Kleinschmidt, A., Steinmetz, H., Sitzer, M., Merboldt, K.-D., and Frahm, J. (1995). Magnetic resonance imaging of regional cerebral blood oxygenation changes under acetazolamide in carotid occlusive disease. *Stroke* 26, 106–110. doi:10.1161/01.STR.26.1.106

Lattanzi, S., Carbonari, L., Pagliariccio, G., Bartolini, M., Cagnetti, C., Viticchi, G., et al. (2018). Neurocognitive functioning and cerebrovascular reactivity after carotid endarterectomy. *Neurology* 90, e307–e315. doi:10.1212/WNL.0000000000004862

Le, L. N. N., Wheeler, G. J., Blockley, N. P., and Fan, A. P. (2023). "Quantitative BOLD with variational bayesian inference: model comparisons with monte carlo simulations and in an elderly cohort," in ISMRM, Toronto, Canada, 03-08 June 2023.

Lee, H., Englund, E. K., and Wehrli, F. W. (2018). Interleaved quantitative BOLD: combining extravascular r2′ - and intravascular r2-measurements for estimation of deoxygenated blood volume and hemoglobin oxygen saturation. *NeuroImage* 174, 420–431. doi:10.1016/j.neuroimage.2018.03.043

Leenders, K. L., Perani, D., Lammertsma, A. A., Heather, J. D., Buckingham, P., Jones, T., et al. (1990). Cerebral blood flow, blood volume and oxygen utilization: normal values and effect of age. *Brain* 113, 27–47. doi:10.1093/brain/113.1.27

Li, X., Wang, D., Auerbach, E. J., Moeller, S., Ugurbil, K., and Metzger, G. J. (2015). Theoretical and experimental evaluation of multi-band EPI for high-resolution whole brain pCASL Imaging. *NeuroImage* 106, 170–181. doi:10.1016/j.neuroimage.2014.10.029

Lin, Z., Lim, C., Jiang, D., Soldan, A., Pettigrew, C., Oishi, K., et al. (2023). Longitudinal changes in brain oxygen extraction fraction (OEF) in older adults: relationship to markers of vascular and alzheimer's pathology. *Alzheimer's Dementia* 19, 569–577. doi:10.1002/alz.12727

Liu, Y., Li, S., Tian, X., Leung, T. W., Liu, L., Liebeskind, D. S., et al. (2023). Cerebral haemodynamics in symptomatic intracranial atherosclerotic disease: A narrative review of the assessment methods and clinical implications. *Stroke Vasc. Neurol.*–2023-002333.svn-2023-002333. doi:10.1136/svn-2023-002333

Makris, N., Goldstein, J. M., Kennedy, D., Hodge, S. M., Caviness, V. S., Faraone, S. V., et al. (2006). Decreased volume of left and total anterior insular lobule in schizophrenia. *Schizophr. Res.* 83, 155–171. doi:10.1016/j.schres.2005.11.020

Mandell, D. M., Han, J. S., Poublanc, J., Crawley, A. P., Stainsby, J. A., Fisher, J. A., et al. (2008). Mapping cerebrovascular reactivity using blood oxygen level-dependent MRI in patients with arterial steno-occlusive disease: comparison with arterial spin labeling mri. *Stroke* 39, 2021–2028. doi:10.1161/STROKEAHA.107.506709

Mikl, M., Mareček, R., Hluštík, P., Pavlicová, M., Drastich, A., Chlebus, P., et al. (2008). Effects of spatial smoothing on fMRI group inferences. *Magn. Reson. Imaging* 26, 490–503. doi:10.1016/j.mri.2007.08.006

Nemoto, E. M., Yonas, H., Kuwabara, H., Pindzola, R. R., Sashin, D., Meltzer, C. C., et al. (2004). Identification of hemodynamic compromise by cerebrovascular reserve and oxygen extraction fraction in occlusive vascular disease. *J. Cereb. Blood Flow. Metab.* 24, 1081–1089. doi:10.1097/01.WCB.0000125887.48838.37

Ni, W., Christen, T., Zun, Z., and Zaharchuk, G. (2015). Comparison of R2′ measurement methods in the normal brain at 3 tesla. *Magn. Reson. Med.* 73, 1228–1236. doi:10.1002/mrm.25232

Ni, W. W., Christen, T., Rosenberg, J., Zun, Z., Moseley, M. E., and Zaharchuk, G. (2017). Imaging of cerebrovascular reserve and oxygenation in Moyamoya disease. *J. Cereb. Blood Flow. Metab.* 37, 1213–1222. doi:10.1177/0271678X16651088

Nicoll, D., Lu, C. M., Pignone, M., and McPhee, S. J. (2012). *Pocket guide to diagnostic tests*. 6. McGraw Hill: Access Medicine. Available at: https://accessmedicine.mhmedical.com/content.aspx?bookid=503&sectionid=43474712.

Olman, C. A., Davachi, L., and Inati, S. (2009). Distortion and signal loss in medial temporal lobe. *PLOS ONE* 4, e8160. doi:10.1371/journal.pone.0008160

Pinheiro, J. C., and Bates, D. M. (1996). Unconstrained parametrizations for variance-covariance matrices. *Stat. Comput.* 6, 289–296. doi:10.1007/BF00140873

Pinto, J., Chappell, M. A., Okell, T. W., Mezue, M., Segerdahl, A. R., Tracey, I., et al. (2020). Calibration of arterial spin labeling data—Potential pitfalls in post-processing. *Magn. Reson. Med.* 83, 1222–1234. doi:10.1002/mrm.28000

Richiardi, J., Monsch, A. U., Haas, T., Barkhof, F., Van de Ville, D., Radü, E. W., et al. (2015). Altered cerebrovascular reactivity velocity in mild cognitive impairment and Alzheimer's disease. *Neurobiol. Aging* 36, 33–41. doi:10.1016/j.neurobiolaging.2014.07.020

Robb, W. H., Khan, O. A., Ahmed, H. A., Li, J., Moore, E. E., Cambronero, F. E., et al. (2022). Lower cerebral oxygen utilization is associated with Alzheimer's disease-related neurodegeneration and poorer cognitive performance among apolipoprotein E ε4 carriers. *J. Cereb. Blood Flow. Metab. Off. J. Int. Soc. Cereb. Blood Flow. Metab.* 42, 642–655. doi:10.1177/0271678X211056393

Rolfe, D. F., and Brown, G. C. (1997). Cellular energy utilization and molecular origin of standard metabolic rate in mammals. *Physiol. Rev.* 77, 731–758. doi:10.1152/physrev.1997.77.3.731

Silvestrini, M., Pasqualetti, P., Baruffaldi, R., Bartolini, M., Handouk, Y., Matteis, M., et al. (2006). Cerebrovascular reactivity and cognitive decline in patients with Alzheimer disease. *Stroke* 37, 1010–1015. doi:10.1161/01.STR.0000206439.62025.97

Simon, A. B., Dubowitz, D. J., Blockley, N. P., and Buxton, R. B. (2016). A novel Bayesian approach to accounting for uncertainty in fMRI-derived estimates of cerebral oxygen metabolism fluctuations. *NeuroImage* 129, 198–213. doi:10.1016/j.neuroimage.2016.01.001

Smeeing, D. P. J., Hendrikse, J., Petersen, E. T., Donahue, M. J., and de Vis, J. B. (2016). Arterial spin labeling and blood oxygen level-dependent MRI cerebrovascular reactivity in cerebrovascular disease: A systematic review and meta-analysis. *Cerebrovasc. Dis.* 42, 288–307. doi:10.1159/000446081

Smith, S. M. (2002). Fast robust automated brain extraction. *Hum. Brain Mapp.* 17, 143–155. doi:10.1002/hbm.10062

Spees, W. M., Yablonskiy, D. A., Oswood, M. C., and Ackerman, J. J. H. (2001). Water proton MR properties of human blood at 1.5 tesla: magnetic susceptibility, t1, t2, t2*, and non-lorentzian signal behavior. *Magn. Reson. Med.* 45, 533–542. doi:10.1002/mrm.1072

Stone, A. J., and Blockley, N. P. (2017). A streamlined acquisition for mapping baseline brain oxygenation using quantitative BOLD. *NeuroImage* 147, 79–88. doi:10.1016/j.neuroimage.2016.11.057

Stone, A. J., Harston, G. W. J., Carone, D., Okell, T. W., Kennedy, J., and Blockley, N. P. (2019). Prospects for investigating brain oxygenation in acute stroke: experience with a non-contrast quantitative bold based approach. *Hum. Brain Mapp.* 40, 2853–2866. doi:10.1002/hbm.24564

Sukstanskii, A. L., and Yablonskiy, D. A. (2001). Theory of FID NMR signal dephasing induced by mesoscopic magnetic field inhomogeneities in biological systems. *J. Magn. Reson.* 151, 107–117. doi:10.1006/jmre.2001.2363

Tam, C. W. C., Burton, E. J., McKeith, I. G., Burn, D. J., and O'Brien, J. T. (2005). Temporal lobe atrophy on MRI in Parkinson disease with dementia: A comparison with alzheimer disease and dementia with lewy bodies. *Neurology* 64, 861–865. doi:10.1212/01.WNL.0000153070.82309.D4

Tchistiakova, E., Crane, D. E., Mikulis, D. J., Anderson, N. D., Greenwood, C. E., Black, S. E., et al. (2015). Vascular risk factor burden correlates with cerebrovascular reactivity but not resting state coactivation in the default mode network. *J. Magn. Reson. Imaging JMRI* 42, 1369–1376. doi:10.1002/jmri.24917

Uchida, Y., Kan, H., Inoue, H., Oomura, M., Shibata, H., Kano, Y., et al. (2022). Penumbra detection with oxygen extraction fraction using magnetic susceptibility in patients with acute ischemic stroke. *Front. Neurology* 13, 752450. doi:10.3389/fneur.2022.752450

Václavů, L., Petr, J., Petersen, E. T., Mutsaerts, H. J. M. M., Majoie, C. B. L., Wood, J. C., et al. (2020). Cerebral oxygen metabolism in adults with sickle cell disease. *Am. J. Hematol.* 95, 401–412. doi:10.1002/ajh.25727

Vestergaard, M. B., Iversen, H. K., Simonsen, S. A., Lindberg, U., Cramer, S. P., Andersen, U. B., et al. (2023). Capillary transit time heterogeneity inhibits cerebral oxygen metabolism in patients with reduced cerebrovascular reserve capacity from steno-occlusive disease. *J. Cereb. Blood Flow. Metab.* 43, 460–475. doi:10.1177/0271678X221139084

Vorstrup, S., Henriksen, L., and Paulson, O. B. (1984). Effect of acetazolamide on cerebral blood flow and cerebral metabolic rate for oxygen. *J. Clin. Invest.* 74, 1634–1639. doi:10.1172/JCI111579

Wang, K., Smith, Z. M., Buxton, R. B., Swenson, E. R., and Dubowitz, D. J. (2015). Acetazolamide during acute hypoxia improves tissue oxygenation in the human brain. *J. Appl. Physiol. Bethesda Md* 119, 1494–1500. doi:10.1152/japplphysiol.00117.2015

Wang, Y., Fellah, S., Fields, M. E., Guilliams, K. P., Binkley, M. M., Eldeniz, C., et al. (2021). Cerebral oxygen metabolic stress, microstructural injury, and infarction in adults with sickle cell disease. *Neurology* 97, e902–e912. doi:10.1212/WNL.0000000000012404

Watchmaker, J. M., Juttukonda, M. R., Davis, L. T., Scott, A. O., Faraco, C. C., Gindville, M. C., et al. (2018). Hemodynamic mechanisms underlying elevated oxygen extraction fraction (OEF) in moyamoya and sickle cell anemia patients. *J. Cereb. Blood Flow. Metab.* 38, 1618–1630. doi:10.1177/0271678X16682509

Watts, M. E., Pocock, R., and Claudianos, C. (2018). Brain energy and oxygen metabolism: emerging role in normal function and disease. *Front. Mol. Neurosci.* 11, 216. doi:10.3389/fnmol.2018.00216

Woolrich, M. W., Chiarelli, P., Gallichan, D., Perthen, J., and Liu, T. T. (2006). Bayesian inference of hemodynamic changes in functional arterial spin labeling data. *Magn. Reson. Med.* 56, 891–906. doi:10.1002/mrm.21039

Xu, F., Liu, P., Pekar, J. J., and Lu, H. (2015). Does acute caffeine ingestion alter brain metabolism in young adults? *NeuroImage* 110, 39–47. doi:10.1016/j.neuroimage.2015.01.046

Yablonskiy, D. A., and Haacke, E. M. (1994). Theory of NMR signal behavior in magnetically inhomogeneous tissues: the static dephasing regime. *Magn. Reson. Med.* 32, 749–763. doi:10.1002/mrm.1910320610

Yablonskiy, D. A., Sukstanskii, A. L., and He, X. (2013). Blood oxygenation level-dependent (BOLD)-based techniques for the quantification of brain hemodynamic and metabolic properties - theoretical models and experimental approaches. *NMR Biomed.* 26, 963–986. doi:10.1002/nbm.2839

Yamaguchi, T., Kanno, I., Uemura, K., Shishido, F., Inugami, A., Ogawa, T., et al. (1986). Reduction in regional cerebral metabolic rate of oxygen during human aging. *Stroke* 17, 1220–1228. doi:10.1161/01.STR.17.6.1220

Yamauchi, H., Okazawa, H., Kishibe, Y., Sugimoto, K., and Takahashi, M. (2004). Oxygen extraction fraction and acetazolamide reactivity in symptomatic carotid artery disease. *J. Neurol. Neurosurg. Psychiatry* 75, 33–37.

Yin, Y., Shu, S., Qin, L., Shan, Y., Gao, J.-H., and Lu, J. (2021). Effects of mild hypoxia on oxygen extraction fraction responses to brain stimulation. *J. Cereb. Blood Flow. Metab.* 41, 2216–2228. doi:10.1177/0271678X21992896

Yin, Y., Zhang, Y., and Gao, J.-H. (2018). Dynamic measurement of oxygen extraction fraction using a multiecho asymmetric spin echo (MASE) pulse sequence. *Magnetic Reson. Med.* 80, 1118–1124. doi:10.1002/mrm.27078

Zhang, J., Cho, J., Zhou, D., Nguyen, T. D., Spincemaille, P., Gupta, A., et al. (2018). Quantitative susceptibility mapping-based cerebral metabolic rate of oxygen mapping with minimum local variance. *Magnetic Reson. Med.* 79, 172–179. doi:10.1002/mrm.26657

frontiers | Frontiers in Physiology

TYPE Original Research
PUBLISHED 03 January 2024
DOI 10.3389/fphys.2023.1271254

OPEN ACCESS

EDITED BY
Alex Bhogal,
Utrecht University, Netherlands

REVIEWED BY
Luis Hernandez-Garcia,
University of Michigan, United States
Michael Germuska,
Cardiff University, United Kingdom

*CORRESPONDENCE
Sriranga Kashyap,
sriranga.kashyap@uhn.ca
Kâmil Uludağ,
kamil.uludag@uhn.ca

RECEIVED 02 August 2023
ACCEPTED 27 November 2023
PUBLISHED 03 January 2024

CITATION
Kashyap S, Oliveira ÍAF and Uludağ K (2024), Feasibility of high-resolution perfusion imaging using arterial spin labeling MRI at 3 Tesla.
Front. Physiol. 14:1271254.
doi: 10.3389/fphys.2023.1271254

Feasibility of high-resolution perfusion imaging using arterial spin labeling MRI at 3 Tesla

Sriranga Kashyap[1]*, Ícaro Agenor Ferreira Oliveira[1] and Kâmil Uludağ[1,2,3,4,5]*

[1]Krembil Brain Institute, University Health Network, Toronto, ON, Canada, [2]Department of Medical Biophysics, University of Toronto, Toronto, ON, Canada, [3]Center for Neuroscience Imaging Research, Institute for Basic Science, Suwon, Republic of Korea, [4]Department of Biomedical Engineering, Sungkyunkwan University, Suwon, Republic of Korea, [5]Physical Sciences, Sunnybrook Research Institute, Toronto, ON, Canada

Cerebral blood flow (CBF) is a critical physiological parameter of brain health, and it can be non-invasively measured with arterial spin labeling (ASL) MRI. In this study, we evaluated and optimized whole-brain, high-resolution ASL as an alternative to the low-resolution ASL employed in the routine assessment of CBF in both healthy participants and patients. Two high-resolution protocols (i.e., pCASL and FAIR-Q2TIPS (PASL) with 2 mm isotropic voxels) were compared to a default clinical pCASL protocol ($3.4 \times 3.4 \times 4\ mm^3$), all of whom had an acquisition time of ≈ 5 min. We assessed the impact of high-resolution acquisition on reducing partial voluming and improving sensitivity to the perfusion signal, and evaluated the effectiveness of z-deblurring on the ASL data. We compared the quality of whole-brain ASL acquired using three available head coils with differing number of receive channels (i.e., 20, 32, and 64ch). We found that using higher coil counts (32 and 64ch coils as compared to 20ch) offers improved signal-to-noise ratio (SNR) and acceleration capabilities that are beneficial for ASL imaging at 3 Tesla (3 T). The inherent reduction in partial voluming effects with higher resolution acquisitions improves the resolving power of perfusion without impacting the sensitivity. In conclusion, our results suggest that high-resolution ASL (2 to 2.5 mm isotropic voxels) has the potential to become a new standard for perfusion imaging at 3 T and increase its adoption into clinical research and cognitive neuroscience applications.

KEYWORDS

arterial spin labeling, brain perfusion, high spatial resolution, 3 Tesla, RF coil, neuroimaging frontiers

1 Introduction

Arterial spin labeling (ASL) is a non-invasive neuroimaging technique that uses magnetically labeled arterial blood water as an endogenous tracer to measure cerebral blood flow (CBF) (Detre et al., 1992; Williams et al., 1992). ASL provides a safe and repeatable method for assessing brain state and function without any risk of toxicity or allergic reactions from exogenous contrast agents. ASL can also be utilized to assess the quantitative CBF in units of mL/100 g/min at an individual voxel level (Williams et al., 1992; Buxton et al., 1998).

In recent years, technological advances in MRI scanner hardware and software, and new cutting-edge analysis methods have positively impacted the range of ASL applications and

resulted in a notable increase in the number of publications (Detre et al., 2012; Iutaka et al., 2023; Lindner et al., 2023). Another factor for its increasing popularity in clinical research is the community effort to standardize acquisition methods, data structures, and analyses (Alsop et al., 2015; Clement et al., 2022; Hernandez-Garcia et al., 2022). However, widely adopted standards (e.g., described in the ASL "white paper" (Alsop et al., 2015)) prescribe spatial resolutions of 3–4 mm in-plane and 4–8 mm slice thickness for ASL scans that are maximally 5–6 min long (typical length of clinical research/standard-of-care MRI protocols) but may not be optimal anymore with current hardware and MRI sequences. Although these protocols may suffice for macroscopic effects (such as pattern of large regions of hypo-perfusion), they are insufficient to detect subtle abnormalities that may represent early stage of neurological diseases or small lesions (Mora Álvarez et al., 2019). Therefore, ASL at higher spatial resolution (< 3 mm nominal, isotropic) is highly desirable.

Another reason for going to high spatial resolutions is to reduce partial volume (PV) effects, which occur when the voxel signal contains fractional contributions from more than one tissue type, for example, gray matter (GM), white matter (WM), and cerebrospinal fluid (CSF). This can introduce inaccuracies in perfusion quantification of the tissue of interest, resulting in either or both underestimation and over-estimation, depending on the PV fractions in the voxels. For instance, Asllani et al. (2008) showed that a voxel mixture of 80:20% gray:white matter (this ratio would be inclusive after the threshold, in most cases) would result in a 24% perfusion underestimation. Another example is the study by Donahue et al. (2006), investigating the impact of a higher resolution ASL protocol compared to low-resolution positron emission tomography (PET) scans, and they demonstrated that uncorrected CBF PET images might underestimate the gray matter (GM) CBF by 20%. In fact, in 2006, Donahue et al. actually envisioned the future of ASL imaging at 3 Tesla (3 T) to be spatial resolutions of 2.5 mm in-plane or higher. Seventeen years later, 3 T ASL imaging is still routinely carried out with voxel sizes > 3 mm, and the voxels are almost never isotropic, which can lead to underestimation of lesions and even misdiagnosis in the direction of the lowest spatial resolution. Although there have been methods and algorithms developed that can provide a means to *post hoc* correct for PV effects (Kirk et al., 2020a; Kirk et al., 2020b; Chappell et al., 2021), they usually cannot recreate lost information, and therefore, the most straight-forward and preferred approach is to just acquire the data at higher spatial resolutions.

This is notwithstanding high-resolution ASL studies carried out at field strengths higher (4.7 T, 7 T) than those typically used in the clinic (1.5 T, 3 T). For example, Mora Álvarez et al. (2019) demonstrated the feasibility of a high-resolution continuous ASL (CASL) at 4.7 T within a clinical time frame of 6 min. The study also observed reduced PV averaging at $1.5 \times 1.5 \times 3$ mm^3 resolution. Another interesting example is the study published by Zuo et al. (2013) where they employed Turbo-FLASH (fast low angle shot) ASL, both pseudo-continuous ASL (pCASL) and pulsed ASL (PASL) at 7 T showing the feasibility of achieving an in-plane resolution of 0.85×1.7 mm^2. At 7 T, recent functional MRI (fMRI) studies also showed the feasibility of using perfusion-weighted contrast with ASL at sub-millimeter spatial resolutions of 0.9 mm isotropic (Kashyap et al., 2021) and 0.7 mm isotropic (Ivanov et al., 2018; Kashyap et al., 2022) using a 3D-EPI (Poser et al., 2010) readout with a FAIR (Kim, 1995) QUIPSS II (Wong et al., 1997; Wong et al., 1998) labeling scheme.

Although there is evidence of the transformative potential that ultra-high-field scanners can have for clinical research and cognitive neuroscience applications, they are limited in availability compared to the ubiquity of 3 T scanners. Therefore, a translation of high-resolution ASL to widely available 3 T clinical platforms is urgently needed to catalyze clinical research as well as further advance the standards of care. This requires systematic optimization attuned to easily accessible workflows, which is currently not explored in the existing ASL literature.

The current study addresses these aforementioned challenges and gaps in the literature by first developing, testing, and evaluating high-resolution ASL protocols at 3 T in clinically feasible times, and then it compares them to a vendor default protocol that is typically used in routine clinical scanning. To this end, we developed optimized 2 mm isotropic pCASL and PASL protocols that balance the trade-off between signal-to-noise ratio (SNR) and acquisition time (TA) to be feasible for clinical application (TA ≈ 5 min). Furthermore, we also evaluated the impact of the choice of standard head coils on 3 T perfusion imaging. We systematically evaluated our protocols and the clinical default protocol with all three commercially available head coils (20-channel head and neck coil, 32-channel head coil only, and 64-channel head and neck coil) to ascertain the optimal hardware for high-resolution acquisitions. In addition, we quantify and demonstrate the reduction in partial voluming enabled by the high-resolution acquisitions. Finally, the lengthening of the readout with 3D-GRASE is recognized to result in through-plane (z-axis) blurring, resulting in loss of spatial resolution (Tan et al., 2011; Paschoal et al., 2021). We also assess the impact of advanced post-processing methods such as z-deblurring to improve spatial fidelity of the acquired data.

2 Materials and methods

2.1 Participants

Eight healthy volunteers (four female and four male volunteers, mean age = 29 ± 4 years) participated in the study and provided written informed consent prior to scanning. All participants were screened healthy individuals, non-smokers, not taking any medications, and with no history of neurological or neurovascular conditions. All procedures in this study conformed to the standards set by the Declaration of Helsinki and was approved by the Research Ethics Board of University Health Network according to the guidelines of Health Canada.

2.2 Data acquisition

Data were acquired on a Siemens MAGNETOM Prisma 3 T MRI scanner (Siemens Healthineers, Erlangen, Germany) at the Slaight

Family Centre for Advanced MRI (Toronto Western Hospital, Toronto ON, Canada); the scanner has a maximum gradient strength of 80 mT/m and a slew rate of 200 T/m/s, and runs on the XA30A IDEA software platform. We used three commercial MRI coils, namely, a 20ch head and neck coil, a 32ch head coil only, and a 64ch head and neck coil for receiving, and the transmission was carried out by the body coil. Participants were positioned by taking the eye centers as a reference for the magnet isocentering to minimize B_0 offsets for the labeling in the neck. All data of participants were acquired in the same scan session. The participants were brought out of the scanner, coils were exchanged, and the participants were repositioned to the magnet's isocenter. The sequential order of coils was pseudo-randomized between participants to avoid any systematic biases.

2.2.1 Anatomical imaging

Structural scans were acquired with the 32ch head coil. Whole-brain anatomical data were acquired using a 3D multi-echo magnetization-prepared rapid gradient echo (3D-MEMPRAGE) sequence (van der Kouwe et al., 2008) that uses volumetric EPI navigators combined with selective data reacquisition (Tisdall et al., 2012) to produce (prospectively) motion-corrected T_1w images (Tisdall et al., 2016) that were used in the study. The 3D-MEMPRAGE data were acquired at 0.8 mm isotropic resolution (TI = 1000 ms, TEs_{1-4} = 1.81, 3.6, 5.39, 7.18 ms, TR = 2500 ms, α = 8°, 208 sagittal slices, matrix = 320 × 320, GRAPPA = 2, Ref. lines = 32, partial $Fourier_{slice}$ = 6/8, echo spacing = 11.2 ms, bandwidth = 740 Hz/px, turbo factor = 168, total acquisition time ≈ 8 min). The four echoes were combined (using root mean squares, RMS) into a high-fidelity T_1-weighted image following the scanner's on-line reconstruction. Quantitative T_1 mapping was carried out using a 3D magnetization-prepared 2 rapid gradient echoes (3D-MP2RAGE) sequence (Marques et al. 2010). The MP2RAGE T_1 maps were only used to facilitate perfusion quantification and thus were acquired at a 1.2 mm isotropic resolution (TIs_{1-2} = 700, 2500 ms, α_{1-2} = 4°, 5°, TE = 4.04 ms, TR = 3200 ms, 144 axial slices, matrix = 192 × 192, GRAPPA = 2, Ref. lines = 32, partial $Fourier_{phase}$ = 6/8, echo spacing = 9.08 ms, bandwidth = 150 Hz/px, turbo factor = 144, total acquisition time ≈ 4 min). T_1 maps were calculated in-line using the Siemens MapIt package (Siemens Healthineers, Erlangen, Germany).

2.2.2 Perfusion imaging

All ASL protocols were developed using the Siemens Advanced 3D-ASL work-in-progress (WIP) sequence (courtesy of Siemens Healthineers, Erlangen, Germany) available for the XA30A baseline platform. The ASL data were acquired with a segmented 3D-GRASE readout for improved SNR (Fernández-Seara et al., 2008; Feinberg et al., 2009; Vidorreta et al., 2014). Three ASL protocols were acquired per coil in each participant: 1) the clinical default protocol ($3.4 \times 3.4 \times 4$ mm^3, "Clinical" in Table 1), 2) a high-resolution (or hires) pCASL protocol (2 mm isotropic, 'Hires' in Table 1), and 3) a hires PASL protocol employing a FAIR-Q2TIPS (Luh et al., 1999) labeling scheme (2 mm isotropic, "PASL Hires" in Table 1). For clinical and hires ASL variants, two steady-state magnetization (M_0) calibration images were acquired without any labeling, but with matched readout and TR increased to 20 s, one of M_0 had the opposite phase encoding for distortion correction. The new hires protocols developed in this study were acquired in approximately the same total time as the spatially anisotropic clinical ASL scan (≈ 5 min).

2.3 Data processing

2.3.1 Anatomical imaging

The RMS-combined, motion-corrected, T_1-weighted 3D-MEMPRAGE was processed using FreeSurfer v 7.3.2 (Dale et al., 1999; Fischl et al., 1999; Fischl et al., 2002) (https://surfer.nmr.mgh.harvard.edu/) using a brain mask that was generated using *mri_synthstrip* (Hoopes et al., 2022) and was provided as an additional input to the *recon-all* pipeline.

2.3.2 Perfusion imaging

The first volume of the ASL timeseries was discarded as separate M_0 scans had been acquired for quantification. The pre-processing steps were carried out using FSL (Smith et al., 2004) included motion and distortion correction, where all control and label volumes were independently realigned to the first volume of the ASL scan. The separately acquired M_0 scans were rigidly registered to the first volume of the ASL scan, and then distortion correction was performed using FSL's *topup* (Andersson et al., 2003) with the two M_0 images. The perfusion timeseries was calculated using sinc-subtraction as implemented in FSL's *perfusion_subtract*. The M_0 images, perfusion-weighted data, and the MP2RAGE T_1 maps (co-registered to M_0) were used as input to *oxasl* (Chappell et al., 2009) (https://github.com/physimals/oxasl) for voxelwise perfusion quantification. M_0 images were co-registered to the anatomical image using FreeSurfer's *bbregister* (Greve and Fischl, 2009) to obtain CBF maps in both native and structural space. No adaptive spatial smoothing (Groves et al., 2009) or partial volume correction (Chappell et al., 2011) was applied. Next, all anatomical scans were carefully registered to the 1 mm isotropic MNI non-linear 2009c asymmetric template space (Fonov et al., 2009; 2011) using the ANTs SyN algorithm (Avants et al., 2014; 2011) (https://github.com/ANTsX/ANTs). Native space maps from *oxasl* were resampled in a single step to the MNI space using *antsApplyTransforms*. The stability of the perfusion signal over time (temporal SNR, tSNR) was calculated dividing the temporal mean by the temporal standard deviation of the perfusion-weighted data (also referred to as perfusion tSNR). The SNR (consequently, tSNR) of a voxel is expected to scale proportionally with its volume, and this condition makes it challenging to compare datasets of highly different spatial resolutions. Therefore, to better appreciate the tSNR relative to a dataset's spatial resolution, the perfusion tSNR map from the hires scan was scaled by the ratio of the voxel volumes of clinical to hires datasets (46.24 $mm^3/8$ $mm^3 = 5.78$).

2.3.3 Partial volume analysis

In order to visualize the impact of the higher spatial resolution acquisition, participant-wise T_1-weighted images were resampled to the nominal spatial resolution of the clinical protocol ($3.4 \times 3.4 \times 4.0$ mm^3) or the hires protocol (2.0 mm isotropic). The resampled T_1-weighted images were segmented using FSL's *fsl_anat*

TABLE 1 Sequence parameters for the three ASL protocols in the present study.

Parameter	Clinical	Hires	PASL hires
Labeling	pCASL	pCASL	FAIR-Q2TIPS
TR/TE_{eff}	4720/20.40 ms	4000/16.80 ms	4000/16.80 ms
Tag control pairs	12	12	12
BS	Gray–White strong	Gray–White	Gray–White
Bolus (TI_1)/PLD (TI_2)	1800/1800 ms	1600/1800 ms	700/1800 ms
FOV	220 × 220	192 × 192	192 × 192
Matrix	64 × 64	96 × 96	96 × 96
Slice oversampling	20%	22.5%	22.5%
Acceleration	GRAPPA 2	2D-CAIPI 3	2D-CAIPI 3
Slices	30	66	66
Partial Fourier	Off	6/8 yz	6/8 yz
Bandwidth	2442 Hz/px	1930 Hz/px	1930 Hz/px
Echo spacing[1]	0.49 ms	0.68 ms	0.68 ms
EPI factor	31	23	23
Segments (k_z)	3	3	3
Turbo factor[2]	12	20	20
Echo-train length[3]	245 ms	336 ms	336 ms
Acquisition time	05:09 min	05:11 min	05:11 min

Although the study focuses on the two pCASL protocols, the PASL protocol is included here for completeness.
TR, repetition time; TE, echo time; FA, flip angle; BS, background suppression (gray–white = 2, gray–white strong = 4 non-selective pulses); PLD, post-labeling delay; TI, inversion time (for PASL); FOV, field-of-view.
[1] echo spacing, time between echoes in the 2D readout;
[2] turbo factor, number of echoes acquired after excitation;
[3] echo-train length≈TE×turbo factor.

(Zhang et al., 2001) to obtain PV estimates. The cortical gray matter segmentation from FreeSurfer was morphologically dilated by one voxel and resampled to the two resolutions, and this resampled, dilated cortical mask was used as the ROI for the PV analyses. To this end, we used a histogram-based analysis to first sort the voxels into different PV fraction bins. Then, to compare the two different acquisition resolutions, the number of voxels in each histogram bin was scaled by their voxel volumes of 46.24 mm^3 and 8 mm^3, respectively, for the clinical and hires protocols, giving us the volume of PV voxels in each bin. This normalization enabled a direct comparison of the PV. A difference between the hires and clinical histograms (after rescaling) was computed for all values above a PV fraction threshold of 0.5 for each of the three tissue classes, namely, GM, WM, and CSF.

2.3.4 Deblurring analysis

In an additional analysis, ASL data acquired from the 32ch coil were pre-processed using *oxasl_deblur* (https://github.com/physimals/oxasl_deblur). We evaluated two different methods for deblurring the data, namely, fast Fourier transform division (FFT) and Lucy–Richardson deconvolution (Lucy) as implemented in *oxasl_deblur*, with three different kernel options (direct estimation, Lorentzian, and Lorentzian with a Weiner filter). Smoothness of the deblurred data was estimated using AFNI's (Cox, 1996; Cox and Hyde, 1997) *3dFWHMx* (Cox et al., 2017) function.

3 Results

3.1 Comparison of clinical and hires ASL data

Figure 1 shows the group average absolute CBF (in units of mL/100 g/min) maps from clinical and hires pCASL protocols presented in three orthogonal views (middle panel) for the three

10.3389/fphys.2023.1271254

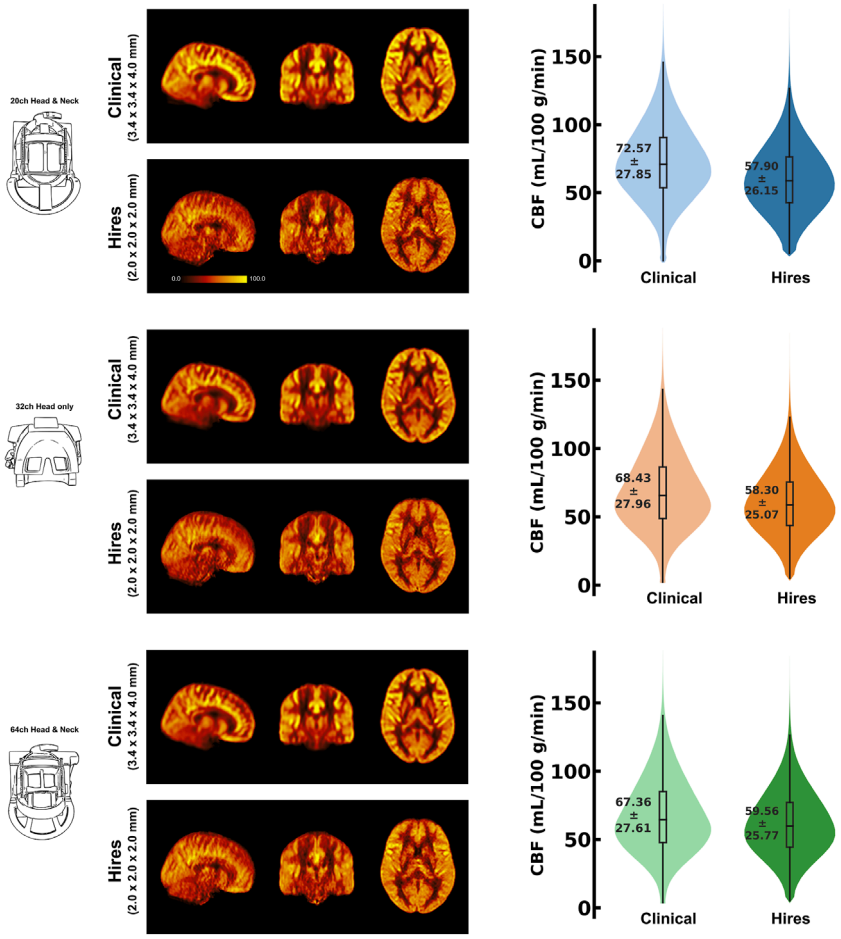

FIGURE 1
Mosaic of orthogonal views of the group average (n = 8) CBF (in mL/100 g/min) for data acquired using the three respective head coils (drawing on the left). In the middle column, the maps obtained from the clinical and hires pCASL acquisitions are displayed in the top and bottom rows, respectively. (Right) Violin plots of the CBF distribution across all participants' data (n = 8) for the two acquisitions. The annotation represents the mean ± standard deviation of the distribution.

head coils used to acquire the data (drawing in left panel). The panel on the right shows the distribution of the CBF values in GM across the participants' data as a violin plot with the CBF values represented on the *y*-axis for the two protocols. The figure annotation represents the mean ± standard deviation of the distribution. A comparison of the group average perfusion weighting and relative CBF (rCBF, in arbitrary units) for the two protocols and three head coils is shown in Supplementary Figure S1. It is important to note that the rCBF calculated using *oxasl* is the perfusion-weighted image (PWI) following kinetic model inversion (i.e., one step before M_0 calibration to physiological units of mL/100 g/min) and is not relative to the whole brain mean or normal white matter (Chappell et al., 2023). For the clinical and hires protocols, we observe that the mean CBF values are very similar for all three coils. The CBF values obtained from the clinical protocols are ≈ 17% greater than those obtained from the hires data, and both measures are in the acceptable range for healthy volunteers (Alsop et al. 2015). Summary statistics for all the different perfusion metrics calculated from the data are tabulated in Supplementary Tables S2–S6.

3.2 Analysis of the partial voluming

One of the primary advantages of acquiring higher spatial resolution data is the reduction of the partial voluming of the signal of interest. As shown in Figure 2, the differences in voxel volumes (hires−clinical) are plotted at each partial volume fraction bin ranging from 0.5 to 1.0 (50% to "pure" single-tissue composition) for three tissue classes, that is, GM (a), WM (b), and CSF (c), using a dilated GM ROI. Data from each participant are shown as a colored dot, with the mean across participants plotted as a black dashed line. In Figure 2A, we observe that on average, above a PV fraction of 0.6 (60% GM), there is a net positive change in the volume of GM and remains positive for all higher PV fractions. In other words, even within the dilated GM ROI, there is a larger volume (total ≈ 6713 mm^3) of "pure" GM in hires than in the clinical data; therefore, partial voluming is reduced. This finding is corroborated by the spatial maps of PV, as illustrated in the right panels with the PV map of hires and clinical shown on top and bottom rows, respectively. A similar pattern is observed in Figures 2B, C that

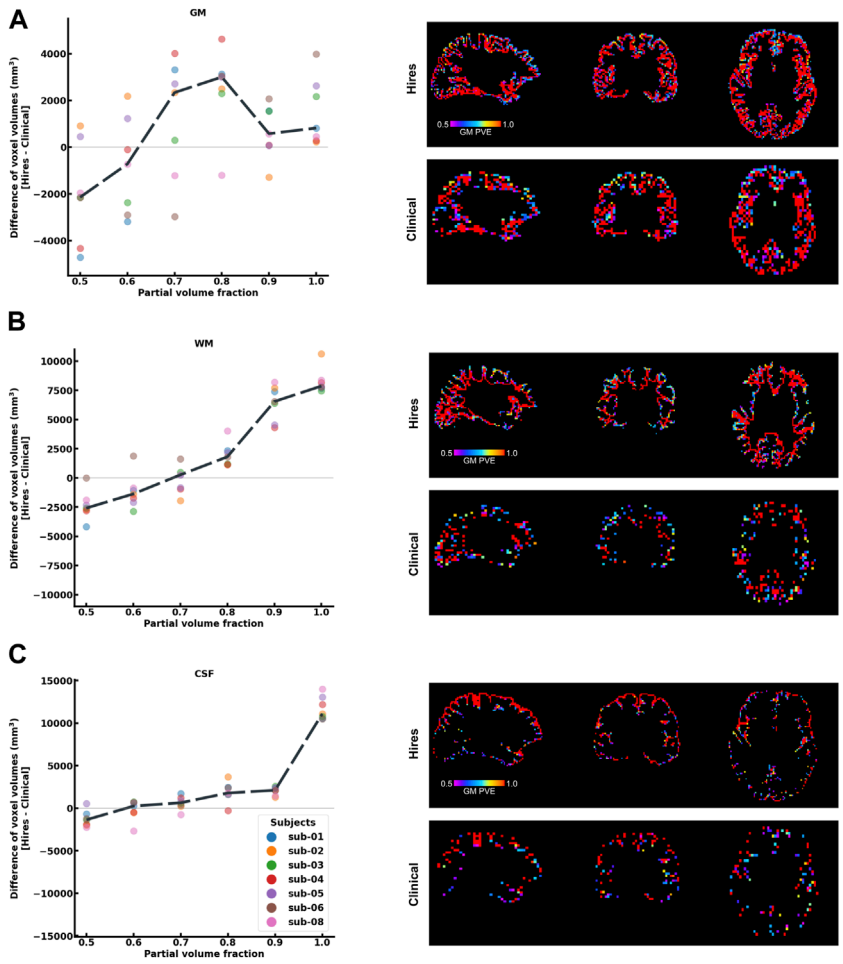

FIGURE 2
Histogram difference plot for all bins ≥0.5 threshold of PV fraction for **(A)** GM, **(B)** WM, and **(C)** CSF tissue classes of the hires and clinical acquisitions. Value from each participant is represented as a color-coded circle, and the group average is plotted as a black dotted line. A single-participant PV estimate map is shown in the right panel for the clinical and hires spatial scales, spatially illustrating the findings of the histogram analysis. It is to be noted that sub-07 is excluded from this analysis as *fsl_anat* could not be completed.

quantifies the PV in WM and CSF, respectively. In other words, within the dilated GM ROI used to extract these results, there is a significantly larger volume of "pure" WM (total ≈ 16,938 mm^3) and "pure" CSF (total ≈ 15,422 mm^3). As GM is bound on either side with WM and CSF, we can infer that the greater the number of "pure" non-GM voxels, the lower the amount of voxels which are PV with GM, and this finding is corroborated by the spatial maps of PV.

3.3 Deblurring analysis of 3D-GRASE ASL

Table 2 shows that the effective spatial resolution of both the clinical and hires datasets is different from what is indicated in the protocol, also referred to as the nominal spatial resolution (in this study, $3.4 \times 3.4 \times 4.0\ mm^3$ and 2.0 mm isotropic, respectively). Systematic evaluation of five parameter combinations in *oxasl_deblur* (Supplementary Table S2) shows that all five combinations result in an improvement in a reduction in the full width at half maximum (FWHM). We found that using the FFT method with direct kernel estimation yields the smallest effective FWHM (clinical: 6.38 ± 0.33 mm vs. hires: 2.38 ± 0.13 mm, Supplementary Table S2). Table 2 shows FWHM estimated from AFNI's *3dFWHMx* for x, y, and *z* axes as well as the effective FWHM (ACF). We observe that irrespective of the acquisition resolution, the smoothness is maximal along the *z*-axis (clinical: 8.73 ± 0.65 mm, hires: 4.01 ± 0.31 mm), and this is the axis along which *oxasl_deblur* is most effective, reducing the smoothness estimate to 5.22 ± 0.49 mm and 1.41 ± 0.12 mm for clinical and hires data, respectively. The change in the estimated FWHM along z after deblurring ($\Delta FWHM_{clinical}/\Delta FWHM_{hires}$) is 1.35 times larger for the hires dataset than that for the clinical data. Figure 3 shows the group average CBF maps for the clinical and hires datasets before ("orig") and after ("deblurred") deblurring, and the distribution of CBF values across all participants' data is also shown as a violin plot.

TABLE 2 FWHM (in mm) estimated using AFNI's *3dFWHMx* for the clinical and hires 3D-GRASE datasets deblurred using the FFT method and direct kernel estimation as implemented in *oxasl_deblur*.

FWHM	Clinical	Clinical deblurred	Hires	Hires deblurred
x	5.51 ± 0.27	5.49 ± 0.76	3.08 ± 0.18	2.65 ± 0.21
y	6.24 ± 0.20	5.91 ± 0.55	2.85 ± 0.17	2.42 ± 0.22
z	8.73 ± 0.65	5.22 ± 0.49	4.01 ± 0.31	1.41 ± 0.12
ACF	10.08 ± 0.67	7.24 ± 0.58	4.83 ± 0.36	2.69 ± 0.12

A comparison of FWHM for different deblurring methods can be found in Supplementary Table S2.
Numerical values presented are mean ± std. dev across participants.

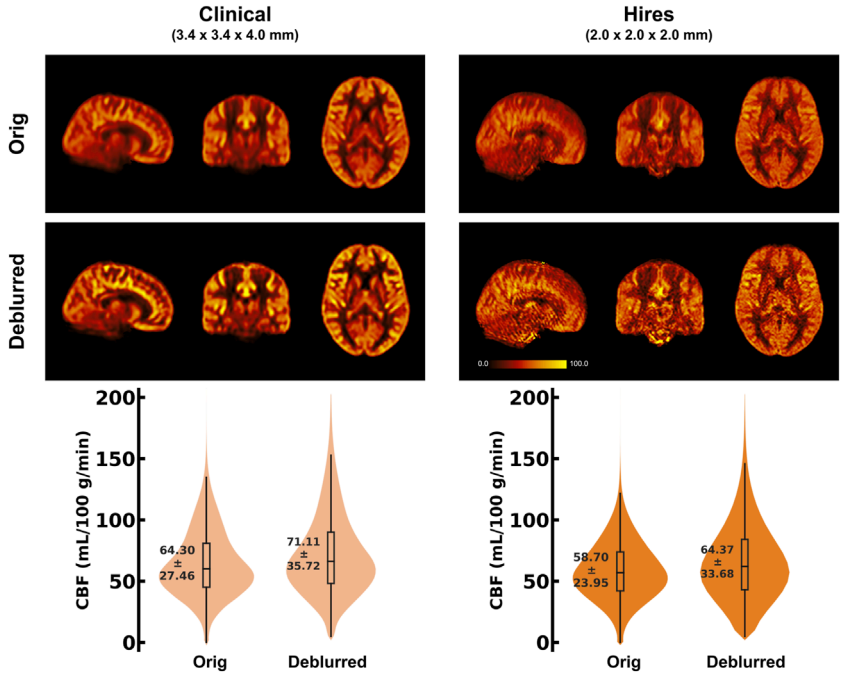

FIGURE 3
(Top) Orthogonal views of the group average CBF maps (in mL/100 g/min) (n = 8) obtained using the 32-channel head coil, before and after deblurring using the FFT method and direct kernel estimation as implemented in *oxasl_deblur*. (Bottom) Violin plots of the CBF distribution across all participants' data (n = 8) for the two acquisitions before and after deblurring. The annotation represents the mean ± standard deviation of the distribution.

3.4 Impact of head coil choice for imaging perfusion

Figure 1 demonstrates that robust CBF maps can be acquired independently of the coil choice. However, the spatial distribution of the CBF maps from the hires protocol shows a preference for 32 and 64ch. Figure 4 (top and middle rows) illustrates the impact of perfusion tSNR across the three coils. In the case of the clinical protocol, the increasing coil count has ≈ 2–2.5% gain in perfusion tSNR, whereas the hires protocol has ≈ 34–42% gain in perfusion tSNR with increasing coil count (Supplementary Table S5). The perfusion tSNR maps of the hires data, rescaled by the ratio of voxel volume (Figure 4, bottom row), illustrate the improvement of tSNR with 32 and 64 coils over 20ch. In addition, Supplementary Table S4 shows that the inter-quartile range (IQR) of the perfusion weighting increases with increasing coil count (20/32/64 ch: for clinical, 312.50/334.30/338.79 a. u., and for hires, 386.34/423.67/440.03 a. u.) for both protocols. The IQR of perfusion weighting between the three coils behaves similarly with the hires PASL protocol (20/32/64 ch: 396.12/447.66/454.97 a. u., Supplementary Table S9). Therefore, it is the SNR benefits afforded by higher coil count rather than the quality or type of labeling used that is responsible of the improvement in the higher IQR of perfusion values.

4 Discussion

In this study, we demonstrate that it is feasible to measure perfusion robustly and repeatably using ASL at a high spatial resolution of 2 mm isotropic within clinically feasible times of

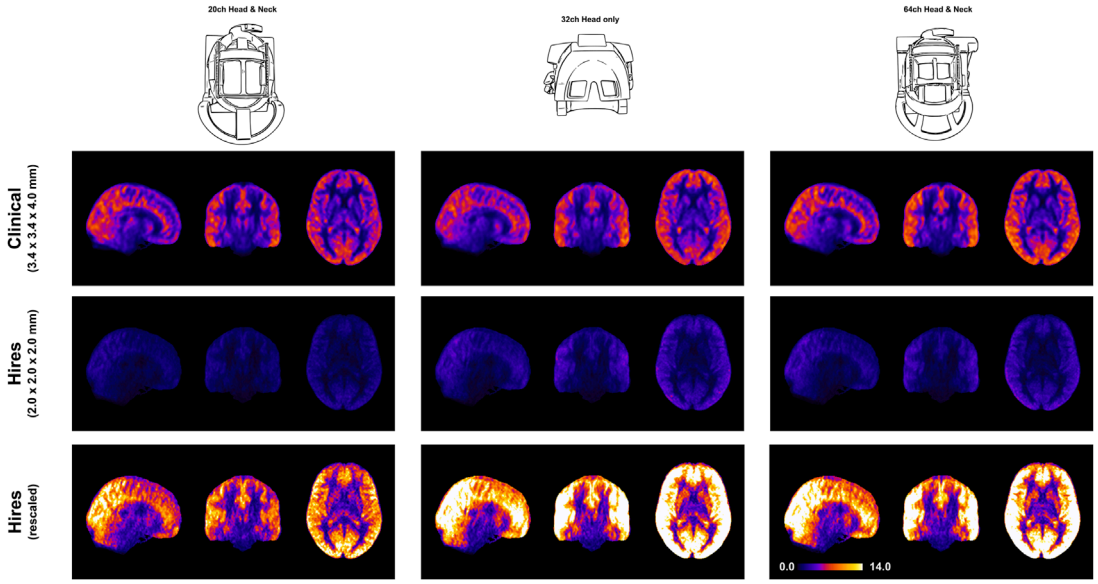

FIGURE 4
Orthogonal views of the group average perfusion tSNR maps (n = 8) where the pCASL clinical and hires maps are presented in the top and middle rows, respectively. The bottom row shows the hires tSNR data (middle row) but with rescaled values.

≈ 5 min. In this study, we used the updated version of the vendor provided 3D-GRASE ASL sequence (Siemens Advanced 3D-ASL WIP), and no custom sequence developments were carried out to enable widespread usage without the necessity to developing custom MR sequences or image reconstruction, despite the continuous progress being made on the development of ASL methods (Hernandez-Garcia et al., 2022). Therefore, we expect the sequence parameter choices made in this study can be selected in the 3D-GRASE ASL sequence available from the vendor on most modern scanners. We show that the increased spatial resolution does result in a reduction of partial voluming compared to the default clinical protocol. We show that through-plane blurring is a problem for 3D-GRASE ASL independent of the protocol being used. We find z-deblurring to be more effective on the hires than the clinical data. Finally, the choice of head coil for imaging perfusion with ASL at 3 T does play an important role with 32 and 64 ch being particularly well suited. Consistent with the results of deblurring, the hires datasets benefit most from perfusion tSNR improvements with higher coil counts.

4.1 Impact of spatial resolution on ASL imaging

We show that increasing the spatial resolution of ASL 5.78×, the clinical resolution does not have a detrimental effect on the measuring perfusion (Figure 1) and takes the same duration as a clinical scan (≈ 5 min). The mean perfusion-weighting values in the high-resolution data were found to be similar to the clinical data (e.g., 32 channel: 608.55 ± 256.24 vs. 605.91 ± 313.30 a. u.) (Supplementary Table S4). Importantly, however, the hires perfusion-weighted images exhibited approximately 27% greater IQR (32ch: clinical 334.3 vs. 423.67 a. u.) than the clinical data. As the IQR is a measure of spread around the mean, this measure is indicative of the dynamic range of perfusion in the data. Being capable of resolving a wider range of perfusion values is critical to detect subtle abnormalities and early detection of neurological diseases (Clement et al., 2018), therefore emphasizing the importance of high spatial resolution imaging (Mora Álvarez et al., 2019) in clinical research and cognitive neuroscience applications.

Acquiring data at a higher spatial resolution supports the observed improvement in dynamic range and concurrently reduces PV effects. The cortical GM is bound on either side by WM and CSF, and PV occurs when a GM voxel contains fractional distributions from these adjacent tissue classes that influence cortical perfusion measures. Figure 2 shows that hires ASL data consistently yield a greater volume of "pure" tissue voxels than the clinical data (GM: ≈ 6713 mm^3, WM: ≈ 16,938 mm^3, CSF: ≈ 15,422 mm^3) (It is to be noted that these PV fractions were derived from a dilated, cortical GM ROI, that is, the ROI does not consist of the large ventricles or the majority of WM in the brain). The increased number of "pure" WM and CSF voxels indicates that the hires data can enable a more effective separation of non-GM signal contributors to the perfusion signal of interest.

Partial volume correction was not performed at any stage of processing of the datasets (Chappell et al., 2011; Chappell et al., 2021). In the absence of PV correction of the lower resolution clinical protocol data, the lower CBF in WM partial voluming with GM would result in a reduction of the average CBF in GM. However, PV of GM with CSF (or rather vessels in CSF) can have the opposite effect, resulting in higher than expected CBF values in GM, which is likely the case here. It is also important to note the default clinical protocol was not subject to any optimization in the present work. Although seemingly contrary to expectations, for

parameter sets similar to the default clinical protocol, the CBF values in our data are consistent with those of studies that use a similar sequence (Vidorreta et al., 2014). Other reasons could be the fact that high-resolution acquisitions inherently reduce partial voluming effects and, therefore, can be more sensitive to the CBF variability within GM. Maps including that of the perfusion weighting and rCBF are shown in Supplementary Figures S1 (clinical vs. hires) and Supplementary Figure S2 (pCASL vs. PASL). We found that the hires PASL results are in good agreement with the hires pCASL (Supplementary Figure S2). Consistent with the previous work (Wu et al., 2007; Chen et al., 2011), the pCASL labeling scheme exhibits approximately 22%–26% higher perfusion tSNR than FAIR-Q2TIPS for the hires acquisitions in our study.

4.2 Impact of deblurring on 3D-GRASE ASL data

Because high spatial resolution is required, the total echo-train length (TE × TF) can exceed 300 ms ($\gg \pi \times T_2^*$ of tissue), resulting in increased blurring (Qin, 2012; Liang et al., 2014; Zhao et al., 2018), that occurs maximally in the slice direction (through-plane or *z*-axis). Thus, requiring post-processing correction or making compromises would render whole-brain acquisitions infeasible. We find that the application of z-deblurring has a demonstrable effect on the improvement of the spatial fidelity (or reducing the estimated FWHM) of the ASL data, as shown in Table 2. It is interesting to note that FWHM along z for the deblurred clinical data (5.22 ± 0.49 mm) is still larger than the non-deblurred hires data (4.01 ± 0.31 mm). This has an important implication in clinical settings where advanced image post-processing is often unavailable. Importantly, the hires ASL protocols enable researchers and clinicians to resolve perfusion changes with a higher spatial fidelity (without requiring advanced image processing) than the *post hoc* deblurred clinical datasets. Furthermore, post-processing deblurring methods have their limitations and they cannot synthesize resolution from information lost in acquisition. Although lengthening the echo-train is an important concern, our findings (Table 2) indicate that deblurring methods are more effective for high-resolution ASL imaging.

4.3 Impact of coil choice on ASL imaging

We demonstrate that robust rCBF maps can be acquired independently of the coil choice (Figure 1); however, higher coil counts (32 and 64ch) offer substantial gains in perfusion tSNR than the 20ch coil (Figure 4). We find that increasing coil count results in ≈ 2–2.5% gain in perfusion tSNR for the clinical protocol compared to ≈ 34–42% gain for the hires protocol (Supplementary Table S5). One reason for this difference could be that data acquired with clinical protocol in Figure 1 are relatively insensitive to the choice of coil due to its low spatial resolution (i.e., low thermal noise) and acceleration (i.e., no g-factor penalty) requirements. On the other hand, the hires protocols accelerate higher and have increased thermal noise than the clinical protocol, owing to the smaller voxel sizes, and therefore benefit from the increased number of coils (Figure 4).

Interestingly, Figure 4 shows that reducing the voxel size (i.e., higher spatial resolution) actually results in a gain in perfusion SNR (clinical vs. hires (scaled)), which may seem counterintuitive from the standpoint of conventional fMRI where the SNR of the BOLD signal decreases with increasing resolution. However, this is due to the different signal origins of the BOLD and perfusion contrasts. By reducing PV with veins and macro-vasculature, we are reducing the signal contributors of the BOLD signal, whereas these same signal components are sources of noise in perfusion imaging, as they have very low perfusion signals. In addition, reducing WM contribution of voxels dominated by GM improves the fidelity of GM perfusion values and reduced influence of physical noise stemming from WM. Therefore, reducing PV increases our sensitivity to the cortical microvasculature signal and reduces noise and signal contribution from WM and CSF. In other words, higher spatial resolution not only decreases image SNR in both BOLD and perfusion methods due to reduction in the number of protons (i.e., voxel volume) but also reduces noise sources in perfusion imaging stemming from CSF, veins, and WM.

4.4 Limitations

Although we demonstrate clear benefits of high-resolution ASL imaging for clinical research and cognitive neuroscience applications (group studies), the present study is limited in its ability to comment on a potential impact in daily clinical practice (single subject, diagnostic). Nevertheless, we believe future studies investigating the impact of ASL sequence parameters in routine clinical practice should use a modestly higher isotropic resolution (e.g., 2.5 mm) to enable better visualization of localized differences in perfusion. Here, we also opted for modest acceleration schemes (Table 1) as the protocols were to be compared on all three available head coils and the 20ch coil would be the lowest common denominator. The availability of the 3D-GRASE readout with 2D-CAIPIRINHA undersampling enabled us to achieve higher isotropic spatial resolution for perfusion imaging (Vidorreta et al., 2014; Ivanov et al., 2017; Boland et al., 2018). For a future non-comparison type of study, this protocol optimization can be pushed further to take advantage of the higher coil count and achieve higher acceleration. A systematic exploration of different CAIPI acceleration schemes or trajectories, impact of reduced g-factor noise amplification on image quality, is, unfortunately, beyond the scope of the present work.

4.5 Concluding remarks

Taking together, this study demonstrates the feasibility and benefits of imaging perfusion using high-resolution isotropic ASL for clinical research and cognitive neuroscience applications at 3 T. We have shown that increasing the spatial resolution does not compromise the accuracy and quality of the perfusion maps, and allows for a wider dynamic range of perfusion values. We have shown that high-resolution data can more effectively separate out the non-GM signal contributors (reduce PV effects), which improves the sensitivity to cortical microvasculature and tissue in GM. In addition, post-processing methods such as z-deblurring are

important considerations for whole-brain perfusion imaging using 3D-GRASE ASL to improve the spatial fidelity of the data. High-resolution acquisitions take advantage of the higher coil counts and offer substantial gains in perfusion tSNR with 32 and 64ch coils. Echoing what Donahue and colleagues envisioned in 2006, we strongly believe that high-resolution ASL (2–2.5 mm isotropic) can be a new standard for perfusion imaging using ASL at 3 T and be adopted into clinical and cognitive neuroscience research workflows.

Data availability statement

Data from this study can be accessed via the Canadian Open Neuroscience Platform (https://n2t.net/ark:/70798/d7mfwmtmr15hw6xwwg).

Ethics statement

The studies involving humans were approved by the Research Ethics Board of University Health Network according to the guidelines of Health Canada. The studies were conducted in accordance with the local legislation and institutional requirements. The participants provided their written informed consent to participate in this study.

Author contributions

SK: conceptualization, data curation, formal analysis, investigation, methodology, visualization, writing–original draft, and writing–review and editing. ÍO: investigation, methodology, validation, visualization, writing–original draft, and writing–review and editing. KU: conceptualization, funding acquisition, methodology, project administration, resources, supervision, writing–original draft, and writing–review and editing.

Funding

The author(s) declare financial support was received for the research, authorship, and/or publication of this article. The study was supported by the Institute for Basic Science, Suwon, Republic of Korea (IBS-R015-D1) to KU.

Acknowledgments

The authors thank Asma Naheed, MRT for the scanning support at the Slaight Family Centre for Advanced MRI, Toronto Western Hospital, University Health Network, Toronto, Canada. They would like to thank Dr. Thomas F. Kirk for the invaluable discussions about the partial voluming problem in ASL MRI data. They would like to thank Dr. Dimo Ivanov for his insights into ASL acquisition. They thank Dr. Gerald R. Moran and Dr. Josef Pfeuffer for their collaboration and for providing the Advanced 3D ASL WIP package for the Siemens XA30 platform.

Conflict of interest

The authors declare that the research was conducted in the absence of any commercial or financial relationships that could be construed as a potential conflict of interest.

Publisher's note

Supplementary material

The Supplementary Material for this article can be found online at: https://www.frontiersin.org/articles/10.3389/fphys.2023.1271254/full#supplementary-material

References

Alsop, D. C., Detre, J. A., Golay, X., Günther, M., Hendrikse, J., Hernandez-Garcia, L., et al. (2015). Recommended implementation of arterial spin-labeled perfusion MRI for clinical applications: a consensus of the ISMRM perfusion study group and the european consortium for ASL in dementia. *Magn. Reson. Med.* 73, 102–116. doi:10.1002/mrm.25197

Andersson, J. L., Skare, S., and Ashburner, J. (2003). How to correct susceptibility distortions in spin-echo echo-planar images: application to diffusion tensor imaging. *Neuroimage* 20, 870–888. doi:10.1016/S1053-8119(03)00336-7

Asllani, I., Borogovac, A., and Brown, T. R. (2008). Regression algorithm correcting for partial volume effects in arterial spin labeling mri. *Magnetic Reson. Med.* 60, 1362–1371. doi:10.1002/mrm.21670

Avants, B. B., Tustison, N. J., Song, G., Cook, P. A., Klein, A., and Gee, J. C. (2011). A reproducible evaluation of ants similarity metric performance in brain image registration. *Neuroimage* 54, 2033–2044. doi:10.1016/j.neuroimage.2010.09.025

Avants, B. B., Tustison, N. J., Stauffer, M., Song, G., Wu, B., and Gee, J. C. (2014). The Insight ToolKit image registration framework. *Front. Neuroinform.* 8, 44. doi:10.3389/fninf.2014.00044

Boland, M., Stirnberg, R., Pracht, E. D., Kramme, J., Viviani, R., Stingl, J., et al. (2018). Accelerated 3d-grase imaging improves quantitative multiple post labeling delay arterial spin labeling. *Magnetic Reson. Med.* 80, 2475–2484. doi:10.1002/mrm.27226

Buxton, R. B., Frank, L. R., Wong, E. C., Siewert, B., Warach, S., and Edelman, R. R. (1998). A general kinetic model for quantitative perfusion imaging with arterial spin labeling. *Magn. Reson Med.* 40, 383–396. doi:10.1002/mrm.1910400308

Chappell, M. A., Groves, A. R., MacIntosh, B. J., Donahue, M. J., Jezzard, P., and Woolrich, M. W. (2011). Partial volume correction of multiple inversion time arterial spin labeling mri data. *Magn. Reson Med.* 65, 1173–1183. doi:10.1002/mrm.22641

Chappell, M. A., Groves, A. R., Whitcher, B., and Woolrich, M. W. (2009). Variational bayesian inference for a nonlinear forward model. *Trans. Sig. Proc.* 57, 223–236. doi:10.1109/TSP.2008.2005752

Chappell, M. A., Kirk, T. F., Craig, M. S., McConnell, F. A. K., Zhao, M. Y., MacIntosh, B. J., et al. (2023). BASIL: A toolbox for perfusion quantification using arterial spin labelling. *Imaging Neurosci.* 1, 1–16. doi:10.1162/imag_a_00041

Chappell, M. A., McConnell, F. A., Golay, X., Günther, M., Hernandez-Tamames, J. A., van Osch, M. J., et al. (2021). Partial volume correction in arterial spin labeling perfusion mri: a method to disentangle anatomy from physiology or an analysis step too far? *Neuroimage* 238, 118236. doi:10.1016/j.neuroimage.2021.118236

Chen, Y., Wang, D. J., and Detre, J. A. (2011). Test-retest reliability of arterial spin labeling with common labeling strategies. *J. Magnetic Reson. Imaging* 33, 940–949. doi:10.1002/jmri.22345

Clement, P., Castellaro, M., Okell, T., Thomas, D. L., Vandemaele, P., Elgayar, S., et al. (2022). Asl-bids, the brain imaging data structure extension for arterial spin labeling. *Sci. Data* 9, 543. doi:10.1038/s41597-022-01615-9

Clement, P., Mutsaerts, H. J., Václavů, L., Ghariq, E., Pizzini, F. B., Smits, M., et al. (2018). Variability of physiological brain perfusion in healthy subjects - a systematic review of modifiers. considerations for multi-center asl studies. *J. Cereb. Blood Flow Metabolism* 38, 1418–1437. doi:10.1177/0271678X17702156

Cox, R. W. (1996). AFNI: software for analysis and visualization of functional magnetic resonance neuroimages. *Comput. Biomed. Res.* 29, 162–173. doi:10.1006/cbmr.1996.0014

Cox, R. W., Chen, G., Glen, D. R., Reynolds, R. C., and Taylor, P. A. (2017). FMRI clustering in AFNI: false-positive rates redux. *Brain Connect.* 7, 152–171. doi:10.1089/brain.2016.0475

Cox, R. W., and Hyde, J. S. (1997). Software tools for analysis and visualization of fmri data. *NMR Biomed.* 10, 171–178. doi:10.1002/(sici)1099-1492(199706/08)10:4/5<171::aid-nbm453>3.0.co;2-l

Dale, A. M., Fischl, B., and Sereno, M. I. (1999). Cortical surface-based analysis. i. segmentation and surface reconstruction. *Neuroimage* 9, 179–194. doi:10.1006/nimg.1998.0395

Detre, J. A., Leigh, J. S., Williams, D. S., and Koretsky, A. P. (1992). Perfusion imaging. *Magn. Reson Med.* 23, 37–45. doi:10.1002/mrm.1910230106

Detre, J. A., Rao, H., Wang, D. J. J., Chen, Y. F., and Wang, Z. (2012). Applications of arterial spin labeled mri in the brain. *J. Magn. Reson Imaging* 35, 1026–1037. doi:10.1002/jmri.23581

Donahue, M. J., Lu, H., Jones, C. K., Pekar, J. J., and van Zijl, P. C. (2006). An account of the discrepancy between mri and pet cerebral blood flow measures. a high-field mri investigation. *NMR Biomed.* 19, 1043–1054. doi:10.1002/nbm.1075

Feinberg, D. A., Ramanna, S., and Guenther, M. (2009). "Evaluation of new asl 3d grase sequences using parallel imaging, segmented and interleaved k-space at 3T with 12- and 32-channel coils," in Proceedings of the 17Th Annual Meeting of ISMRM, Honolulu, Hawaii, USA. (Honolulu, Hawaii, USA).

Fernández-Seara, M. A., Edlow, B. L., Hoang, A., Wang, J., Feinberg, D. A., and Detre, J. A. (2008). Minimizing acquisition time of arterial spin labeling at 3T. *Magn. Reson Med.* 59, 1467–1471. doi:10.1002/mrm.21633

Fischl, B., Salat, D. H., Busa, E., Albert, M., Dieterich, M., Haselgrove, C., et al. (2002). Whole brain segmentation: automated labeling of neuroanatomical structures in the human brain. *Neuron* 33, 341–355. doi:10.1016/s0896-6273(02)00569-x

Fischl, B., Sereno, M. I., and Dale, A. M. (1999). Cortical surface-based analysis. ii: inflation, flattening, and a surface-based coordinate system. *Neuroimage* 9, 195–207. doi:10.1006/nimg.1998.0396

Fonov, V., Evans, A., McKinstry, R., Almli, C., and Collins, D. (2009). Unbiased nonlinear average age-appropriate brain templates from birth to adulthood. *NeuroImage* 47, S102. doi:10.1016/S1053-8119(09)70884-5

Fonov, V., Evans, A. C., Botteron, K., Almli, C. R., McKinstry, R. C., Collins, D. L., et al. (2011). Unbiased average age-appropriate atlases for pediatric studies. *Neuroimage* 54, 313–327. doi:10.1016/j.neuroimage.2010.07.033

Greve, D. N., and Fischl, B. (2009). Accurate and robust brain image alignment using boundary-based registration. *Neuroimage* 48, 63–72. doi:10.1016/j.neuroimage.2009.06.060

Groves, A. R., Chappell, M. A., and Woolrich, M. W. (2009). Combined spatial and non-spatial prior for inference on mri time-series. *Neuroimage* 45, 795–809. doi:10.1016/j.neuroimage.2008.12.027

Hernandez-Garcia, L., Aramendia-Vidaurreta, V., Bolar, D. S., Dai, W., Fernández-Seara, M. A., Guo, J., et al. (2022). Recent technical developments in ASL: a review of the state of the art. *Magnetic Reson. Med.* 88, 2021–2042. doi:10.1002/mrm.29381

Hoopes, A., Mora, J. S., Dalca, A. V., Fischl, B., and Hoffmann, M. (2022). Synthstrip: skull-stripping for any brain image. *NeuroImage* 260, 119474. doi:10.1016/j.neuroimage.2022.119474

Iutaka, T., de Freitas, M. B., Omar, S. S., Scortegagna, F. A., Nael, K., Nunes, R. H., et al. (2023). Arterial spin labeling: techniques, clinical applications, and interpretation. *RadioGraphics* 43, e220088. doi:10.1148/rg.220088

Ivanov, D., Kashyap, S., Haast, R. A., Janssens, S., Huber, L., Poser, B. A., et al. (2018). "Whole-brain sub-millimeter isotropic resolution cerebral blood flow map in humans," in Proceedings of the Annual Meeting of the International Society for Magnetic Resonance in Medicine (ISMRM), Paris, France, 2301.

Ivanov, D., Pfeuffer, J., Gardumi, A., Uludağ, K., and Poser, B. A. a. (2017). "2d caipirinha improves accelerated 3d grase asl," in Proceedings of the Annual Meeting of the International Society for Magnetic Resonance in Medicine (ISMRM), Honolulu, USA, 3630.

Kashyap, S., Ivanov, D., Haast, R. A. M., Fritz, F. J., Harms, R. L., Huber, L., et al. (2022). "The impact of optimal RF coil combination on whole-brain sub-millimetre resolution perfusion imaging at 7T," in Proceedings of the Annual Meeting of the International Society for Magnetic Resonance in Medicine (ISMRM), London, UK, 1145.

Kashyap, S., Ivanov, D., Havlicek, M., Huber, L., Poser, B. A., and Uludağ, K. (2021). Sub-millimetre resolution laminar fMRI using arterial spin labelling in humans at 7 T. *PLOS ONE* 16, e0250504. doi:10.1371/journal.pone.0250504

Kim, S.-G. (1995). Quantification of relative cerebral blood flow change by flow-sensitive alternating inversion recovery (FAIR) technique: application to functional mapping. *Magnetic Reson. Med.* 34, 293–301. doi:10.1002/mrm.1910340303

Kirk, T., McConnell, F. K., Ivanov, D., Kashyap, S., Craig, M., and Chappell, M. (2020a). "Partial volume effect correction of arterial spin labelling data using surface segmentations," in Proceedings of the Annual Meeting of the International Society for Magnetic Resonance in Medicine (ISMRM) (Virtual), 3292.

Kirk, T. F., Coalson, T. S., Craig, M. S., and Chappell, M. A. (2020b). Toblerone: surface-based partial volume estimation. *IEEE Trans. Med. Imaging* 39, 1501–1510. doi:10.1109/TMI.2019.2951080

Liang, X., Connelly, A., Tournier, J.-D., and Calamante, F. (2014). A variable flip angle-based method for reducing blurring in 3d grase asl. *Phys. Med. Biol.* 59, 5559–5573. doi:10.1088/0031-9155/59/18/5559

Lindner, T., Bolar, D. S., Achten, E., Barkhof, F., Bastos-Leite, A. J., Detre, J. A., et al. (2023). Current state and guidance on arterial spin labeling perfusion mri in clinical neuroimaging. *Magnetic Reson. Med.* 89, 2024–2047. doi:10.1002/mrm.29572

Luh, W.-M., Wong, E. C., Bandettini, P. A., and Hyde, J. S. (1999). QUIPSS II with thin-slice TI1 periodic saturation: a method for improving accuracy of quantitative perfusion imaging using pulsed arterial spin labeling. *Magnetic Reson. Med.* 41, 1246–1254. doi:10.1002/(sici)1522-2594(199906)41:6<1246::aid-mrm22>3.0.co;2-n

Marques, J. P., Kober, T., Krueger, G., van der Zwaag, W., Van de Moortele, P.-F., and Gruetter, R. (2010). Mp2rage, a self bias-field corrected sequence for improved segmentation and t1-mapping at high field. *Neuroimage* 49, 1271–1281. doi:10.1016/j.neuroimage.2009.10.002

Mora Álvarez, M. G., Stobbe, R. W., and Beaulieu, C. (2019). High resolution continuous arterial spin labeling of human cerebral perfusion using a separate neck tagging RF coil. *PLoS ONE* 14, e0215998. doi:10.1371/journal.pone.0215998

Paschoal, A. M., Leoni, R. F., Pastorello, B. F., and van Osch, M. J. P. (2021). Three-dimensional gradient and spin-echo readout for time-encoded pseudo-continuous arterial spin labeling: influence of segmentation factor and flow compensation. *Magnetic Reson. Med.* 86, 1454–1462. doi:10.1002/mrm.28807

Poser, B. A., Koopmans, P. J., Witzel, T., Wald, L. L., and Barth, M. (2010). Three-dimensional echo-planar imaging at 7 tesla. *NeuroImage* 51, 261–266. doi:10.1016/j.neuroimage.2010.01.108

Qin, Q. (2012). Point spread functions of the t2 decay in k-space trajectories with long echo train. *Magn. Reson. Imaging* 30, 1134–1142. doi:10.1016/j.mri.2012.04.017

Smith, S. M., Jenkinson, M., Woolrich, M. W., Beckmann, C. F., Behrens, T. E., Johansen-Berg, H., et al. (2004). Advances in functional and structural mr image analysis and implementation as fsl. *Neuroimage* 23, S208–S219. doi:10.1016/j.neuroimage.2004.07.051

Tan, H., Hoge, W., Hamilton, C., Günther, M., and Kraft, R. (2011). 3d grase propeller: improved image acquisition technique for arterial spin labeling perfusion imaging. *Magnetic Reson. Med.* 66, 168–173. doi:10.1002/mrm.22768

Tisdall, M. D., Hess, A. T., Reuter, M., Meintjes, E. M., Fischl, B., and van der Kouwe, A. J. (2012). Volumetric navigators for prospective motion correction and selective reacquisition in neuroanatomical mri. *Magn. Reson Med.* 68, 389–399. doi:10.1002/mrm.23228

Tisdall, M. D., Reuter, M., Qureshi, A., Buckner, R. L., Fischl, B., and van der Kouwe, A. J. W. (2016). Prospective motion correction with volumetric navigators (vnavs) reduces the bias and variance in brain morphometry induced by subject motion. *Neuroimage* 127, 11–22. doi:10.1016/j.neuroimage.2015.11.054

van der Kouwe, A. J. W., Benner, T., Salat, D. H., and Fischl, B. (2008). Brain morphometry with multiecho mprage. *Neuroimage* 40, 559–569. doi:10.1016/j.neuroimage.2007.12.025

Vidorreta, M., Balteau, E., Wang, Z., De Vita, E., Pastor, M. A., Thomas, D. L., et al. (2014). Evaluation of segmented 3d acquisition schemes for whole-brain high-resolution arterial spin labeling at 3 t. *NMR Biomed.* 27, 1387–1396. doi:10.1002/nbm.3201

Williams, D. S., Detre, J. A., Leigh, J. S., and Koretsky, A. P. (1992). Magnetic resonance imaging of perfusion using spin inversion of arterial water. *Proc. Natl. Acad. Sci. U. S. A.* 89, 212–216. doi:10.1073/pnas.89.1.212

Wong, E. C., Buxton, R. B., and Frank, L. R. (1997). Implementation of quantitative perfusion imaging techniques for functional brain mapping using pulsed arterial spin labeling. *NMR Biomed.* 10, 237–249. doi:10.1002/(sici)1099-1492(199706/08)10:4/5⟨237::aid-nbm475⟩3.0.co;2-x

Wong, E. C., Buxton, R. B., and Frank, L. R. (1998). Quantitative imaging of perfusion using a single subtraction (QUIPSS and QUIPSS II). *Magnetic Reson. Med.* 39, 702–708. doi:10.1002/mrm.1910390506

Wu, W.-C., Fernandez-Seara, M., Detre, J. A., Wehrli, F. W., and Wang, J. (2007). A theoretical and experimental investigation of the tagging efficiency of pseudocontinuous arterial spin labeling. *Magnetic Reson. Med.* 58, 1020–1027. doi:10.1002/mrm.21403

Zhang, Y., Brady, M., and Smith, S. (2001). Segmentation of brain mr images through a hidden markov random field model and the expectation-maximization algorithm. *IEEE Trans. Med. Imaging* 20, 45–57. doi:10.1109/42.906424

Zhao, L., Chang, C.-Y. E., and Alsop, D. C. (2018). Controlling t2 blurring in 3d rare arterial spin labeling acquisition through optimal combination of variable flip angles and k-space filtering. *Magnetic Reson. Med.* 80, 1391–1401. doi:10.1002/mrm.27118

Zuo, Z., Wang, R., Zhuo, Y., Xue, R., Lawrence, K. S. S., and Wang, D. J. J. (2013). Turbo-FLASH based arterial spin labeled perfusion MRI at 7 t. *PLOS ONE* 8, e66612. doi:10.1371/journal.pone.0066612

frontiers | Frontiers in Physiology

TYPE Original Research
PUBLISHED 25 April 2024
DOI 10.3389/fphys.2024.1238533

OPEN ACCESS

EDITED BY
Silvia Capuani,
National Research Council (CNR), Italy

REVIEWED BY
Paul Summers,
European Institute of Oncology (IEO), Italy
Vera Catharina Keil,
VU Medical Center, Netherlands

*CORRESPONDENCE
Vittorio Stumpo,
vittorio.stumpo@usz.ch

RECEIVED 12 June 2023
ACCEPTED 02 April 2024
PUBLISHED 25 April 2024

CITATION
Stumpo V, Sayin ES, Bellomo J, Sobczyk O, van Niftrik CHB, Sebök M, Weller M, Regli L, Kulcsár Z, Pangalu A, Bink A, Duffin J, Mikulis DD, Fisher JA and Fierstra J (2024), Transient deoxyhemoglobin formation as a contrast for perfusion MRI studies in patients with brain tumors: a feasibility study. *Front. Physiol.* 15:1238533. doi: 10.3389/fphys.2024.1238533

Transient deoxyhemoglobin formation as a contrast for perfusion MRI studies in patients with brain tumors: a feasibility study

Vittorio Stumpo[1]*, Ece Su Sayin[2,3], Jacopo Bellomo[1], Olivia Sobczyk[3,4], Christiaan Hendrik Bas van Niftrik[1], Martina Sebök[1], Michael Weller[5], Luca Regli[1], Zsolt Kulcsár[6], Athina Pangalu[6], Andrea Bink[6], James Duffin[2,3], David D. Mikulis[4], Joseph A. Fisher[2,3] and Jorn Fierstra[1]

[1]Department of Neurosurgery, Clinical Neuroscience Center, University Hospital Zurich, University of Zurich, Zurich, Switzerland, [2]Department of Physiology, University of Toronto, Toronto, ON, Canada, [3]Joint Department of Medical Imaging and the Functional Neuroimaging Lab, University Health Network, Toronto, ON, Canada, [4]Department of Anesthesia and Pain Management, University Health Network, University of Toronto, Toronto, ON, Canada, [5]Department of Neurology, Clinical Neuroscience Center, University Hospital Zurich, University of Zurich, Zurich, Switzerland, [6]Department of Neuroradiology, Clinical Neuroscience Center, University Hospital Zurich, University of Zurich, Zurich, Switzerland

Background: Transient hypoxia-induced deoxyhemoglobin (dOHb) has recently been shown to represent a comparable contrast to gadolinium-based contrast agents for generating resting perfusion measures in healthy subjects. Here, we investigate the feasibility of translating this non-invasive approach to patients with brain tumors.

Methods: A computer-controlled gas blender was used to induce transient precise isocapnic lung hypoxia and thereby transient arterial dOHb during echo-planar-imaging acquisition in a cohort of patients with different types of brain tumors (n = 9). We calculated relative cerebral blood volume (rCBV), cerebral blood flow (rCBF), and mean transit time (MTT) using a standard model-based analysis. The transient hypoxia induced-dOHb MRI perfusion maps were compared to available clinical DSC-MRI.

Results: Transient hypoxia induced-dOHb based maps of resting perfusion displayed perfusion patterns consistent with underlying tumor histology and showed high spatial coherence to gadolinium-based DSC MR perfusion maps.

Conclusion: Non-invasive transient hypoxia induced-dOHb was well-tolerated in patients with different types of brain tumors, and the generated rCBV, rCBF and MTT maps appear in good agreement with perfusion maps generated with gadolinium-based DSC MR perfusion.

KEYWORDS

MR perfusion, deoxyhemoglobin, brain tumor, glioblastoma, advanced imaging

Introduction

Magnetic resonance imaging (MRI) perfusion plays an important role in the diagnostic work-up and ongoing surveillance of patients with brain tumors. Dynamic susceptibility contrast (DSC) perfusion MRI traces the passage of a bolus of contrast through the cerebral vasculature. Most commonly, the systemic injection of gadolinium-based contrast agents (GBCA) is used to acquire resting perfusion measures, such as cerebral blood volume (CBV), cerebral blood flow (CBF) and mean transit time (MTT). This can either be obtained in an absolute fashion, with the use of an arterial input function (AIF), or more commonly relatively to healthy tissue (e.g., contralateral white matter) (Boxerman et al., 2020). DSC perfusion imaging exploits the volume diffusion theory, whereby the injected bolus of contrast agent causes a transient signal drop on spin echo and gradient echo planar imaging and this can be used to infer time dependent changes in tissue concentration of contrast agent, which is relatable to tissue perfusion (Calamante, 2013). Within this theorem, the paramagnetic properties of deoxyhemoglobin (dOHb) have recently been explored as an endogenous contrast agent (Poublanc et al., 2021; Vu et al., 2021). In fact, a bolus of dOHb acts as susceptibility contrast, generating similar rCBV, rCBF, MTT perfusion maps to those obtained with GBCA in healthy subjects and in patients with cerebrovascular steno-occlusive disease (Poublanc et al., 2021; Vu et al., 2021; Sayin et al., 2022; Sayin et al., 2023a). This is obtained, as previously demonstrated, by means of a gas blender with a sequential gas delivery breathing circuit to implement rapid "bolus-like" changes in the partial pressure of oxygen of the arterial blood (Slessarev et al., 2007; Poublanc et al., 2021; Sayin et al., 2022). The viability of this technique presents potential advantages such as avoidance of an exogenous gadolinium-based contrast agent, with its connected drawbacks, in a patient population requiring serial longitudinal imaging follow-up. For this reason, after promising reports in healthy subjects and in patients with cerebrovascular steno-occlusive disease, in the present study we sought to investigate the feasibility of using transient hypoxia-induced dOHb as a contrast agent for perfusion imaging in a patient cohort with different types of brain tumors.

Methods

The study was approved by the ethics board of the Canton of Zurich, Switzerland (research protocol KEK-ZH-No.2020-02314) and all participants provided informed consent prior to inclusion into the study. For this feasibility study, in the period from March to October 2022, subjects admitted at the Department of Neurosurgery of the University Hospital Zurich, Switzerland, with a newly diagnosed brain tumor planned for surgical resection, irrespectively of suspected tumor histology, were prospectively included to undergo a transient hypoxia induced-dOHb imaging study with a standardized breathing protocol before the intervention. At inclusion, the patients were also offered a follow-up scan. Exclusion criteria were as follows: presence of known severe cardiopulmonary disease, i.e., (severe heart insufficiency, pulmonary diffusion impairment disease, severe COPD or severe asthma), standard MRI contraindications including allergy to GBCA, pregnancy, glaucoma, metallic tattoo dyes, severe renal insufficiency and metallic prosthesis, age < 18 years, inability or refusal to sign informed consent.

MRI protocol

Patients were scanned on a 3 T Skyra VE11 (Siemens, Erlangen, Germany) scanner with a 32-channel head coil. An axial 2D T2*-weighted gradient echoplanar sequence (50 slices with interleaved acquisition) planned on the ACPC line plus 20° anticlockwise on a sagittal image was used to acquire the BOLD data, with voxel size 2.5 × 2.5 × 2.5 mm^3, repetition time (TR)/TE 1800/30 m, flip angle 80°, bandwidth 2168 Hz/Px, field of view (FOV) 220 × 220 mm^2. During the echo-planar imaging (EPI) sequence acquisition, 160 volumes were acquired corresponding to a duration of circa 5 minutes. Acquisition parameters of T1-CE, FLAIR, T2 as per standard brain tumor protocol have been described in previously published article (Stumpo et al., 2021). For a subgroup of patients, clinical-diagnostic work-up required execution of a gadolinium (Dotarem) enhanced DSC-MRI GRE-EPI, FOV 100 × 100 mm^2, resolution 128 × 128, TR/TE 2040/36, FA 90°.

Respiratory protocol

A custom-built computer controlled gas blender (RepirAct™ Gen 4, Thornhill Medical, Toronto, Canada) was used to precisely control partial pressure of end-tidal O_2 ($P_{ET}O_2$) and CO_2 ($P_{ET}CO_2$) with the prospective gas targeting algorithm based on (Slessarev et al., 2007). BOLD signal changes were induced by a rapid double hypoxic stimulus as previously proposed by and Sayin et al. (Poublanc et al., 2021; Sayin et al., 2022; Sayin et al., 2023a) The programmed $P_{ET}O_2$ stimulus pattern was 4-min and 20 s long and consisted of a 60 s baseline $P_{ET}O_2$ of 95 mmHg (normoxia), a step decrease in $P_{ET}O_2$ to 40 mmHg (hypoxia) for 60 s, a return to normoxia for 20–40 s, a second step decrease in $P_{ET}O_2$ to 40 mmHg for 60 s, followed by a return to normoxia for 40-60 s (see also Figure 1).

Processing of BOLD and T1-weighted volumes

The acquired transient hypoxia induced-dOHb images were first slice-time corrected and volume re-registered for motion correction within the time-series. Next the BOLD images were realigned to their respective axial anatomical T1-weighted images using Analysis of Functional Neuroimaging (AFNI) software Version 22.0.04'Hadrian'. (National Institutes of Health, Bethesda, Maryland) (Cox, 1996; Cox and Hyde, 1997). Using Statistical Parameter Mapping (SPM 12, Wellcome Trust Centre for Neuroimaging, Institute of Neurology, University College London; http://www.fil.ion.ucl.ac.uk/spm), automated segmentation of the T1-weighted image yielded grey and white matter, cerebrospinal fluid, skull and skin probability maps. T2, FLAIR, and T1-CE volumes were co-registered and resliced to the high-resolution T1 image acquired in the same session as the BOLD.

Calculation of resting perfusion maps

For quality control, we calculated the goodness of fit (Rsquared) of the percentage BOLD signal change and the $P_{ET}O_2$ time series was

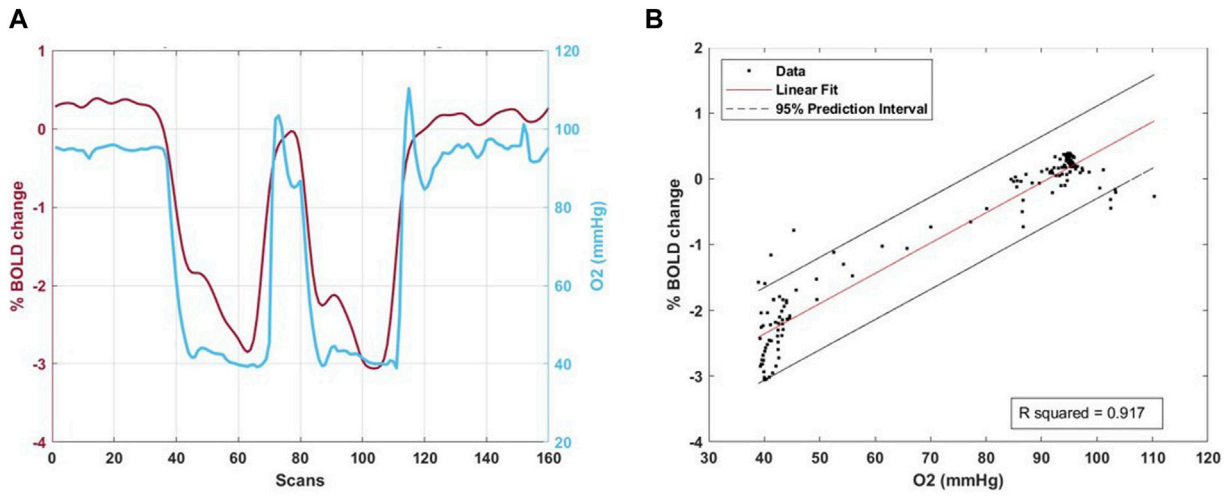

FIGURE 1
Right panel **(A)**. The percentage mean BOLD signal change in the combined grey and white matter mask plus the combined whole lesion including contrast-enhancement, necrosis and edema is shown in one patient during the hypoxic respiratory protocol. After 60 s at 95 mmHg PETO2 two hypoxic stimuli at 40 mmHg PETO2 lasting 60 s each with 20–40 s return to normoxia in between could be induced with optimal results (blue line). The corresponding percentage BOLD signal change during gas manipulation is shown (dark red line). Left Panel **(B)** shows the relative linear fit plot.

TABLE 1 Study population.

Identifier	Age	Sex	Tumor	Side	Location	Tumor volume (mL)	Edema volume (mL)	Gad-DSC
1	77	M	Lung adenocarcinoma metastasis	L	Frontal	11.1	10.7	No
2	58	M	Glioblastoma	L	Frontobasal	41.3	25.9	Yes
3	59	M	Astrocytoma PXA G3	R	Mediobasal	64.0	49.1	No
4a	60	F	Glioblastoma	L	Multifocal (precuneus, cuneus)	17.9	10.2	Yes
4b	-	-	-	-	-	-	-	Yes
5	51	F	Oligodendroglioma G3	R	Frontobasal	82.6	50.1	No
6	57	M	Glioblastoma	L	Superior temporal gyrus	18.6	12.8	No
7	29	F	Astrocytoma G2	R	Middle temporal gyrus			Yes
8	41	M	Meningioma	L	Falx	42.7	41.9	No
9	72	M	Glioblastoma	L	Temporopolar	63.2	47.0	Yes

Abbreviations. F, female; G, grade; Gad, gadolinium; L, left; M, male; mL, milliliter; PXA, pleomorphic xanthoastrocytoma; R, right; DSC, dynamic susceptibility contrast.

regressed using a linear least square fitting to the BOLD time series on a voxel-per-voxel basis.

Perfusion measures using transient hypoxia induced-dOHb were calculated with a conventional analysis using an arterial input function (AIF) chosen over the middle cerebral artery and a deconvolution-based model as previously described by (Poublanc et al., 2021). First, an AIF was chosen over a voxel in the middle cerebral artery. The signal was smoothed voxel-wise using an adaptive mean filtering of width 7 mm. The tracer kinetics relationship was applied in the signal domain and rCBV and MTT metrics were determined using a least square fitting procedure, with MTT bound between 1 and 8 s. The model uses a mono-exponential residue function. Using the central volume theorem, rCBF was then calculated as rCBF = rCBV/MTT (Østergaard, 2005) and scaled by 30 arbitrary units (a.u.).

Automatic segmentation and region-of-interest (ROI) determination

Region of interest masks (contrast enhancement, necrosis and edema) were automatically segmented using Oncohabitats Software (Juan-Albarracín et al., 2018) for glioblastomas and manually segmented for the other tumor types. Automatically segmented tumor region-of-interest were visually inspected for accuracy and required no subsequent manual correction.

TABLE 2 Transient hypoxia induced-dOHb perfusion measures in Gray Matter, White Matter, Contrast-Enhancement, Flipped Contrast-Enhancement, Edema, Flipped Edema of included patients.

	GM			WM			CE			Flipped CE			Edema			Flipped edema		
	MTT	CBV	CBF	MTT	CBV	CBF	MTT	CBV	CBF	MTT	CBV	CBF	MTT	CBV	CBF	MTT	CBV	CBF
Identifier																		
1	2.7	2.0	45.6	3.2	1.8	35.0	3.6	2.4	67.3	5.4	1.0	15.7	5.9	1.6	24.0	6.9	1.3	13.5
2	3.7	4.4	59.8	3.9	4.3	59.2	3.8	5.2	71.2	3.8	3.2	55.1	2.6	4.0	69.9	3.6	3.7	74.0
4a	4.2	5.2	61.6	4.9	4.1	46.8	4.8	7.8	94.1	6.5	4.3	42.2	4.7	4.6	46.6	5.4	4.3	42.5
5	3.8	4.3	55.5	4.4	3.0	39.3	5.0	12.7	122.6	5.2	6.4	63.7	4.8	9.0	93.3	5.1	10.5	108.4
6	5.6	1.7	16.3	6.2	1.3	14.1	5.2	4.9	49.2	5.9	3.5	29.8	5.7	1.7	14.8	5.9	1.8	17.3
7*	3.1	2.6	46.2	3.9	2.0	34.4	-	-	-	-	-	-	-	-	-	-	-	-
8	1.9	2.2	95.2	2.0	2.0	83.1	1.6	4.5	210.2	2.3	1.6	61.9	1.4	2.6	132.9	1.3	1.4	74.4
9	2.7	1.1	30.2	2.9	1.0	29.2	3.4	1.4	34.6	3.8	0.9	23.3	2.6	1.1	32.6	2.9	1.0	32.1
Mean (SD)	3.5 (1.1)	2.9 (1.4)	51.3 (21.9)	3.9 (1.2)	2.4 (1.2)	42.6 (19.6)	4.0 (1.2)	5.3 (3.6)	90.7 (56.7)	4.6 (1.3)	2.7 (1.9)	39.5 (20.0)	3.7 (1.5)	3.6 (2.5)	63.8 (35.5)	4.1 (4.1)	3.5 (3.1)	57.3 (29.2)
Min-Max	1.9–3.8	1.1–5.2	16.3–95.2	2.0–6.2	1.0–4.3	14.1–83.1	1.6–5.2	1.4–12.7	34.6–210.2	2.3–6.5	0.9–6.4	15.7–63.7	1.4–5.9	1.1–4.6	14.8–93.3	1.3–6.9	1.0–10.5	13.5–108.4

Abbreviations. CBF, cerebral blood flow; CBV, cerebral blood volume; Max, maximum; Min, minimum; MTT, mean transit time; SD, standard deviation.

10.3389/fphys.2024.1238533

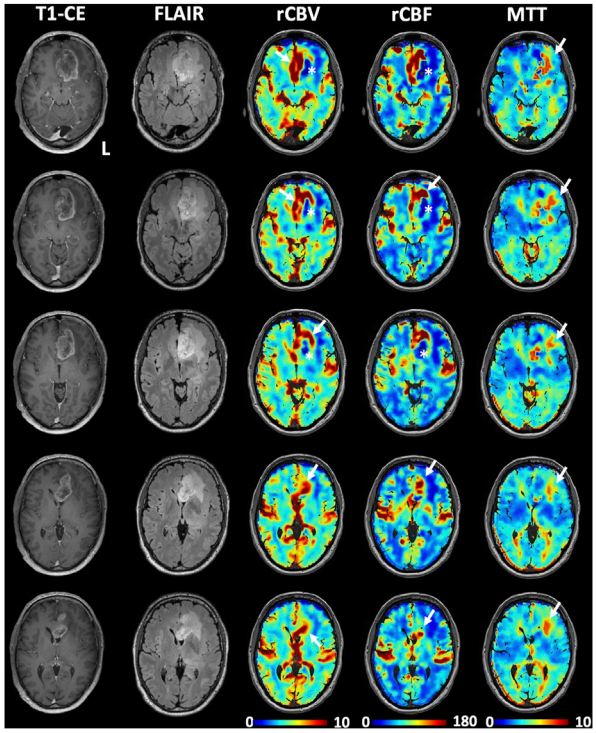

FIGURE 2
Illustrative perfusion maps obtained with the transient hypoxia induced-dOHb protocol during BOLD-MRI acquisition in a patient with left frontal glioblastoma. High perfusion, as represented by increased CBV and CBF, can be observed in correspondence of the contrast-enhancing lesion (white arrows), while decreased rCBV and rCBF can be observed in the central necrotic area (white asterisks) as well as the in the FLAIR hyperintensity typical of perilesional edema. Note that only a partial correspondence of increased perfusion is observed at the posterolateral margin of the contrast-enhancing lesion. High MTT values can be observed mostly in the perilesional edema (white arrows in the MTT maps).

Calculation of perfusion measures in ROIs

MRI volumes were analyzed using MATLAB 2019 (The MathWorks, Inc., Natick, United States). rCBV, rCBF and MTT values were calculated in the grey and white matter after masking out the whole tumor (including edema) and for each of the aforementioned tumor ROIs. Two additional ROI were defined: tumor, i.e., contrast-enhancement + necrosis and whole lesion, including surrounding edema; and the corresponding volumes in the contralateral hemisphere identified using proprietary Matlab programme. Perfusion metrics were overlayed onto their respective anatomical images using SPM software and qualitatively compared to the co-registered T1CE and FLAIR to identify perfusion patterns in tumor ROIs (contrast enhancement, edema, necrosis).

DSC-MRI analysis

In a subgroup of patients, a DSC-MRI was acquired during clinical workup for diagnostic purposes. The acquired sequences were analyzed (including leakage correction) using Olea Software version 3.0 to calculate rCBV, rCBF, MTT maps. The perfusion maps were exported, co-registered and resliced to the high-resolution T1 anatomical images and qualitatively compared with the resting perfusion measures obtained with transient hypoxia induced-dOHb. Average rCBV, rCBF and MTT were calculated in the same above-mentioned ROI and contralateral flipped masks and compared with transient hypoxia induced-dOHb estimated values.

Results

Study population

Eleven patients provided informed consent for participation in the study. Of these, nine patients completed the imaging protocol and were included in the final study population, reasons of dropout of the two excluded patients being in one patient interruption of study due to dyspnea during the respiratory protocol, in the other discomfort and claustrophobia during MRI acquisition. One patient underwent the imaging protocol twice, the second being after tumor resection. Mean age was 56 (SD 13.8; 3 female subjects). The baseline characteristics are provided in Table 1.

The study population included patients with different types of brain tumors: 1 metastasis, 1 meningioma, 1 astrocytoma WHO grade 2, 1 pleomorphic xanthoastrocytoma WHO grade 3, 1 oligodendroglioma WHO grade 3, 4 glioblastomas (1 patient was also scanned post-operatively). The histopathological diagnosis was based on the 2021 WHO classification (Louis et al., 2021). Patient 3 was excluded from the following analysis due to excessively noisy BOLD signal, caused by suboptimal stimulus during the examination. Four of the included patients received during diagnostic work-up a standard gadolinium perfusion MRI, with one of them receiving it at another center before referral.

An illustrative BOLD signal change and linear fit plot is shown in Figure 1 and is reported for each patient in Supplementary Figure S1.

Resting transient hypoxia induced-dOHb resting perfusion measures

Transient hypoxia induced-dOHb resting perfusion measures in the abovementioned regions-of-interest were calculated for each patient as previously reported (Poublanc et al., 2021). The relative measurements are reported in Table 2.

Qualitative visual analysis

Figure 2 shows an illustrative case, i.e., patient 2, 58 y. o. male with a left frontobasal glioblastoma. The perfusion maps show high CBV, CBF in the contrast-enhanced lesion regions, while these metrics are very low in the central necrotic area with high agreement with the morphological high-resolution sequences. MTT is mostly increased in peritumoral edematous tissue. Figure 3 displays perfusion patterns in different tumor types. Qualitative image analysis shows perfusion to be higher in grey matter than in white matter and increased CBV and CBF were observed in contrast-

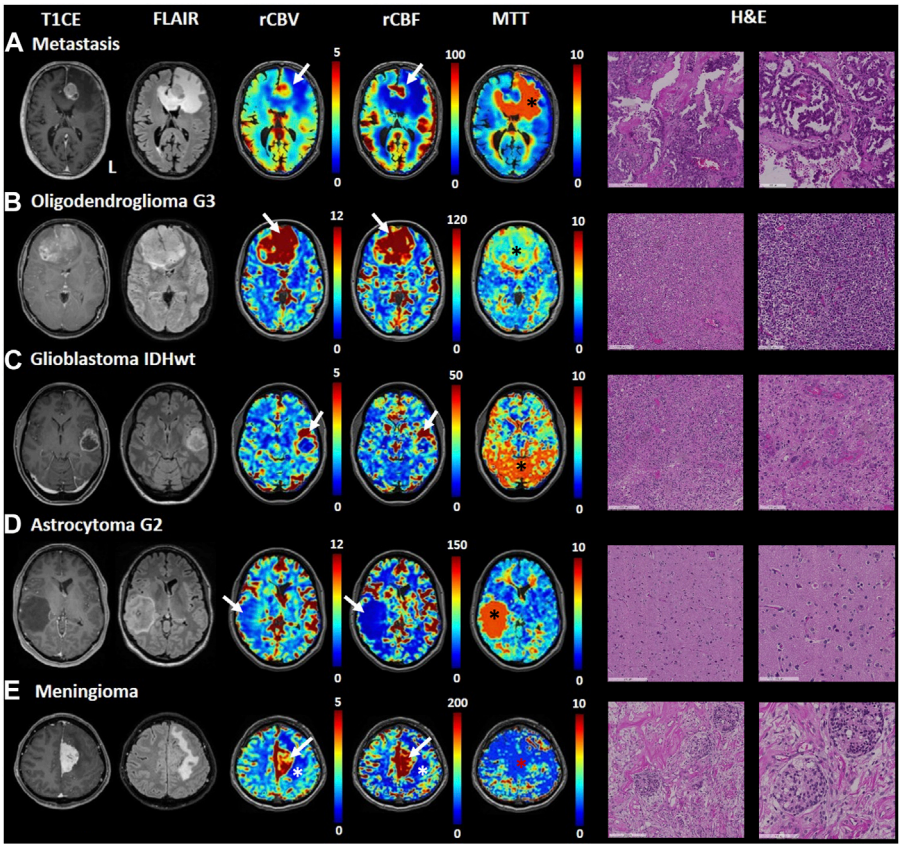

FIGURE 3
Transient hypoxia induced-dOHb MRI perfusion patterns in some common brain tumors. T1-CE, T2-FLAIR, rCBV, rCBF and MTT transient hypoxia induced-dOHb MRI perfusion maps and H&E sections are displayed for each tumor type included. **(A)**. Patient with a left frontal lung adenocarcinoma metastasis. Around the contrast-enhancing lesion, displaying high CBV and CBF (white arrow) can be appreciated an extensive perilesional edema (FLAIR hyperintensity, low CBV and CBF, high MTT - black asterisk). **(B)**. Patient with frontobasal oligodendroglioma grade 3, displaying strongly increased CBV and CBF (white arrows) as well as moderately increased MTT (black asterisk). **(C)**. Patient with left superior temporal gyrus glioblastoma. The contrast-enhancing lesion (high CBV and CBF, white arrows) surrounding a central necrotic area can be appreciated. The MTT map shows spot-like increased values, particularly evident in the posterior circulation (black asterisk) which we speculate could be attributed to noisier signal/suboptimal stimulus, **(D)**. Patient with right middle temporal gyrus astrocytoma grade 2. The lesion does not show contrast uptake, is hyperintense in FLAIR sequence and displays lower perfusion than healthy parenchyma (low CBV and CBF shown by white arrow) as well as strongly increased mean transit time (black asterisk). **(E)**. Patient with a left-sided falx meningioma. FLAIR sequence shows hyperintense edema around the contrast-enhancing lesion (note increased CBV and CBF as pointed by white arrows). The MTT map shows no increased mean transit time in the lesion (red asterisk).

enhancing lesion of metastases (Figure 3A), oligodendroglioma WHO grade 3 (Figure 3B), glioblastoma (Figure 3C) and meningioma (Figure 3E) with respect to healthy tissue. On the contrary, lower CBV and CBF were observed in the astrocytoma WHO grade 2 (Figure 3D). MTT was shown to be higher in areas of edema identified by T2 FLAIR (Figures 3A, B) as well as in the astrocytoma WHO grade 2 dense cellular tissue (Figure 3D).

Comparison of transient hypoxia induced-dOHb BOLD and DSC-MRI

In the three patients who underwent a pre-operative DSC-MRI in our institution, this was compared with the transient hypoxia induced-dOHb perfusion maps for visual qualitative examination and rCBV, rCBF and MTT were calculated in each of the two techniques. The transient hypoxia induced-dOHb BOLD perfusion and corresponding gadolinium DSC-MRI are shown for three patients (2 glioblastomas and 1 astrocytoma WHO grade 2) in Figure 4. The values of rCBV, rCBF, MTT obtained by gadolinium-based DSC-MRI and analyzed with Olea-Software were compared to the transient hypoxia induced-dOHb estimated values in grey matter, white matter, identified tumor ROIs and flipped masks (Figure 5). In particular, the plots show congruent measurements in the different ROIs and contralateral flipped masks between the two techniques with similar trends.

Based on the availability of 2 transient hypoxia induced-dOHb perfusion scans for patient 4, a multifocal glioblastoma with lesions in left cuneus and precuneus, follow-up imaging from pre-to post-operative is shown and compared with gadolinium DSC (Figure 6). Transient hypoxia induced-dOHb BOLD perfusion maps display good spatial agreement with gadolinium-based DSC perfusion also in the longitudinal follow-up of a glioblastoma patient.

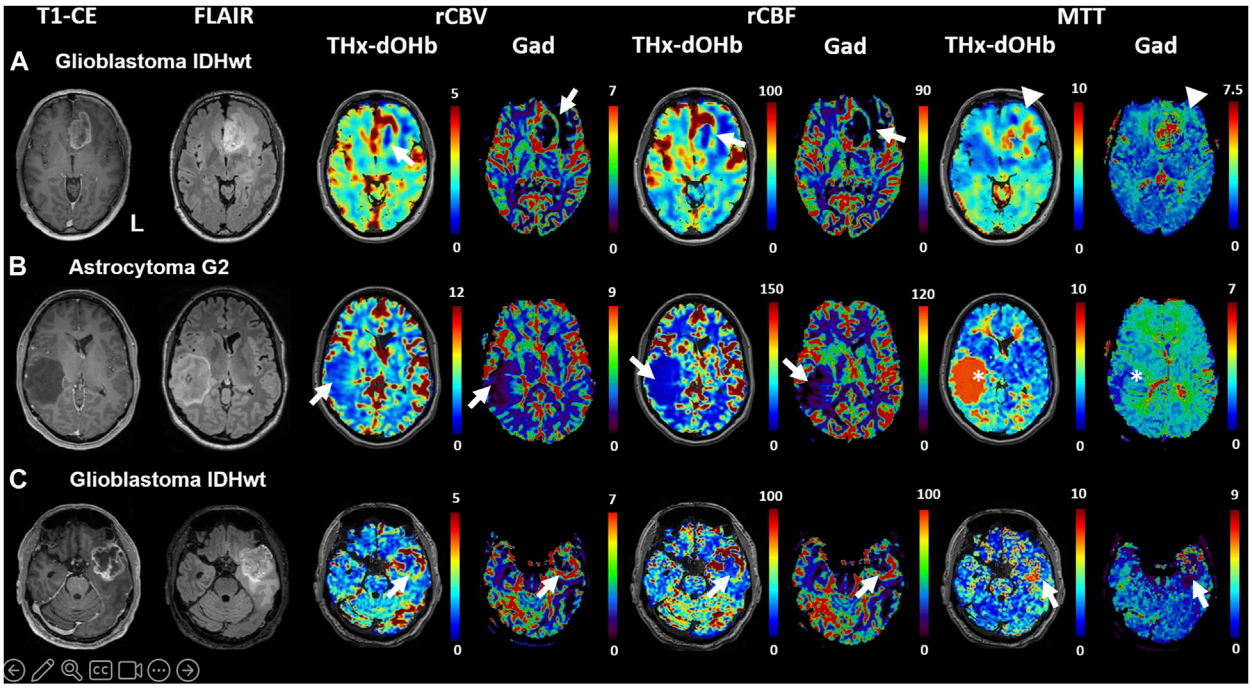

FIGURE 4
Comparison of transient hypoxia induced-dOHb perfusion maps with DSC-Gad MRI perfusion maps in three illustrative patients with diffuse cerebral glioma. T1-CE, T2-FLAIR, rCBV, rCBF and MTT obtained with transient hypoxia induced-dOHb and standard gadolinium MRI perfusion maps are displayed for three patients with cerebral diffuse glioma. **(A)**. Patient 2, left frontobasal glioblastoma. **(B)**. Patient 7, right middle temporal gyrus astrocytoma G2. **(C)**. Patient 9, left temporopolar glioblastoma. Arrowheads pointing at relevant tumor areas to facilitate comparison between transient hypoxia induced-dOHb and gadolinium perfusion. Note: There is excellent congruence between Gd and d-OHb maps except for patient B, where tumor MTT values are much higher in the transient hypoxia induced-dOHb perfusion maps as compared to the gadolinium perfusion (asterisk). The reason for this is uncertain but the finding could point to higher sensitivity of the dOHb method to MTT abnormalities.

Discussion

Summary of study findings

Our preliminary study shows good feasibility of transient controlled hemoglobin desaturation by means of a standardized hypoxic stimulus to obtain resting perfusion parameters in a population of patients with brain tumor. At the single patient level, we found the calculated transient hypoxia induced-dOHb perfusion maps to be in good agreement with intrinsic tumor characteristics that would be expected in a GBCA perfusion, i.e., increased CBV and CBF in highly perfused tumors such as brain metastasis, glioblastomas, oligodendroglioma and meningioma compared to healthy tissue; decreased CBV, CBF in astrocytoma grade 2 as well as increased MTT in edematous or dense cellular tissue. For the subgroup of patients for whom a DSC-MRI was available, the relative ROI-level patterns estimated using transient hypoxia induced-dOHb well reflect the measurement obtained in standard gadolinium perfusion. Moreover, the longitudinal assessment in one patient shows good qualitative agreement with the relative DSC-MRI. The investigated technique, which exploits the BOLD-related drop in MRI signal induced by a bolus of paramagnetic deoxyhemoglobin as a possible alternative for gadolinium contrast, has been recently introduced in seminal publications by (Vu et al., 2021; Poublanc et al., 2021; Sayin et al., 2022) in healthy subjects as well as in patients with steno-occlusive cerebrovascular disease (Sayin et al., 2023a).

Perfusion MRI in brain tumor assessment–"status quo"

Perfusion assessment is clinically relevant in brain tumor diagnosis and follow-up, as increased perfusion correlates with tumor's aggressiveness and can be used in the differential diagnosis of cerebral lesions as well as to distinguish post-treatment changes from tumor recurrence/progression (Guida et al., 2022; Stumpo et al., 2022). However, in a proportion of brain tumors the blood brain barrier is either disrupted or dysfunctional (e.g., glioblastomas, metastasis) (Arvanitis et al., 2020; Guan et al., 2021), making contrast leakage in the extravascular extracellular space a significant confounder to reliable and reproducible measurements (Shiroishi et al., 2015; Leu et al., 2017; Boxerman et al., 2020). For this reason, GBCA perfusion techniques require appropriate correction and rely most commonly on a loading dose of contrast agent administered prior to the acquisition to minimize T1 changes during first pass, and/or on mathematic correction algorithms (Leu et al., 2017; Boxerman et al., 2020).

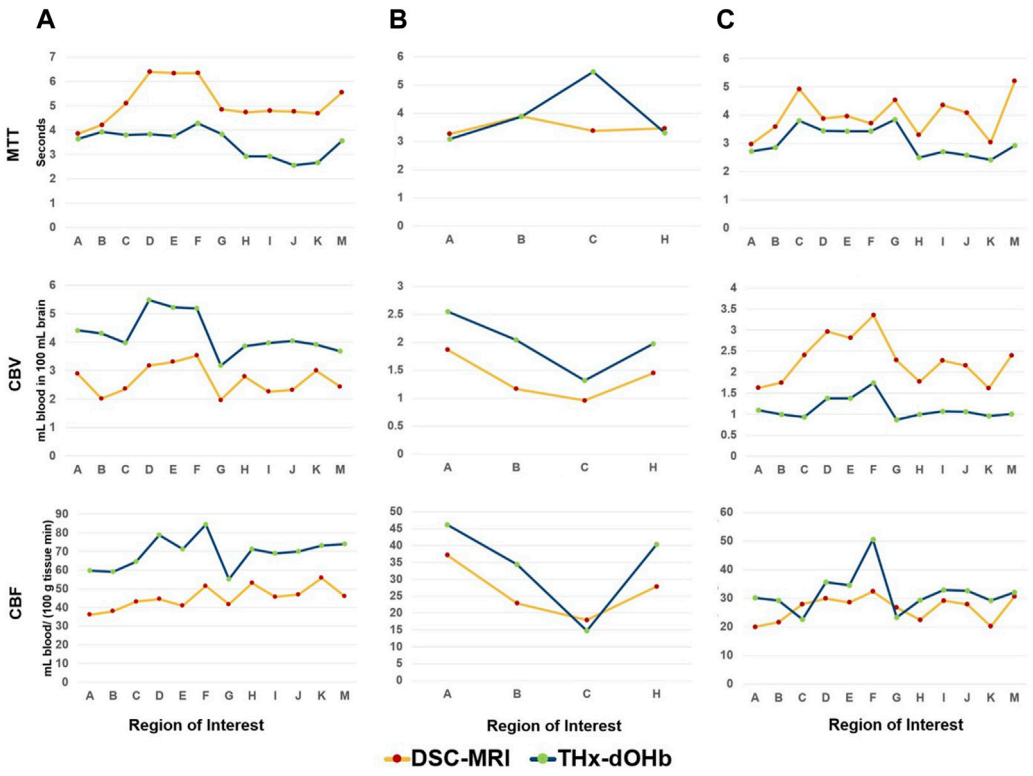

FIGURE 5
Comparison of transient hypoxia induced-dOHb perfusion and DSC-MRI measurements in selected region-of-interest in 3 patients with brain tumor. The measurements of rCBV, rCBF and MTT in grey and white matter, selected tumor ROI and contralateral flipped masks are shown for patients 2 **(A)**, 7 **(B)** and 9 **(C)** for both transient hypoxia induced-dOHb and DSC-MRI. Note that for Patient 7, i.e., middle temporal gyrus astrocytoma grade 2, only four ROIs are shown as in this tumor type no contrast-enhancement, necrosis or perilesional edema could be identified consistent with the radiological presentation of this tumor entity. Legend. **(A)**. Grey Matter, **(B)**. White Matter, **(C)**. Whole Lesion (Contrast-Enhancement + Necrosis + Edema), **(D)**. Tumor Lesion (Contrast-Enhancement + Necrosis), **(E)**. Contrast-Enhancement, **(F)**. Necrosis, **(G)**. Edema, **(H)**. Contralateral Whole Lesion, **(I)**. Contralateral Tumor, **(J)**. Contralateral Contrast-Enhancement, **(K)**, Contralateral Necrosis, **(M)**. Contralateral Edema.

Transient hypoxia induced-dOHb for perfusion assessment: differences from gadolinium perfusion–technical aspects, model and potential

Previous literature has focused on BOLD-contrast for functional MRI and task-based pre-surgical mapping (as neural activation induces changes in regional blood flow) (Glover, 2011; Zacà et al., 2014), or resting-state fMRI for functional architecture inference (Lee et al., 2013; Stoecklein et al., 2020), as well as characterization of cerebrovascular reactivity during vasodilatory stimulus (Fierstra et al., 2013; Fierstra et al., 2016; Fierstra et al., 2018; Fisher et al., 2018; Muscas et al., 2020; Sebök et al., 2020; Sebök et al., 2021). Only recently has the possibility to induce a reproducible and standardized transient bolus of deoxygenated blood (while controlling for competing PCO_2 effects) - in combination with the high temporal resolution of EPI sequence - become focus of attention in the setting of perfusion quantification (Poublanc et al., 2021; Vu et al., 2021; Sayin et al., 2022; Sebök et al., 2023a). BOLD imaging contrast is well suited for this technique as it derives from the different physical properties of hemoglobin in its saturated and desaturated state which result in a diamagnetic *versus* a paramagnetic signal response, respectively (Buxton, 2013; Gauthier and Fan, 2019). Perfusion patterns observed in our study are in agreement to what is reported in the literature for different tumor histologies (Tamrazi et al., 2016; Guida et al., 2022; Stumpo et al., 2022) and display, even if with some spatial differences, remarkably good qualitative agreement with DSC-MRI. To which extent the spatial as well as quantitative differences observed are determined by intrinsic tumor characteristics exhibiting differential response to a contrast medium *versus* an endogenous deoxyhemoglobin bolus remains to be further investigated in future studies. Nevertheless, development and validation of the transient hypoxia induced-dOHb technique for perfusion measurement in patients with brain tumors would present several benefits with respect to gadolinium contrast. We expect that endogenous deoxyhemoglobin, as opposed to GBCA, remains completely intravascular even in cases of BBB leakage. As such it could be even more sensitive to certain vascular properties of some tumors with respect to gadolinium, despite caution need to be taken due to the described magnetic distortion generated by deoxyhemoglobin also in the extravascular space. (Buxton, 2013). The potential advantages of this technique include avoidance of an exogenous contrast agent with its connected drawbacks, i.e., potential of allergic reactions (Gracia Bara et al., 2022), known accumulation of gadolinium in the brain (Gulani et al., 2017), difficult handling in nephropathic patients due to concerns of nephrotoxicity (Weinreb et al., 2021) and a higher repeatability of the scan during treatment follow-up. These benefits are also shared from arterial spin labeling (ASL) MRI, which in recent years has been extensively investigated in the setting of cerebral perfusion assessment and also in patients with brain tumor. Despite promising results, this technique

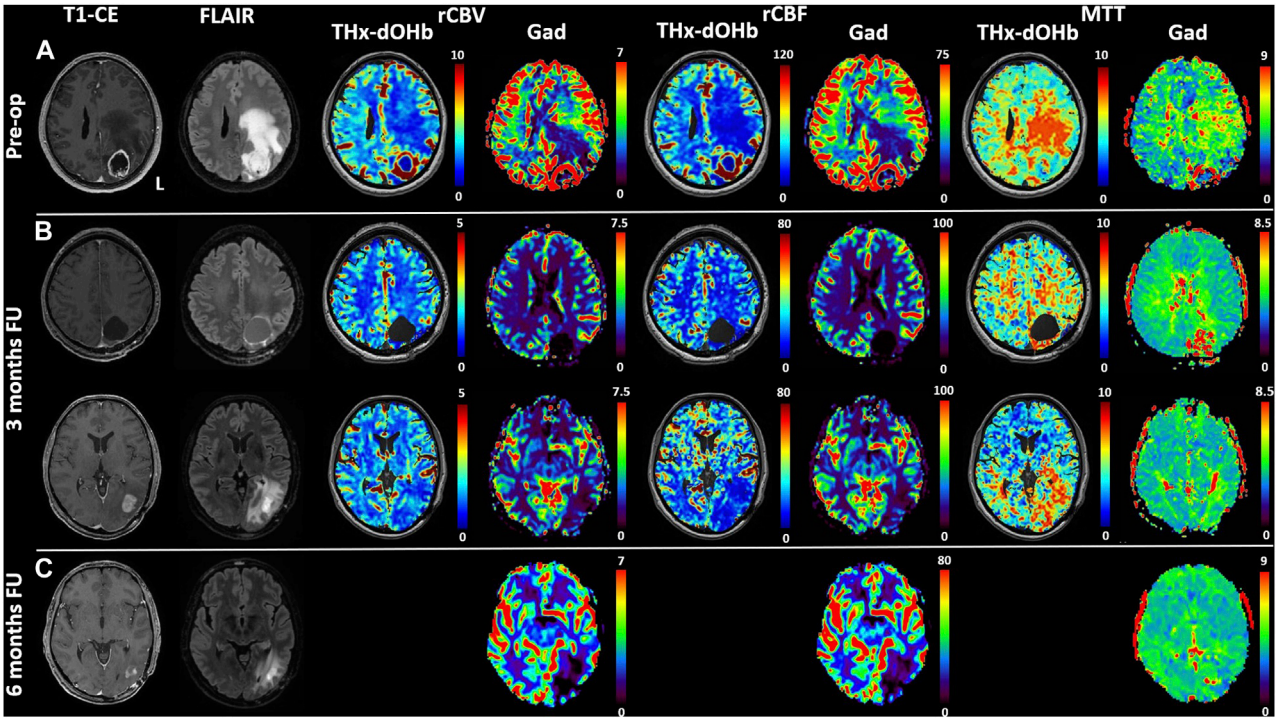

FIGURE 6
Comparison of transient hypoxia induced-dOHb and DSC-Gad MRI perfusion maps in a glioblastoma patient before resection **(A)** and during follow-up at 3 **(B)** and 6 months **(C)**. Baseline and follow-up comparison of transient hypoxia induced-dOHb and gadolinium DSC-MRI perfusion maps in patient with multifocal glioblastoma with lesions in left cuneus and precuneus. Pre-operative T1-CE, FLAIR and transient hypoxia induced-dOHb perfusion as well as corresponding gadolinium DSC-MRI maps **(A)** as well as 3 months **(B)** and 6 months follow-up MRI **(C)**, only DSC-MRI available). The patient was referred to our center after receiving an MRI on prescription from the general practitioner following persistent parietal headaches episodes, vertigo, visual disturbances, memory loss and speech difficulties. The first MRI showed, as depicted in Figure 5, a contrast-enhancing lesion surrounding a central necrotic area in the left precuneus with extensive perilesional edema as well as a smaller contrast-enhancing lesion in the left cuneus. Consistently with known higher perfusion in glioblastomas, both DSC-MRI and transient hypoxia induced-dOHb showed higher rCBV and rCBF in tumor tissue. Gross total resection of the two lesions was performed. Histological analysis confirmed the diagnosis of glioblastoma. As a consequence, after surgery the patient received concomitant radiochemoterapy with temozolomide followed by maintenance chemotherapy as per standard of care (Stupp Protocol). MGMT promoter methylation analysis revealed an unmethylated promoter. At 3 months follow-up, both DSC and transient hypoxia induced-dOHb MRI were repeated. Figure 5 (upper panel) shows the resection cavity with normal perfusion at its margins. The same follow-up MRI showed however an area of contrast enhancement surrounded by FLAIR hyperintensity caudally to the resected tumor. This lesion did not display neither in DSC- nor transient hypoxia induced-dOHb MRI increased perfusion, with the two techniques showing perfusion maps with good qualitative agreement. (Figure 5, lower panel). Another MRI performed at 6 months showed a regression of contrast enhancement and edema. This clinical case shows how transient hypoxia induced-dOHb preliminarily achieved good agreement with gadolinium DSC perfusion also in the follow-up of a glioblastoma patient, warranting further longitudinal validation in the follow-up of treated glioma patients as well as in treated brain metastases.

lagged somewhat behind in the clinical implementation. (Cebeci et al., 2014; Alsop et al., 2015; Haller et al., 2016; Alsaedi et al., 2018).

On the other hand, possible drawbacks include susceptibility artifacts that limit the study of tumors with hemorrhagic component (e.g., melanoma metastasis), reduced contrast to noise ratio and higher predisposition to movement artifacts. Optimization of pre-processing steps (smoothening, etc.) should be also pursued to find the optimal trade-off between decreasing noise and maintaining a fair spatial specificity useful in brain tumor assessment. In order to characterize the relative effect of such confounders, as well as differences and similarities between traditional DSC-MRI *versus* transient hypoxia induced-dOHb, future validation studies should ideally adopt the same acquisition parameters.

Further, blood desaturation for investigation of brain tumor vascularity could exploit analysis technique different than bolus tracking method such as carpet plot analysis (Bhogal et al., 2022) or transfer function analysis (Sayin et al., 2023b), with these having already provided encouraging results in healthy subjects. Moving away from resting perfusion assessment, other approaches may be employed to investigate intrinsic tissue features by dissecting specific BOLD signal changes characteristics during gas control. A preliminary study demonstrated the feasibility of such technique, with a small cohort of glioblastoma patients exhibiting unique tissue response patterns during hypoxic, hyperoxic and hypercapnic stimuli (Stumpo et al., 2021). For this reason, a longitudinal cohort study after optimization of the hypoxic stimulus is currently ongoing. The potential to better characterize tumoral tissue and peritumoral tissue infiltration with such approach relies not only on the observed magnitude of signal change during evoked stimulus, but also the complementary information derived from a refined analysis including other parameters such as goodness-of-fit, contrast-to-noise ratio and temporal lag. In fact, these variables allow further categorization of dynamic functional tissue characteristics that may not be appreciated in static conditions by traditional perfusion analysis. Moreover, advanced data-driven analysis methods such as time-series clustering could also be exploited to identify subgroups of voxels based on stimulus-evoked hemodynamic patterns to correlate with physiological *versus*

pathological vasculature and underlying histological and functional properties of the tissue studied (Baudelet and Gallez, 2003).

Limitations

Our study has several limitations. Despite visual analysis of the calculated maps show high similarity with expected perfusion patterns in different tumors, its qualitative nature as well as the small sample size prevents us from drawing more robust conclusions on the underlying quantitative data. Moreover, at the present stage, while not requiring the injection of a contrast agent, this technique has other drawbacks including longer post-processing times as compared with the clinically available software for DSC-MRI perfusion analysis, higher costs related to gas and masks procurement and, lastly, potential reduced tolerance to the mask and to the hypoxic stimulus may also lead to higher dropout rate in poorly cooperative patients. The time required for the acquisition of the EPI sequence is not significantly longer than the one used in clinical setting for the DSC perfusion. Of note, extensive literature in DSC-gadolinium perfusion MRI described thoroughly confounders of absolute perfusion quantification in brain tumors due to a variety of factors (e.g., flip angle, echo time, temporal resolution, baseline and post-bolus data points, post-processing techniques and leakage correction, etc.) (Boxerman et al., 2020). In this context, the results of our preliminary qualitative analysis warrant future both intra- and inter-subject repeatability assessment. Only 4 patients included in our study received a gadolinium-contrast DSC-MRI to compare transient hypoxia induced-dOHb perfusion and with different acquisition parameters, with one of them receiving it at an external institution. Regardless, qualitative analysis in these 4 patients suggests high concordance of gadolinium perfusion and deoxyhemoglobin-based perfusion with inter-ROI relative measurement showing similar patterns between the two techniques. A validation study in a larger patient population with defined tumor subgroups is currently underway to validate the quantitative measurements obtained by deoxyhemoglobin perfusion against a clinical DSC-MRI gadolinium perfusion.

Conclusion

In this feasibility study, transient and precise hemoglobin desaturation by controlled hypoxic gas modulation is feasible and repeatable in patients with brain tumor. The induced signal change allows for resting brain tissue perfusion measurements, which qualitatively are in good agreement with gadolinium-based perfusion in the study cohort. Based on promising preliminary data, deoxyhemoglobin-based perfusion warrants further quantitative validation against gadolinium in a larger, heterogenous cohort of patients with brain tumor.

Data availability statement

The raw data supporting the conclusions of this article will be made available by the authors upon reasonable request.

Ethics statement

The studies involving humans were approved by Ethics board of the Canton of Zurich, Switzerland (research protocol KEK-ZH-No.2020-02314). The studies were conducted in accordance with the local legislation and institutional requirements. The participants provided their written informed consent to participate in this study.

Author contributions

Conception and Design: VS and JFie. Data Acquisition: VS and JB. Data Analysis: VS, ES, JB, and CHBvN. Manuscript Drafting: VS, JB, ES, and JFie. Critical Review of the Manuscript: OS, CHBvN, MS, MW, LR, ZK, AP, AB, JD, DM, JF and JFie. Study Supervision: JFie.

Funding

Swiss Cancer Research Foundation (KFS-3975-08-2016-R). Vittorio Stumpo is supported by the UZH Candoc Grant FK-23-048.

Conflict of interest

JF and DM contributed to the development of the automated end-tidal targeting device, RespirAct™ (Thornhill Research Inc., TRI) used in this study and have equity in the company. ES, OS, and JD are part time employees of TRI. TRI did not commission, provide support for the study, or review the manuscript. MW has received research grants from Quercis and Versameb, and honoraria for lectures or advisory board participation or consulting from Bayer, Curevac, Medac, Novartis, Novocure, Orbus, Philogen, Roche and Sandoz.

The remaining authors declare that the research was conducted in the absence of any commercial or financial relationships that could be construed as a potential conflict of interest.

Publisher's note

Supplementary material

The Supplementary Material for this article can be found online at: https://www.frontiersin.org/articles/10.3389/fphys.2024.1238533/full#supplementary-material

References

Alsaedi, A., Thomas, D., Bisdas, S., and Golay, X. (2018). Overview and critical appraisal of arterial spin labelling technique in brain perfusion imaging. *Contrast Media and Mol. Imaging* 2018, e5360375. doi:10.1155/2018/5360375

Alsop, D. C., Detre, J. A., Golay, X., Günther, M., Hendrikse, J., Hernandez-Garcia, L., et al. (2015). Recommended implementation of arterial spin-labeled perfusion MRI for clinical applications: a consensus of the ISMRM perfusion study group and the European consortium for ASL in dementia. *Magnetic Reson. Med.* 73, 102–116. doi:10.1002/mrm.25197

Arvanitis, C. D., Ferraro, G. B., and Jain, R. K. (2020). The blood–brain barrier and blood–tumour barrier in brain tumours and metastases. *Nat. Rev. Cancer* 20, 26–41. doi:10.1038/s41568-019-0205-x

Baudelet, C., and Gallez, B. (2003). Cluster analysis of BOLD fMRI time series in tumors to study the heterogeneity of hemodynamic response to treatment. *Magnetic Reson. Med.* 49, 985–990. doi:10.1002/mrm.10468

Bhogal, A. A., Sayin, E. S., Poublanc, J., Duffin, J., Fisher, J. A., Sobczyk, O., et al. (2022). Quantifying cerebral blood arrival times using hypoxia-mediated arterial BOLD contrast. *NeuroImage* 261, 119523. doi:10.1016/j.neuroimage.2022.119523

Boxerman, J. L., Quarles, C. C., Hu, L. S., Erickson, B. J., Gerstner, E. R., Smits, M., et al. (2020). Consensus recommendations for a dynamic susceptibility contrast MRI protocol for use in high-grade gliomas. *Neuro Oncol.* 22, 1262–1275. doi:10.1093/neuonc/noaa141

Buxton, R. B. (2013). The physics of functional magnetic resonance imaging (fMRI). *Rep. Prog. Phys.* 76, 096601. doi:10.1088/0034-4885/76/9/096601

Calamante, F. (2013). Arterial input function in perfusion MRI: a comprehensive review. *Prog. Nucl. Magnetic Reson. Spectrosc.* 74, 1–32. doi:10.1016/j.pnmrs.2013.04.002

Cebeci, H., Aydin, O., Ozturk-Isik, E., Gumus, C., Inecikli, F., Bekar, A., et al. (2014). Assesment of perfusion in glial tumors with arterial spin labeling; comparison with dynamic susceptibility contrast method. *Eur. J. Radiology* 83, 1914–1919. doi:10.1016/j.ejrad.2014.07.002

Cox, R. W. (1996). AFNI: software for analysis and visualization of functional magnetic resonance neuroimages. *Comput. Biomed. Res.* 29, 162–173. doi:10.1006/cbmr.1996.0014

Cox, R. W., and Hyde, J. S. (1997). Software tools for analysis and visualization of fMRI data. *NMR Biomed.* 10, 171–178. doi:10.1002/(SICI)1099-1492(199706/08)10:4/5<171::AID-NBM453>3.0.CO;2-L

Fierstra, J., Sobczyk, O., Battisti-Charbonney, A., Mandell, D. M., Poublanc, J., Crawley, A. P., et al. (2013). Measuring cerebrovascular reactivity: what stimulus to use? *J. Physiology* 591, 5809–5821. doi:10.1113/jphysiol.2013.259150

Fierstra, J., van Niftrik, B., Piccirelli, M., Burkhardt, J. K., Pangalu, A., Kocian, R., et al. (2016). Altered intraoperative cerebrovascular reactivity in brain areas of high-grade glioma recurrence. *Magn. Reson. Imaging* 34, 803–808. doi:10.1016/j.mri.2016.02.003

Fierstra, J., van Niftrik, C., Piccirelli, M., Bozinov, O., Pangalu, A., Krayenbühl, N., et al. (2018). Diffuse gliomas exhibit whole brain impaired cerebrovascular reactivity. *Magn. Reson. Imaging* 45, 78–83. doi:10.1016/j.mri.2017.09.017

Fisher, J. A., Venkatraghavan, L., and Mikulis, D. J. (2018). Magnetic resonance imaging–based cerebrovascular reactivity and hemodynamic reserve. *Stroke* 49, 2011–2018. doi:10.1161/STROKEAHA.118.021012

Gauthier, C. J., and Fan, A. P. (2019). BOLD signal physiology: models and applications. *NeuroImage* 187, 116–127. doi:10.1016/j.neuroimage.2018.03.018

Glover, G. H. (2011). Overview of functional magnetic resonance imaging. *Neurosurg. Clin. N. Am.* 22, 133–139. doi:10.1016/j.nec.2010.11.001

Gracia Bara, M. T., Gallardo-Higueras, A., Moreno, E. M., Laffond, E., Muñoz Bellido, F. J., Martin, C., et al. (2022). Hypersensitivity to gadolinium-based contrast media. *Front. Allergy* 3, 813927. doi:10.3389/falgy.2022.813927

Guan, Z., Lan, H., Cai, X., Zhang, Y., Liang, A., and Li, J. (2021). Blood–brain barrier, cell junctions, and tumor microenvironment in brain metastases, the biological prospects and dilemma in therapies. *Front. Cell Dev. Biol.* 0, 722917. doi:10.3389/fcell.2021.722917

Guida, L., Stumpo, V., Bellomo, J., van Niftrik, C. H. B., Sebök, M., Berhouma, M., et al. (2022). Hemodynamic imaging in cerebral diffuse glioma - Part A: concept, differential diagnosis and tumor grading. *Cancers* 14, 1432. doi:10.3390/cancers14061432

Gulani, V., Calamante, F., Shellock, F. G., Kanal, E., Reeder, S. B., and International Society for Magnetic Resonance in Medicine (2017). Gadolinium deposition in the brain: summary of evidence and recommendations. *Lancet Neurology* 16, 564–570. doi:10.1016/S1474-4422(17)30158-8

Haller, S., Zaharchuk, G., Thomas, D. L., Lovblad, K.-O., Barkhof, F., and Golay, X. (2016). Arterial spin labeling perfusion of the brain: emerging clinical applications. *Radiology* 281, 337–356. doi:10.1148/radiol.2016150789

Juan-Albarracín, J., Fuster-Garcia, E., Pérez-Girbés, A., Aparici-Robles, F., Alberich-Bayarri, Á., Revert-Ventura, A., et al. (2018). Glioblastoma: vascular habitats detected at preoperative dynamic susceptibility-weighted contrast-enhanced perfusion MR imaging predict survival. *Radiology* 287, 944–954. doi:10.1148/radiol.2017170845

Lee, M. H., Smyser, C. D., and Shimony, J. S. (2013). Resting-state fMRI: a review of methods and clinical applications. *Am. J. Neuroradiol.* 34, 1866–1872. doi:10.3174/ajnr.A3263

Leu, K., Boxerman, J. L., and Ellingson, B. M. (2017). Effects of MRI protocol parameters, preload injection dose, fractionation strategies, and leakage correction algorithms on the fidelity of dynamic-susceptibility contrast MRI estimates of relative cerebral blood volume in gliomas. *Am. J. Neuroradiol.* 38, 478–484. doi:10.3174/ajnr.A5027

Louis, D. N., Perry, A., Wesseling, P., Brat, D. J., Cree, I. A., Figarella-Branger, D., et al. (2021). The 2021 WHO classification of tumors of the central nervous system: a summary. *Neuro-Oncology* 23, 1231–1251. doi:10.1093/neuonc/noab106

Muscas, G., van Niftrik, C. H. B., Sebök, M., Seystahl, K., Piccirelli, M., Stippich, C., et al. (2020). Hemodynamic investigation of peritumoral impaired blood oxygenation-level dependent cerebrovascular reactivity in patients with diffuse glioma. *Magn. Reson. Imaging* 70, 50–56. doi:10.1016/j.mri.2020.03.012

Østergaard, L. (2005). Principles of cerebral perfusion imaging by bolus tracking. *J. Magnetic Reson. Imaging* 22, 710–717. doi:10.1002/jmri.20460

Poublanc, J., Sobczyk, O., Shafi, R., Sayin, E. S., Schulman, J., Duffin, J., et al. (2021). Perfusion MRI using endogenous deoxyhemoglobin as a contrast agent: preliminary data. *Magnetic Reson. Med.* 86, 3012–3021. doi:10.1002/mrm.28974

Sayin, E. S., Duffin, J., Stumpo, V., Bellomo, J., Piccirelli, M., Poublanc, J., et al. (2023a). Assessing perfusion in steno-occlusive cerebrovascular disease using transient hypoxia-induced deoxyhemoglobin as a dynamic susceptibility contrast agent. *Am. J. Neuroradiol.* 45, 37–43. doi:10.3174/ajnr.A8068

Sayin, E. S., Schulman, J., Poublanc, J., Levine, H. T., Raghavan, L. V., Uludag, K., et al. (2022). Investigations of hypoxia-induced deoxyhemoglobin as a contrast agent for cerebral perfusion imaging. *Hum. Brain Mapp.* 44, 1019–1029. doi:10.1002/hbm.26131

Sayin, E. S., Sobczyk, O., Poublanc, J., Mikulis, D. J., Fisher, J. A., and Duffin, J. (2023b). Transfer function analysis assesses resting cerebral perfusion metrics using hypoxia-induced deoxyhemoglobin as a contrast agent. *Front. Physiol.* 14, 1167857. doi:10.3389/fphys.2023.1167857

Sebök, M., van Niftrik, C. H. B., Halter, M., Hiller, A., Seystahl, K., Pangalu, A., et al. (2020). Crossed cerebellar diaschisis in patients with diffuse glioma is associated with impaired supratentorial cerebrovascular reactivity and worse clinical outcome. *Cerebellum* 19, 824–832. doi:10.1007/s12311-020-01174-y

Sebök, M., van Niftrik, C. H. B., Muscas, G., Pangalu, A., Seystahl, K., Weller, M., et al. (2021). Hypermetabolism and impaired cerebrovascular reactivity beyond the standard MRI-identified tumor border indicate diffuse glioma extended tissue infiltration. *Neuro-Oncology Adv.* 3, vdab048. doi:10.1093/noajnl/vdab048

Shiroishi, M. S., Castellazzi, G., Boxerman, J. L., D'Amore, F., Essig, M., Nguyen, T. B., et al. (2015). Principles of T2*-weighted dynamic susceptibility contrast MRI technique in brain tumor imaging. *J. Magnetic Reson. Imaging* 41, 296–313. doi:10.1002/jmri.24648

Slessarev, M., Han, J., Mardimae, A., Prisman, E., Preiss, D., Volgyesi, G., et al. (2007). Prospective targeting and control of end-tidal CO2 and O2 concentrations. *J. Physiology* 581, 1207–1219. doi:10.1113/jphysiol.2007.129395

Stoecklein, V. M., Stoecklein, S., Galiè, F., Ren, J., Schmutzer, M., Unterrainer, M., et al. (2020). Resting-state fMRI detects alterations in whole brain connectivity related to tumor biology in glioma patients. *Neuro-Oncology* 22, 1388–1398. doi:10.1093/neuonc/noaa044

Stumpo, V., Guida, L., Bellomo, J., Van Niftrik, C. H. B., Sebök, M., Berhouma, M., et al. (2022). Hemodynamic imaging in cerebral diffuse glioma - Part B: molecular correlates, treatment effect monitoring, prognosis, and future directions. *Cancers* 14, 1342. doi:10.3390/cancers14051342

Stumpo, V., Sebök, M., van Niftrik, C. H. B., Seystahl, K., Hainc, N., Kulcsar, Z., et al. (2021). Feasibility of glioblastoma tissue response mapping with physiologic BOLD imaging using precise oxygen and carbon dioxide challenge. *Magn. Reson Mater Phy* 35, 29–44. doi:10.1007/s10334-021-00980-7

Tamrazi, B., Shiroishi, M. S., and Liu, C.-S. J. (2016). Advanced imaging of intracranial meningiomas. *Neurosurg. Clin. N. Am.* 27, 137–143. doi:10.1016/j.nec.2015.11.004

Vu, C., Chai, Y., Coloigner, J., Nederveen, A. J., Borzage, M., Bush, A., et al. (2021). Quantitative perfusion mapping with induced transient hypoxia using BOLD MRI. *Magnetic Reson. Med.* 85, 168–181. doi:10.1002/mrm.28422

Weinreb, J. C., Rodby, R. A., Yee, J., Wang, C. L., Fine, D., McDonald, R. J., et al. (2021). Use of intravenous gadolinium-based contrast media in patients with kidney disease: consensus statements from the American College of radiology and the national kidney foundation. *Radiology* 298, 28–35. doi:10.1148/radiol.2020202903

Zacà, D., Jovicich, J., Nadar, S. R., Voyvodic, J. T., and Pillai, J. J. (2014). Cerebrovascular reactivity mapping in patients with low grade gliomas undergoing presurgical sensorimotor mapping with BOLD fMRI. *J. Magnetic Reson. Imaging* 40, 383–390. doi:10.1002/jmri.24406

Frontiers in Physiology

Understanding how an organism's components work together to maintain a healthy state

The second most-cited physiology journal, promoting a multidisciplinary approach to the physiology of living systems - from the subcellular and molecular domains to the intact organism and its interaction with the environment.

Discover the latest Research Topics

See more →

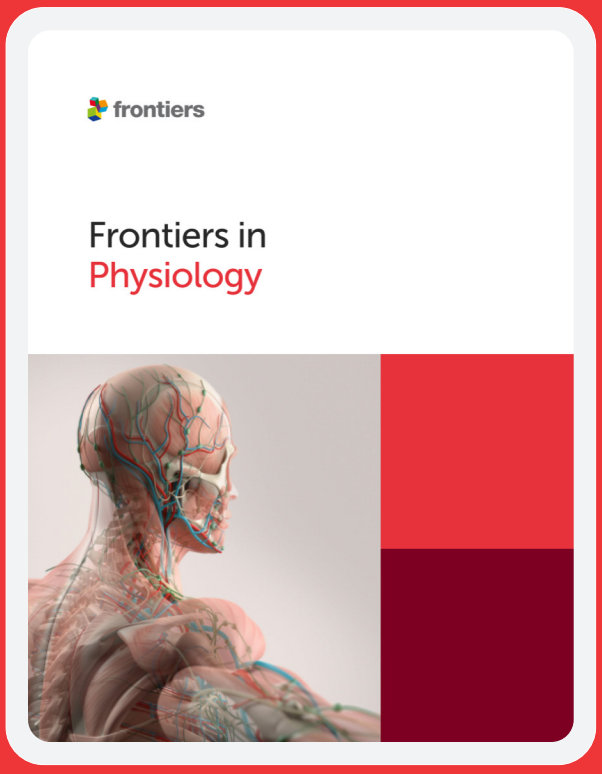

Frontiers

Avenue du Tribunal-Fédéral 34
1005 Lausanne, Switzerland
frontiersin.org

Contact us

+41 (0)21 510 17 00
frontiersin.org/about/contact